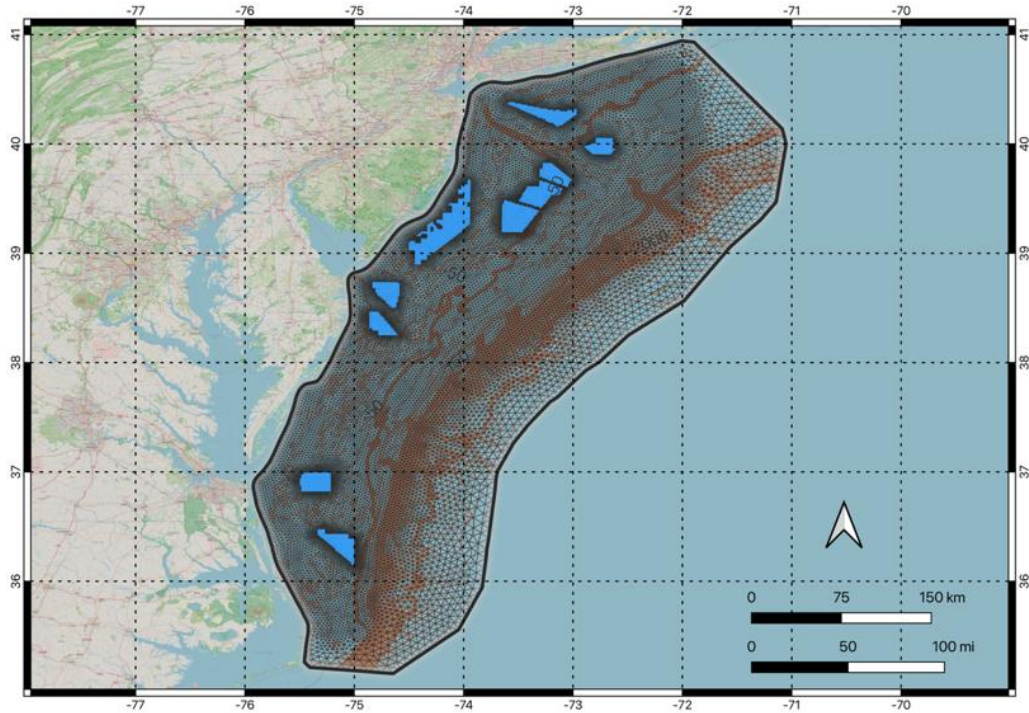


Offshore Wind Impact on Oceanographic Processes: North Carolina to New York, Volume 1 - RPS



Offshore Wind Impact on Oceanographic Processes: North Carolina to New York, Volume 1 - RPS

October 2024

Authors:

Nickitas Georgas¹, Lysel Garavelli², Daniel Codiga¹, Emily Day¹, Lilian Engel², Lenaïg Hemery², William Misa¹, Mahmud Monim¹, Hanieh Moghadam¹, Alicia Morandi¹, Amin Ilia¹, John Speers¹, Tayebah Tajallibakhsh¹.

Prepared under 140M0123C0001

by
RPS Ocean Science, a Tetra Tech company¹
55 Village Square Drive
South Kingstown, RI 14879

and
Pacific Northwest National Laboratory²
1100 Dexter Ave N
Seattle, WA 98109

DISCLAIMER

This study concept, oversight, and funding were provided by the U.S. Department of the Interior, Bureau of Ocean Energy Management (BOEM), Environmental Studies Program, Washington, DC, under Contract Number 140M0123C0001 with RPS Ocean Science and Pacific Northwest National Laboratory. This report has been technically reviewed by BOEM, and it has been approved for publication. The views and conclusions contained in this document are those of the authors and should not be interpreted as representing the opinions or policies of BOEM, nor does mention of trade names or commercial products constitute endorsement or recommendation for use.

REPORT AVAILABILITY

Download a PDF file of this report at https://epis.boem.gov/Final%20Reports/BOEM_2025-016.pdf. To search other studies completed by BOEM's Environmental Studies Program, visit <https://www.boem.gov/environment/environmental-studies/environmental-studies-information/>.

CITATION

Georgas N, Garavelli L, Codiga D, Day E, Engel L, Hemery L, Misa W, Monim M, Moghadam H, Morandi A, Ilia A, Speers J, Tajallibakhsh T (RPS Ocean Science, South Kingston, RI, and Pacific Northwest National Laboratory, Seattle, WA). 2025. Offshore wind impact on oceanographic processes: North Carolina to New York, Volume 1 - RPS. Sterling (VA): U.S. Department of the Interior, Bureau of Ocean Energy Management. 360 p. Obligation No.: 140M0123C0001. Report No.: BOEM 2025-016.

ABOUT THE COVER

Mid-Atlantic Bight Model domain, North Carolina to New York, with bathymetric contours (brown, labels in meters), and offshore Wind Energy Areas included in this study (blue). Used with permission. All rights reserved.

ACKNOWLEDGMENTS

This project was supported by the Bureau of Safety and Environmental Enforcement (BSEE), the U.S. Department of the Interior (DOI), on behalf of the Bureau of Ocean Energy Management (BOEM) under contract number 140M0123C0001. We would like to thank the BOEM supervisors for this project: Jennifer Draher (Oceanographer and Contracting Officer Representative), Thomas Kilpatrick (Oceanographer), Brian Hooker (Lead Biologist), Ursula Howson (Fish Biologist), Travis Washington (Physical Scientist) and Kyle Baker (Marine Biologist) all of whom provided us valuable advice and suggestions for this study. We are also grateful to Jennifer Moreci (BSEE) and Timothy White. Special thanks to Marlein Geraeds for her input and discussion about velocity interpolation in Delft3D-FM and Chris Orphanides (Marine Resource Management Specialist, NOAA NMFS) for his participation in project meetings and his very helpful comments and suggestions. We thank Nicholas Baccari, Christina Buxton, Sandra Deeb, and Fei Xing for their editing assistance.

Contents

Contents	i
List of Figures	iv
List of Tables	xvi
List of Abbreviations and Acronyms	xviii
Executive Summary	19
1 Introduction	22
2 Area of Interest and Wind Farm Scenarios	24
2.1 Area of Interest.....	24
2.2 Simulation Scenarios	24
3 Physical Observations	26
3.1 Surface Waves	26
3.2 Sea Surface Height	28
3.3 Ocean Currents	32
3.4 Seawater Temperature	34
3.5 Salinity	37
3.6 Surface Meteorology	39
4 Wind Wake Modeling	41
4.1 Selection of Model.....	41
4.2 PyWake Validation Setup.....	46
4.3 Specification of Reference Wind Turbine.....	46
4.4 Selection of Wind Deficit Model	48
4.5 Selection of Engineering Wind Farm Models.....	50
4.6 Selection of Resolution of Computational Grid	56
4.7 Impact of Wind Speed on Wake.....	58
4.8 Impact of Computational Domain Extension on Wake	67
4.9 Comparison of PyWake-derived Wind Reduction with Christiansen et al. (2022).....	70
4.10 Steps for Wake Calculation.....	71
5 Hydrodynamic Modeling – Calibration and Validation	74
5.1 Model Overview.....	74
5.2 Model Grid.....	74
5.3 Boundary Forcing.....	75
5.3.1 Water Level Boundary.....	75
5.3.2 Water Temperature and Salinity	76
5.3.3 Surface Boundary Conditions	77
5.4 Storage and Computational Requirements.....	78
5.5 Model Calibration and Stability.....	79
5.5.1 Sea Surface Height	80
5.5.2 Water Temperature	86
5.5.3 Salinity.....	98
5.5.4 Currents.....	102
5.6 Validation.....	105
5.6.1 Sea Surface Height	105
5.6.2 Water Temperature	116
5.6.3 Salinity.....	126
5.6.4 Current	129

5.7	Model Skill Summary of Validation and Calibration Periods.....	136
5.8	Hydrodynamic Modeling of Scenarios 2 and 3 with WEA Buildout.....	137
6	Surface Wave Modeling.....	139
6.1	Introduction.....	139
6.2	Wave Model Description	139
6.3	Wave Model Grid and Bathymetry	139
6.4	Wave Model Forcings	140
6.5	Model Parameters and Calibration.....	144
6.6	Wave Model Validation	155
6.6.1	Wind Forcing Validation (ERA5)	155
6.6.2	Significant Wave Height Validation (Scenario 1, SWAN)	158
6.6.3	Mean Wave Direction Validation (Scenario 1, SWAN)	165
6.6.4	Mean Wave Period Validation (Scenario 1, SWAN)	172
6.6.5	Conclusion on SWAN Baseline (Scenario 1) Validation	179
7	Impact of Offshore Wind Farms on Winds	180
7.1	Wind Wake Effects	180
7.2	Effects on Wind Climatology	180
7.3	Transient Effects	188
8	Impact Of Offshore Wind Farms on Wave Conditions	190
8.1	Impact to Significant Wave Height	190
8.2	Impact to Mean Wave Period.....	198
9	Impact Of Offshore Wind Farms on Hydrodynamics	206
9.1	Background	206
9.1.1	Middle-Atlantic Bight General Circulation	206
9.1.2	Cold Pool.....	207
9.1.3	Hydrodynamic Effects of Offshore Wind Developments.....	217
9.2	Effects of WEA Development on Cold Pool and Regional Currents.....	218
9.2.1	Cold Pool.....	218
9.2.2	Effects on Currents	220
9.3	Impact Analysis at Specific Locations.....	224
9.3.1	Annualized and Seasonal Changes.....	225
9.3.2	Impacts at Weekly Timescale Relative to Baseline Variability.....	230
9.4	Effects on Stratification and Thermocline	290
10	Impact Of Offshore Wind Farms on Bed Shear Stress and Sediment Mobility.....	295
10.1	Methodology.....	295
10.2	Bed Shear Stress	295
10.3	Sediment Mobility.....	298
11	Selection of Species of Interest	301
11.1	Literature Review and Species Selection	301
11.2	Larval Biological Parameters	301
12	Larval Transport Modeling and Impact of Offshore Wind Farms on Larval Connectivity	306
12.1	Introduction.....	306
12.2	Methods.....	307
12.2.1	Hydrodynamic Model	307
12.2.2	Biophysical Larval Dispersal Model	307
12.2.3	Larval Dispersal Model Setup	308
12.2.4	Model Configurations	311

12.2.5	Analysis	311
12.3	Results	312
12.3.1	Influence of Hydrodynamics on Larval Connectivity	312
12.3.2	Effect of DVM on Larval Connectivity	322
12.3.3	Effect of Temperature Tolerance on Larval Connectivity.....	326
12.3.4	Effect of DVM and Temperature Tolerance on Larval Connectivity.....	331
12.3.5	Summary of Larval Connectivity Statistics.....	336
12.4	Discussion.....	339
13	Study Conclusions	342
14	References	344
15	Appendices	355

List of Figures

Figure 1. BOEM wind lease areas between North Carolina and New York.	23
Figure 2. WTG coverage through the wind lease areas considered in this study.	24
Figure 3. Surface wave observations stations.	27
Figure 4. NOS tide gauge locations.	29
Figure 5. Sea Surface Height observations coverage	31
Figure 6. Ocean Currents observation coverage.	33
Figure 7. Sea Water Temperature observations coverage.	36
Figure 8. Salinity observations coverage.	38
Figure 9. Surface meteorology (wind/pressure) observation stations.	40
Figure 10. Velocity deficit curves derived from SAR observation for isolated wake cases at the Global Tech wind farm (thin black lines).	43
Figure 11. Modular architecture of PyWake.	45
Figure 12. Location and layout of hypothetical wind farm used in PyWake analysis.	46
Figure 13. Power and thrust curve (upper panel) and aerodynamic thrust coefficient (lower panel) for NREL 15 MW reference turbine (modified from Gaertner et al., 2020).	48
Figure 14. Example comparison of applying different Wind Deficit Models to capture wind wake expansion at the hub-height of the turbine (150m).	49
Figure 15. Example comparison of applying different Wind Deficit Models to capture wind wake expansion at 10m elevation above surface. Wind units are m/s.	50
Figure 16. Comparison of engineering wind farm models at hub-height (direction 0°, 45°, and 90°). Axes units in km. All wind units are m/s.	51
Figure 17. Comparison of engineering wind farm models at hub-height (direction 135°, 180°, and 225°). Axes units in km. All wind units are m/s.	52
Figure 18. Comparison of engineering wind farm models at hub-height (direction 270° and 315°). Axes units in km. All wind units are m/s.	53
Figure 19. Comparison of engineering wind farm models at 10m elevation (direction 0°, 45°, 90°, and 135°). Axes units in km. All wind units are m/s.	54
Figure 20. Comparison of engineering wind farm models at 10m elevation (direction 180°, 225°, 270°, and 315°). Axes units in km. All wind units are m/s.	55
Figure 21. Comparison of simulation time for different engineering wind farm models at different wind direction at hub-height (left panel) and at 10m elevation (right panel).	56
Figure 22. Comparison of different grid resolutions at turbine hub-height. All wind values are in m/s.	57
Figure 23. Comparison of different grid resolutions at 10m elevation. All wind values are in m/s.	58
Figure 24. Comparison of wind wake for different free-stream inflow speeds (3 - 8m/s) at the hub-height. Axes units in km. All wind units are m/s.	59
Figure 25. Comparison of wind wake for different free-stream inflow speeds (9 - 14m/s) at the hub-height. Axes units in km. All wind units are m/s.	60
Figure 26. Comparison of wind wake for different free-stream inflow speeds (15 - 20m/s) at the hub- height. Axes units in km. All wind units are m/s.	61

Figure 27. Comparison of wind wake for different free-stream inflow speeds (21 - 25m/s) at the hub-height. Axes units in km. All wind units are m/s.	62
Figure 28. Comparison of wind wake for different free-stream inflow speeds (3 - 8m/s) at 10m elevation. Axes units in km. All wind units are m/s.	63
Figure 29. Comparison of wind wake for different free-stream inflow speeds (9 - 14m/s) at 10m elevation. Axes units in km. All wind units are m/s.	64
Figure 30. Comparison of wind wake for different free-stream inflow speeds (15 -19 m/s) at 10m elevation. Axes units in km. All wind units are m/s.	65
Figure 31. Comparison of hub-height wind speed reduction (see Figure 24 to Figure 27) at the downstream boundary on the west (left panel) and maximum wind speed reduction inside the windfarm (right panel) with different free-stream inflow speeds.	66
Figure 32. Comparison of 10-m elevation mean wind speed deficit (% reduction, see Figure 28 to Figure 30) at the downstream edge of the wind turbine clusters with different free-stream inflow speeds at 10m elevation.	67
Figure 33. Comparison of wind speed reduction (at hub-height) at the downstream boundary on the west with different clearance distance (between wind farm and the boundary).	68
Figure 34. Comparison of wind speed reduction (at 10m elevation) at the downstream boundary on the west with different clearance distance (between wind farm and the boundary).	69
Figure 35. Comparison of wind speed reduction (at hub-height) at the downstream boundary on the west (left panel) and simulation time (right panel) with different model extension/clearance distance (between wind farm and the boundary).	70
Figure 36. Comparison of mean wind speed reduction (at 10m) at the downstream boundary on the west (left panel) and simulation time (right panel) with different model extension/clearance.	70
Figure 37. Comparison of PyWake-derived wake with Christiansen et al. (2022).	71
Figure 38. Example of wind turbines (Scenario 2) clustered into individual wind farms (from #1 to #8) off the East Coast.	72
Figure 39. Mid-Atlantic Bight shelf model grid. (a) Left panel: Numerical model grid. (b) Right panel: Grid bathymetry.	75
Figure 40. Surface water temperature and salinity color maps for time stamp, January 7, 2018 00:00:00 output from the model.	77
Figure 41. Representative timestamp of surface boundary conditions applied.	78
Figure 42. Water level comparison between hydrodynamic model and NOS tide gauge at Sandy Hook, New Jersey.	80
Figure 43. Water level simulated in the model versus observed from the NOS tide gauge at Sandy Hook, New Jersey.	81
Figure 44. Water level comparison between hydrodynamic model and NOS tide gauge at Atlantic City, New Jersey.	81
Figure 45. Water level simulated in the model versus observed from the NOS tide gauge at Atlantic City, New Jersey.	82
Figure 46. Water level comparison between hydrodynamic model and NOS tide gauge at Lewes, Delaware.	82
Figure 47. Water level simulated in the model versus observed from the NOS tide gauge at Lewes, Delaware.	83
Figure 48. Water level comparison between hydrodynamic model and NOS tide gauge at Duck, North Carolina.	83

Figure 49. Water level simulated in the model versus observed from the NOS tide gauge at Duck, North Carolina	84
Figure 50. Sea Surface Height comparison between Model and Doppio dataset for calibration period. ...	85
Figure 51. Binned bathymetry map of AOI (every 20m).	86
Figure 52. Temperature timeseries comparison; NDBC Buoy 44009 (blue) and calibrated model (red) ...	87
Figure 53. Temperature timeseries comparison; NDBC Buoy 44014 (blue) and calibrated model (red) ...	88
Figure 54. Temperature timeseries comparison; NDBC Buoy 44025 (blue) and calibrated model (red) ...	88
Figure 55. Temperature timeseries comparison; NDBC Buoy 44065 (blue) and calibrated model (red) ...	89
Figure 56. Temperature timeseries comparison; NDBC Buoy 44066 (blue) and calibrated model (red) ...	89
Figure 57. Temperature timeseries comparison; NDBC Buoy 44086 (blue) and calibrated model (red) ...	90
Figure 58. Temperature timeseries comparison; NDBC Buoy 44088 (blue) and calibrated model (red) ...	90
Figure 59. Temperature timeseries comparison; NDBC Buoy 44089 (blue) and calibrated model (red) ...	91
Figure 60. Temperature timeseries comparison; NDBC Buoy 44091 (blue) and calibrated model (red) ...	91
Figure 61. Temperature timeseries comparison; NDBC Buoy 44095 (blue) and calibrated model (red) ...	92
Figure 62. Temperature timeseries comparison; NDBC Buoy 44099 (blue) and calibrated model (red) ...	92
Figure 63. Temperature timeseries comparison; NDBC Buoy 44100 (blue) and calibrated model (red) ...	93
Figure 64. Surface temperature comparison between Model and Doppio dataset for calibration period. .	94
Figure 65. Surface temperature comparison between Model and NOAA Optimally Interpolated High Resolution SST for calibration period.....	95
Figure 66. Bottom temperature comparison between Model and Doppio dataset for calibration period. ..	96
Figure 67. Temperature comparison between glider observation and model.	97
Figure 68. Surface salinity comparison between Model and Doppio dataset for calibration period.	99
Figure 69. Bottom salinity comparison between Model and Doppio dataset for calibration period.	100
Figure 70. Salinity comparison between glider observation and model for calibration period.....	101
Figure 71. Surface current comparison (current magnitude, speed) between Model and Doppio dataset for calibration period.....	103
Figure 72. Surface current comparison between Model and HF Radar dataset for calibration period.....	104
Figure 73. Bottom current comparison between Model and Doppio dataset for calibration period.....	105
Figure 74. Water level comparison between hydrodynamic model and NOS tide gauge at Sandy Hook, New Jersey.....	107
Figure 75. Water level simulated in the model versus observed from the NOS tide gauge at Sandy Hook, New Jersey.....	108
Figure 76. Water level comparison between hydrodynamic model and NOS tide gauge at Atlantic City, New Jersey.....	109
Figure 77. Water level simulated in the model versus observed from the NOS tide gauge at Atlantic City, New Jersey.....	110
Figure 78. Water level comparison between hydrodynamic model and NOS tide gauge at Lewes, Delaware	111
Figure 79. Water level simulated in the model versus observed from the NOS tide gauge at Lewes, Delaware	112

Figure 80. Water level comparison between hydrodynamic model and NOS tide gauge at Duck, North Carolina	113
Figure 81. Water level simulated in the model versus observed from the NOS tide gauge at Duck, North Carolina	114
Figure 82. Sea Surface Height comparison between Model and Doppio dataset for validation period. ...	116
Figure 83. Temperature timeseries validation; NDBC Buoy 44009 (blue) and calibrated model (red)	118
Figure 84. Temperature timeseries validation; NDBC Buoy 44014 (blue) and calibrated model (red)	118
Figure 85. Temperature timeseries validation; NDBC Buoy 44025 (blue) and calibrated model (red)	118
Figure 86. Temperature timeseries validation; NDBC Buoy 44065 (blue) and calibrated model (red)	119
Figure 87. Temperature timeseries validation; NDBC Buoy 44066 (blue) and calibrated model (red)	119
Figure 88. Temperature timeseries validation; NDBC Buoy 44086 (blue) and calibrated model (red)	120
Figure 89. Temperature timeseries validation; NDBC Buoy 44089 (blue) and calibrated model (red)	120
Figure 90. Temperature timeseries validation; NDBC Buoy 44091 (blue) and calibrated model (red)	121
Figure 91. Temperature timeseries validation; NDBC Buoy 44095 (blue) and calibrated model (red)	121
Figure 92. Temperature timeseries validation; NDBC Buoy 44099 (blue) and calibrated model (red)	122
Figure 93. Temperature timeseries validation; NDBC Buoy 44100 (blue) and calibrated model (red). ...	122
Figure 94. Surface temperature comparison between Model and Doppio dataset for validation period..	123
Figure 95. Surface temperature comparison between Model and NOAA Optimally Interpolated High Resolution SST for validation period.....	124
Figure 96. Bottom temperature comparison between Model and Doppio dataset for validation period...	125
Figure 97. Temperature comparison between glider observation and model for validation period.....	126
Figure 98. Surface salinity comparison between Model and Doppio dataset for validation period.	127
Figure 99. Bottom salinity comparison between Model and Doppio dataset for validation period. A).....	128
Figure 100. Salinity comparison between glider observation and model for calibration period. a)	129
Figure 101. Current speed comparison between Empire Wind observation and model at 9.6m	130
Figure 102. Current speed comparison between Empire Wind observation and model at 19.6m	131
Figure 103. Current speed comparison between Empire Wind observation and model at 33.6m	131
Figure 104. Current rose comparison at Empire Wind at 9.6m, observation (left) and model (right).	132
Figure 105. Current rose comparison at Empire Wind at 19.6m, observation (left) and model (right).	132
Figure 106. Current rose comparison at Empire Wind at 33.6m, observation (left) and model (right).	133
Figure 107. Surface current comparison between Model and Doppio dataset for validation period.	134
Figure 108. Surface current comparison between Model and HF Radar dataset for validation period....	135
Figure 109. Bottom current comparison between Model and Doppio dataset for validation period.....	136
Figure 110. Taylor Diagram of calibrated model compared to observational and DOPPIO data.....	137
Figure 111. The wave model grid (left panel) and bathymetry (right panel) is the same as the hydrodynamic model grid.	140
Figure 112. Wave model boundary conditions.....	142
Figure 113. Wind roses (02/01/2018-01/31/2020) at ERA5 points in the project domain.	143

Figure 114. Significant wave height comparison with measurements at NDBC station 44066 for ST6 and Westh. approach.	145
Figure 115. Significant wave height comparison with measurements at NDBC station 44025 for ST6 and Westh. approach.	146
Figure 116. Significant wave height comparison with measurements at NDBC station 44065 for ST6 and Westh. approach.	147
Figure 117. Significant wave height comparison with measurements at NDBC station 44091 for ST6 and Westh. approach.	148
Figure 118. Significant wave height comparison with measurements at NDBC station 44099 for ST6 and Westh. approach.	149
Figure 119. Significant wave height comparison with measurements at NDBC station 44089 for ST6 and Westh. approach.	149
Figure 120. Significant wave height comparison with measurements at NDBC station 44099 for ST6 and Westh. approach.	150
Figure 121. Significant wave height comparison with measurements at NDBC station 44014 for ST6 and Westh. approach.	151
Figure 122. Significant wave height comparison with measurements at NDBC station 44100 for ST6 and Westh. approach.	152
Figure 123. Significant wave height comparison with measurements at NDBC station 44086 for ST6 and Westh. approach.	153
Figure 124. Significant wave height comparison with measurements at NDBC station 44095 for ST6 and Westh. approach.	154
Figure 125. ERA5 – Simulated wind speed vs. measurements at NDBC station 44009	156
Figure 126. ERA5 – Simulated wind speed vs. measurements at NDBC station 44014	156
Figure 127. ERA5 – Simulated wind speed vs. measurements at NDBC station 44025	156
Figure 128. ERA5 – Simulated wind speed vs. measurements at NDBC station 44065	157
Figure 129. ERA5 – Simulated wind speed vs. measurements at NDBC station 44066	157
Figure 130. Overall evaluation of wind speed at NDBC stations 44009 (left panel) and 44014 (right panel)	157
Figure 131. Overall evaluation of wind speed at NDBC stations 44025 (left panel) and 44065 (right panel)	158
Figure 132. Overall evaluation of wind speed at NDBC station 44066.....	158
Figure 133. Simulated significant wave height vs. measurements at NDBC station 44009.....	159
Figure 134. Simulated significant wave height vs. measurements at NDBC station 44014.....	160
Figure 135. Simulated significant wave height vs. measurements at NDBC station 44025.....	160
Figure 136. Simulated significant wave height vs. measurements at NDBC station 44065.....	160
Figure 137. Simulated significant wave height vs. measurements at NDBC station 44066.....	161
Figure 138. Simulated significant wave height vs. measurements at NDBC station 44086.....	161
Figure 139. Simulated significant wave height vs. measurements at NDBC station 44088.....	161
Figure 140. Simulated significant wave height vs. measurements at NDBC station 44089.....	162
Figure 141. Simulated significant wave height vs. measurements at NDBC station 44091.....	162

Figure 142. Simulated significant wave height vs. measurements at NDBC station 44095.....	162
Figure 143. Simulated significant wave height vs. measurements at NDBC station 44099.....	162
Figure 144. Simulated significant wave height vs. measurements at NDBC station 44100.....	163
Figure 145. Overall evaluation of simulated significant wave height at NDBC stations 44009 (left panel) and 44014 (right panel)	163
Figure 146. Overall evaluation of simulated significant wave height at NDBC stations 44025 (left panel) and 44065 (right panel)	163
Figure 147. Overall evaluation of simulated significant wave height at NDBC stations 44066 (left panel) and 44086 (right panel)	164
Figure 148. Overall evaluation of simulated significant wave height at NDBC stations 44088 (left panel) and 44089 (right panel)	164
Figure 149. Overall evaluation of simulated significant wave height at NDBC stations 44091 (left panel) and 44095 (right panel)	165
Figure 150. Overall evaluation of simulated significant wave height at NDBC stations 44099 (left panel) and 44100 (right panel)	165
Figure 151. Simulated mean wave direction (blue) vs. measurements (red) at NDBC station 44009.	166
Figure 152. Simulated mean wave direction (blue) vs. measurements (red) at NDBC station 44014.	166
Figure 153. Simulated mean wave direction (blue) vs. measurements (red) at NDBC station 44025.	167
Figure 154. Simulated mean wave direction (blue) vs. measurements (red) at NDBC station 44065.	167
Figure 155. Simulated mean wave direction (blue) vs. measurements (red) at NDBC station 44066.	167
Figure 156. Simulated mean wave direction (blue) vs. measurements (red) at NDBC station 44086.	168
Figure 157. Simulated mean wave direction (blue) vs. measurements (red) at NDBC station 44088.	168
Figure 158. Simulated mean wave direction (blue) vs. measurements (red) at NDBC station 44089.	168
Figure 159. Simulated mean wave direction (blue) vs. measurements (red) at NDBC station 44091.	169
Figure 160. Simulated mean wave direction (blue) vs. measurements (red) at NDBC station 44095.	169
Figure 161. Simulated mean wave direction (blue) vs. measurements (red) at NDBC station 44099.	169
Figure 162. Simulated mean wave direction (blue) vs. measurements (red) at NDBC station 44100.	170
Figure 163. Overall evaluation of simulated mean wave direction at NDBC stations 44009 (left panel) and 44014 (right panel)	170
Figure 164. Overall evaluation of simulated mean wave direction at NDBC stations 44025 (left panel) and 44065 (right panel)	170
Figure 165. Overall evaluation of simulated mean wave direction at NDBC stations 44066 (left panel) and 44086 (right panel)	171
Figure 166. Overall evaluation of simulated mean wave direction at NDBC stations 44088 (left panel) and 44089 (right panel)	171
Figure 167. Overall evaluation of simulated mean wave direction at NDBC stations 44091 (left panel) and 44095 (right panel)	172
Figure 168. Overall evaluation of simulated mean wave direction at NDBC stations 44099 (left panel) and 44100 (right panel)	172
Figure 169. Simulated mean wave period vs. measurements at NDBC station 44009.....	173
Figure 170. Simulated mean wave period vs. measurements at NDBC station 44014.....	173

Figure 171. Simulated mean wave period vs. measurements at NDBC station 44025.....	174
Figure 172. Simulated mean wave period vs. measurements at NDBC station 44065.....	174
Figure 173. Simulated mean wave period vs. measurements at NDBC station 44066.....	174
Figure 174. Simulated mean wave period vs. measurements at NDBC station 44086.....	175
Figure 175. Simulated mean wave period vs. measurements at NDBC station 44088.....	175
Figure 176. Simulated mean wave period vs. measurements at NDBC station 44089.....	175
Figure 177. Simulated mean wave period vs. measurements at NDBC station 44091.....	176
Figure 178. Simulated mean wave period vs. measurements at NDBC station 44095.....	176
Figure 179. Simulated mean wave period vs. measurements at NDBC station 44099.....	176
Figure 180. Simulated mean wave period vs. measurements at NDBC station 44100.....	177
Figure 181. Overall evaluation of simulated mean wave period at NDBC stations 44009 (left panel) and 44014 (right panel)	177
Figure 182. Overall evaluation of simulated mean wave period at NDBC stations 44025 (left panel) and 44065 (right panel)	178
Figure 183. Overall evaluation of simulated mean wave period at NDBC stations 44066 (left panel) and 44086 (right panel)	178
Figure 184. Overall evaluation of simulated mean wave period at NDBC stations 44088 (left panel) and 44089 (right panel)	178
Figure 185. Overall evaluation of simulated mean wave period at NDBC stations 44091 (left panel) and 44095 (right panel)	179
Figure 186. Overall evaluation of simulated mean wave period at NDBC stations 44099 (left panel) and 44100 (right panel)	179
Figure 187. Example of wind speed maps used as input for hydrodynamic and wave modeling.	181
Figure 188. Averaged wind speed maps for January 2018.	182
Figure 189. 50 th (top left) and 75 th (bottom left) percentile wind speeds, m/s, over the model domain for the 2-year period of simulation.....	183
Figure 190. Time series of wind speed for each of the three simulation scenarios for locations A (top) and B (bottom) shown on Figure 189 over the 2-year period.	184
Figure 191. Frequency distributions of wind speeds at locations A (top) and B (bottom) shown in Figure 189 for each of the three scenarios.....	185
Figure 192. Winter (Dec-Feb) differences (color shading) of mean wind speed in Scenario 2 (left) and Scenario 3 (right) relative to baseline. Arrows show winter mean baseline wind. The cyan lines indicate the location of the 0.5m/s deficit contours.....	186
Figure 193. Spring (Mar-May) differences (color shading) of mean wind speed in Scenario 2 (left) and Scenario 3 (right) relative to baseline. Arrows show spring mean baseline wind. The cyan lines indicate the location of the 0.5m/s deficit contours.....	186
Figure 194. Summer (Jun-Aug) differences (color shading) of mean wind speed in Scenario 2 (left) and Scenario 3 (right) relative to baseline. Arrows show summer mean baseline wind. The cyan (magenta) lines indicate the location of the 0.5m/s deficit contours simulated in this work (in work by Golbazi et al. 2022).....	187
Figure 195. Fall (Sep-Nov) differences (color shading) of mean wind speed in Scenario 2 (left) and Scenario 3 (right) relative to baseline. Arrows show fall mean baseline wind. The cyan lines indicate the location of the 0.5m/s deficit contours.	187

Figure 197. 99 th percentile of the transient wind reduction based on the time series of absolute wind speed difference between Scenario 2 and baseline (left) and Scenario 3 and baseline (right).	188
Figure 198. Probability distributions of absolute wind speed difference between Scenario 2 and baseline (top) and Scenario 3 and baseline (bottom) at locations A and B shown in Figure 192.	189
Figure 199. Median significant wave heights change and the 99 th percentile of the instantaneous difference.	191
Figure 200. Mean value of the difference between the median wave heights of OWT Scenarios and Baseline for every bathymetric bin.	192
Figure 201. Mean value of 99 th percentile of OWTs Scenarios and Baseline significant wave height instantaneous absolute differences for every bathymetry bin.	193
Figure 202. Changes to 1% and 10% significant wave height.	194
Figure 203. Changes to 90% and 99% significant wave height.	195
Figure 204. Mean value of the difference between the 90 th percentile wave heights of OWT Scenarios and Baseline for every bathymetry bins.	196
Figure 205. Mean value of the difference between the 99 th percentile wave heights of OWT Scenarios and Baseline for every bathymetry bins.	197
Figure 206. Stick plot of significant wave height and peak wave direction at Point F shown in Figure 198.	197
Figure 207. Median mean wave period change and the 99 th percentile of the instantaneous difference.	199
Figure 208. Mean value of the difference between the median Mean Wave Period of OWT Scenarios and Baseline for every bathymetry bin.	200
Figure 209. Mean value of 99 th percentile of OWTs Scenarios and Baseline mean wave period absolute instantaneous differences for every bathymetry bins.	201
Figure 210. Change in 1 st percentile and 10 th percentile mean wave period.	202
Figure 211. Change in 90 th percentile and 99 th percentile mean wave period.	203
Figure 212. Mean value of the difference between the 90 th percentile of Mean Wave Period of OWT Scenarios and Baseline for every bathymetry bins.	204
Figure 213. Mean value of the difference between the 99 th percentile of Mean Wave Period of OWT Scenarios and Baseline for every bathymetry bins.	205
Figure 214. Annual mean currents recorded by High Frequency Radar system between May 1999 and May 2000 (Kohut et al., 2004). Reproduced with permission.	206
Figure 215. Delft3D FM modeled mean surface currents from Feb 2018 to Jan 2020.	207
Figure 216. Locations of cross-shelf temperature transects.	209
Figure 217. Temperature contours under baseline conditions from March to October 2018 at transect 1.	210
Figure 218. Temperature contours under baseline conditions from March to October 2019, at transect 1.	211
Figure 219. Temperature contours under baseline conditions from March to October 2018, at transect 2.	212
Figure 220. Temperature contours under baseline conditions from March to October 2019, at transect 2.	213

Figure 221. Temperature contours under baseline conditions from March to October 2018, at transect 3.	214
Figure 222. Temperature contours under baseline conditions from March to October 2019, at transect 3.	215
Figure 223. Temperature contours under baseline conditions from March to October 2018, at transect 4.	216
Figure 224. Temperature contours under baseline conditions from March to October 2019, at transect 4.	217
Figure 225. Temperature contours under baseline (solid black line) and Scenario 2 (dashed blue line) conditions, from March to October 2018, at transect 2.	219
Figure 226. Temperature contours under baseline (solid black line) and Scenario 3 (dashed blue line) conditions, from March to October 2018, at transect 2.	220
Figure 227. Change in the median and 99th percentile depth-averaged current speed.	222
Figure 228. Change in the median and 99th percentile Low-Pass-Filtered depth-averaged current speed.	223
Figure 229. Difference of depth-averaged velocity between Scenario 2 and baseline (upper panel), and Scenario 3 and baseline (lower panel).	224
Figure 230. Locations of time series stations used in oceanographic impact analyses.	225
Figure 231. Weekly mean (left panels), and weekly differences for Scenario 2 - baseline (middle panels) and Scenario 3 - baseline (right panels) for wind speed and current speed (surface, bottom, and depth-averaged) at station 15.	235
Figure 232. Weekly mean (left panels), and weekly differences for Scenario 2 - baseline (middle panels) and Scenario 3 - baseline (right panels) for wind speed and current speed (surface, bottom, and depth-averaged) at station 17.	236
Figure 233. Weekly mean (left panels), and weekly differences for Scenario 2 - baseline (middle panels) and Scenario 3 - baseline (right panels) for wind speed and current speed (surface, bottom, and depth-averaged) at station 19.	237
Figure 234. Weekly mean (left panels), and weekly differences for Scenario 2 - baseline (middle panels) and Scenario 3 - baseline (right panels) for wind speed and current speed (surface, bottom, and depth-averaged) at station 20.	238
Figure 235. Weekly mean (left panels), and weekly differences for Scenario 2 - baseline (middle panels) and Scenario 3 - baseline (right panels) for wind speed and current speed (surface, bottom, and depth-averaged) at station 21.	239
Figure 236. Weekly mean (left panels), and weekly differences for Scenario 2 - baseline (middle panels) and Scenario 3 - baseline (right panels) for wind speed and current speed (surface, bottom, and depth-averaged) at station 23.	240
Figure 237. Weekly mean (left panels), and weekly differences for Scenario 2 - baseline (middle panels) and Scenario 3 - baseline (right panels) for wind speed and current speed (surface, bottom, and depth-averaged) at station 25.	241
Figure 238. Weekly mean (left panels), and weekly differences for Scenario 2 - baseline (middle panels) and Scenario 3 - baseline (right panels) for surface (upper panels) and bottom temperature (lower panels) at station 15.	243
Figure 239. Weekly mean (left panels), and weekly differences for Scenario 2 - baseline (middle panels) and Scenario 3 - baseline (right panels) for surface (upper panels) and bottom temperature (lower panels) at station 17.	244

Figure 240. Weekly mean (left panels), and weekly differences for Scenario 2 - baseline (middle panels) and Scenario 3 – baseline (right panels) for surface (upper panels) and bottom temperature (lower panels) at station 19.	245
Figure 241. Weekly mean (left panels), and weekly differences for Scenario 2 - baseline (middle panels) and Scenario 3 – baseline (right panels) for surface (upper panels) and bottom temperature (lower panels) at station 20.	246
Figure 242. Weekly mean (left panels), and weekly differences for Scenario 2 - baseline (middle panels) and Scenario 3 – baseline (right panels) for surface (upper panels) and bottom temperature (lower panels) at station 21.	247
Figure 243. Weekly mean (left panels), and weekly differences for Scenario 2 - baseline (middle panels) and Scenario 3 – baseline (right panels) for surface (upper panels) and bottom temperature (lower panels) at station 23.	248
Figure 244. Weekly mean (left panels), and weekly differences for Scenario 2 - baseline (middle panels) and Scenario 3 – baseline (right panels) for surface (upper panels) and bottom temperature (lower panels) at station 25.	249
Figure 245. Weekly mean (left panels), and weekly differences for Scenario 2 - baseline (middle panels) and Scenario 3 – baseline (right panels) for different heat fluxes at station 15.	251
Figure 246. Weekly mean (left panels), and weekly differences for Scenario 2 - baseline (middle panels) and Scenario 3 – baseline (right panels) for different heat fluxes at station 17.	252
Figure 247. Weekly mean (left panels), and weekly differences for Scenario 2 - baseline (middle panels) and Scenario 3 – baseline (right panels) for different heat fluxes at station 19.	253
Figure 248. Weekly mean (left panels), and weekly differences for Scenario 2 - baseline (middle panels) and Scenario 3 – baseline (right panels) for different heat fluxes at station 20.	254
Figure 249. Weekly mean (left panels), and weekly differences for Scenario 2 - baseline (middle panels) and Scenario 3 – baseline (right panels) for different heat fluxes at station 21.	255
Figure 250. Weekly mean (left panels), and weekly differences for Scenario 2 - baseline (middle panels) and Scenario 3 – baseline (right panels) for different heat fluxes at station 23.	256
Figure 251. Weekly mean (left panels), and weekly differences for Scenario 2 - baseline (middle panels) and Scenario 3 – baseline (right panels) for different heat fluxes at station 25.	257
Figure 252. Weekly mean (left panels), and weekly differences for Scenario 2 - baseline (middle panels) and Scenario 3 – baseline (right panels) for turbulent vertical eddy viscosity (surface and bottom) at station 15.	259
Figure 253. Weekly mean (left panels), and weekly differences for Scenario 2 - baseline (middle panels) and Scenario 3 – baseline (right panels) for turbulent vertical eddy viscosity (surface and bottom) at station 17.	260
Figure 254. Weekly mean (left panels), and weekly differences for Scenario 2 - baseline (middle panels) and Scenario 3 – baseline (right panels) for turbulent vertical eddy viscosity (surface and bottom) at station 19.	261
Figure 255. Weekly mean (left panels), and weekly differences for Scenario 2 - baseline (middle panels) and Scenario 3 – baseline (right panels) for turbulent vertical eddy viscosity (surface and bottom) at station 20.	262
Figure 256. Weekly mean (left panels), and weekly differences for Scenario 2 - baseline (middle panels) and Scenario 3 – baseline (right panels) for turbulent vertical eddy viscosity (surface and bottom) at station 21.	263
Figure 257. Weekly mean (left panels), and weekly differences for Scenario 2 - baseline (middle panels) and Scenario 3 – baseline (right panels) for turbulent vertical eddy viscosity (surface and bottom) at station 23.	264

Figure 258. Weekly mean (left panels), and weekly differences for Scenario 2 - baseline (middle panels) and Scenario 3 – baseline (right panels) for turbulent vertical eddy viscosity (surface and bottom) at station 25.....	265
Figure 259. Weekly mean (left panels), and weekly differences for Scenario 2 - baseline (middle panels) and Scenario 3 – baseline (right panels) for TKE (surface and bottom) at station 15.	267
Figure 260. Weekly mean (left panels), and weekly differences for Scenario 2 - baseline (middle panels) and Scenario 3 – baseline (right panels) for TKE (surface and bottom) at station 17.	268
Figure 261. Weekly mean (left panels), and weekly differences for Scenario 2 - baseline (middle panels) and Scenario 3 – baseline (right panels) for TKE (surface and bottom) at station 19.	269
Figure 262. Weekly mean (left panels), and weekly differences for Scenario 2 - baseline (middle panels) and Scenario 3 – baseline (right panels) for TKE (surface and bottom) at station 20.	270
Figure 263. Weekly mean (left panels), and weekly differences for Scenario 2 - baseline (middle panels) and Scenario 3 – baseline (right panels) for TKE (surface and bottom) at station 21.	271
Figure 264. Weekly mean (left panels), and weekly differences for Scenario 2 - baseline (middle panels) and Scenario 3 – baseline (right panels) for TKE (surface and bottom) at station 23.	272
Figure 265. Weekly mean (left panels), and weekly differences for Scenario 2 - baseline (middle panels) and Scenario 3 – baseline (right panels) for TKE (surface and bottom) at station 25.	273
Figure 266. Weekly mean (left panels), and weekly differences for Scenario 2 - baseline (middle panels) and Scenario 3 – baseline (right panels) for Richardson Number (surface and bottom) at station 15.	275
Figure 267. Weekly mean (left panels), and weekly differences for Scenario 2 - baseline (middle panels) and Scenario 3 – baseline (right panels) for Richardson Number (surface and bottom) at station 17.	276
Figure 268. Weekly mean (left panels), and weekly differences for Scenario 2 - baseline (middle panels) and Scenario 3 – baseline (right panels) for Richardson Number (surface and bottom) at station 19.	277
Figure 269. Weekly mean (left panels), and weekly differences for Scenario 2 - baseline (middle panels) and Scenario 3 – baseline (right panels) for Richardson Number (surface and bottom) at station 20.	278
Figure 270. Weekly mean (left panels), and weekly differences for Scenario 2 - baseline (middle panels) and Scenario 3 – baseline (right panels) for Richardson Number (surface and bottom) at station 21.	279
Figure 271. Weekly mean (left panels), and weekly differences for Scenario 2 - baseline (middle panels) and Scenario 3 – baseline (right panels) for Richardson Number (surface and bottom) at station 23.	280
Figure 272. Weekly mean (left panels), and weekly differences for Scenario 2 - baseline (middle panels) and Scenario 3 – baseline (right panels) for Richardson Number (surface and bottom) at station 25.	281
Figure 273. Weekly mean (left panels), and weekly differences for Scenario 2 - baseline (middle panels) and Scenario 3 – baseline (right panels) for thermocline depth and strength at station 15.	283
Figure 274. Weekly mean (left panels), and weekly differences for Scenario 2 - baseline (middle panels) and Scenario 3 – baseline (right panels) for thermocline depth and strength at station 17.	284
Figure 275. Weekly mean (left panels), and weekly differences for Scenario 2 - baseline (middle panels) and Scenario 3 – baseline (right panels) for thermocline depth and strength at station 19.	285
Figure 276. Weekly mean (left panels), and weekly differences for Scenario 2 - baseline (middle panels) and Scenario 3 – baseline (right panels) for thermocline depth and strength at station 20.	286

Figure 277. Weekly mean (left panels), and weekly differences for Scenario 2 - baseline (middle panels) and Scenario 3 – baseline (right panels) for thermocline depth and strength at station 21.	287
Figure 278. Weekly mean (left panels), and weekly differences for Scenario 2 - baseline (middle panels) and Scenario 3 – baseline (right panels) for thermocline depth and strength at station 23.	288
Figure 279. Weekly mean (left panels), and weekly differences for Scenario 2 - baseline (middle panels) and Scenario 3 – baseline (right panels) for thermocline depth and strength at station 25.	289
Figure 280. Change in thermal stratification for Scenario 2 (partial build out) and Scenario 3 (full buildout) against baseline conditions for August 2018.	290
Figure 281. Wind velocity (top first panel), current velocity (second panel), and temperature with depth (panel 3-5) for all three scenarios during April 15 - April 30, 2019 at station 19.	292
Figure 282. Wind velocity (first panel), current velocity (second panel), and temperature with depth (panel 3-5) for all three scenarios during August 1 - August 15, 2019 at station 25.	294
Figure 283. Change in median, 95th percentile, and 99th percentile of bed shear stress due to currents.	296
Figure 284. Change in median, 95th percentile, and 99th percentile of bed shear stress due to waves.	297
Figure 285. Change in median, 95th percentile, and 99th percentile of bed shear stress due to combined currents and waves.	298
Figure 286. Sediment mobility changes.	300
Figure 287. Distribution of Atlantic sea scallop (<i>Placopecten magellanicus</i>) spawning beds off the Northeast coast of North America (figure from Hart and Chute, 2004).	303
Figure 288. Distribution of Atlantic surfclam (<i>Spisula solidissima</i>) in the Mid-Atlantic (figure from Cargnelli et al., 1999).	304
Figure 289. Distribution of black sea bass (<i>Centropristis striata</i>) eggs collected during NOAA-NEFSC ichthyoplankton surveys (figure from Drohan et al., 2007).	305
Figure 290. Plot a shows the center points on two adjoining triangles (blue or black dot) of the mesh grid with distances from the edge that connects them, d1 and d2.	308
Figure 291. Larvae release (spawning) and settlement zones for sea scallop (green, a, b, c), surfclam (blue, d, e, f), and sea bass (red, g, h, i).	310
Figure 292. Trajectories of all larvae released on May 1, 2018 for simulation M1.	313
Figure 293. Density of all successfully settled larvae for simulation M1. This image is a zoomed-in portion of the total domain near the northern WEAs.	314
Figure 294. Larval dispersal distance between release and settlement locations for Scenario 1 (no turbines, white), Scenario 2 (partial buildout; light shading), and Scenario 3 (full buildout; dark shading).	316
Figure 295. Connectivity matrix for each species for simulation M1; top row (a, b, c) is sea scallop, middle row (d, e, f) is surfclam, and bottom row (g, h, i) is sea bass.	318
Figure 296. Maps of settlement success per settlement zone for Scenario 1 (baseline, left column, a, d, g) for each species – top row sea scallop (a, b, c), center row surfclam (d, e, f), bottom row sea bass (g, h, i) for simulation M1.	319
Figure 297. Scallop trajectories (a, b, c), connectivity matrices (d, e, f), distance distribution (g), and successfully settled end location density plot (h, i, j) for 10,000 released larvae (M2).	321
Figure 298. Trajectories over time for all larvae released on May 1, 2018 with DVM (simulation M3). Top row (a, b, c) sea scallop, middle row (d, e, f) surfclam, and bottom row (g, h, i) sea bass.	323

Figure 299. Density of all successfully settled larvae for simulation M3. This image is a zoomed in portion of the total domain near the northern WEAs.....	324
Figure 300. Distance between larvae release and settle for Scenario 1 (baseline, no turbines, white), Scenario 2 (partial buildout, light shading), and Scenario 3 (full buildout, dark shading). ...	325
Figure 301. Connectivity matrix for each species with DVM (simulation M3); top row (a, b, c) is sea scallop, middle row (d, e, f) is surfclam, and bottom row (g, h, i) is sea bass.....	326
Figure 302. Trajectories over time for all larvae released on May 1, 2018 with temperature dependence (simulation M4).....	328
Figure 303. Density of all successfully settled larvae for simulation M4. This image is a zoomed in portion of the total domain near the northern WEAs.....	329
Figure 304. Larval dispersal distance between larvae release and settlement for Scenario 1 (baseline, no turbines, white), Scenario 2 (partial buildout, light shading), and Scenario 3 (full buildout, dark shading).....	330
Figure 305. Connectivity matrix for each species with temperature dependence (simulation M4); top row (a, b, c) is scallop, middle row (d, e, f) is surfclam, and bottom row (g, h, i) is sea bass.....	331
Figure 306. Trajectories over time for all larvae released on May 1, 2018 with DVM and temperature dependence (simulation M5).....	333
Figure 307. Density map of all successfully settled larvae for simulation M5. This image is a zoomed in portion of the total domain near the northern WEAs.....	334
Figure 308. Larval dispersal distance between larvae release and settlement for scenario 1 (baseline, no turbines, white), scenario 2 (partial buildout, light shading), and scenario 3 (full buildout, dark shading).....	335
Figure 309. Connectivity matrix for each species with DVM and temperature dependence (simulation M5); top row (a, b, c) is sea scallop, middle row (d, e, f) is surfclam, and bottom row (g, h, i) is sea bass.....	336

List of Tables

Table 1. Simulation scenarios.....	25
Table 2. Surface wave observation station information and basic statistics.....	27
Table 3. NOS coastal stations information and basic statistics.....	28
Table 4. Satellite sea surface height observations information and basic statistics.....	30
Table 5. Ocean current observations including basic statistics.....	32
Table 6. Sea water temperature observations including basic statistics.....	35
Table 7. Salinity observations including basic statistics.....	37
Table 8. Surface meteorology observations.....	39
Table 9. Compilation of wind speed deficit α and wake length σ from SAR observations and airborne measurements.....	43
Table 10. Physical dimensions of reference wind turbine (NREL 15MW).....	47
Table 11. Tidal constituents computed with T_TIDE.....	76
Table 12. Model parameters tested in calibration.....	79
Table 13. Model calibration statistics for water elevation (m) at 4 NOS stations.....	84

Table 14. Model skill metrics against NDBC observations of water temperature for calibration period.	87
Table 15. Monthly model skill metrics against glider observations of water temperature for calibration period.	98
Table 16. Monthly model skill metrics against glider observations of water salinity for calibration period.	102
Table 17. Model validation statistics for water elevation (m) at 4 NOS stations.	115
Table 18. Model skill metrics against NDBC observations of surface water temperature for validation period.	117
Table 19. Model skill metrics against Empire Wind current speed observations.	131
Table 20. Specifics of the wave datasets used for forcing SWAN model.	141
Table 21. Specifics of the wind datasets used for forcing SWAN model.	141
Table 22. SWAN model setup parameters.	144
Table 23. Wind speed validation metrics (ERA5) at NDBC station locations.	155
Table 24. Significant wave height validation metrics at NDBC station locations.	159
Table 25. Mean wave direction validation metrics at NDBC station locations.	166
Table 26. Mean wave period validation metrics at NDBC station locations.	173
Table 27. Simulated annualized mean Scenario 1 (Baseline) parameters and their difference between Scenario 3 (Full buildout) and Scenario 1 at 7 of the stations shown in Figure 225.	228
Table 28. Relative percent increase (+) or decrease (-) of simulated seasonal mean parameters between Scenario 3 (Full buildout) and Scenario 1 (Baseline) at 7 of the stations shown in Figure 225.	229
Table 29. Percentage of weeks that the z-score exceeds 95th percentile for Scenario 2 - baseline.	232
Table 30. Percentage of weeks that the z-score exceeds 95th percentile for Scenario 3 - baseline.	233
Table 31. Summary of pertinent larval biological parameters for each target species specific to the Mid Atlantic Bight.	302
Table 32: Relevant biological parameters for the larval dispersal model for each species.	308
Table 33: Summary of parameters included in the different model configurations. Model configurations M2 was performed for Atlantic sea scallop only due to computing constraints.	311
Table 34: Summary of results obtained for all model simulations (see Table 3 for details) for Atlantic sea scallop. Disp. Dist. is dispersal distance, min is minimum, max is maximum.	337
Table 35: Summary of results obtained for all model simulations (see Table 3 for details) for Atlantic surfclam. Disp. Dist. is dispersal distance, min is minimum, max is maximum.	337
Table 36: Summary of results obtained for all model simulations (see Table 3 for details) for Black sea bass. Disp. Dist. is dispersal distance, min is minimum, max is maximum.	338
Table 37: P-value statistics for each of the metrics shown in Table 34, Table 35, and Table 36 calculated over all simulations for each species comparing the variance between the hydrodynamic scenarios. A p-value above 0.05 means there is no statistical difference between the three hydrodynamic scenarios for that summary statistic for that species.	339

List of Abbreviations and Acronyms

Short form	Long form
ABL	atmospheric boundary layer
ABM	agent based model
AEP	Annual Energy Production
AOI	area of interest
CFD	computational fluid dynamics
CFSRv2	Climate Forecast System Reanalysis v2
DFLOW	hydrodynamic module of Delft3D system
DTU	Technical University of Denmark
DVM	diurnal vertical migration
ECMWF	European Center for Medium Range Weather Forecasts
ERA5	ECMWF Reanalysis Version 5
GEBCO	General Bathymetric Map of the Oceans
IOA	Index of Agreement
LES	large eddy simulation
LiDAR	light detecting and ranging
MAB	Middle Atlantic Bight
MAE	mean absolute error
MPAS	Model for Prediction Across Scales
MPI	Message Passing Interface
MSL	mean sea level
MW	megawatt
NCEI	National Centers for Environmental Information
NDBC	National Data Buoy Center
NEFSC	Northeast Fisheries Science Center
NOS	National Ocean Service
NREL	National Renewables Energy Laboratory
NYHOPS	New York Harbor Ocean Prediction System
OSS	offshore substation
OWT	offshore wind turbine
PPT	parts per thousand
PSU	practical salinity units
R ²	coefficient of determination
RANS	Reynolds-Averaged Navier-Stokes
RMS	root mean square
RMSE	root mean square error
ROMS	Regional Ocean Modeling System
SAR	synthetic aperture radar
SMS	Surface-Water Modeling System
SST	sea surface temperature
ST6	Source Term 6, observation-based wave parameterization
STD	standard deviation
SWAN	Simulating Waves Nearshore
T_TIDE	Tidal analysis software by Pawlowicz et al. (2002)
UTC	Coordinated Universal Time
WAsP	Wind Atlas Analysis and Application Program
WEA	Wind Energy Area
Westh	Westhuysen, parameterization used in SWAN
WRF	Weather Research and Forecasting
WTG	wind turbine generator
WW3	WaveWatch III

Summary

Proposed development of offshore wind energy areas in the Mid-Atlantic Bight has raised concerns among stakeholders about potential changes to coastal and oceanic environmental conditions. To build on two previous BOEM studies, this project developed a validated modeling system that incorporates individual wind turbines and wind energy resource facilities for the U.S. North Atlantic Ocean from North Carolina to New York and used it to generate detailed simulations that enable more accurate assessments of possible impacts of proposed wind energy facilities. The objective of the study was to determine the effects of offshore wind energy facilities on coastal and oceanic environmental conditions and habitat by examining how oceanic characteristics will change after turbine installation, particularly for bottom stress, turbulent mixing, along and cross-shelf currents, wind-wave interactions, and larval transport.

We used numerical modeling and statistical analysis of model results to answer these questions. We treated three modeling scenarios: baseline conditions without wind turbines (Scenario 1), “partial buildout” of proposed Wind Energy Areas (WEAs) based on Construction and Operations Plans (Scenario 2), and complete buildout to include the development of the remaining leased WEAs on the shelf as of October 2022 (Scenario 3). A two-year period was modeled from February 2018 through January 2020, inclusive. The hydrodynamic model employed is the unstructured mesh Delft3D-FM, extending from the nearshore to beyond the shelf break, with a hybrid terrain-following and horizontal level vertical grid. Boundary forcing is from the validated and calibrated Doppio data-assimilative operational model based on the Regional Ocean Modeling System (ROMS), and meteorological forcing is from the European Center for Medium Range Weather Forecasts 5th generation global reanalysis (ERA5). The waves model is the Simulating WAVes Nearshore (SWAN), run on the same unstructured mesh as Delft3D-FM and driven by surface meteorology and boundary wave conditions both also from ERA5. Modeled hydrodynamic and wave parameters were calibrated and validated using skill metrics and extensive observations including water level, currents, temperature, salinity, surface meteorology, and waves from tide gauge, mooring, satellite, high frequency radar, and glider sources. The index of agreement, root mean square error, and other metrics are on par with published values from comparable state of the art modeling studies.

For the modeling scenarios with wind energy area development (Scenarios 2 and 3), simulation of wind turbine effects and wind wakes used the analytical model PyWake from the Technical University of Denmark, for its computational efficiency and configurable modular architecture. Turbine speed, generator power, and thrust coefficient are from the National Renewable Energy Laboratory reference type, with 15-megawatt capacity, 150 m hub-height, 240 m rotor diameter, and fixed-bottom monopile structure. We constructed winds affected by wind energy arrays across the entire domain by superposing on unmodified winds the spatially and temporally varying wind reductions (wind wake deficits), which can overlap, computed for multiple clusters of turbines. These winds forced the hydrodynamic and wave models, together with enhanced hydrodynamic drag at the location of each monopile turbine foundation based on previously published CFD modeling applied to the turbines of this study.

Results quantify wind reductions (wakes) within and downwind of the wind energy areas. Due to the turbine thrust coefficient curve, reductions are largest for wind speeds between the cut-in speed of about 3 m/s and the hub-height speed at which the rated power is reached, about 11 m/s. Reductions to climatological winds at 10 m height (which force the hydrodynamic model) are higher for complete buildout (Scenario 3) than partial buildout (Scenario 2) and can reach or exceed 20% in limited areas within turbine arrays and 10% downwind of them. Reductions weaken markedly tens of km from the arrays but extend as far as 100-200 km away downwind. Relatively rare and transient maximal wind

reductions, occurring about 1% of the time, can reach 30%–50% for 10 m/s wind speeds, and are more widespread across the domain.

Effects of weakened winds on surface waves occur mostly local to areas with reduced winds, especially within and around WEAs with geometries aligned with prevalent wind directions. Median significant wave heights are reduced by up to 4 cm and 7 cm for the partial and complete build-out scenarios, respectively, which is about 5% of climatology or less in the WEAs nearer to the coast, and relatively less further offshore. Median dominant wave periods slightly increased by up to 0.16 s within WEAs due to the relative increase in swell to the total wave field, as the higher-period remotely generated swell is relatively unaffected in wind energy areas compared to the locally generated wind waves that are reduced there.

Our results indicate that wind farms cause statistically significant changes in annual- and seasonal-mean winds; surface heat fluxes; surface and bottom temperatures; surface, bottom, and vertical-mean currents; water column stability; and thermocline depth. Currents are more strongly affected by the reduced winds than by the local influence of flow interactions with turbine foundations, simulated here by enhanced hydrodynamic drag. Scenario results indicate wind energy areas cause 50th, 95th, and 99th percentile total current (not low-pass filtered) speeds to decrease modestly (less than 2mm/s on the median, less than 1cm/s on the upper percentiles), with smaller-magnitude (less than 1cm/s) local increases also seen especially shoreward of the northern wind energy areas along the NY Bight and NJ coast at the 99th percentile level.

The main characteristic of Mid-Atlantic Bight general circulation is a 2–12 cm/s alongshore southward flowing mean current over the shelf, driven mainly by the southward regional alongshore pressure gradient and influenced by wind stress (Lentz, 2010; Chen and Yang, 2024). The Scenario 2 and 3 tidal residual, low-passed, mean current vectors of the southward general circulation strengthen along the wind energy areas. These changes appear to be due to alterations in larger-scale circulation patterns resulting from wind wake effects, rather than increased turbulence and mixing around the turbine foundations. A consistent interpretation is that weaker winds due to wind energy areas shift the dynamical balance of alongshore flow to enhance its southward component. Another feature in the scenario results is increased horizontal shear of currents, due to weakening of southward flow adjacent to wind energy areas where it has increased.

In the two scenarios with reduced winds due to wind energy area buildout, surface temperatures are higher over the WEAs, and the thermocline shoals on the lee side of them, characteristics that are hypothesized to be due to suppressed wind-driven vertical turbulence in the surface mixed layer locally and increased positive vorticity and upwelling at their offshore edge. The strength of the seasonal thermocline increases, with surface to bottom temperature stratification higher in the full buildout scenario by as much as about 1°C in certain areas during mid-summer. Although the seasonal cold pool formation and evolution is not fundamentally altered, the cold pool may be advected further south in the summer. Consistent with these effects, statistical analysis of representative stations shows that parameters most likely to have weekly-mean values that differ between complete buildout and baseline by more than the within-week baseline variability are temperature (both near-bottom and surface), near-surface stability, and thermocline depth and strength. In contrast, this is less likely for wind speed, current speed, vertical turbulent eddy viscosity, and turbulent kinetic energy. The effect of weakened winds on bed shear stress and sediment mobility is modest reductions near the coast and in areas near the installations, which are more pronounced for the 95th and 99th percentiles than median values, and stronger for complete buildout than partial buildout. These impacts are due to reduced waves, not reduced currents, but bottom currents do tend to decrease slightly within the wind energy areas.

We completed a literature review of commercial value, spawning characteristics, larval distributions, and behavior for key life stages of numerous fishery species of the region. A consultation process with Bureau

of Ocean Energy Management (BOEM) and National Oceanic and Atmospheric Administration (NOAA) colleagues, which considered various factors including the applicability of the larval dispersal model and data availability, led to the identification of Atlantic sea scallop (*Placopecten magellanicus*), Atlantic surfclam (*Spisula solidissima*), and black sea bass (*Centropristis striata*) as the three species of interest, for which larval dispersal was modeled. We used a biophysical larval dispersal model, coupling the individual-based Lagrangian model Ichthyop with the hydrodynamic model, to simulate larval transport of these three commercial species. The effects of hydrodynamic conditions in three dimensions were assessed based on species-specific inputs for larvae including spawning location, spawning depth, spawning time, larval dispersal duration, settlement depth, settlement habitat, diel vertical migration behavior, and temperature tolerance. The model configurations included a case for each species, for each of the three scenarios, with (a) passive larvae, (b) diel vertical migration behavior, and (c) temperature-dependent mortality. Larval trajectories, settlement success, connectivity patterns, and dispersal distances were assessed.

Results for all three species from the model with passive larvae showed only general transport from the northern to the southern part of the study domain, and higher larval connectivity in the north. Larvae were transported away from their spawning zones due to changes in hydrodynamic features associated with the presence of wind energy areas, including stronger along-shelf flow in some areas, reduced mixing, and stronger stratification. For simulations adding diel vertical migration behavior, the mean and range of larval dispersal distances were larger and mean larval connectivity increased (to about 3.0%–3.5% from 0.5% to 1.5%), relative to passive larvae, consistent with larvae spending more time higher in the water column where currents are generally stronger. Simulations adding only temperature-dependent mortality showed a decrease in larval connectivity due to high mortality, likely because of exposure to a wider range of temperatures than in laboratory studies on which threshold temperatures are based. The consistent connectivity patterns and effects of wind energy areas observed across model configurations suggest that larval connectivity is primarily influenced by hydrodynamic processes. While the calculated larval connectivity values did not differ significantly between the tested hydrodynamic scenarios, the larval dispersal model for these three commercial species predicted reduced local retention, especially in the northern region, and increased larval dispersal distances in some regions where wind energy areas are present. The increased larval dispersal distances in the presence of wind energy areas may prevent larvae from settling in habitats close to their spawning areas, potentially altering the species' distribution range over time. At the scale of the Mid-Atlantic Bight, the presence of wind energy areas does not qualitatively influence larval connectivity patterns. However, more regional long-term studies are needed to better understand the effects of wind energy areas on the larval dynamics of commercially important species.

The simulated minor reductions on wave conditions, bed shear stress, and sediment mobility due to wind energy farms are likely not of substantial impact relative to natural variability; because the effects of buildout are more pronounced within wind energy arrays and weaker outside them, impacts generally are minor on regionwide water column oceanographic processes, for example the seasonal development of stratification and formation and evolution of the cold pool. However, the increased water temperature and stratification strength, especially within the WEAs, may be of sufficient magnitude to potentially alter ecology, particularly when superposed on climate warming that is causing warm-water species guilds to displace cold-water guilds northward. More work is needed to examine whether the changes seen in this work may be locally significant to ecosystems and communities along the mid-Atlantic coast.

1 Introduction

The planned development of offshore wind energy lease areas in the Mid-Atlantic Bight (Figure 1) has raised concern among stakeholders regarding the potential changes in the region's hydrodynamic circulation resulting from the build-out of one or several offshore wind energy facilities. To address this concern, the Bureau of Ocean Energy Management (BOEM) has funded studies looking into the cumulative impacts of offshore wind facilities on regional circulation patterns, nutrient and sediment transport, and larval dispersal. With other projects focused on lease areas offshore of Massachusetts to New York, this study aimed to model the potential changes in physical and biological processes associated with the offshore wind lease areas in North Carolina north of Cape Hatteras, Virginia, Maryland, Delaware, and New Jersey, planned for development on continental shelf waters shoreward of the shelf break. This study focused only on lease blocks (Figure 1), and not all BOEM offshore planning areas that include areas outside the continental shelf. The study includes an examination of the effect of two wind farm layout scenarios within these lease areas during average seasonal conditions, a literature review on species of interest relevant to the study area, and an assessment of the effective scale of change in larval transport around wind energy areas (WEAs).

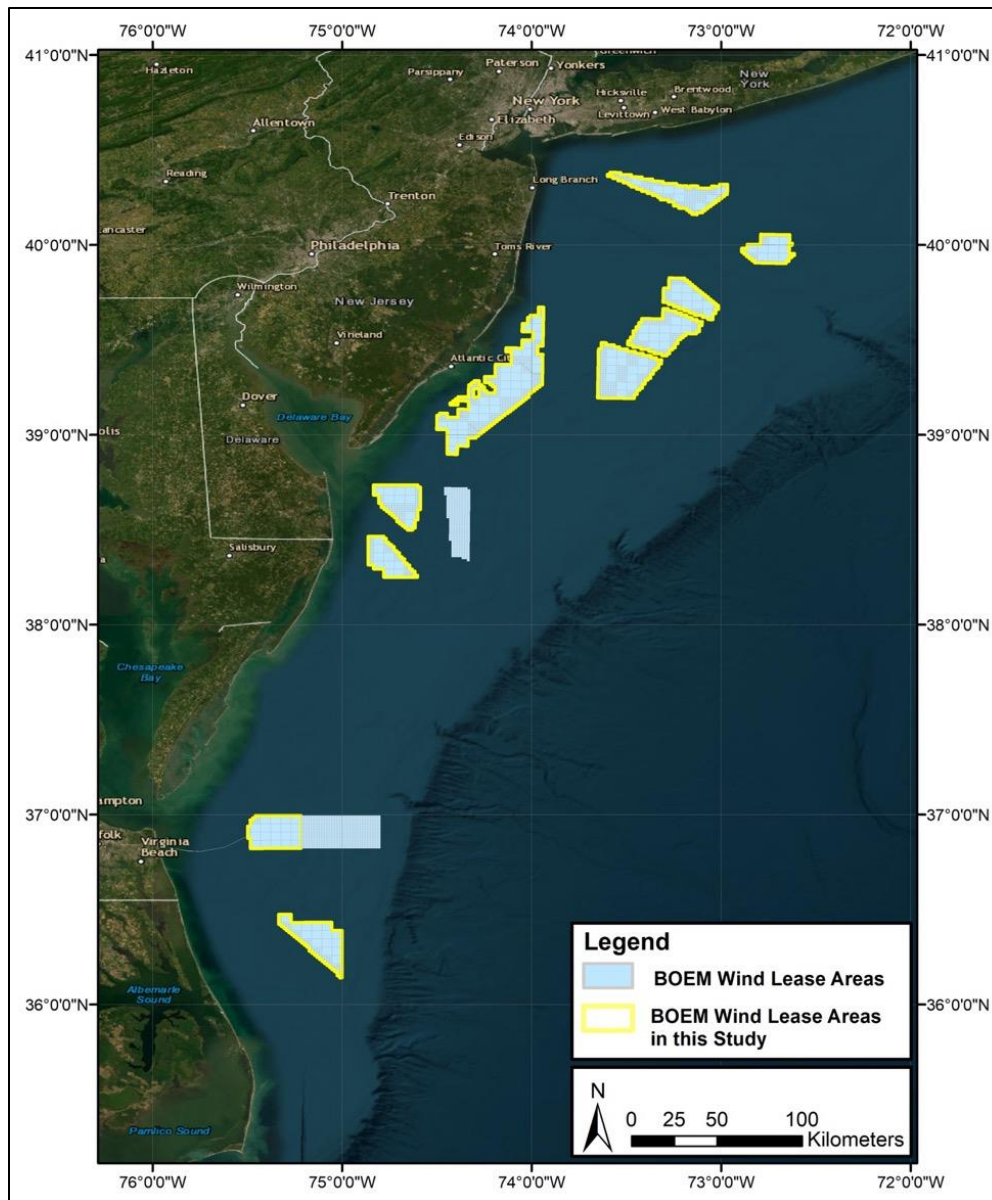


Figure 1. BOEM wind lease areas between North Carolina and New York.

Wind lease areas in this study are highlighted with yellow. Two areas unhighlighted were leased on August 14, 2024 and were not included in the contracted scope of work for this study that commenced in October 2022. The major objective of the present study under the funded Solicitation 140M0123C0001 was to accurately assess the potential effects of offshore wind energy facilities in the Mid-Atlantic Bight Shelf between Cape Hatteras, North Carolina, and New York on ocean circulation, environmental conditions, and larval transport. This was done by examining how oceanic responses may change after the build-out of offshore wind turbines and energy facilities, particularly for bottom stress, turbulent mixing, wind-wave interactions, and general circulation features relevant to fisheries such as the mid-Atlantic Cold Pool. This was done through numerical model development and comparisons of model scenarios with and without wind farms on the Mid-Atlantic Bight Shelf. The subsequent changes in biological processes, namely the larval dispersal of selected species of interest, were also evaluated.

2 Area of Interest and Wind Farm Scenarios

2.1 Area of Interest

Given the geographic scope of this study which is the Mid-Atlantic Bight shelf between Cape Hatteras, NC and the New York Bight, and given the focus of the study on capturing the effect of the wind wake generated in and around the proposed wind farms on the hydrodynamic circulation, wind waves, and larval transport, the agreed upon modeling domain is shown in Figure 2, in relation to the wind farms proposed at the time modeling started. The domain encompasses the Mid-Atlantic Bight shelf from Cape Hatteras in the southwest to the Fire Island barrier line off Long Island in the northeast. It extends beyond the continental shelf break by about 80 to 100km thus including the shelf break and parts of the deep ocean plateau. That deep-water extension was made to accommodate the possibility of wind wake effects from wind farms close to the shelf break as well as boundary effects.

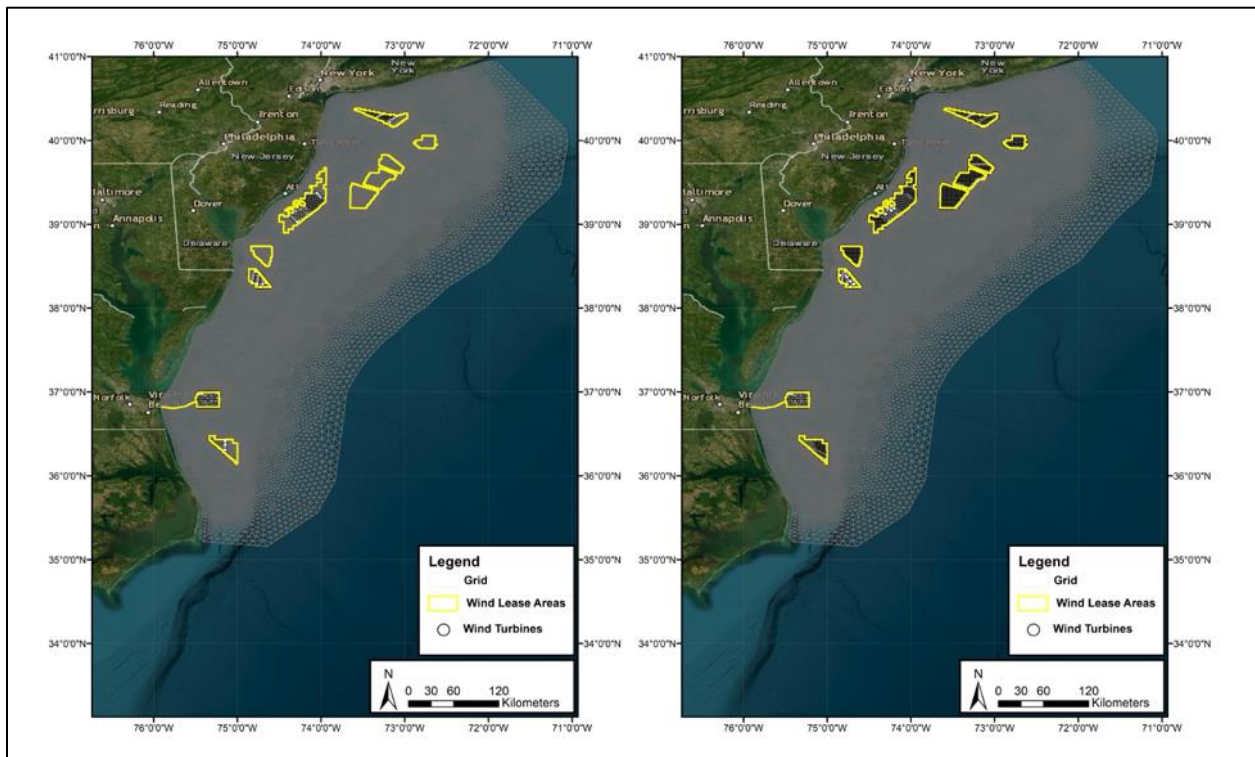


Figure 2. WTG coverage through the wind lease areas considered in this study. (a) Left panel: Scenario 2 Publicly Available Locations. (b) Right panel: Scenario 3—full build-out.

2.2 Simulation Scenarios

To achieve goals associated with the Net Zero transition of the US economy, support in adopting renewable energy strategies such as solar power, hydrogen renewable energy storage, and wind energy harvesting have grown in recent years. As part of this strategy, installation of fields of offshore wind turbine generators (WTG), connected to offshore substations (OSS) are planned for Mid-Atlantic Bight WEAs. Several lease parcels, concentrated in 10 lease areas within the area of interest (AOI) are considered in this study (Figure 1).

The study will consider three scenarios for these 10 lease areas, listed in Table 1.

Table 1. Simulation scenarios.

Scenario	Description
1 - Baseline	No wind turbines in the WEAs.
2 – 15 MW Partial build-out	1,852 WTGs, 15 MW NREL type, at all locations identified using publicly available Construction and Operation Plans (Figure 2-a).
3 – 15 MW Complete build-out	6,353 WTGs, 15 MW NREL type, Scenario 2 locations plus a 0.6 nm by 0.6 nm grid across the remainder of the lease areas (Figure 2-b).

Wind turbine specifications and WTG placement grid for each of the two scenarios with WTG (Scenarios 2 and 3) are included in Section 4.3 of this report.

3 Physical Observations

The numerical models for waves and hydrodynamics are validated, in particular the baseline case (Scenario 1), against a multitude of observations collected over the two-year period of February 1, 2018 to January 31, 2020. Observational methods include buoys, satellites, gliders, HF-Radar and other techniques, covering numerous numerical model output variables. To set the stage for the modeling, the following subsections present the collected observations, their coverage, types, and statistics, organized by type. The model domain shown in the following figures is the part of the complete numerical model domain that is on the area of interest, the continental shelf.

3.1 Surface Waves

Surface wave observations comprise significant wave height, average wave period, and mean wave direction at available National Data Buoy Center (NDBC) locations shown in Figure 3 and summarized in Table 2.

Table 2. Surface wave observation station information and basic statistics.

Data Type	Data Provider	Start Date	End Date	Num Locations	Min Obs	Max Obs	Mean Obs	Std Obs	Min Lat (°N)	Max Lat (°N)	Min Long (°W)	Max Long (°W)
Significant Wave Height (m)	NOAA (NDBC)	2/1/2018	1/31/2020	11	0.19	8.49	1.241	0.727	35.750	40.369	72.644	75.722
Average Wave Period (s)	NOAA (NDBC)	2/1/2018	1/31/2020	11	2.41	13.86	5.302	1.199	35.750	40.369	72.644	75.722
Mean Wave Direction (deg)	NOAA (NDBC)	2/1/2018	1/31/2020	11	0	360	123.694	68.063	35.750	40.369	72.644	75.722



Figure 3. Surface wave observations stations.

3.2 Sea Surface Height

Sea surface height (SSH) and water elevation observations in the AOI were collected for four coastal National Ocean Service (NOS) tidal stations (Table 3 and Figure 4), and from available satellites (Table 4 and Figure 5) in the form of the Doppio 7-km gridded products produced from along-track satellite measurements. All sea surface height values in meters MSL (1983-2001 National Tidal Datum Epoch).

Table 3. NOS coastal stations information and basic statistics.

Station Name	NOS ID #	Start, UTC	End, UTC	Min Obs	Max Obs	Mean Obs	Std Obs	Lat (°N)	Long (°W)
Sandy, Hook, NJ	8531680	2/1/2018 00:00	1/31/2020 23:54	-1.593	1.887	0.161	0.551	40.467	74.010
Atlantic City, NJ	8534720	2/1/2018 00:00	1/31/2020 23:54	-1.432	1.672	0.153	0.484	39.357	74.418
Lewes, DE	8557380	2/1/2018 00:00	1/31/2020 23:54	-1.330	1.742	0.166	0.486	38.783	75.120
Duck, NC	8651370	2/1/2018 00:00	1/31/2020 23:54	-1.019	1.656	0.155	0.401	36.183	75.747

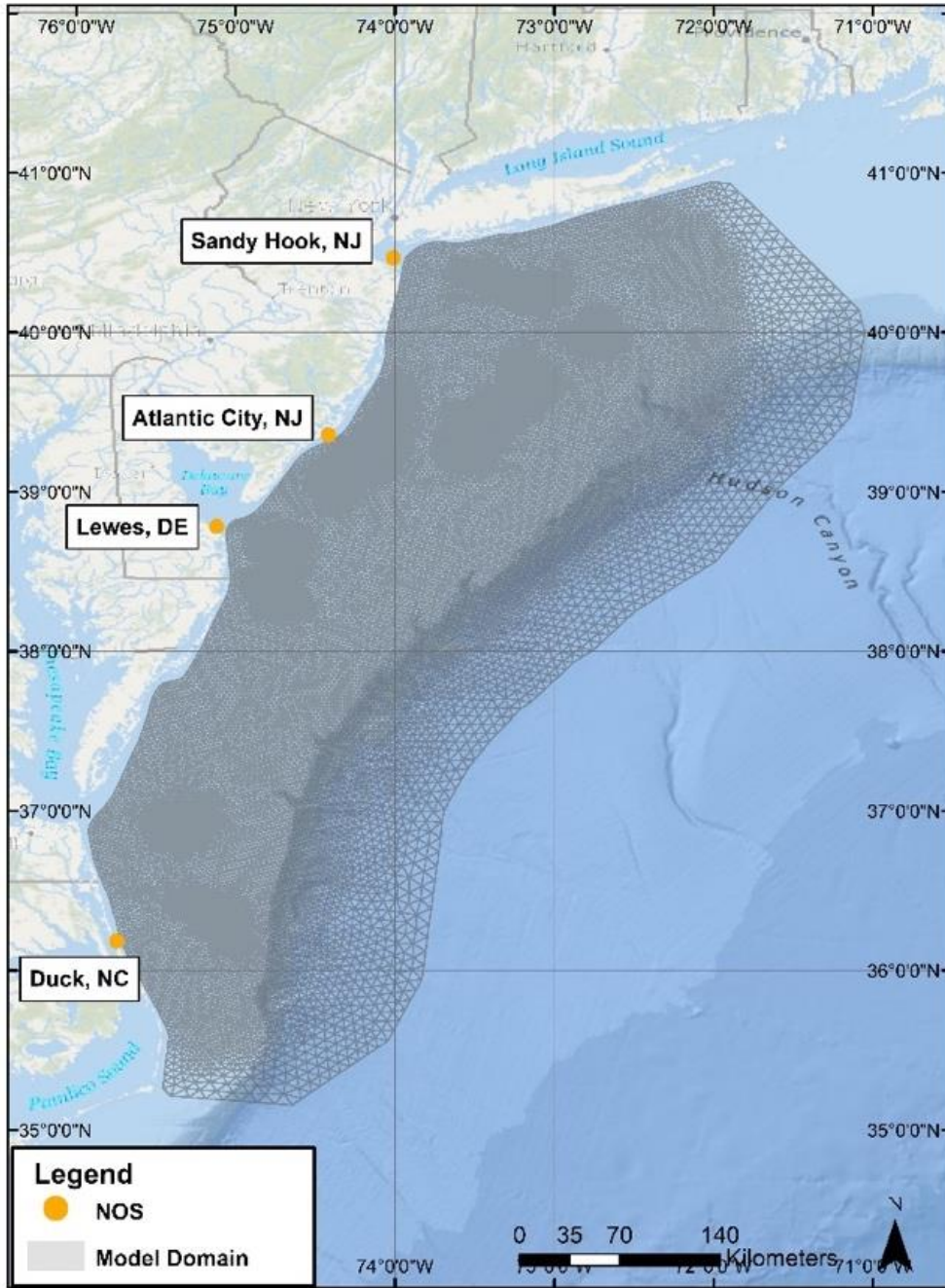


Figure 4. National Ocean Service tide gauge locations.

Table 4. Satellite sea surface height observations information and basic statistics.

Data Provider	Start, UTC	End, UTC	Num Locations	Min Obs	Max Obs	Mean Obs	Std Obs	Min Lat (°N)	Max Lat (°N)	Min Long (°W)	Max Long (°W)
Cryosat	2/1/2018 12:20	1/31/2020 2:42	4,592	-1.147	1.116	-0.111	0.392	35.492	40.809	71.848	75.790
Altika	2/1/2018 9:15	1/10/2020 11:28	4,133	-1.116	1.048	-0.079	0.384	35.484	40.809	71.858	75.824
Alt. Super Obs	11/16/2018 9:45	7/24/2019 11:26	17	-0.487	0.114	-0.250	0.186	36.348	40.348	72.896	75.445
Jason 2	2/4/2018 4:54	9/28/2019 18:00	2,409	-1.048	0.996	-0.105	0.361	35.485	40.772	71.851	75.882
Jason 3	2/2/2018 5:14	1/27/2020 4:00	2,539	-1.781	1.340	-0.059	0.439	37.807	40.522	72.370	74.863
Sentinel 3a	2/3/2018 0:57	1/29/2020 2:47	4,984	-1.210	1.154	-0.064	0.396	35.765	40.804	72.034	75.807
Sentinel 3b	3/6/2019 1:19	1/30/2020 16:25	2,486	-1.142	0.876	-0.027	0.368	35.488	40.744	71.918	75.536

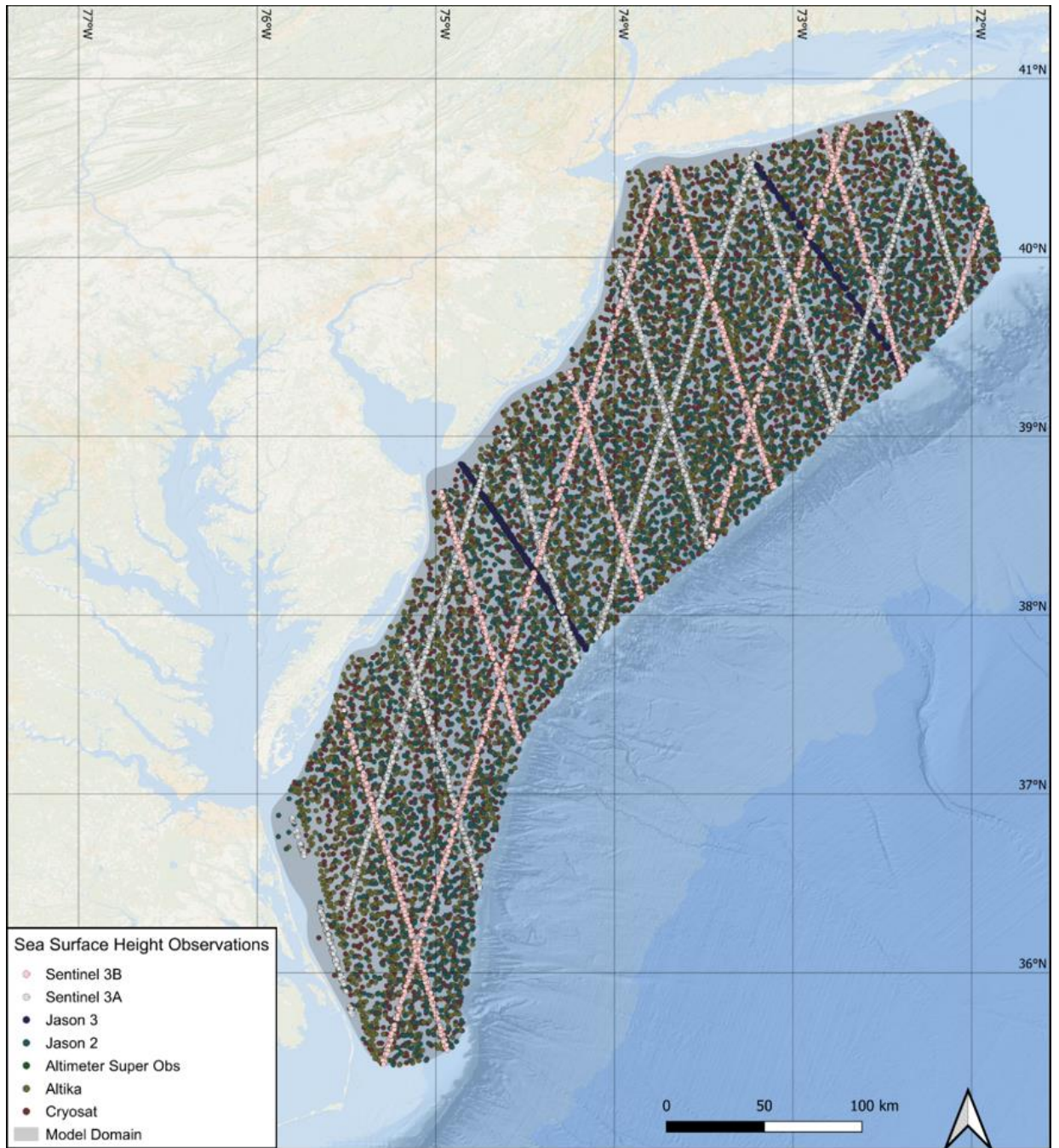


Figure 5. Sea Surface Height observations coverage.

3.3 Ocean Currents

Available ocean current data, in units of m/s, were collected from buoys and CODAR HF-Radar coverage instruments (Table 5 and Figure 6).

Table 5. Ocean current observations including basic statistics.

Data Type	Data Provider	Start Date	End Date	Num Locs	Min Obs	Max Obs	Mean Obs	Std Obs	Min Lat (°N)	Max Lat (°N)	Min Long (°W)	Max Long (°W)	Min Depth (m)	Max Depth (m)
Current Speed (m/s)	Empire Wind Moored Current Meter	12/1/2018	2/1/2020	1	0.0001	3.6284	0.1274	0.1152	40.2985	40.2985	73.3336	73.3336	9.6	33.6
U (m/s)	CODAR	2/1/2018	1/31/2020	206	-1.219	1.535	-0.034	0.156	35.545	40.684	71.924	75.699	2	2
V (m/s)	CODAR	2/1/2018	1/31/2020	206	-1.175	0.950	-0.063	0.128	35.545	40.684	71.924	75.699	2	2

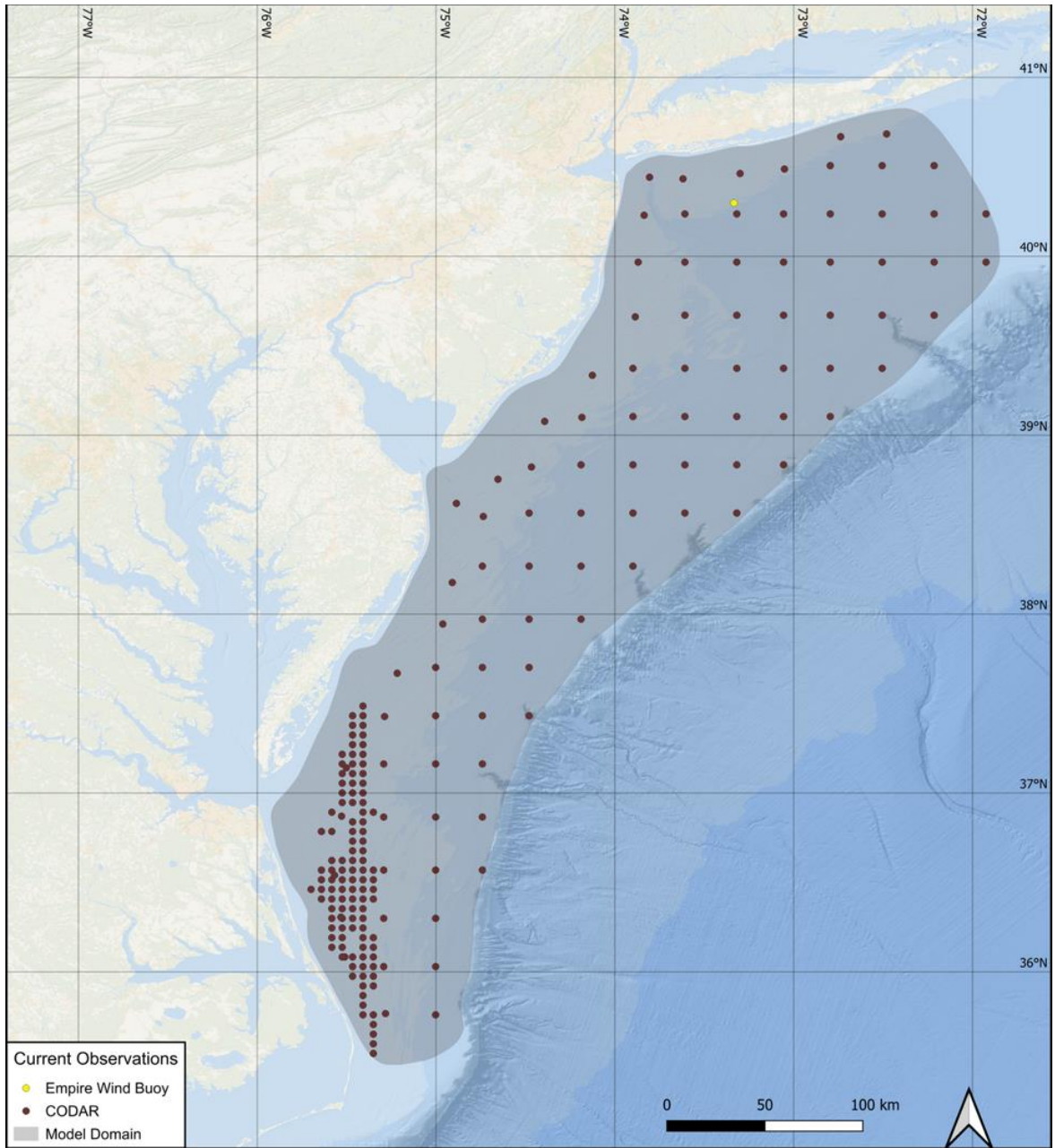


Figure 6. Ocean currents observation coverage.

3.4 Seawater Temperature

Available sea temperature observations, both at the sea surface (SST) and at depth, in units of degrees Celsius, were collected from the various sources (Table 6 and Figure 7).

Table 6. Sea water temperature observations including basic statistics.

Data Provider	Start, UTC	End, UTC	Num Locations	Min Obs	Max Obs	Mean Obs	Std Obs	Min Lat (°N)	Max Lat (°N)	Min Long (°W)	Max Long (°W)
OSMC Other	5/3/2018 1:30	5/6/2018 7:58	15	7.618	12.468	9.193	1.389	37.416	37.511	74.453	74.700
OSMC Argo	2/15/2018 9:42	10/28/2018 22:00	1,025	5.966	28.653	15.111	6.344	35.485	40.317	72.063	75.338
OSMC Floats	5/7/2018 7:56	9/12/2018 1:20	71	7.241	26.859	12.068	5.564	37.414	39.002	73.316	75.084
OSMC VOS	10/6/2018 5:27	10/6/2018 6:26	2	11.450	22.200	17.283	4.227	39.556	39.683	72.436	72.450
SST Super Obs.	2/7/2018 9:20	1/29/2020 16:00	1,358	3.118	31.180	20.837	6.507	35.504	40.738	71.858	75.886
OSMC Ships	2/25/2018 0:00	5/4/2018 6:30	20	5.900	12.500	8.170	1.743	39.288	40.442	72.500	73.826
AVHRR	2/1/2018 0:31	1/31/2020 14:00	1,370	0.150	30.799	17.116	7.139	35.504	40.738	71.858	75.886
GOES	3/10/2019 21:29	9/19/2019 18:45	4	6.335	23.770	15.031	6.454	35.850	40.527	72.398	75.771
Pioneer	2/1/2018 11:47	1/31/2020 20:48	166	3.363	26.459	13.304	6.236	37.556	40.077	71.858	74.352
WSAT	2/1/2018 6:14	1/30/2020 0:00	1,164	0.028	33.621	16.205	7.027	35.504	40.612	71.858	75.642
AMSR	6/2/2018 7:28	1/31/2020 17:12	1,521	2.306	31.631	18.581	6.902	35.504	40.808	71.858	75.905
VIIRS	2/15/2018 12:18	10/27/2018 16:00	646	6.114	28.735	14.678	6.497	35.485	40.288	71.867	75.289
Glider Super Obs	2/15/2018 10:13	11/15/2019 14:48	5,705	3.833	28.942	15.011	5.726	35.485	40.724	71.868	75.427
IOOS Glider DAC	5/3/2018 1:30	5/6/2018 7:58	15	32.770	35.451	33.481	0.507	37.416	37.511	74.453	74.700

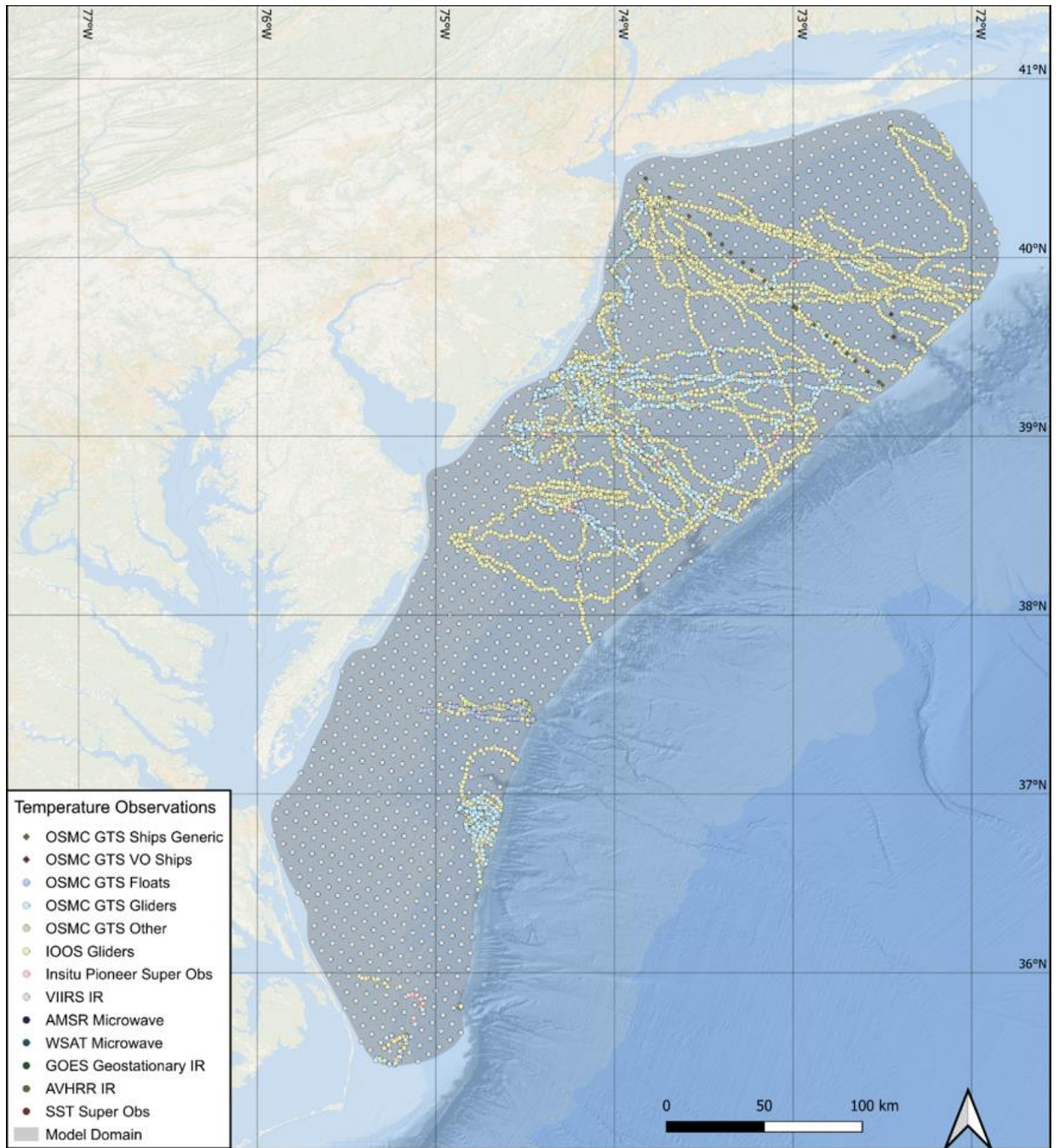


Figure 7. Sea water temperature observations coverage.

3.5 Salinity

Available salinity observations throughout the water column in practical salinity units (psu ~ parts per thousand), were collected from gliders and other sources (Table 7 and Figure 8). In Table 7, “Glider Super Obs” refers to “super observations”; these are combinations of multiple observations of the same type that fall within a single model grid cell and are closely spaced in time, in this case from the 7-km Doppio grid (Levin et al, 2020).

Table 7. Salinity observations including basic statistics.

Data Provider	Start, UTC	End, UTC	Num Locations	Min Obs	Max Obs	Mean Obs	Std Obs	Min Lat (°N)	Max Lat (°N)	Min Long (°W)	Max Long (°W)	Min Depth	Max Depth
OSMC Other	2/15/2018 9:42	10/28/2018 22:00	1,026	28.827	35.856	32.721	1.038	35.485	40.317	72.063	75.338	2.5	137.5
OSMC Gliders	5/7/2018 7:56	9/12/2018 1:20	71	29.963	35.511	32.757	0.909	37.414	39.002	73.316	75.084	2.5	137.5
OSMC Floats	3/10/2019 21:29	9/19/2019 18:45	4	30.289	35.423	32.387	1.261	35.850	40.527	72.398	75.771	2.5	45.0
Pioneer	2/15/2018 12:18	10/27/2018 16:00	646	28.414	35.946	32.702	1.109	35.485	40.288	71.867	75.289	2.5	137.5
Glider Super Obs	2/15/2018 10:13	11/15/2019 14:48	5,705	27.269	36.276	32.971	1.255	35.485	40.724	71.868	75.427	2.5	137.5
OSMC Other	2/15/2018 9:42	10/28/2018 22:00	1,026	28.827	35.856	32.721	1.038	35.485	40.317	72.063	75.338	2.5	137.5
OSMC Gliders	5/7/2018 7:56	9/12/2018 1:20	71	29.963	35.511	32.757	0.909	37.414	39.002	73.316	75.084	2.5	137.5

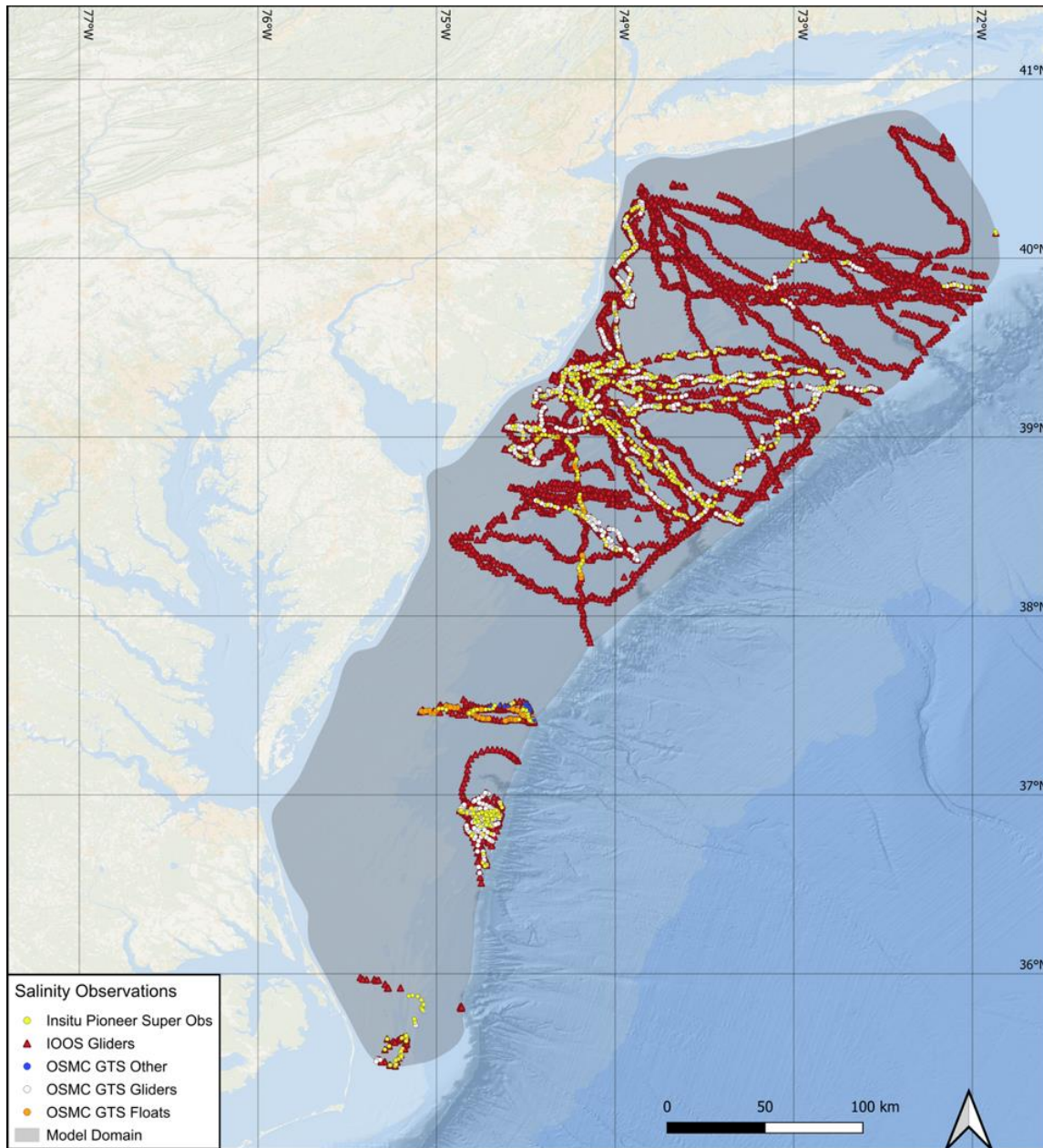


Figure 8. Salinity observations coverage.

3.6 Surface Meteorology

Available meteorological observations, namely wind speed, in m/s, and barometric pressure near sea level, in hPa, were collected from NDBC buoys (Table 8 and Figure 9).

Table 8. Surface meteorology observations

Data Type	Data Provider	Start date, UTC	End date, UTC	Num Locs	Min Obs	Max Obs	Mean Obs	Std Obs	Min Lat (°N)	Max Lat (°N)	Min Long (°W)	Max Long (°W)
Wind Speed (m/s)	NDBC	2/1/2018	1/31/2020	12	0	28.3	6.429	3.372	36.609	40.369	72.644	74.842
Sea Level Pressure (hPa)	NDBC	2/1/2018	1/31/2020	12	980.3	1044.1	1017.251	7.851	36.609	40.369	72.644	74.842

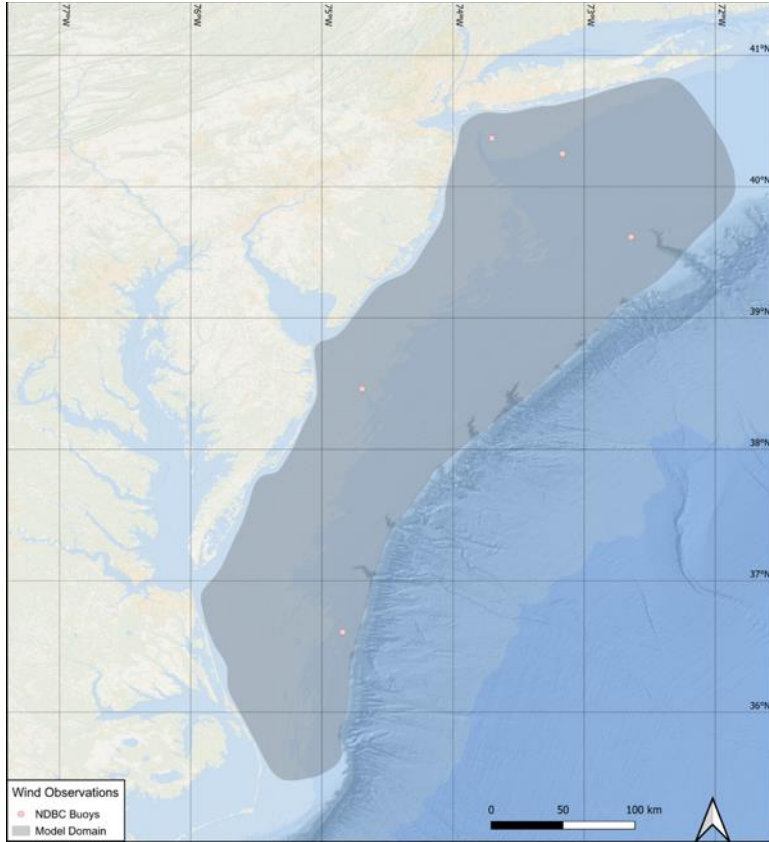


Figure 9. Surface meteorology (wind/pressure) observation stations.

4 Wind Wake Modeling

To generate renewable energy through offshore wind farms, kinetic energy is extracted from the atmosphere which results in atmospheric wakes. This phenomenon of increased atmospheric turbulence and horizontal momentum reduction on the downstream side of wind turbines can be foremost characterized by the decrease in wind speed (Christiansen et al., 2022, Dörenkämper and Steinfeld, 2022) and the formation of wind shadow zones reaching the surface of the ocean.

4.1 Selection of Model

To calculate the atmospheric wakes in the lee of wind turbine installations, several approaches can be used (NAS 2023):

- Computational fluid dynamics (CFD)
- Mesoscale modeling
- Analytical modeling methods
- Empirical top-down methods

There are several CFD frameworks such as Reynolds averaged Navier–Stokes (RANS) models with various levels of sophistication which range from 3D with actuator disks to parabolic, linearized, unsteady, or 2D, and large-eddy simulation (LES) with actuator disks or lines. Among these options, high-resolution LES provides the most accurate result as it solves the fine-scale details of the wakes around the turbines at a grid resolution of 10 m or less. However, LES is computationally uneconomic on the spatial scale of application considered in this study.

Mesoscale modeling, on the other hand, is less computationally expensive than CFD and can be implemented in real-world scenarios where there is a feedback loop between atmospheric boundary layer (ABL) and the wind farms. In the mesoscale modeling approach, horizontal resolution is in the order of kilometers while vertical resolution is in tens of meters within the ABL. These frameworks allow for a strong physical coupling between hydrodynamics and meteorology but, at a spatial resolution limited by computational needs and physical constraints, cannot resolve individual turbines and either parameterize them as an elevated momentum sink (Volker et al., 2015) or as an elevated momentum sink and a source of turbulence (Fitch et al., 2012; Abkar and Porté-Agel, 2015; Pan and Archer, 2018).

Several wake models have been parameterized over the years such as Jensen (1983) and Fitch et al., (2012), hereafter referred to as the Jensen model and Fitch scheme, respectively. Ma et al. (2022) found that, although the Fitch Scheme is widely adopted to calculate the wakes of wind farms and their impacts, in many cases it underestimated wake losses and overpredicted the power output of wind farms, especially when the wind is oriented with the turbine columns (Jiménez et al., 2012; Pan and Archer, 2018). However, it was found that the Jensen model shows more consistency in terms of performing well in different setup of wind farms and for all directions. This model assumes a top-hat distribution of the velocity deficit in every turbine wake and then uses superposition methods to consider the interaction among multiple wakes. However, the Jensen model was developed based on the assumption of having the same upstream undisturbed wind speed and direction for all turbines within the wind farm; this is not ideal as significant variability in the distribution of wind speed and direction within a wind farm is expected because of surface heterogeneity and mesoscale weather systems (van der Laan et al., 2017; Peña et al., 2018). Not considering horizontal variability within large wind farms could lead to errors into the annual energy production and power density prediction calculation. For this reason, Ma et al. (2022) parameterized the Jensen wake model and implemented and inserted it into two commonly used atmospheric numerical models: the Weather Research and Forecasting (WRF) model and the Model for Prediction Across Scales (MPAS). In this implementation, the internal variability in wind speed and

direction within a wind farm can be considered. However, to implement this algorithm, an atmospheric modeling study needs to be carried out using WRF at a sub-km scale resolution that is cost prohibitive for this project.

Christiansen et al. (2022) described a very simplified, empirical way to calculate the downstream wind wake at the scale of wind farms (hereafter referred to as the Christiansen method) by making a “zero-order” approximation for wind farms in the German Bight that simplifies or neglects dependencies arising from specific wind turbines and wind farm characteristics, turbulence changes, and effects on within-farm weather conditions. This approach parameterized the wind speed deficits resulting from operating wind farms and reduced the mean wind speed in dependence of the respective wind direction. The wind velocity impacted by the wake effect was empirically described as a function of the downstream wind speed deficit:

$$u(x, y) = u_0(1 - \Delta u) \quad \text{Eq. 1}$$

where

x is the downstream distance aligned to the prevailing wind direction,

y defines the perpendicular distance from the central wake axis of a wind farm,

u_0 is the undisturbed or free-flowing (upstream) wind field, and

Δu is the downstream wind speed deficit.

The parameterization for the downstream wind speed reduction from the above equation, is generally based on earlier studies (Frandsen, 1992; Frandsen et al., 2006). It consists of two components describing the downstream wake recovery and the width of the wake structure.

The formulation of the downstream velocity deficit is based on the concept described by Emeis (2010) which is a top-down approach, i.e., each wind farm is considered as one unit of additional roughness and the wake recovery in the farm’s lee is represented using an exponential decay function. This model was validated in multiple studies, where it was depicted that the exponential approach can reproduce airborne measurements of atmospheric wakes fairly well at scale (Cañadillas et al., 2020; Platis et al., 2020, 2021). Christiansen’s method followed a similar exponential approach to formulate the wind speed deficits on the lee side of wind farms in the German Bight. In this approach the wind speed magnitude decreases the strongest close to the offshore wind farms and recovers exponentially over the downstream distance:

$$\Delta u(x) = \alpha e^{-x/\sigma} \quad \text{Eq. 2}$$

where

α is the maximum relative deficit

σ is the exponential decay constant, and

x is the downstream distance aligned to the prevailing wind direction.

As the model described by Emeis (2010) considers turbine wakes at hub height, Christiansen et al. (2022) made some modification to calculate the wake deficit α and the decay constant σ . The individual values for α and σ are determined by multiple factors such as the wind field, atmospheric stability, vertical momentum fluxes, wind farm density, and the wind turbine drag. As no empirical equation accounted for these factors for wind deficit and wake length, typical mean values for α and σ were selected, based on

values from some local studies in the German Bight (Table 9) and calculated statistics from Synthetic Aperture Radar (SAR) measurements (Figure 10, copied here).

Table 9. Compilation of wind speed deficit α and wake length σ from SAR observations and airborne measurements.

	Wake deficit α [%]	Wake length σ [km]
Cañadillas et al. (2020)	-	14–70
Christiansen and Hasager (2005, 2006)	8–9	5–20
Djath et al. (2018) and Djath and Schulz-Stellenfleth (2019)	5–10	30–60
Hasager et al. (2015)	-	15–70
Mean Value	8.0	35.5

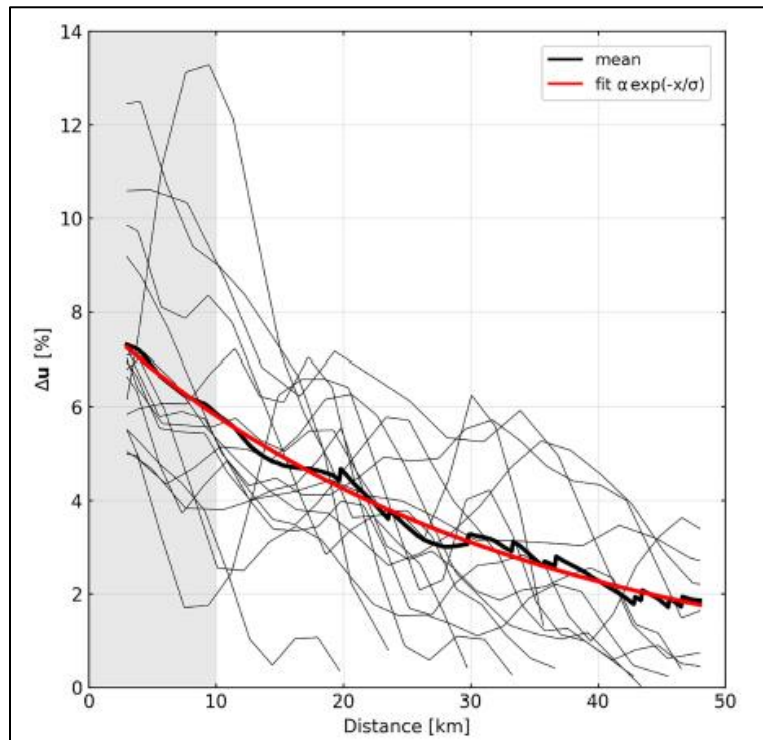


Figure 10. Velocity deficit curves derived from SAR observation for isolated wake cases at the Global Tech wind farm (thin grey lines).

Thick black line indicates the average velocity deficit, and the red curve represents the best fit, $\alpha=7.5\%$ and $\sigma=32\text{km}$. From Christiansen et al. (2022). Reproduced with permission.

The atmospheric wake has a cross-sectional shape which can be expressed by a symmetric exponential function (scaled by the characteristic wind farm width L). This function was also validated with airborne observation (Cañadillas et al., 2020). However, Djath and Schulz-Stellenfleth (2019) suggested that the cross-sectional shape of a wake at 10-m height is more distinguishable near the wake edges. For this reason, Christiansen et al. (2022) chose an exponential decay constant of $\gamma = L/3$, to narrow the wake cross section at sea surface height (in comparison with the hub height assumption) and proposed

$$\Delta u(y) = e^{-\left(\frac{y}{L}\right)^2}$$

Eq. 3

where

L is wind farm width, and

y defines the distance from the central wake axis.

Because of this simplistic approach, the Christiansen et al. (2022) algorithm might be considered an efficient way to calculate the wake impacted wind field at first order. However, this approach does not allow for the spatial variation of wake inside a windfarm, nor does it account for the modeling of the specific 15MW wind turbines considered in this project.

There are some software packages that allow calculation of wake interaction in a wind farm in a computationally tractable way for a range of steady state conditions. PyWake is a Python-based, open-source code developed at the Technical University of Denmark that can be used to compute the wake losses for a specific wind farm layout configuration, power production of individual turbines, as well as the Annual Energy Production (AEP) of a wind farm (Pedersen et al., 2023). PyWake is efficient in computing the wake propagation within a wind farm and can quantify the interaction between turbines. The code has a highly modular architecture (Figure 11) which enables the users to combine different AEP modelling blocks in different ways which, in turn, allows building a sophisticated model that can simulate real-world problems more accurately. As this approach provides copious options to build a highly customized model, the user needs to be diligent in terms of selecting the models.

FLow Redirection and Induction in Steady State (FLORIS) is another Python based open-source wind plant optimization tool developed by National Renewable Energy Laboratory (NREL) and Delft University of Technology with support from the U.S. Department of Energy Wind Energy Technologies Office. This software incorporates steady-state wake models (Jensen 1983, Bastankhah and Porté-Agel, 2014, Niayifar and Porté-Agel, 2016) into a performance-focused Python framework, similar to PyWake.

Beside the open-source software mentioned above, there exist commercial software tools for wind resource assessment, such as WAsP (Wind Atlas Analysis and Application Program, Technical University of Denmark, Wind and Energy Systems, based on original work by Troen and Petersen, 1989). WAsP can be used for all kinds of terrain and provides models and tools for every step in the process of calculating the energy yield for a wind farm. WAsP also facilitates calculation of wind farm efficiency, wind resource and turbulence mapping over selected areas, computation of the mutual wake effects between the turbines in a wind farm, and siting of wind turbines and wind farms (Katic et al., 1986). However, calculating the wake effects for multiple big windfarms over a large area is onerous to accomplish through WAsP. Because the software creates only output of one wind turbine at a time, calculating the modified wind field for all the turbines in all the windfarms, for every timestep and for all downstream space, takes a lot of manual effort.

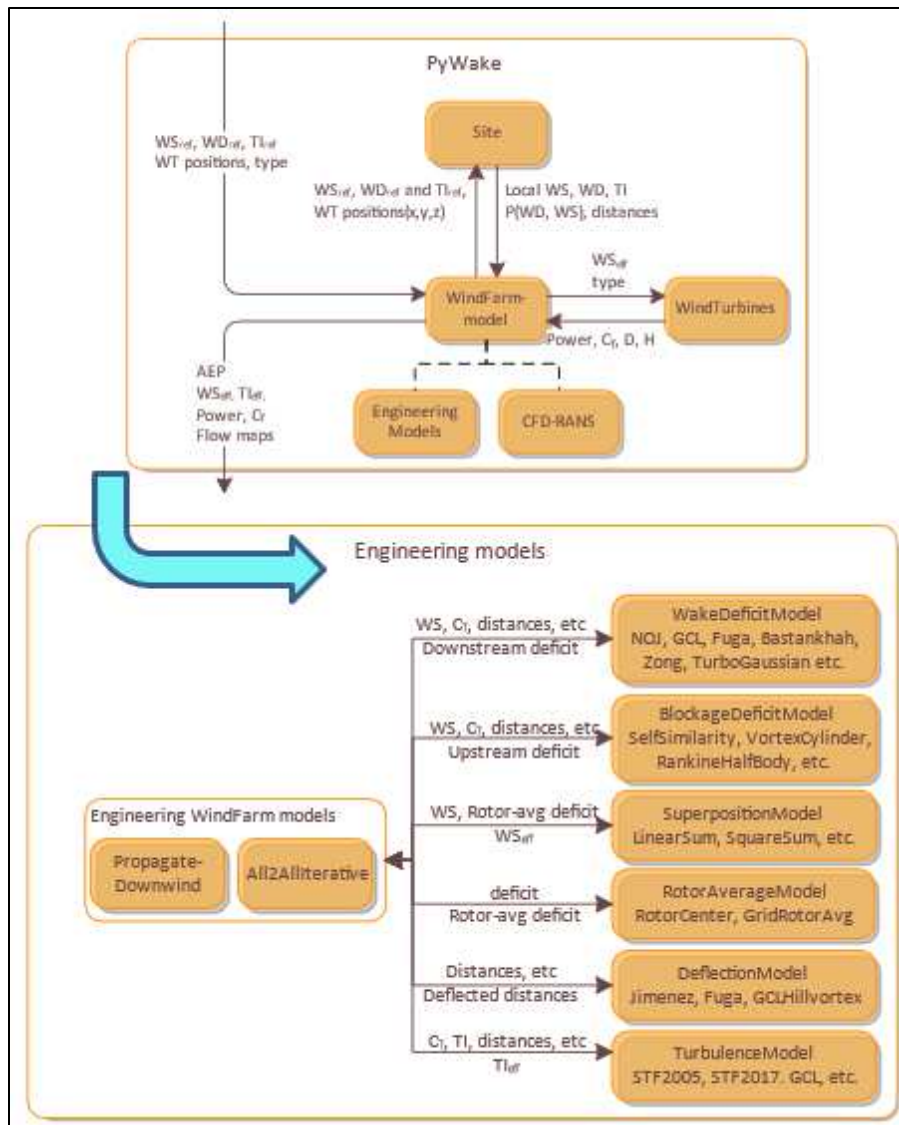


Figure 11. Modular architecture of PyWake.

Source: <https://topfarm.pages.windenergy.dtu.dk/PyWake/notebooks/Overview.html>

In summary, although CFD frameworks such as RANS models can calculate the wind wake effect, they are computationally uneconomic. Coupling hydrodynamics to very high-resolution meteorological model simulation—for example building and coupling to a high-resolution WRF model—can investigate turbine interactions that go beyond the primary effect of wind reduction (e.g., as it pertains to changes in heat fluxes) offering a comprehensive solution but similarly remain computationally very expensive on the scales considered in this project (NAS 2023). On the other hand, 0-order approaches such as the Christiansen model can be highly efficient but also highly simplified and specific to the availability of SAR data, not available for this study as the wind farms considered are yet to be built. As a result, an analytical approach facilitated by an open-source tool—PyWake (Pedersen et al., 2023)—was selected for this project. PyWake is computationally efficient and able to capture the wind wake (wind reduction) in the leeward side of a wind turbine (Pedersen et al., 2022). This tool also has a modular architecture which also enables its users to combine different modelling blocks in different ways, in turn allowing the construction of a sophisticated model.

4.2 PyWake Validation Setup

To build the wind farms setup within the PyWake framework, multiple wind turbine parameters such as power, hub-height, and rotor diameter are required. Also, appropriate PyWake parameters such as computational grid domain, wind-deficit models, and available engineering wind farm models were analyzed for an accurate simulation. To test these parameters, a cluster of hypothetical wind turbines near the North Carolina coastline was imported and set up in PyWake (Figure 12). In the following discussion results are provided based on these experiments. Once these experiments were completed, the parameters were applied to the other wind farms (with different size and layout) in the AOI.

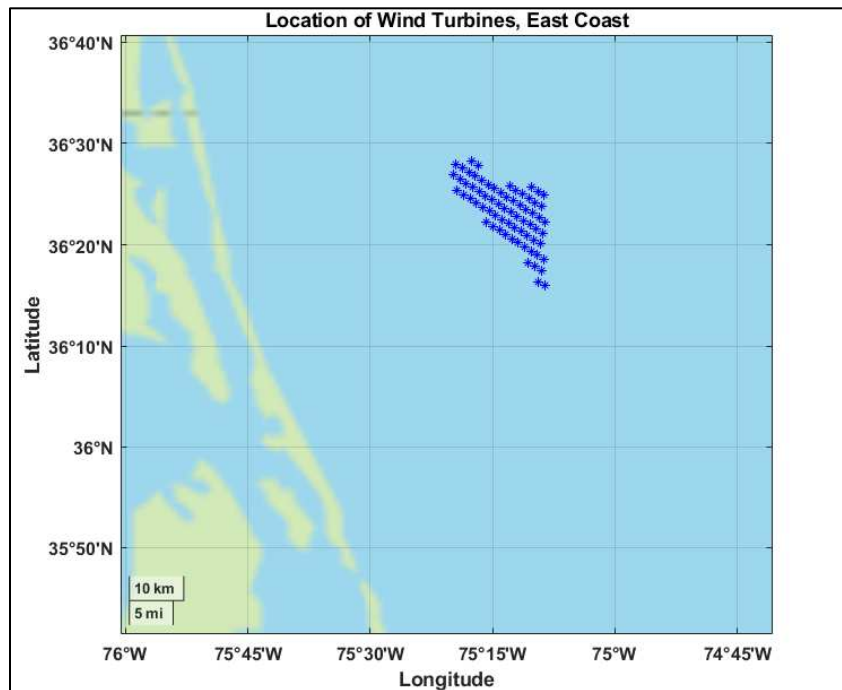


Figure 12. Location and layout of hypothetical wind farm used in PyWake analysis.

4.3 Specification of Reference Wind Turbine

For the simulation, wind turbine specifications were selected based on a reference turbine which was developed by a joint effort of National Renewable Energy Laboratory (NREL), Technical University of Denmark (DTU), and University of Maine (UMaine) (Gaertner et al., 2020). This offshore wind turbine has a rated capacity of 15-MW, has hub-height and rotor diameter of 150 m and 240 m respectively, and is supported by a fixed-bottom monopile structure (Table 10). For input in PyWake, the turbine's speed, generator power (violet curve in the upper panel of Figure 13) and thrust coefficient (red curve in the lower panel of Figure 13) were used (along with hub-height and rotor diameter) from the reference turbine.

Table 10. Physical dimensions of reference wind turbine (NREL 15MW).

Item	Description	Dimension
Turbine Hub Height	The average height of wind turbine above water surface.	150 m
Turbine tower diameter	The tower diameter was enhanced with marine growth to increase the diameter and increase hydrodynamic roughness.	10 m with 10 cm marine growth added
Turbine tower scour protection diameter	Scour protection was simulated around the base of the turbine tower monopile.	50 m
Turbine tower scour protection height	Scour protection was simulated around the base of the turbine tower monopile and had a height above the surrounding seabed.	1 m
Rotor swept diameter	Rotor diameter is used in the wind wake loss calculations.	240 m
Cut-in wind speed	Cut-in wind speed is used in the wind wake loss calculation.	3 m/s
Cut-out wind speed	Cut-out wind speed is used in the wind wake loss calculation.	25 m/s

The power coefficient, (Figure 13), is a measure of the efficiency with which a wind turbine converts kinetic energy in the wind to electrical power within its operational range. It indicates how effectively a turbine can extract energy from the wind, bound by the theoretical Betz limit of 0.593. The thrust coefficient, (Figure 13), is a measure of the axial force exerted by the wind on the rotor blades. Figure 13 defines how the wind turbine is expected to operate between its operational wind speed range. In Region 1.5 (3 m/s to about 7 m/s) the efficiency of the turbine as measured by increases toward its expected maximum, 0.489, which it attains in Region 2 (about 7 m/s to 11 m/s). As winds exceed that speed, in Region 3, the turbine's controller starts pitching its blades from 0° to about 22° toward the 25 m/s cut-out wind speed maintaining maximal design rotor speed, saturated generator torque, and 15 MW rated power generation (Gaertner et al., 2020) while avoiding overspeed and excessive stress and damage. The rotor thrust, thrust coefficient, and the effectiveness of the conversion of available wind energy to power decrease monotonically as a result in that Region.

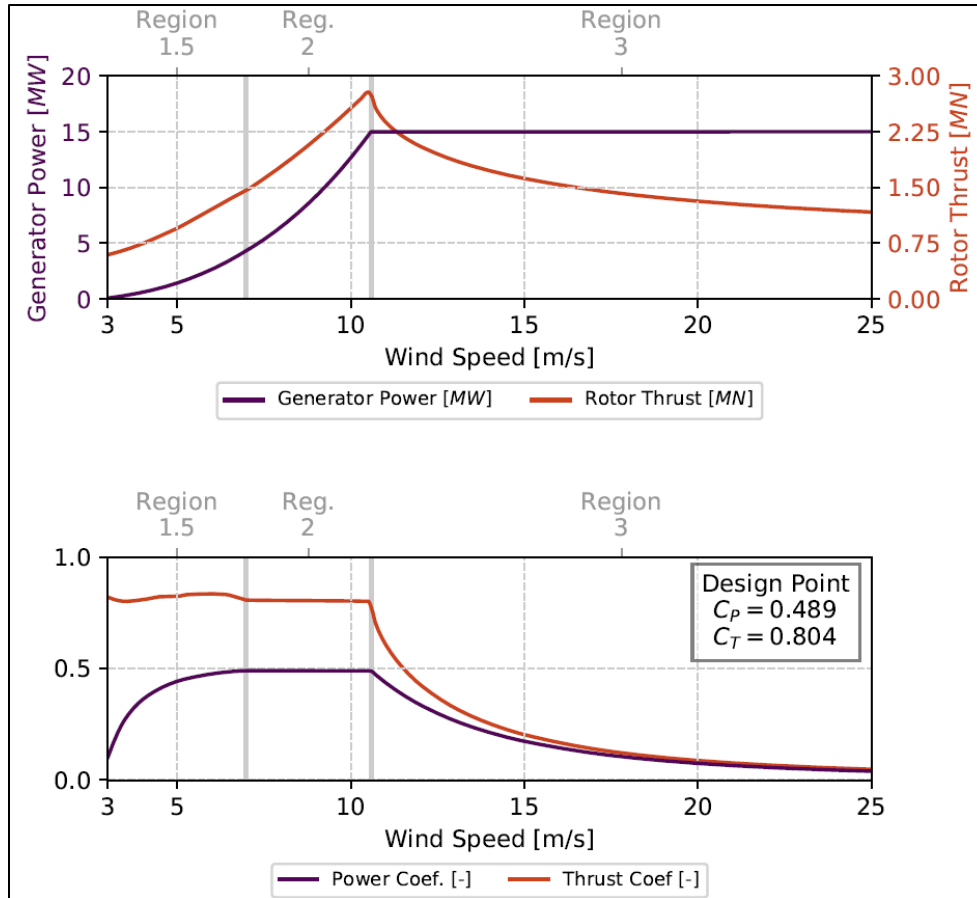


Figure 13. Power and thrust curve (upper panel) and aerodynamic thrust coefficient (lower panel) for NREL 15 MW reference turbine. Modified from Gaertner et al., 2020.

4.4 Selection of Wind Deficit Model

One of the main components of PyWake modular architecture is the Wake Deficit Model that computes the wake deficit caused by a single wind turbine. Although there are multiple deficit models available for use in PyWake, most of them are known to underpredict the wake. Fischereit et al. (2021) compared various approaches to calculate the wake effect and found that RANS and WRF models performs better compared to PyWake models in terms of capturing the wake from an upstream wind farm. To address this, Pedersen et al. (2022) developed a new wake model (Turbo Gaussian Deficit), to accurately capture both internal wind farm wakes and cluster wakes from neighboring wind farms extending over long distances. In our analysis, we compared this newly developed model with the other models discussed in Fischereit et al. (2021) and verified that the Turbo Gaussian Deficit is the best model to capture the expansion of the wind wake in the downstream direction of the wind farm. The wake-analysis was done both at the hub-height of 150 m elevation (Figure 14) and 10 m elevation (Figure 15).

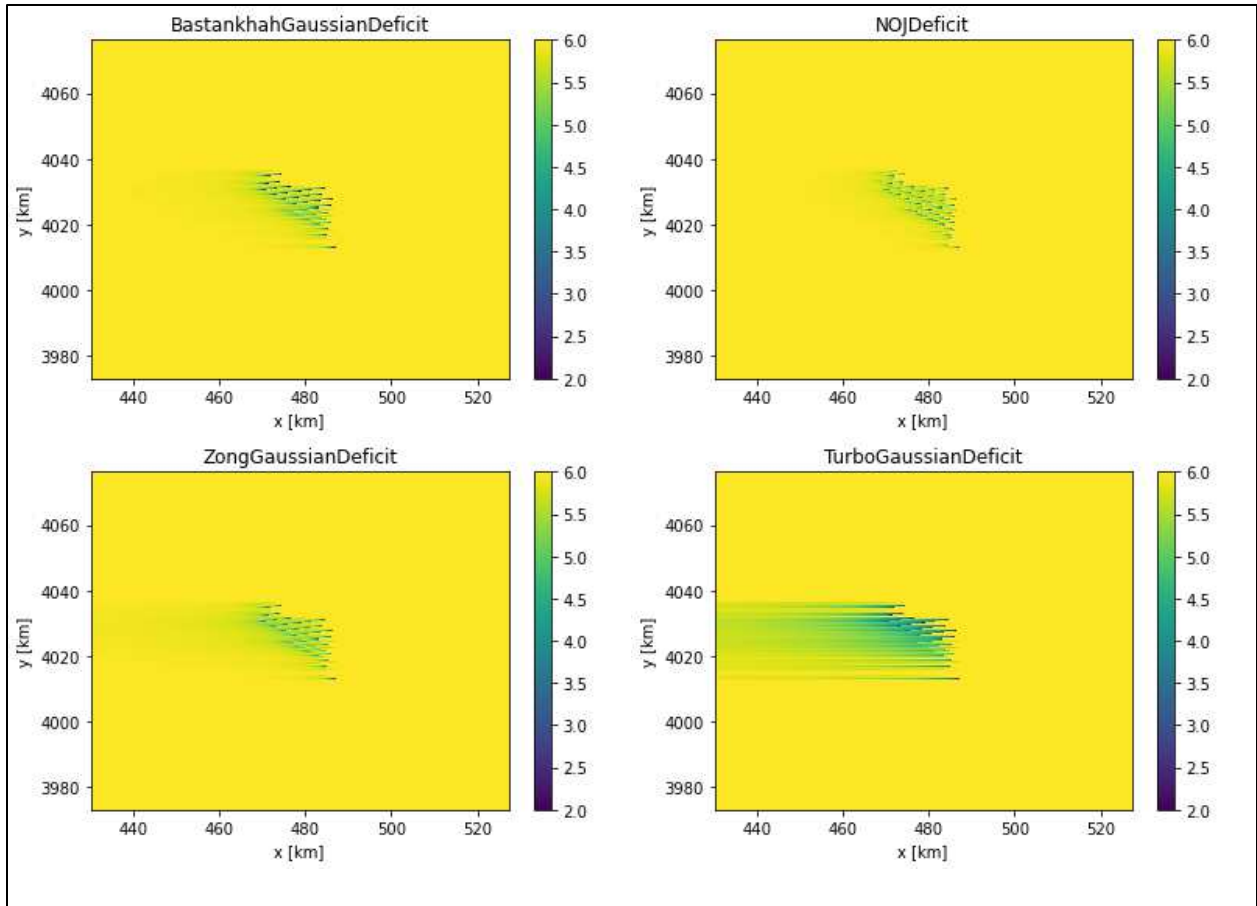


Figure 14. Example comparison of applying different Wind Deficit Models to capture wind wake expansion at the hub-height of the turbine (150 m). Wind units are m/s. Incident wind westward.

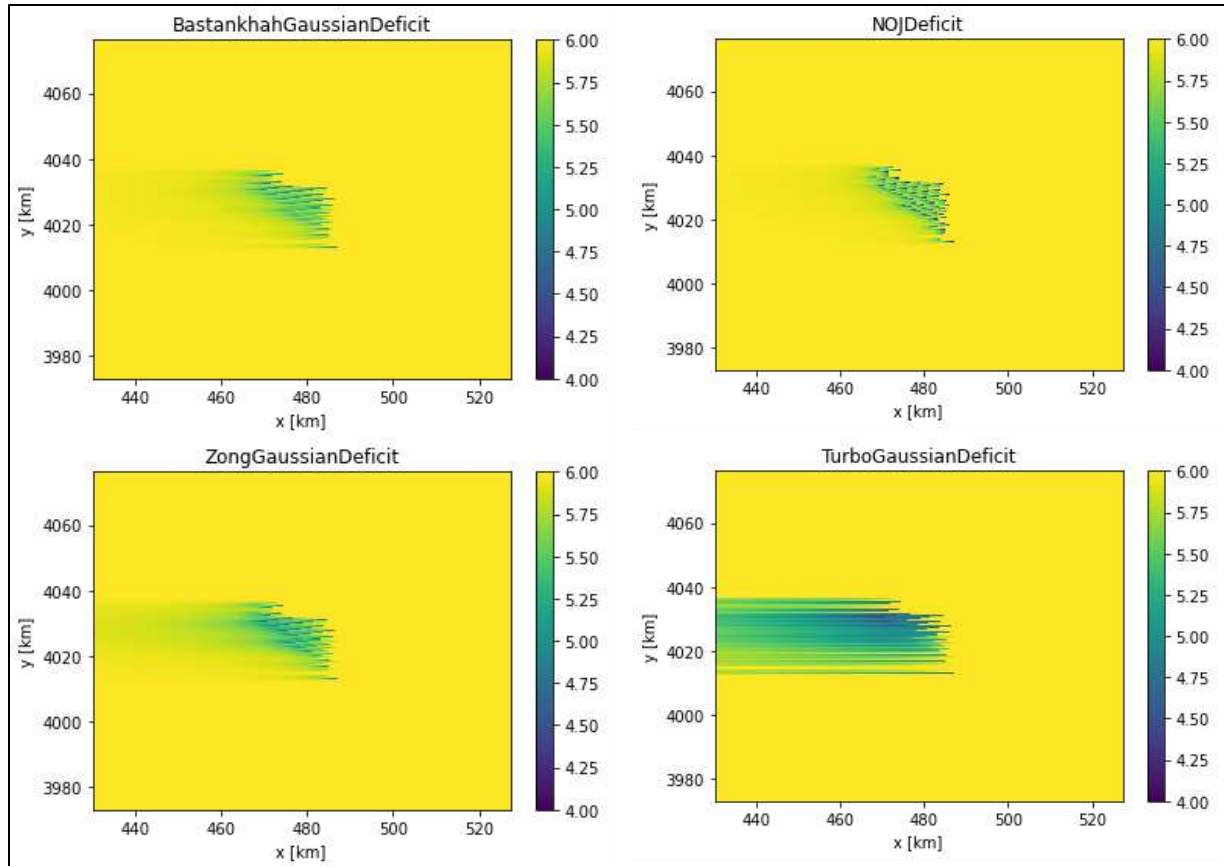


Figure 15. Example comparison of applying different Wind Deficit Models to capture wind wake expansion at 10 m elevation above surface. Wind units are m/s.

4.5 Selection of Engineering Wind Farm Models

The engineering wind farm models provide two different approaches to calculate wind deficit – PropagateDownwind and All2AllIterative. The PropagateDownwind wind farm model is presumably faster, as it performs a minimum of deficit calculations by iterating over all turbines in downstream order. In each iteration it calculates the effective wind speed at the current wind turbine as the free stream wind speed minus the sum of the deficit from upstream sources. Based on this effective wind speed, it computes the deficit caused by the current turbine on all downstream locations. On the other hand, All2AllIterative is presumably slower as in each iteration it sums up the deficit from all wind turbine sources and calculates the deficit caused by all wind turbines on all wind turbines (Pedersen et al., 2023). For this study, both approaches were compared to see how they impact the simulation result assuming spatially invariant upstream wind input. For a constant speed of 6 m/s, the freestream inflow wind direction was varied at the turbine hub-height (Figure 16, Figure 17, Figure 18) and at 10 m elevation (Figure 19 and Figure 20). Based on the wake maps shown, both engineering wind farm models resulted in the same solution at all wind directions.

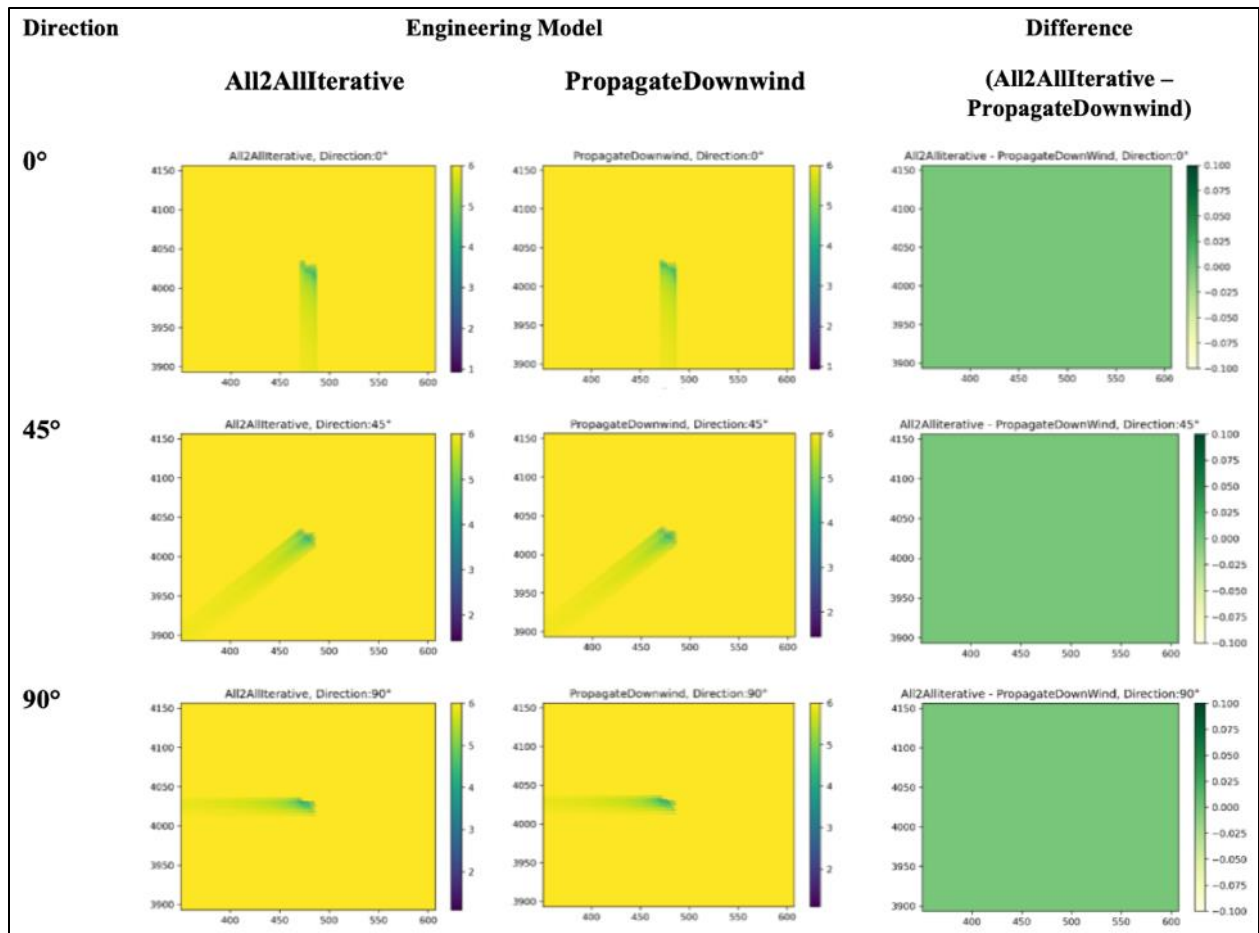


Figure 16. Comparison of engineering wind farm models at hub-height (direction 0°, 45°, and 90°). Axes units in km. All wind units are m/s.

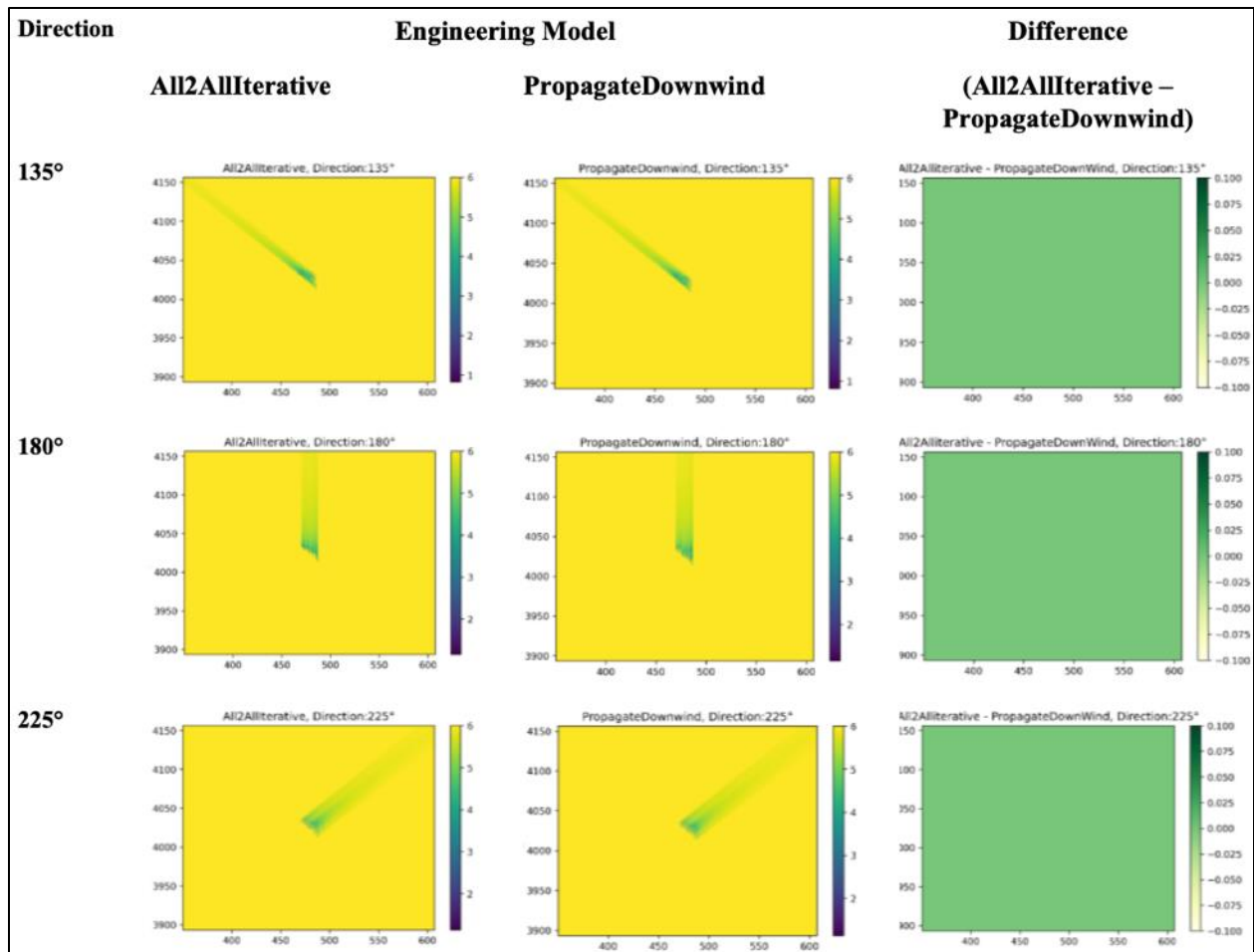


Figure 17. Comparison of engineering wind farm models at hub-height (direction 135°, 180°, and 225°). Axes units in km. All wind units are m/s.

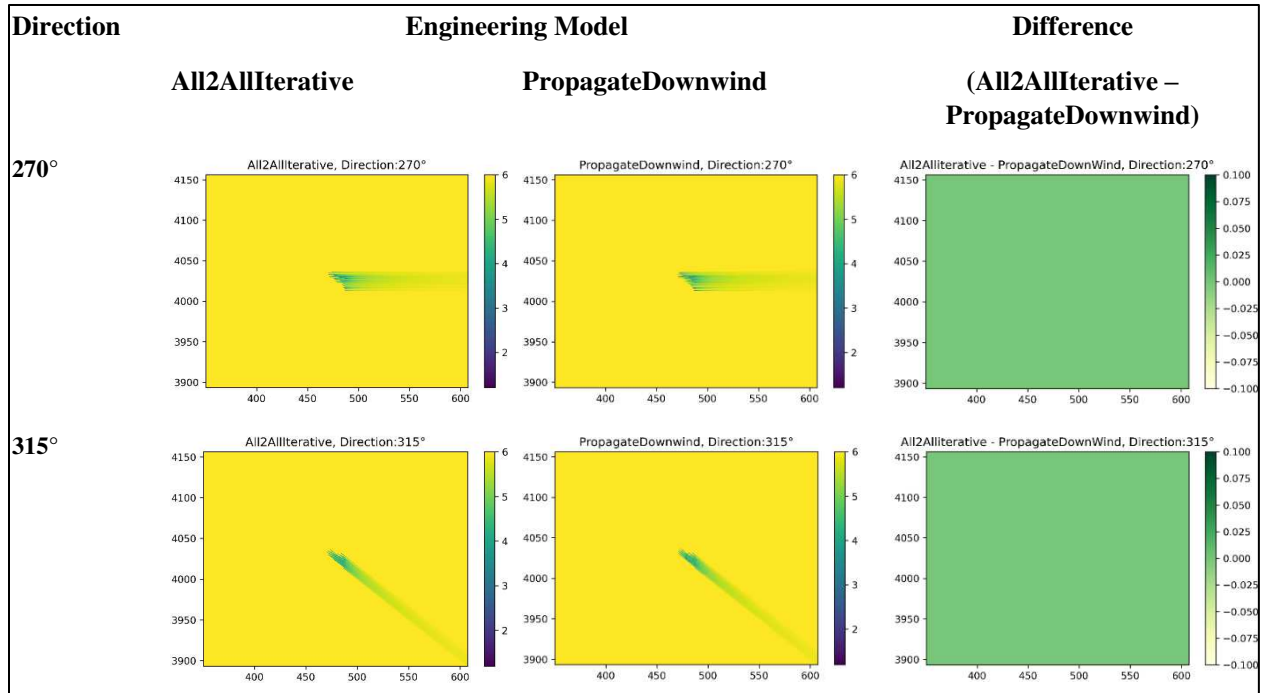


Figure 18. Comparison of engineering wind farm models at hub-height (direction 270° and 315°). Axes units in km. All wind units are m/s.

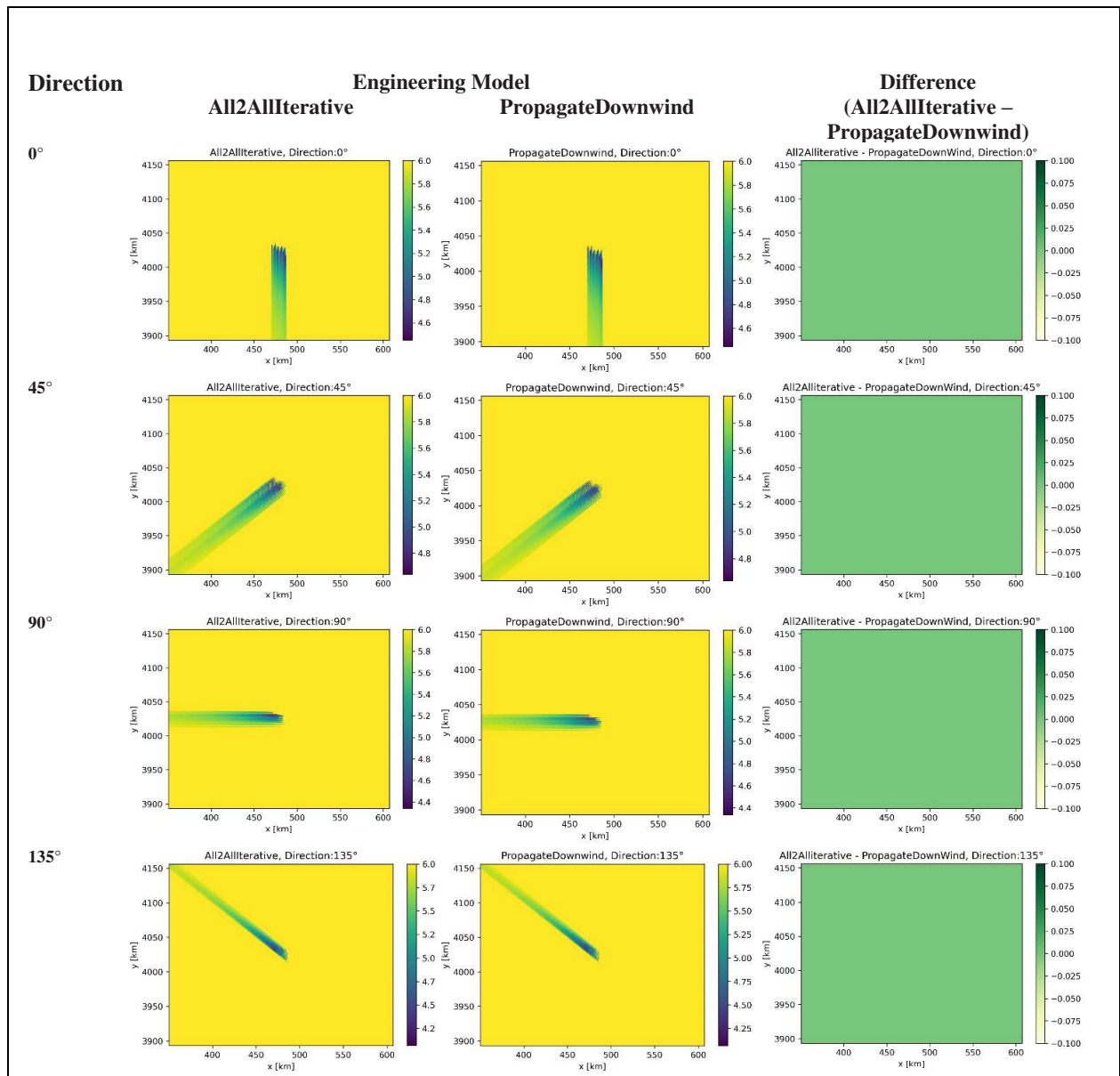


Figure 19. Comparison of engineering wind farm models at 10 m elevation (direction 0°, 45°, 90°, and 135°). Axes units in km. All wind units are m/s.

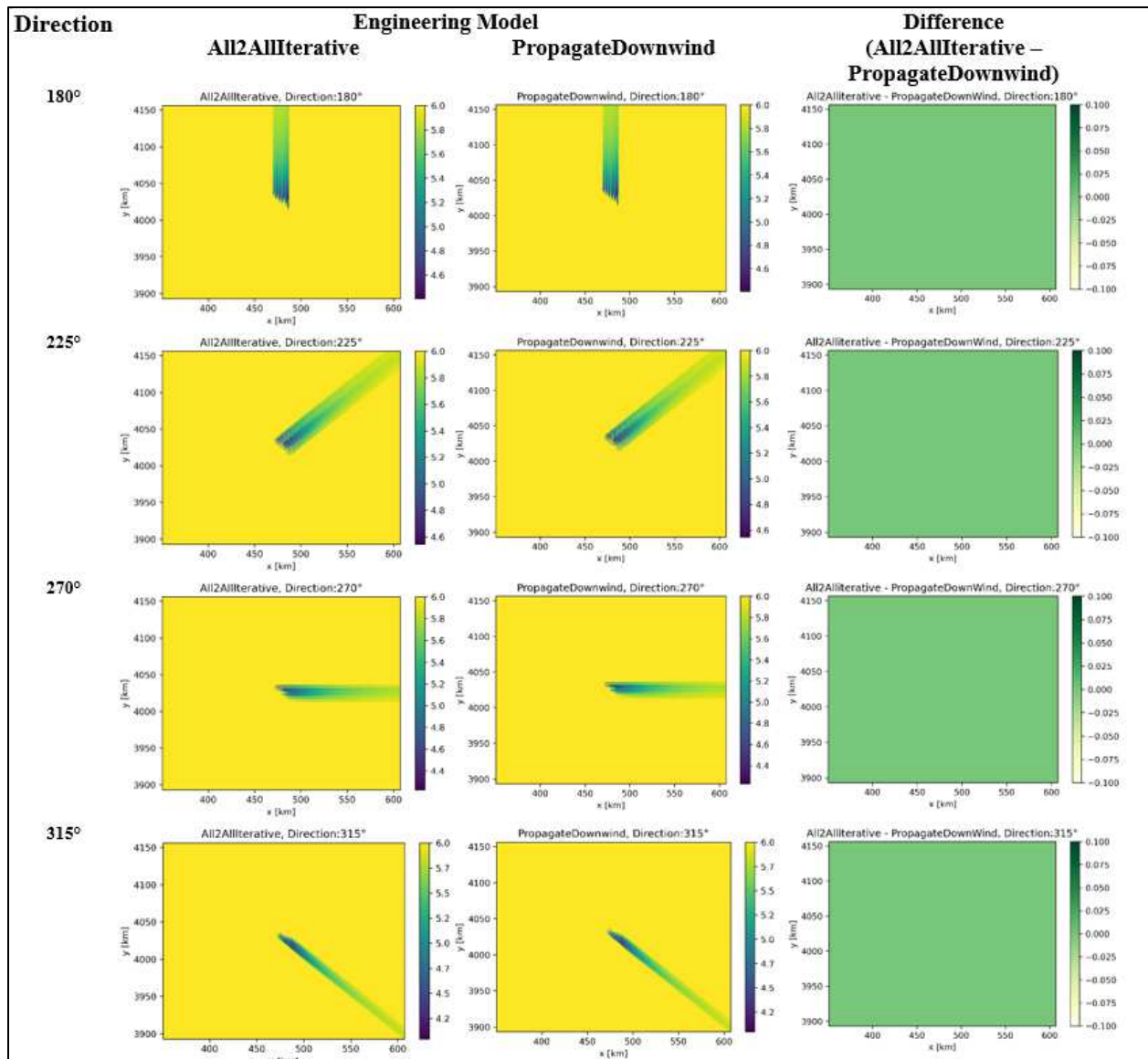


Figure 20. Comparison of engineering wind farm models at 10 m elevation (direction 180°, 225°, 270°, and 315°).

Axes units in km. All wind units are m/s.

The simulation time for each of the directions were also compared for All2AllIterative and PropagateDownwind wind farm models (Figure 21). No significant difference was found in terms of computational expense between the two models in this setting. It is hypothesized that the All2AllIterative model may provide better results, at a higher computational cost, in later implementations of the PyWake model that may enable robust import of spatially variable wind fields into PyWake. Therefore, All2AllIterative is used.

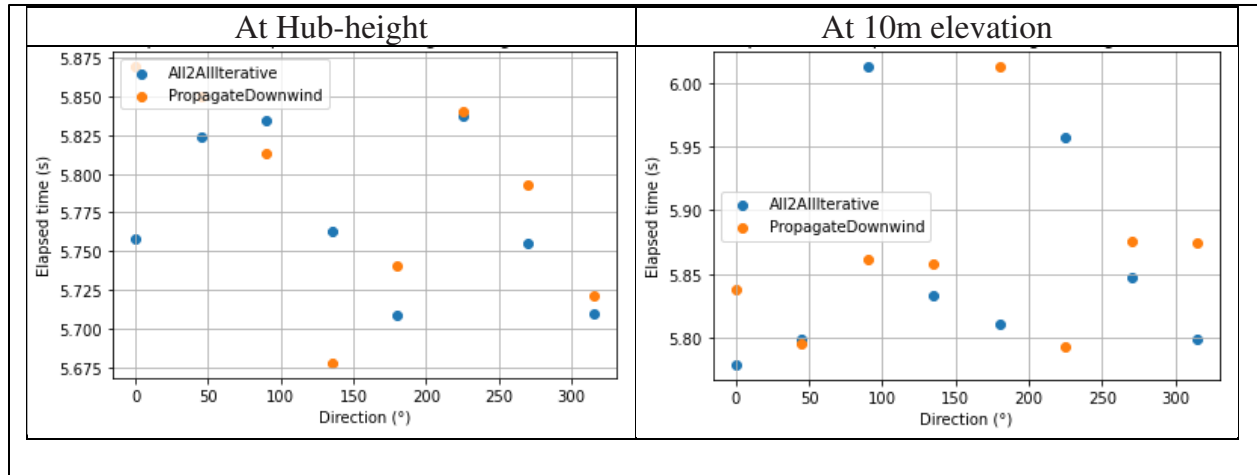


Figure 21. Comparison of simulation time for different engineering wind farm models at different wind direction at hub-height (left panel) and at 10 m elevation (right panel).

4.6 Selection of Resolution of Computational Grid

In order to capture the wake inside the wind farm, the resolution of the computational grid was analyzed. The minimum distance between two adjacent turbines in the simulation was approximately 1km, so multiple values smaller than 1 km were tested as spatial resolution in the model domain at hub height (Figure 22) and at 10 m elevation (Figure 23). Based on this analysis, the grid with 250m resolution captures the wake better than 500 m grid. However, the grids with finer resolutions (< 250 m) do not show significant improvement over 250 m grid, as expected for turbines with 240 m rotor diameter. As expected, the higher the resolution, the slower the runtime.

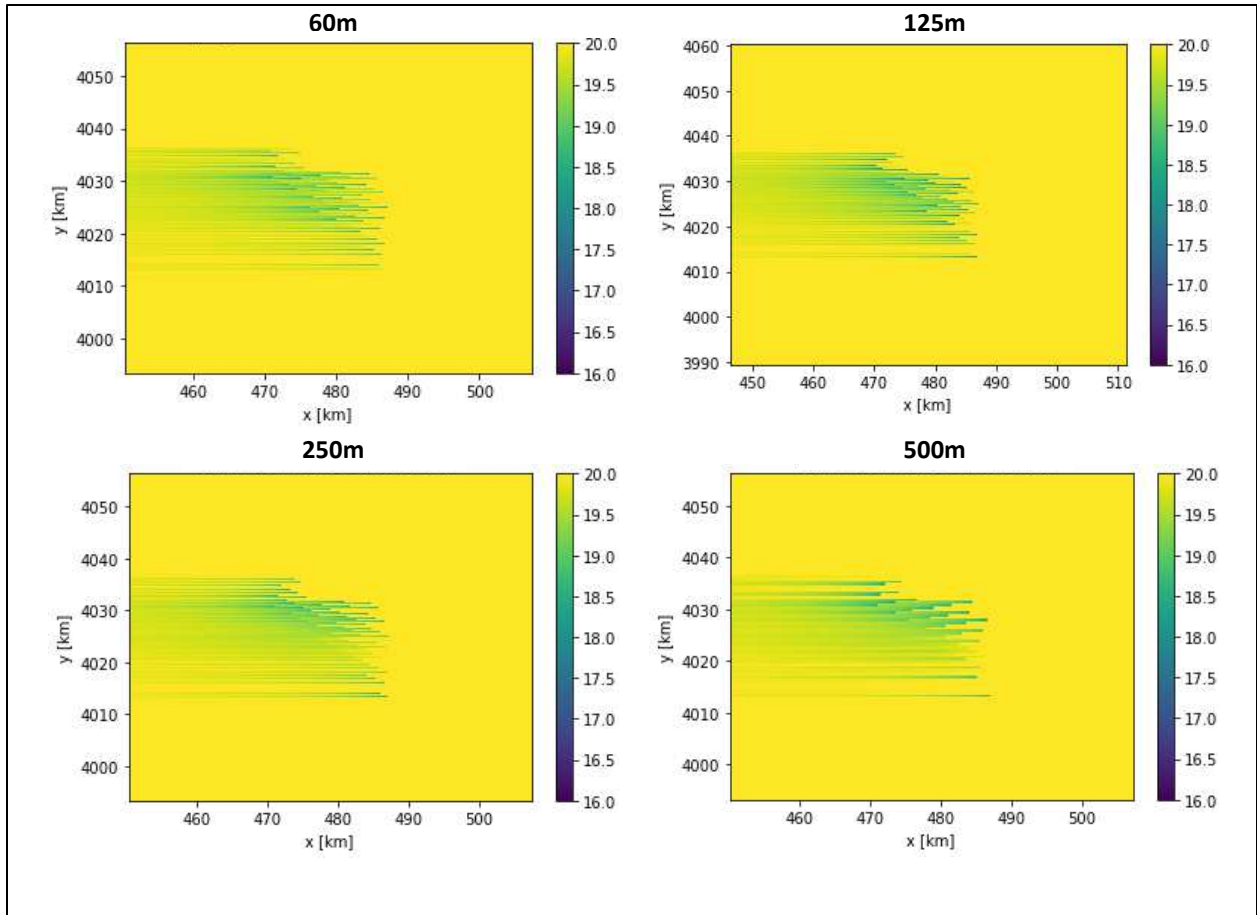


Figure 22. Comparison of different grid resolutions at turbine hub-height. All wind values are in m/s.

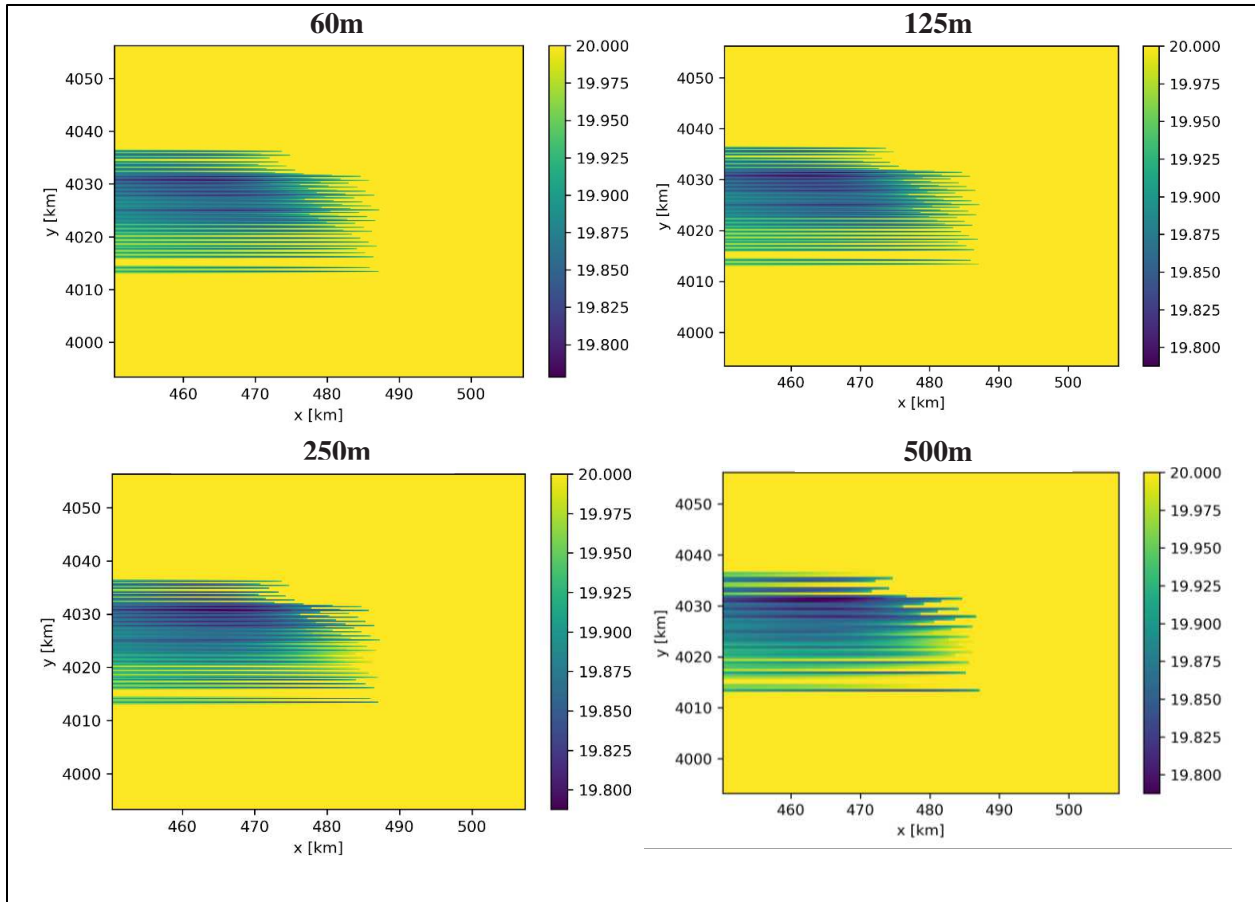


Figure 23. Comparison of different grid resolutions at 10 m elevation. All wind values are in m/s.

4.7 Impact of Wind Speed on Wake

To understand and validate how the maximum reduction of wind speed changes with free-stream inflow speed in PyWake given the wind turbine specifications from Section 4.3, the wind wake was simulated for different wind speeds in-between the cut-in and cut-off (25 m/s) speeds at the hub-height (Figure 24 to Figure 27) and 10 m elevation (Figure 28 to Figure 30). The wind speed reduction at lower speeds (3–11 m/s) is higher inside the wind farm compared to higher speeds. The scale in each panel varies individually between the maximum (free) and minimum calculated wind speeds within the domain. In this context, the figures clearly illustrate that the reduction in wind speed, for instance, from 14 m/s free speed to around 10 m/s, is much smaller compared to the reduction from 9 m/s free speed to approximately 1 m/s.

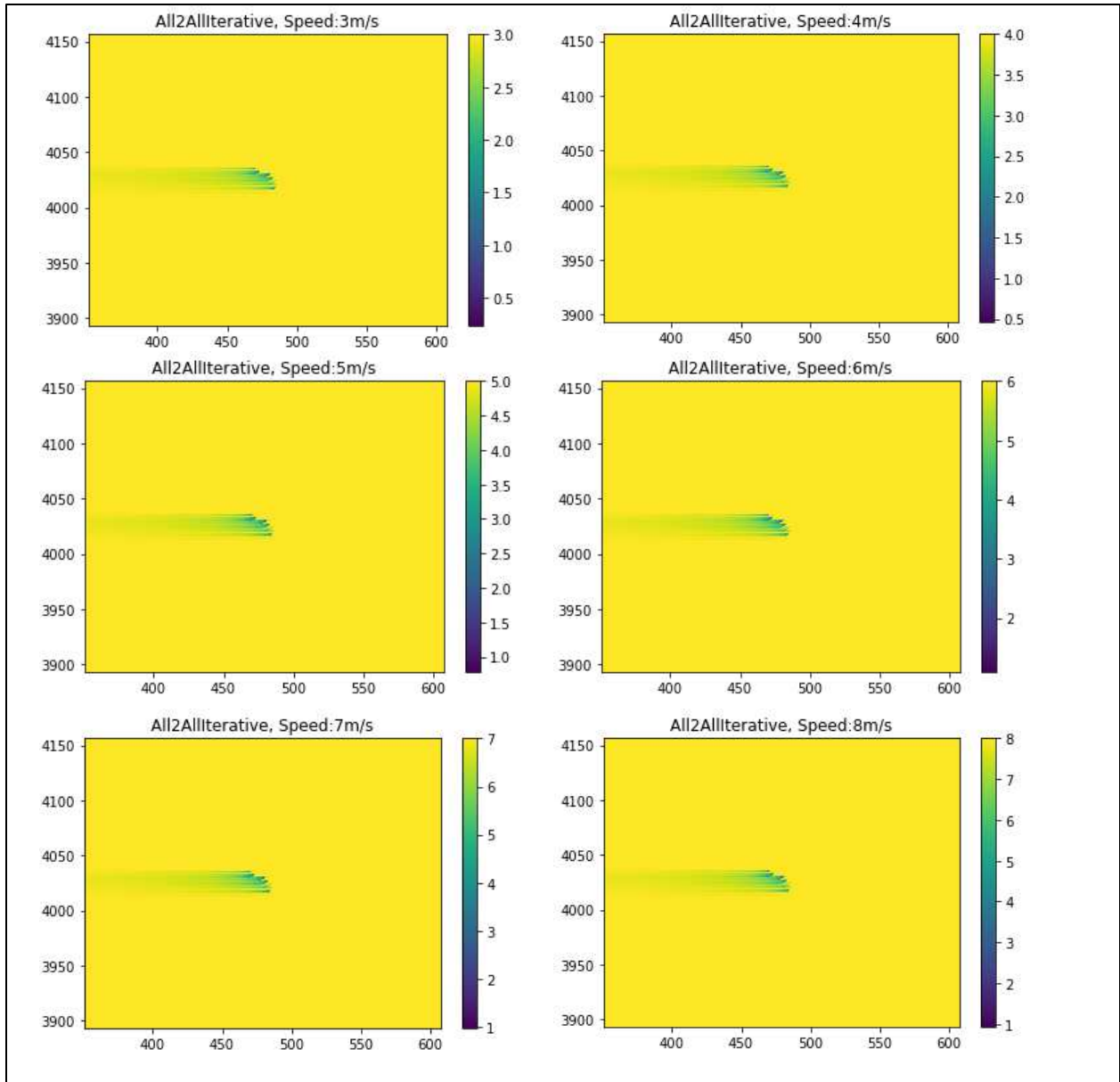


Figure 24. Comparison of wind wake for different free-stream inflow speeds (3–8 m/s) at the hub-height. Axes units in km. All wind units are m/s.

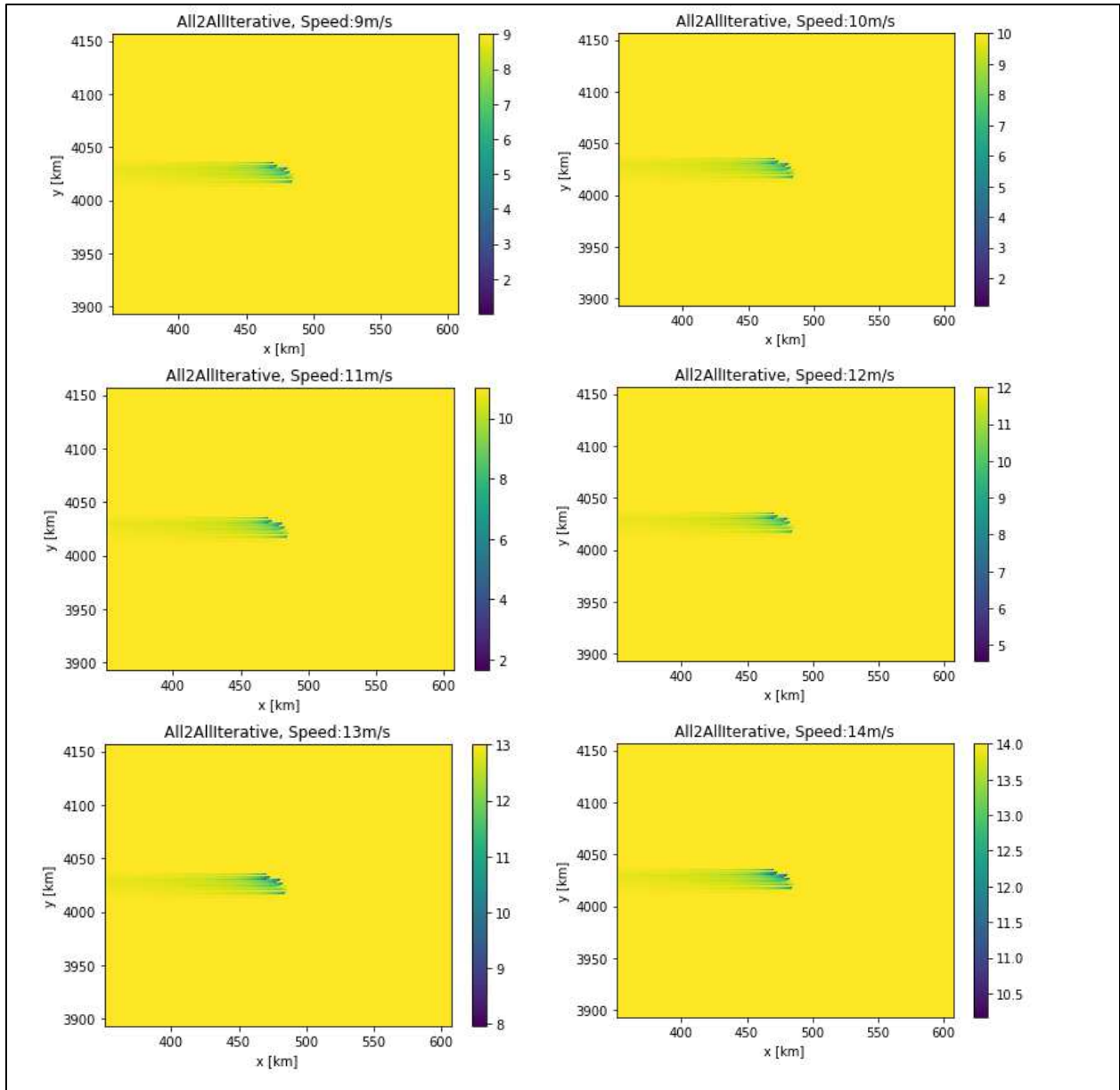


Figure 25. Comparison of wind wake for different free-stream inflow speeds (9–14 m/s) at the hub-height. Axes units in km. All wind units are m/s.

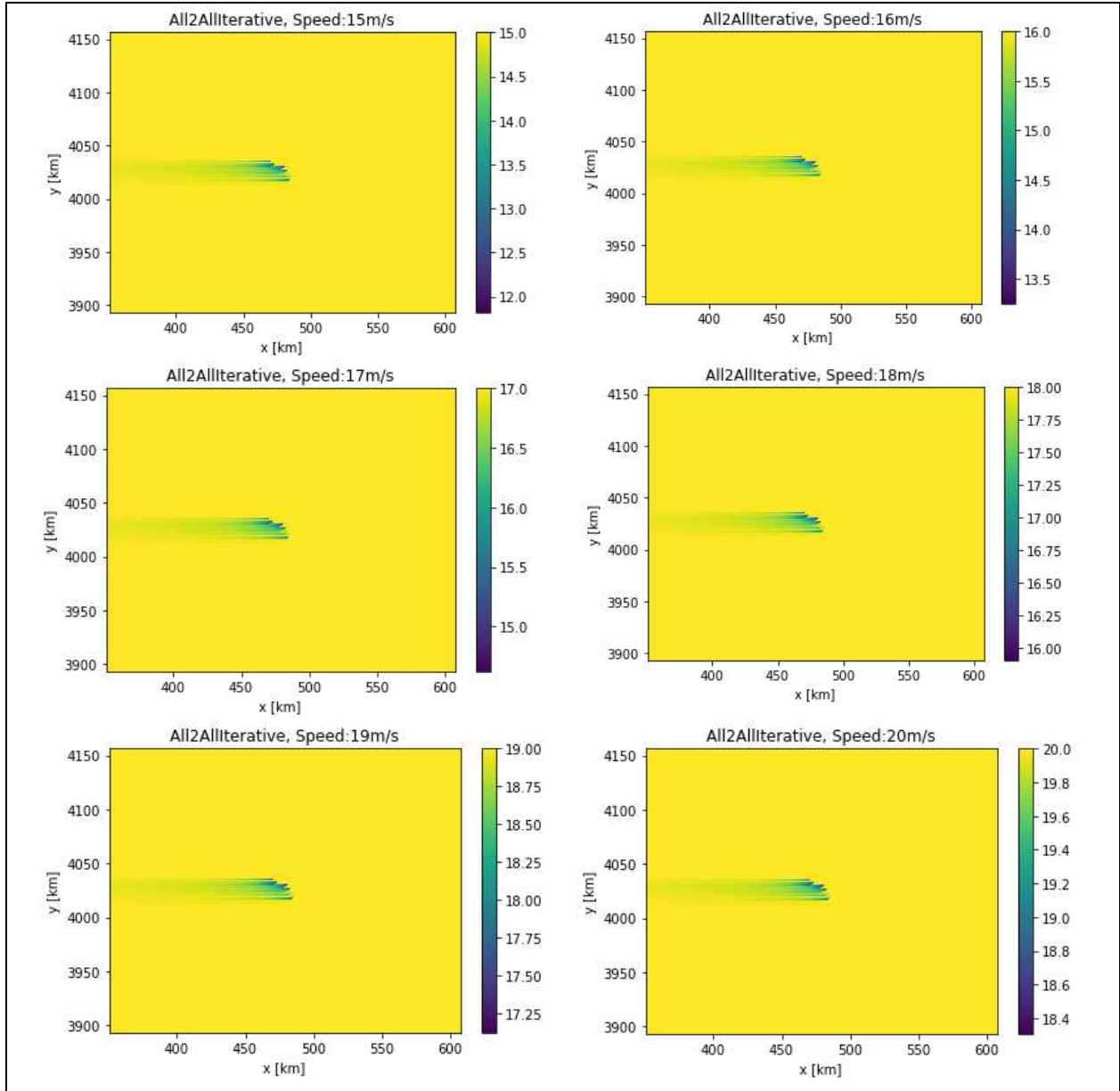


Figure 26. Comparison of wind wake for different free-stream inflow speeds (15–20 m/s) at the hub-height. Axes units in km. All wind units are m/s.

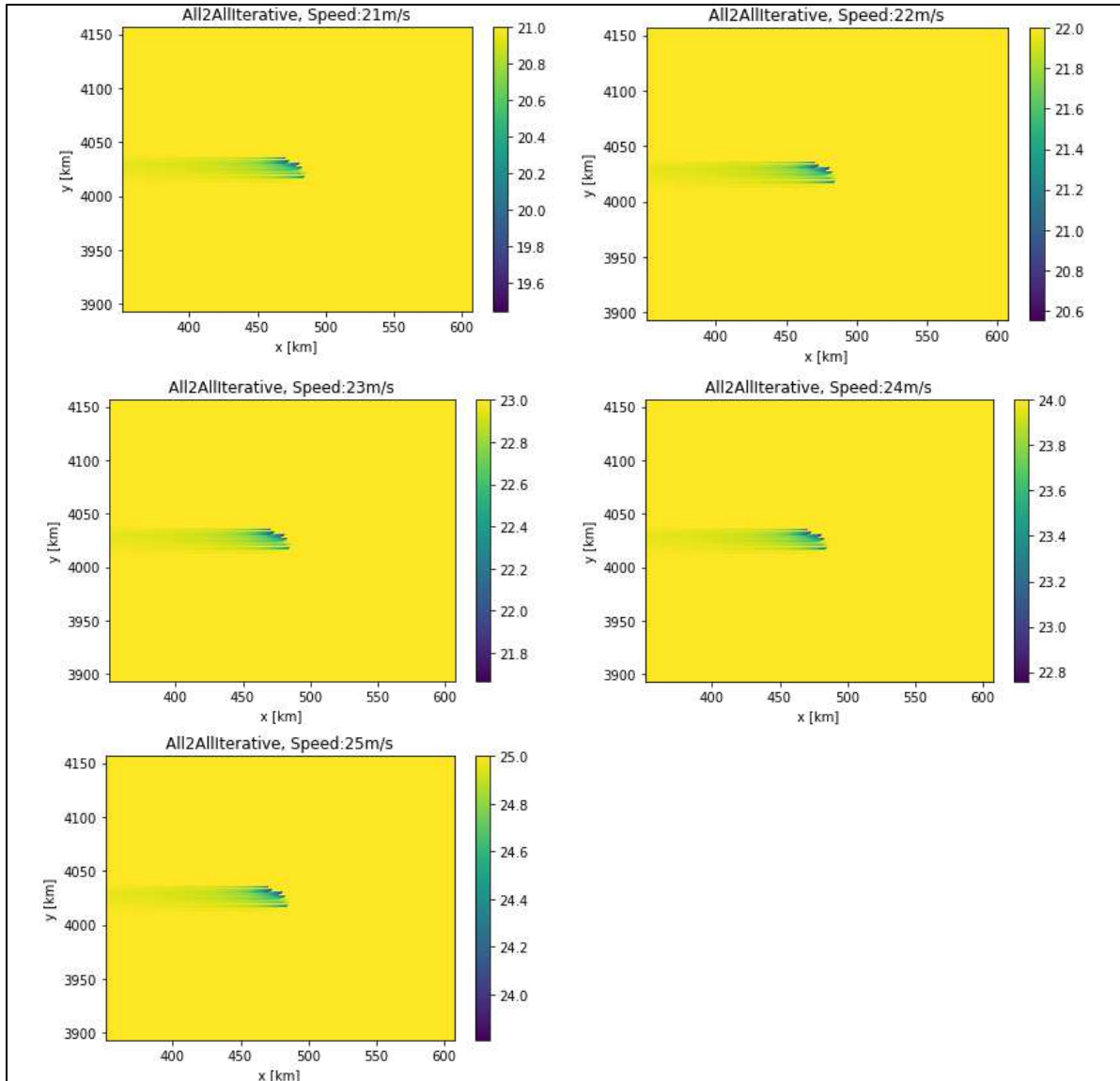


Figure 27. Comparison of wind wake for different free-stream inflow speeds (21–25 m/s) at the hub-height. Axes units in km. All wind units are m/s.

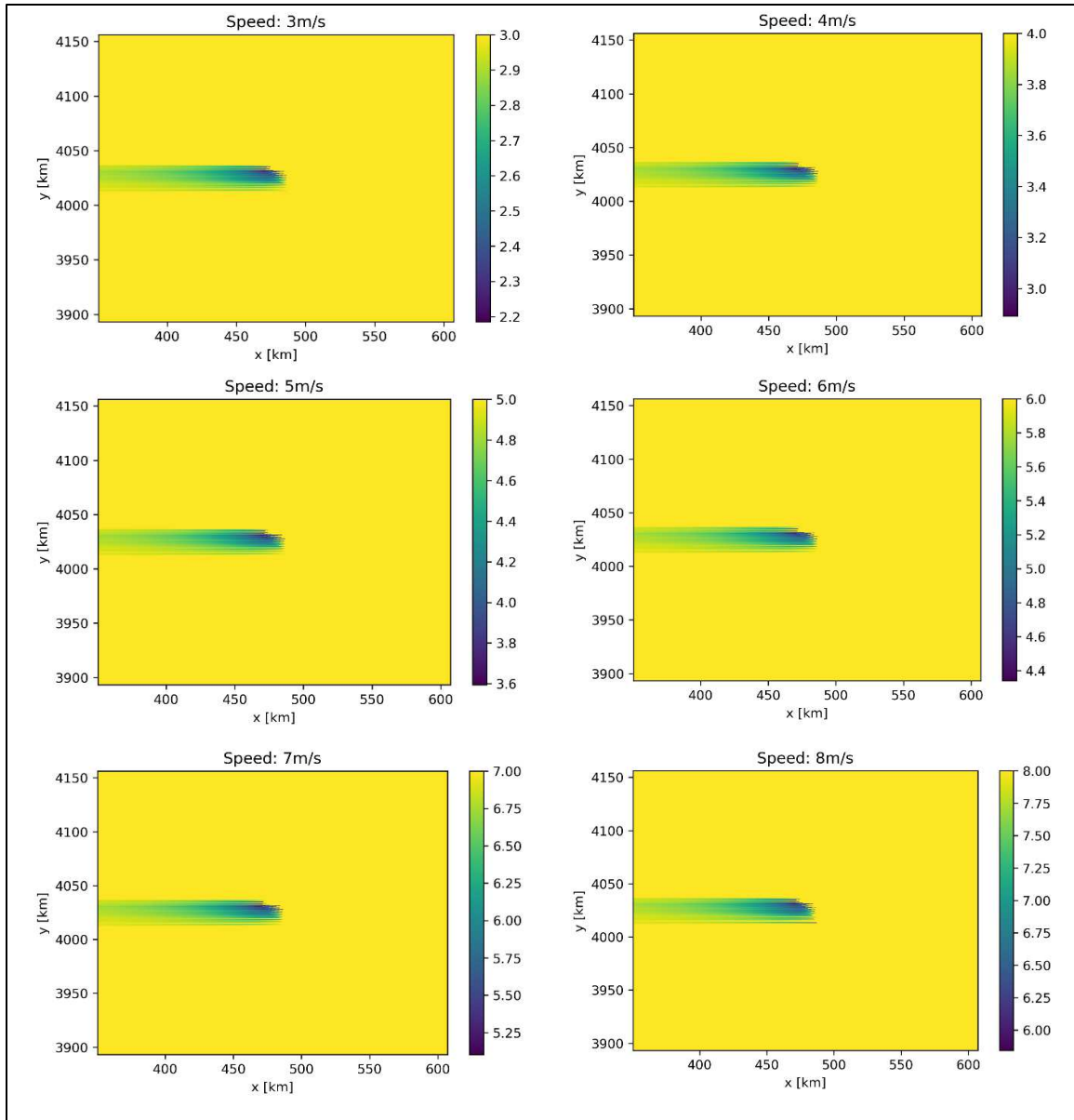


Figure 28. Comparison of wind wake for different free-stream inflow speeds (3–8 m/s) at 10 m elevation. Axes units in km. All wind units are m/s.

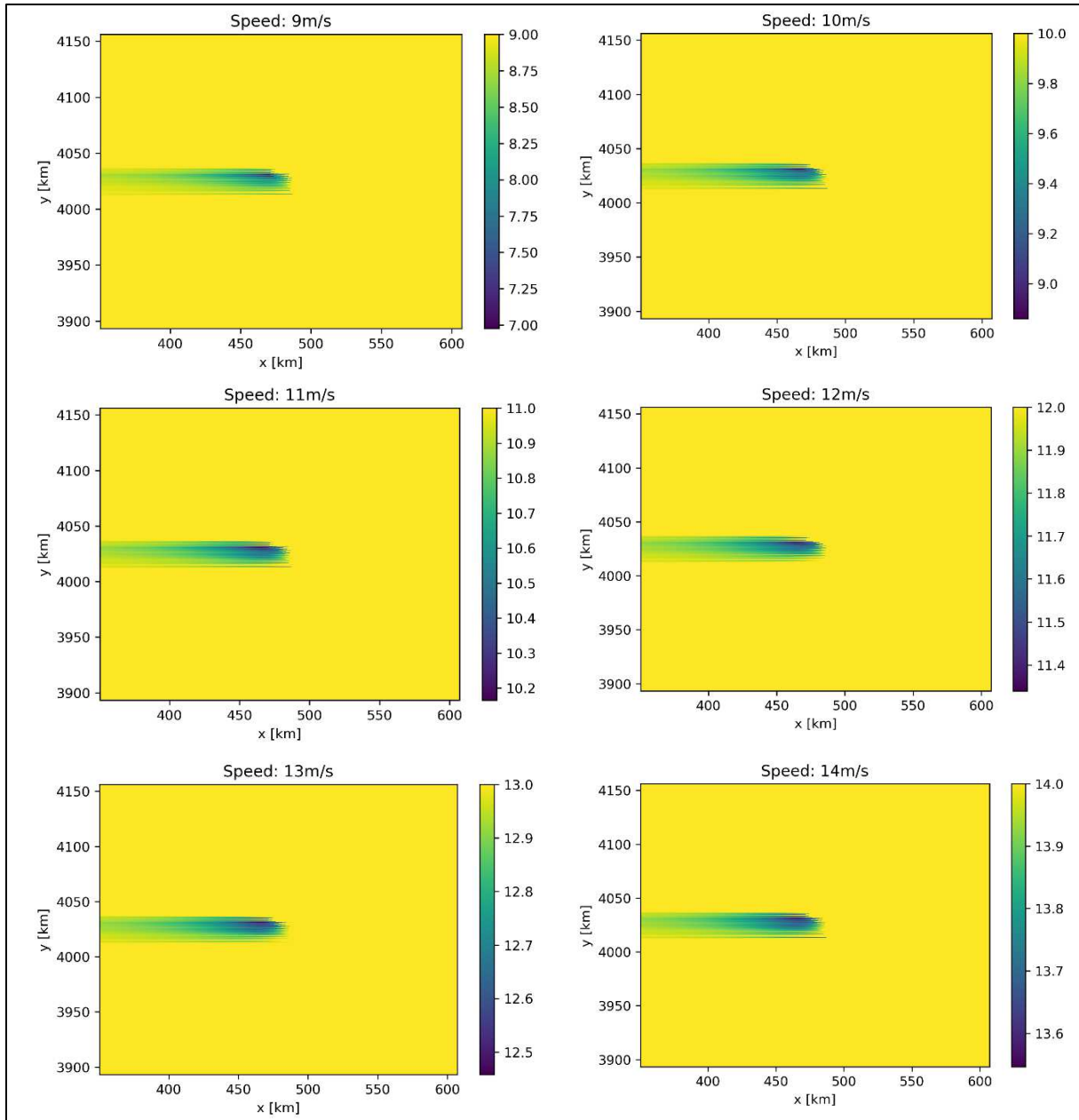


Figure 29. Comparison of wind wake for different free-stream inflow speeds (9–14 m/s) at 10 m elevation. Axes units in km. All wind units are m/s.

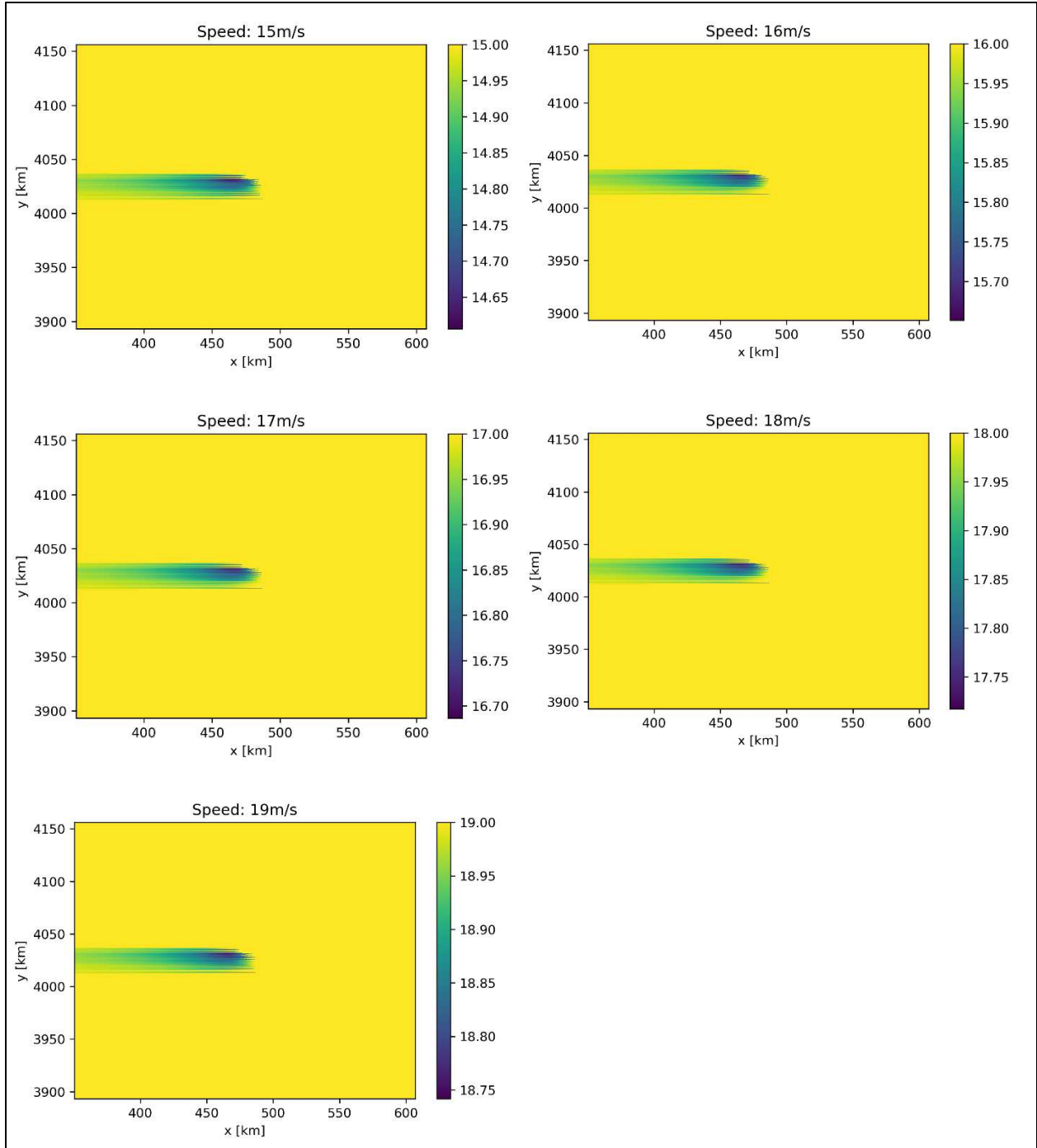


Figure 30. Comparison of wind wake for different free-stream inflow speeds (15–19 m/s) at 10 m elevation. Axes units in km. All wind units are m/s.

Wind speed deficits (wake-associated % reduction) at hub-height both at the western boundary of the model domain and inside the windfarm were calculated as the ratio of the resulting wind speed divided by the free stream (equal to inflow) wind speed. Figure 31 shows that from 3–11 m/s, the wind speed deficit is high. However, when wind speed exceeds about 11 m/s, the deficit decreases rapidly. When the speed reaches 20 m/s, the deficit is relatively much smaller. This trend of wind reduction follows well the thrust coefficient (CT) curve shown in (Figure 13, lower panel), which also has an inflection point around 11m/s free stream speed, above which a stand-alone reference wind turbine is expected to be generating maximum (15MW) power (Figure 13, upper panel).

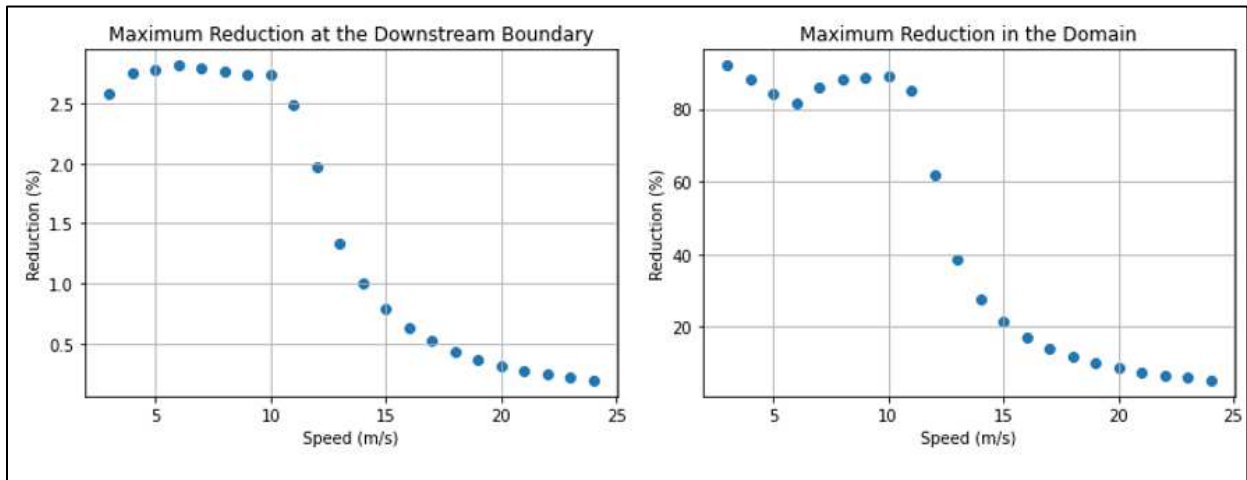


Figure 31. Comparison of hub-height wind speed reduction (see Figure 24 to Figure 27) at the downstream boundary on the west (left panel) and maximum wind speed reduction inside the windfarm (right panel) with different free-stream inflow speeds. Both are given as percent from free-stream speed.

Figure 32 shows mean wind speed deficit (wake-associated % reduction) at 10m elevation at the western edge of the wind turbine clusters. The change of mean reduction with different speeds also shows the same pattern as the maximum deficit (Figure 31) and the thrust coefficient curve.

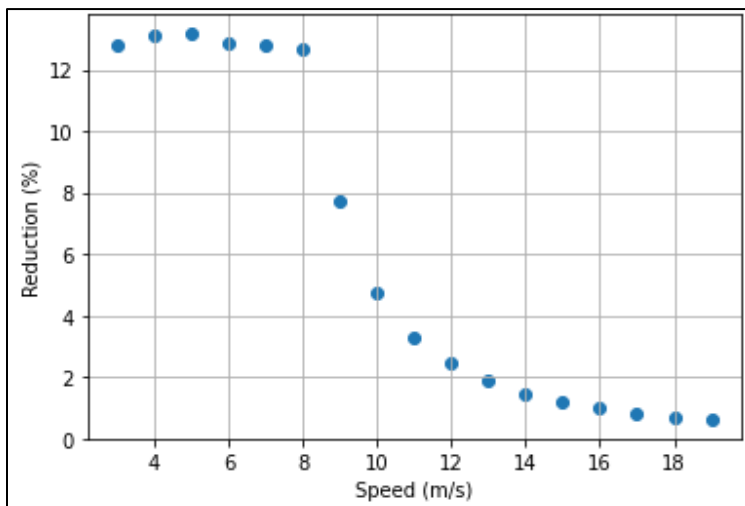


Figure 32. Comparison of 10-m elevation mean wind speed deficit (% reduction, see Figure 28 to Figure 30) at the downstream edge of the wind turbine clusters with different free-stream inflow speeds at 10 m elevation.

4.8 Impact of Computational Domain Extension on Wake

As the deficit at the downstream boundary is maximum between 3 and 11 m/s (Figure 31), the size/extent of the computational grid was analyzed by using a free-stream inflow speed of 6 m/s varying the distance between the boundary of the domain and the nearest turbine. By extending the computational domain, PyWake was able to capture most of the wake-affected zone and the wind recovery increased at the downstream boundary with increasing clearance between wind farm and boundary: Figure 33 is for winds at hub height, while Figure 34 is for winds at 10 m above surface. Please note change in colorbar scale.

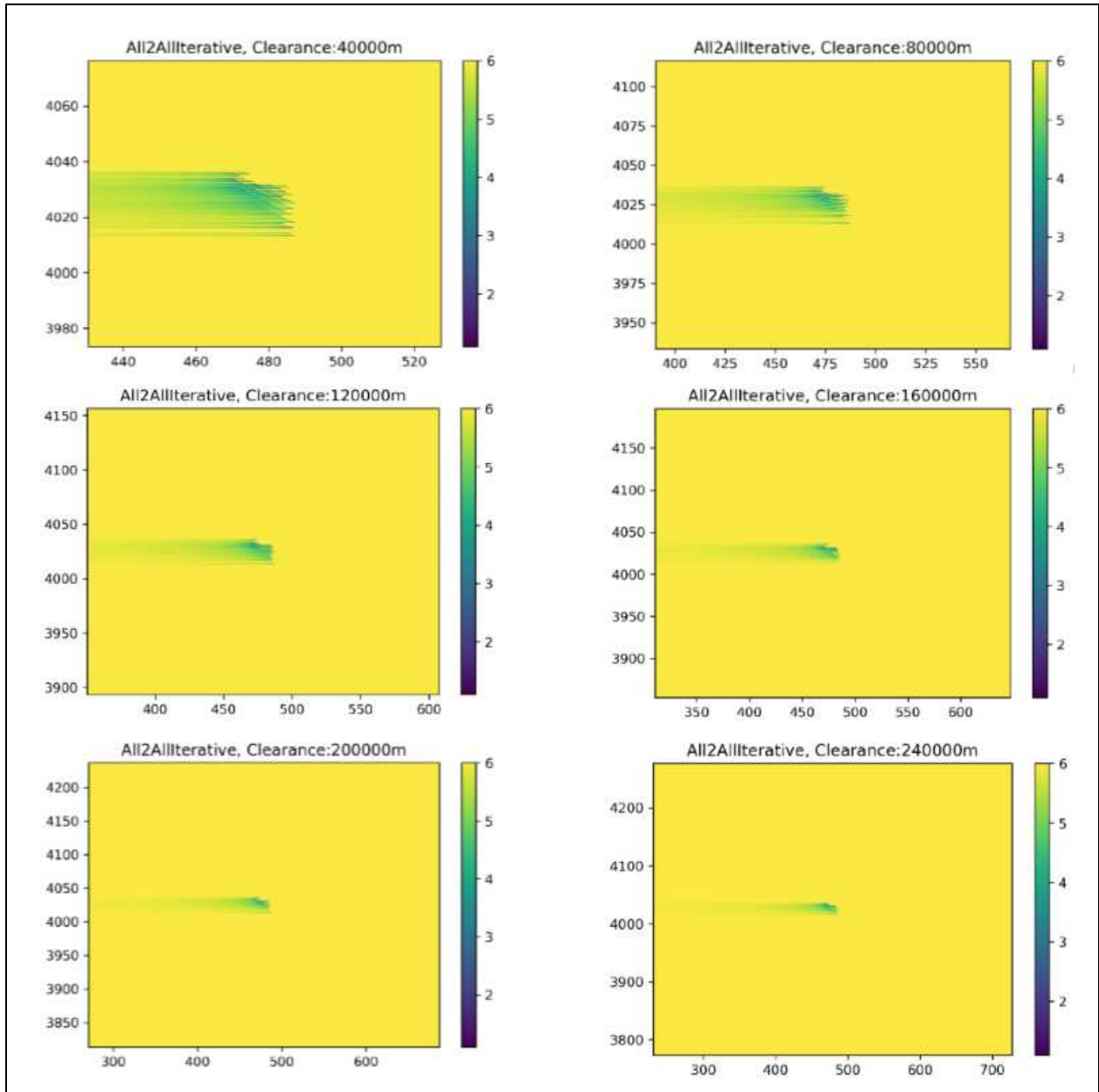


Figure 33. Comparison of wind speed reduction (at hub-height) at the downstream boundary on the west with different clearance distance (between wind farm and the boundary). Axes units in km. All wind units are m/s.

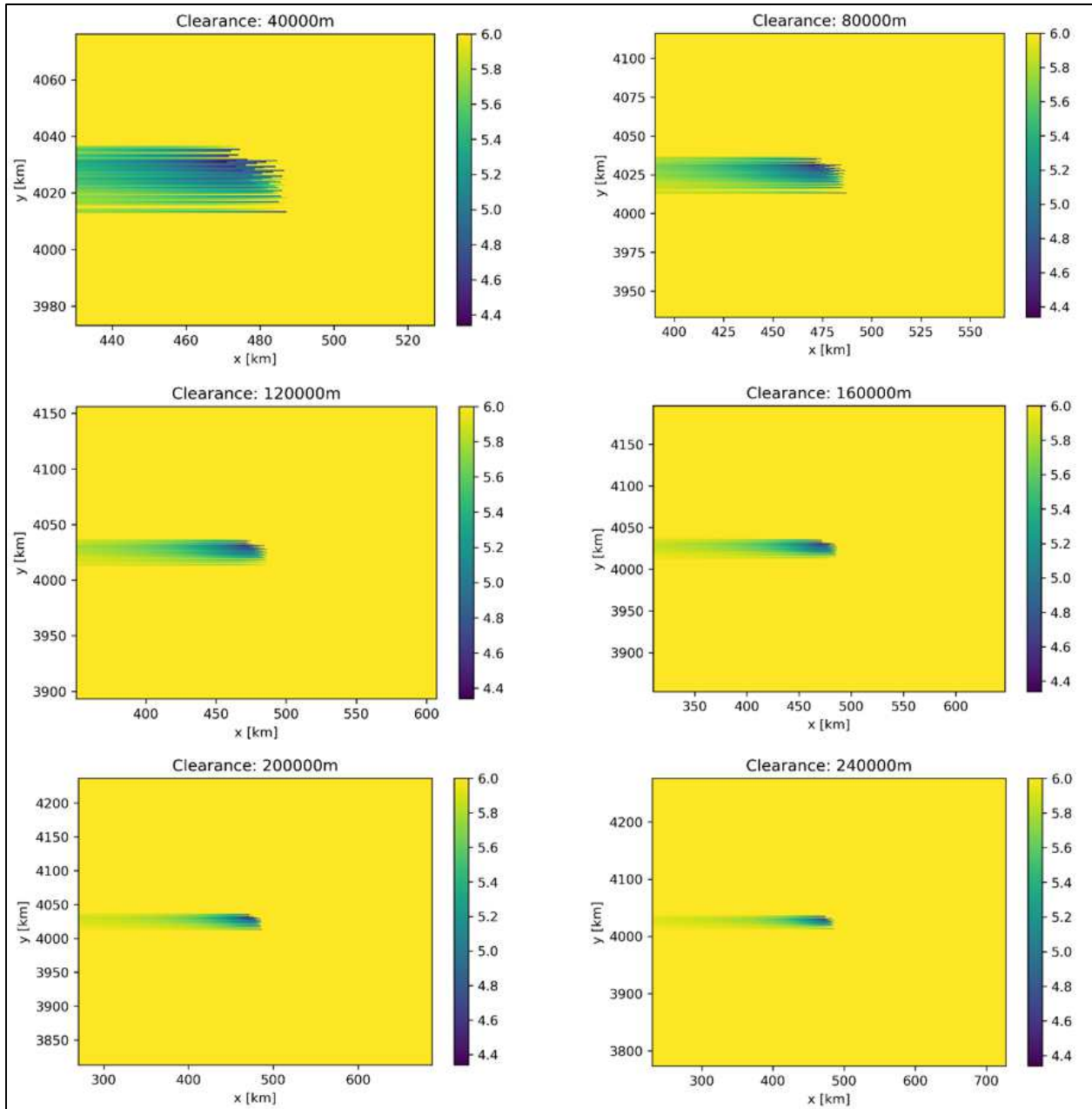


Figure 34. Comparison of wind speed reduction (at 10 m elevation) at the downstream boundary on the west with different clearance distance (between wind farm and the boundary). Axes units in km. All wind units are m/s.

The wind speed deficit at hub-height (left panel of Figure 35) at the western boundary of the domain decreases rapidly with increasing clearance distance between wind farm and the domain boundary. After 120 km, the increment in clearance distance does not significantly impact the wind deficit (left panel of Figure 35). However, it significantly increases the computational time (elapsed time) (right panel of Figure 35). Beyond 120 km, the resulting maximum reduction (<3%) is less than 0.17 m/s for the 6 m/s wind speed. The maximum reduction at the downstream boundary from Figure 31, which also used 120 km, is about 0.25 m/s at 10 m/s free stream velocity, considered similar to the maximum accuracy of any reanalysis field (i.e., ERA5 here) used to force the numerical hydrodynamic models. Therefore, 120 km is used.

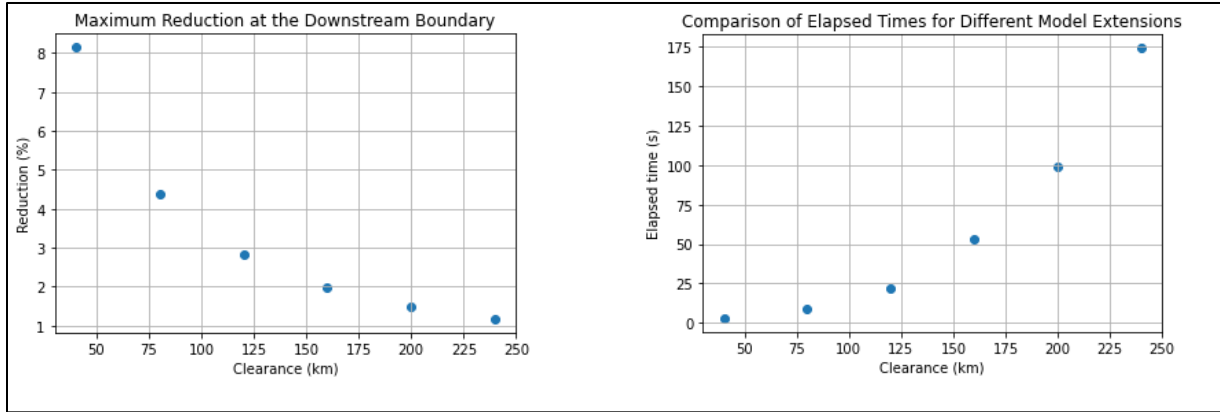


Figure 35. Comparison of wind speed reduction (at hub-height) at the downstream boundary on the west (left panel) and simulation time (right panel) with different model extension/clearance distance (between wind farm and the boundary).

Figure 36 shows mean wind speed reductions and the computational time at the western boundary of the domain for 10 m above surface elevation. The change of mean reduction and model run-time with increasing clearance distance shows the same pattern as the maximum reduction and run-time for wake simulation at hub-height (Figure 35).

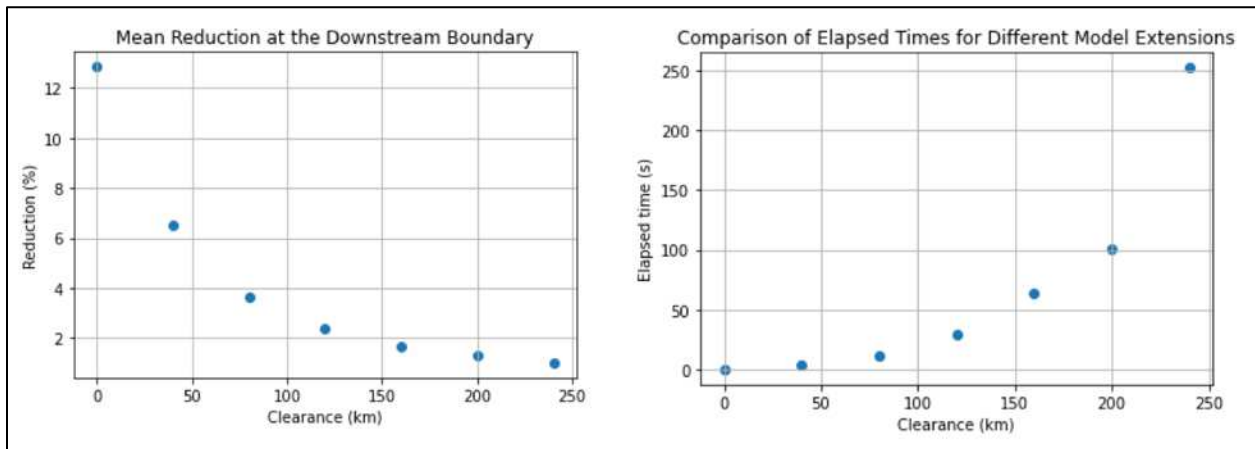


Figure 36. Comparison of mean wind speed reduction (at 10 m) at the downstream boundary on the west (left panel) and simulation time (right panel) with different model extension/clearance.

4.9 Comparison of PyWake-derived Wind Reduction with Christiansen et al. (2022)

To understand how PyWake-derived wind reduction compares with the mean, SAR-based wind deficit from Christiansen et al. (2022) (Figure 10), a qualitative analysis was carried out on a wind farm which has a similar size to Global Tech wind farm (used in Christiansen et al., 2022). Different wind turbine powers were used for this analysis: 5 MW turbines similar to the ones present in Global Tech wind farm, 12 MW Turbines described in Johnson et al. (2021), and 15 MW used in the present work (Figure 37).

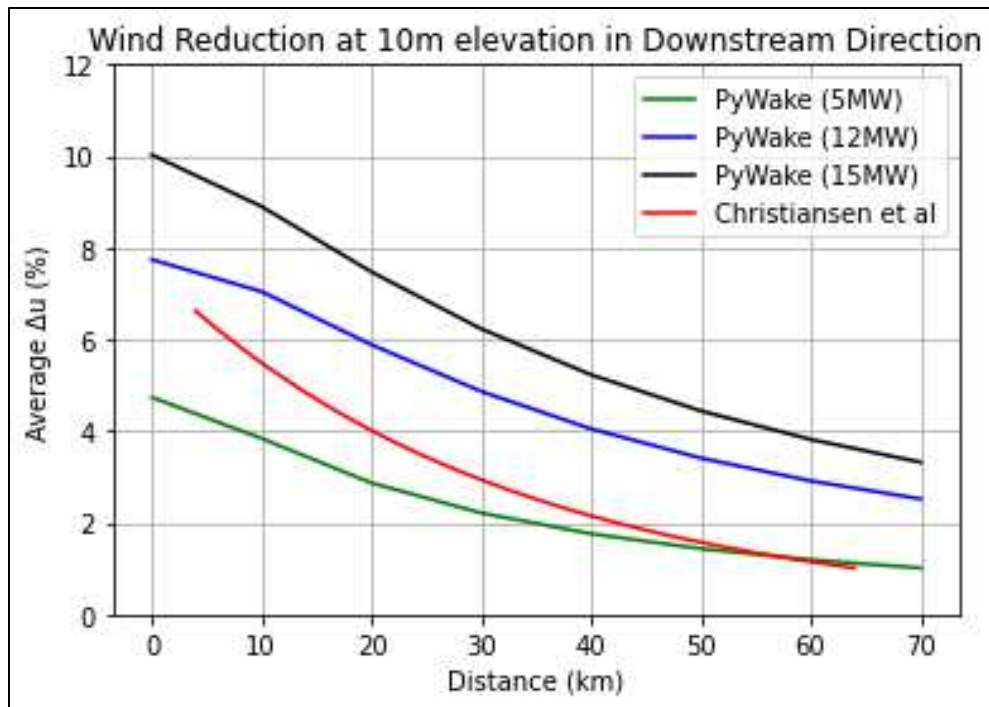


Figure 37. Comparison of PyWake-derived wake with Christiansen et al. (2022). The figure shows average wind reduction in the lee side of the wind farm. For a farm with 5 MW turbines (similar to Global Tech I wind farm), the wind reduction is about 5% at the edge of the turbine. In the first 40 km from the windfarm, the wind deficit is slightly smaller than what Christiansen et al. (2022) showed. This difference can be caused by the smaller number of turbines (69) used in the PyWake experimental farm compared to 80 turbines deployed in the Global Tech wind farm. Also, the differences in arrangement of turbines in windfarms as well as the wind direction causing the wake effect can contribute to the difference between PyWake and Christiansen et al. (2022).

The PyWake calculation of wind reduction using 12 MW and 15 MW monopiles (used in Johnson et al., 2021) shows that, with increasing size of turbine, reduction in wind speed will grow, reaching 10% for 15 MW turbines, and resulting in a longer wake. It is important to note that the wind wake model outlined by Johnson et al. (2021) does not extend beyond the spatial boundaries of the offshore wind farm. This limitation arises from the use of a "simplified energy model" to capture the wind wake, along with the relatively coarse resolution of the CFSR wind dataset employed in the simulation.

4.10 Steps for Wake Calculation

After finalizing the calibration of all the PyWake parameters, the following steps were taken to calculate the wake-affected wind field used to force the numerical models in the presence of wind farms:

The starting point is reading (free-stream) wind speed and direction time series from the ERA5 reanalysis and interpolating it into a higher resolution (~500 m) rectilinear grid. This new grid later facilitated integrating PyWake results into Hydrodynamic and Wave model input.

Considering each farm's domain separately, ERA5 wind time series were extracted from the grid point located in the middle of the wind farm (8 wind time series for Scenario 2, one for each farm, Figure 38).

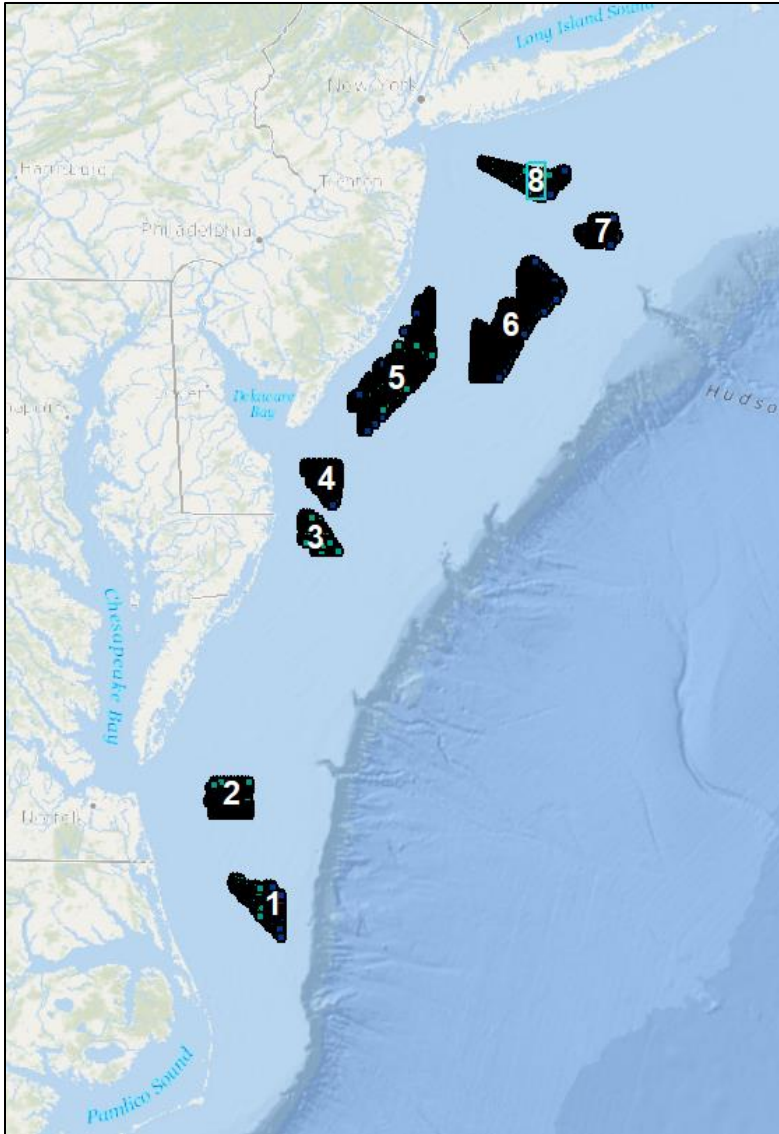


Figure 38. Example of wind turbines (Scenario 2) clustered into individual wind farms (from #1 to #8) off the East Coast.

As ERA5 provides 10m over-ocean wind field, 10 m elevation wind was specified as input to PyWake. Because the wake calculation needs speed at the rotor-center of the turbines, PyWake then converted 10m speed to the hub-height speed using the following expression (Bratton and Womeldorf, 2011):

$$V_2 = V_1 \left(\frac{H_2}{H_1} \right)^\alpha \tag{Eq. 4}$$

where the wind speed velocity V_2 at height H_2 can be estimated using the wind speed velocity V_1 recorded for a different elevation H_1 at the same site with the wind shear exponent, α . The wind shear exponent relates to terrain roughness and for open water the value is 0.1.

Then, for each wind farm:

- Wind farms were set up in a 500 m grid that covers the wind farm and the nearby areas which might be impacted by the wake caused by the wind farm.
- Wind speeds were divided in 12 bins (from minimum as 3m/s to maximum operational wind speed of 25 m/s with an interval of 2m/s) and wind directions into 12 bins (from 0° to 360° with an interval of 30°).
- PyWake was run for each wind speed bin and direction (12 * 12 = 144 runs in example above).
- Wind reduction factors were calculated for each binned (steady state) case (for that farm) which resulted in 144 maps (data fields) of reduction factors for each farm (based on the example above).

The above steps were then repeated for all farms (8 * 144 = 1,152 reduction factor maps)

Then, for each time in the global ERA5 wind field:

- Concurrent 8 speed/direction value pairs were retrieved from wind time series, one pair “representative” for each farm, and each rounded to its closest bin from above 144 bins.
- For each of these pairs (for each wind farm), applicable reduction maps were retrieved for that pair (8 PyWake map grids, one for each farm’s representative wind at that time) and then applied to the part of the main rectilinear wind input grid (covering whole Mid Atlantic Bight (MAB) area; described in the first bullet point) associated with the wind farm/ reduction map to calculate the reduced wind field.
- The combined wake impacted wind field were calculated by averaging over the reduced wind fields caused by all the wind farms. This step took consideration of areas which are affected by wakes from multiple farms.
- Wind-wake-effect-accounting wind field were saved into the main rectilinear wind input grid.
- The next ERA5 time step was repeated to create the new wind field for hydrodynamic/wave grid.

5 Hydrodynamic Modeling–Calibration and Validation

5.1 Model Overview

Hydrodynamic modeling of the area is conducted with Deltares Delft3D Flexible Mesh (Delft3D FM) Modeling Suite using its hydrodynamic module, DFLOW (Deltares, 2022). The Delft3D FM modeling suite can carry out simulations of non-steady flows, sediment transports, waves, water quality, morphological developments and ecology in three-dimensional coordinates with a flexible mesh and finite volume code. The grid mesh can be constructed using a variety of polygonal elements, with up to six sides. This allows for easy construction of model grids that conform well to complex shorelines and sinuous channels and can include high degrees of mesh resolution in areas only where it is desired, as in the case of the wind farms in this project. The vertical dimension can be specified with boundary fitted sigma-coordinates or a strictly horizontal Z-grid. DFLOW simulates tidally and/or meteorologically forced two-dimensional (2DH, depth-averaged) or three dimensional (3D) unsteady flow and transport phenomena (Deltares, 2022).

5.2 Model Grid

Given the requirements for localized high-resolution areas in the BOEM wind turbine lease areas, a high-resolution unstructured numerical model grid (unstructured mesh) has been created for this work. The grid covers the area of interest between south Long Island and Cape Hatteras, bound by the 10m onshore isobaths and a 70–80 km extension past the continental shelf break. The unstructured mesh uses triangular finite elements of variable resolution with a total of 23,668 vertices (nodes). Resolution varies between 7 km and 10 km at the offshore boundary, to 3km at the nearshore boundary, and to less than 1km within and around the WEAs. The highest resolved areas are at and around the WEAs. Orthogonality and smoothness have been considered while creating the mesh, with orthogonality in Universal Transverse Mercator around 0 and smoothness less than 1.76. Forty combination z and sigma (terrain following) layers are used in the vertical. The vertical layer breakdown consists of 25 z layers present in depths below 150 m and 15 sigma layers present in depths above 150 m to the surface. Thus, most of the continental shelf is segmented in terrain-following sigma layers, while the shelf break and deep ocean plateau below 150 m depth uses the more appropriate z layering that reduces erroneous numerical diffusion associated with steep bathymetric gradients. Model bathymetry was sourced from GEBCO (the General Bathymetric Map of the Oceans, at 425 m resolution) and NCEI (the National Centers for Environmental Information, 1/9 and 1/3 arcsecond resolution–nominal 3m and 10m, respectively). The bathymetry was mosaiced and mapped on the numerical grid. Grid resolution and bathymetry are shown in Figure 39. The model has been set up and boundary forcing conditions were created for its validation, calibration, and required simulations. This grid is shared with the surface wave model introduced in Section 6.

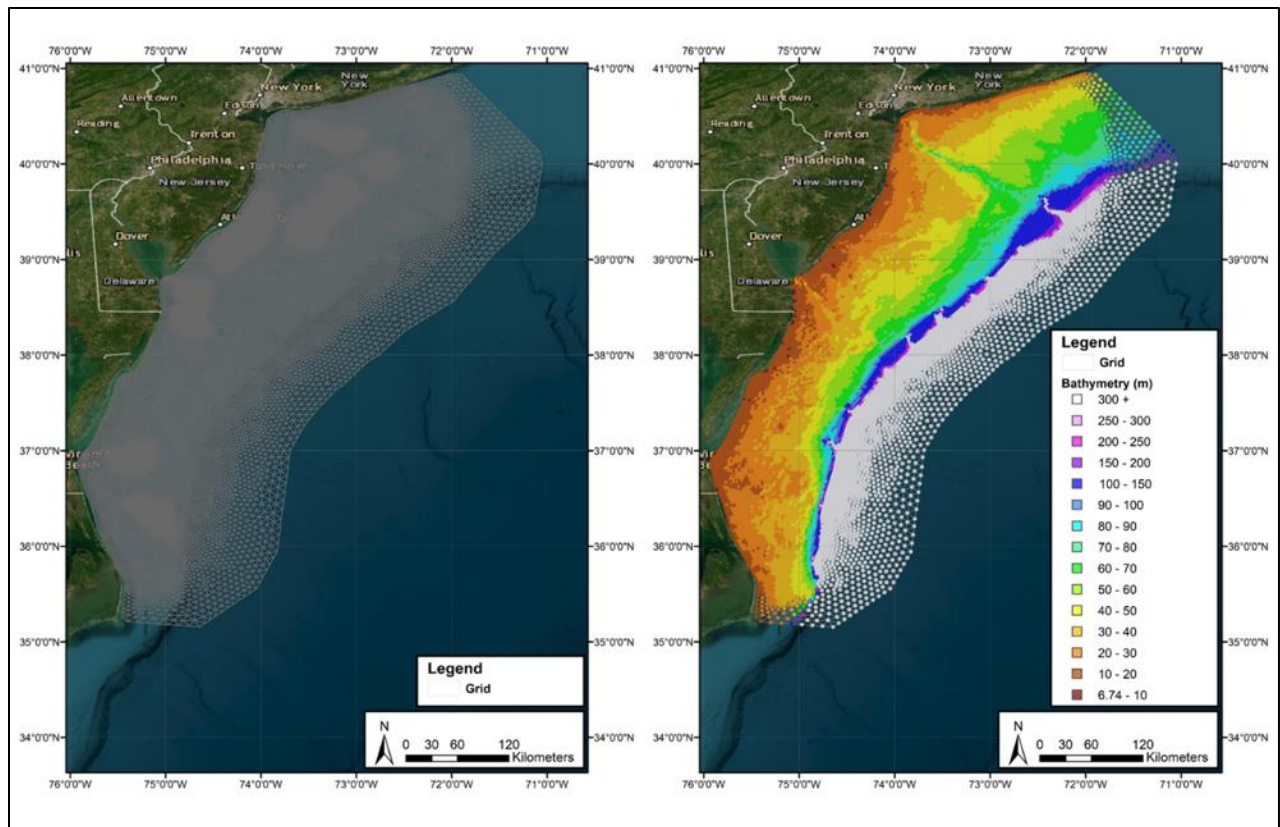


Figure 39. Mid-Atlantic Bight shelf model grid. (a) Left panel: numerical model grid. (b) Right panel: grid bathymetry.

5.3 Boundary Forcing

The hydrodynamic model forcing entails water level timeseries applied along the onshore and offshore open boundaries, temperature and salinity applied along the vertical layers at the open boundary, as well as wind, zenith-calculated solar radiation at the top of the atmosphere, total cloud cover, barometric pressure, atmospheric air temperature, and relative humidity applied at the surface of the model grid as meteorological forcing. Wind forcing will include the effects of wind farm wakes in Scenarios 2 and 3 (Table 1) as modeled by pyWake (Section 4).

5.3.1 Water Level Boundary

The water level boundary runs along the perimeter of the model domain as an open boundary. Tidal data were extracted from Doppio, a ROMS-based (Region Ocean Modeling System) validated and calibrated, data-assimilative model of the Mid Atlantic Bight and Gulf of Maine (López, et al., 2020). The haversine distance formula was applied to determine Doppio nodes within 10 km of the hydrodynamic model's open boundary nodes. Each node at the open boundary had at least two and at most nine Doppio nodes within a 10 km range. Water level timeseries extracted from each Doppio node were run through T_TIDE, a toolbox for harmonic analysis of oceanic tides, to compute tidal constituents and predicted (astronomical) tidal timeseries (Pawlowicz, et al, 2002) (Table 11). Tidal constituents computed with T_TIDE displays which tidal constituents were computed. The Doppio Tidal Residual was computed subtracting the predicted tidal from the original water level timeseries at each node. An inverse distance weighting formulation between the model's boundary nodes and Doppio nodes with the 10 km range was applied to each of the tidal constituents and residual timeseries. The weighted tidal constituents were

processed through T_TIDE and the output tidal time series was added to the weighted residual. Smooth tidal solutions were thus created along the open ocean boundary, validated against raw Doppio results, and in 3D barotropic (uniform density) test simulations.

Table 11. Tidal constituents computed with T_TIDE

Tidal Constituent	Description
2N2	Lunar elliptical semidiurnal second-order constituent
K1	Lunar diurnal constituent
K2	Lunisolar semidiurnal constituent
M2	Principal lunar semidiurnal constituent
M4	Shallow water overtides of principal lunar constituent
MF	Lunisolar fortnightly constituent
MM	Lunar monthly constituent
MN4	Shallow water quarter diurnal constituent
MS4	Shallow water quarter diurnal constituent
N2	Larger lunar elliptic semidiurnal constituent
O1	Lunar diurnal constituent
P1	Solar diurnal constituent
Q1	Larger lunar elliptic diurnal constituent
S1	Solar diurnal constituent
S2	Principal solar semidiurnal constituent

5.3.2 Water Temperature and Salinity

Water temperature and salinity time series were imposed at the model’s lateral open boundary across the 40 vertical depth layers. Data were extracted from the Doppio model and transformed from the vertical s coordinates that support ROMS’ vertical stretching terrain following model to the Delft sigma- z equivalent depth levels. The Haversine Distance formula matched the closest individual Doppio node to each open boundary node and the temperature and salinity data were interpolated to the model’s 40 vertical layers (combination of z and sigma layers). Representations of surface water temperature and salinity for a single timestep over the model domain are shown in Figure 40. Initial temperature and salinity conditions in the Delft model were also interpolated from Doppio.

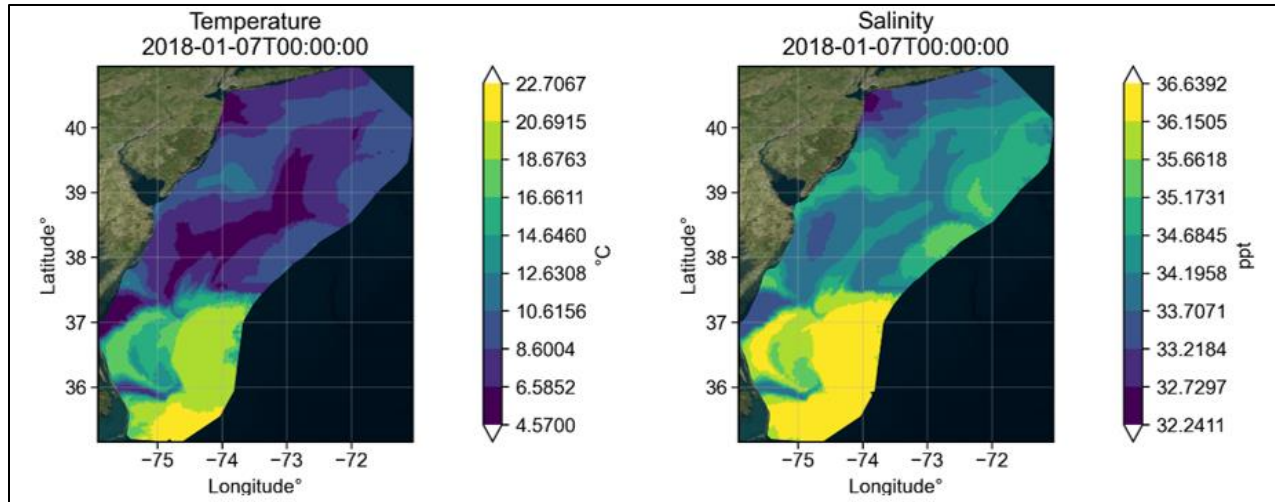


Figure 40. Surface water temperature and salinity color maps for time stamp, January 7, 2018 00:00:00 output from the model.

5.3.3 Surface Boundary Conditions

ERA5 is the fifth generation ECMWF reanalysis for global climate weather (Hersbach, et al., 2023). Wind at 10 m above surface, surface barometric pressure reduced to mean sea level, atmospheric air temperature at 2 m above surface, total cloud cover and relative humidity at 2 m above surface were extracted from ERA5 and applied to the model baseline run to internally calculate surface stress and heat flux boundary conditions. A composite ocean heat flux model is applied to the model domain based upon Gill (1982) and Lane (1989). The composite ocean heat flux model computes incoming solar radiation at the top of the atmosphere based on time and astronomical arguments and accounts for heat exchange from the solar insolation that is directed through the atmosphere and ocean's surface. The model considers effective back radiation and heat losses due to evaporation and convection including computations for latent and sensible heat during occurrence of free convection, defined in the heat balance equation. Relative humidity, air temperature and the fraction of the sky covered by clouds is prescribed (in %) from ERA5. This model formulation typically applies for large water bodies.

Heat Balance (Delft 2023)

$$Q_{tot} = Q_{sn} + Q_{an} - Q_{br} - Q_{ev} - Q_{co} - Q_{evfree} - Q_{cofree} \quad \text{Eq. 5}$$

Q_{tot} = total heat flux

Q_{sn} = net incident solar radiation (short wave)

Q_{an} = net incident atmospheric radiation (long wave)

Q_{br} = back radiation

Q_{ev} = evaporative heat flux (latent heat)

Q_{co} = convective heat flux (sensible heat)

Q_{evfree} = evaporative heat flux (free convection latent heat)

Q_{cofree} = convective heat flux (free convection sensible heat)

Spatially and time varying (hourly) data are input into the Delft model. An example for a single timestamp of the variables is shown in Figure 41. For the buildout scenarios the windfarm wake winds are applied as the wind forcing boundary condition and in the composite heat flux model.

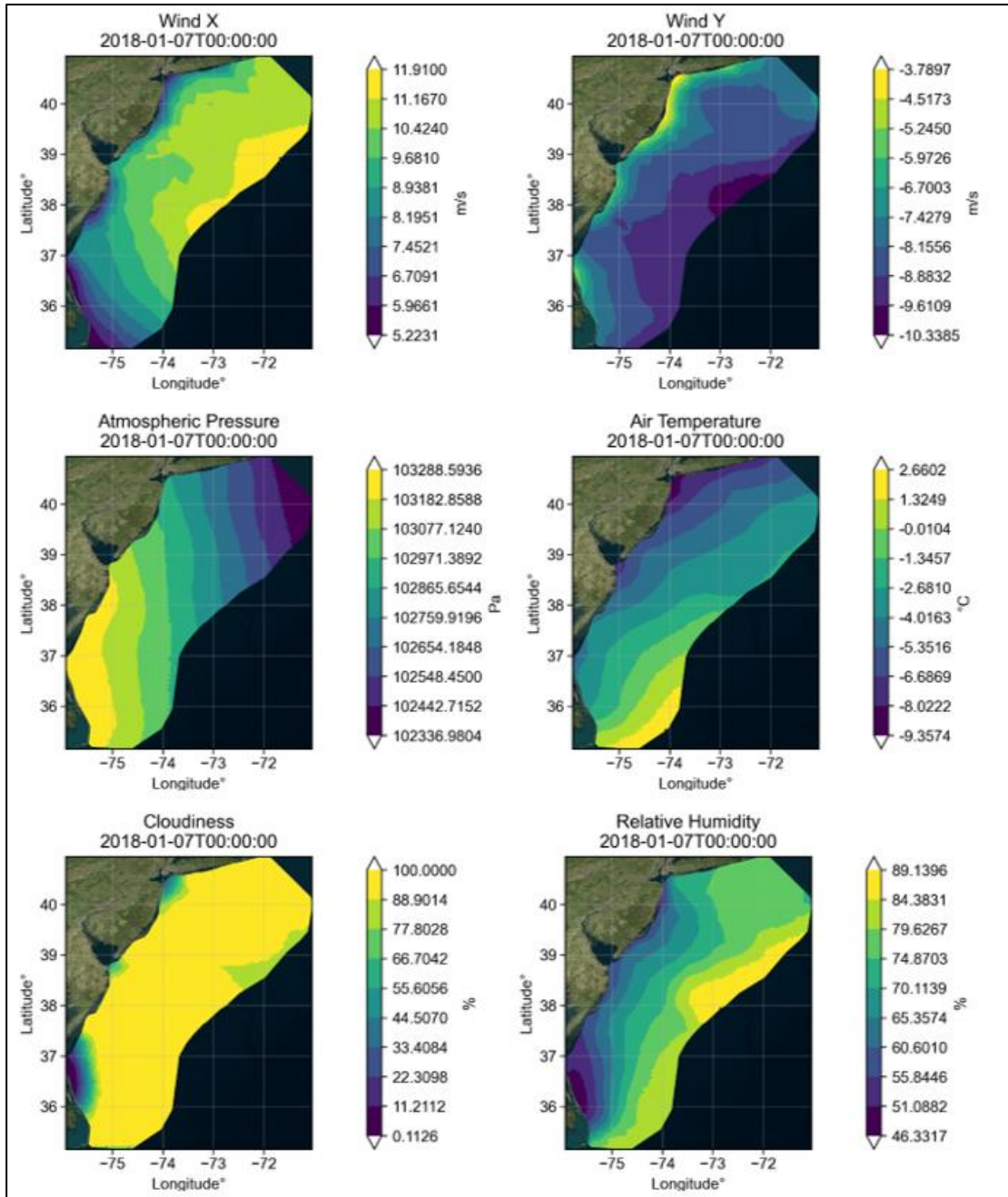


Figure 41. Representative timestamp of surface boundary conditions applied. (a) Upper Left Panel: Eastward wind velocity at 10 m over surface (b) Upper Right Panel: Northward wind velocity at 10 m over surface (c) Mid Left Panel: Surface Atmospheric Pressure reduced to MSL (d) Mid Right Panel: Air Temperature, 2 m over surface (e) Lower Left Panel: Total Cloudiness (f) Lower Right Panel: Relative Humidity, 2 m over surface.

5.4 Storage and Computational Requirements

Storage and computational processing requirements for the model were robust. Following model testing the model was run in three-day chunks with restart files. Each three-day model is approximately 30 gb of data and took around 10 to 13 hours to run presently in serial model. Using MPI parallelism and extra

storage, the model takes about a week to finish a two-year run on 64 core virtual machines with 128 GiB memory on the RPS Azure cloud.

5.5 Model Calibration and Stability

Calibration of the fully forced hydrodynamic model was performed for a 12-month period, February 2018 to January 2019, inclusive, while the next 12-month period was used for model validation. Calibration was challenging and included the application and adjustment of various model parameters to optimize model skill metrics and reduce instabilities present. RPS conducted a literature review regarding modification of model parameters to stabilize the model and referred to research by Mudiyansele (2021). Adjustments to the model’s Smagorinsky factor for horizontal turbulence, coefficients for horizontal eddy diffusivity and viscosity as well as vertical eddy diffusivity and viscosity were made. Boundary hydrostatic stability was also checked. Application of a horizontal momentum filter resolved early issues present along the Gulf Stream by suppressing spurious oscillations in the vertical velocities along the open boundary affecting the horizontal velocities. Multiple turbulence closure schemes are included with Delft3D, and the k-epsilon closure model was employed in this study. Several schemes employing large eddy diffusivity applied along the ocean nodal boundary and surrounding area were tested and ultimately helped stabilize the velocities in the region. Further model refinement following the application of the horizontal momentum filter and localized eddy diffusivity included adjustments to Secchi depth, a measure of the clarity of water, used to formulate light attenuation in the water column contributing to the calculations for surface heat flux penetration, addition of a sponge layer to the open boundary, and combined tidal and current boundary conditions (Table 12. Model parameters tested in calibration). The calibrated model parameters were chosen by performing various statistical analyses comparing each model run using different settings to observed current, temperature, and salinity data to maximize performance metrics. The overall skill of the calibrated model using the chosen set of parameters can be seen in the normalized Taylor Diagram in Figure 110.

Table 12. Model parameters tested in calibration.

Parameter	Coefficient Explanation	Min	Max	Selected
Smagorinsky	Horizontal Turbulence Factor	0.5	2	1
Dalton	Evaporative Heat Flux	0.0012	0.002115	Variable, equal to Wind Drag coefficient
Stanton	Convective Heat Flux	0.0012	0.002115	Variable, equal to Wind Drag coefficient
Vicouv, bgnd	Background Horizontal Eddy Viscosity	0.1	15	0.3 – 15 at Boundary
Vicoww, bgnd	Background Vertical Eddy Viscosity	5E-5	1E-6	1E-5
Dicouv, bgnd	Background Horizontal Eddy Diffusivity	0.1	15	0.3 – 15 at Boundary
Dicoww, bgnd	Background Vertical Eddy Diffusivity	0.1	2	1E-5
Secchi depth	Water Clarity	2	15	4
Rhoair	Air Density	1.15	1.4	1.2

5.5.1 Sea Surface Height

The hydrodynamic model sea surface height calibration included the comparison of existing and forecast conditions within the Mid-Atlantic Bight. Time varying sea surface height from NOS tidal gauges and spatially and time varying sea surface height from Doppio, a ROMS-based (Regional Ocean Modeling System) model of the Mid-Atlantic Bight and Gulf of Main regions were compared to the model.

5.5.1.1 Model against NOS Station Data

Sea surface height comparisons between the model and NOS tidal gauges were used to verify the tidal signal. NOS tide gauges, located in the nearshore region of the model domain spanning the Southern and Northern extents, were used in the calibration (Figure 4). Model calibration was performed on the fully forced hydrodynamic model, over a one-year period from February 2018 to January 2019, following a month of spin-up. Sea surface height time series comparing the model and NOS tide gauge data, as well as scattered density plots of simulated versus observed sea surface height were compared between the multiple calibration runs. The selected run's results are displayed for each station in Figure 42 through Figure 49. Calibration statistics are summarized in Table 13. The model performs well compared to the NOS tide gauges located over the model domain, based on the coefficient of determination (R^2) and Root-Mean-Square-Error (RMSE); the coefficient of determination varies between 0.955 to 0.978, while the Root-Mean-Square-Error ranges from 8.5 cm to 14.9 cm.

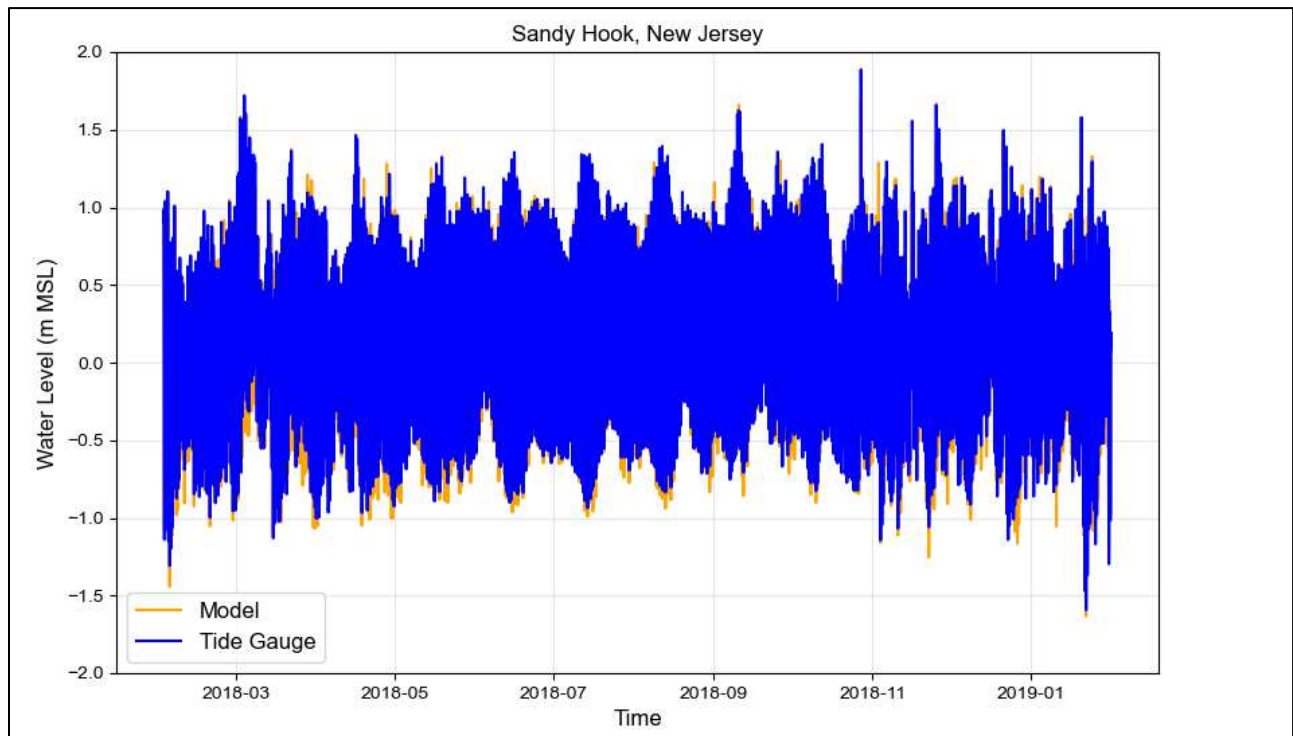


Figure 42. Water level comparison between hydrodynamic model and NOS tide gauge at Sandy Hook, New Jersey.

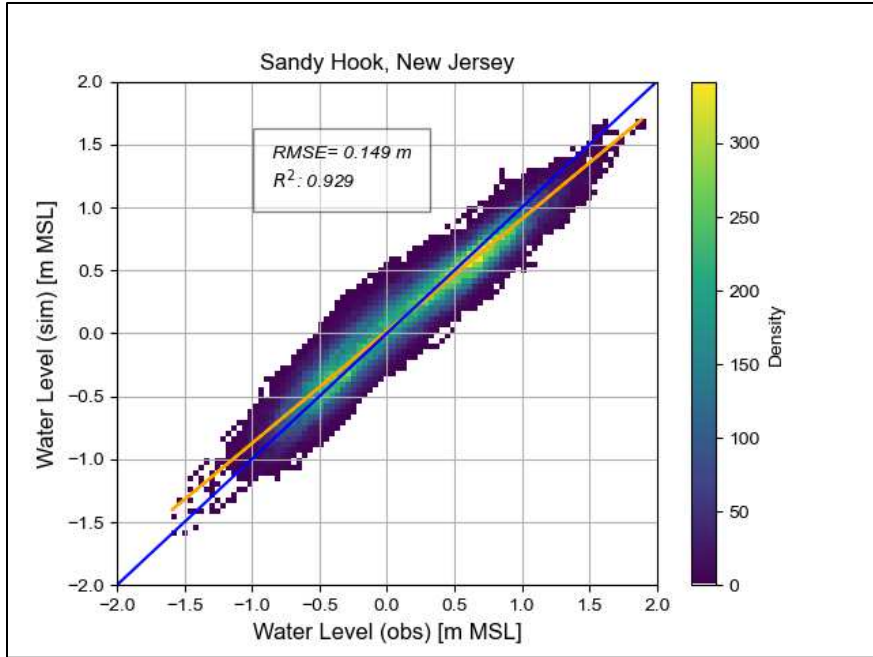


Figure 43. Water level simulated in the model versus observed from the NOS tide gauge at Sandy Hook, New Jersey.

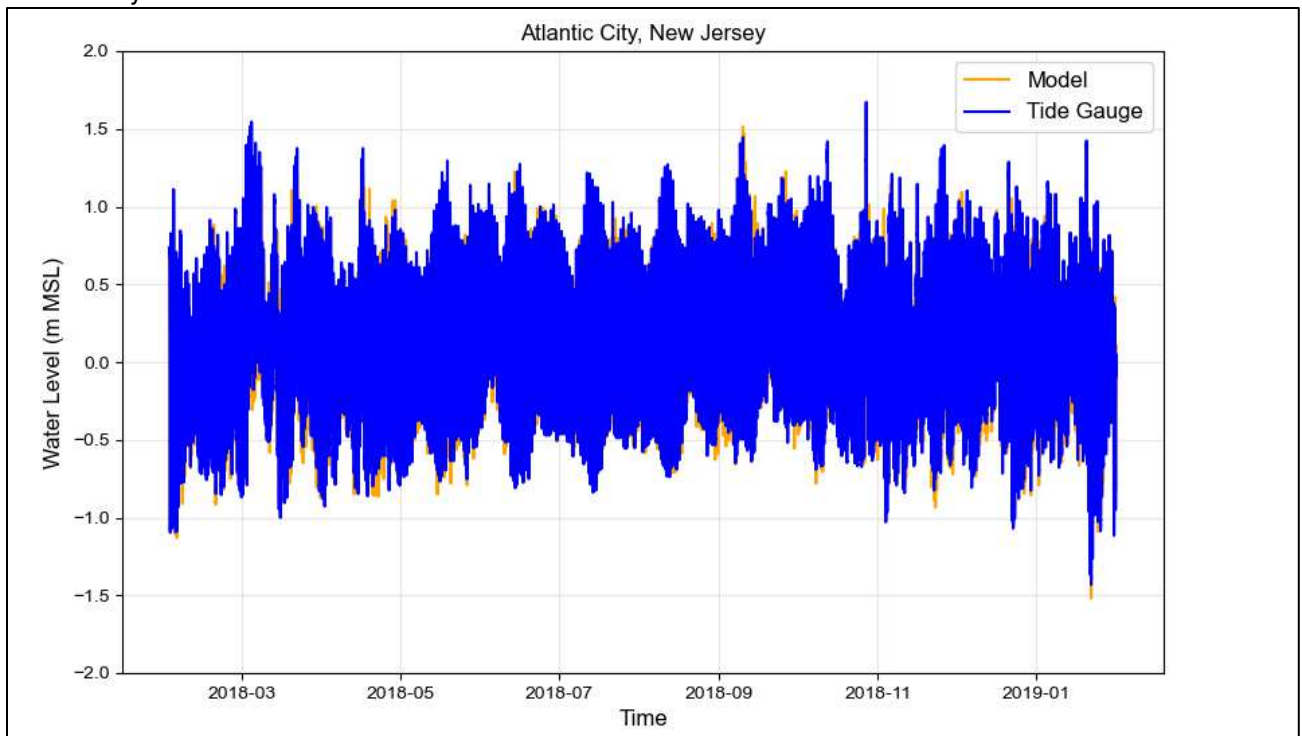


Figure 44. Water level comparison between hydrodynamic model and NOS tide gauge at Atlantic City, New Jersey.

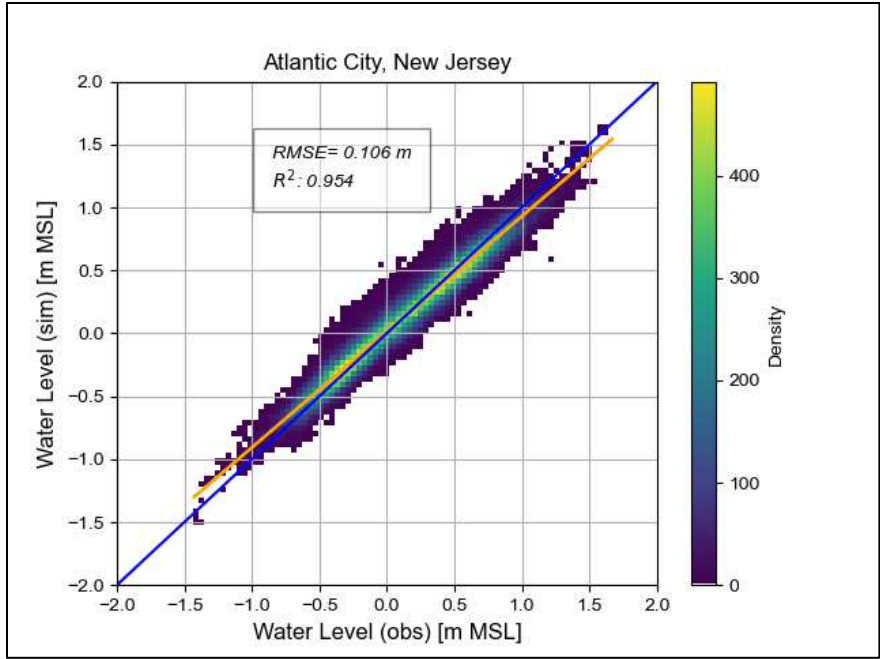


Figure 45. Water level simulated in the model versus observed from the NOS tide gauge at Atlantic City, New Jersey.

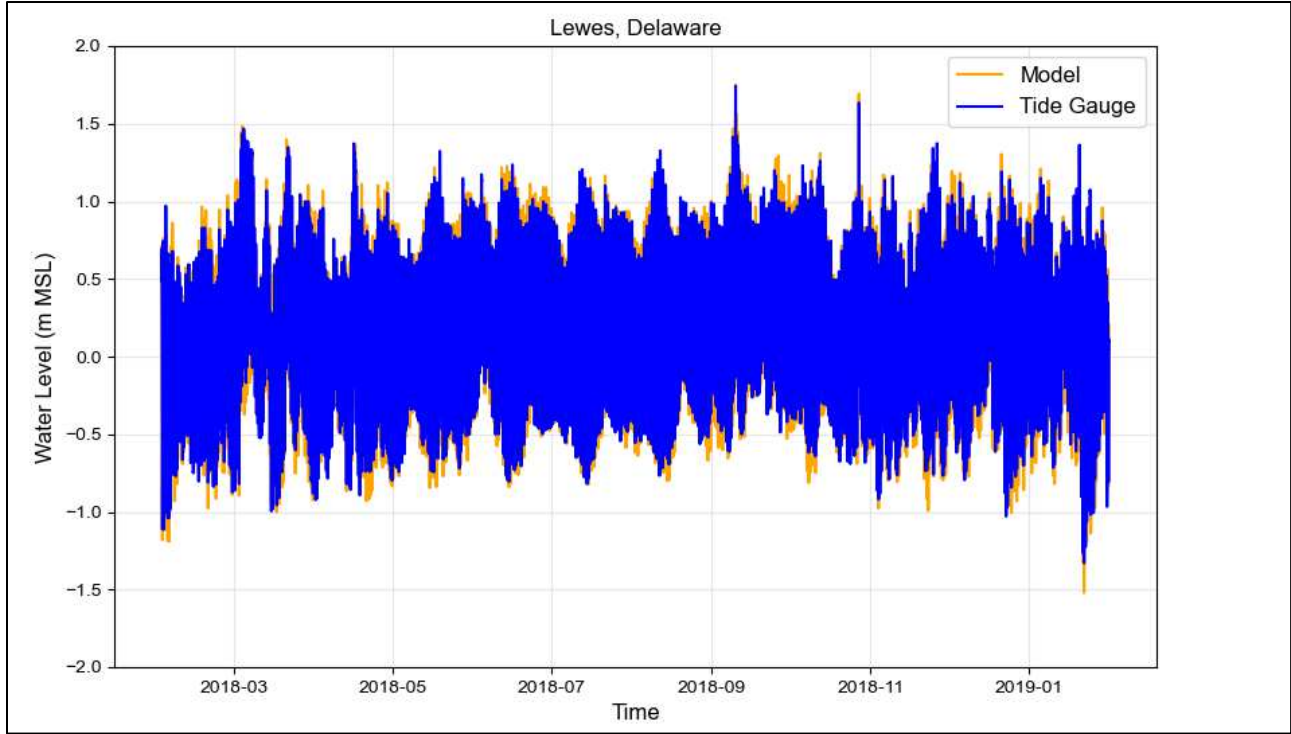


Figure 46. Water level comparison between hydrodynamic model and NOS tide gauge at Lewes, Delaware.

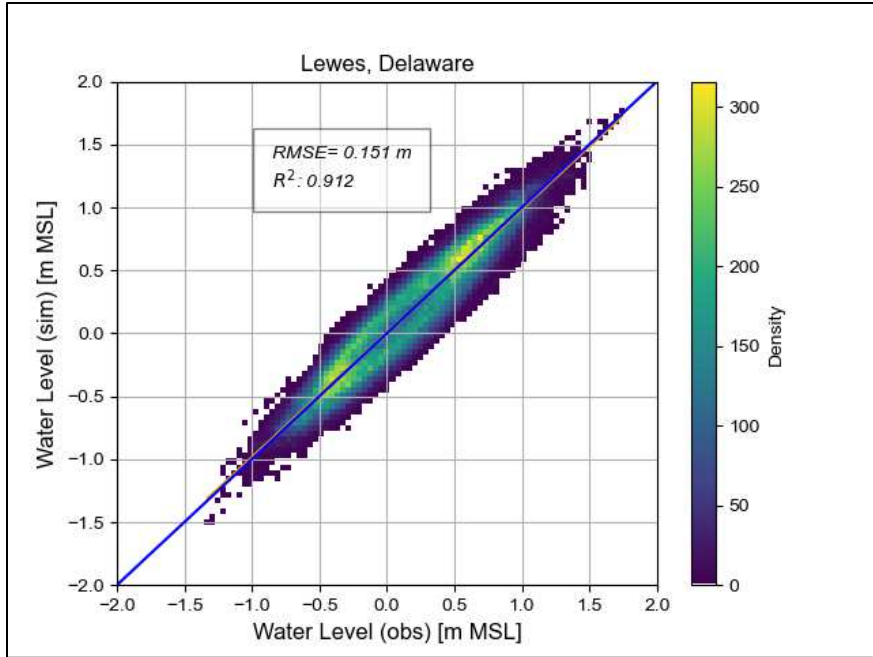


Figure 47. Water level simulated in the model versus observed from the NOS tide gauge at Lewes, Delaware.

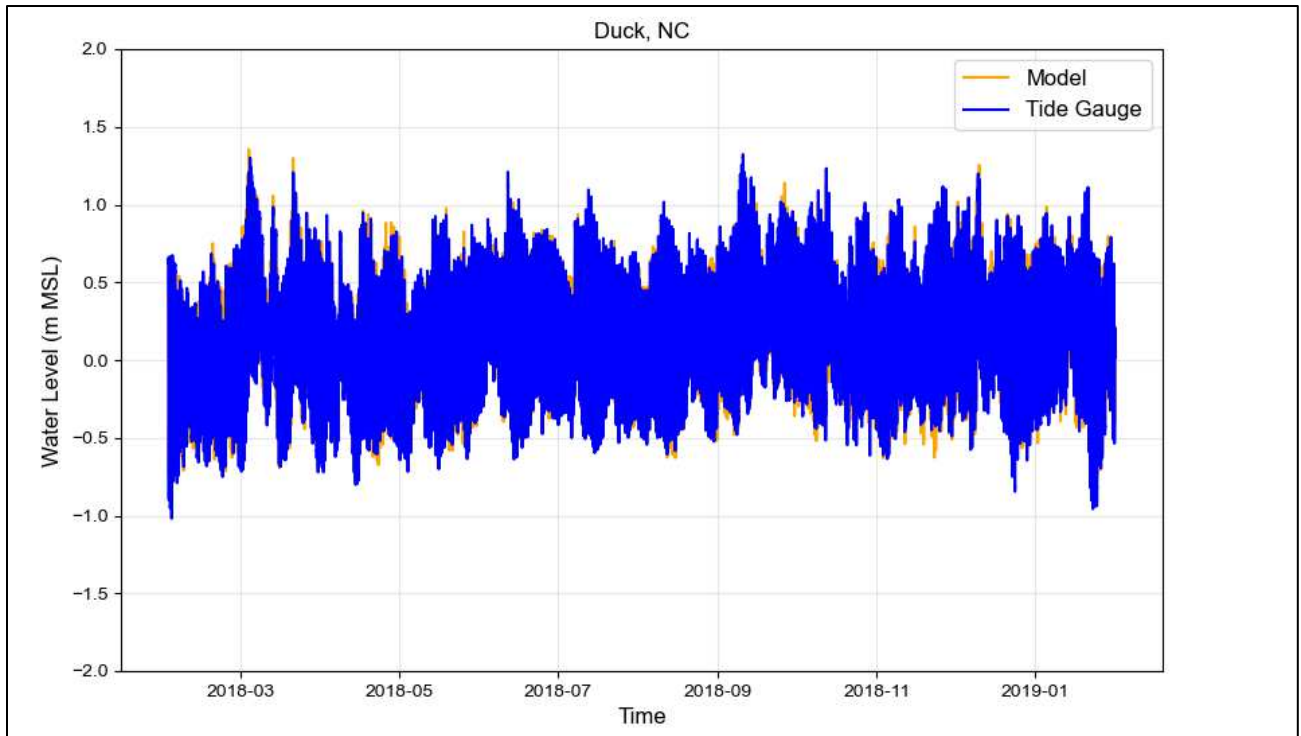


Figure 48. Water level comparison between hydrodynamic model and NOS tide gauge at Duck, North Carolina.

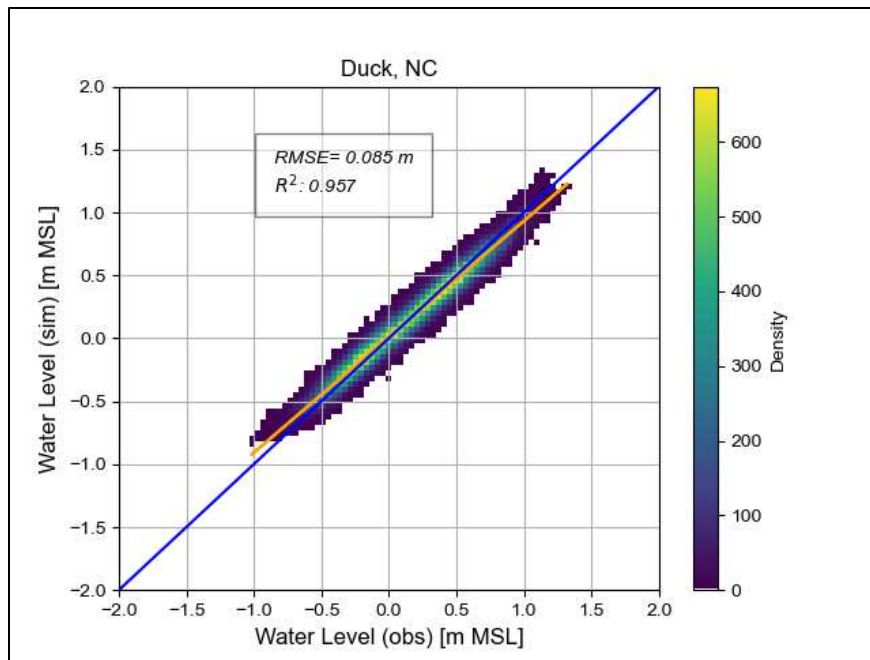


Figure 49. Water level simulated in the model versus observed from the NOS tide gauge at Duck, North Carolina.

Table 13. Model calibration statistics for water elevation (m) at 4 NOS stations.

Station Name	NOS ID #	RMSE, meters	R	R ²
Sandy Hook, New Jersey	8531680	0.149	0.964	0.929
Atlantic City, New Jersey	8534720	0.106	0.976	0.954
Lewes, Delaware	8557380	0.151	0.955	0.912
Duck, North Carolina	8651370	0.085	0.978	0.957

5.5.1.2 Model against Doppio SSH

Model calibration of sea surface height considered spatially and time varying data from the Doppio ROMS model. Doppio sea surface height was compared to the hydrodynamic model for the one-year calibration period, February 2018 to January 2019. Skill metrics including bias, root mean square error, index of agreement, correlation, standard deviation of the model and observed, and mean of observed were analyzed and summarized in histogram and tabular form to showcase variation along the shelf (Figure 50). Index of agreement, developed by Willmott, is a dimensionless metric from 1 to 0, that defines the agreement of the predicted to the observed data, a value of 1 represents a perfect agreement between the datasets (Willmott, 1981). Visualization of the bathymetric bins used to show variation of skill metrics across the model domain is shown in Figure 51. The model sea surface height exhibits low bias and high index of agreement across all bathymetric bins compared to Doppio. Spatial maps of monthly average sea surface height of the model, Doppio dataset, and difference over the calibration period are included in Appendix A.1.

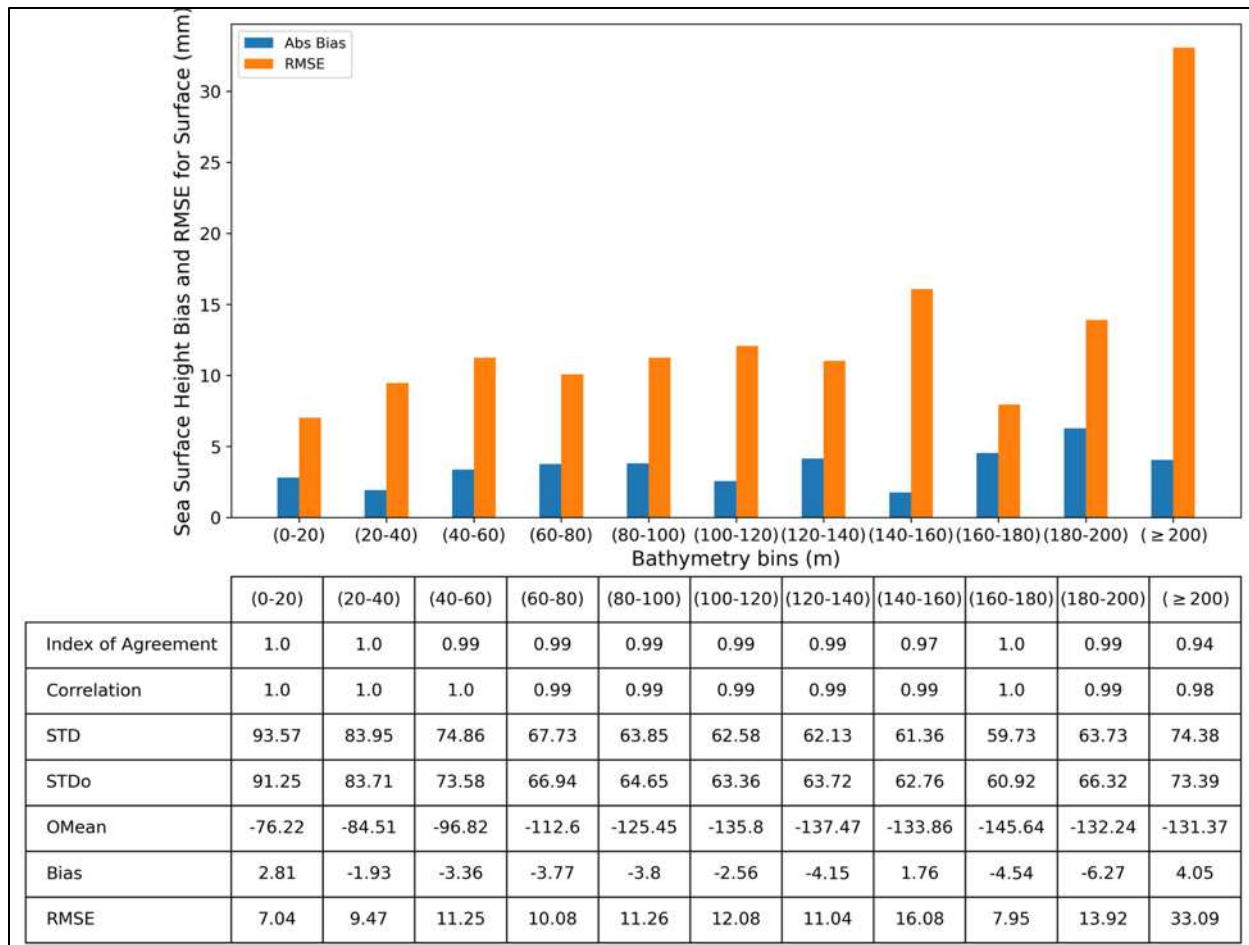


Figure 50. Sea Surface Height comparison between Model and Doppio dataset for calibration period. Top: The histogram presents bias and RMSE, in mm. Bottom: The table shows model skill metrics.

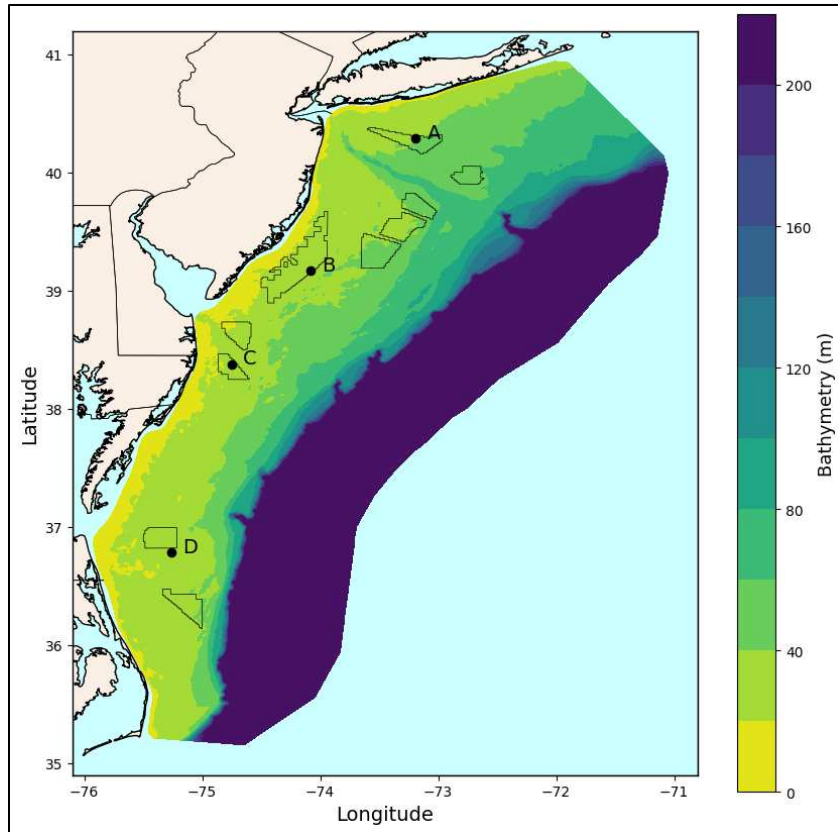


Figure 51. Binned bathymetry map of AOI (every 20 m).

5.5.2 Water Temperature

The hydrodynamic model water temperature calibration included comparison of existing and predicted conditions within the Mid-Atlantic Bight. Time varying surface temperature from NDBC stations, spatially and time varying surface and bottom temperature data from the Doppio, ROMS-based (Regional Ocean Modeling System) model of the Mid-Atlantic Bight and Gulf of Main regions, spatially varying monthly surface temperature data from NOAA Optimally Interpolated High-Resolution SST (OISSTV2), and spatially scattered time varying temperature data provided from gliders were compared to the model.

5.5.2.1 Model against NDBC

The model's water temperature predictions were calibrated against NDBC station time series. The time series comparisons of the model to the 12 NDBC stations from February 2018 to January 2019 are presented in Figure 52 through Figure 63. Table 14 shows the stats of calibrated model against the temperature observations at NDBC stations. The comparisons show a good agreement between modeled surface temperature and NDBC observations.

Table 14. Model skill metrics against NDBC observations of water temperature for calibration period.

Station Name	Correlation	Index of Agreement	Bias (°C)	RMSE (°C)
44095 Oregon Inlet NC	0.96	0.96	0.99	2.64
44086 Nags Head NC	0.99	0.99	0.36	1.20
44100 Duck FRF NC	0.99	0.99	0.06	1.32
44088 Virginia Beach Offshore VA	0.93	0.93	-0.50	2.54
44014 Virginia	0.93	0.94	-0.54	2.87
44099 Cape Henry VA	0.99	0.99	-0.17	1.12
44089 Wallops Island VA	1.00	1.00	0.02	0.82
44009 Delaware Bay	0.99	0.99	-0.22	1.22
44091 Barnegat NJ	0.99	0.99	-0.69	1.37
44065 New York Harbor Entrance	0.99	1.00	0.05	0.93
44025 Long Island	0.99	0.99	0.60	1.30
44066 East Long Beach NJ	0.98	0.98	0.59	1.22

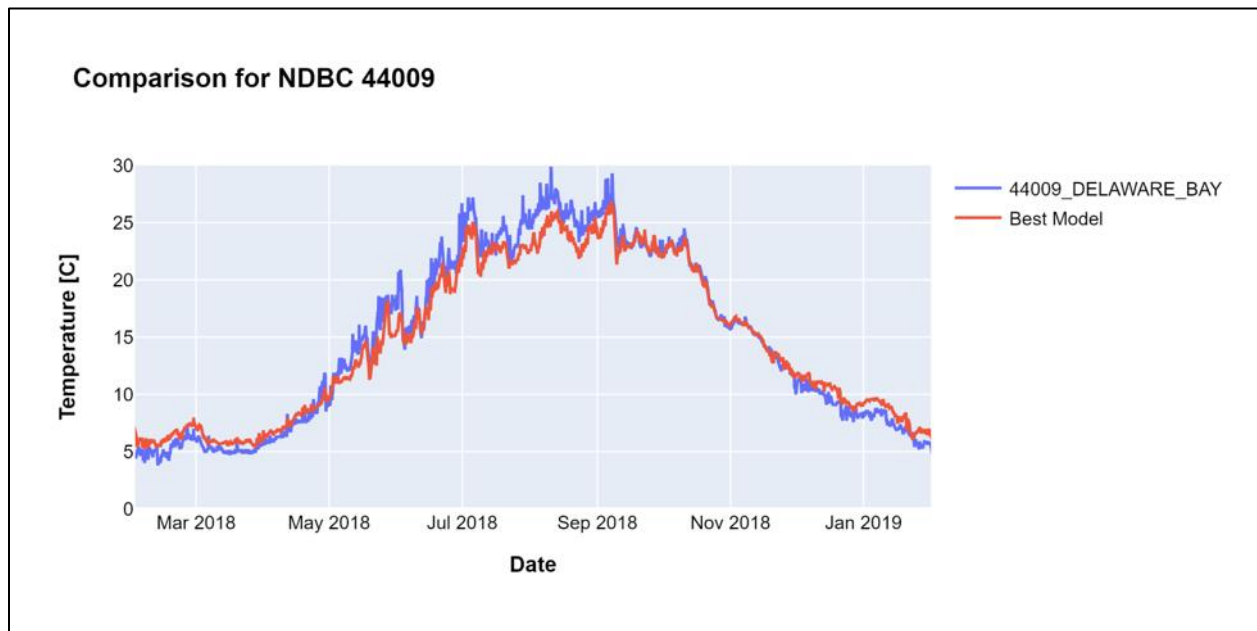


Figure 52. Temperature timeseries comparison; NDBC Buoy 44009 (blue) and calibrated model (red).

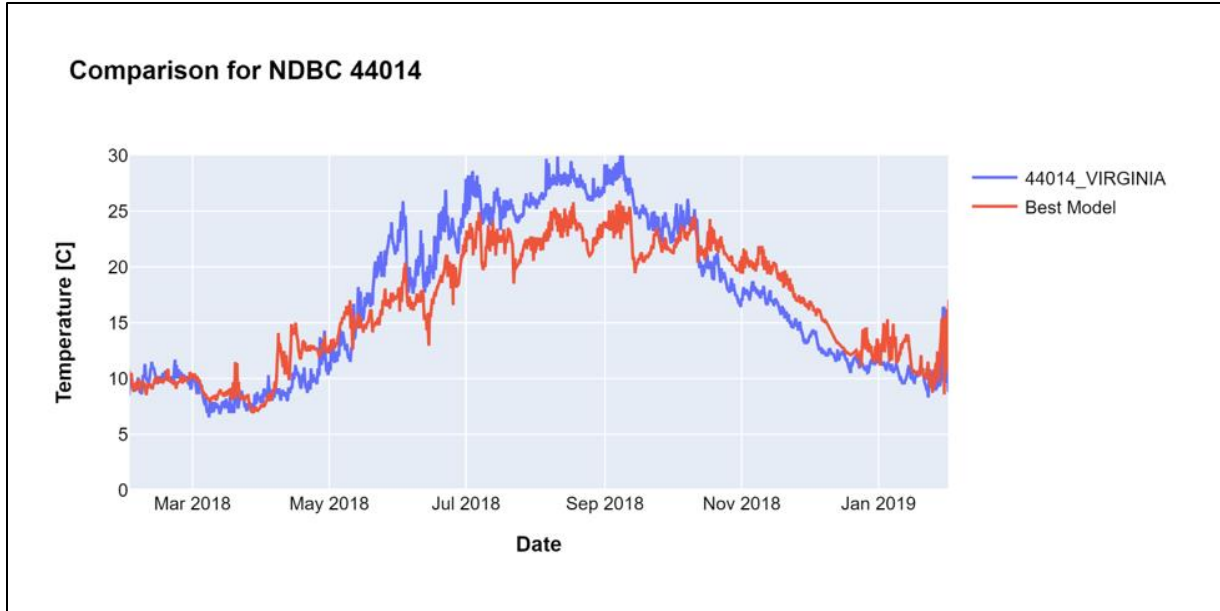


Figure 53. Temperature timeseries comparison; NDBC Buoy 44014 (blue) and calibrated model (red).



Figure 54. Temperature timeseries comparison; NDBC Buoy 44025 (blue) and calibrated model (red).

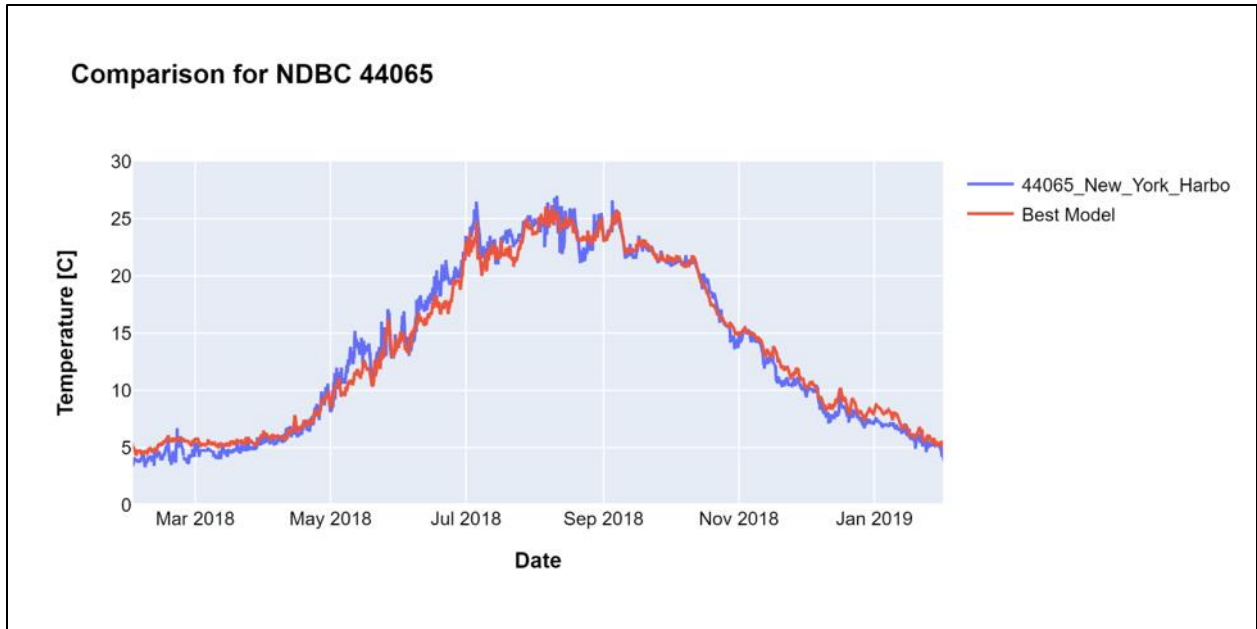


Figure 55. Temperature timeseries comparison; NDBC Buoy 44065 (blue) and calibrated model (red).



Figure 56. Temperature timeseries comparison; NDBC Buoy 44066 (blue) and calibrated model (red).



Figure 57. Temperature timeseries comparison; NDBC Buoy 44086 (blue) and calibrated model (red).



Figure 58. Temperature timeseries comparison; NDBC Buoy 44088 (blue) and calibrated model (red).

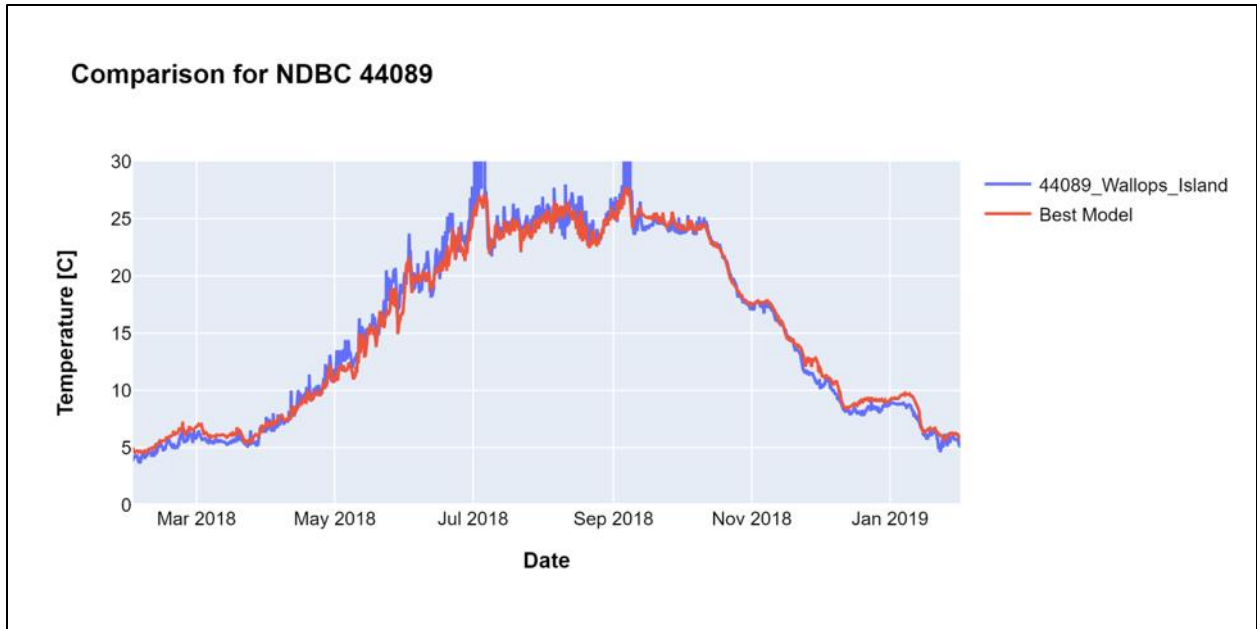


Figure 59. Temperature timeseries comparison; NDBC Buoy 44089 (blue) and calibrated model (red).

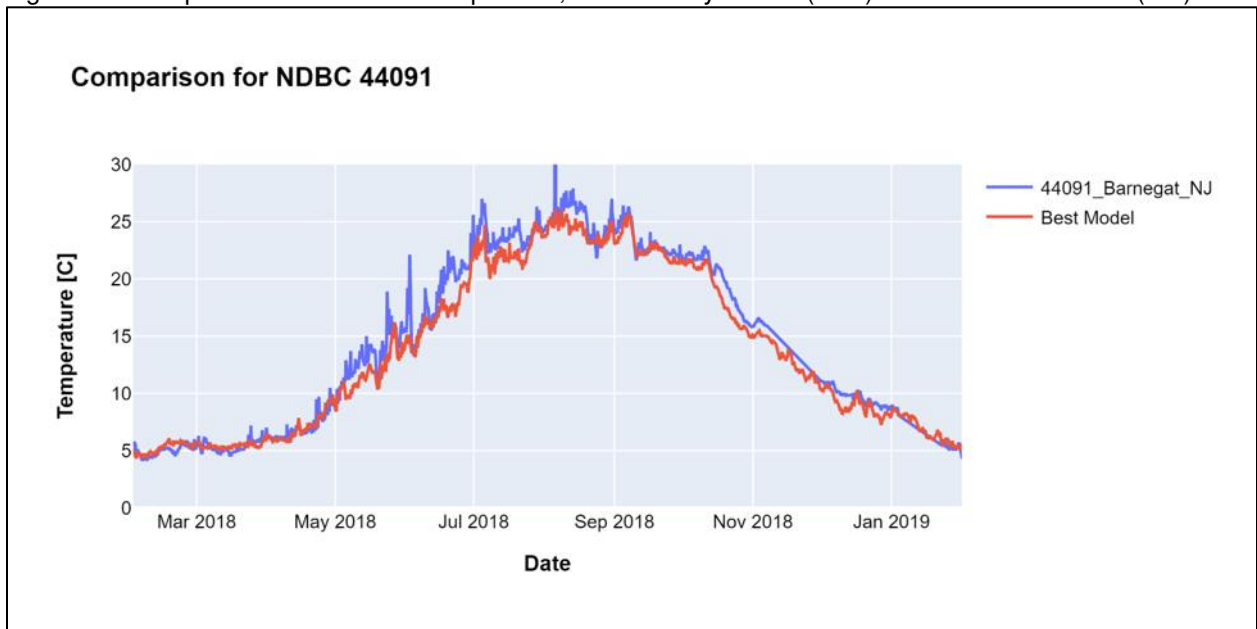


Figure 60. Temperature timeseries comparison; NDBC Buoy 44091 (blue) and calibrated model (red).

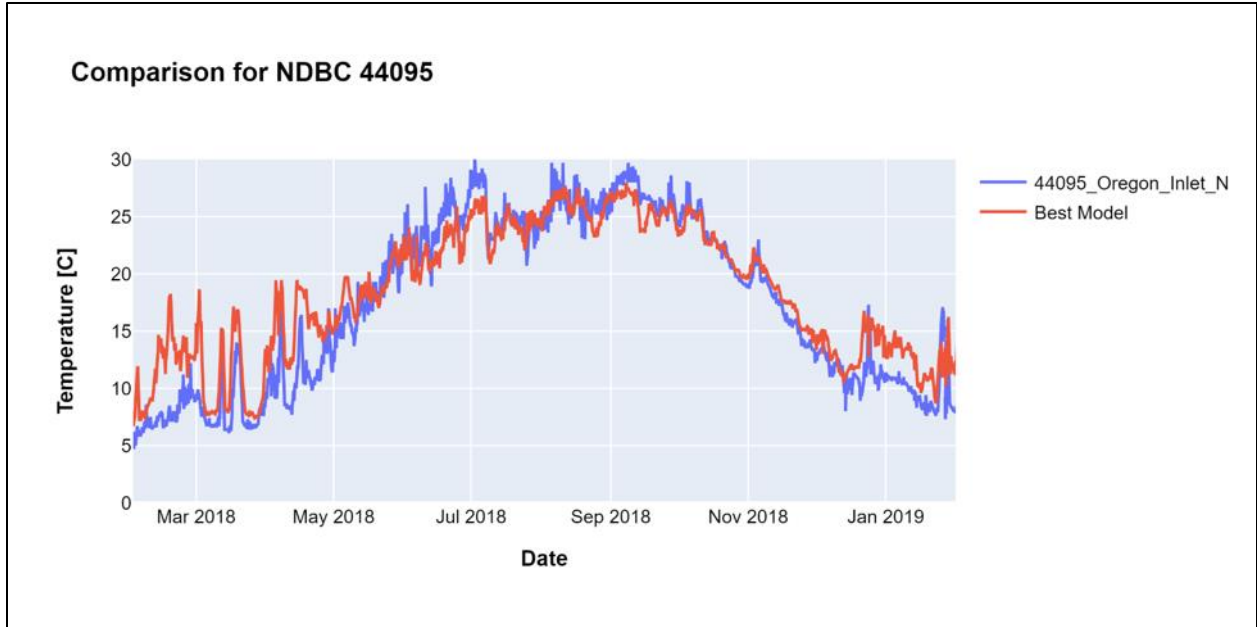


Figure 61. Temperature timeseries comparison; NDBC Buoy 44095 (blue) and calibrated model (red).



Figure 62. Temperature timeseries comparison; NDBC Buoy 44099 (blue) and calibrated model (red).



Figure 63. Temperature timeseries comparison; NDBC Buoy 44100 (blue) and calibrated model (red).

5.5.2.2 Model against Doppio Surface Temperature

Model calibration of surface temperature considered spatially and time varying data from the Doppio ROMS model. Doppio surface temperature was compared to the hydrodynamic model for a one-year time period, February 2018 to January 2019. Skill metrics including bias, root mean square error, index of agreement, correlation, standard deviation of the model and observed, and mean of observed were analyzed and summarized in histogram and tabular form to showcase variation along the shelf (Figure 64). The model's surface temperature exhibits RMSE ranging from 0.54°C to 1.33°C and bias from -0.48°C to -0.08°C . The index of agreement is above 0.98 for all bathymetric bins ranging from 0 to 200+m depth. Spatial maps of monthly average surface temperature of the model, Doppio dataset, and difference over the calibration period are included in Appendix A.2.

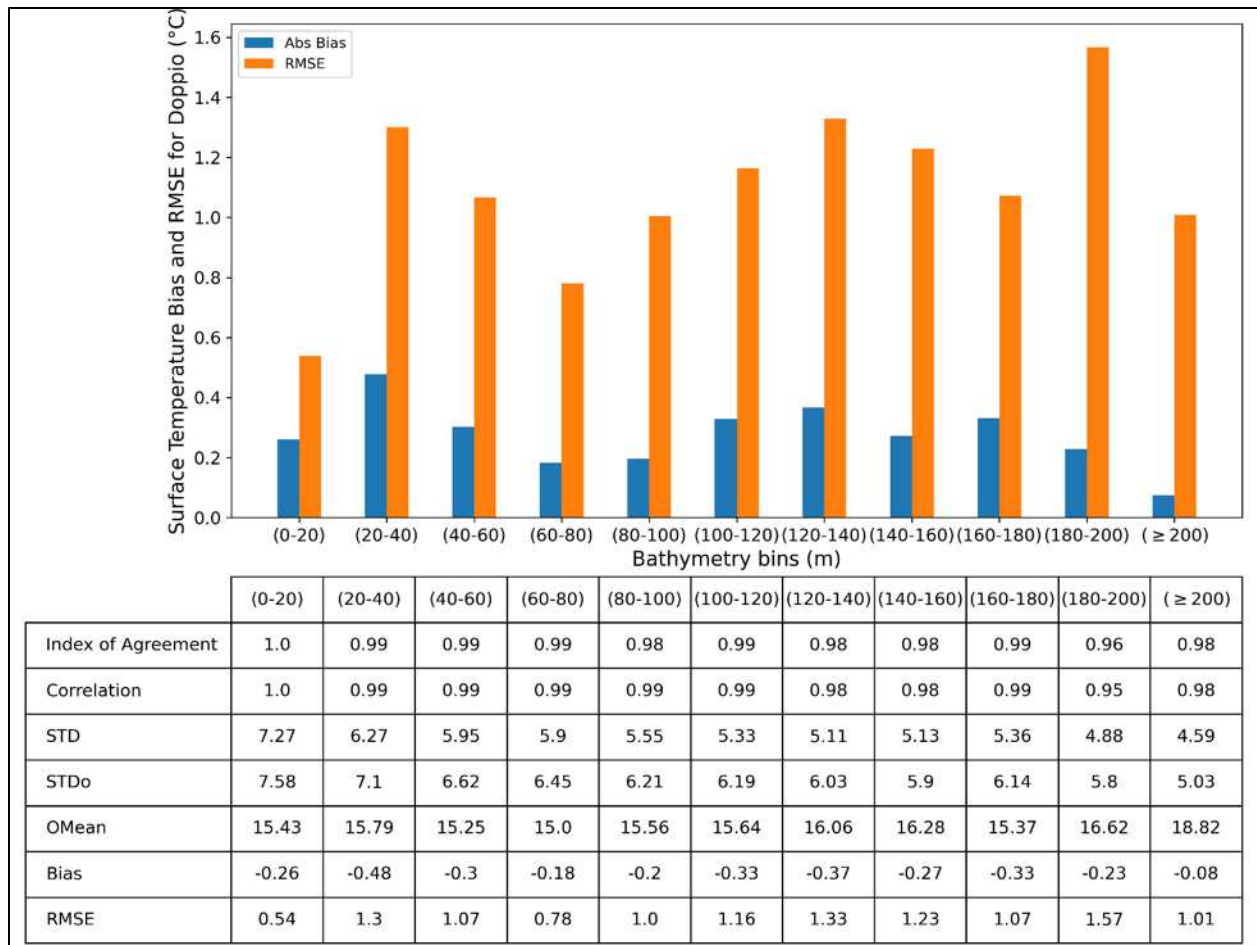


Figure 64. Surface temperature comparison between Model and Doppio dataset for calibration period. Top: The histogram presents bias and RMSE in °C. Bottom: The table shows model skill metrics.

5.5.2.3 Model against NOAA High-Resolution Optimally Interpolated SST (OISSTV2)

Model calibration of surface temperature considered spatially varying monthly data from the NOAA High-Resolution Optimally Interpolated SST satellite-derived dataset. NOAA surface temperature was compared to the hydrodynamic model for a one-year time period, February 2018 to January 2019. Skill metrics including bias, root mean square error, index of agreement, correlation, standard deviation of the model and observed, and mean of observed were analyzed and summarized in histogram and tabular form to showcase variation along the shelf (Figure 65). The model's surface temperature exhibits high index of agreement and correlation over all depth ranges. The lowest bias is shown in depths between 60m to 80m as well as depths past the shelf break. The RMSE varies more over the model domain. Spatial maps of monthly average surface temperature of the model, NOAA OISSTV2 dataset, and difference over the calibration time period are included in Appendix A.3.

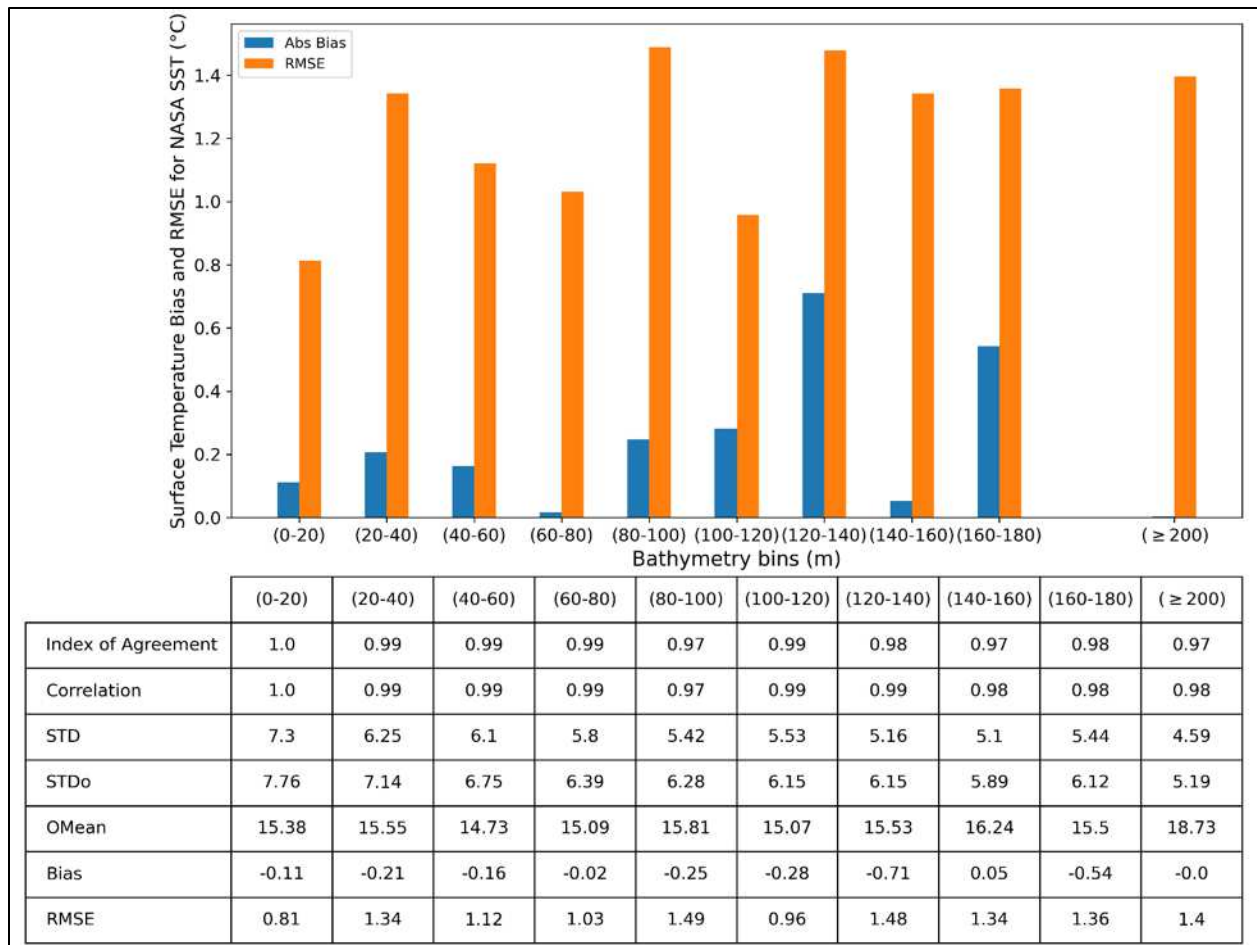


Figure 65. Surface temperature comparison between Model and NOAA Optimally Interpolated High Resolution SST for calibration period.

Top: The histogram presents bias and RMSE, °C. Bottom: The table shows model skill metrics.

5.5.2.4 Model against Doppio Near-Bottom Water Temperature

Model calibration of bottom temperature considered spatially and time varying data from the Doppio ROMS model. Doppio bottom temperature from the multiple calibration runs was compared to the hydrodynamic model for a one-year period, February 2018 to January 2019. Skill metrics including bias, root mean square error, index of agreement, correlation, standard deviation of the model and observed, and mean of observed were analyzed and summarized in histogram and tabular form to showcase variation along the shelf (Figure 66). The selected model's bottom temperature exhibits high model skill in depths ranging from 0m to 40m with high index of agreement and correlation and low bias ranging from -0.07° C to 0.21° C. Agreement between Delft and Doppio bottom temperatures decreases moving into deeper waters. Doppio bottom temperatures are poorly constrained due to a lack of bottom observations from the glider datasets that Doppio assimilates. Spatial maps of the monthly average bottom temperature of the model, Doppio dataset, and difference over the calibration time period are included in Appendix A.4.

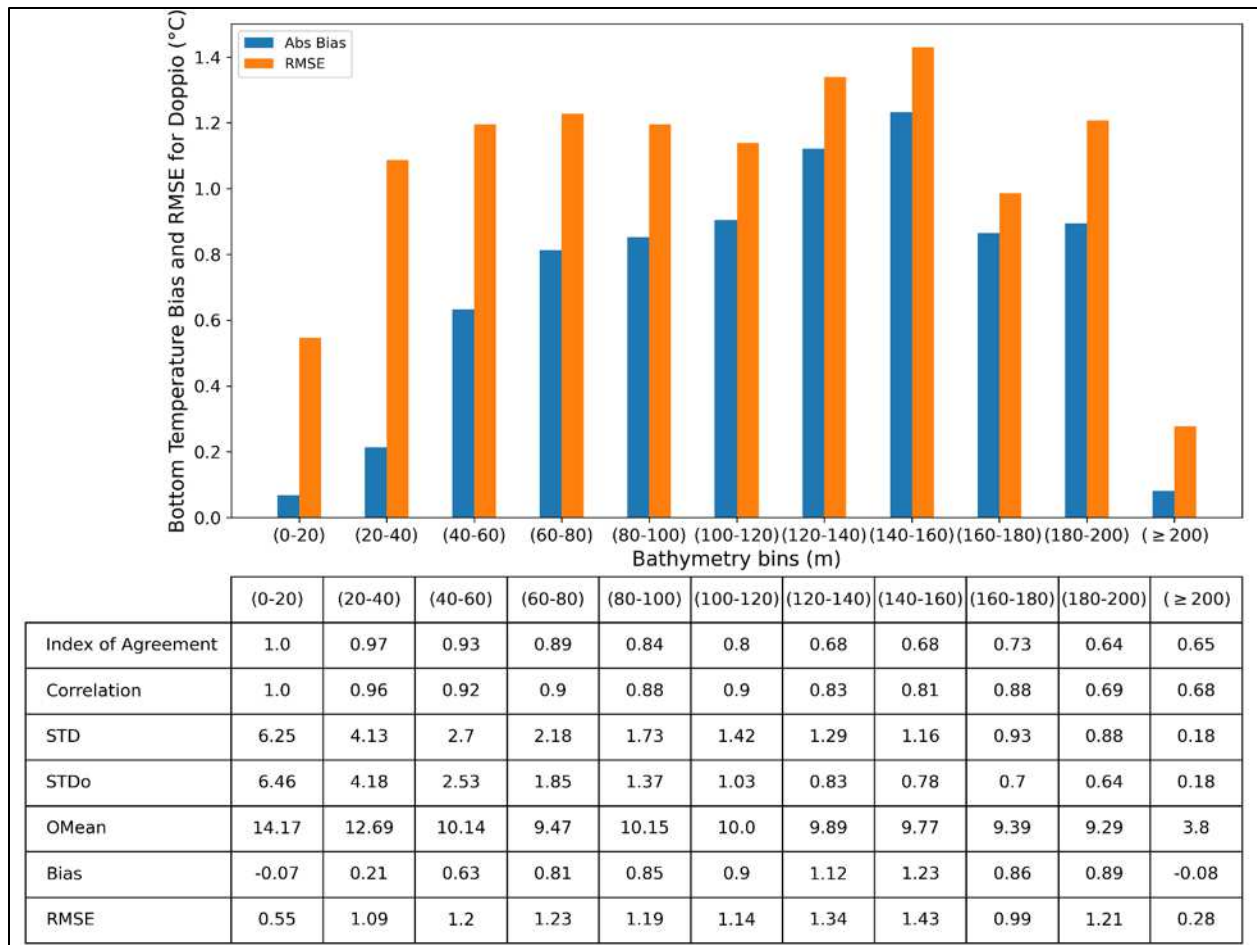


Figure 66. Bottom temperature comparison between Model and Doppio dataset for calibration period. Top: The histogram presents bias and RMSE, °C. Bottom: The table shows model skill metrics.

5.5.2.5 Model against Glider Temperature

Model calibration of temperature considered data recorded by gliders. The glider observations are spatially scattered. The gliders traveled from near the surface (2.5 m) to a depth of 175 m. Figure 67 depicts the histogram and skill statistics parameters of the selected model's results compared to the glider observations for the calibration period, Feb 2018 to Jan 2019, for temperature. Notably, the model exhibits its highest skill in very shallow and moderate depths (< 20 m and between 120 m and 160m). The monthly model skills also presented in the Table 15 for temperature. The highest model skill for temperature regarding glider observation is in summer, while the lowest model skills are observed in winter especially in January 2019.

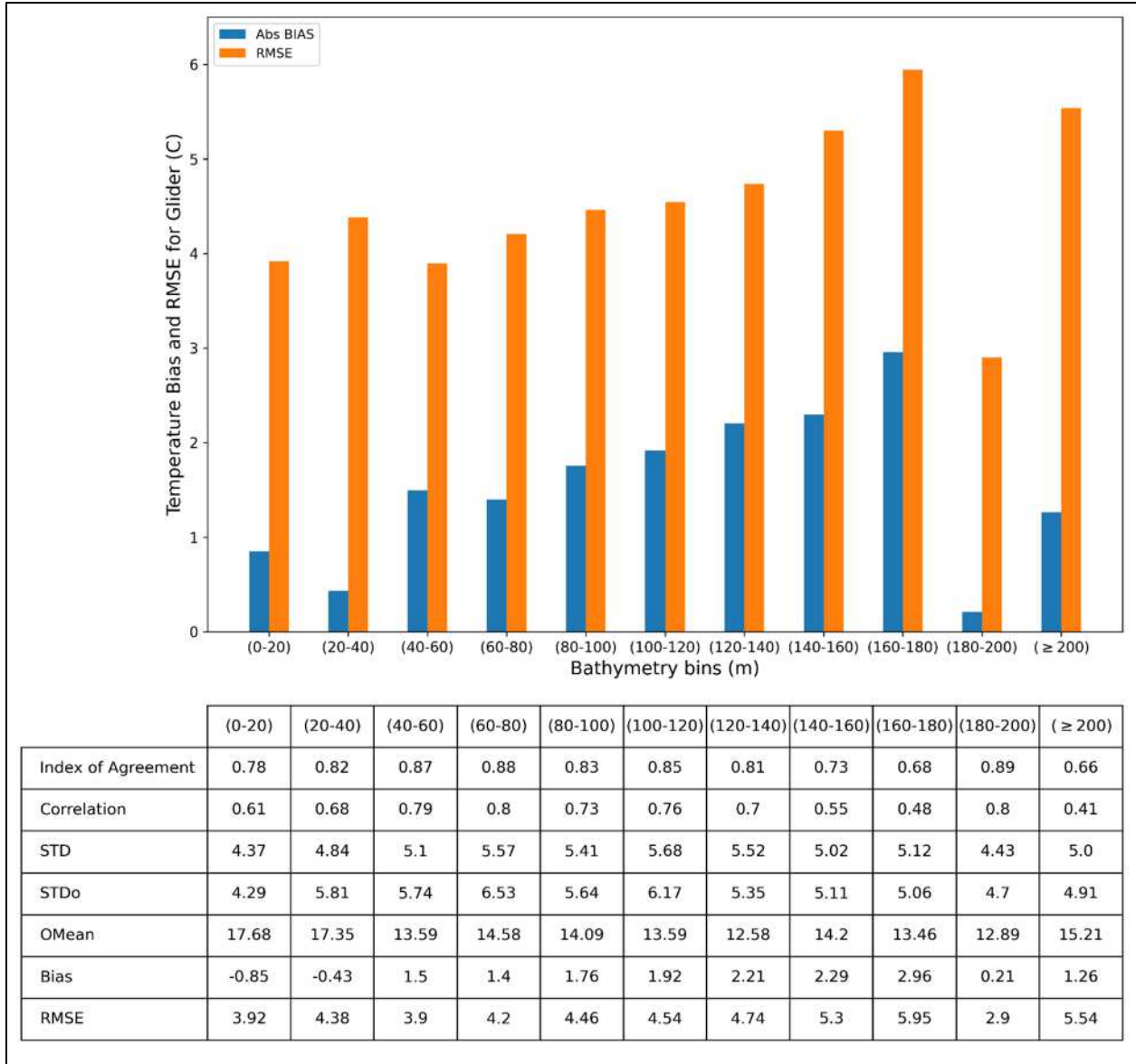


Figure 67. Temperature comparison between glider observation and model.
 Top: The histogram presents bias and RMSE, °C. Bottom: The table shows model skill metrics.

Table 15. Monthly model skill metrics against glider observations of water temperature for calibration period.

Month	Correlation	Index of Agreement	Bias (°C)	RMSE (°C)
January	-0.37	0.19	3.15	7.12
February	0.31	0.53	1.05	4.49
March	0.49	0.65	1.45	4.18
April	0.12	0.37	3.12	6.49
May	0.19	0.45	0.18	4.08
June	0.35	0.61	0.33	6.05
July	0.57	0.70	2.90	6.40
August	0.73	0.83	0.24	4.74
September	0.57	0.74	0.78	5.12
October	0.29	0.57	1.79	4.55
November	0.24	0.51	1.00	3.98
December	0.09	0.44	1.66	5.08

5.5.3 Salinity

The hydrodynamic model salinity calibration included comparison of the candidate runs to existing and predicted conditions within the Mid-Atlantic Bight. Spatially and time varying surface and bottom salinity data from the Doppio, ROMS-based (Regional Ocean Modeling System) model of the Mid-Atlantic Bight and Gulf of Maine regions, and spatially scattered time varying salinity data from gliders were compared to the model.

5.5.3.1 Model against Doppio Surface Salinity

Model calibration of surface salinity considered spatially and time varying data from the Doppio ROMS model. Doppio surface salinity was compared to the hydrodynamic model for a one-year period, February 2018 to January 2019. Skill metrics for each candidate run included bias, root mean square error, index of agreement, correlation, standard deviation of the model and observed, and mean of observed. These were analyzed and summarized in histogram and tabular form to showcase variation along the shelf (Figure 68). The model's surface salinity exhibits a higher index of agreement 0.94 in the nearshore region in depths ranging from 0–20 m versus depths higher than 20 m, the index of agreement ranges from 0.79 to 0.86. Correlation ranges from 0.84 to 0.94 in depths of 0 to 80 m. Spatial maps of monthly average surface salinity of the model, Doppio dataset, and difference over the calibration period are included in Appendix A.5.

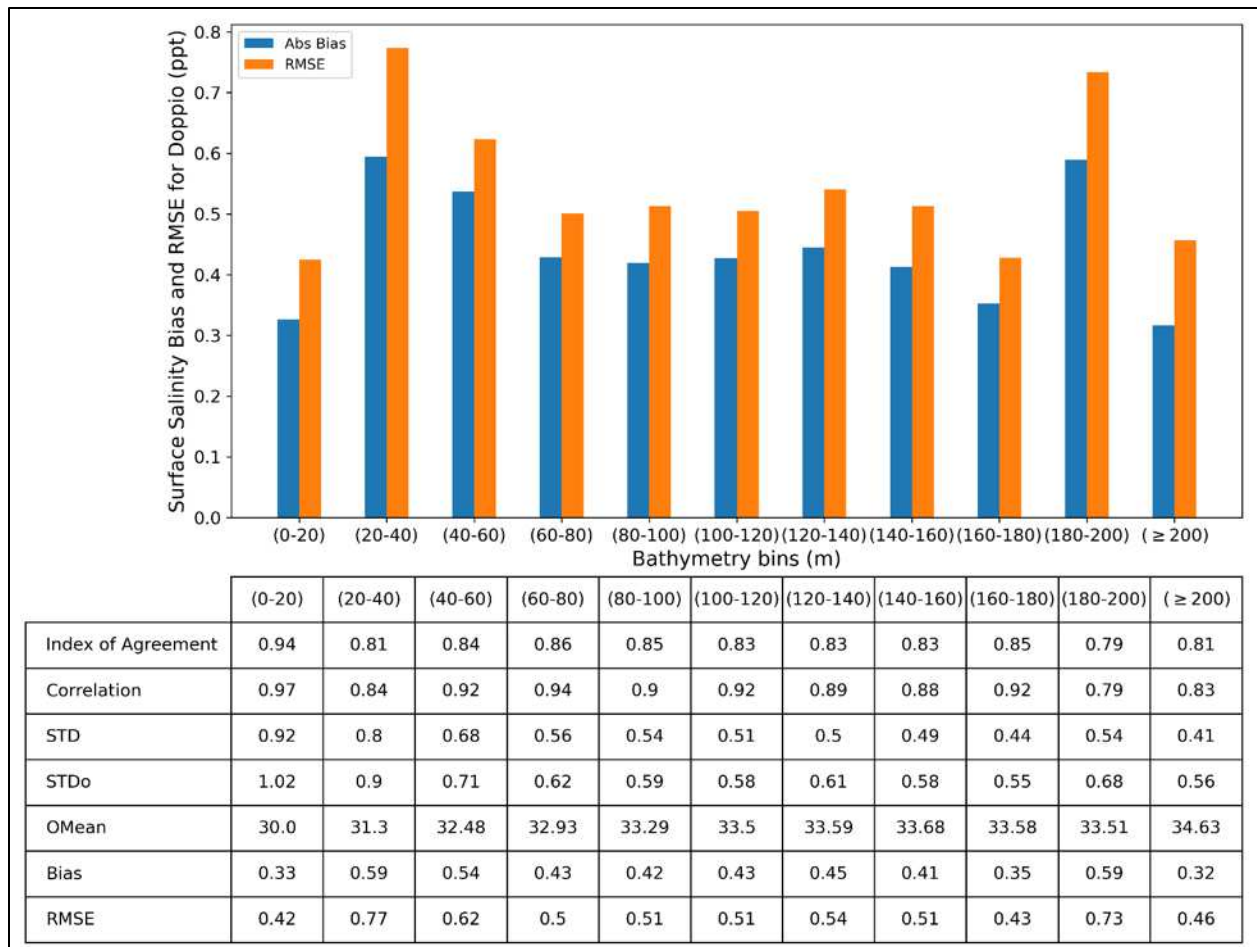


Figure 68. Surface salinity comparison between Model and Doppio dataset for calibration period. Top: The histogram presents bias and RMSE, psu. Bottom: The table shows model skill metrics.

5.5.3.2 Model against Doppio Near Bottom Salinity

Model calibration of bottom salinity considered spatially and time varying data from the Doppio ROMS model. Doppio bottom salinity was compared to the hydrodynamic model for a one-year period, February 2018 to January 2019. Skill metrics including bias, root mean square error, index of agreement, correlation, standard deviation of the model and observed, and mean of observed were analyzed and summarized in histogram and tabular form to showcase variation along the shelf (Figure 69). The model's bottom salinity exhibits high skills in the shallow regions between 0 to 40 m compared to mid-range and deeper depths. As for bottom temperatures, Doppio bottom salinities are poorly constrained due to a lack of bottom observations from the glider datasets that Doppio assimilates. Spatial maps of monthly average bottom salinity of the model, Doppio dataset, and difference over the calibration period are included in Appendix A.6.

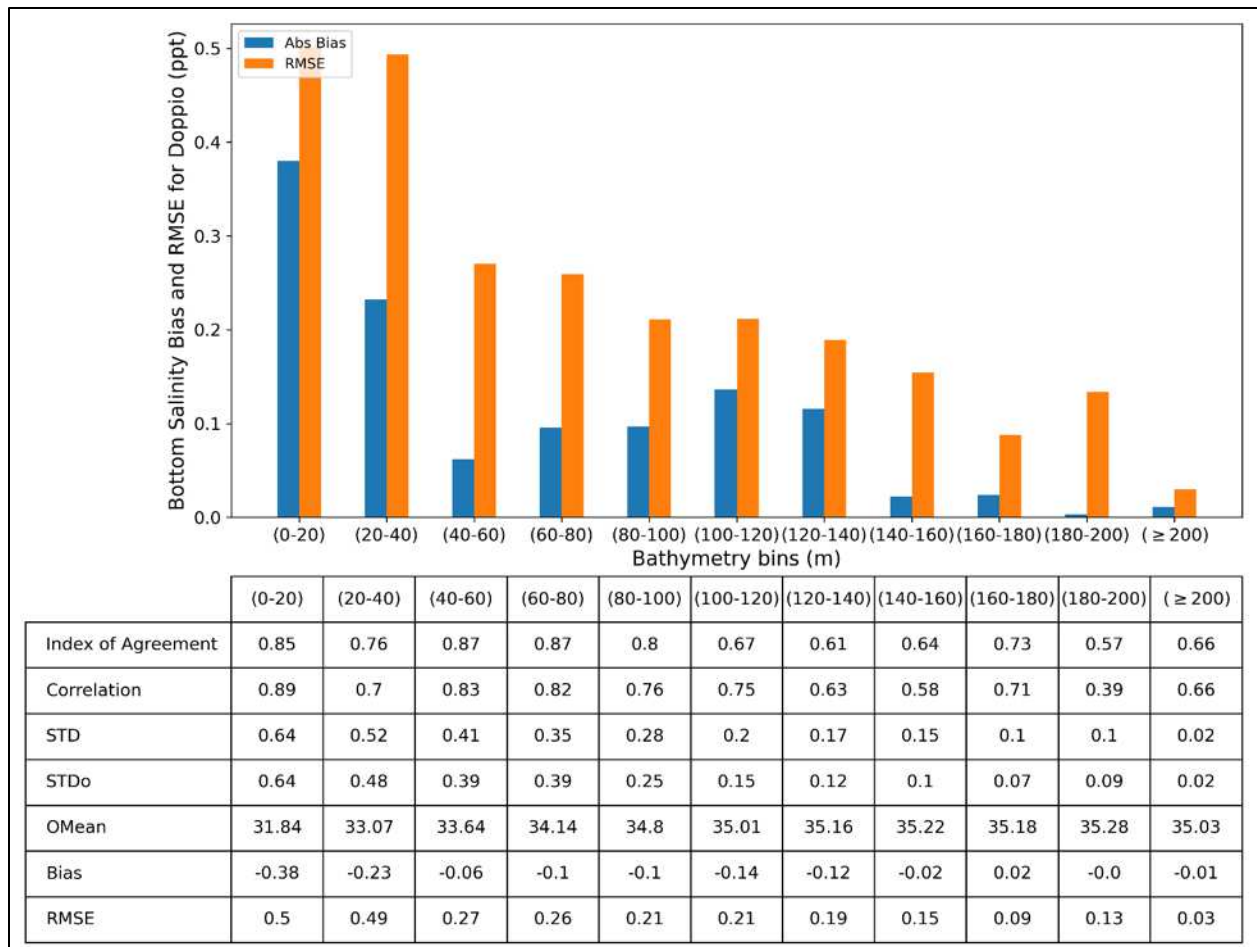


Figure 69. Bottom salinity comparison between Model and Doppio dataset for calibration period. Top: The histogram presents bias and RMSE, psu. Bottom: The table shows model skill metrics

5.5.3.3 Model against Glider Salinity

Model calibration of salinity considered data recorded by gliders. Figure 70 depicts the salinity histogram and skill parameters of the model compared to the glider observations for the calibration period, February 2018 to January 2019. Notably, the model exhibits its highest skill in very shallow and moderate depths (< 20 m and between 120 m and 160 m). The monthly model skills are also presented in Table 16 for salinity. The highest model skill for salinity regarding glider observation is in summer, while the lowest model skills are observed in winter.

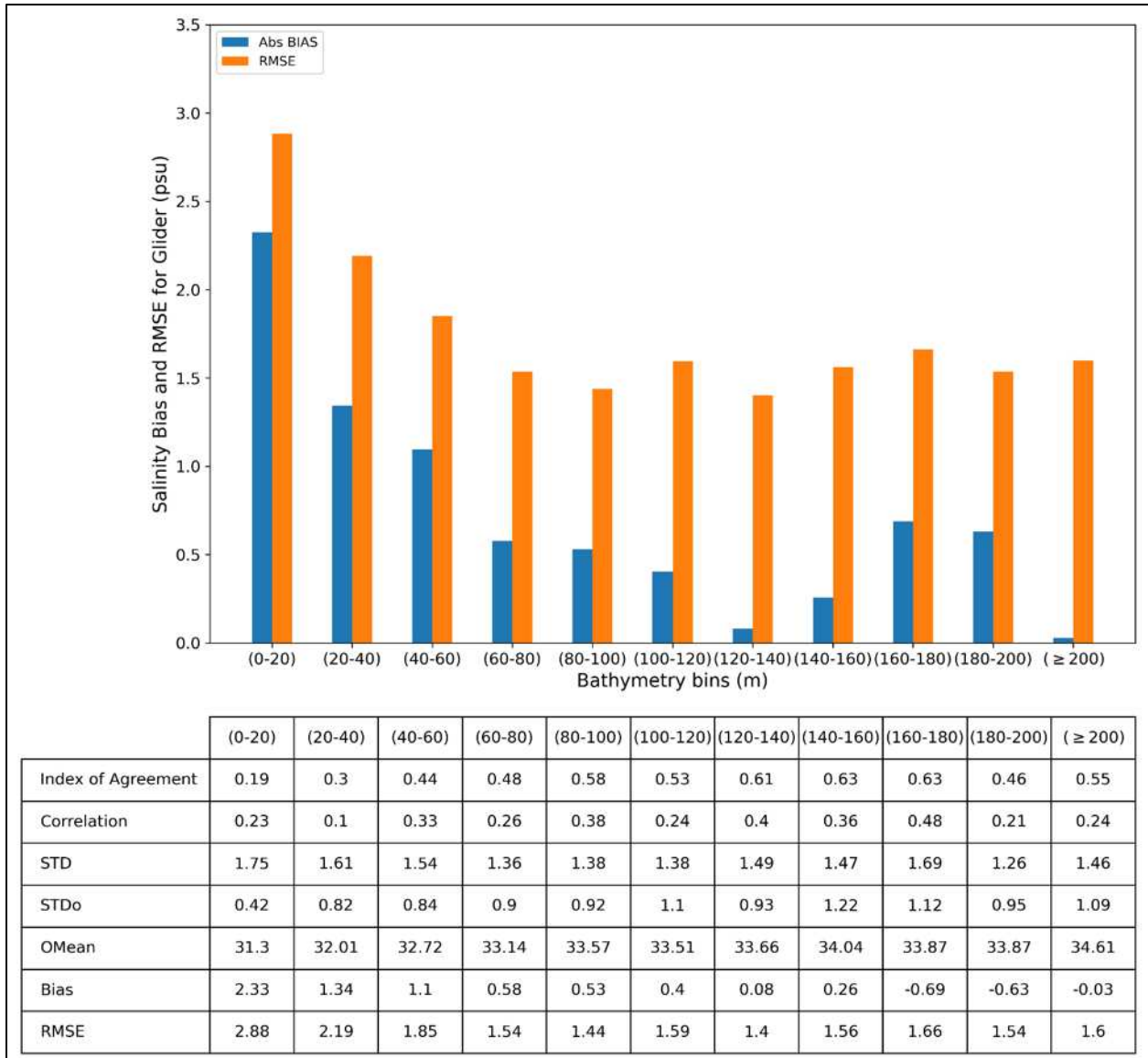


Figure 70. Salinity comparison between glider observation and model for calibration period. Top: The histogram presents bias and RMSE, psu. Bottom: The table shows model skill metrics.

Table 16. Monthly model skill metrics against glider observations of water salinity for calibration period.

Month	Correlation	Index of Agreement	Bias (psu)	RMSE (psu)
January	-0.23	0.29	0.64	1.50
February	0.25	0.54	0.12	0.76
March	0.39	0.59	0.47	0.96
April	0.23	0.52	0.60	1.42
May	0.10	0.44	0.19	1.90
June	0.10	0.47	0.16	1.29
July	-0.06	0.43	0.95	1.73
August	0.27	0.56	0.38	1.70
September	0.08	0.42	0.34	1.83
October	-0.02	0.41	0.02	2.21
November	0.01	0.46	0.23	2.11
December	0.16	0.50	0.57	1.37

5.5.4 Currents

The hydrodynamic model current calibration entailed comparison of existing and forecast conditions within the Mid-Atlantic Bight. Spatially and time varying bottom and surface current data from the Doppio, ROMS-based (Regional Ocean Modeling System) model of the Mid-Atlantic Bight and Gulf of Maine regions and surface current data from CODAR HF Radar were compared to the model.

5.5.4.1 Model against Doppio Surface Current

Model calibration of surface current considered spatially and time varying data from the Doppio ROMS model. Doppio surface current was compared to the hydrodynamic model for a one-year time period, February 2018 to January 2019. Skill metrics including bias, root mean square error, index of agreement, correlation, standard deviation of the model and observed, and mean of observed were analyzed and summarized in histogram and tabular form to showcase variation along the shelf (Figure 71). The model's surface current exhibits higher model skill in the shallow to mid-depth regions (0 m to 120 m); the bias ranges from -0.01 m/s to 0.02 m/s and RMSE ranges from 0.03 m/s to 0.04 m/s. Spatial maps of monthly average surface current of the model, Doppio dataset, and difference over the calibration period are included in Appendix A.7.

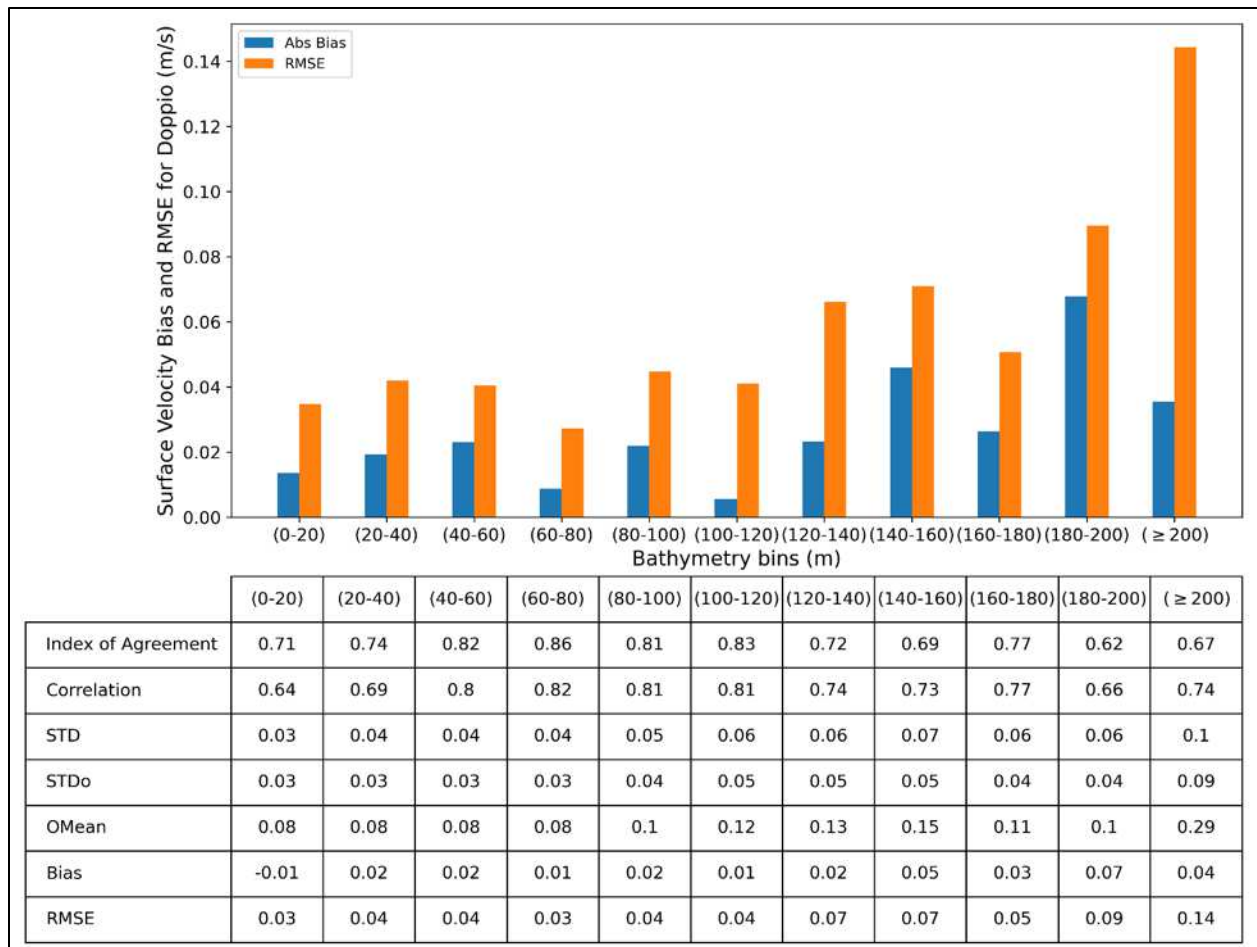


Figure 71. Surface current comparison (current magnitude, speed) between Model and Doppio dataset for calibration period.

Top: The histogram presents bias and RMSE, m/s. Bottom: The table shows model skill metrics.

5.5.4.2 Model against HF Radar Surface Current

Model calibration of surface current speed considered spatially and time varying data from CODAR HF Radar. HF Radar surface current speed was compared to the hydrodynamic model for a one-year period, February 2018 to January 2019. Skill metrics including bias, root mean square error, index of agreement, correlation, standard deviation of the model and observed, and mean of observed were analyzed and summarized in histogram and tabular form to showcase variation along the shelf (Figure 72). The model's surface current exhibits good model skill in shallow and mid-depth regions (0 m to 140 m); the bias ranges from -0.02 m/s to 0.03 m/s and RMSE ranges from 0.04 m/s to 0.07 m/s. The higher absolute differences (Bias and RMSE) above the 140 m isobath are influenced by the strong Shelf Break Jet and the Gulf Stream in the southern edge of the modeling domain that have much higher speeds than the continental shelf itself. The correlation and index of agreement metrics however, which are scaled to observations, though lower, are reasonable in these areas as well. Spatial maps of monthly average surface current magnitude of the model, HF Radar dataset, and difference over the calibration period are included in Appendix A.8.

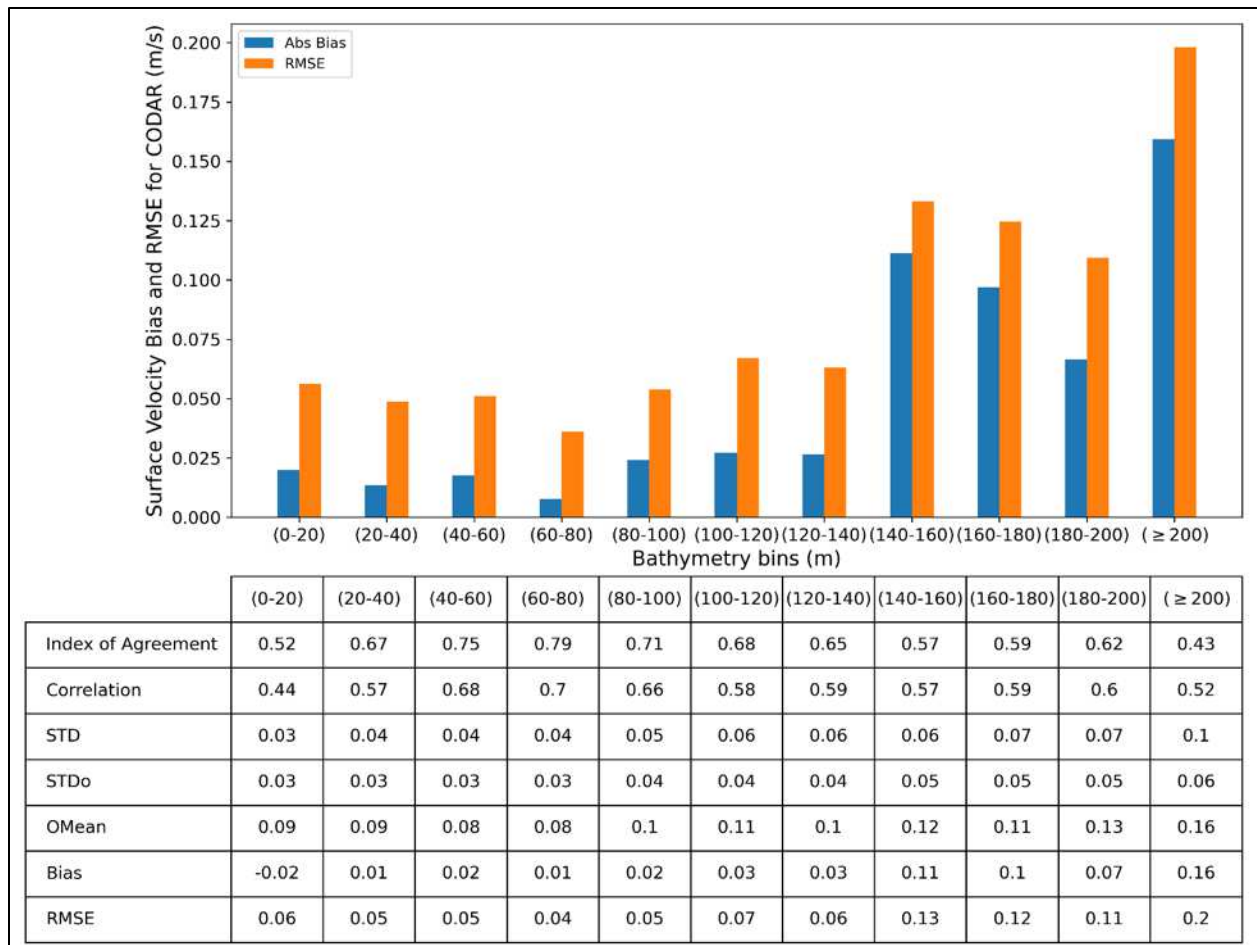


Figure 72. Surface current comparison between Model and HF Radar dataset for calibration period. Top: The histogram presents bias and RMSE, m/s. Bottom: The table shows model skill metrics.

5.5.4.3 Model against Doppio Bottom Current

Model calibration of bottom current considered spatially and time varying data from the Doppio ROMS model. Doppio bottom current was compared to the hydrodynamic model for a one-year period, February 2018 to January 2019. Skill metrics including bias, root mean square error, index of agreement, correlation, standard deviation of the model and observed, and mean of observed were analyzed and summarized in histogram and tabular form to showcase variation along the shelf (Figure 73). The model's bottom current exhibits the lowest bias and RMSE in depths from 0 m to 80 m; the bias ranges from 0m/s to 0.01 m/s and RMSE ranges from 0.01 m/s to 0.02 m/s. Although there is a high model skill with higher index of agreement and correlation in the shallow and mid-depth regions, bottom current in depths beyond 80 m have lower index of agreement and correlation. Spatial maps of monthly average bottom current of the model, Doppio dataset, and difference over the calibration period are included in Appendix A.9.

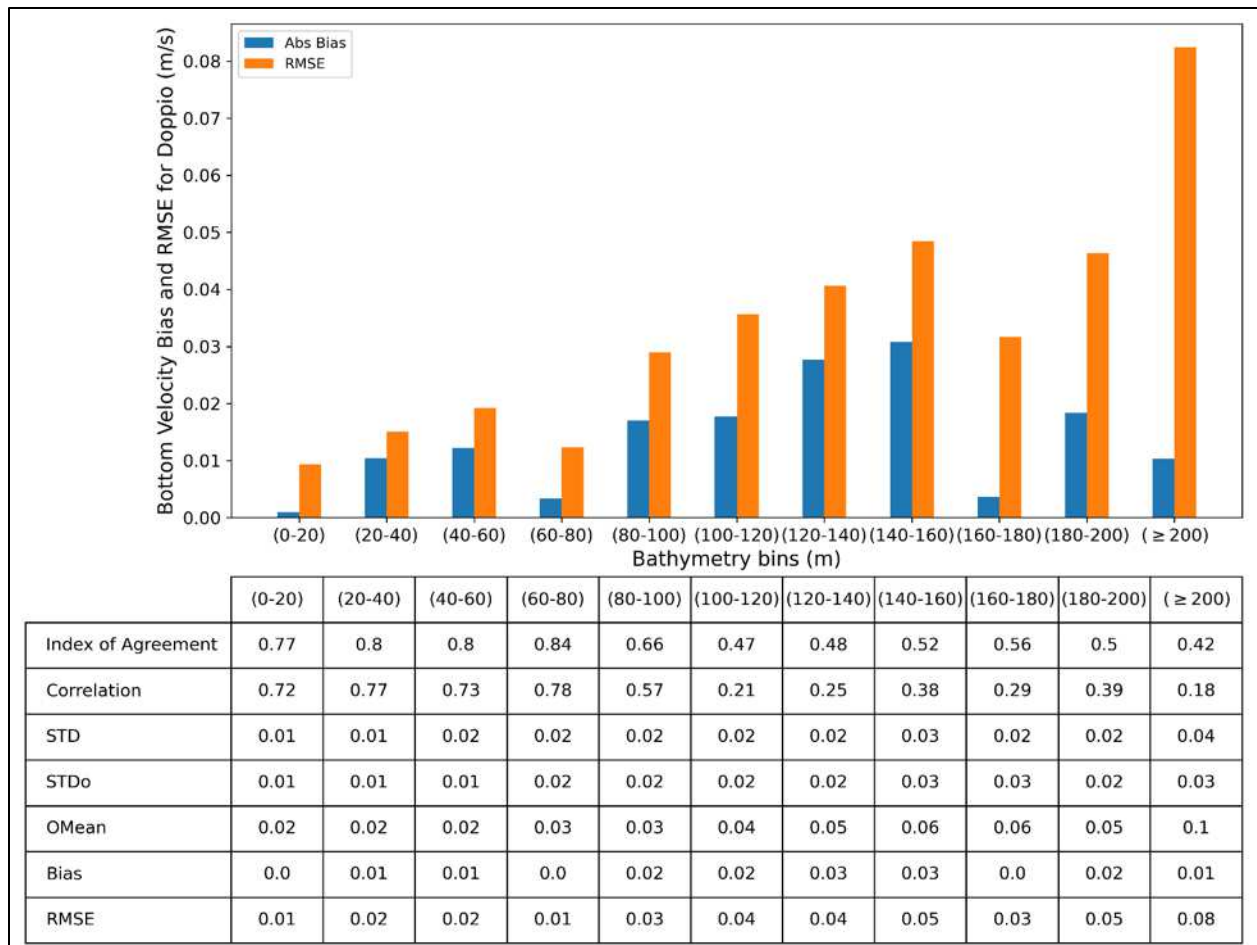


Figure 73. Bottom current comparison between Model and Doppio dataset for calibration period. Top: The histogram presents bias and RMSE, m/s. Bottom: The table shows model skill metrics.

5.6 Validation

The hydrodynamic model was validated for the one-year period following calibration, February 2019 to January 2020. Validation of the hydrodynamic model encompassed sea surface height, water temperature, salinity, and currents from the same datasets as the calibration period.

5.6.1 Sea Surface Height

The hydrodynamic model sea surface height validation included the comparison of existing and forecast conditions within the Mid-Atlantic Bight. Time varying sea surface height from NOS tidal gauges and spatially and time varying sea surface height from Doppio, ROMS-based (Regional Ocean Modeling System) model of the Mid-Atlantic Bight and Gulf of Main regions were compared to the model.

5.6.1.1 Model against NOS Station Data

The model's sea surface height was validated to NOS tidal gauges. Four NOS tidal gauges spanning North and South of the model domain, were compared to the hydrodynamic model for a one-year time period following calibration, February 2019 to January 2020. Sea surface height time series comparing the model and NOS tide gauge data, as well as scattered density plots of simulated versus observed sea

surface height are displayed for each station in Figure 74 through Figure 81. Validation statistics are summarized in Table 17.

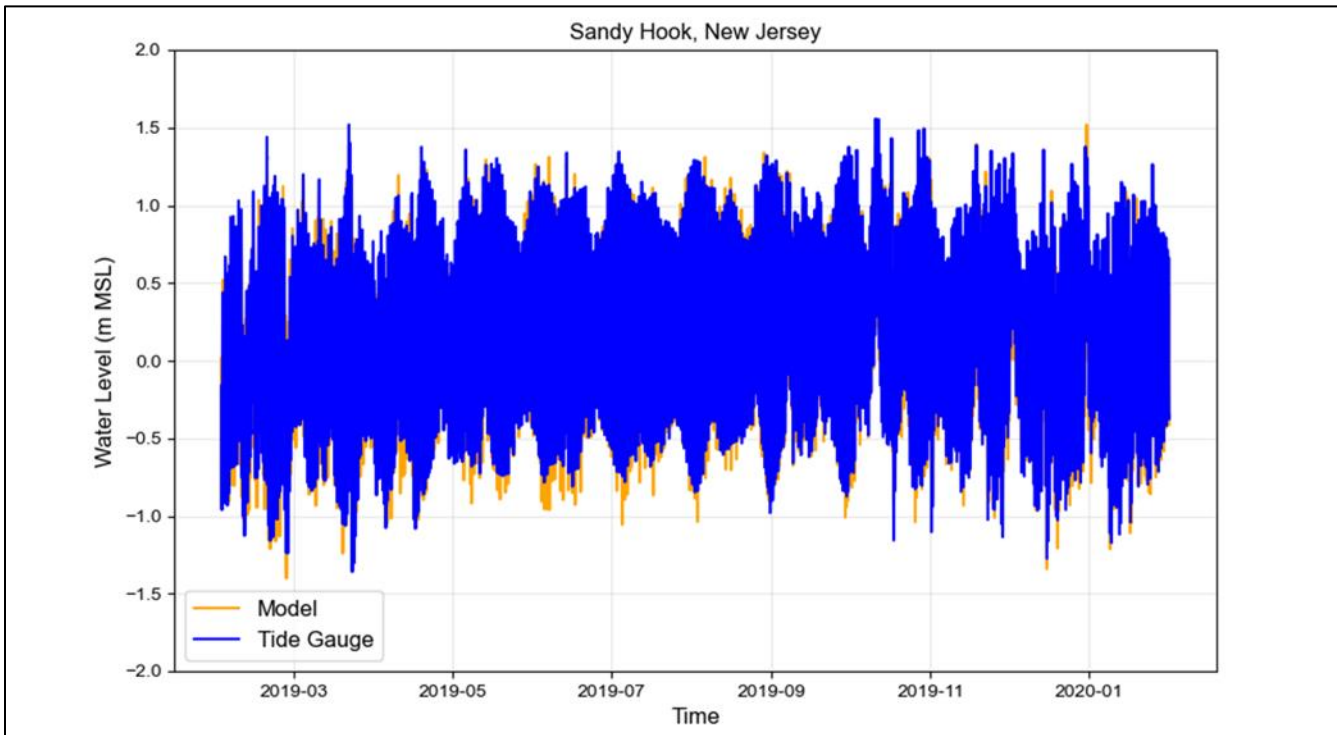


Figure 74. Water level comparison between hydrodynamic model and NOS tide gauge at Sandy Hook, New Jersey.

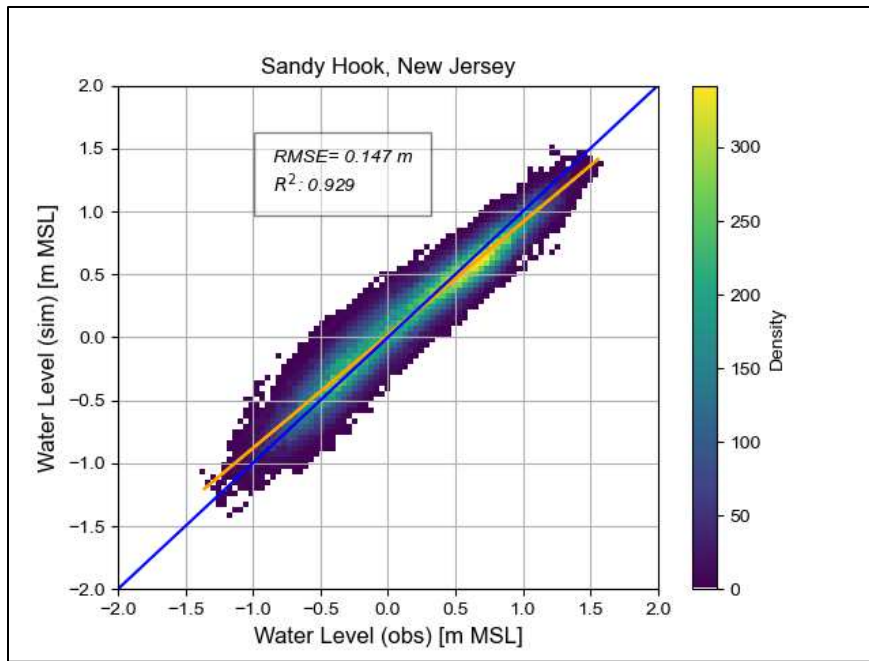


Figure 75. Water level simulated in the model versus observed from the NOS tide gauge at Sandy Hook, New Jersey.

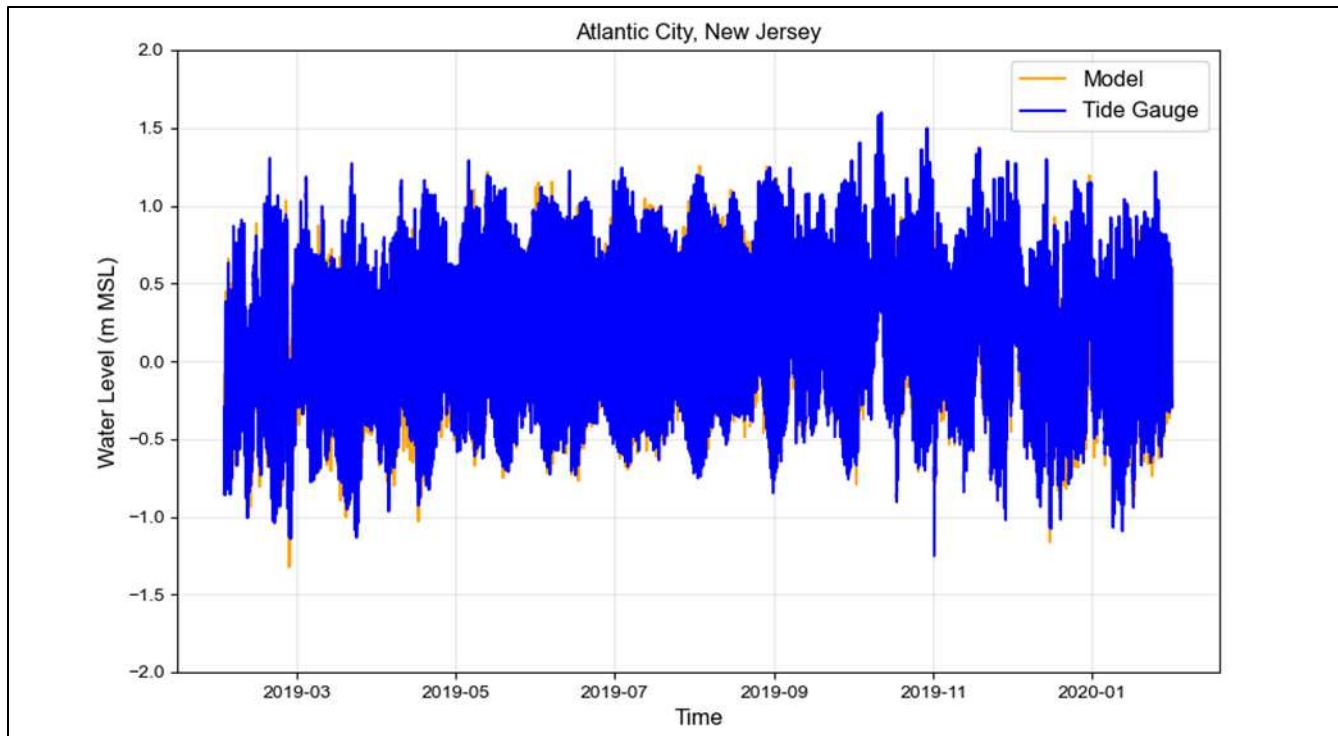


Figure 76. Water level comparison between hydrodynamic model and NOS tide gauge at Atlantic City, New Jersey.

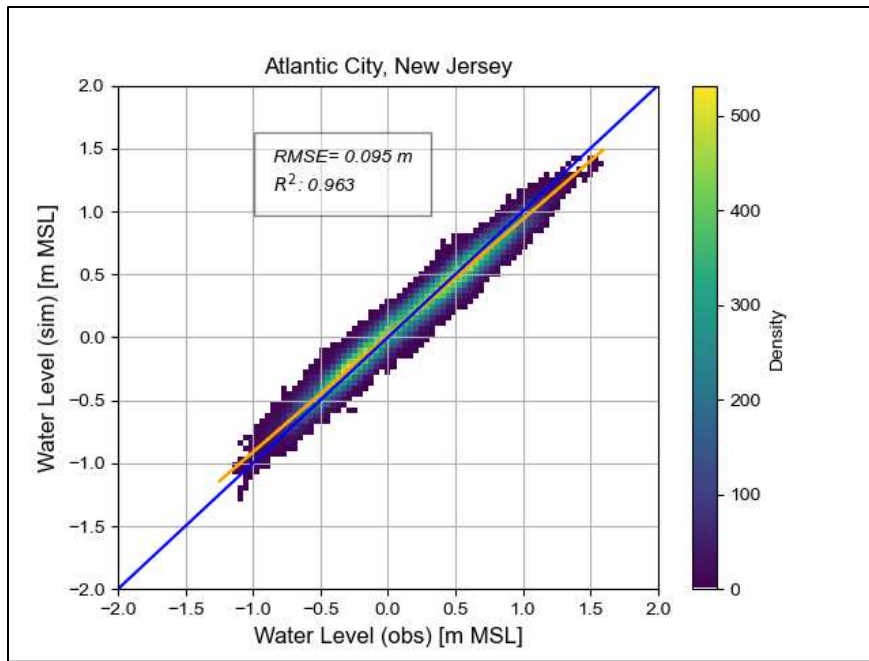


Figure 77. Water level simulated in the model versus observed from the NOS tide gauge at Atlantic City, New Jersey.

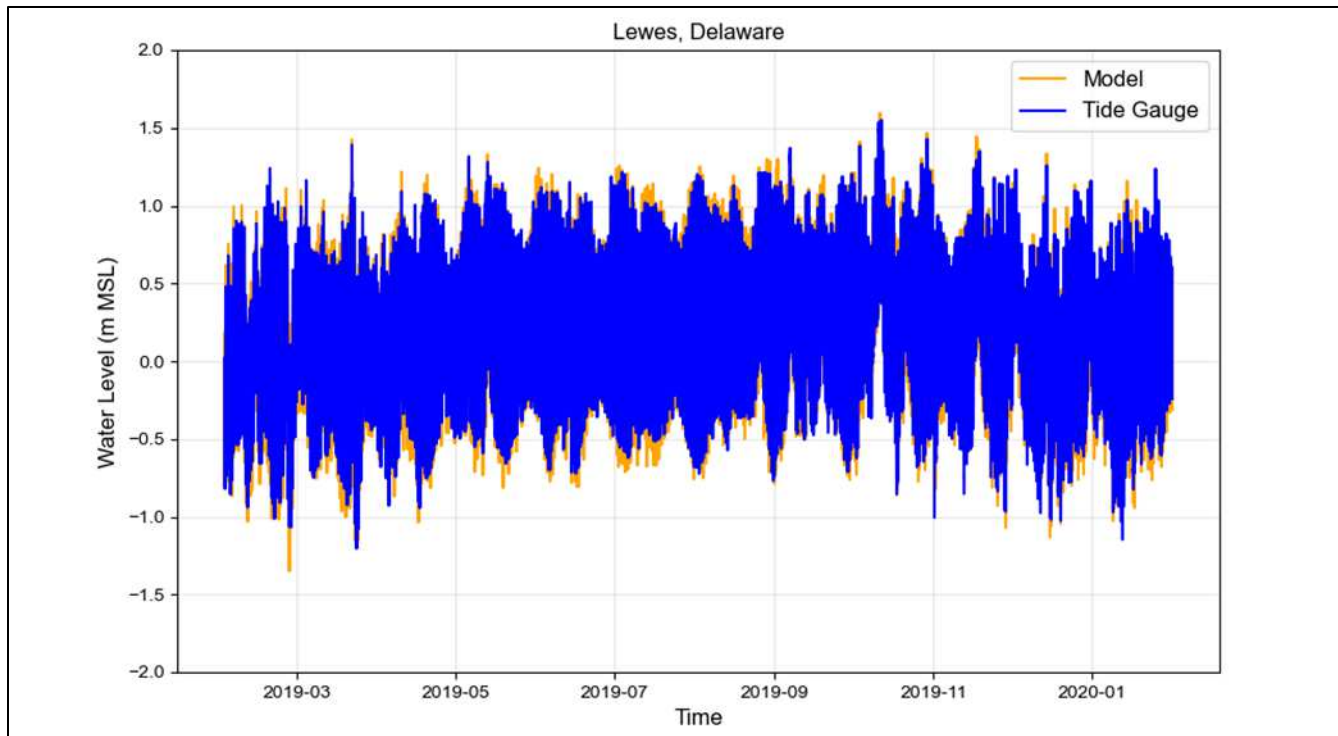


Figure 78. Water level comparison between hydrodynamic model and NOS tide gauge at Lewes, Delaware.

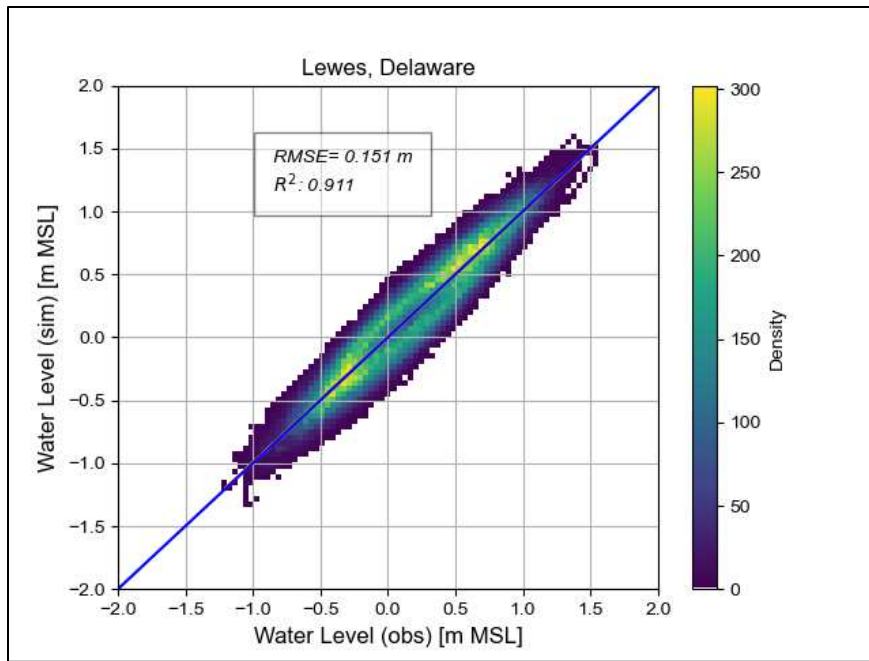


Figure 79. Water level simulated in the model versus observed from the NOS tide gauge at Lewes, Delaware.

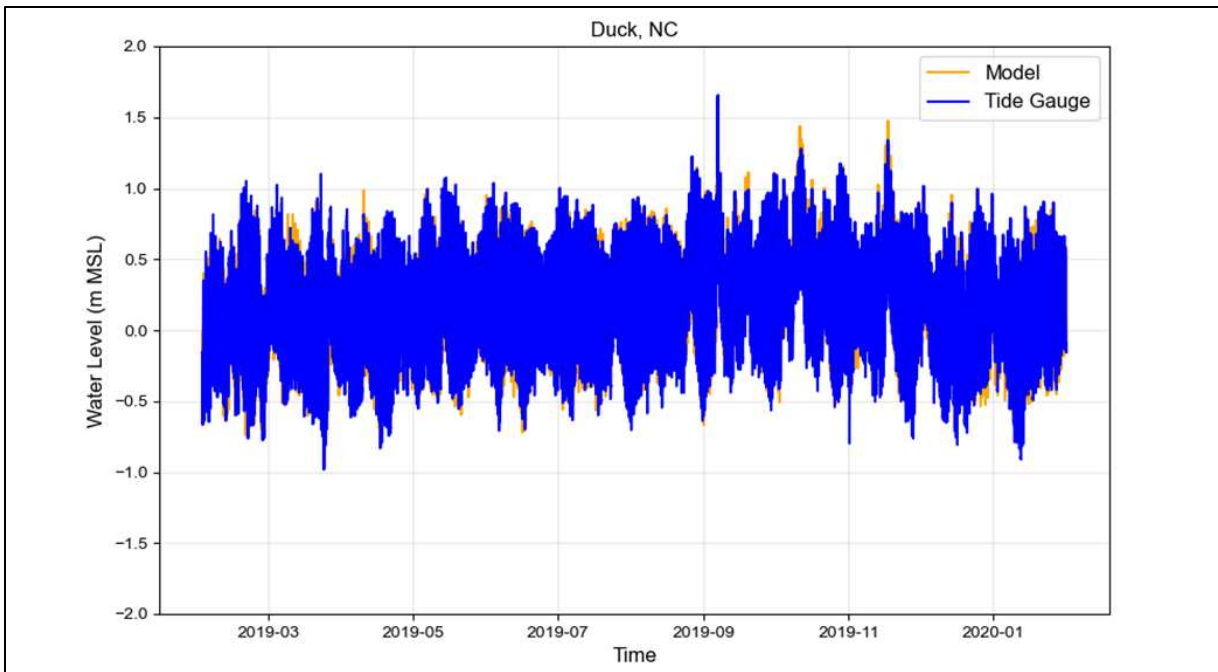


Figure 80. Water level comparison between hydrodynamic model and NOS tide gauge at Duck, North Carolina.

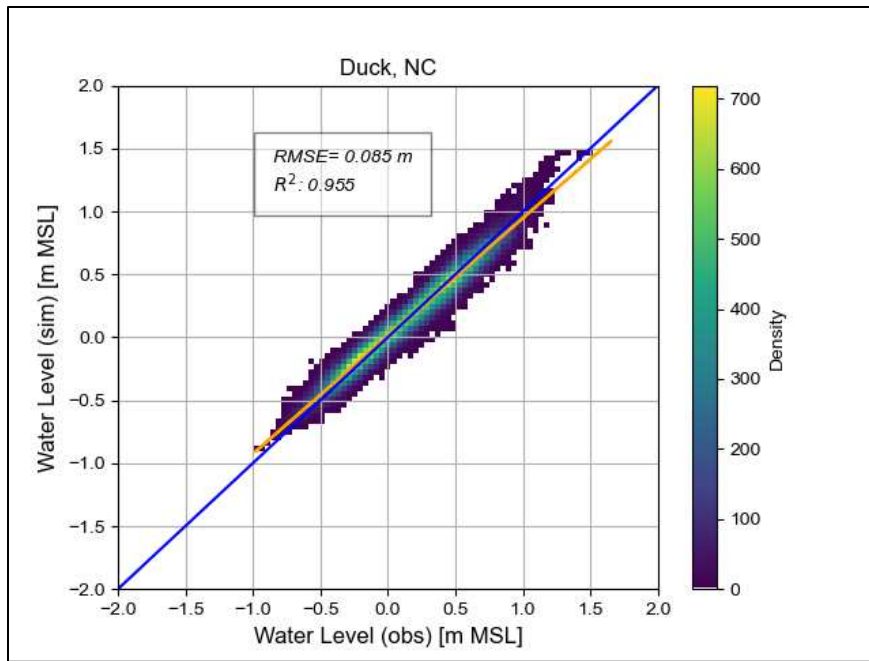


Figure 81. Water level simulated in the model versus observed from the NOS tide gauge at Duck, North Carolina.

Table 17. Model validation statistics for water elevation (m) at four NOS stations.

Station Name	NOS ID #	RMSE, meters	R	R ²
Sandy Hook, New Jersey	8531680	0.147	0.964	0.929
Atlantic City, New Jersey	8534720	0.095	0.981	0.963
Lewes, Delaware	8557380	0.151	0.955	0.911
Duck, North Carolina	8651370	0.085	0.977	0.955

5.6.1.2 Model against Doppio Sea Surface Height

Model validation of sea surface height considered spatially and time varying data from the Doppio ROMS model. Doppio sea surface height was compared to the hydrodynamic model for a one-year period following calibration, February 2019 to January 2020. Skill metrics including bias, root mean square error, index of agreement, correlation, standard deviation of the model and observed, and mean of observed were analyzed and summarized in histogram and tabular form to showcase variation along the shelf (Figure 82). The model sea surface height exhibits low bias and high index of agreement across all bathymetric bins compared to Doppio. Spatial maps of monthly average sea surface height of the model, Doppio dataset, and difference over the validation period are included in Appendix A.1.

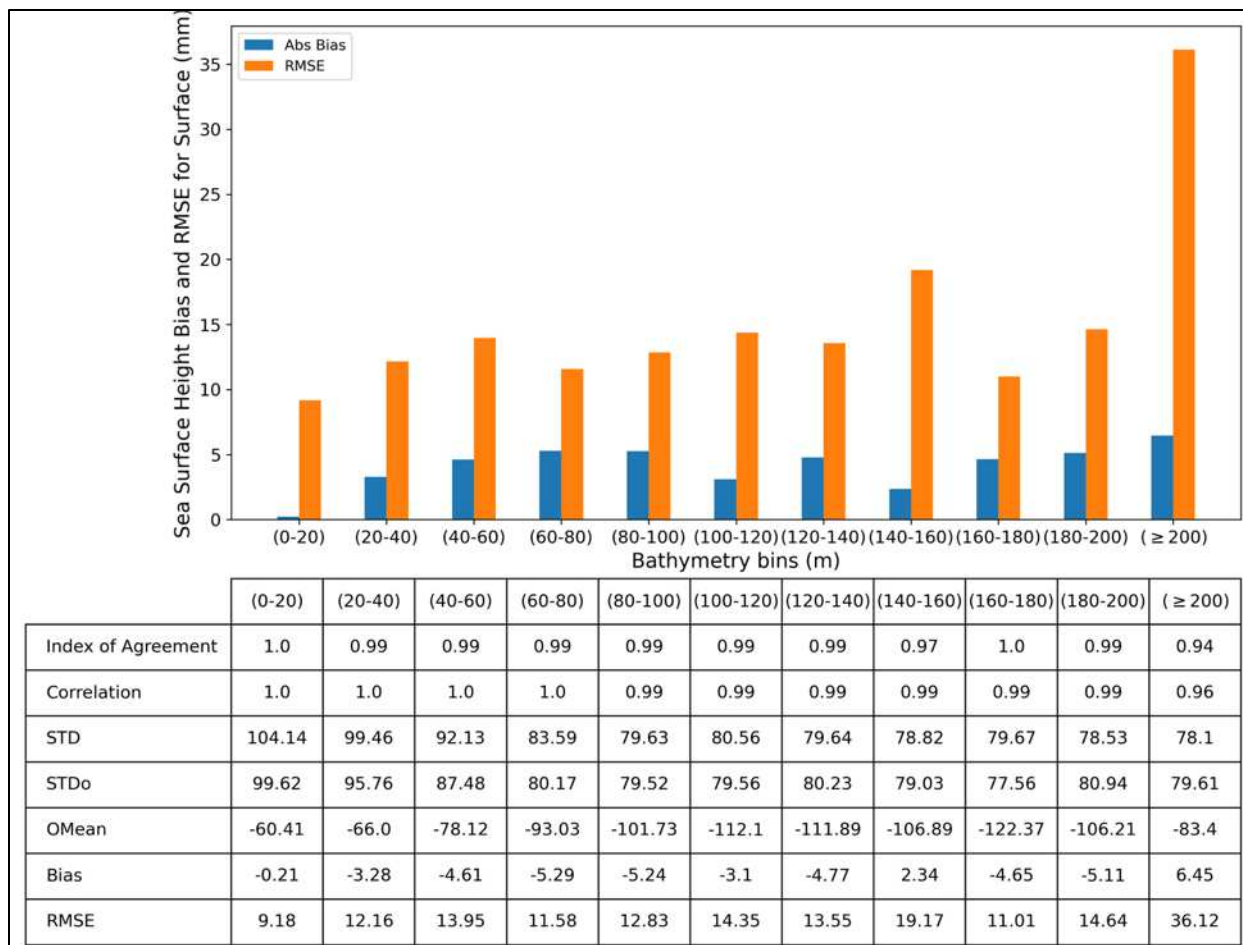


Figure 82. Sea Surface Height comparison between Model and Doppio dataset for validation period. Top: The histogram presents bias and RMSE, mm. Bottom: The table shows model skill metrics.

5.6.2 Water Temperature

The hydrodynamic model water temperature validation included comparison of existing and forecast conditions within the Mid-Atlantic Bight. Time varying surface temperature from NDBC stations, spatially and time varying surface and bottom temperature data from the Doppio, ROMS-based (Regional Ocean Modeling System) model of the Mid-Atlantic Bight and Gulf of Maine regions, spatially varying monthly surface temperature data from NOAA Optimally Interpolated High-Resolution SST (OISSTV2), and spatially scattered time varying temperature data provided from gliders were compared to the model.

5.6.2.1 Model against NDBC Temperature Data

The model's water temperature predictions were validated against NDBC stations time series and NOAA High Resolution Satellite-derived de-clouded Sea Surface Temperature time series (Section 3.4). The time series comparisons of the model to the 12 NDBC stations from February 2019 to January 2020 are presented in Figure 83 through Figure 93. Table 18 shows a statistical comparison of temperature from the validated model against observations at the NDBC stations. The comparisons show a good agreement between modeled surface temperature and NDBC observations for the validation period. Stations that exhibited the lowest skill metrics included NDBC stations 44014 and 44088, both located offshore of Virginia near the shelf break at the southeast portion of the model domain closest to the Gulf Stream (Figure 112). The seasonal variation in the model is less than in the NDBC data there. The model appears

to have a cold water bias in the summer and a warm water bias in the winter. It is not clear what drives these apparent biases at the southern part of the shelf break. However, the monthly maps comparing the model against NOAA SST in Appendix A2 point to a possible increased diffusion of the Gulf Stream in the winter leading to warm bias, paired with an increased impact of the colder shelf break jet in the summer leading to a cold bias, in the region of these buoys.

Table 18. Model skill metrics against NDBC observations of surface water temperature for validation period.

Station Name	Correlation	Index of Agreement	Bias (°C)	RMSE (°C)
44095 Oregon Inlet NC	0.96	0.96	1.22	2.35
44086 Nags Head NC	0.97	0.98	0.82	1.90
44100 Duck FRF NC	0.99	0.99	0.30	1.30
44014 Virginia	0.90	0.86	1.05	3.51
44099 Cape Henry VA	0.99	0.99	0.19	1.00
44089 Wallops Island VA	0.99	1.00	-0.06	0.91
44009 Delaware Bay	0.99	0.99	-0.14	1.13
44091 Barnegat NJ	0.99	0.99	-0.57	1.33
44065 New York Harbor Entrance	0.99	1.00	-0.09	0.80
44025 Long Island	0.99	0.99	0.60	1.21
44066 East Long Beach NJ	0.99	0.99	-0.19	0.91

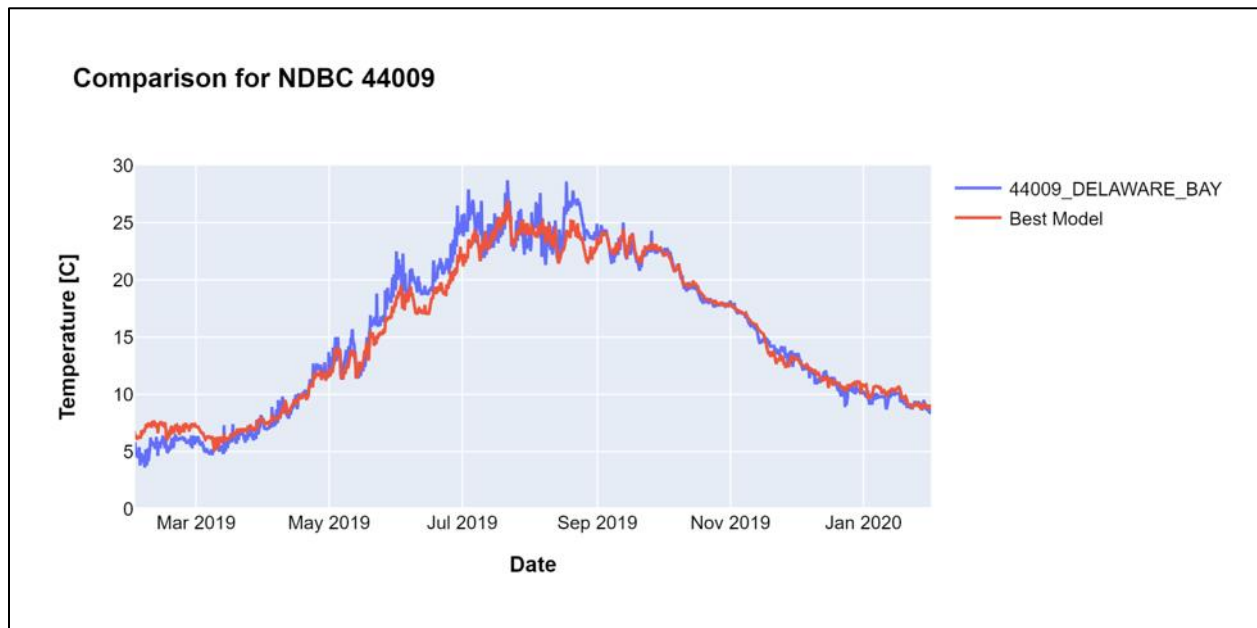


Figure 83. Temperature timeseries validation; NDBC Buoy 44009 (blue) and calibrated model (red).

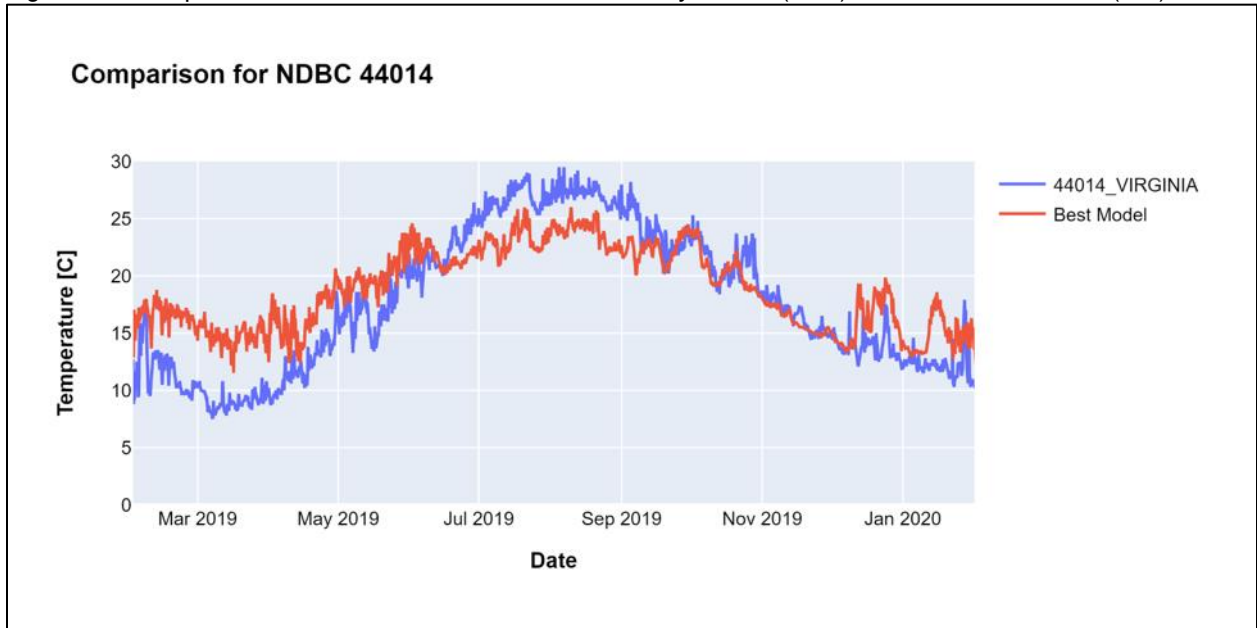


Figure 84. Temperature timeseries validation; NDBC Buoy 44014 (blue) and calibrated model (red).



Figure 85. Temperature timeseries validation; NDBC Buoy 44025 (blue) and calibrated model (red).

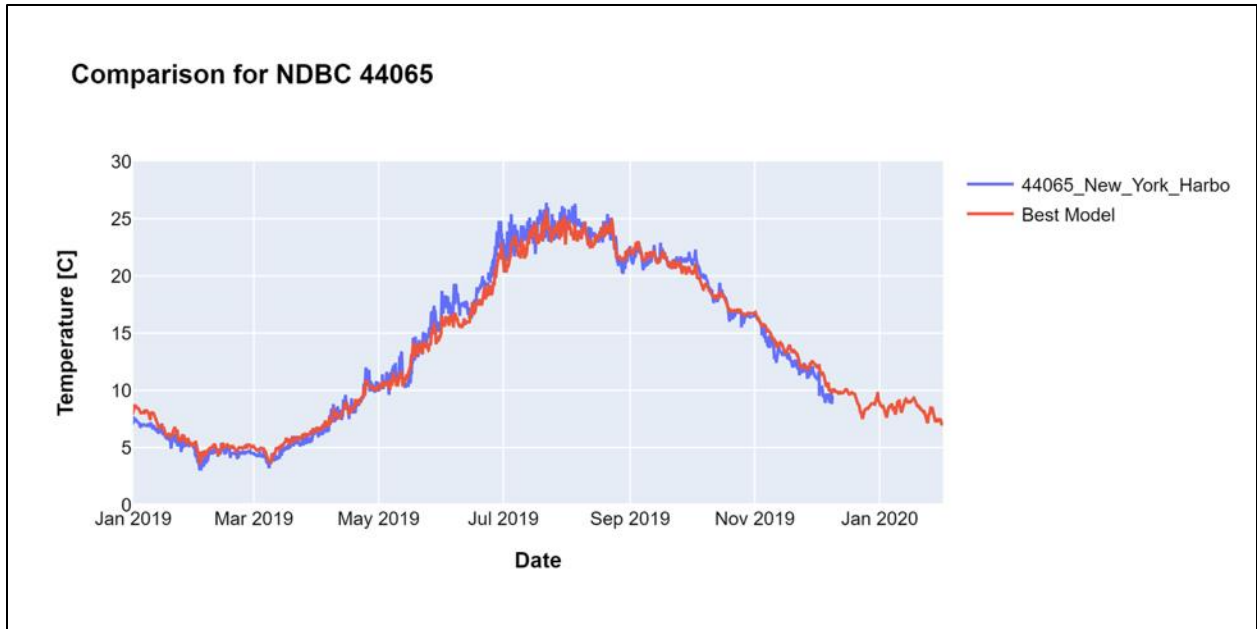


Figure 86. Temperature timeseries validation; NDBC Buoy 44065 (blue) and calibrated model (red).

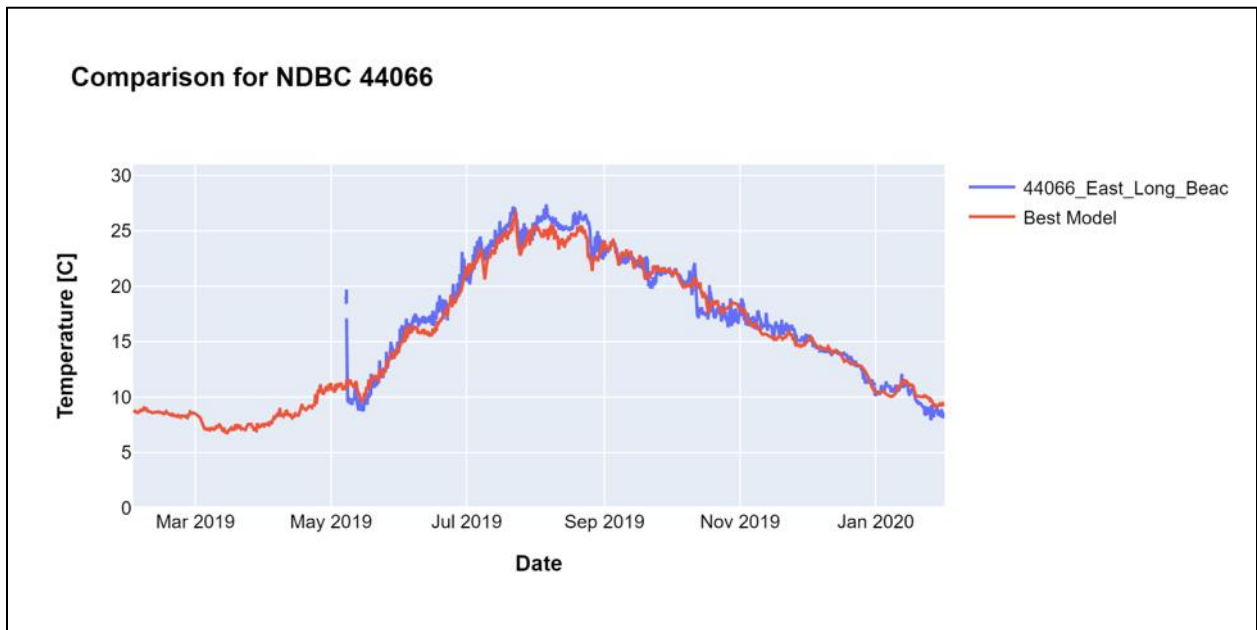


Figure 87. Temperature timeseries validation; NDBC Buoy 44066 (blue) and calibrated model (red).

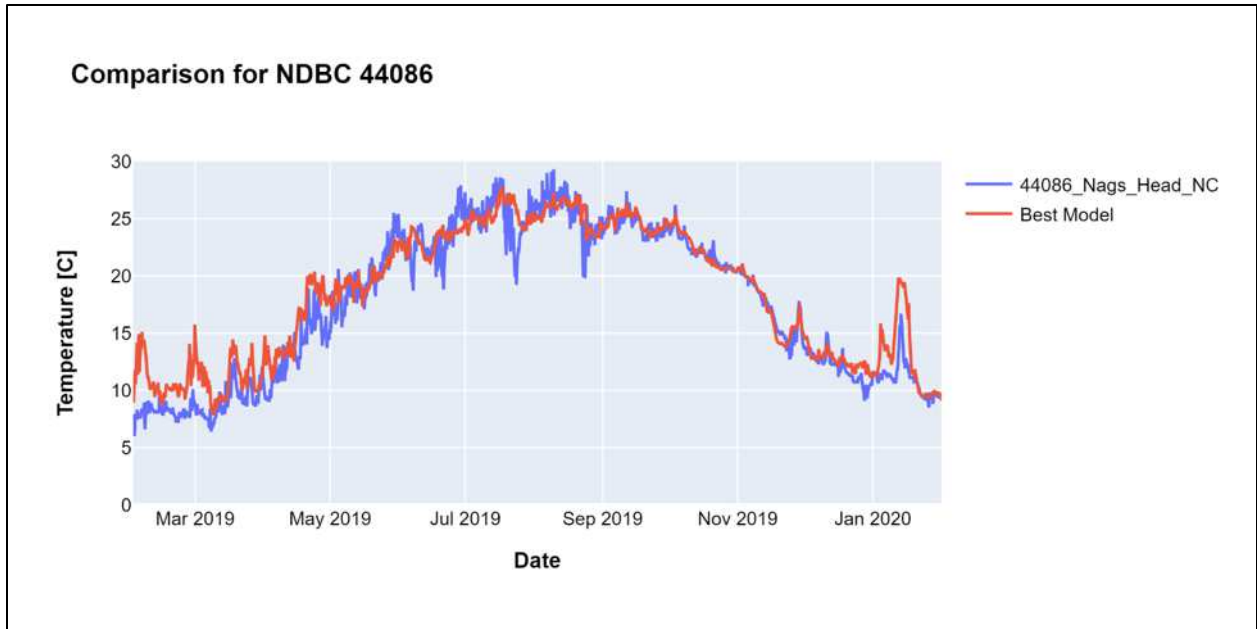


Figure 88. Temperature timeseries validation; NDBC Buoy 44086 (blue) and calibrated model (red).



Figure 89. Temperature timeseries validation; NDBC Buoy 44089 (blue) and calibrated model (red).



Figure 90. Temperature timeseries validation; NDBC Buoy 44091 (blue) and calibrated model (red).

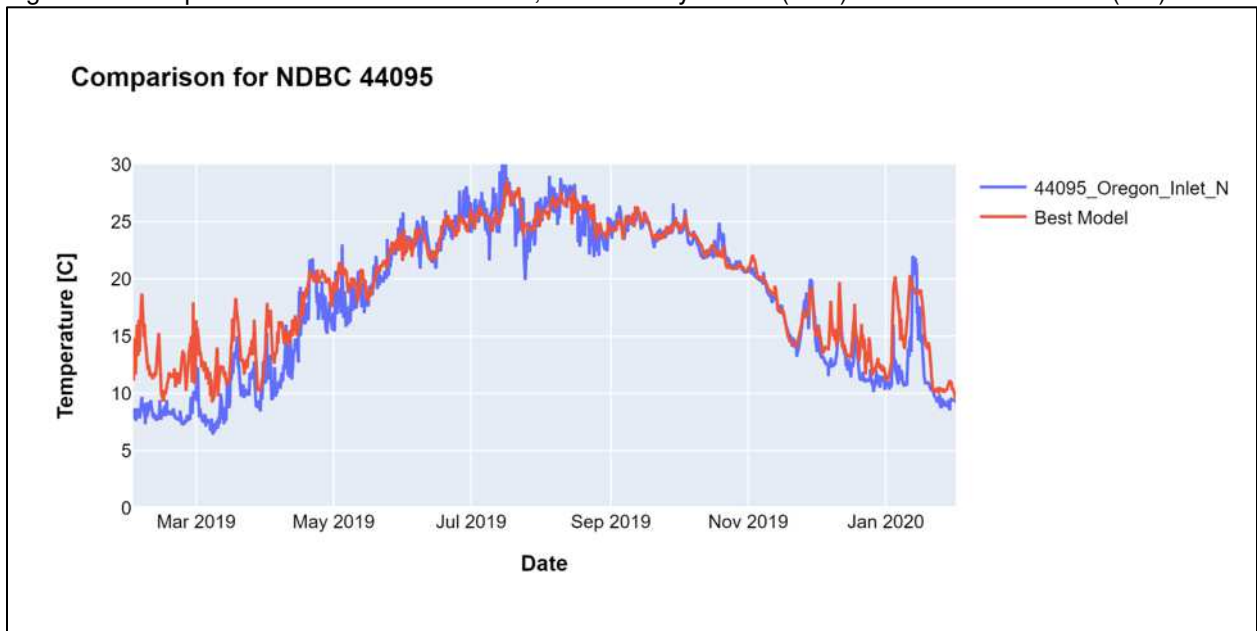


Figure 91. Temperature timeseries validation; NDBC Buoy 44095 (blue) and calibrated model (red).



Figure 92. Temperature timeseries validation; NDBC Buoy 44099 (blue) and calibrated model (red).

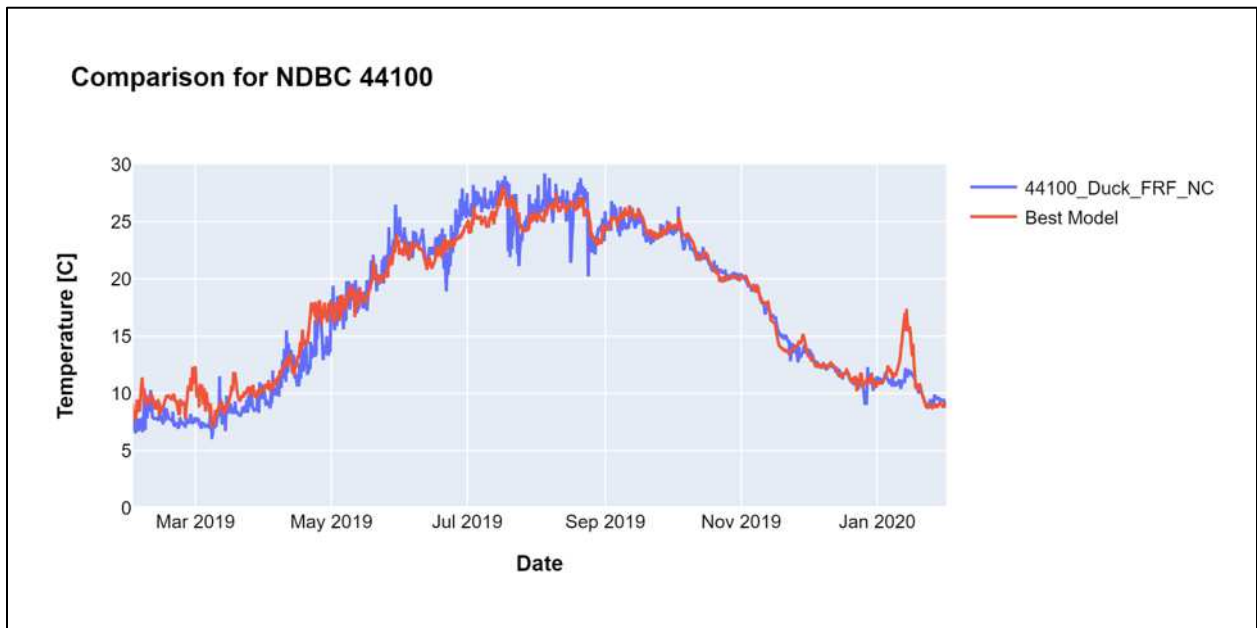


Figure 93. Temperature timeseries validation; NDBC Buoy 44100 (blue) and calibrated model (red).

5.6.2.2 Model against Doppio Surface Temperature

Model validation of surface temperature considered spatially and time varying data from the Doppio ROMS model. Doppio surface temperature was compared to the hydrodynamic model for a one-year period following calibration, February 2019 to January 2020. Skill metrics including bias, root mean square error, index of agreement, correlation, standard deviation of the model and observed, and mean of observed were analyzed and summarized in histogram and tabular form to showcase variation along the

shelf (Figure 94). The model’s surface temperature is in good agreement to the Doppio dataset. This is exhibited in high index of agreement and correlation over the model domain as well as low bias ranging from -0.16°C to 0.15°C . Spatial maps of monthly average surface temperature of the model, Doppio dataset, and difference over the validation period are included in Appendix A.2.

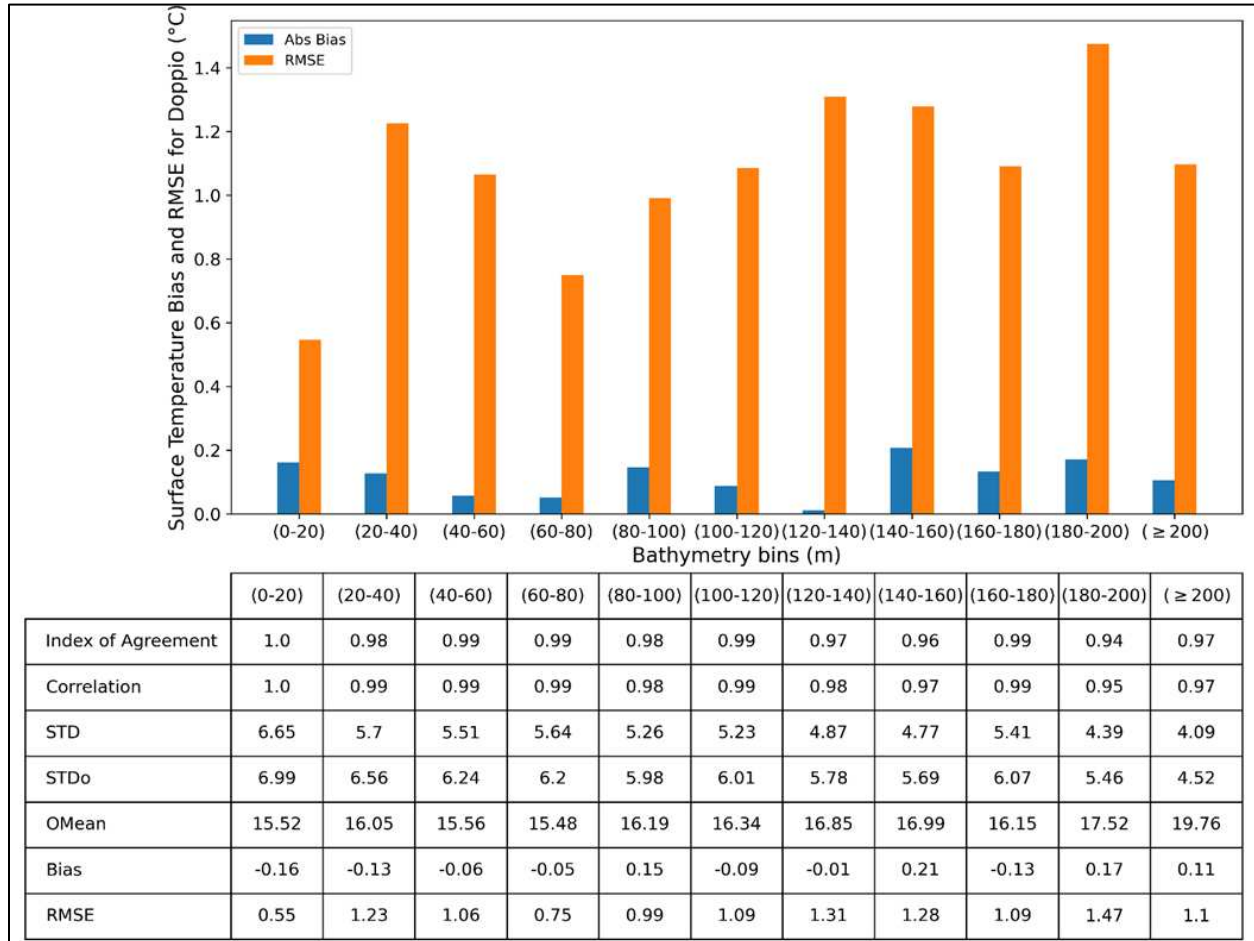


Figure 94. Surface temperature comparison between Model and Doppio dataset for validation period. Top: The histogram presents bias and RMSE, $^{\circ}\text{C}$. Bottom: The table shows model skill metrics.

5.6.2.3 Model against NOAA Optimally Interpolated High-Resolution SST (OISSTV2)

Model validation of surface temperature considered spatially varying monthly data from the NOAA Optimally Interpolated High-Resolution SST. NOAA surface temperature was compared to the hydrodynamic model for the one-year validation period, February 2019 to January 2020. Skill metrics including bias, root mean square error, index of agreement, correlation, standard deviation of the model and observed, and mean of observed were analyzed and summarized in histogram and tabular form to showcase variation along the shelf (Figure 212). The model’s surface temperature exhibits high index of agreement and correlation across the model domain. The shallow regions show the lowest bias between the model and NOAA Optimally Interpolated High-Resolution SST (OISSTV2) dataset. Spatial maps of monthly average surface temperature of the model, NOAA OISSTV2 dataset, and difference over the validation period are included in Appendix A.3.

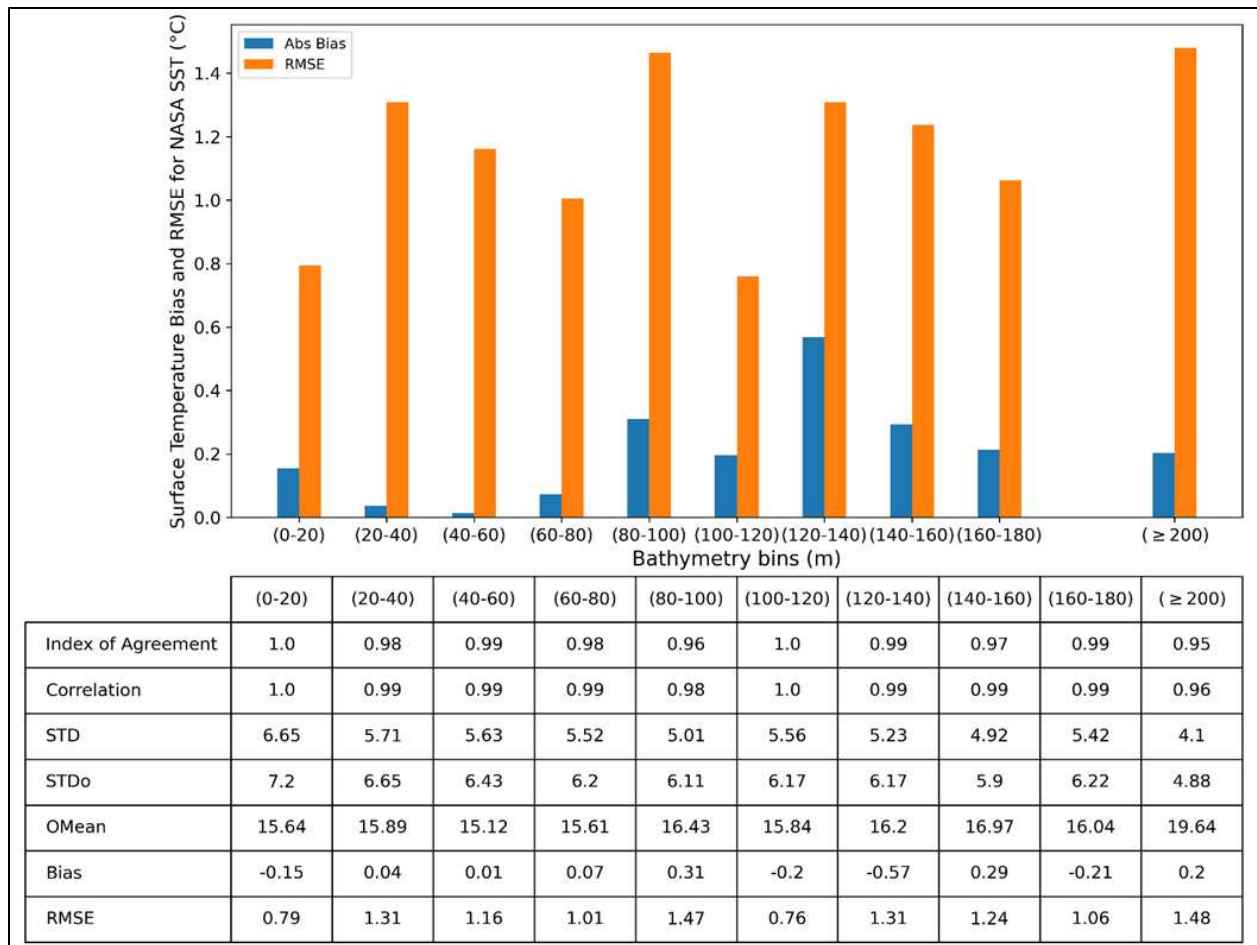


Figure 95. Surface temperature comparison between Model and NOAA Optimally Interpolated High Resolution SST for validation period.

Top: The histogram presents bias and RMSE, °C. Bottom: The table shows model skill metrics.

5.6.2.4 Model against Doppio Bottom Temperature

Model validation of bottom temperature considered spatially and time varying data from the Doppio ROMS model. Doppio bottom temperature was compared to the hydrodynamic model for a one-year period following calibration, February 2019 to January 2020. Skill metrics including bias, root mean square error, index of agreement, correlation, standard deviation of the model and observed, and mean of observed were analyzed and summarized in histogram and tabular form to showcase variation along the shelf (Figure 96). The model’s bottom temperature bias increases from the shallow to mid-depth ranges and remains low beyond the shelf break. The index of agreement between the model and Doppio ranges from 0.91 to 0.99 in depths from 0m to 80m and decreases gradually with increased depth from 0.93 to 0.65. Spatial maps of monthly average bottom temperature of the model, Doppio dataset, and difference over the validation period are included in Appendix A.4.

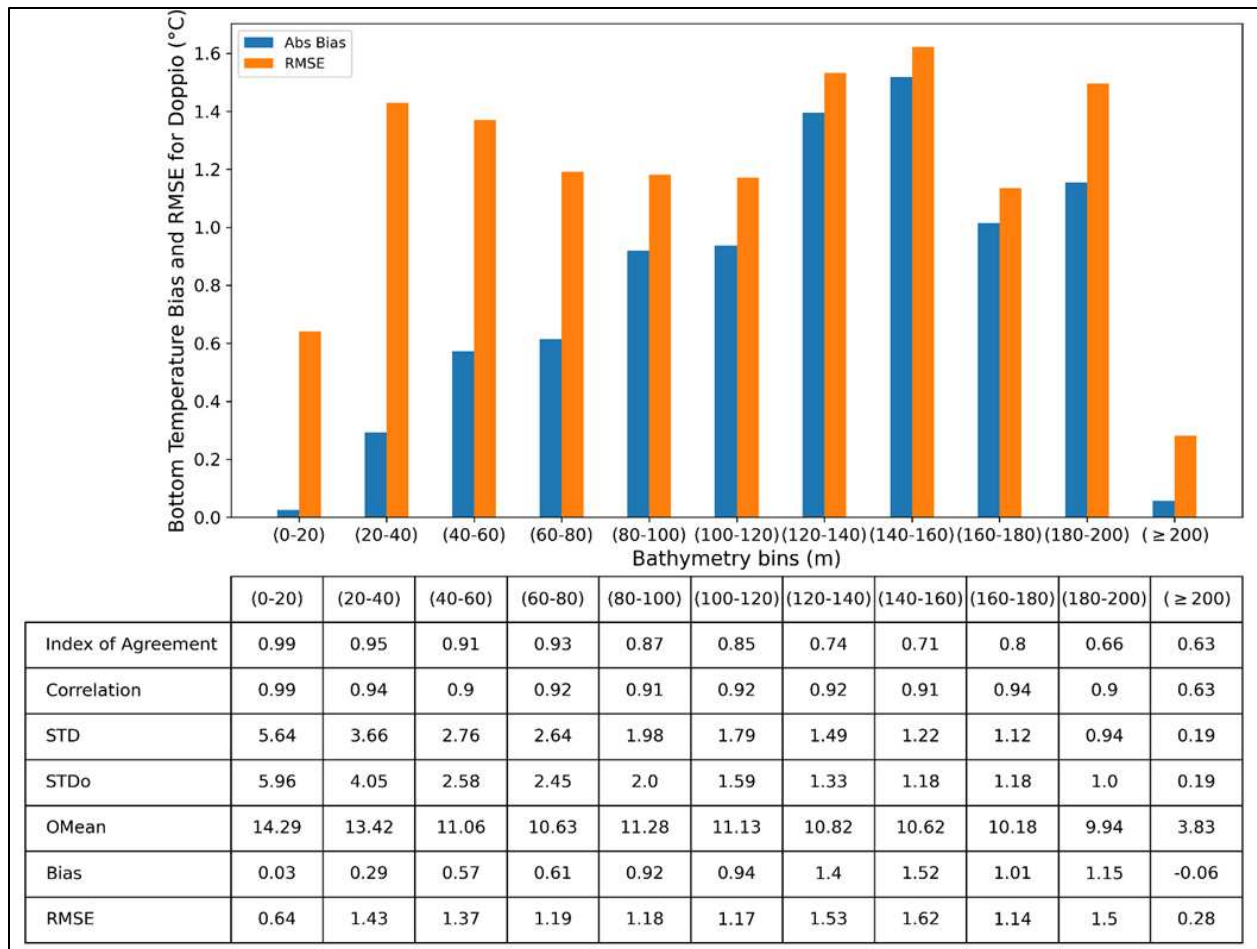


Figure 96. Bottom temperature comparison between Model and Doppio dataset for validation period. Top: The histogram presents bias and RMSE, °C. Bottom: The table shows model skill metrics.

5.6.2.5 Model against Glider Temperature

Model validation of temperature considered data recorded by glider. Figure 102 depicts the temperature histogram and skill parameters of the model compared to the glider observations for the validation period, Feb 2019 to Jan 2020, Notably, the model exhibits its highest skill in very shallow and moderate depths (< 20m and between 120 m and 160 m). At bathymetries above 200 m, the shelf break and deep ocean plateau, the bias is positive (overestimation, see the Table in Figure 97). However, the temperature overestimation is very low for the depth bins less than 200 m.

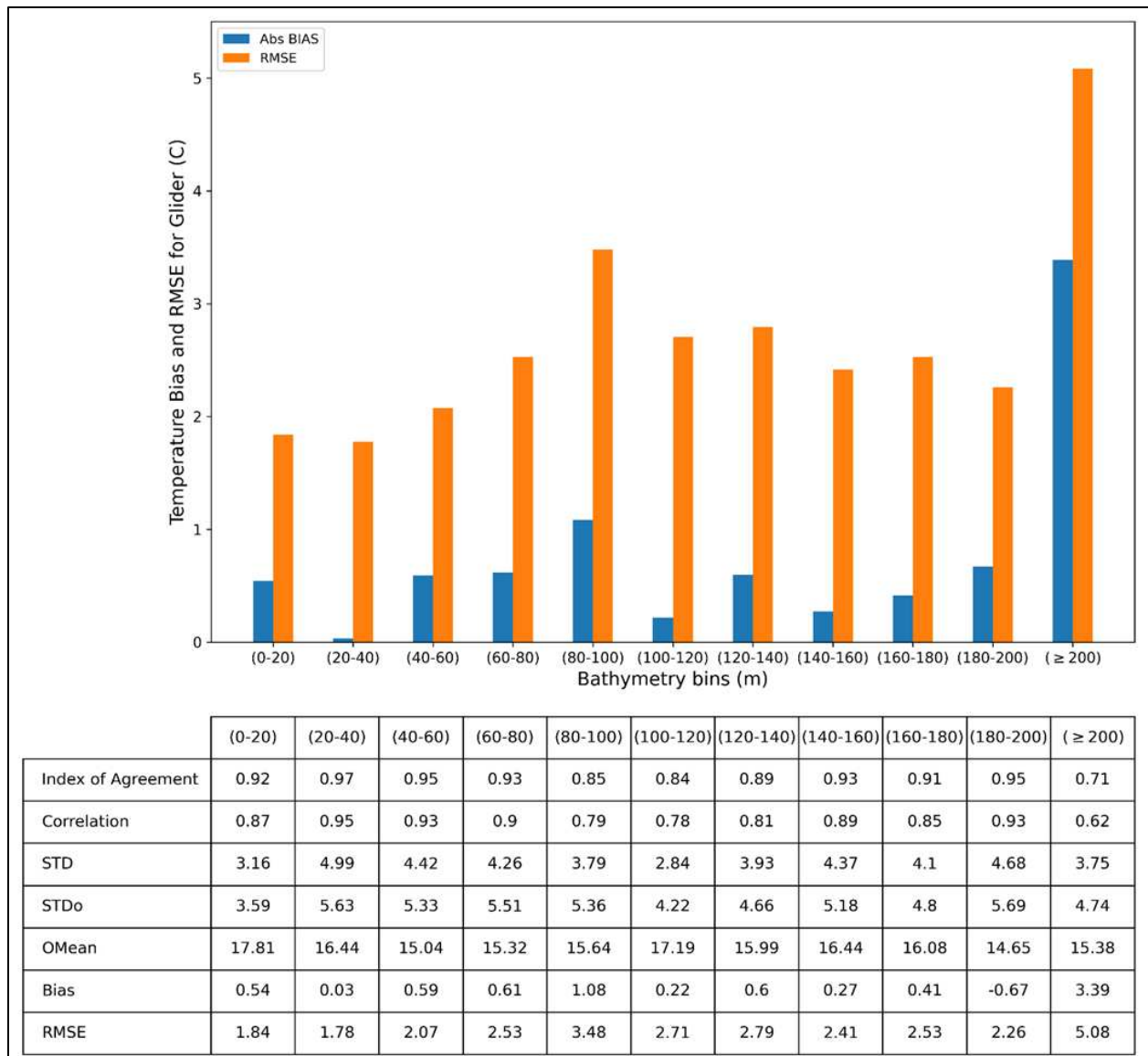


Figure 97. Temperature comparison between glider observation and model for validation period. Top: The histogram presents bias and RMSE, °C. Bottom: The table shows model skill metrics.

5.6.3 Salinity

The hydrodynamic model salinity validation included comparison of existing and forecast conditions within the Mid-Atlantic Bight. Spatially and time varying surface and bottom salinity data from the Doppio, ROMS-based (Regional Ocean Modeling System) model of the Mid-Atlantic Bight and Gulf of Main regions, and spatially scattered time varying salinity data from gliders were compared to the model.

5.6.3.1 Model against Doppio Surface Salinity

Model validation of surface salinity considered spatially and time varying data from the Doppio ROMS model. Doppio surface salinity was compared to the hydrodynamic model for a one-year time period following calibration, February 2019 to January 2020. Skill metrics including bias, root mean square error, index of agreement, correlation, standard deviation of the model and observed, and mean of observed were analyzed and summarized in histogram and tabular form to showcase variation along the

shelf (Figure 98). The model’s surface salinity exhibits highest model skill in depths between 0 to 20 m and slight variation of skill metrics beyond 20 m from the shallow regions to the deeper areas. Spatial maps of monthly average surface salinity of the model, Doppio dataset, and difference over the validation time period are included in Appendix A.5.

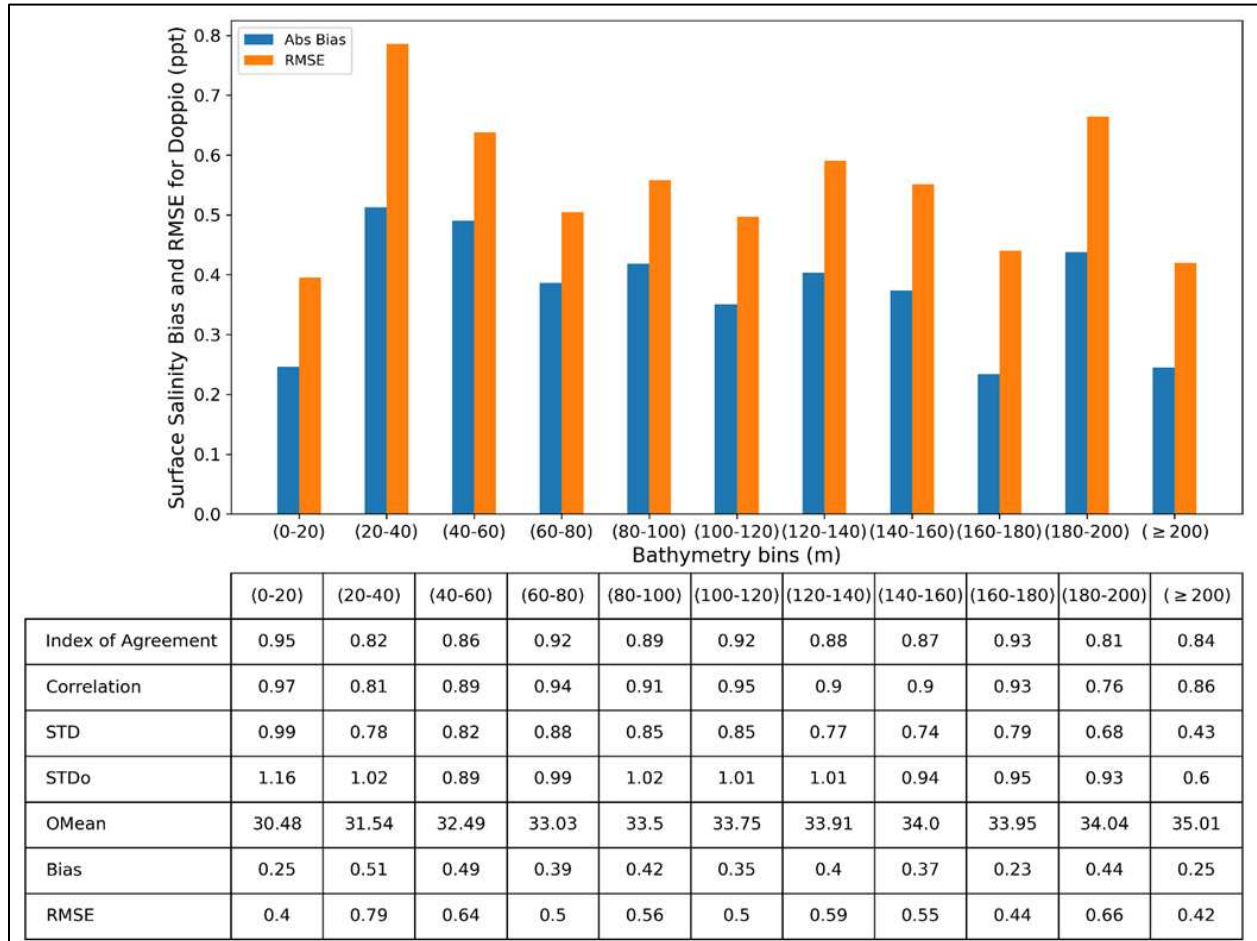


Figure 98. Surface salinity comparison between Model and Doppio dataset for validation period. Top: The histogram presents bias and RMSE, psu. Bottom: The table shows model skill metrics.

5.6.3.2 Model against Doppio Bottom Salinity

Model validation of bottom salinity considered spatially and time varying data from the Doppio ROMS model. Doppio bottom salinity was compared to the hydrodynamic model for a one-year period following calibration, February 2019 to January 2020. Skill metrics including bias, root mean square error, index of agreement, correlation, standard deviation of the model and observed, and mean of observed were analyzed and summarized in histogram and tabular form to showcase variation along the shelf (Figure 99). The model’s bottom salinity performs better with increasing depth, this is shown for bias and RMSE. However, the model has a higher index of agreement in depths ranging from 0 m to 20 m and 40 m to 80 m. Spatial maps of monthly average bottom salinity of the model, Doppio dataset, and difference over the validation period are included in Appendix A.6.

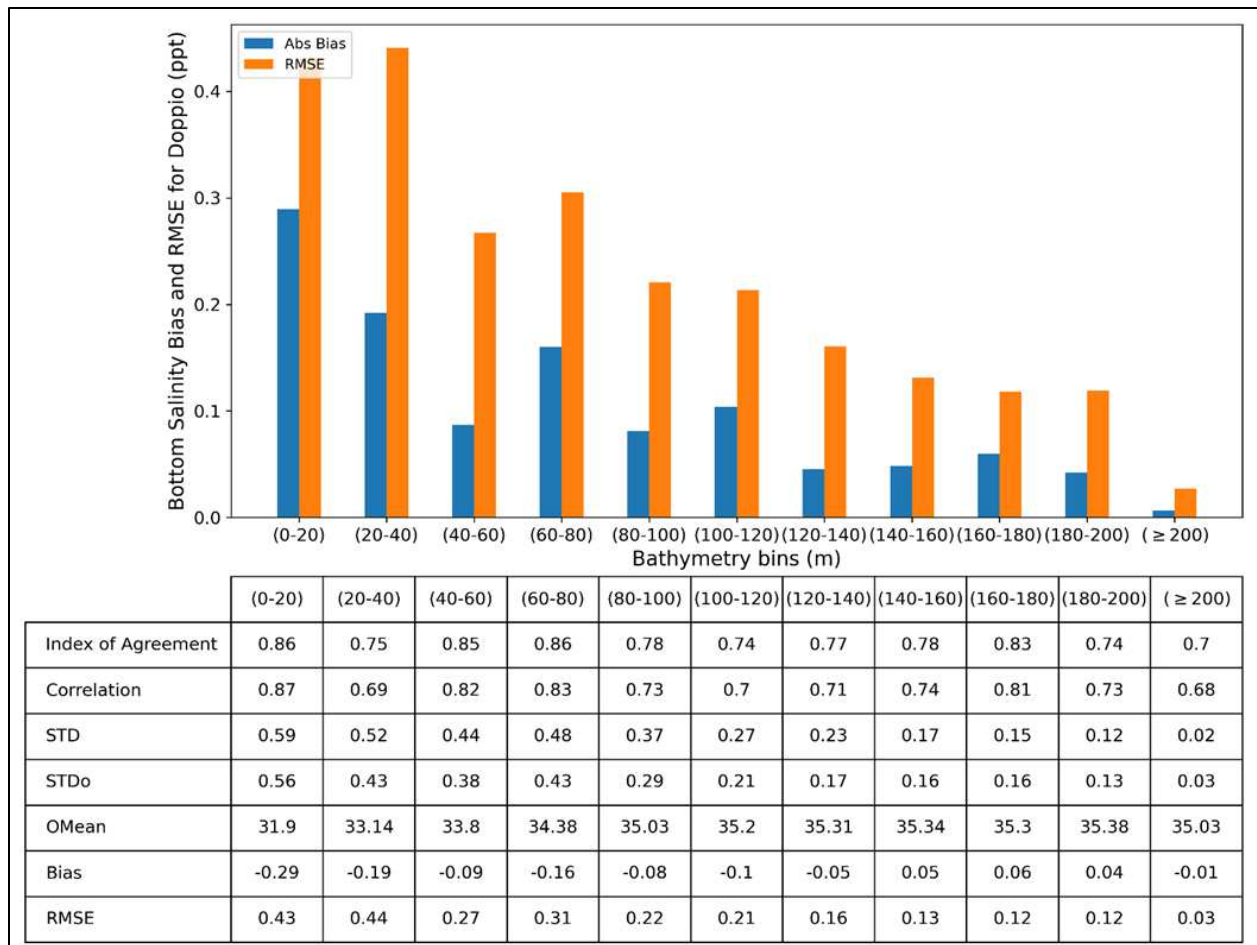


Figure 99. Bottom salinity comparison between Model and Doppio dataset for validation period. A) Top: The histogram presents bias and RMSE, psu. Bottom: The table shows model skill metrics.

5.6.3.3 Model against Glider Salinity

Model validation of salinity considered data recorded by gliders. Figure 100 depicts the salinity histogram and skill parameters of the model compared to the glider observations for the validation period, February 2018 to January 2020. Notably, the model exhibits its highest skill in moderate depths (< 20 m and between 120 m and 160 m). At the [0–20] m bin, agreement between the small amount of glider data there and Delft is quite low. The environment is most dynamic in terms of salinity variations in the nearshore. Thus, model skill reduction is expected compared to deeper waters. However, this low skill cannot be attributed to that fact alone and is unique to glider data.

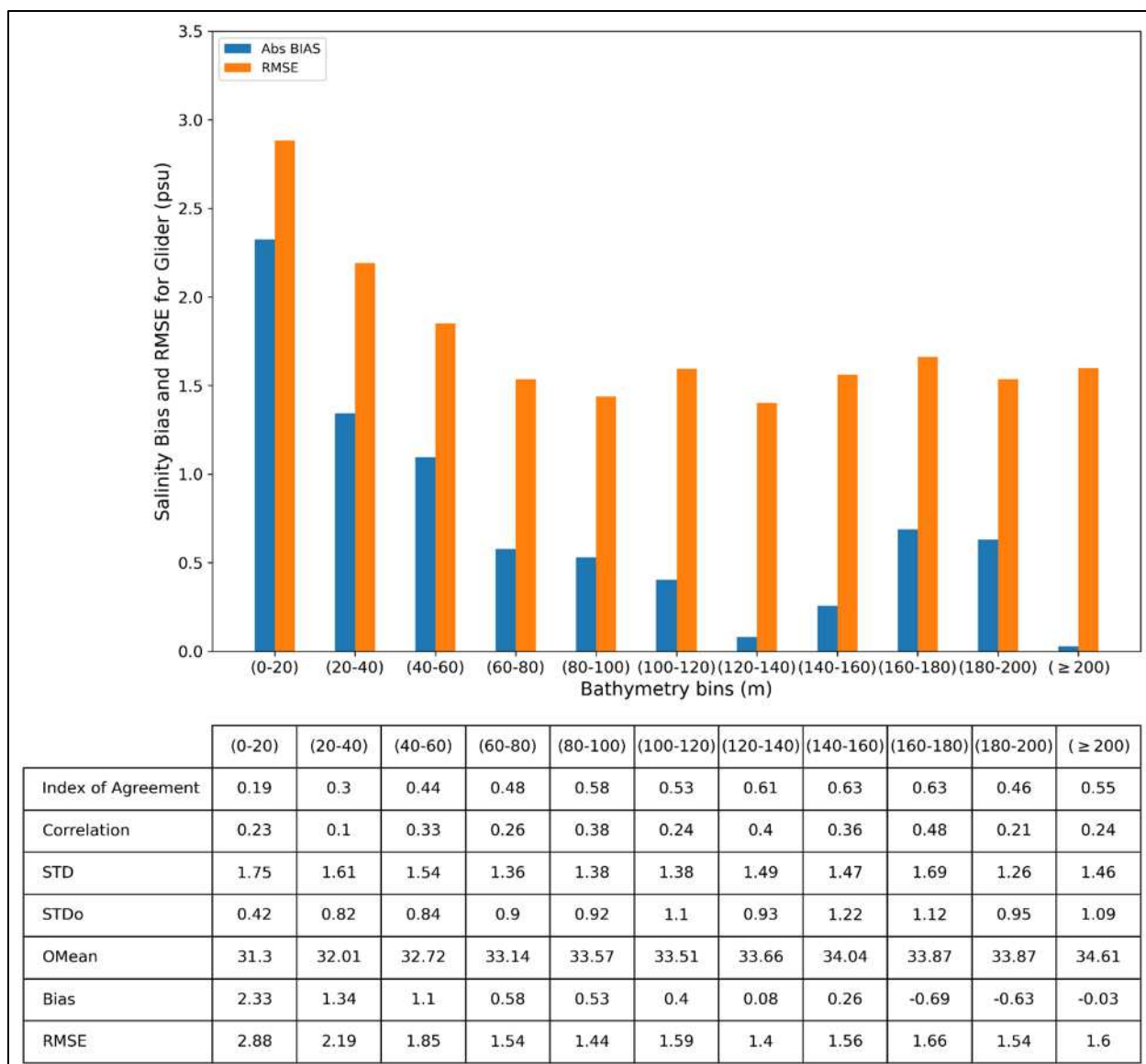


Figure 100. Salinity comparison between glider observation and model for calibration period. a) Top: The histogram presents bias and RMSE, psu. Bottom: The table shows model skill metrics.

5.6.4 Current

Validation of the model’s hydrodynamic conditions included comparison to data extracted from an Empire Wind buoy, spatially and time varying data from Doppio, ROMS-based (Regional Ocean Modeling System) model of the Mid-Atlantic Bight and Gulf of Main regions, and spatially and time varying data from CODAR HF Radar.

5.6.4.1 Model against Empire Wind Data

The Empire Wind observation data include current speeds at the subsurface. These data cover the period from December 2018 to January 2020. They are used for model validation rather than calibration, primarily covering on the second year of the modeling period. The current speeds recorded at three depths 9.6 m, 19.6 m, and 33.6 m. Timeseries comparison of model results and observed current speeds are

shown in Figure 101 to Figure 103. While the correlation seems moderate, the other statistical parameters, such as bias, RMSE, and the Index of Agreement, are good. The current roses comparisons, Figure 104 to Figure 106, also indicate good agreement with current directions.

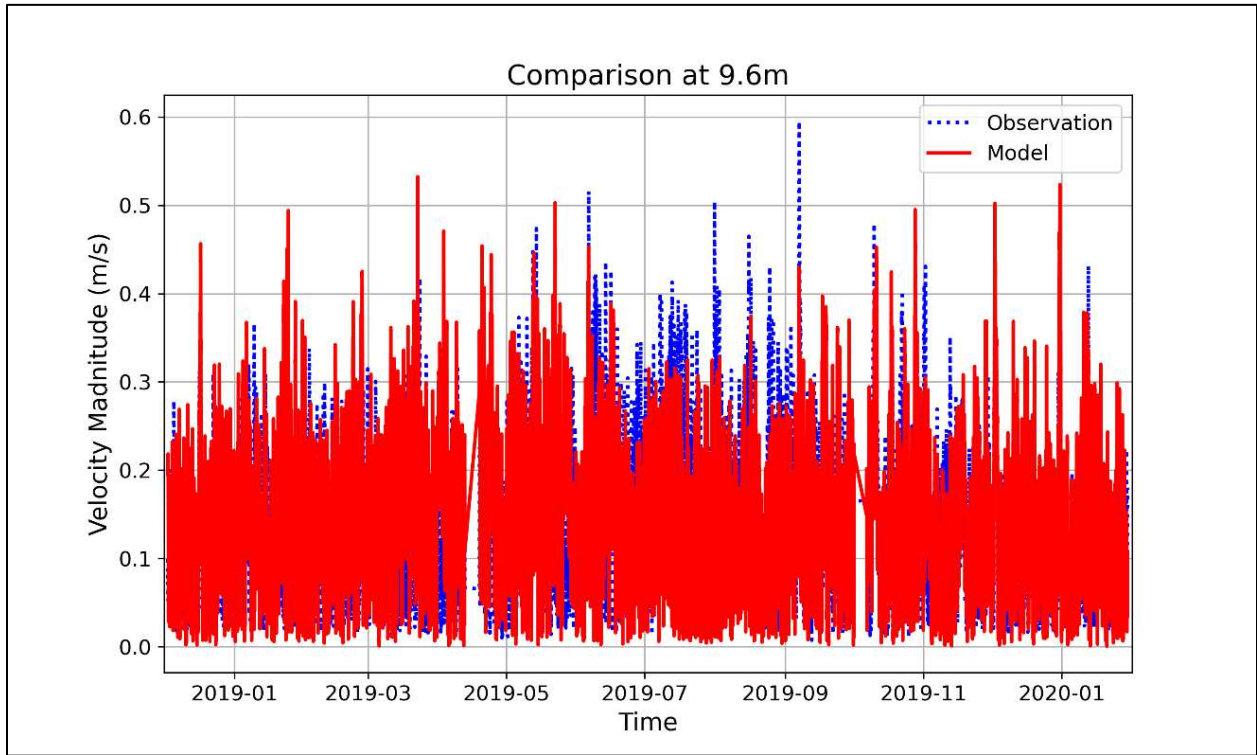


Figure 101. Current speed comparison between Empire Wind observation and model at 9.6 m.

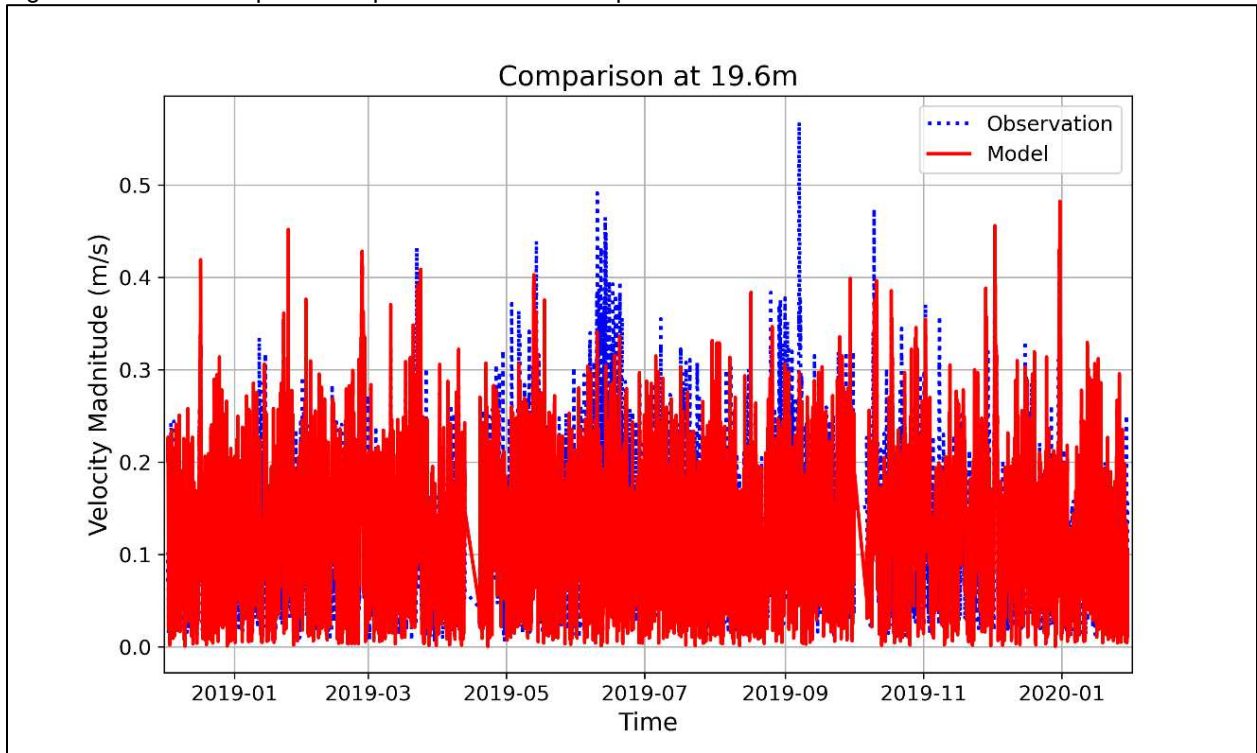


Figure 102. Current speed comparison between Empire Wind observation and model at 19.6 m.

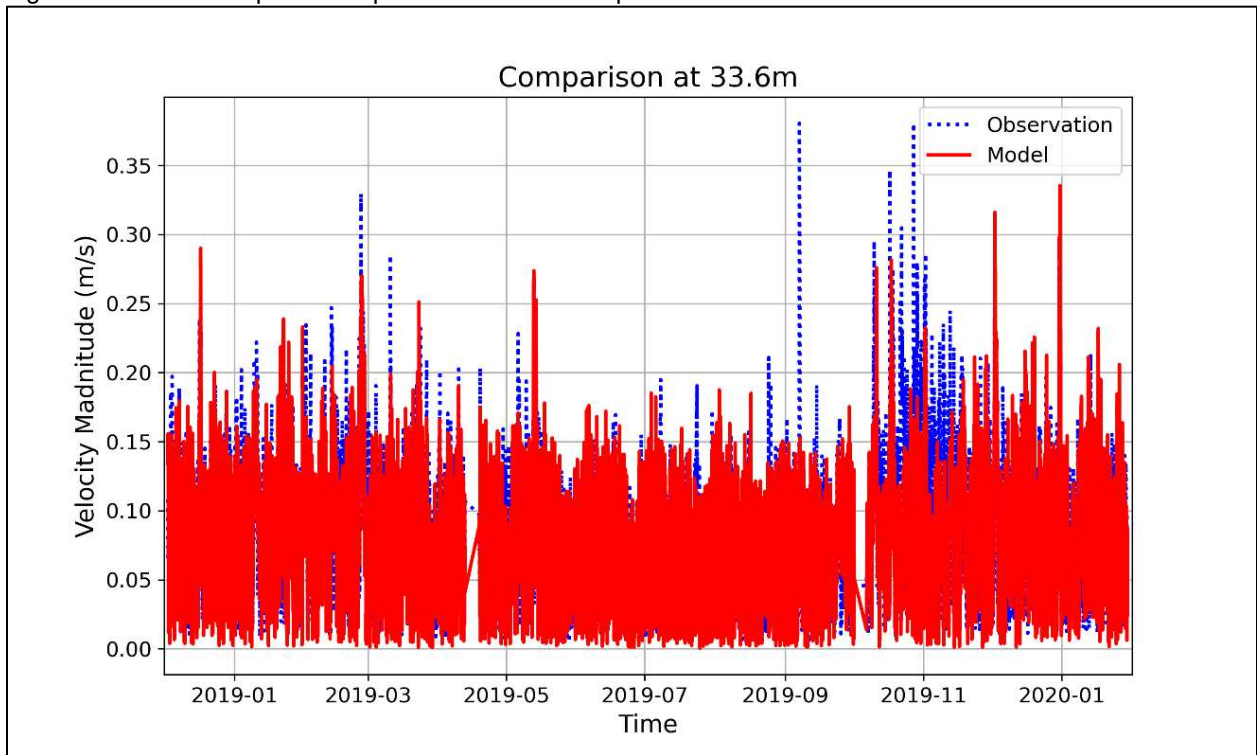


Figure 103. Current speed comparison between Empire Wind observation and model at 33.6 m.

Table 19. Model skill metrics against Empire Wind current speed observations.

Observation Depth. m	Correlation	Index of Agreement	Bias	RMSE
9.6	0.419	0.659	0.005	0.086
19.9	0.463	0.687	0.001	0.073
33.6	0.450	0.677	0.000	0.046

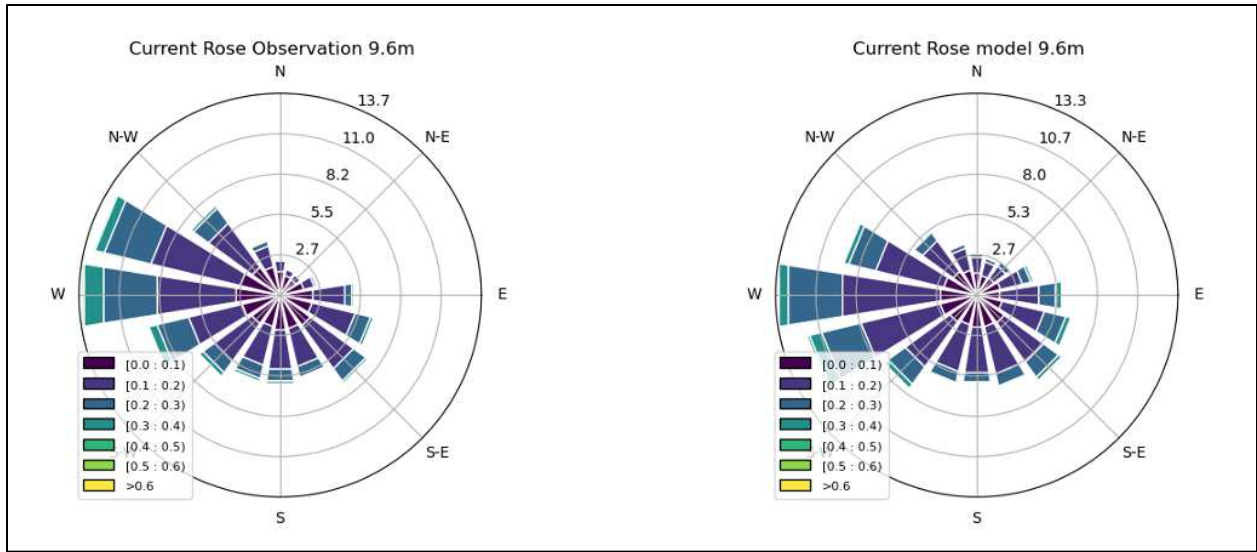


Figure 104. Current rose comparison at Empire Wind at 9.6 m, observation (left) and model (right).

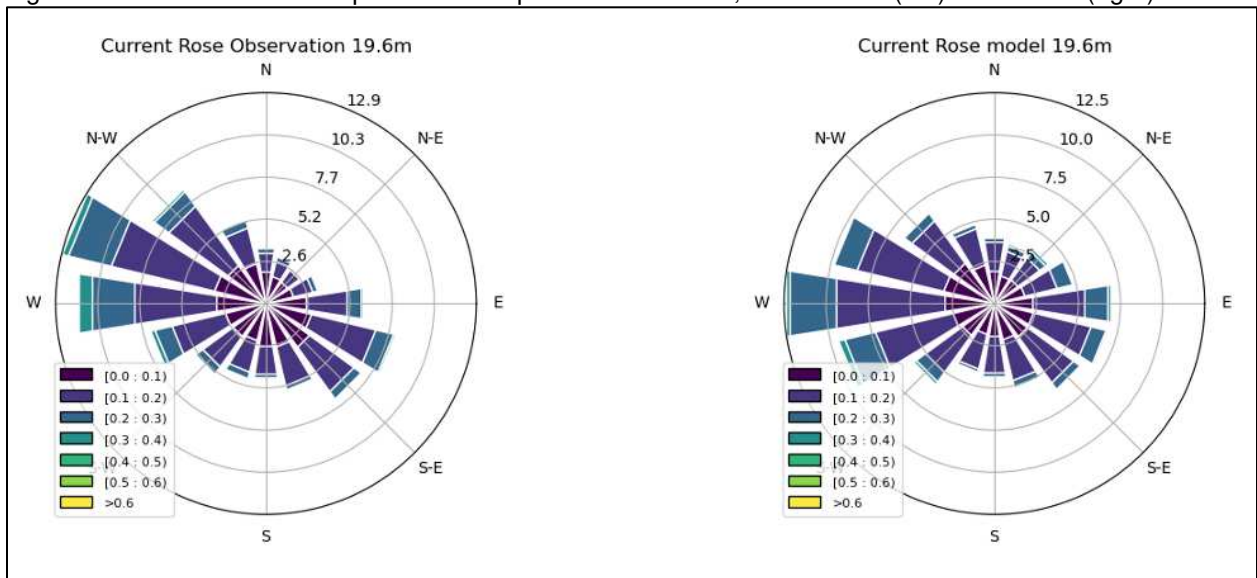


Figure 105. Current rose comparison at Empire Wind at 19.6 m, observation (left) and model (right).

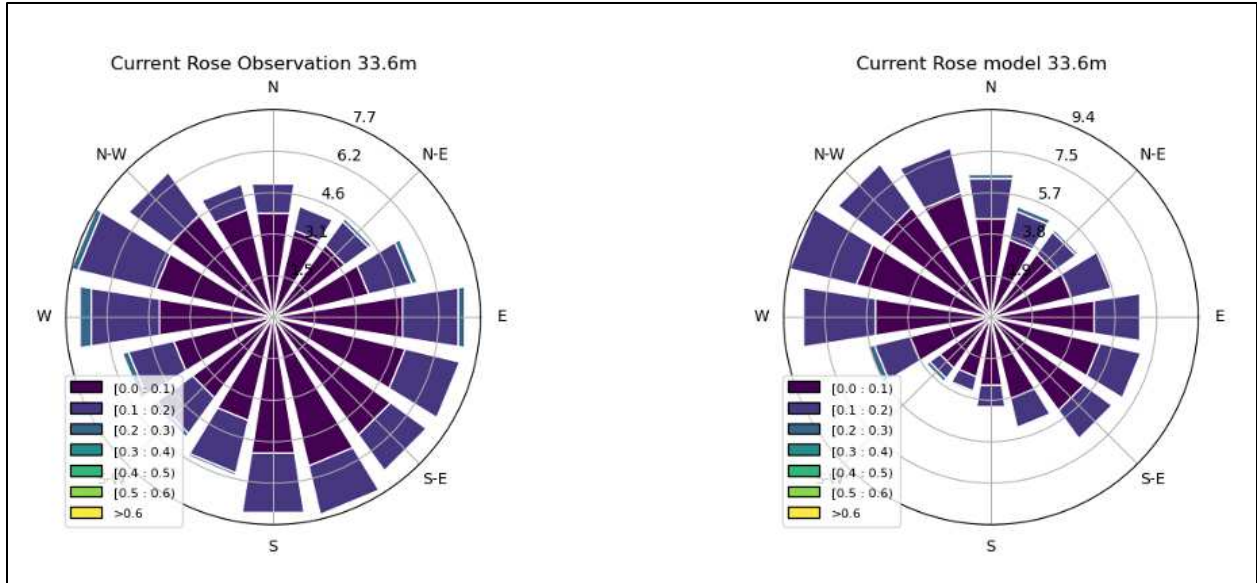


Figure 106. Current rose comparison at Empire Wind at 33.6 m, observation (left) and model (right).

5.6.4.2 Model against Doppio Surface Currents

Model validation of surface current considered spatially and time varying data from the Doppio ROMS model. Doppio surface current was compared to the hydrodynamic model for a one-year period following calibration, February 2019 to January 2020. Skill metrics including bias, root mean square error, index of agreement, correlation, standard deviation of the model and observed, and mean of observed were analyzed and summarized in histogram and tabular form to showcase variation along the shelf (Figure 107). The model's surface current exhibits low bias and RMSE ranging from -0.01 m/s to 0.03 m/s and 0.03 m/s to 0.05 m/s respectively, in depth regions from 0 m to 100 m. In depths larger than 200 m RMSE is 0.16 m/s, larger than the shallower and mid-depth regions. Spatial maps of monthly average surface current of the model, Doppio dataset, and difference over the validation period are included in Appendix A.7.

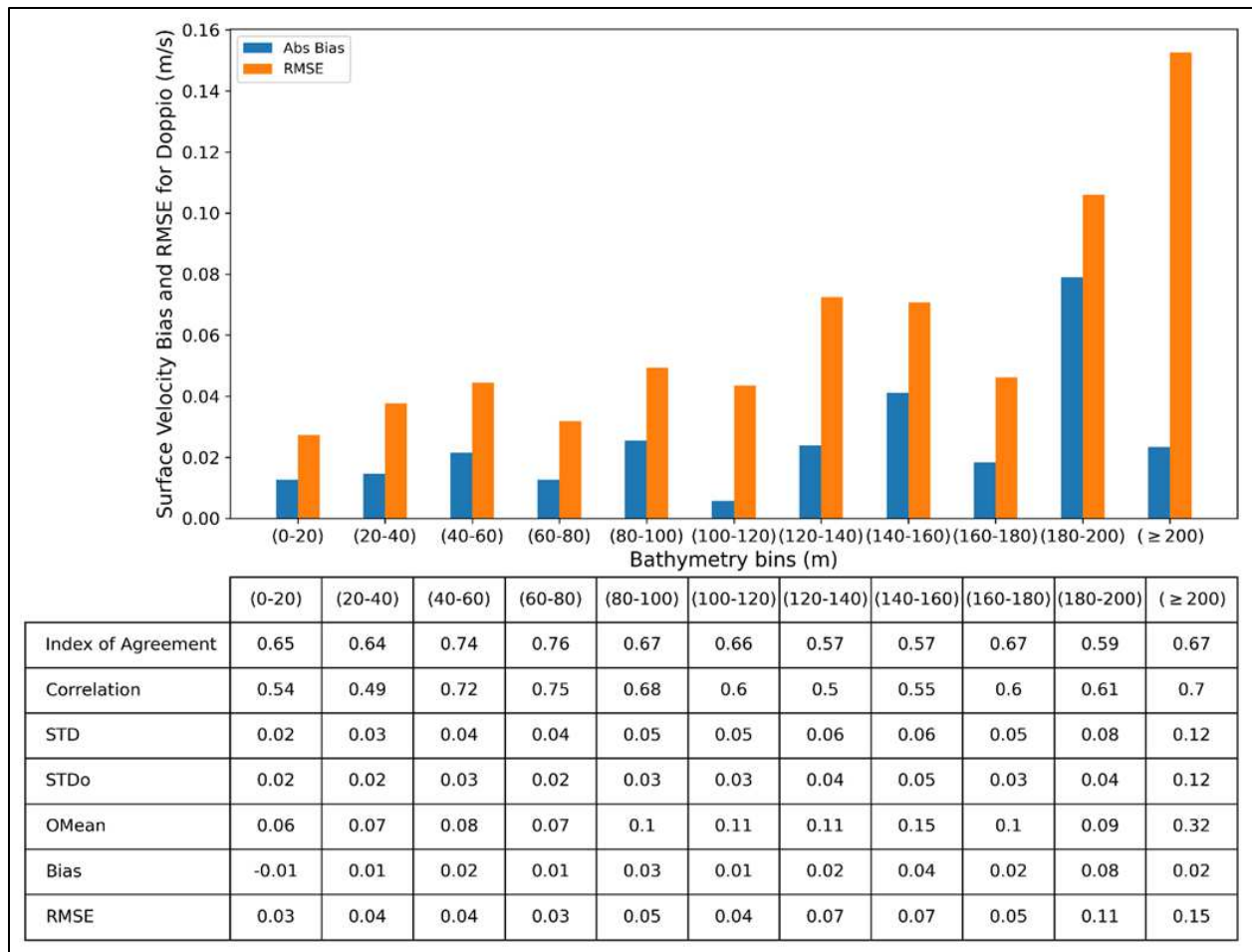


Figure 107. Surface current comparison between Model and Doppio dataset for validation period. Top: The histogram presents bias and RMSE, m/s. Bottom: The table shows model skill metrics.

5.6.4.3 Model against HF Radar Surface Currents

Model validation of surface current speed considered spatially and time varying data from the CODAR HF Radar dataset. Doppio surface current speed was compared to the hydrodynamic model for a one-year period following calibration, February 2019 to January 2020. Skill metrics including bias, root mean square error, index of agreement, correlation, standard deviation of the model and, and mean of observed were analyzed and summarized in histogram and tabular form to showcase variation along the shelf (Figure 108). The model's surface current speed exhibits low bias and RMSE in the shallower to moderate depth regions where depth ranges and is higher past the shelf break. Higher absolute differences (Bias and RMSE) in areas deeper than the 140m isobath in the southern edge of the modeling domain are influenced by the strong Shelf Break Jet and the Gulf Stream, which have much higher speeds than on the continental shelf. The correlation and index of agreement metrics however, which are scaled to observations, though lower, are reasonable in these areas as well, as explained in Section 5.5.4.2. Spatial maps of monthly average surface current of the model, HF Radar dataset, and difference over the validation period are included in Appendix A.8.

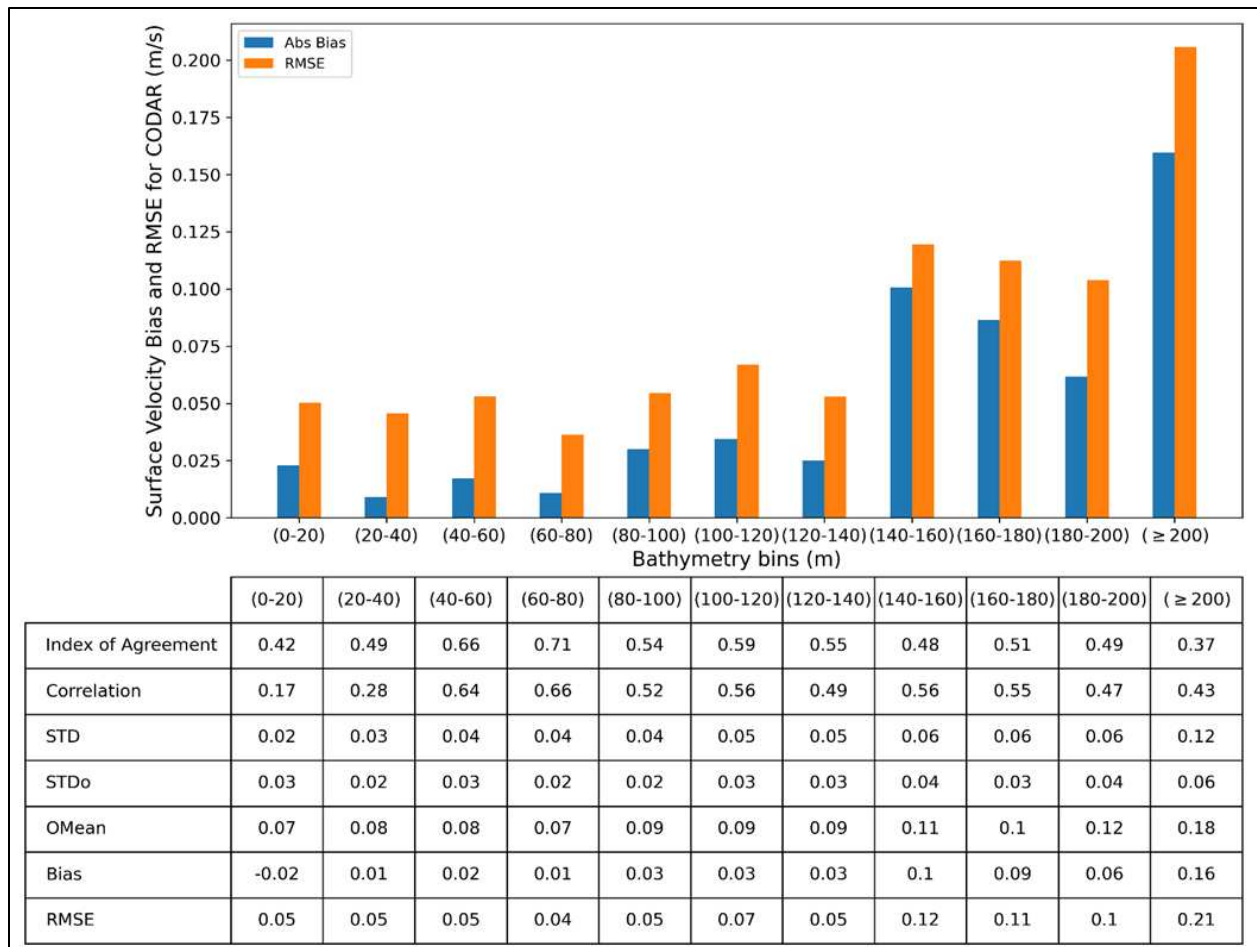


Figure 108. Surface current comparison between Model and HF Radar dataset for validation period. Top: The histogram presents bias and RMSE, m/s. Bottom: The table shows model skill metrics.

5.6.4.4 Model against Doppio Bottom Currents

Model validation of bottom current considered spatially and time varying data from the Doppio ROMS model. Doppio bottom current was compared to the hydrodynamic model for a one-year period following calibration, February 2019 to January 2020. Skill metrics including bias, root mean square error, index of agreement, correlation, standard deviation of the model and observed, and mean of observed were analyzed and summarized in histogram and tabular form to showcase variation along the shelf (Figure 109). The model's bottom current exhibits low bias and RMSE in shallower to mid depth regions (0m to 100 m depth) ranging from 0 m/s to 0.01 m/s and 0.01 m/s to 0.03 m/s respectively. Spatial maps of monthly average bottom current of the model, Doppio dataset, and difference over the validation period are included in Appendix A.9.

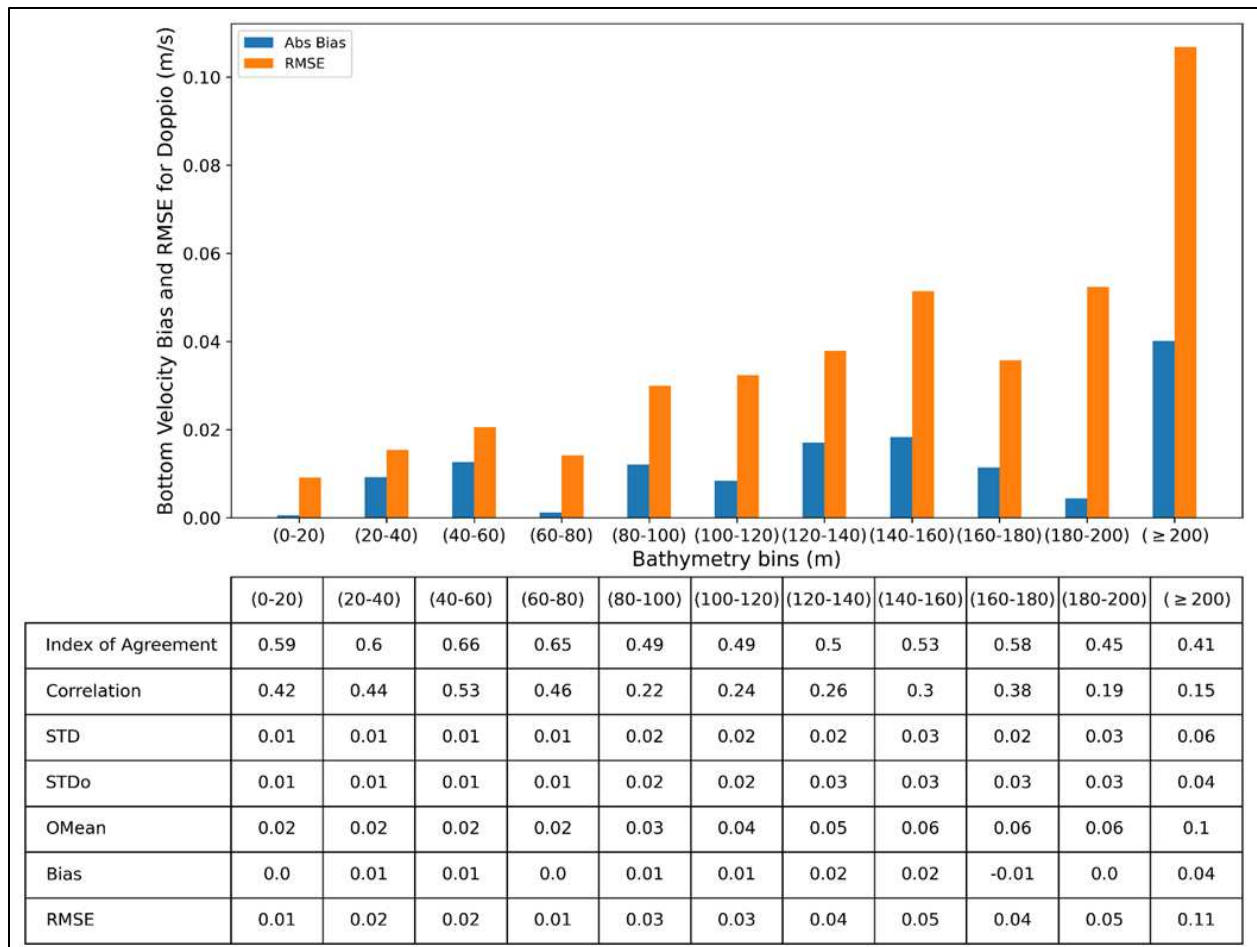


Figure 109. Bottom current comparison between Model and Doppio dataset for validation period. Top: The histogram presents bias and RMSE, m/s. Bottom: The table shows model skill metrics.

5.7 Model Skill Summary of Validation and Calibration Periods

Model skill of the hydrodynamic model runs of calibration and validation time periods is illustrated in the Taylor Diagram shown in Figure 110. The figure displays a comparison between Delft3D model outcomes, observational data, and ROMS Doppio model results. The Taylor Diagram depicts the model's performance during both the calibration period (February 2018 to January 2019) in red and the validation period in blue (February 2019 to January 2020). Notably, the Delft3D FM results exhibit a strong correlation with the ROMS Doppio model, which provides the main part of the lateral forcing for the Delft3D FM model. The primary disparities between these models are evident in bottom current speed, where the normalized RMSE is lowest (indicated by gray curves), likely stemming from differences in model resolution between Doppio and Delft3D FM. Delft3D FM has much higher resolution compared to ROMS Doppio. Regarding agreement with observations, the highest correlation (0.99) and lowest RMSE (0.25) are observed with NDBC temperature data. Following NDBC data, and in decreasing skill order, Delft3D model performance is the best against SST, glider salinity, glider temperature, and HF Radar data, respectively. However, discrepancies between Delft3D FM and HF Radar data are most prominent in the deeper parts of the domain and the Gulf Stream region, not on the shelf region that is the primary area of interest in this study. Overall, the skill metrics are on par with recently published values from state-of-the-art comparable models (e.g., Georgas and Blumberg 2010, Bhushan et al., 2010, Sun et al., 2016, López et al., 2020, Johnson et al., 2021, Wilkin et al., 2022)

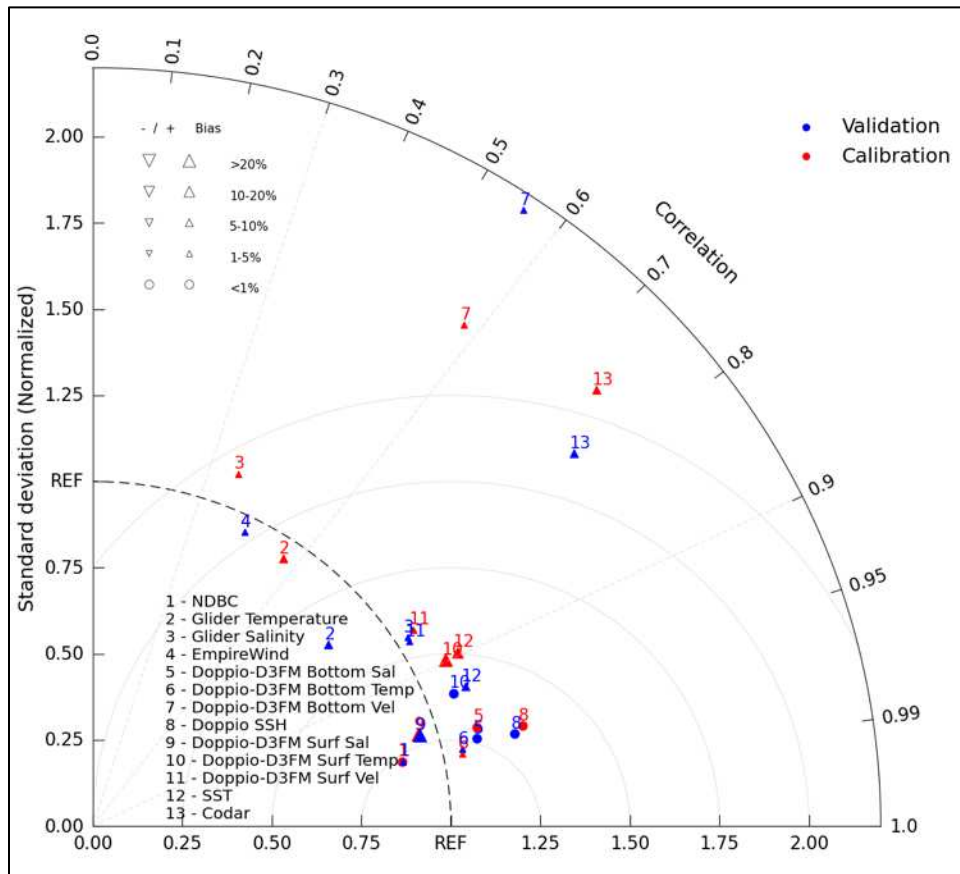


Figure 110. Taylor Diagram of calibrated model compared to observational and DOPPIO data. Sea Surface Temperature, Empire Wind Buoy, Glider Temperature, Glider Salinity, NDBC, DOPPIO model data used for calibration period (Feb 2018–an 2019) and validation period (Feb 2019–Jan 2020)¹.

5.8 Hydrodynamic Modeling of Scenarios 2 and 3 with WEA Buildout

After the baseline hydrodynamic model without WEA development was calibrated and validated (previous sections), the model was set up to run for the same two-year period (Feb-01-2018 to Jan-31-2020, with Jan 2018 used for ramp up) for the two scenarios with wind turbine placement within the WEAs. The wind wake effect for each of these scenarios was accounted for by applying the wind-wake-modified wind fields discussed in Chapter 4 for scenarios 2 and 3 as surface forcing to the validated hydrodynamic model.

Localized flow surrounding turbines within the WEAs for each of scenarios 2 and 3 was accounted for in the hydrodynamic model through the subgrid bridge pillar parameterization in Delft3D. For each build-out scenario (Table 1), the locations of each individual WTG monopile, along with the monopile diameter accounting for biofouling, and a hydrodynamic drag coefficient were provided as input (Table 10). The

¹ Empire Wind data, covering Jan 2019 to Feb 2020, used only for the validation.

drag coefficient is applied within the model as an effective-area-weighted flow restriction within each mesh element with turbines. Its value is based on the study conducted by Johnson et al. (2021) that investigated flow surrounding turbine foundations using a Computational Fluid Dynamic (CFD) model. The CFD model simulated steady stratified flow and determined the drag coefficient induced by the turbine foundation including associated scour protection on the fluid flow to be $C_D=1.034$, which is slightly higher than that of a smooth cylindrical pile (1.0). This value for the drag coefficient was found by Johnson et al. (2021) to be applicable to both 12 MW and 15 MW wind turbine foundations, the latter of which are used in the present study and was adopted for use in the hydrodynamic model.

Results from these two scenarios were compared to the baseline conditions run (Scenario 1) in Chapter 9.

6 Surface Wave Modeling

6.1 Introduction

Following the planned fields of offshore WTGs and OSSs installation for Mid-Atlantic Bight WEAs, the potential effects of offshore wind energy structures and facilities on surface waves are to be investigated. The numerical wave model SWAN (Holthuijsen et al. 1997), is used to provide comparisons of oceanographic conditions with and without turbines considering the three scenarios elaborated in Section 2.2. The following sections include a description of the wave model used for this study, grid and bathymetry used for the wave modeling, the boundary conditions used for forcing the model, different physical formulations and parameters used in the model setup, and calibration and validation of the model using baseline data measured at multiple locations over an annual period.

6.2 Wave Model Description

The SWAN model, developed by the Delft University of Technology, is a flexible and efficient program based on the wave action balance equation that can solve wave conditions in a two-dimensional domain using the iterative Gauss-Seidel technique. An advantage of the iterative technique employed in SWAN is that it can compute spectral wave components for the full 360-degree compass circle. SWAN has been used for simulating wave parameters in coastal areas, lakes, and estuaries using wind, water level, bottom friction, and current conditions (Zijlema, 2010).

For realistic estimation of wave parameters, SWAN includes algorithms to simulate different wave propagation processes such as propagation through geographic space, refraction and shoaling caused by bottom and current variations, and blockage by obstacles. In addition, SWAN considers the dissipation effects caused by bottom friction, wave breaking, and white-capping (van der Westhuysen et al., 2007). The model also resolves the evolution of wind waves in coastal waters with relatively shallow depths by spectral calculation, at user-specified resolution of directions and frequencies (Mao et al., 2016).

6.3 Wave Model Grid and Bathymetry

The grid and bathymetry used in wave modeling is the same grid and bathymetry as the hydrodynamic modeling (also shown here in Figure 111). Using the same grid for both models facilitate the models' communication by reading the hydrodynamic data (water level and current) at the same nodes (i.e. locations) the data were generated for by the hydrodynamic model; thus, no data interpolation is required when coupling hydrodynamic forcing to waves. The high-resolution unstructured grid covers the AOI from south Long Island, New York to Cape Hatteras, North Carolina with grid cell sizes ranging from about 1km (in the BOEM wind turbine lease areas) to about 10km (near the offshore open boundary). The unstructured mesh for SWAN (fort.14 file) was generated by the Surface water Modeling System (SMS) and includes 46,955 triangles with 23,668 vertices and 14 open boundary segments at the model's offshore boundary. The boundary information stored in fort.14 is used when the wave boundary conditions are applied to SWAN.

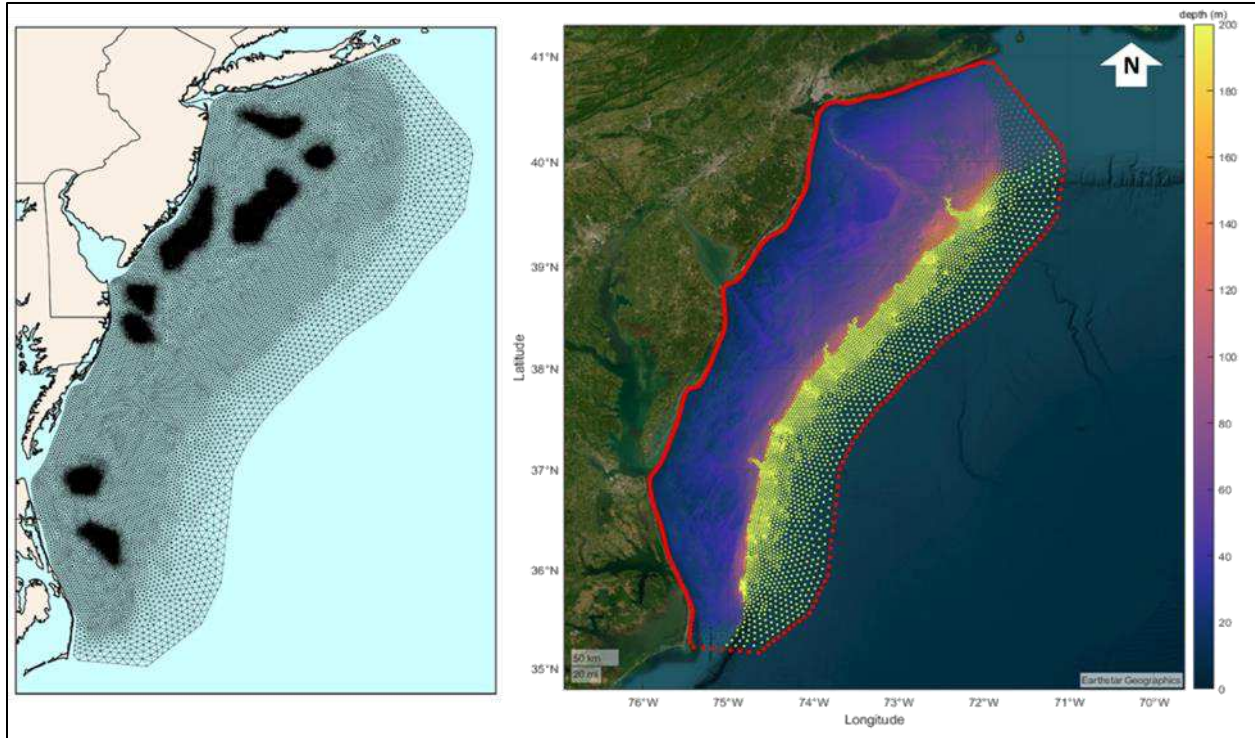


Figure 111. The wave model grid (left panel) and bathymetry (right panel) is the same as the hydrodynamic model grid.

6.4 Wave Model Forcings

The wind and wave data for forcing the wave model were set up using high-quality global reanalysis products, namely the fifth generation of the ECMWF Global Reanalysis (ERA5). The wave parameters at the open boundary obtained from ERA5 (Table 20) included significant wave height, mean wave period, mean wave direction, and directional spreading time series. The ERA5 data are available on an ocean wave model grid with 0.5° horizontal resolution at an hourly time step interval. For the present study, ERA5 wave parameters were spatially interpolated for 14 points (shown with filled white circles in Figure 112) for the 14 open boundary segments, each 45–65km long (segment end points are shown as yellow points in Figure 112). The wind datasets used in this study are also obtained from ERA5 which provides wind data on a global scale (Table 21) with 0.25° horizontal resolution (hollow white points in Figure 112) and an hourly time step interval. Wind roses for the entire two-year simulation period at ERA5 points in the project domain are shown in Figure 113. Note that wind directions over the ocean tend to be aligned with the shoreline and Continental Shelf break.

Table 20. Specifics of the wave datasets used for forcing SWAN model.

Name of Dataset	ERA5 Waves
Coverage (used in this study)	76.10°W – 70.60°W 34.7°N – 41.4°N
Owner/Provider	ECMWF
Horizontal Grid Size	0.5°
Modeling Period	2018 – 2020
Time Step	Hourly

Table 21. Specifics of the wind datasets used for forcing SWAN model.

Name of Dataset	ERA5 Winds
Coverage (used in this study)	76.10°W – 70.60°W 34.7°N – 41.4°N
Owner/Provider	ECMWF
Horizontal Grid Size	0.25°
Modeling Period	2018 – 2020
Time Step	Hourly

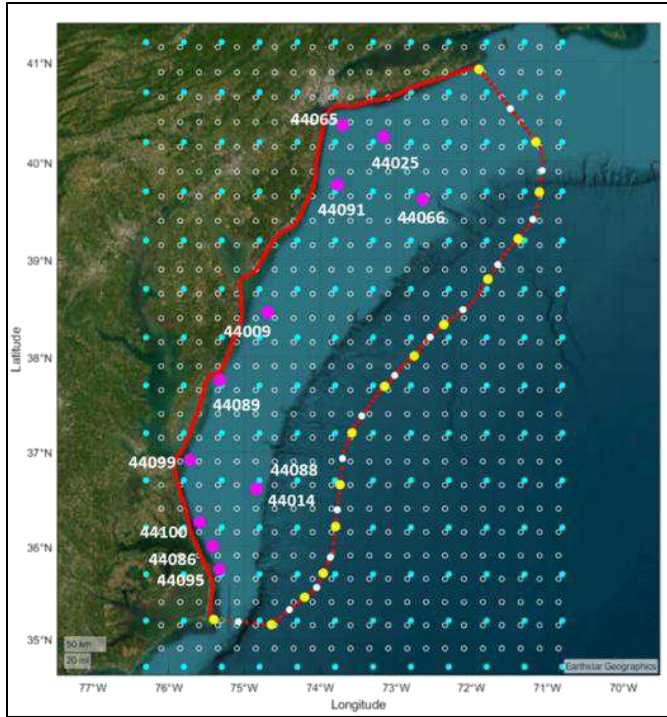


Figure 112. Wave model boundary conditions.

ERA5 wave and wind points (solid cyan and hollow white circles, respectively), SWAN model boundary segment interpolation (solid white circles) and end points (solid yellow circles), and NDBC station locations (solid magenta circles).

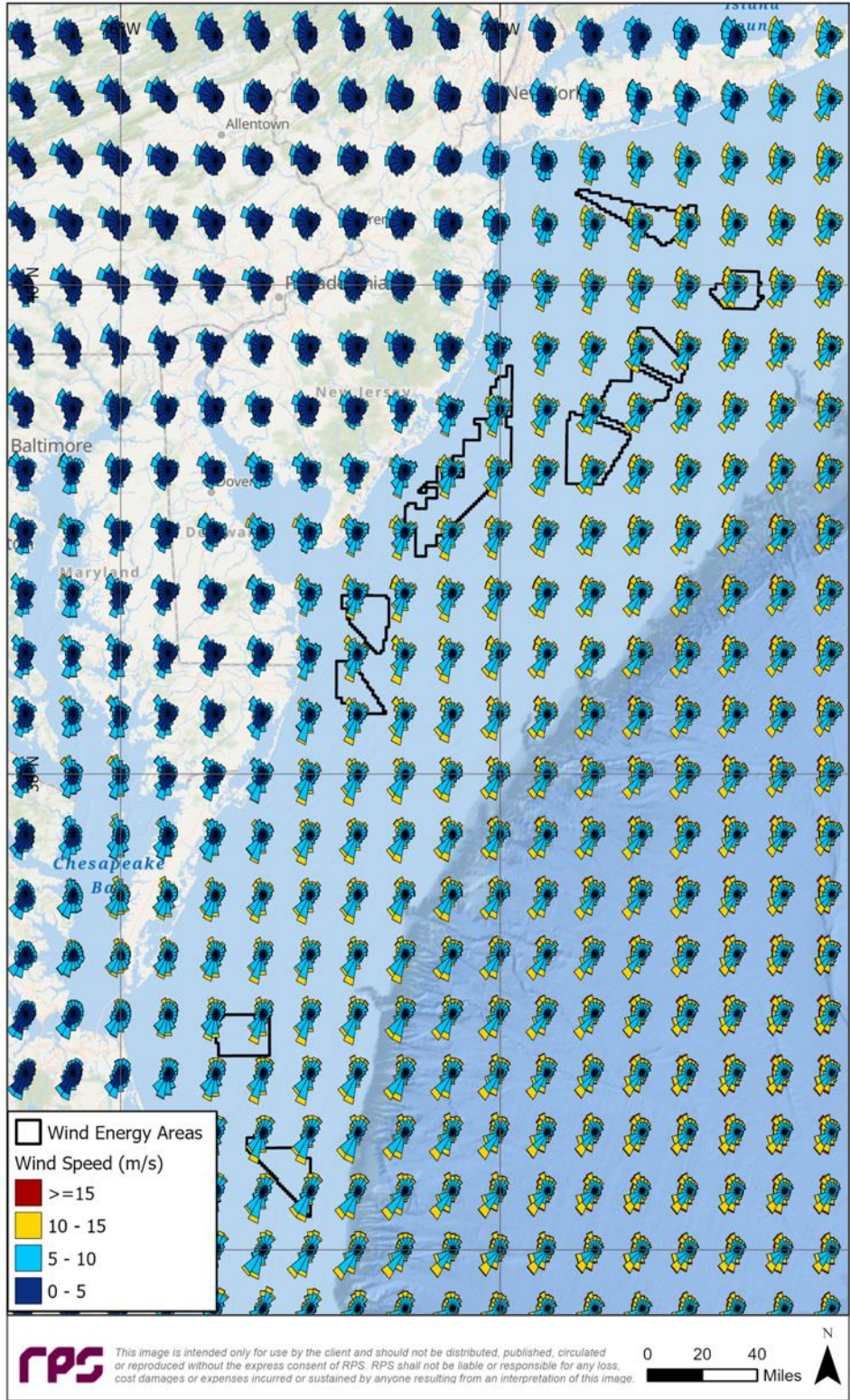


Figure 113. Wind roses (02/01/2018–01/31/2020) at ERA5 points in the project domain.

6.5 Model Parameters and Calibration

Various physical processes are activated in the wave model setup including depth-induced wave breaking, bottom-friction, white-capping, and triad wave-wave interactions. For the process of depth induced wave-breaking, a 0.73 constant breaking factor was used (Eldeberky and J.A. Battjes, 1996). Bottom friction was activated using the JONSWAP bottom friction formulation of Hasselmann et al. (1973). The triad wave-wave interaction in every spectral direction was set up using the Lumped Triad Approximation (Eldeberky et al., 1997). The wave modeling setup is described in Table 22.

Table 22. SWAN model setup parameters.

Model Parameter	Value
Discretization	45 directional bins
Maximum Number of Iterations	10
Time step	15-minute
Mesh resolution	1km to 10km
Wind forcing	ERA5 time series
Wave breaking	Constant ($\gamma = 0.73$)
Bottom friction	JONSWAP friction coefficient = 0.015
Boundary conditions	ERA 5 time series of significant wave height, mean period, mean direction and directional spreading

Model parameters were analyzed before finalizing them for the long-term run. These parameters included number of iterations per timestep, wave boundary application methods (segments or sides), and wind growth formulations. As for the third-generation mode for wind input, all available options (linear growth; exponential growth; nonlinear saturation-based white-capping combined with wind input, or “Westh” for author van der Westhuysen; and ST6 Physics, or “ST6” for source term 6) were tested using a 1.5-month model run. The two approaches that yielded better results (Westh and ST6) were selected to be tested for a longer 3-month time span (26 Aug 2019–26 Nov 2019, covering Hurricane Dorian extreme event). Figure 114 through Figure 124 compare the significant wave height time series for these two runs against measurements at 11 NDBC stations throughout the domain from south Long Island, New York to Cape Hatteras, North Carolina. The RMSE values associated with ST6 approach show a significantly better match with observation data at almost all locations (10.6% average improvement in RMSE) as also found in the latest literature (Aydoğan and Ayat 2021). Therefore, the ST6 formulation was selected for the final setup.

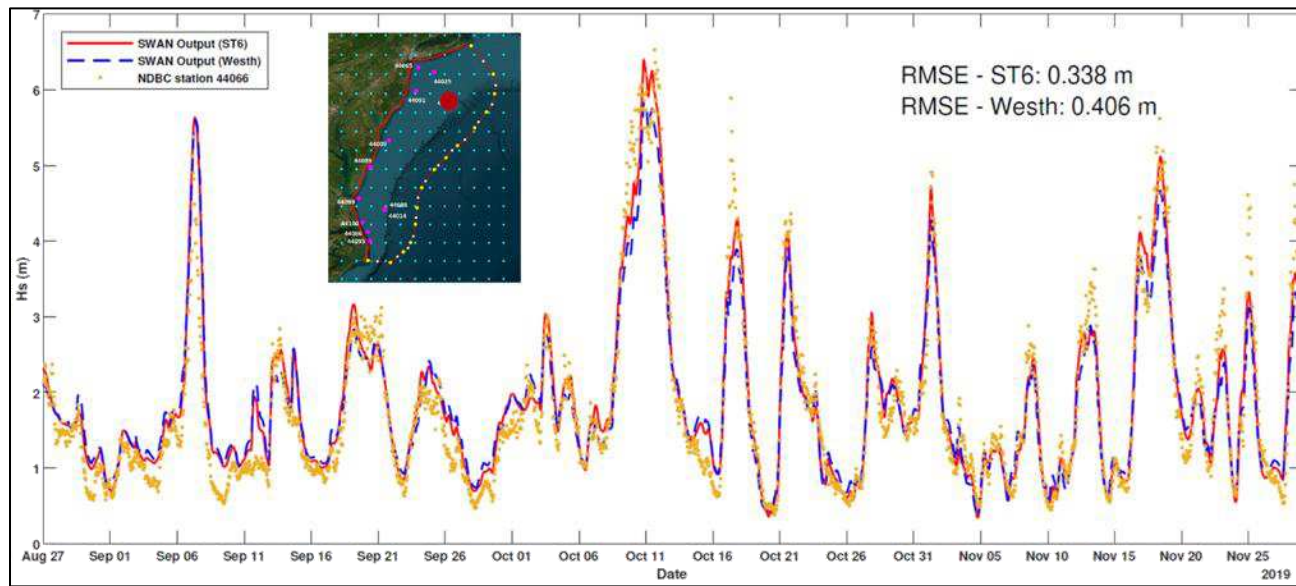


Figure 114. Significant wave height comparison with measurements at NDBC station 44066 for ST6 and Westh. approach.

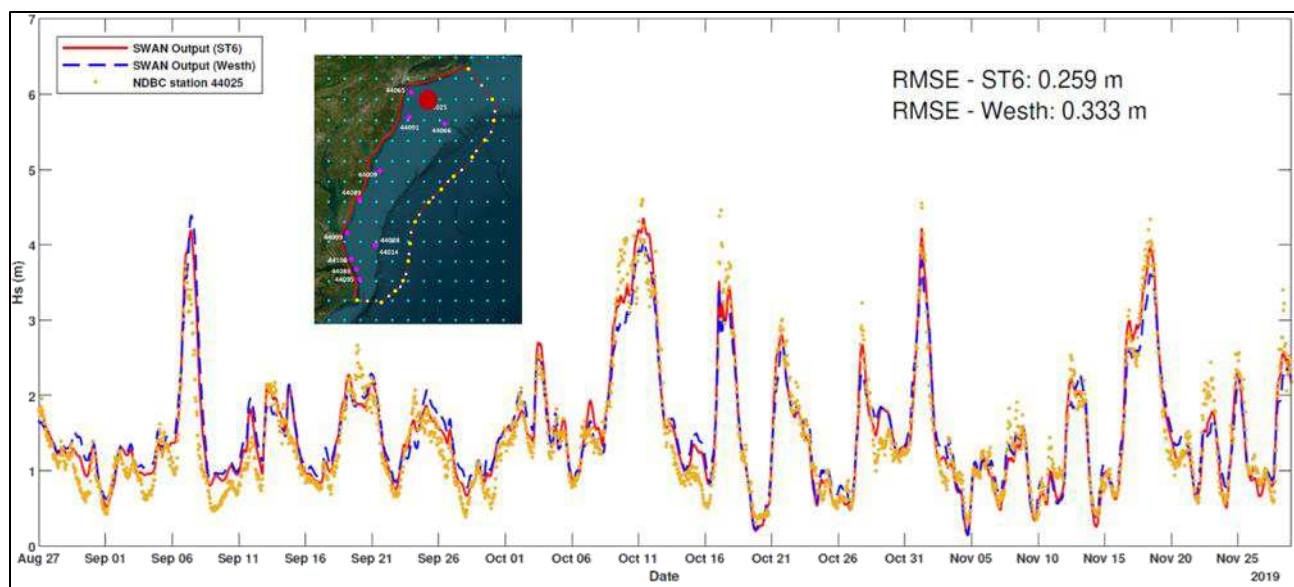


Figure 115. Significant wave height comparison with measurements at NDBC station 44025 for ST6 and Westh. approach.

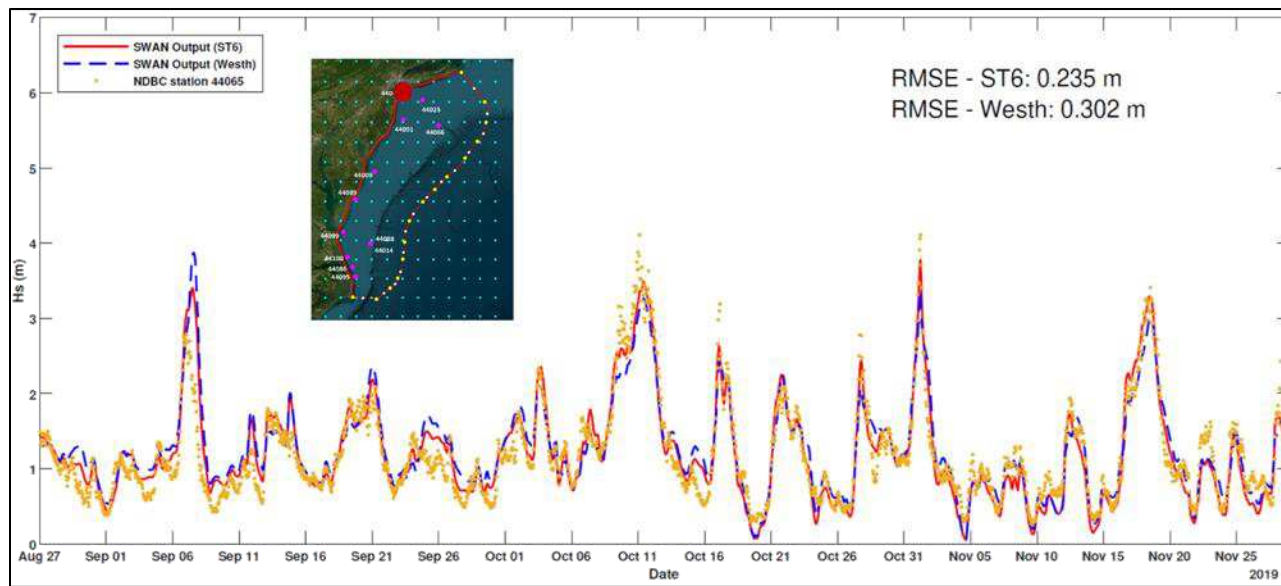


Figure 116. Significant wave height comparison with measurements at NDBC station 44065 for ST6 and Westh. approach.

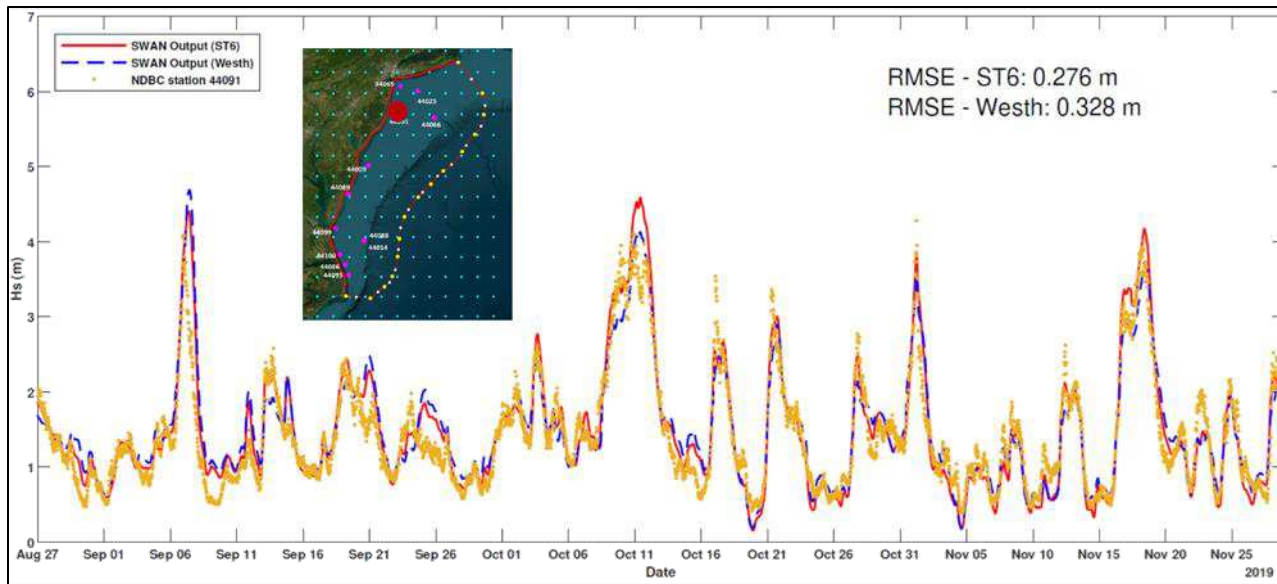


Figure 117. Significant wave height comparison with measurements at NDBC station 44091 for ST6 and Westh. approach.

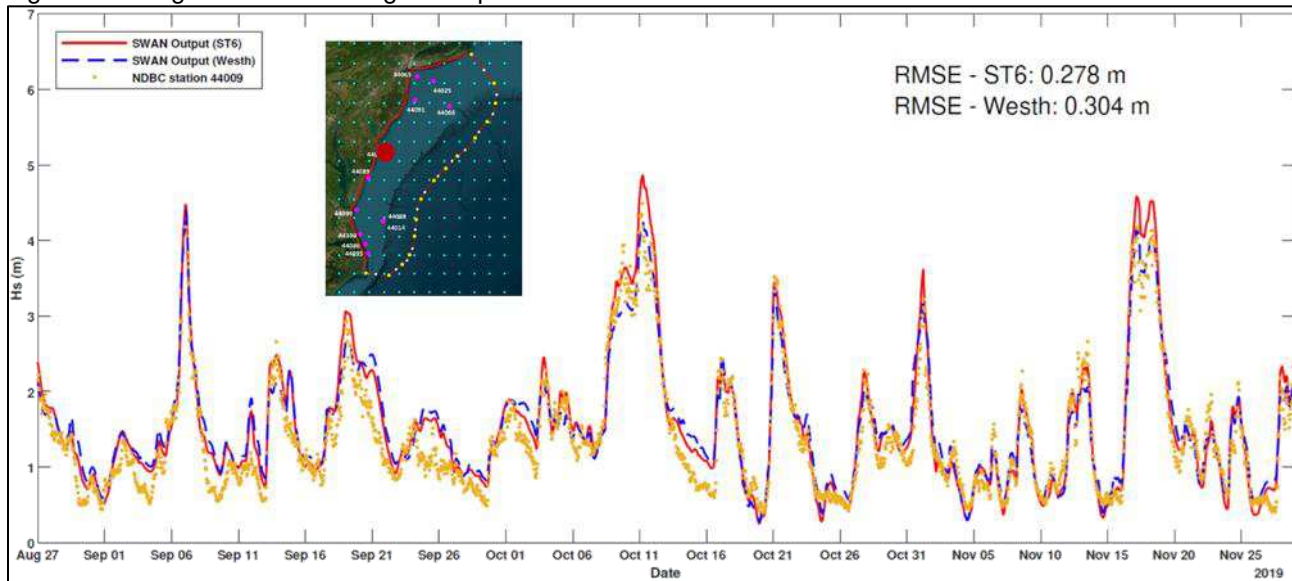


Figure 118. Significant wave height comparison with measurements at NDBC station 44099 for ST6 and Westh. approach.

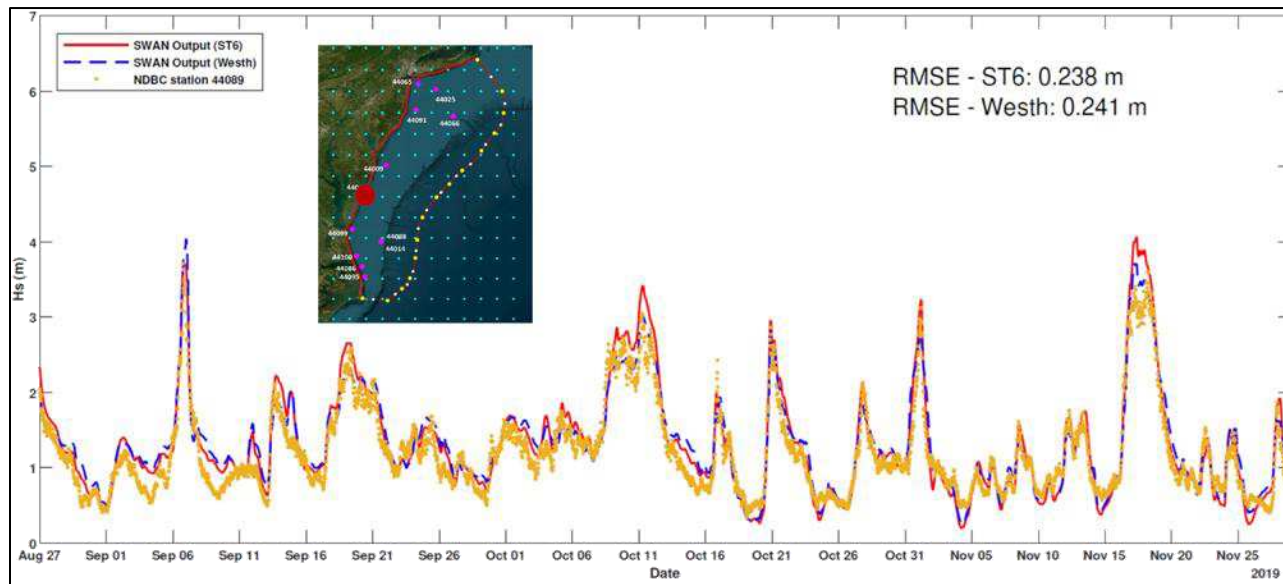


Figure 119. Significant wave height comparison with measurements at NDBC station 44089 for ST6 and Westh. approach.

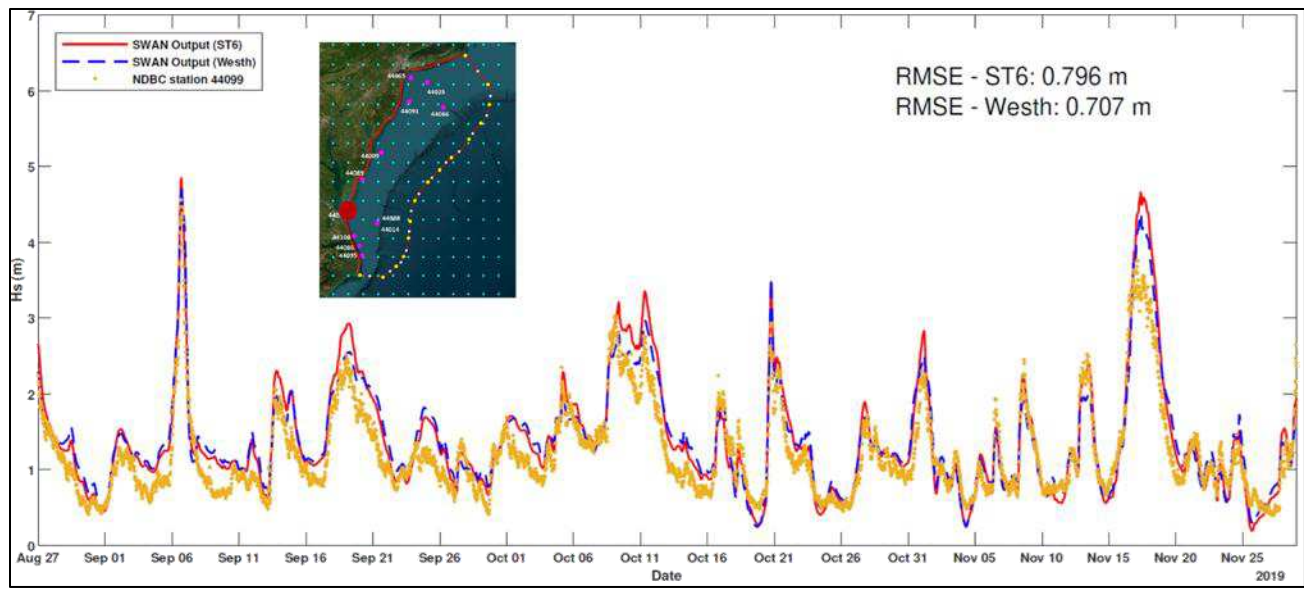


Figure 120. Significant wave height comparison with measurements at NDBC station 44099 for ST6 and Westh. approach.

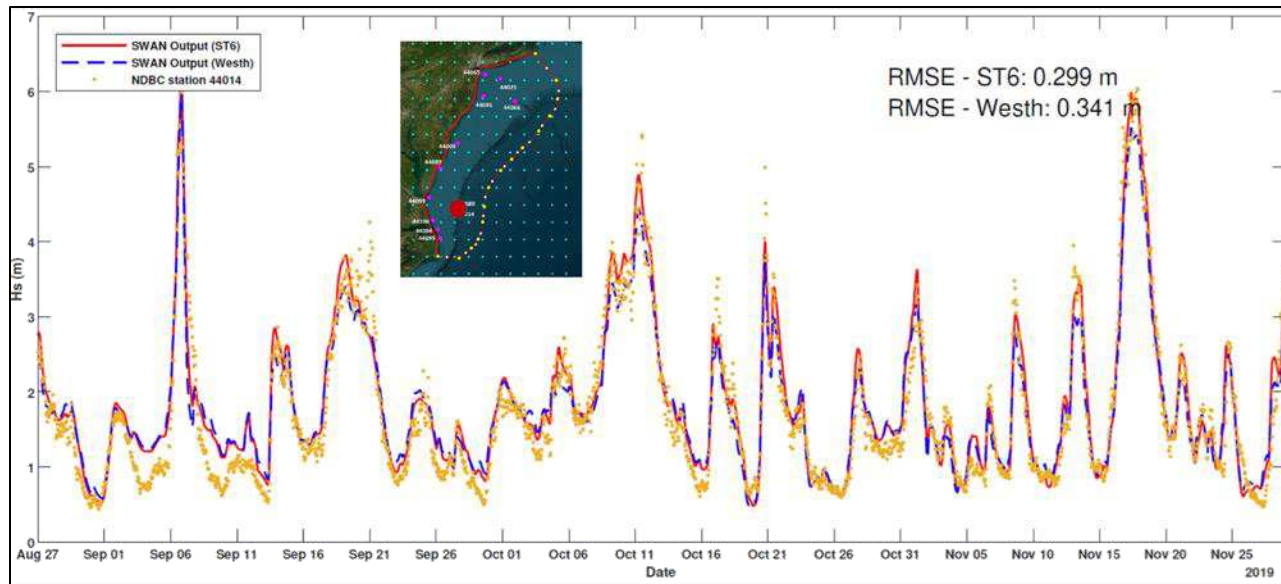


Figure 121. Significant wave height comparison with measurements at NDBC station 44014 for ST6 and Westh. approach.

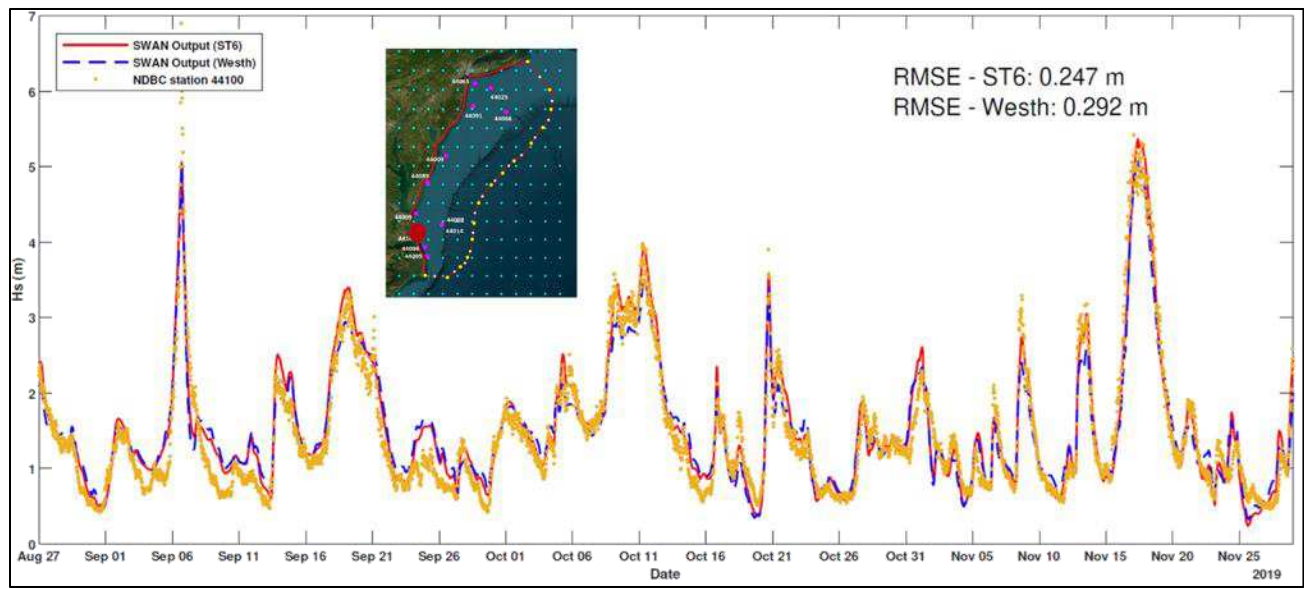


Figure 122. Significant wave height comparison with measurements at NDBC station 44100 for ST6 and Westh. approach.

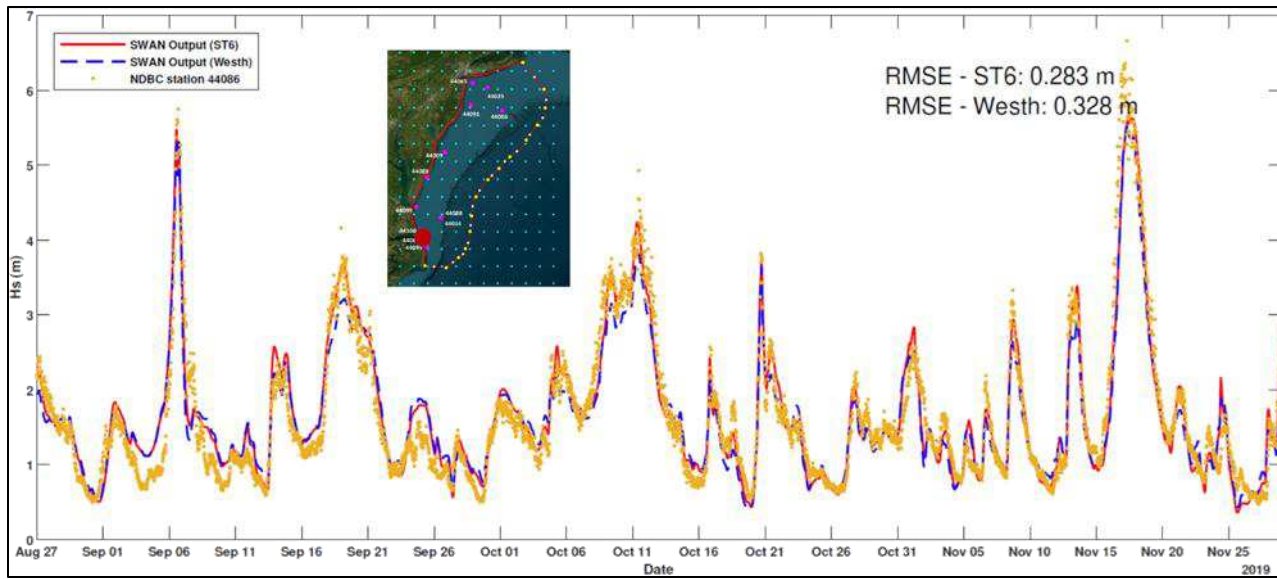


Figure 123. Significant wave height comparison with measurements at NDBC station 44086 for ST6 and Westh. approach.

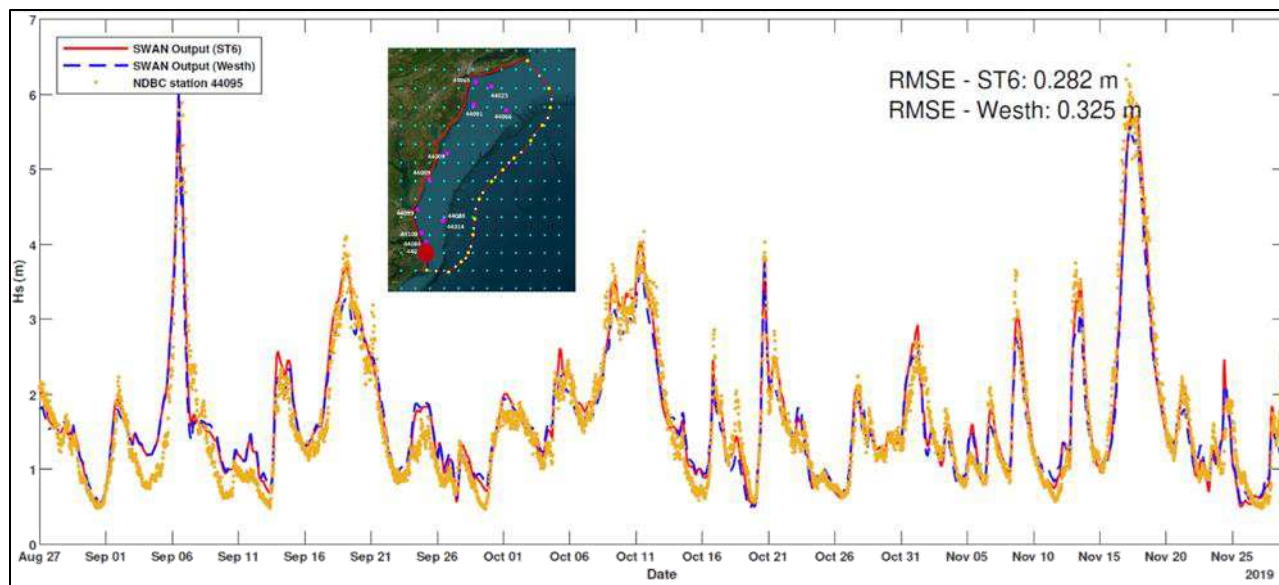


Figure 124. Significant wave height comparison with measurements at NDBC station 44095 for ST6 and Westh. approach.

6.6 Wave Model Validation

After calibration of the model parameters, the SWAN model for the MAB was then run for validation purposes as part of Scenario 1 (Baseline Scenario - no wind turbines) over two full calendar years, February 2018 to February 2020. SWAN was forced by ERA5 winds and waves at its surface and ocean boundaries, respectively.

6.6.1 Wind Forcing Validation (ERA5)

First, the ERA5 wind forcing was validated against in situ observations, converted to 10m above surface using equation (4) from their known anemometer height. Results for wind speed were summarized in Table 23. In general, R^2 values vary between 0.714 at NDBC station 44065 off the entrance of the New York Harbor – which also has the highest RMSE, 1.752 m/s – to 0.834 at 44025 situated further offshore the NY Bight Apex (RMSE=1.412m/s there). These values show that ERA5 provides excellent forcing for wave modeling in the AOI and are very similar to a comprehensive validation performed by Campos et al. (2022) against satellite data. Their results indicated that ERA5 provides high-quality winds for non-extreme conditions, especially at the eastern boundaries, with bias between -0.5 and 0.3 m/s and RMSE below 1.5 m/s. The reanalysis errors were found to be site-dependent, with strong winds at extratropical locations like the MAB well represented, and higher RMSE in tropical regions. Our results, however, do show a tendency of under-prediction of wind speeds by ERA5 at NDBC station 44065 primarily at high wind values, but also overall, as ERA5 was biased low there by 0.915 m/s.

Table 23. Wind speed validation metrics (ERA5) at NDBC station locations.

NDBC Station	RMSE (m/s)	Bias (m/s)	R^2	MAE (m/s)	IOA	Min (m/s)	Max (m/s)	Mean (m/s)	STD (m/s)
44009	1.487	0.149	0.794	1.134	0.934	0.1	23.1	6.188	3.273
44014	1.638	0.589	0.762	1.214	0.939	0.1	28.3	6.165	3.357
44025	1.412	0.065	0.834	1.053	0.955	0.1	20.3	6.751	3.471
44065	1.752	-0.915	0.714	1.398	0.913	0.1	20.7	6.338	3.275
44066	1.414	0.456	0.830	1.014	0.959	0.1	21.7	6.722	3.528

The following time series and correlogram plots (Figure 125 to Figure 132) visually compare the wind forcing from ERA5 against the NDBC anemometer data.

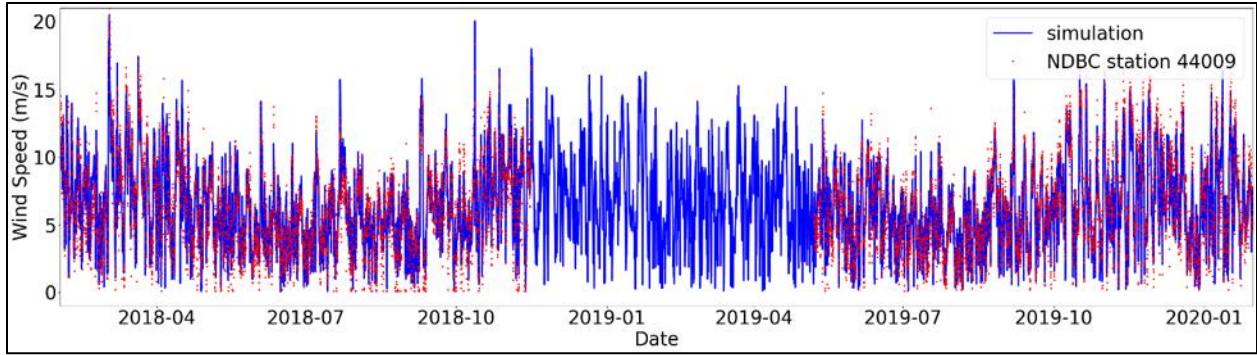


Figure 125. ERA5 – Simulated wind speed vs. measurements at NDBC station 44009.

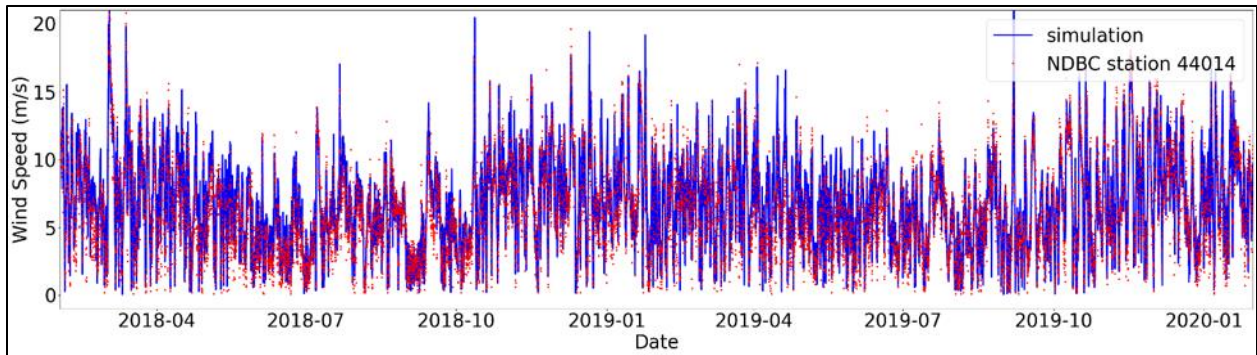


Figure 126. ERA5 – Simulated wind speed vs. measurements at NDBC station 44014.

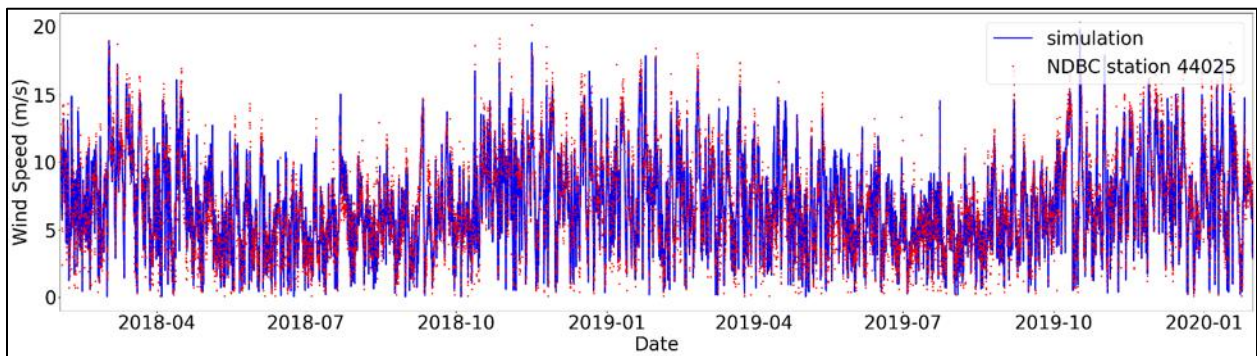


Figure 127. ERA5 – Simulated wind speed vs. measurements at NDBC station 44025.

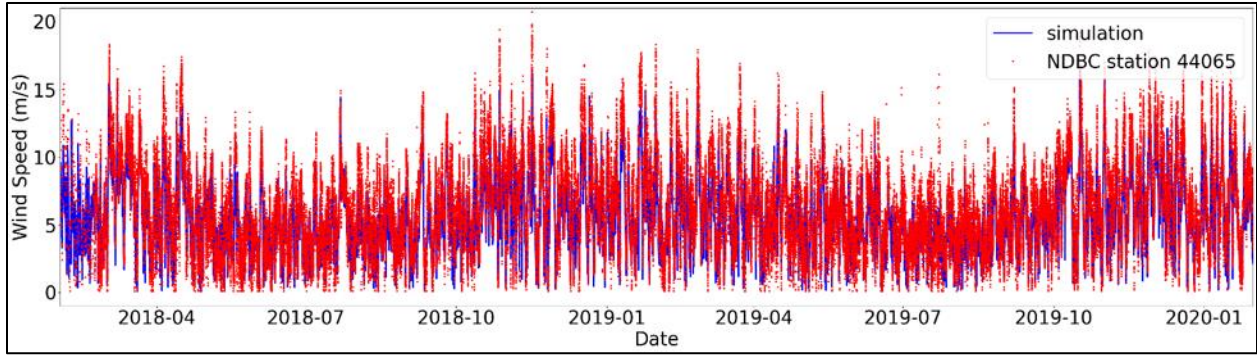


Figure 128. ERA5 – Simulated wind speed vs. measurements at NDBC station 44065.

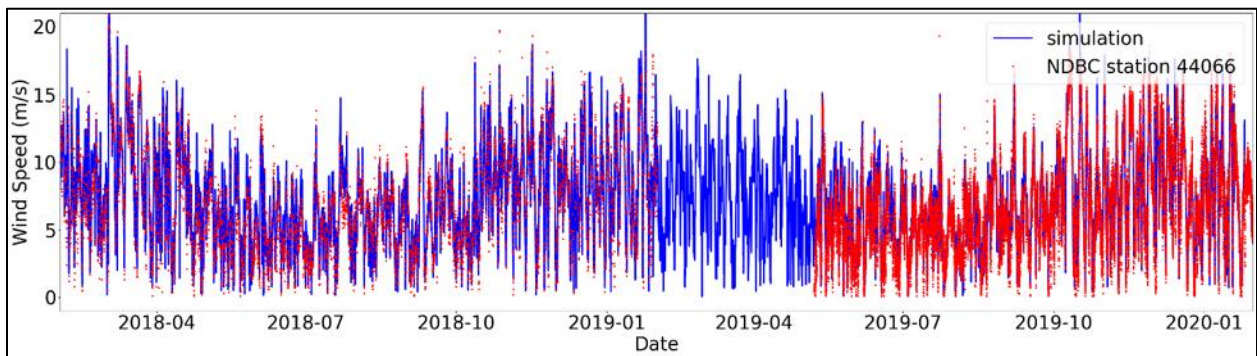


Figure 129. ERA5 – Simulated wind speed vs. measurements at NDBC station 44066.

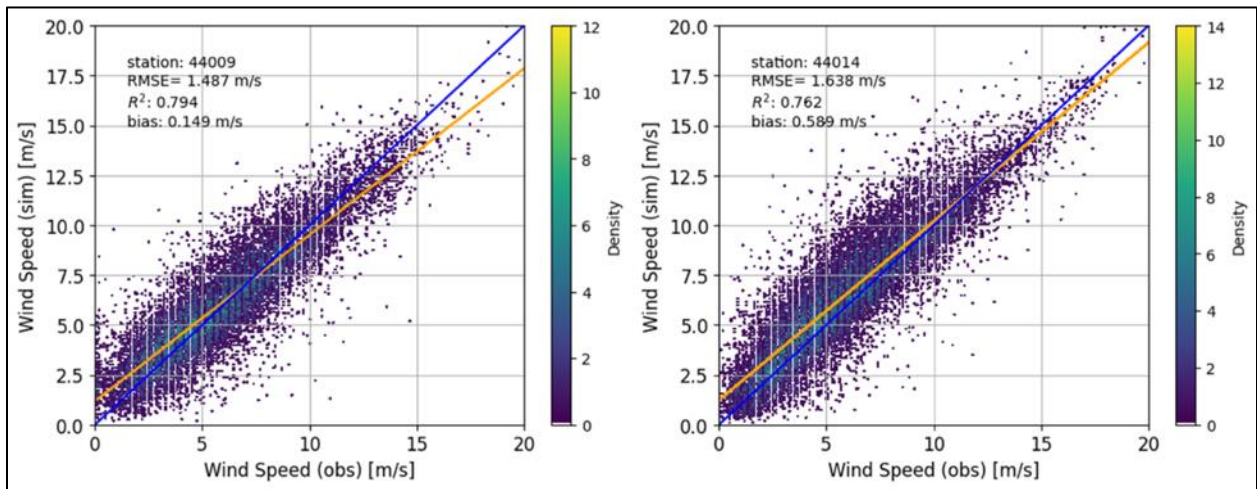


Figure 130. Overall evaluation of wind speed at NDBC stations 44009 (left panel) and 44014 (right panel).

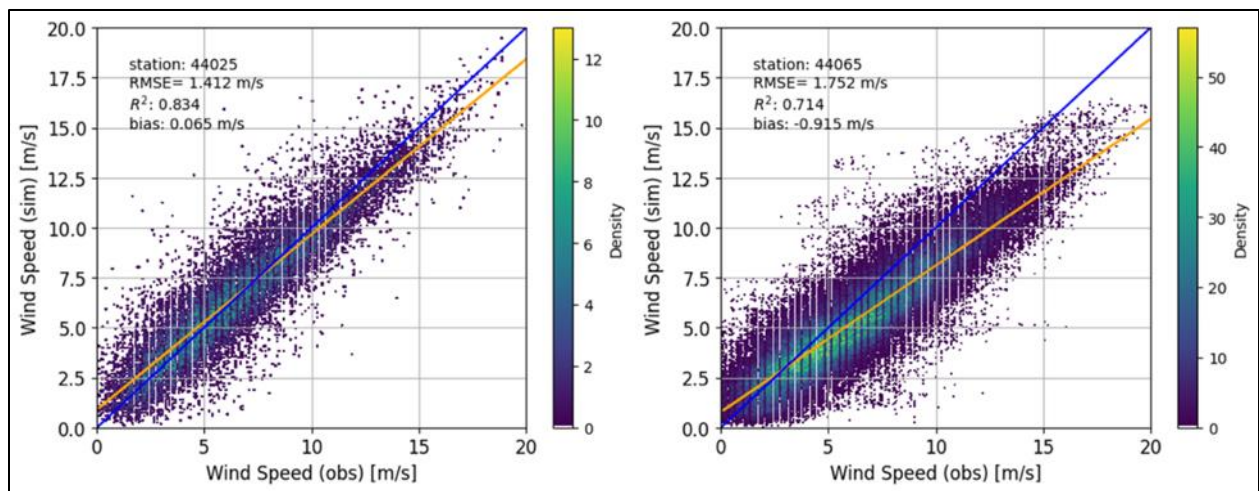


Figure 131. Overall evaluation of wind speed at NDBC stations 44025 (left panel) and 44065 (right panel).

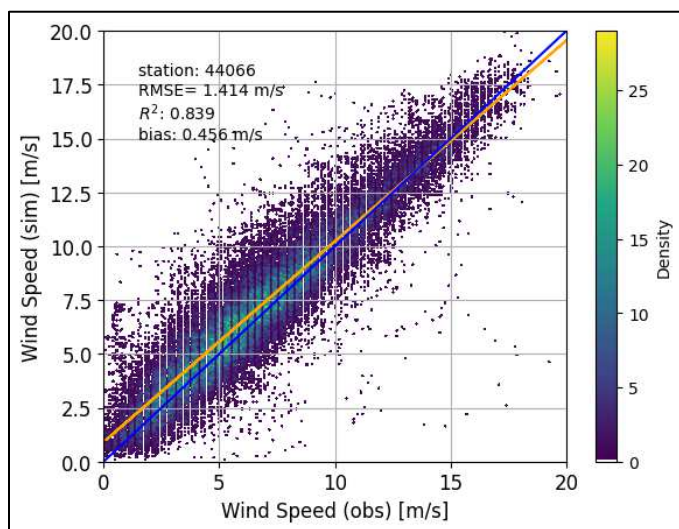


Figure 132. Overall evaluation of wind speed at NDBC station 44066.

6.6.2 Significant Wave Height Validation (Scenario 1, SWAN)

Table 24 shows that the SWAN model of the MAB has very good skill in simulating significant wave height. R^2 values ranged from 0.61 at station 44099 near the Chesapeake Bay entrance, to 0.884 at station 44095. Given that 44065 had somewhat less skill in wind speed, the R^2 value for significant wave height may mean that either the wind observations themselves are biased high for some reason, or, more likely, that the local wind at the entrance of the New York Harbor does not govern the local wave climate which is mostly governed by wind forcing and fetch over the more open areas of the MAB and beyond. RMSE for significant wave height was very low and ranged between 0.260m at 44065 and 0.4m at 44066 at the Hudson River Canyon.

Table 24. Significant wave height validation metrics at NDBC station locations.

NDBC Station	RMSE (m)	Bias (m)	R ²	MAE (m)	IOA	Min Observed (m)	Max Observed (m)	Mean Observed (m)	STD Observed (m/s)
44009	0.323	0.118	0.752	0.235	0.942	0.20	4.92	1.183	0.648
44014	0.310	0.076	0.870	0.235	0.965	0.30	6.75	1.477	0.862
44025	0.290	0.067	0.847	0.208	0.962	0.22	6.31	1.291	0.742
44065	0.260	0.008	0.802	0.193	0.953	0.19	5.43	1.055	0.585
44066	0.400	0.073	0.847	0.274	0.957	0.31	8.49	1.592	1.022
44086	0.284	-0.020	0.861	0.207	0.963	0.34	7.73	1.363	0.762
44088	0.363	0.049	0.879	0.268	0.964	0.38	7.02	1.539	1.047
44089	0.263	0.079	0.735	0.192	0.944	0.25	4.48	1.028	0.511
44091	0.302	0.024	0.796	0.212	0.952	0.24	5.61	1.277	0.668
44095	0.265	0.010	0.884	0.195	0.969	0.35	7.59	1.368	0.778
44099	0.307	0.105	0.610	0.219	0.921	0.29	4.56	1.015	0.491
44100	0.263	0.021	0.849	0.195	0.961	0.30	6.90	1.164	0.677

Figure 133 to Figure 150 visually compare significant wave height simulated in SWAN versus NDBC station data.

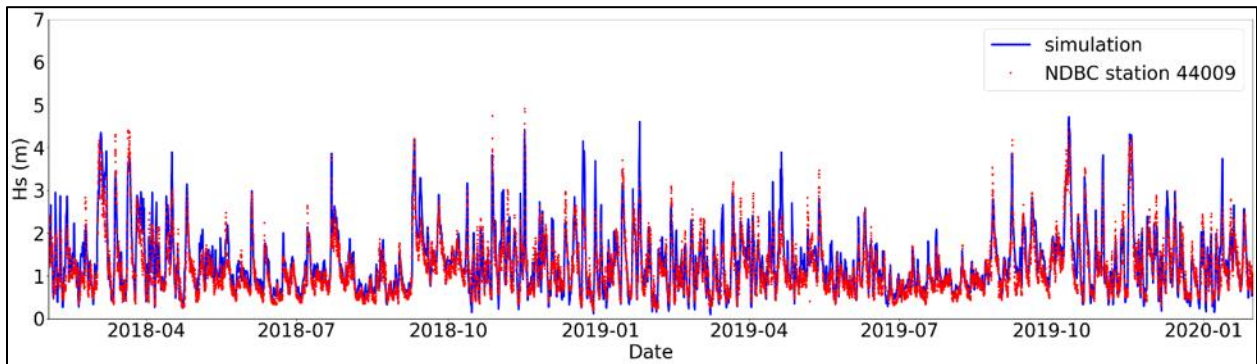


Figure 133. Simulated significant wave height vs. measurements at NDBC station 44009.

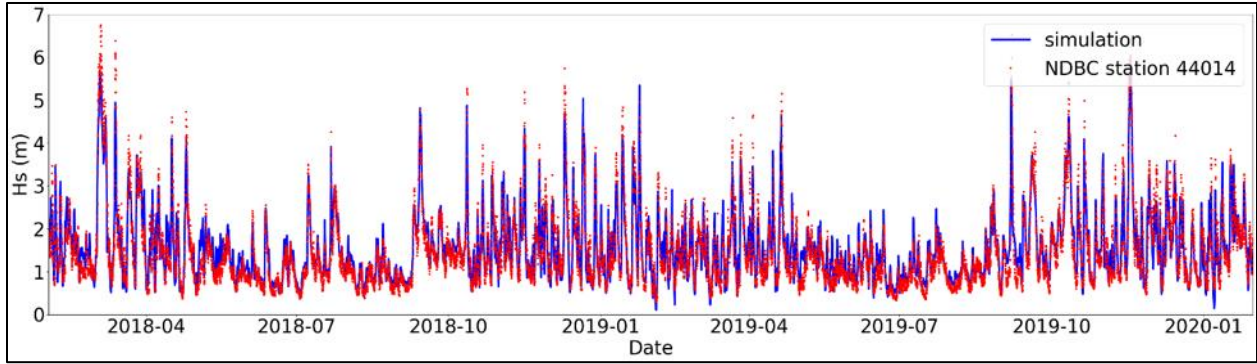


Figure 134. Simulated significant wave height vs. measurements at NDBC station 44014.

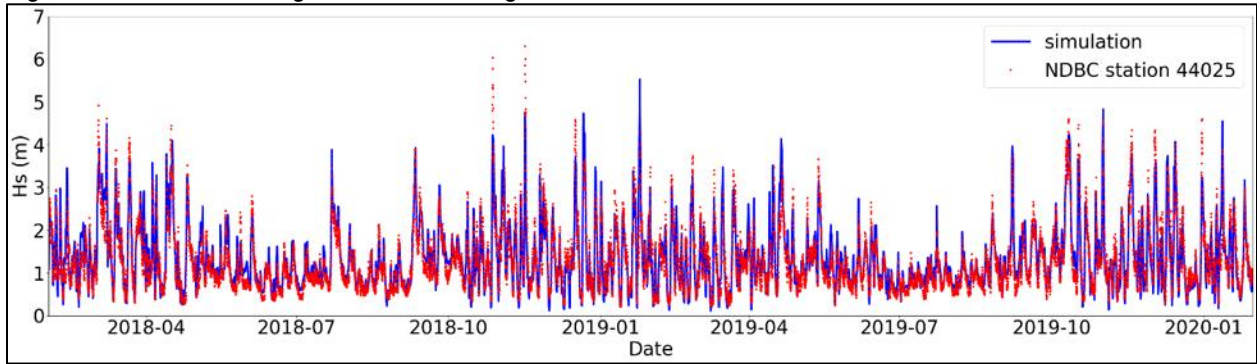


Figure 135. Simulated significant wave height vs. measurements at NDBC station 44025.

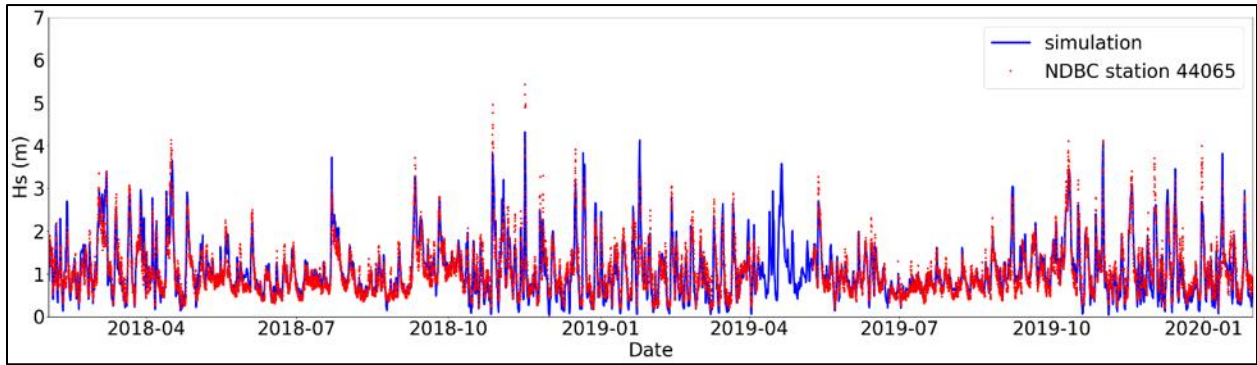


Figure 136. Simulated significant wave height vs. measurements at NDBC station 44065.

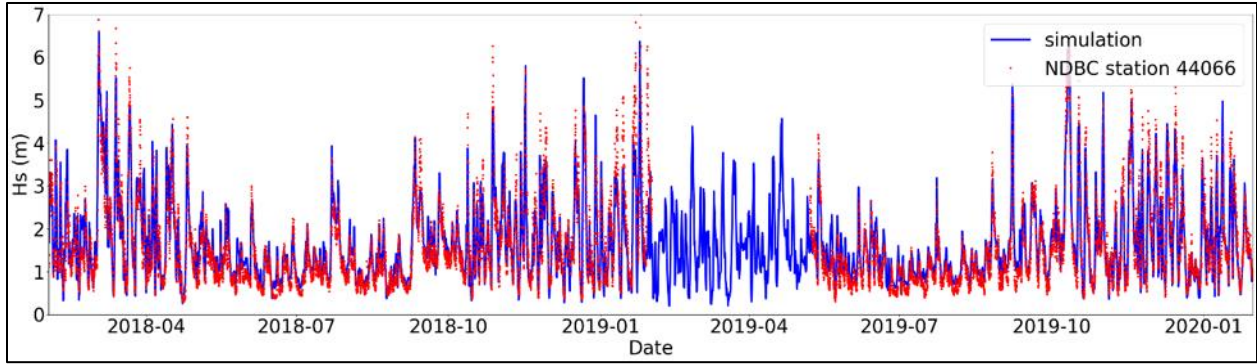


Figure 137. Simulated significant wave height vs. measurements at NDBC station 44066.

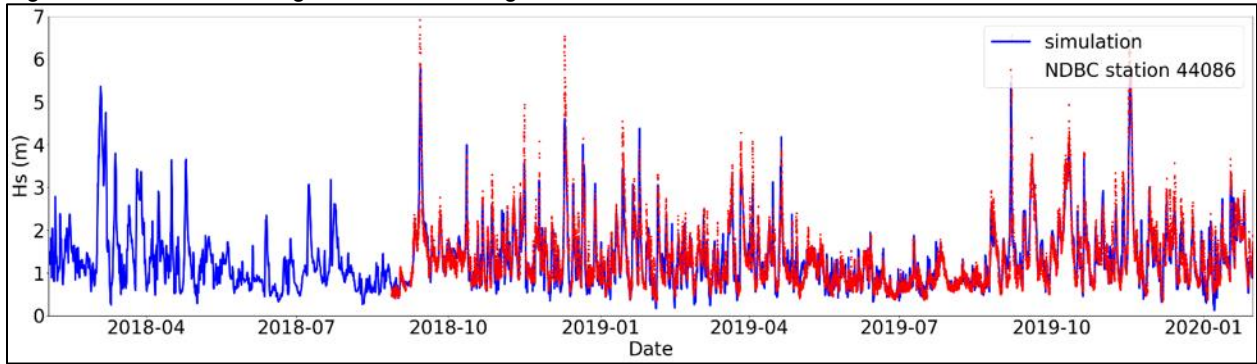


Figure 138. Simulated significant wave height vs. measurements at NDBC station 44086.

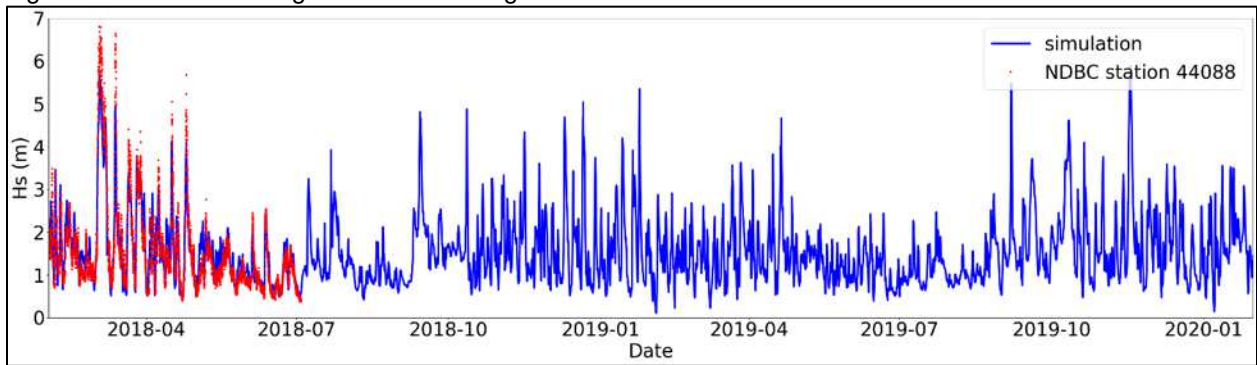


Figure 139. Simulated significant wave height vs. measurements at NDBC station 44088.

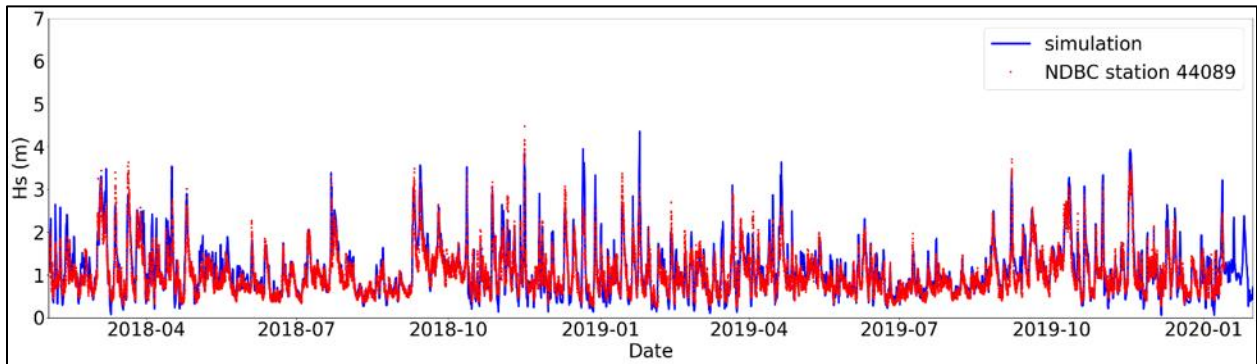


Figure 140. Simulated significant wave height vs. measurements at NDBC station 44089.

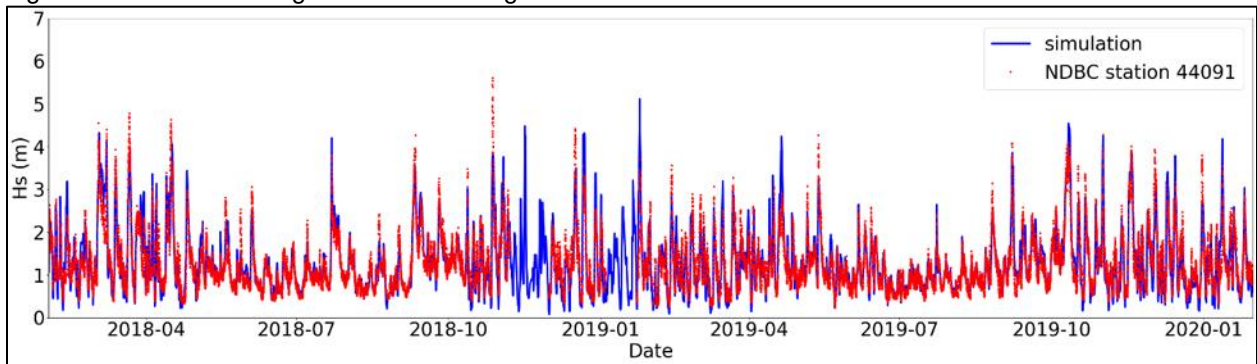


Figure 141. Simulated significant wave height vs. measurements at NDBC station 44091.

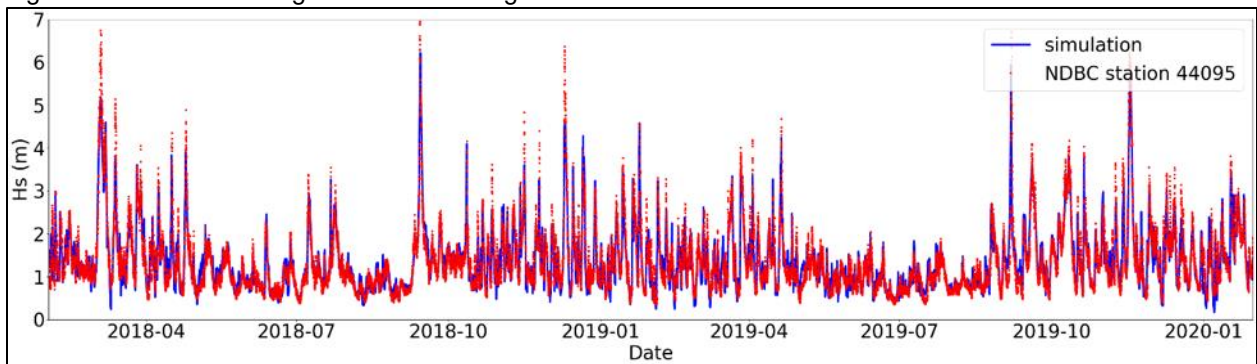


Figure 142. Simulated significant wave height vs. measurements at NDBC station 44095.

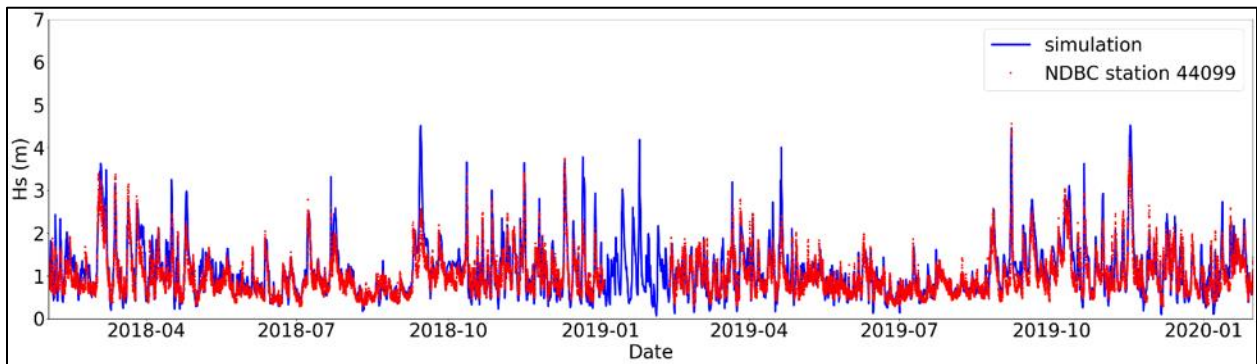


Figure 143. Simulated significant wave height vs. measurements at NDBC station 44099.

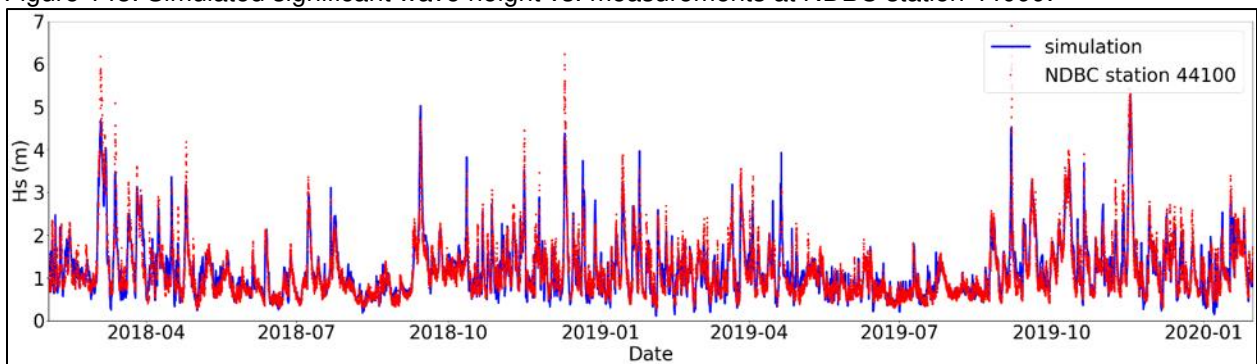


Figure 144. Simulated significant wave height vs. measurements at NDBC station 44100.

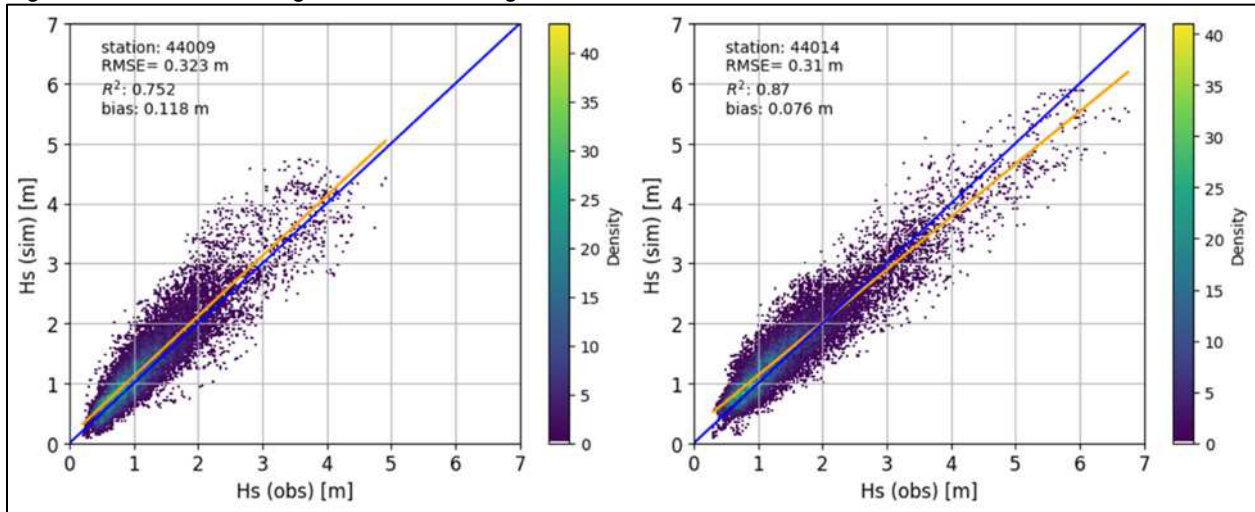


Figure 145. Overall evaluation of simulated significant wave height at NDBC stations 44009 (left panel) and 44014 (right panel).

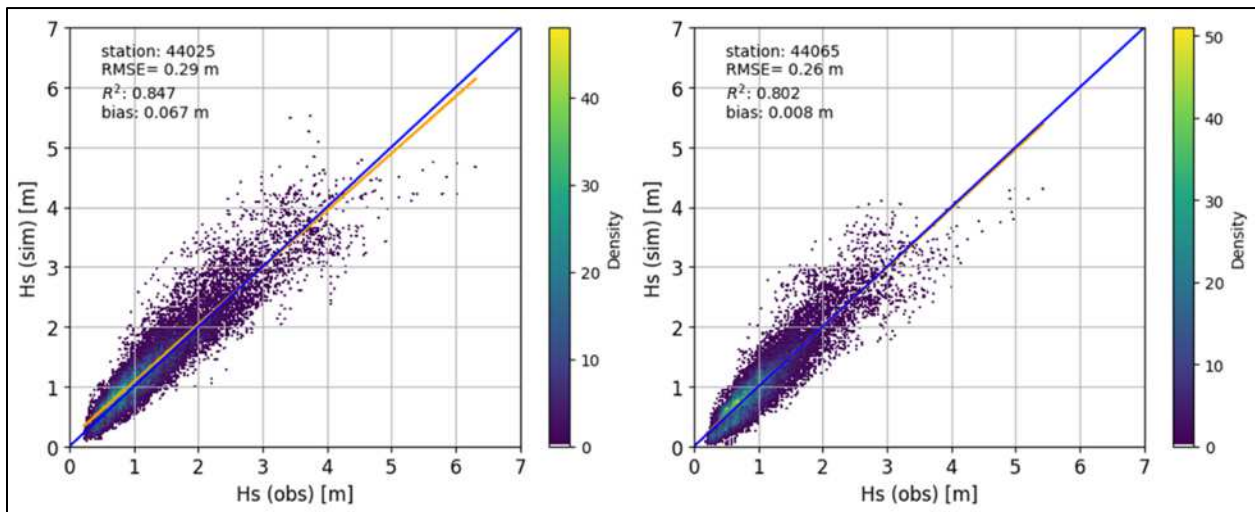


Figure 146. Overall evaluation of simulated significant wave height at NDBC stations 44025 (left panel) and 44065 (right panel).

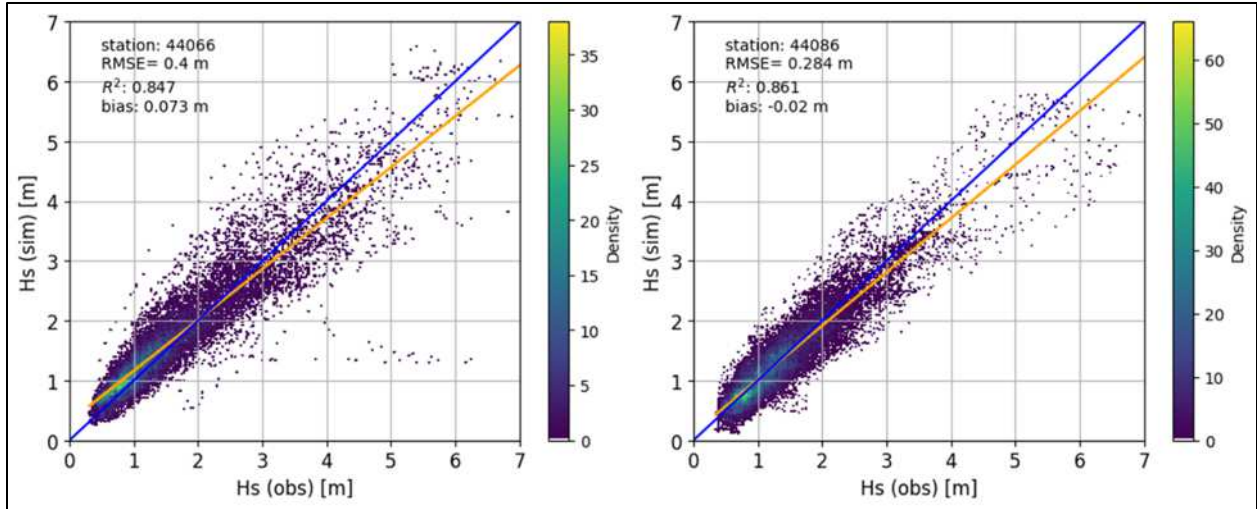


Figure 147. Overall evaluation of simulated significant wave height at NDBC stations 44066 (left panel) and 44086 (right panel).

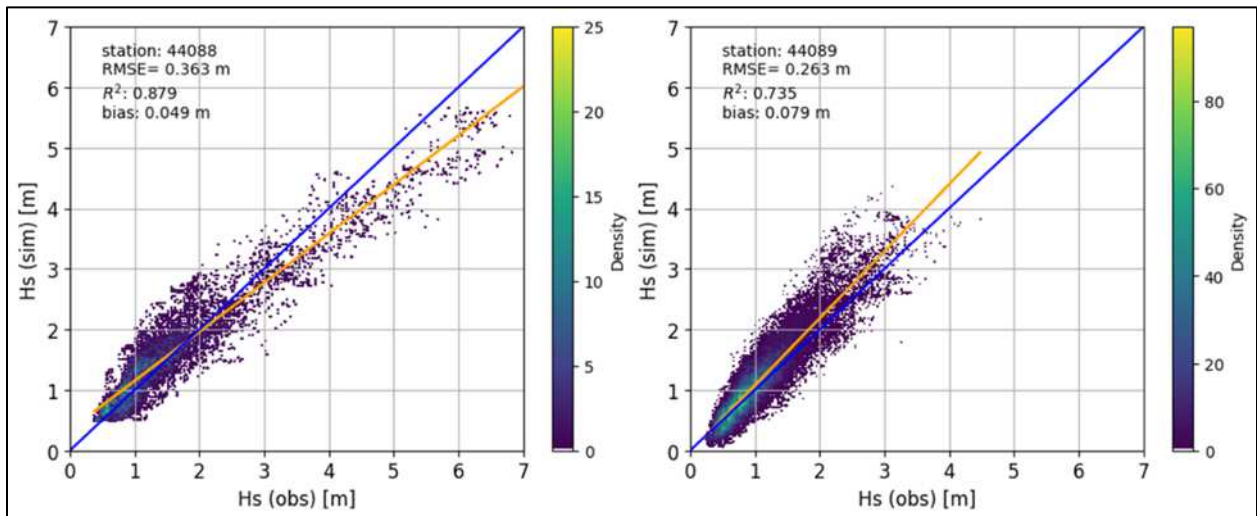


Figure 148. Overall evaluation of simulated significant wave height at NDBC stations 44088 (left panel) and 44089 (right panel).

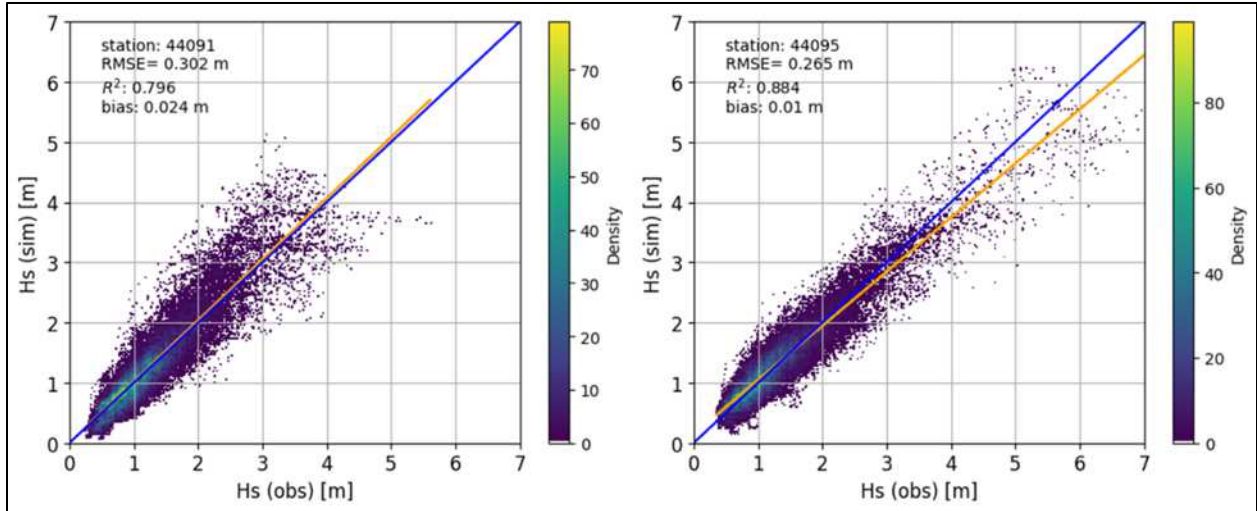


Figure 149. Overall evaluation of simulated significant wave height at NDBC stations 44091 (left panel) and 44095 (right panel).

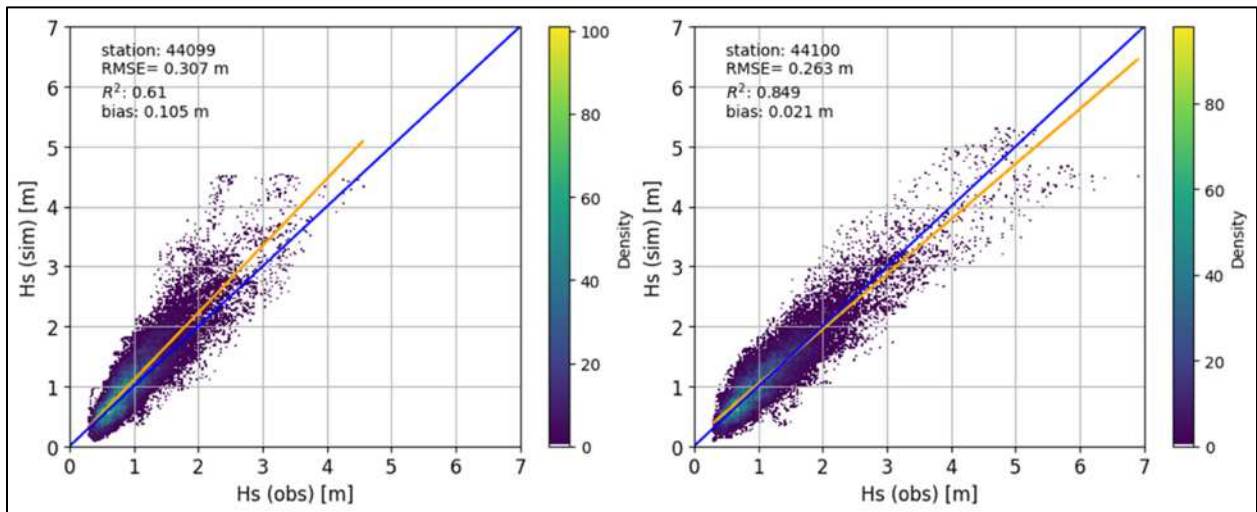


Figure 150. Overall evaluation of simulated significant wave height at NDBC stations 44099 (left panel) and 44100 (right panel).

6.6.3 Mean Wave Direction Validation (Scenario 1, SWAN)

In terms of mean wave direction (Table 25) average RMSE was just above 1/12 of the trigonometric circle (37°) with an average angular bias less than 25° and an average circular correlation of 0.77. Figure 151 to Figure 168 graphically illustrate the comparisons against data.

Table 25. Mean wave direction validation metrics at NDBC station locations.

NDBC Station	RMSE (deg)	Angular Bias (deg)	Circular Correlation	MAE (deg)	IOA
44009	41.983	25.2	0.754	28.282	0.932
44014	39.054	23.8	0.786	26.372	0.946
44025	37.772	22.5	0.797	25.112	0.927
44065	38.593	21.5	0.719	24.584	0.906
44066	39.558	22.4	0.813	25.536	0.941
44086	40.555	23.4	0.785	26.519	0.937
44088	37.844	24.3	0.782	26.321	0.942
44089	35.389	22.2	0.720	24.056	0.906
44091	37.720	22.1	0.743	24.687	0.932
44095	38.311	21.6	0.804	24.565	0.934
44099	33.484	20.4	0.773	22.244	0.926
44100	36.418	22.0	0.762	24.215	0.929

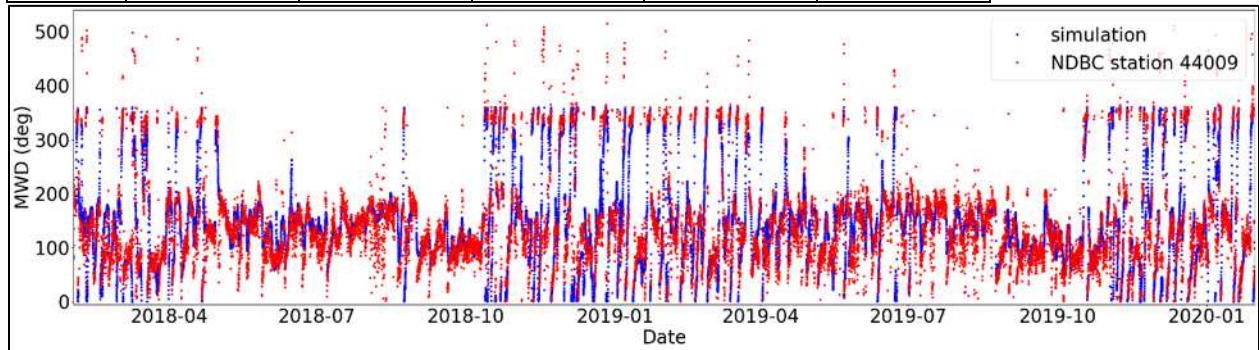


Figure 151. Simulated mean wave direction (blue) vs. measurements (red) at NDBC station 44009.

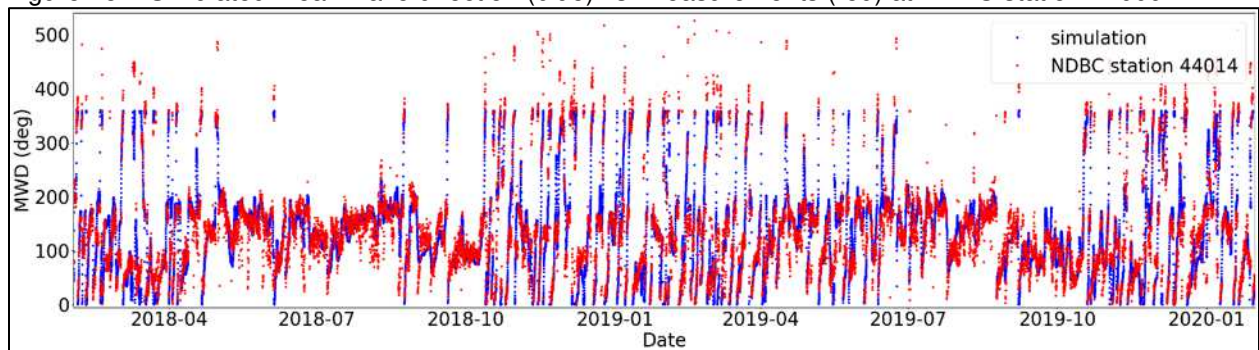


Figure 152. Simulated mean wave direction (blue) vs. measurements (red) at NDBC station 44014.

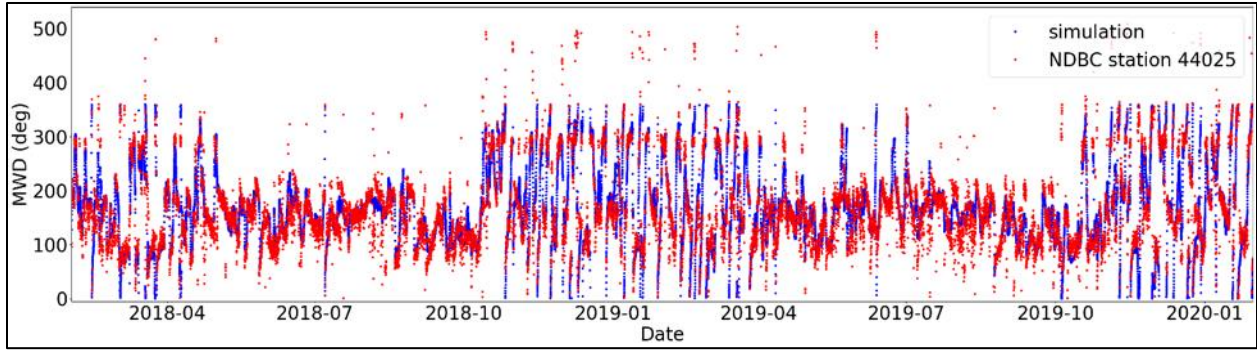


Figure 153. Simulated mean wave direction (blue) vs. measurements (red) at NDBC station 44025.

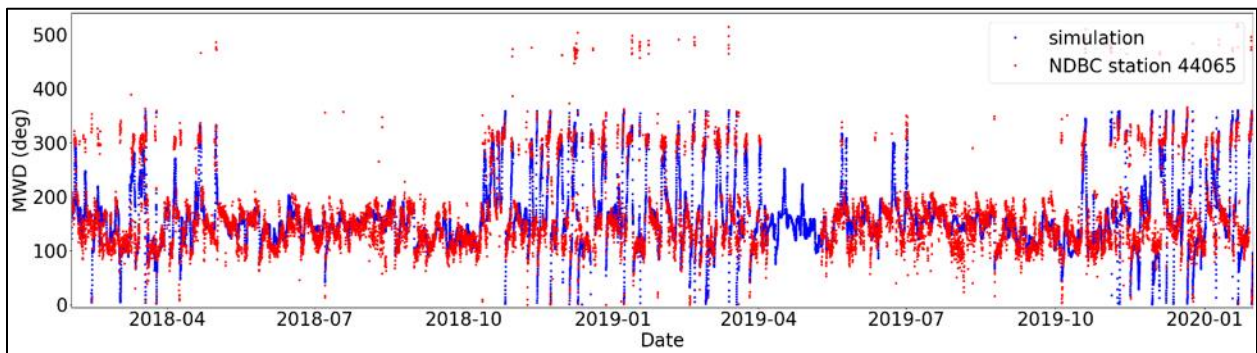


Figure 154. Simulated mean wave direction (blue) vs. measurements (red) at NDBC station 44065.

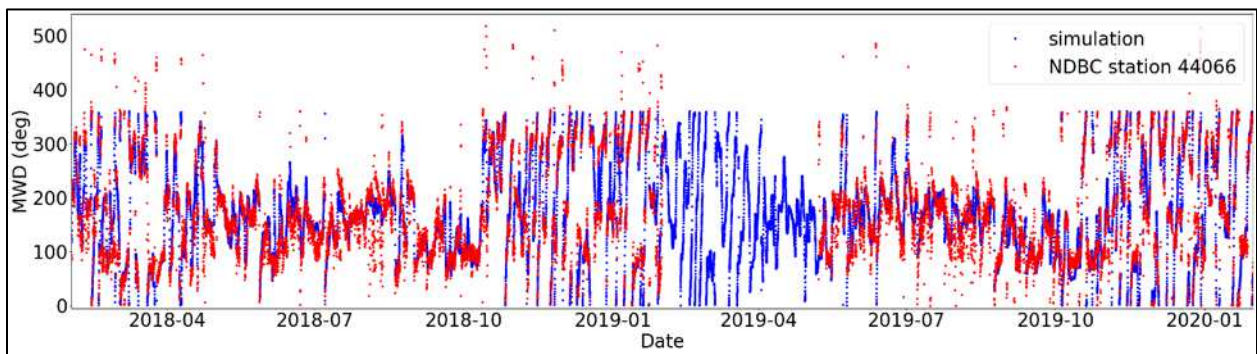


Figure 155. Simulated mean wave direction (blue) vs. measurements (red) at NDBC station 44066.

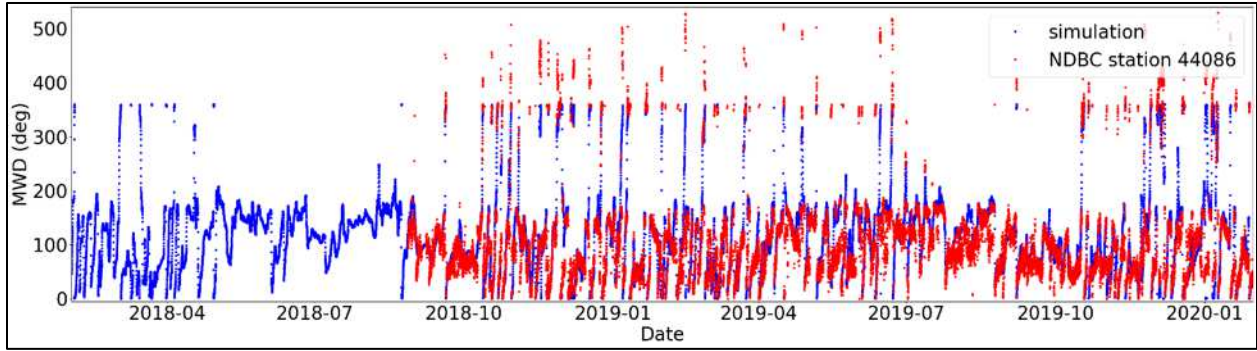


Figure 156. Simulated mean wave direction (blue) vs. measurements (red) at NDBC station 44086.

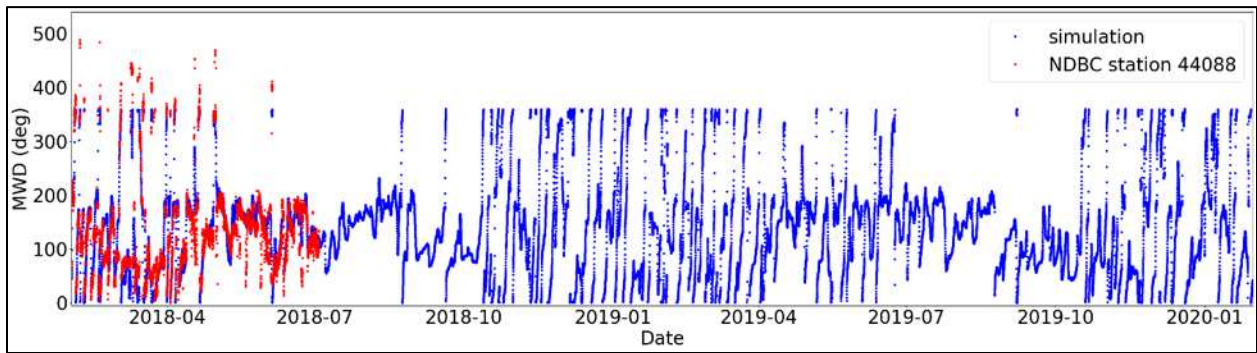


Figure 157. Simulated mean wave direction (blue) vs. measurements (red) at NDBC station 44088.

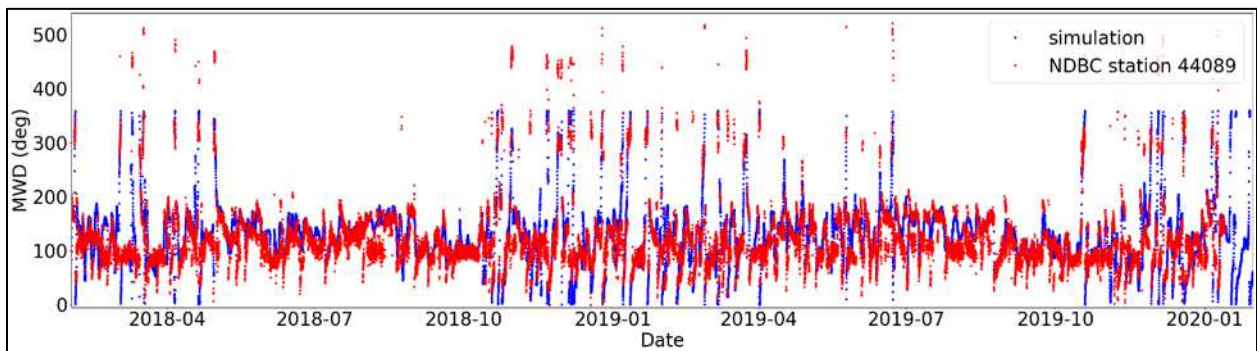


Figure 158. Simulated mean wave direction (blue) vs. measurements (red) at NDBC station 44089.

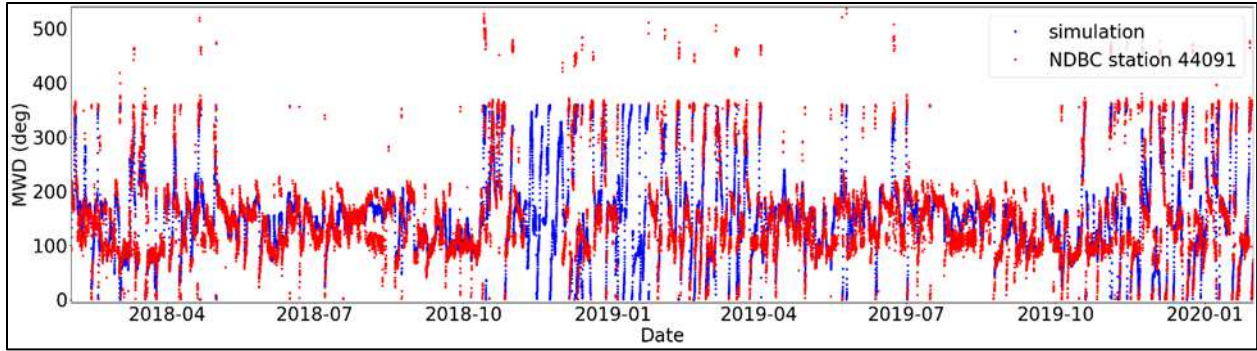


Figure 159. Simulated mean wave direction (blue) vs. measurements (red) at NDBC station 44091.

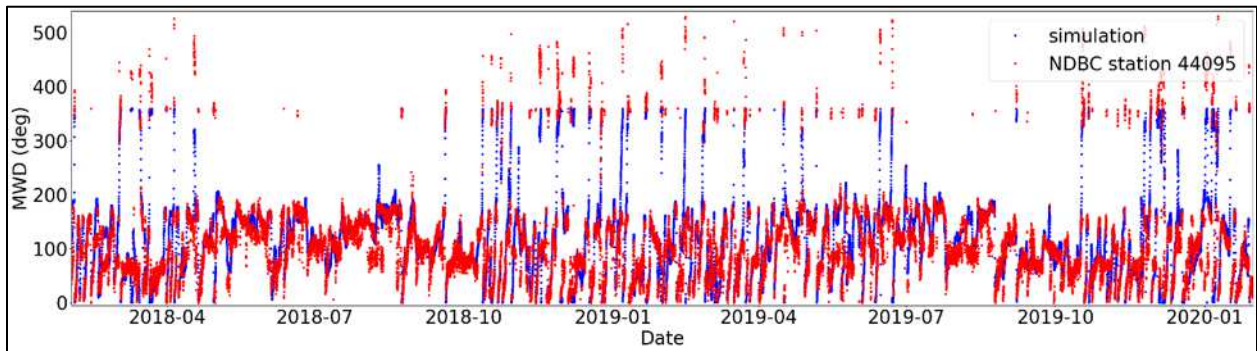


Figure 160. Simulated mean wave direction (blue) vs. measurements (red) at NDBC station 44095.

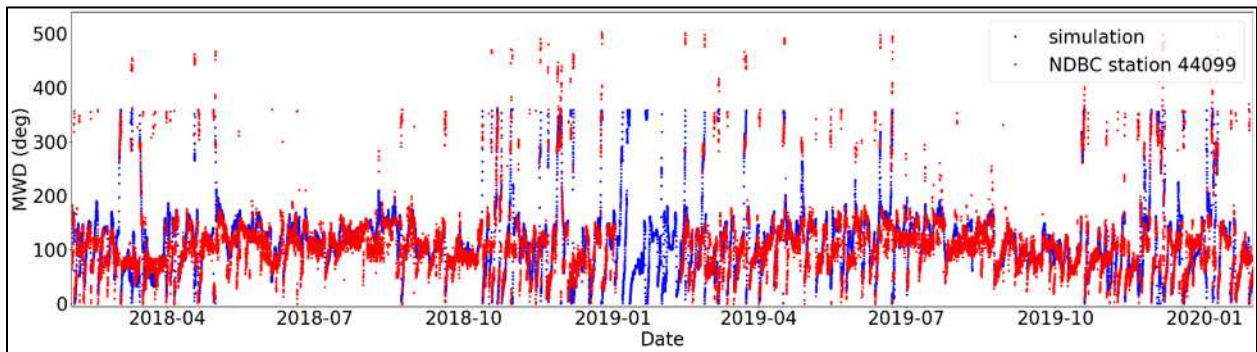


Figure 161. Simulated mean wave direction (blue) vs. measurements (red) at NDBC station 44099.

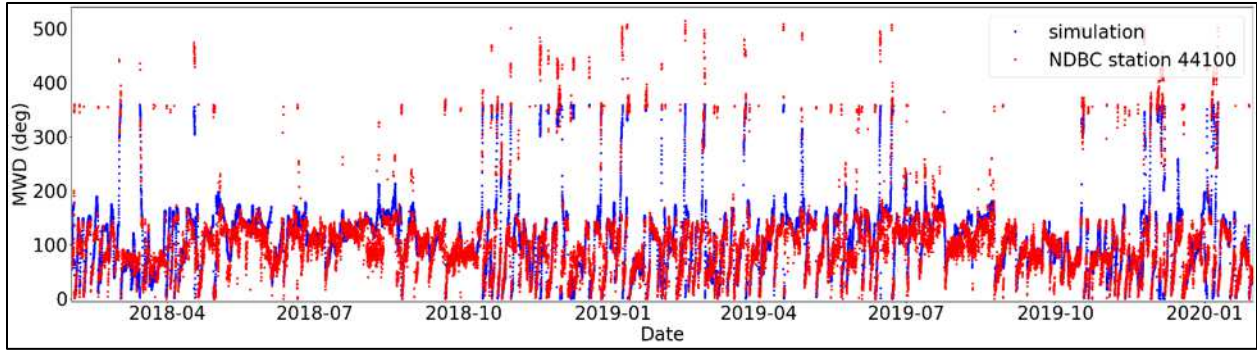


Figure 162. Simulated mean wave direction (blue) vs. measurements (red) at NDBC station 44100.

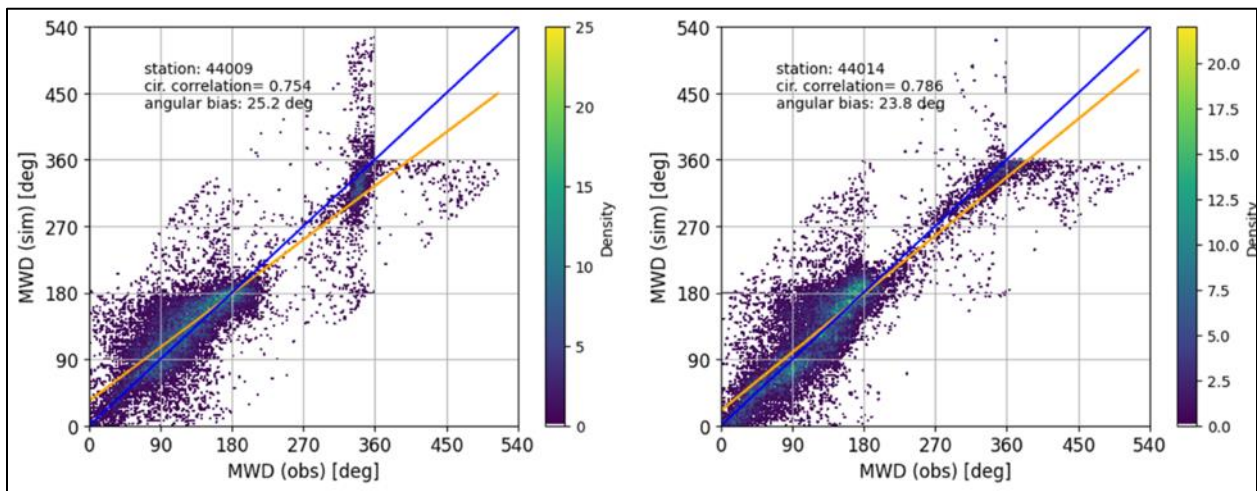


Figure 163. Overall evaluation of simulated mean wave direction at NDBC stations 44009 (left panel) and 44014 (right panel).

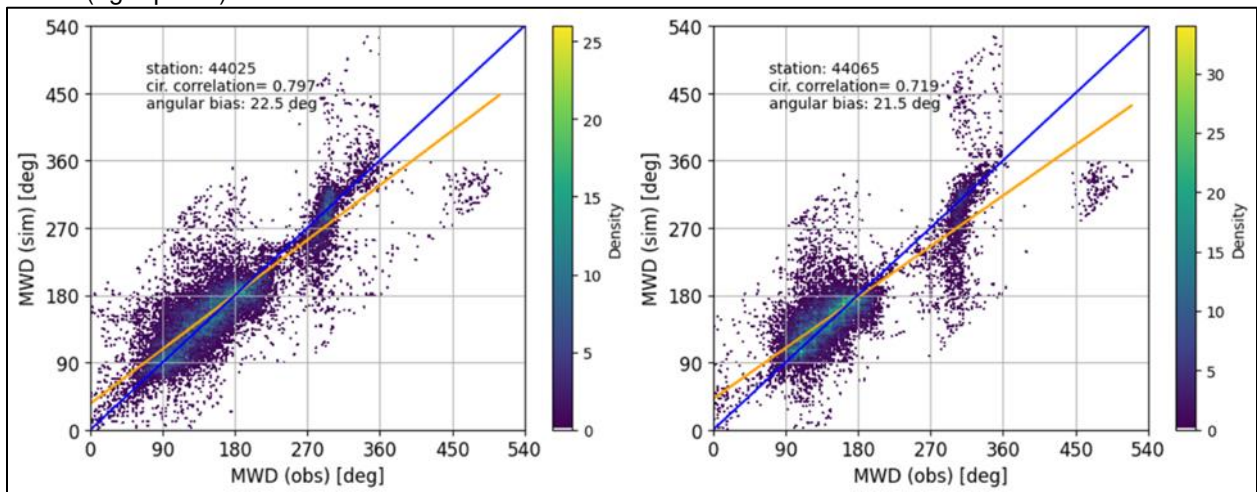


Figure 164. Overall evaluation of simulated mean wave direction at NDBC stations 44025 (left panel) and 44065 (right panel).

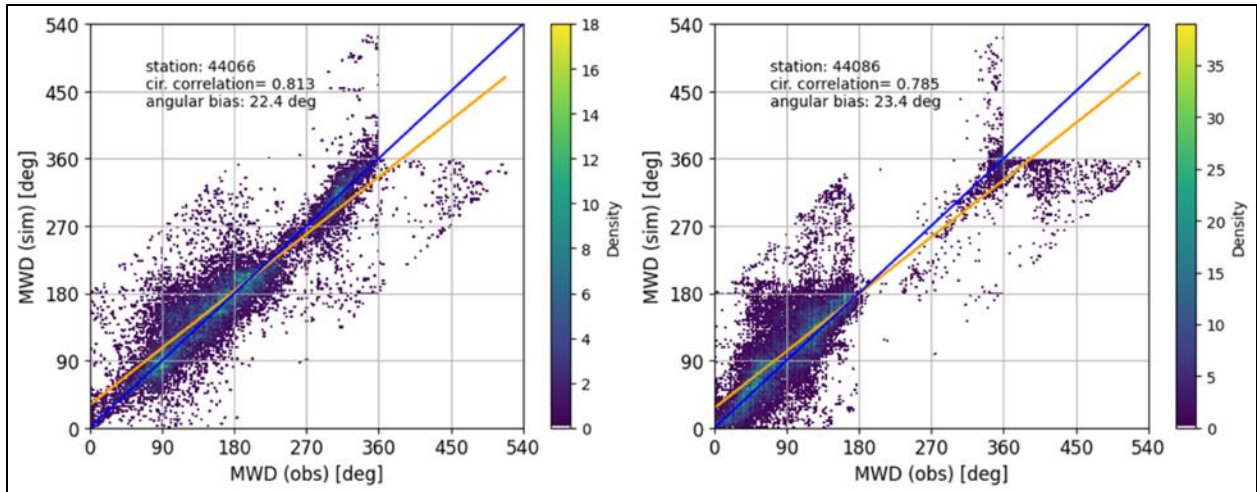


Figure 165. Overall evaluation of simulated mean wave direction at NDBC stations 44066 (left panel) and 44086 (right panel).

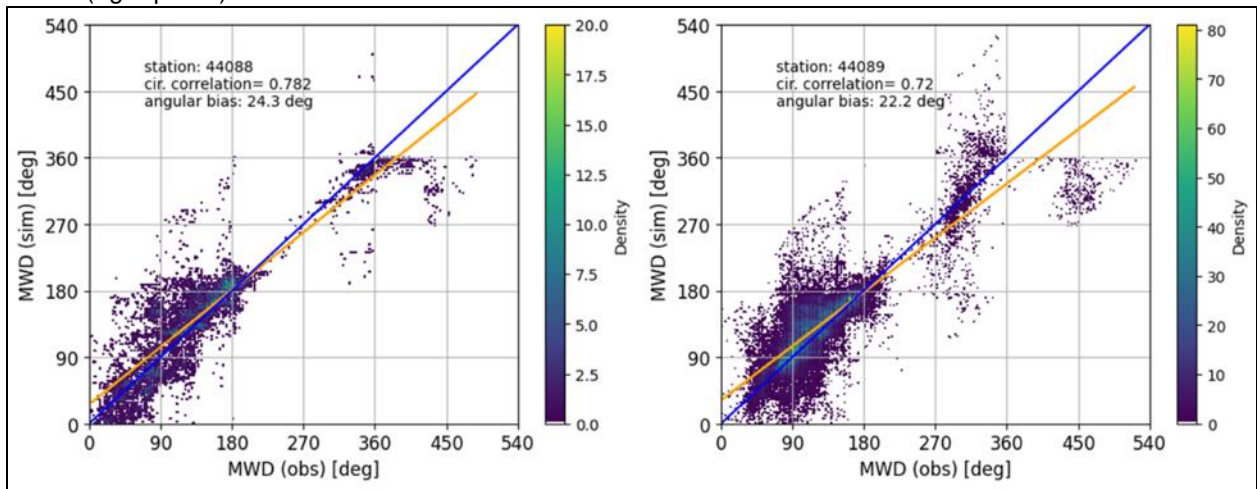


Figure 166. Overall evaluation of simulated mean wave direction at NDBC stations 44088 (left panel) and 44089 (right panel).

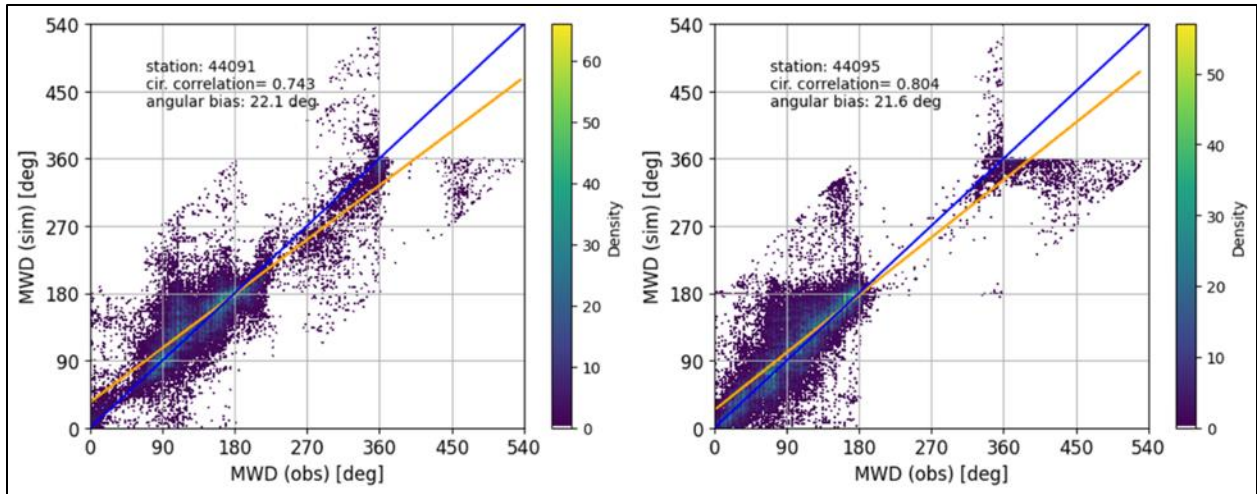


Figure 167. Overall evaluation of simulated mean wave direction at NDBC stations 44091 (left panel) and 44095 (right panel).

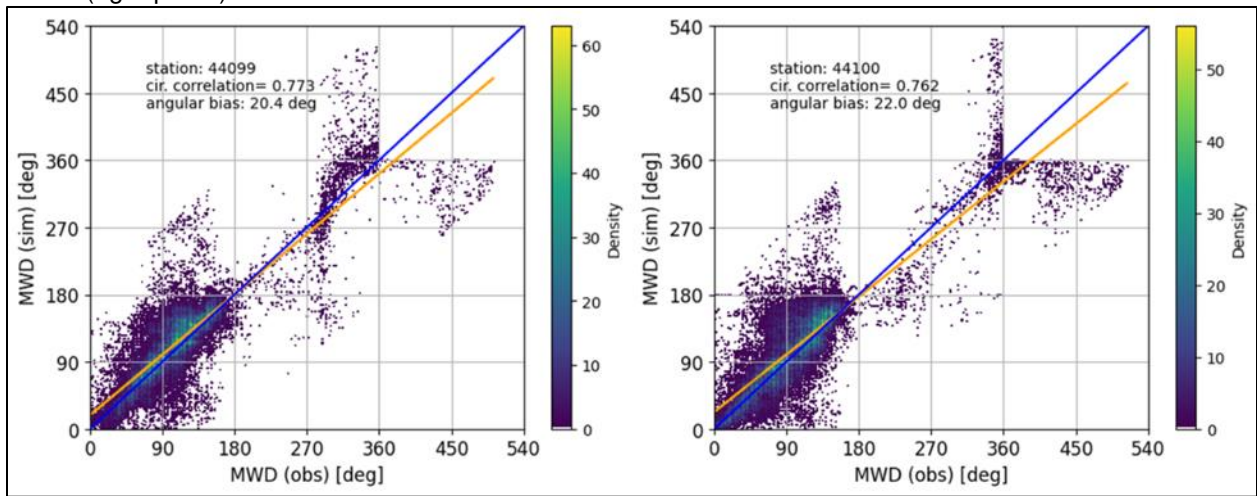


Figure 168. Overall evaluation of simulated mean wave direction at NDBC stations 44099 (left panel) and 44100 (right panel).

6.6.4 Mean Wave Period Validation (Scenario 1, SWAN)

In terms of mean wave period (Table 26), SWAN showed a tendency to be biased low (negative bias) for 6 of 12 NDBC stations with a cross-station average RMSE of 0.82 seconds. Figure 169 to Figure 186 visually compare mean wave period simulated in SWAN versus NDBC station data.

Table 26. Mean wave period validation metrics at NDBC station locations.

NDBC Station	RMSE (s)	Bias (s)	MAE (s)	IOA	Min Observed (s)	Max Observed (s)	Mean Observed (s)	STD Observed (s)
44009	0.839	0.065	0.605	0.872	2.98	11.11	5.075	1.007
44014	0.655	0.116	0.490	0.926	3.04	13.59	5.421	1.141
44025	0.781	0.073	0.559	0.893	2.95	10.31	5.081	1.019
44065	1.059	0.128	0.760	0.849	2.67	11.24	4.939	1.122
44066	0.685	0.012	0.511	0.917	3.24	12.01	5.513	1.105
44086	0.845	-0.194	0.620	0.896	2.91	11.98	5.592	1.223
44088	0.717	-0.303	0.537	0.930	3.36	13.61	5.837	1.434
44089	0.905	-0.111	0.641	0.886	2.71	13.42	5.194	1.281
44091	0.857	0.058	0.599	0.889	2.64	11.19	5.171	1.149
44095	0.744	-0.199	0.543	0.916	3.07	13.86	5.579	1.254
44099	0.888	-0.008	0.645	0.865	2.41	11.42	5.041	1.071
44100	0.857	-0.255	0.624	0.893	2.81	13.08	5.446	1.246

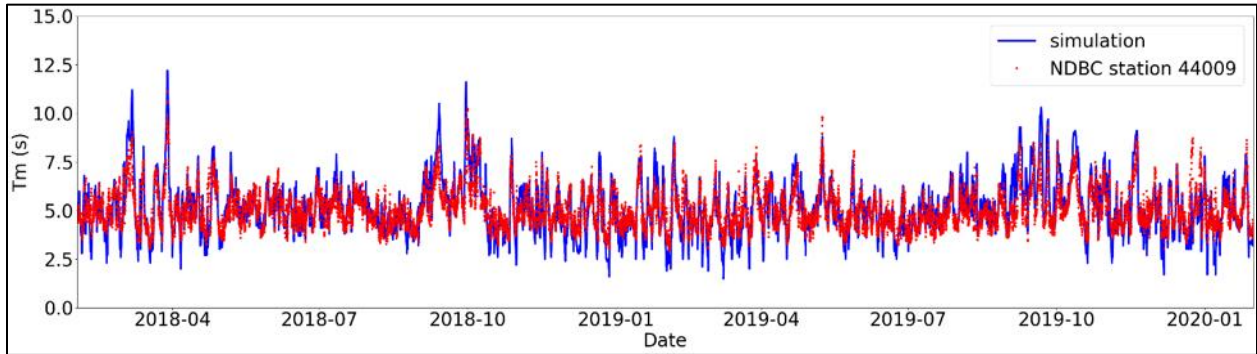


Figure 169. Simulated mean wave period vs. measurements at NDBC station 44009.

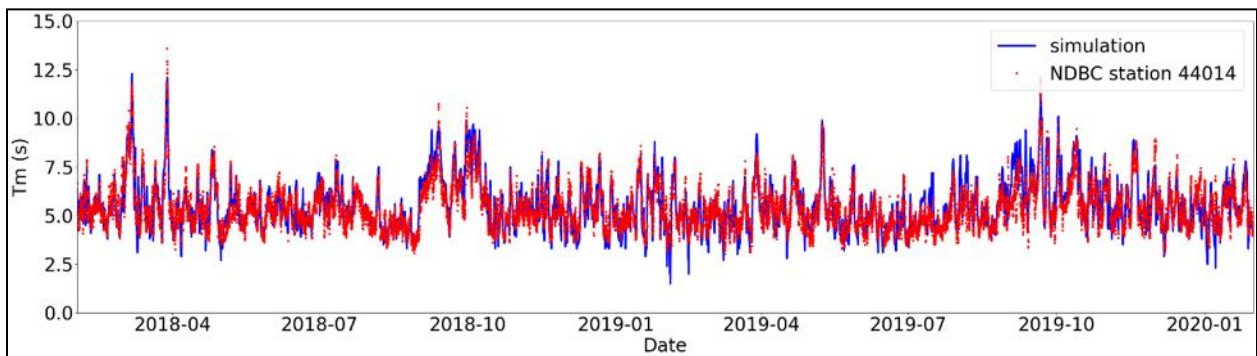


Figure 170. Simulated mean wave period vs. measurements at NDBC station 44014.

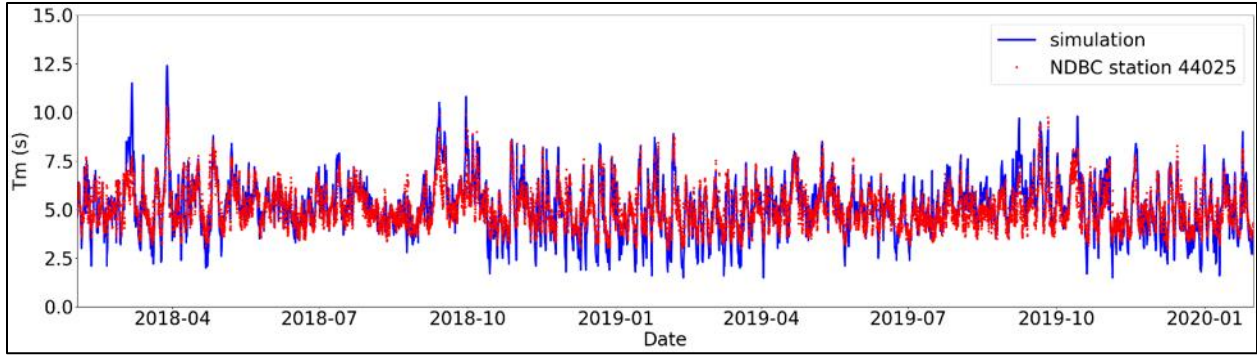


Figure 171. Simulated mean wave period vs. measurements at NDBC station 44025.

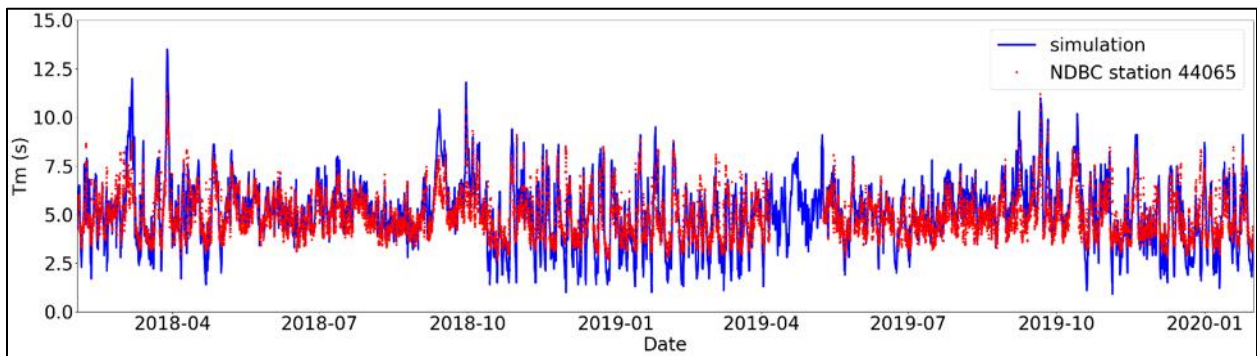


Figure 172. Simulated mean wave period vs. measurements at NDBC station 44065.

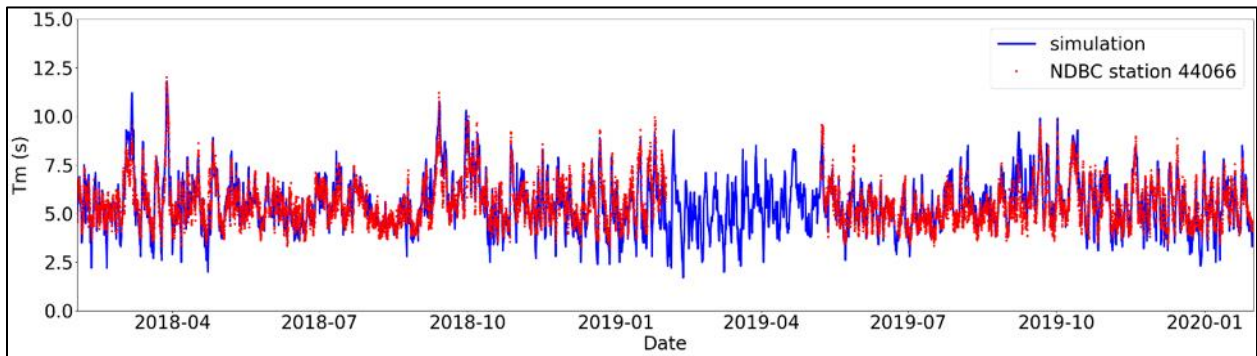


Figure 173. Simulated mean wave period vs. measurements at NDBC station 44066.

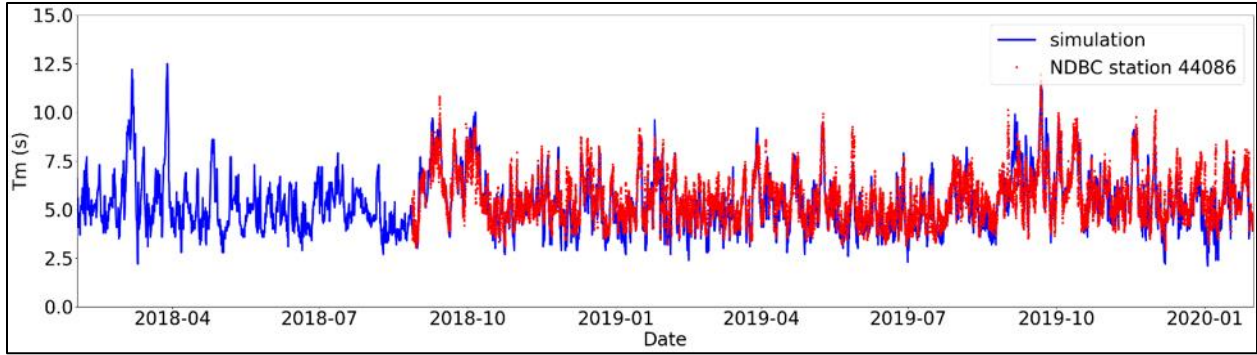


Figure 174. Simulated mean wave period vs. measurements at NDBC station 44086.

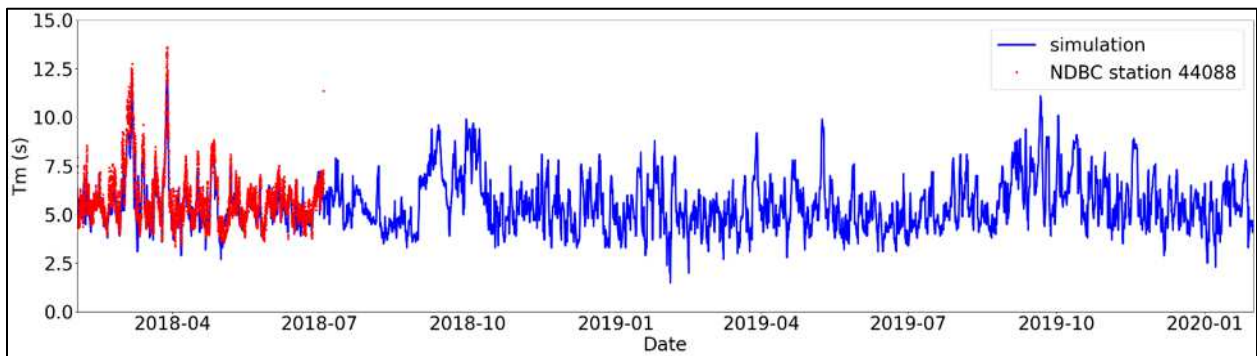


Figure 175. Simulated mean wave period vs. measurements at NDBC station 44088.

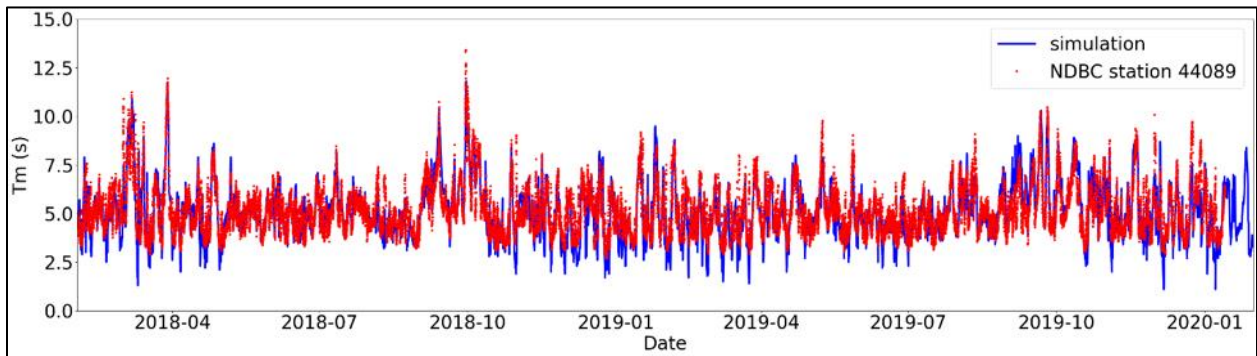


Figure 176. Simulated mean wave period vs. measurements at NDBC station 44089.

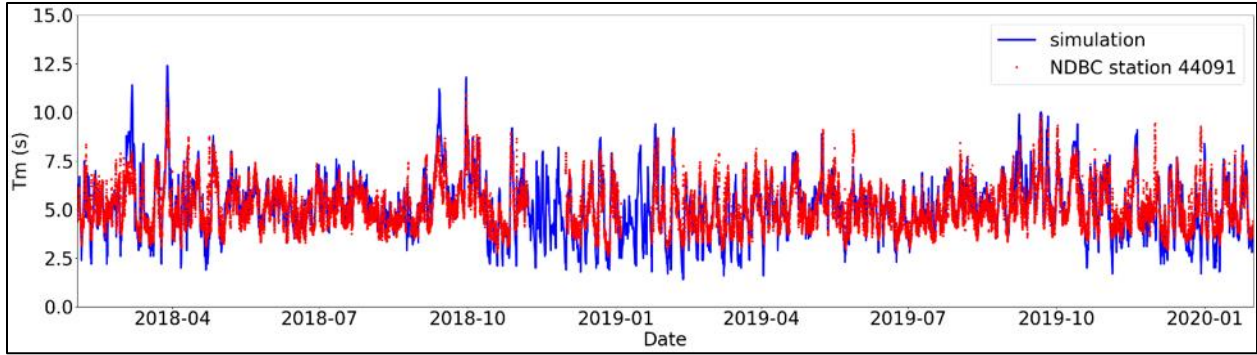


Figure 177. Simulated mean wave period vs. measurements at NDBC station 44091.

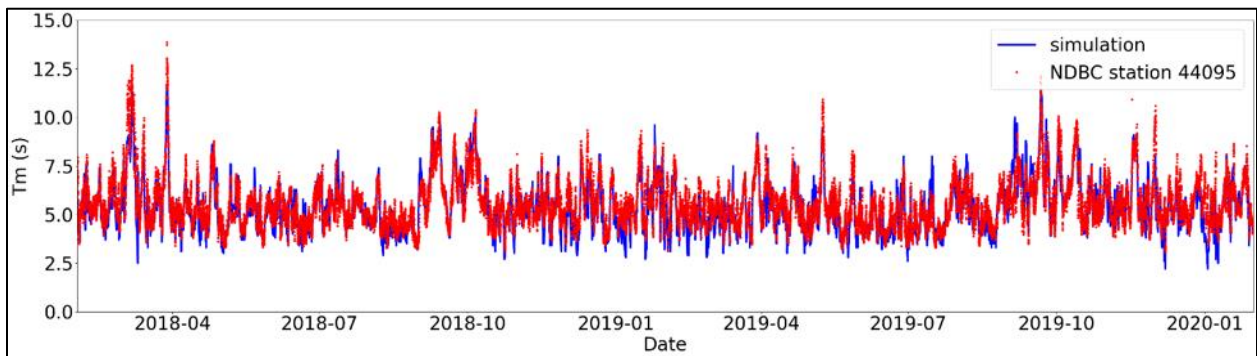


Figure 178. Simulated mean wave period vs. measurements at NDBC station 44095.

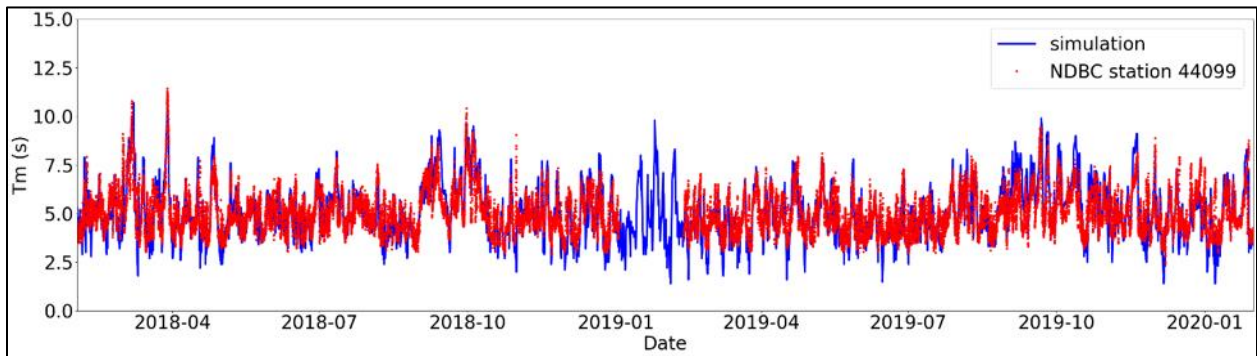


Figure 179. Simulated mean wave period vs. measurements at NDBC station 44099.

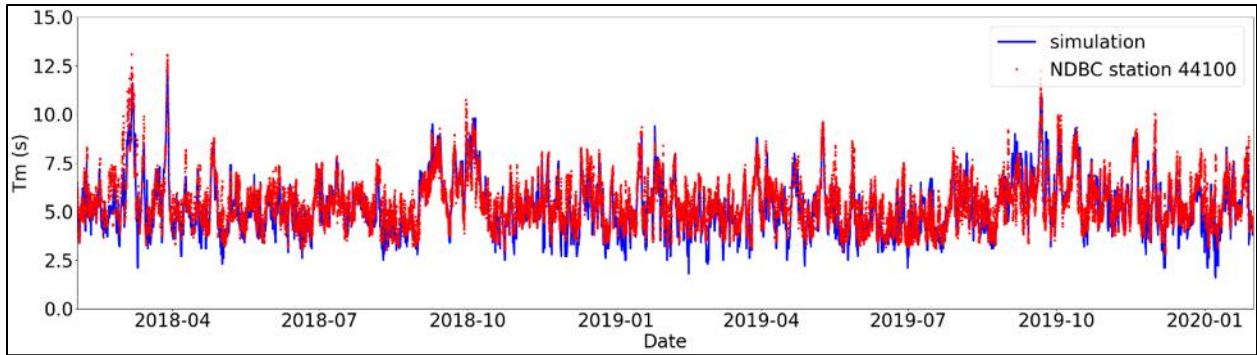


Figure 180. Simulated mean wave period vs. measurements at NDBC station 44100.

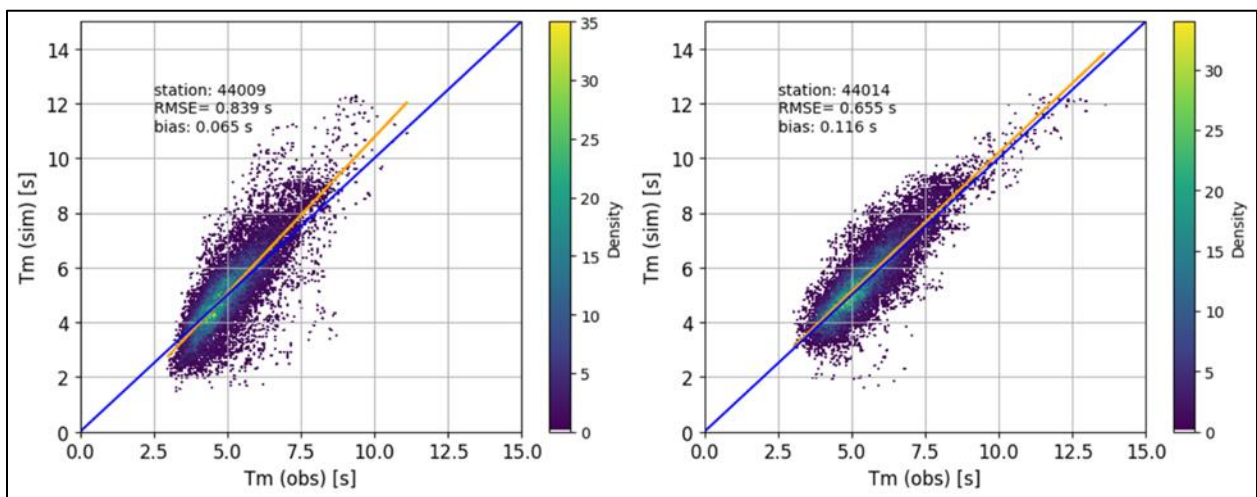


Figure 181. Overall evaluation of simulated mean wave period at NDBC stations 44009 (left panel) and 44014 (right panel).

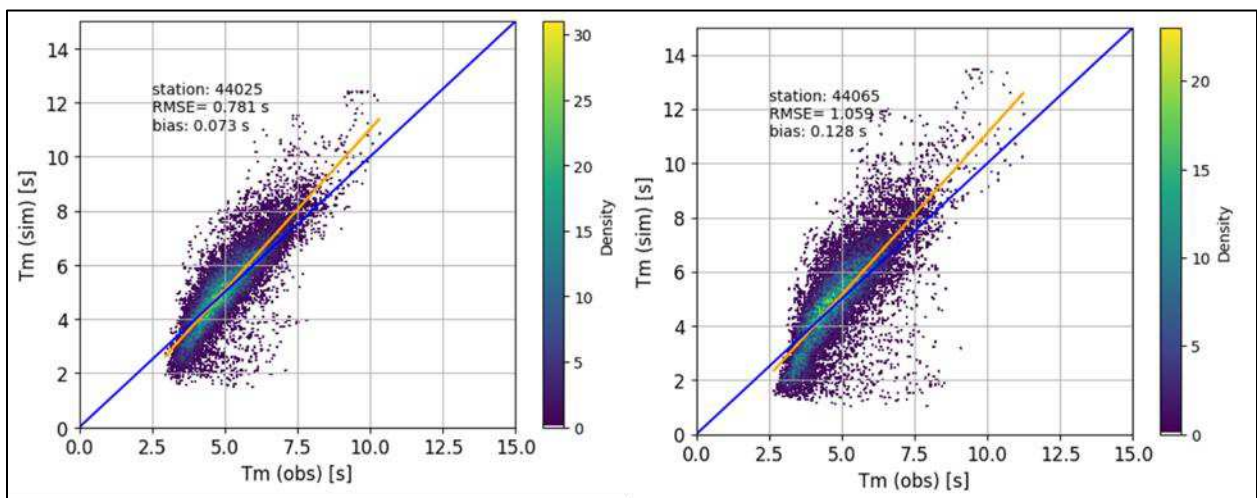


Figure 182. Overall evaluation of simulated mean wave period at NDBC stations 44025 (left panel) and 44065 (right panel).

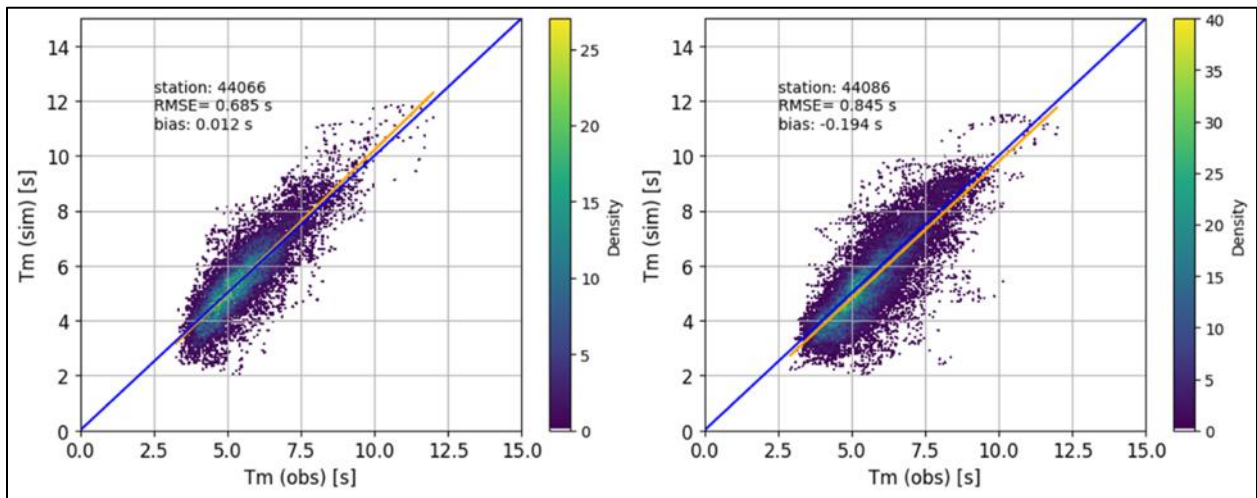


Figure 183. Overall evaluation of simulated mean wave period at NDBC stations 44066 (left panel) and 44086 (right panel).

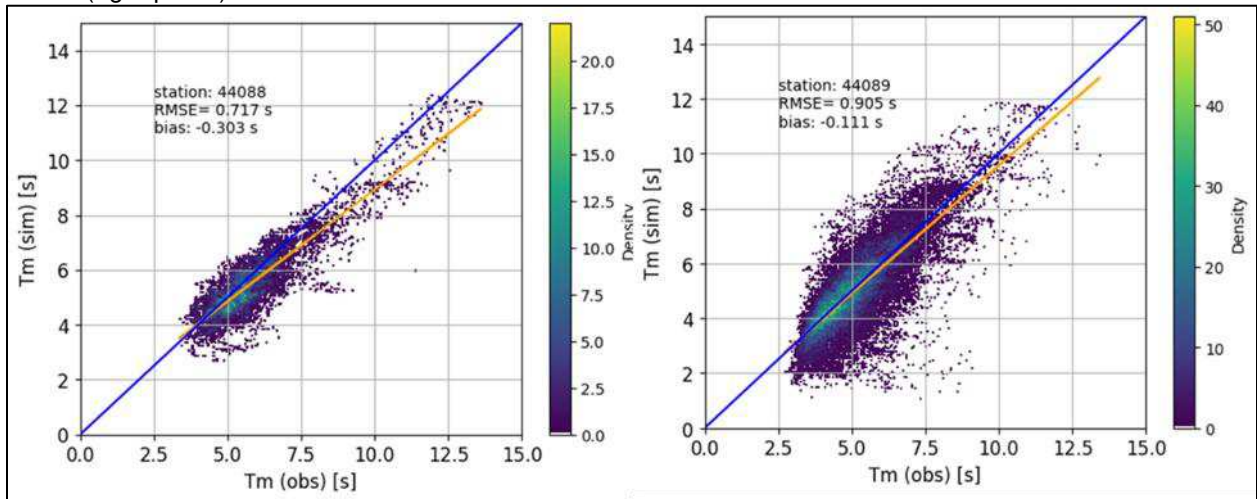


Figure 184. Overall evaluation of simulated mean wave period at NDBC stations 44088 (left panel) and 44089 (right panel).

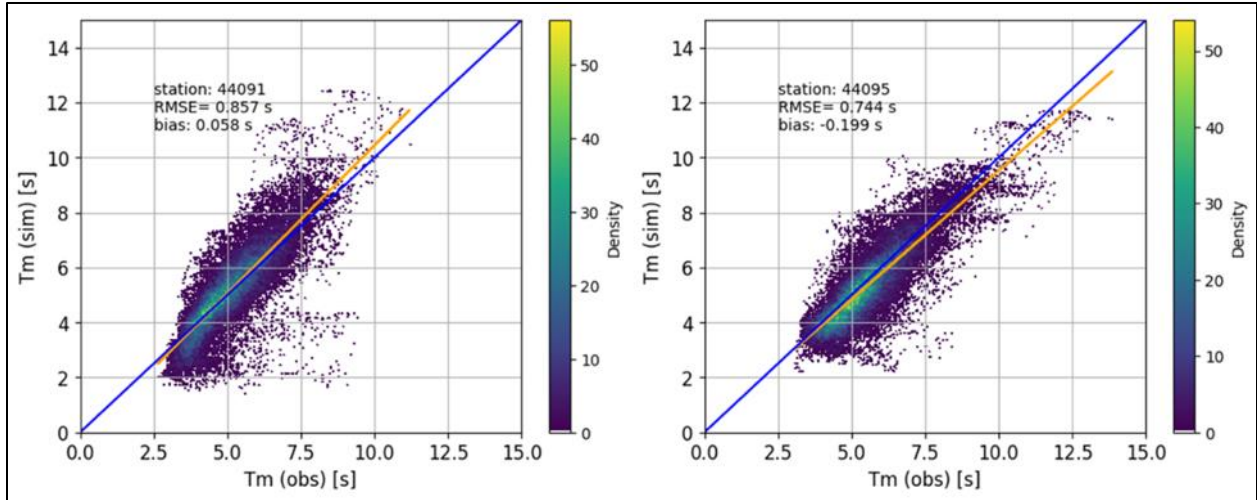


Figure 185. Overall evaluation of simulated mean wave period at NDBC stations 44091 (left panel) and 44095 (right panel).

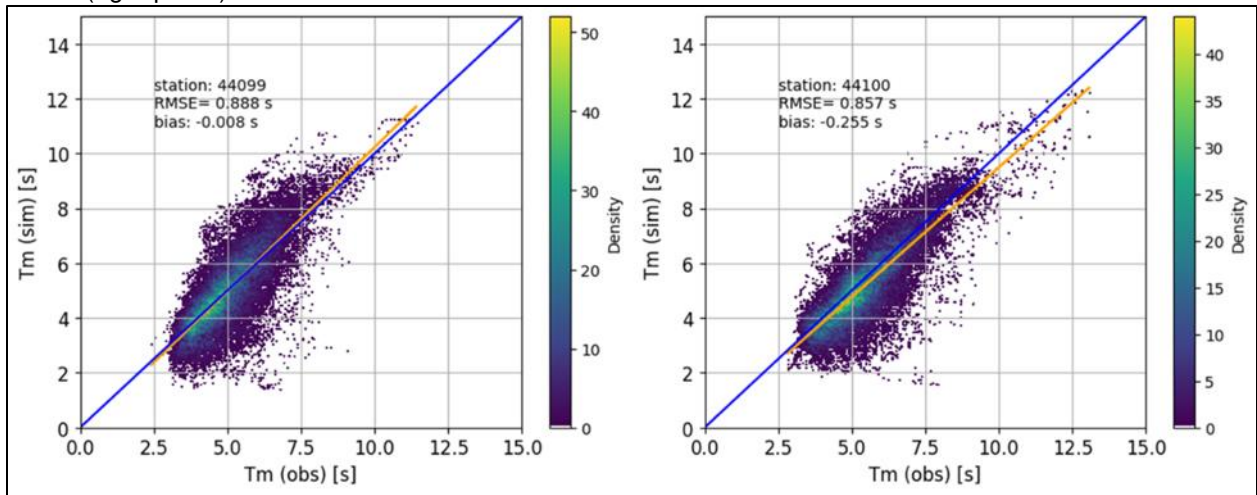


Figure 186. Overall evaluation of simulated mean wave period at NDBC stations 44099 (left panel) and 44100 (right panel).

6.6.5 Conclusion on SWAN Baseline (Scenario 1) Validation

The previous sections included model skill summary tables and validation figures (time series and XY plots). We first compared the wind forcing for ERA5 against the NDBC anemometer data (Section 6.6.1). We then compared the SWAN model simulated wave response for significant wave height (Section 6.6.2), mean wave direction (Section 6.6.3), and mean wave period (Section 6.6.4), at the same and other NDBC buoy locations with such data (shown in Figure 5). Time series show that high wave events were also well captured by the model. Overall, the model skill was excellent and is similar to two other relatively recent wave models of the Mid-Atlantic Bight which used the Wave Watch III (WW3) and/or SWAN models forced with Climate Forecast System Reanalysis (CFSR) winds rather than ERA5 (Allahdadi et al., 2019 and Medina et al., 2020).

7 Impact of Offshore Wind Farms on Winds

This chapter describes the simulated effects of WEA development to 10-meter above surface wind speeds. Wind wake reductions for Scenarios 2 and 3 were simulated as explained in Chapter 4 by applying the wind deficits due to the clusters of WTGs in each scenario that were calculated with PyWake to the ERA5 10 m wind fields (in space and time).

7.1 Wind Wake Effects

Figure 187 shows examples of wind speed maps for different scenarios for the modeling domain at 12:00AM UTC January 25, 2018. The ERA5 wind speed represents Scenario 1 (Baseline) with no wake. Scenario 2 (15MW Partial Build-out) and Scenario 3 (15MW Complete Build-out) are the wakes from turbines from five clusters and eight clusters, respectively. In Scenario 3, wake from some clusters in the north are seen impacting neighboring clusters. However, for both Scenarios, two of the clusters in the south did not show any wake as they are in an area where wind speed is below cut-in speed of 3 m/s. As a reminder, wind deficits relative to the free wind speed were calculated to be higher between the cut-in speed of 3 m/s and 11 m/s, over which they decrease up to the cut-off speed of 25 m/s, for the NREL 15MW turbines (Section 4.7).

Figure 188 shows average wind speed maps for the month of January 2018 for different scenarios as well as the difference between these monthly-mean wind fields between wake scenarios (scenarios 2 and 3) and baseline (Scenario 1). The difference maps show that wake-induced deficits are prominent at the locations of wind turbine clusters and, given the prevailing wind directions during that month, extend mostly along-shore and to the offshore northwest and southwest directions. Although, as noted in Chapter 4, most of the wind reductions from the wind wake deficit are within the developed WEAs (Figure 188, bottom panels), the “shadow zones” (wind wakes) seen in Figure 187 and Figure 188, though substantially weakened, can span 100–200km downstream, consistent with Section 4.8.

7.2 Effects on Wind Climatology

Figure 189 shows both the median and 75th percentile winds during the two-year simulation periods, and their reduction due to the wind wakes for each WEA-development scenario. The strongest climatological winds are generally found offshore, blowing over the deep ocean plateau seaward of the continental shelf slope, at around 7.5m/s and 10m/s for the 50th and 75th percentiles, respectively. Wind speeds gradually decrease over the shelf toward land. At wind farm A shown on Figure 189 south of Long Island, the median wind blows at around 6m/s, while the 75th percentile is near 9 m/s. The Limited Buildout Scenario 2 does not include WTGs in any of the offshore-most WEAs, while some of the farms closer to shore, such as wind farm B (Figure 189) are not fully covered with WTGs in that scenario. At location A, 50th percentile winds are simulated to decrease by ~1 m/s (1.2 m/s) or 15% (20%) in Scenario 2 (Scenario 3) due to the wind wake. Since Scenario 3 has a more expansive buildout, the wake region expands spatially to cover a larger area depending on the prevailing climatological wind directions. Reductions become fairly small moving away from the WEAs both in absolute but also relative magnitude in the offshore direction. Although the NJ Shore region is closer to the WEAs, the climatological wind reduction is not more pronounced because of the prevailing wind directions which are either along-coast or from the coast (note wind roses in Figure 113).

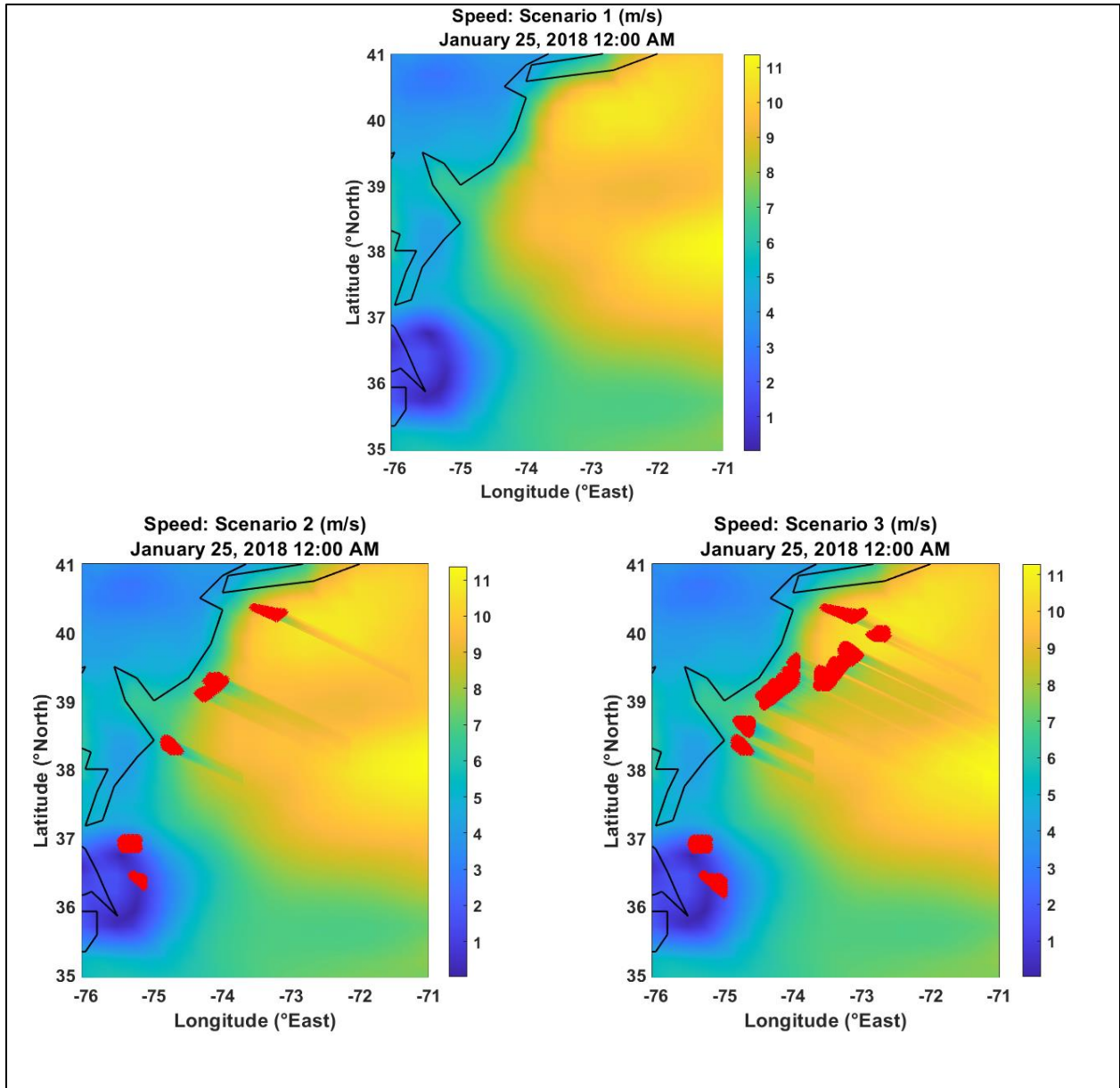


Figure 187. Example of wind speed maps used as input for hydrodynamic and wave modeling. The upper panel represents Scenario 1 (ERA5 field with no wake), the bottom left panel shows the wake impacted wind field for Scenario 2 (15MW Limited - 5 clusters) and the bottom right panel shows the wake impacted wind field for Scenario 2 (15MW Build - out 8 clusters). The red region in the bottom panels shows locations of the wind turbine in the clusters.

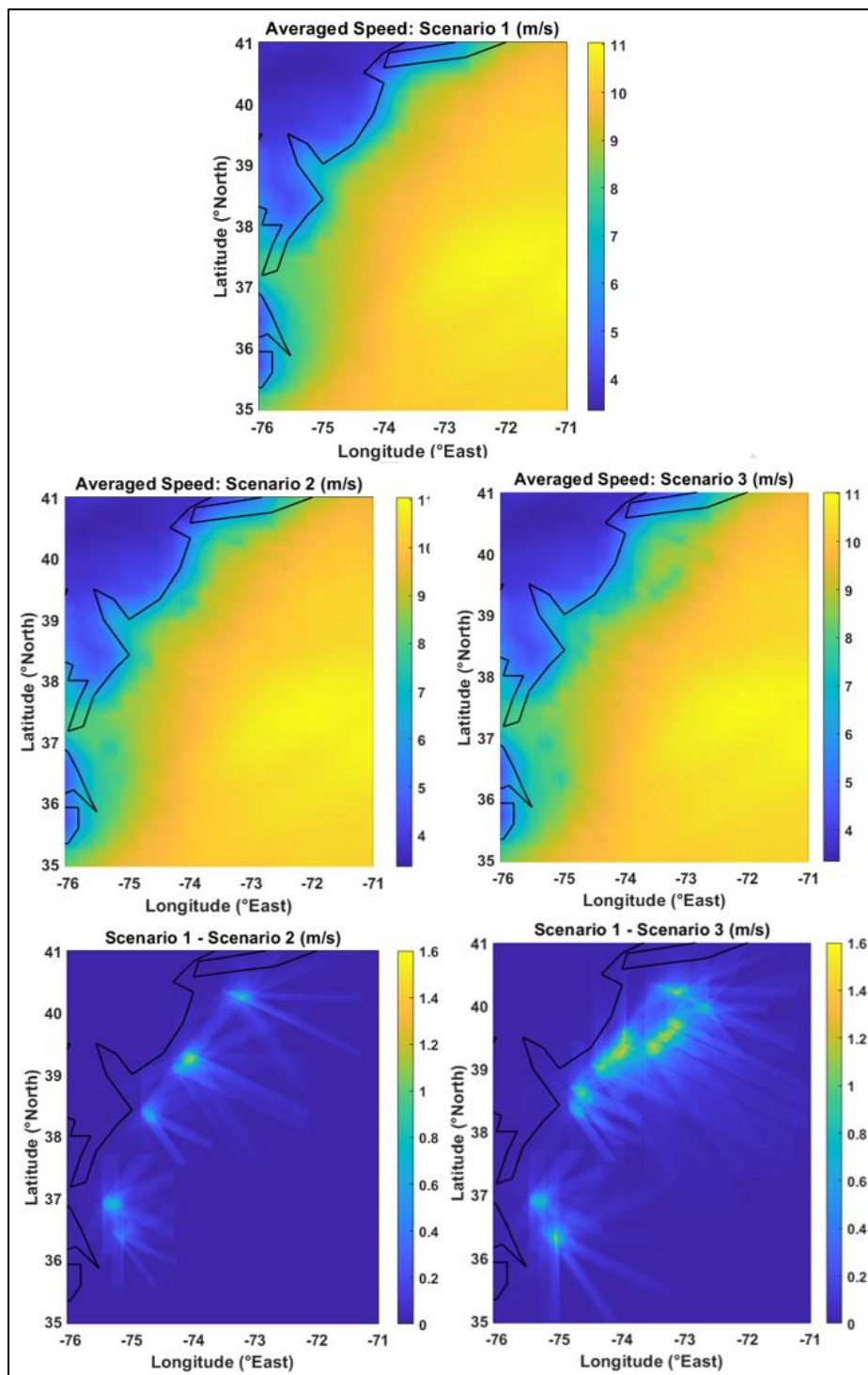


Figure 188. Averaged wind speed maps for January 2018.

The upper panel represents the baseline scenario (Scenario 1), the middle panels exhibit wake scenarios (Scenario 2 and Scenario 3), and the bottom panels show the difference between the baseline and the WEA development scenarios with their wind wake.

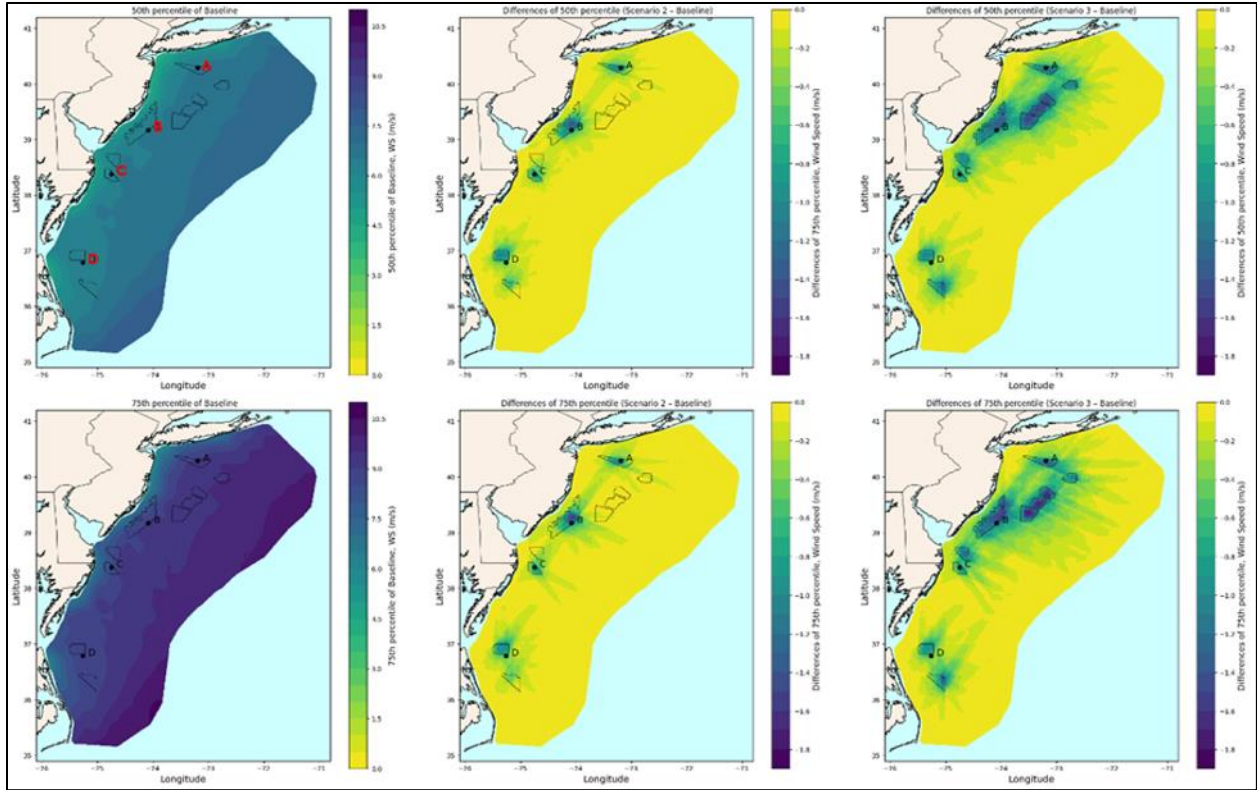


Figure 189. 50th (top left) and 75th (bottom left) percentile wind speeds, m/s, over the model domain for the two-year period of simulation. Locations A, B, C, and D are highlighted in red text in the upper left panel. Center (Scenario 2, Limited Buildout) and right (Scenario 3, Full Buildout) panels show the difference (reduction) in the 50th (top) and 75th (bottom) percentile wind speeds for each WEA-development scenario against baseline conditions (Scenario 1).

Figure 190 shows the two-year time series of the 10 m wind for the three scenarios at locations A and B shown in Figure 189. The corresponding wind-speed frequency distributions at the same locations for each run are illustrated in Figure 191 and show small differences between scenarios 2 and 3 at these locations within WEAs which, though developed in both scenarios, are developed further in Scenario 3. Locations C and D in Figure 189 are within WEAs that are fully built in both scenarios 2 and 3; Their distributions for scenarios 2 and 3 are almost identical, and similarly reduced against baseline (not shown).

The reduction in the climatological winds discussed in the previous paragraphs and seen in Figure 189 and Figure 191 describes a reduction in the mean distribution of winds blowing over the model domain (or specific locations) calculated in the span of the two simulation years. For example, the 75th percentile wind reduction seen in Figure 189 – and deduced from Figure 191 at locations A and B – describes the difference between the 75th higher percentile winds for a buildout scenario against the 75th higher percentile winds for the baseline case, with the percentiles calculated over the 2 year time series at each location, independently. The highest reductions at locations A and B happen around the 50th to 70th percentile: As climatological winds become higher than 11 m/s offshore the wake deficits decrease and reductions to climatological winds start to plateau (Figure 191).

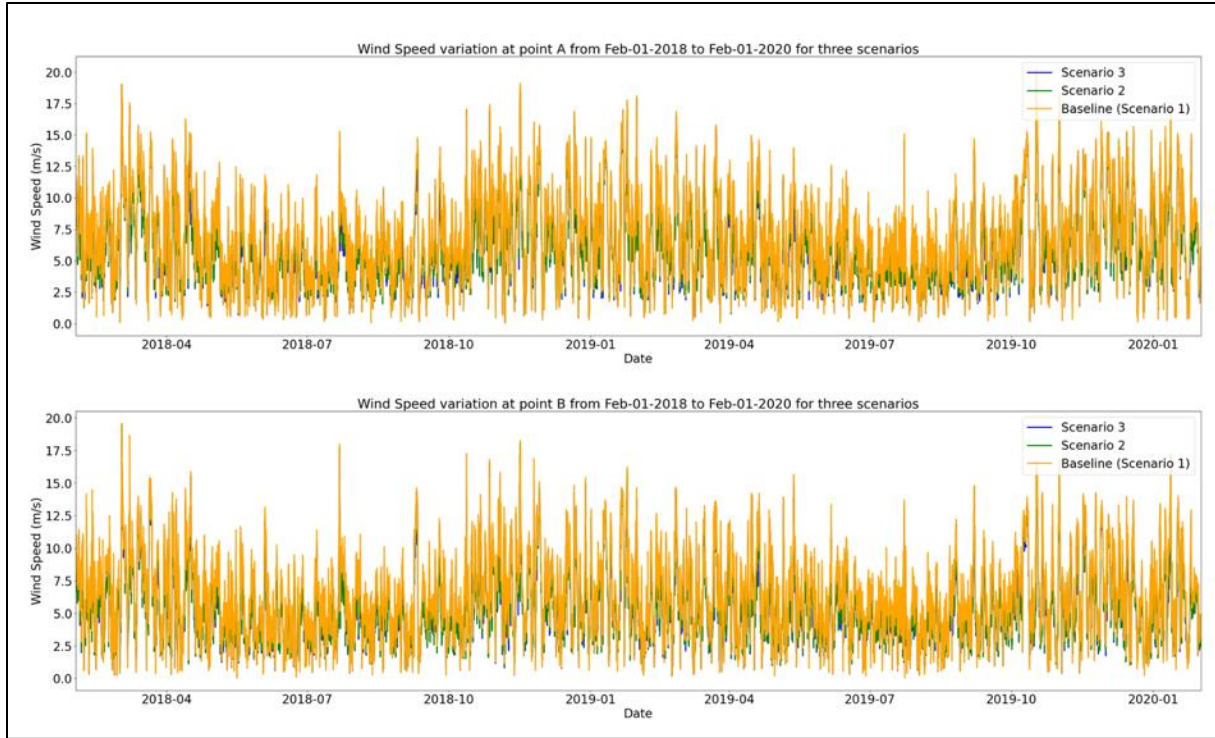


Figure 190. Time series of wind speed for each of the three simulation scenarios for locations A (top) and B (bottom) shown on Figure 189 over the two-year period.

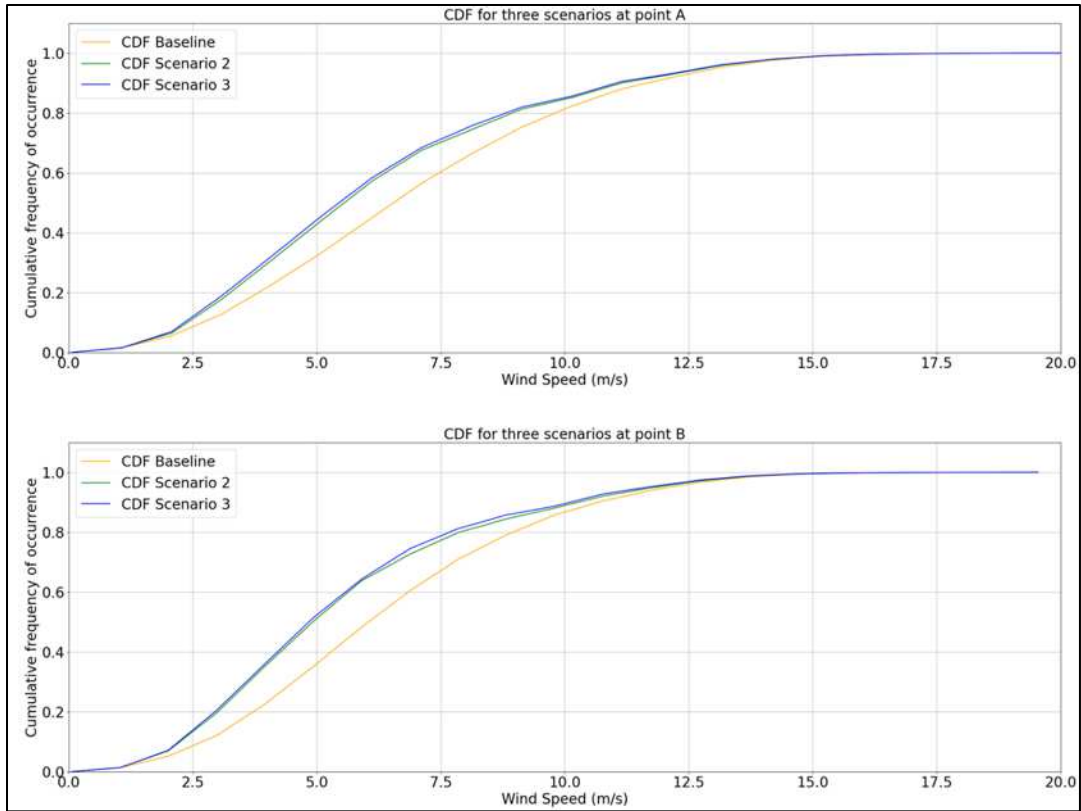


Figure 191. Frequency distributions of wind speeds at locations A (top) and B (bottom) shown in Figure 189 for each of the three scenarios.

Seasonality of the wind wake deficits is presented in Figure 192 (winter), Figure 193 (spring), Figure 194 (summer), and Figure 195 (fall). On each figure the seasonal mean wind of the Baseline is shown as overlaid arrows, to help make clear the predominantly leeward directions of the wind energy areas, where the deficits are strongest. These overlaid arrows consist of offshore/eastward flow and a seasonal cycle that moves between higher-speed winds (reaching 3–4 m/s) toward the southeast during winter, and lower-speed winds (about 1–2 m/s) that are north-northeastward during summer. This demonstrates that the Baseline case is consistent with the well-known seasonal cycle of average winds over the Mid-Atlantic Bight (see, e.g., Fig. 7 of Charles et al., 2012).

In each of the four seasons, the deficits are strongest within the wind energy areas, where they reach maxima of up to about 1.5 m/s for Scenario 2 and about 1.9 m/s for Scenario 3. The deficits extend outside the wind energy areas in all directions, with the distance limited to under about 10 km in the predominantly windward direction and much longer, up to at least 100 km in some areas, in the predominantly leeward direction. The deficits leeward from some wind energy areas therefore overlap with other wind energy areas. The figures include the simulated 0.5 m/s deficit contour which is mostly contained within the wind farms with some spreading between or leeward of them. **Error! Reference source not found.** includes, for reference only, the 0.5 m/s deficit contour from Golbazi et al. (2022), simulated for the summer of 2018 using the WRF model with 10MW turbines and differences in the footprint of some wind energy areas.

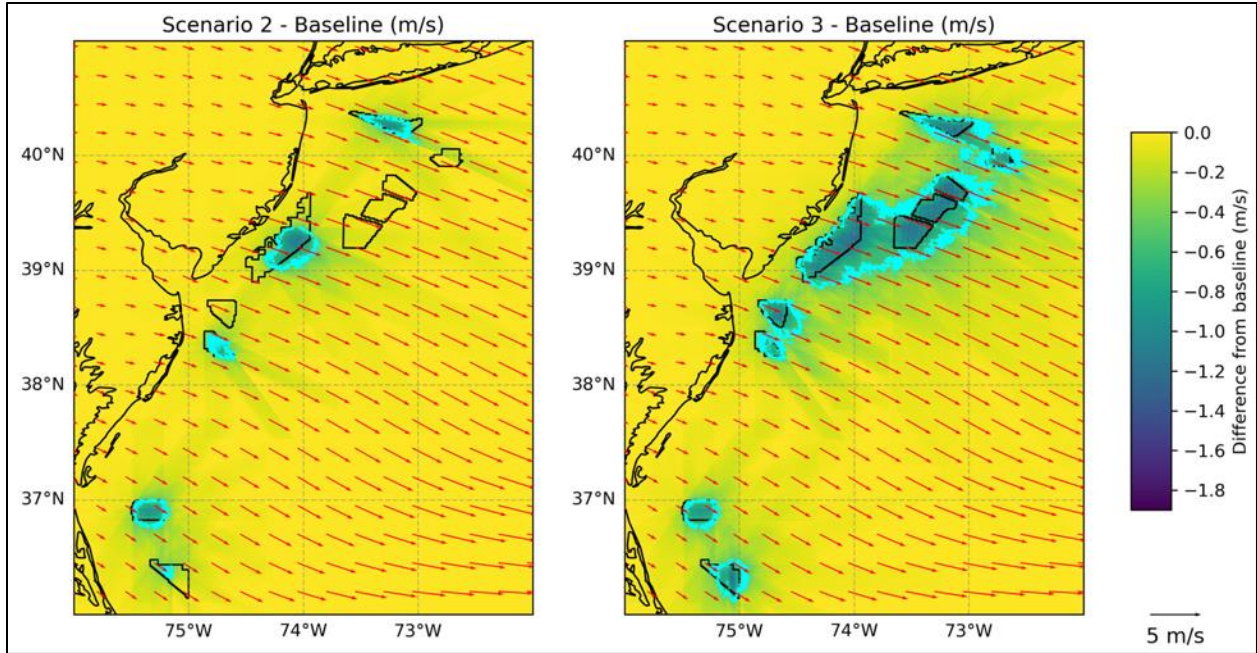


Figure 192. Winter (Dec–Feb) differences (color shading) of mean wind speed in Scenario 2 (left) and Scenario 3 (right) relative to baseline. Arrows show winter mean baseline wind. The cyan coloring indicates the location of the 0.5 m/s deficit contours.

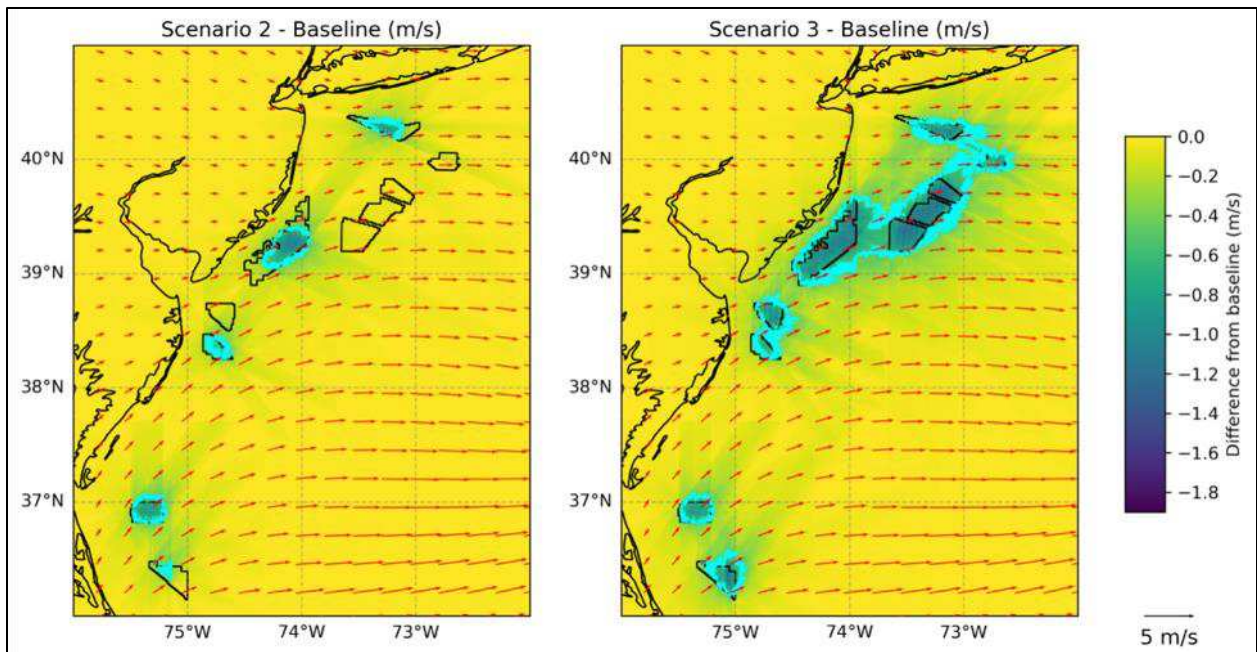


Figure 193. Spring (Mar–May) differences (color shading) of mean wind speed in Scenario 2 (left) and Scenario 3 (right) relative to baseline. Arrows show spring mean baseline wind. The cyan coloring indicates the location of the 0.5m/s deficit contours.

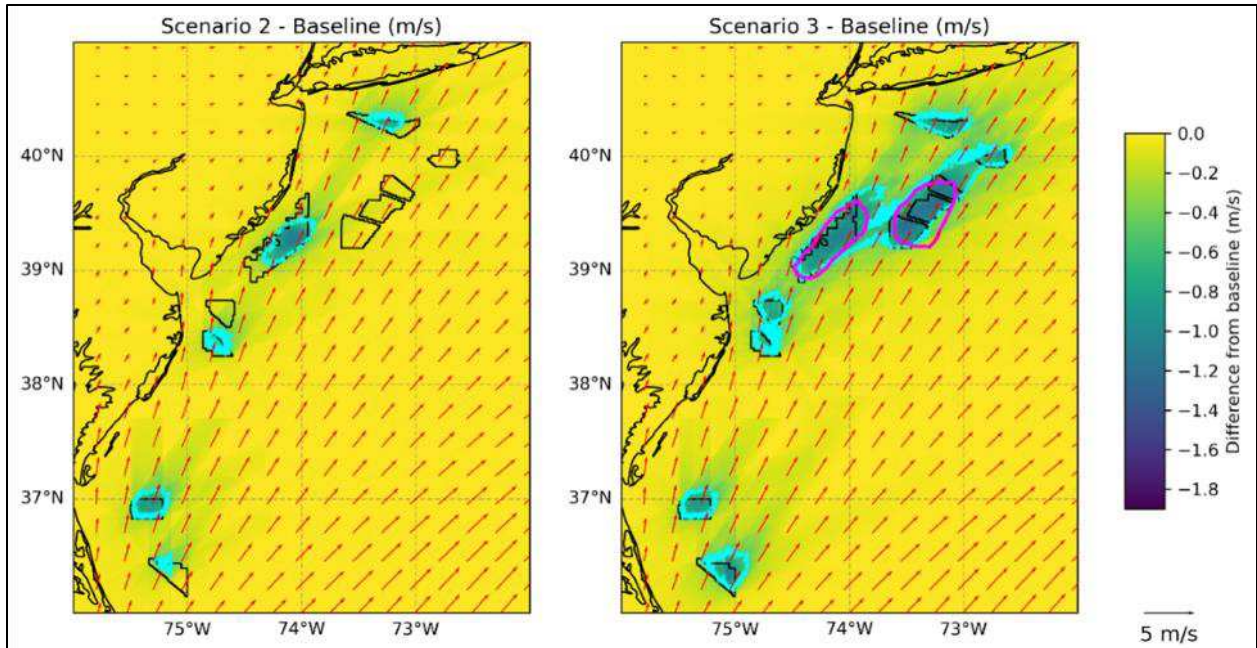


Figure 194. Summer (Jun–Aug) differences (color shading) of mean wind speed in Scenario 2 (left) and Scenario 3 (right) relative to baseline. Arrows show summer mean baseline wind. The cyan lines indicate the location of the 0.5m/s deficit contours simulated in this work (in work by Golbazi et al. 2022 for a different study).

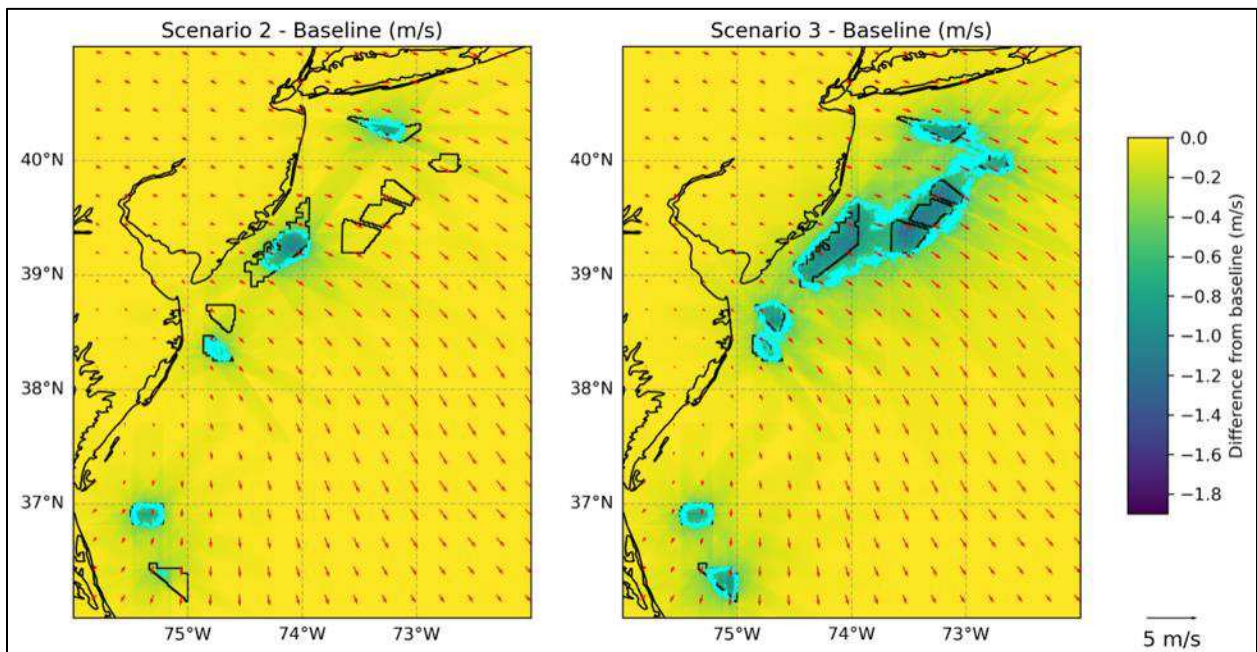


Figure 195. Fall (Sep–Nov) differences (color shading) of mean wind speed in Scenario 2 (left) and Scenario 3 (right) relative to baseline. Arrows show fall mean baseline wind. The cyan coloring indicates the location of the 0.5m/s deficit contours.

7.3 Transient Effects

Compared to the climatological effects described in the previous section, transient wakes and wind reductions are simulated to reach relatively higher values with longer wake spans in build-out scenarios compared to the baseline, depending on specific event conditions. The map in Figure 192 illustrates the 99th percentile of the absolute wind speed difference time series at each point in the modeling domain over the two-year simulations. That is, statistically speaking, for three hours every 12.5 days, reductions can be as high as 3–5 m/s at some WEAs depending on the scenario. Given the findings of Section 4.7, this happens when winds are blowing around 10 m/s. Therefore, these rarer transient reductions can reach 30–50%. The corresponding probability plot for the transient wind reductions at locations A and B is seen in Figure 193.

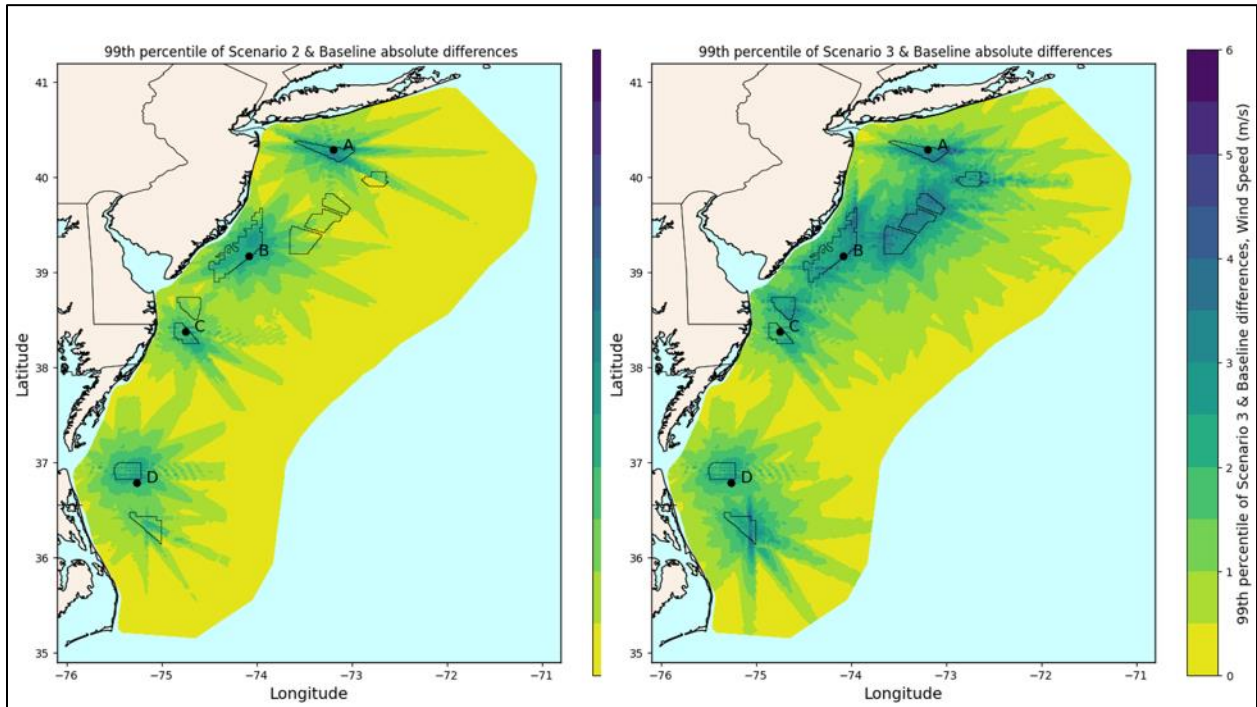


Figure 196. 99th percentile of the transient wind reduction based on the time series of absolute wind speed difference between Scenario 2 and baseline (left) and Scenario 3 and baseline (right).

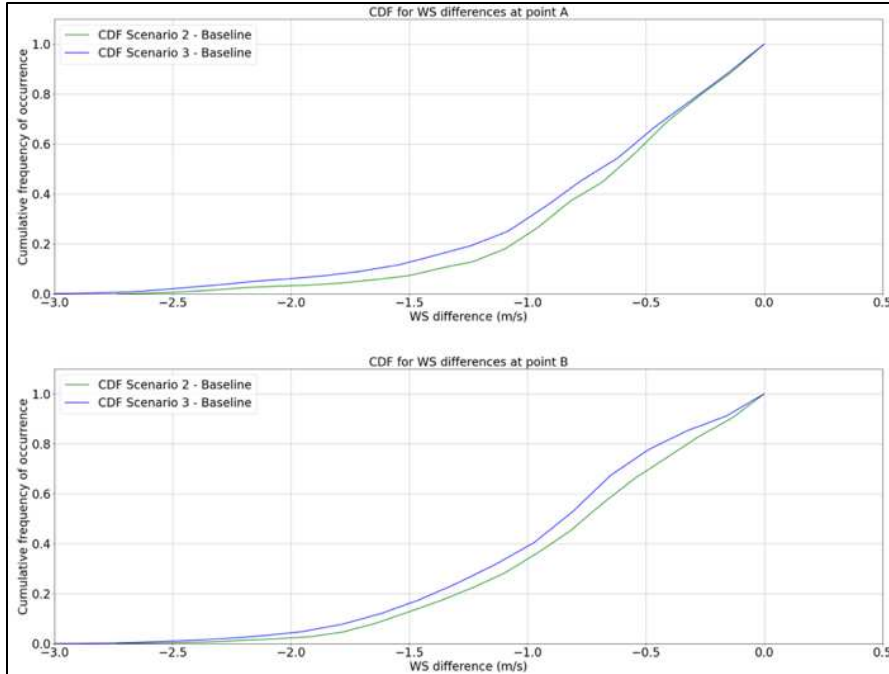


Figure 197. Probability distributions of absolute wind speed difference between Scenario 2 and baseline (top) and Scenario 3 and baseline (bottom) at locations A and B shown in Figure 192.

8 Impact Of Offshore Wind Farms on Wave Conditions

In this section, surface wave model results after wind wake reduction (scenarios 2 and 3) are presented. The model was run for a period of two years (Feb-01-2018 to Jan-31-2020) by applying the wind results discussed in Section 4 for scenarios 2 and 3 to our validated wave model.

8.1 Impact to Significant Wave Height

The simulated wake effects of the offshore wind turbines on significant wave height, H_s , are illustrated in the scenario-difference maps of Figure 194 for each OWT scenario. Both the median (top row) and the 99th percentile (bottom row) of these quantities, and the respective differences of each quantile to the baseline case are shown. Similar to the wind speeds, waves are highest offshore; The median waves are up to 1.8 m and the 99th percentile waves are as high as 6 m (Figure 194, A1 & B1). The reductions in the median waves are presented by darker blue color shades in Figure 194 (A2 & A3) and it indicates maximum reduction of 4 cm and 7 cm in Scenario 2 and 3 OWT layouts, respectively. The highest reductions in median waves are near the windfarms, especially in wind farms that are aligned with the principal wind directions, and they are more pronounced for Scenario 3. The decreases in median significant wave height are also summarized in Figure 195 for each bathymetric depth bin in Figure 51.

Changes in local significant wave heights are the result of wind-wave and swell interactions and wave-wave interactions from the altered wind-wave component. Thus, there is expected nonlinearity in the transient interaction of wind-waves (that are reduced as winds are reduced from the farms) and distant swell (that is not). Figure 196 (B2 & B3) indicate a higher value for 99th percentile of H_s absolute instantaneous differences in Scenario 2 in comparison with Scenario 3. Note that this is the 99th percentile of the instantaneous absolute differences at any moment, rather than the absolute difference of the 99th percentiles of individual scenarios; it is therefore a signature of a transient response. The results are interesting and counter-intuitive, as wind percentiles tend to be lower in Scenario 3 compared to Scenario 2 due to the presence of more wind turbines in Scenario 3, pointing to a non-linear process. Scenario 3 creates wind wake reductions at and near farms that do not have turbines in Scenario 2. However, farms that exist in both scenarios can see reduced winds in Scenario 3 due to wakes from new wave farms built upstream, and thus less instantaneous relative reduction depending on the operating power curve of the wind turbines and the local wind speed encountered during transient events. After analyzing wave height behavior in 20-meter bathymetric bins (Figure 196, 99th percentile), the effect of OWT is slightly greater in deeper areas ($> 60\text{m}$), further from the wind farms, for Scenario 3 compared to Scenario 2. Also, the 99th percentile of wave height difference is the same order of magnitude as the spatial standard deviation of the baseline waves at these bins (line 2, 3, and 4 of the table).

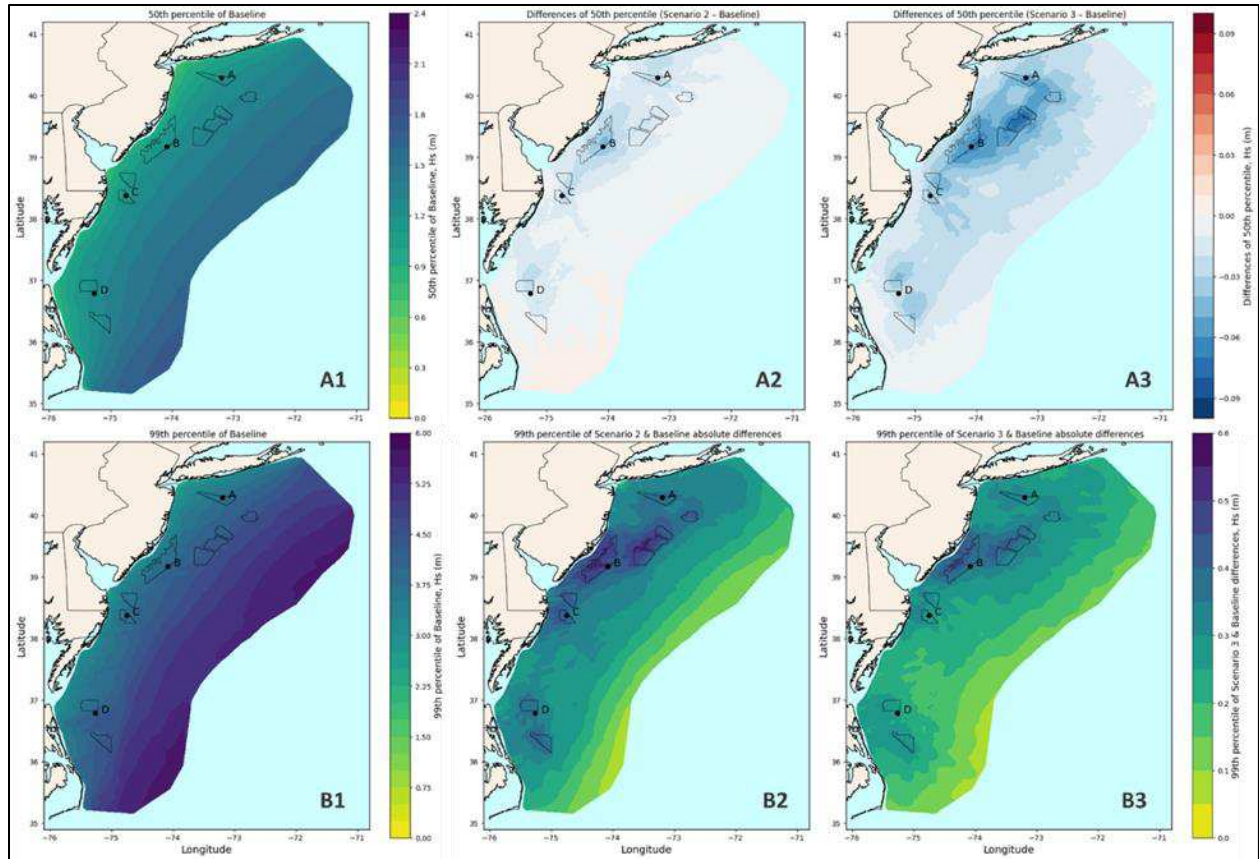


Figure 198. Median significant wave heights change and the 99th percentile of the instantaneous difference.

Top row: Median significant wave height for Feb-01-2018 to Jan-31-2020 (A1) and OWT scenario changes: Median of Scenario 2 - Median of Baseline (A2) and Median of Scenario 3 - Median of Baseline (A3). Bottom row: The same as top row but for the 99th percentile (B1) and the 99th percentile of instantaneous absolute differences for each OWT scenario to the baseline: Scenario 2 (B2) and Scenario 3 (B3).

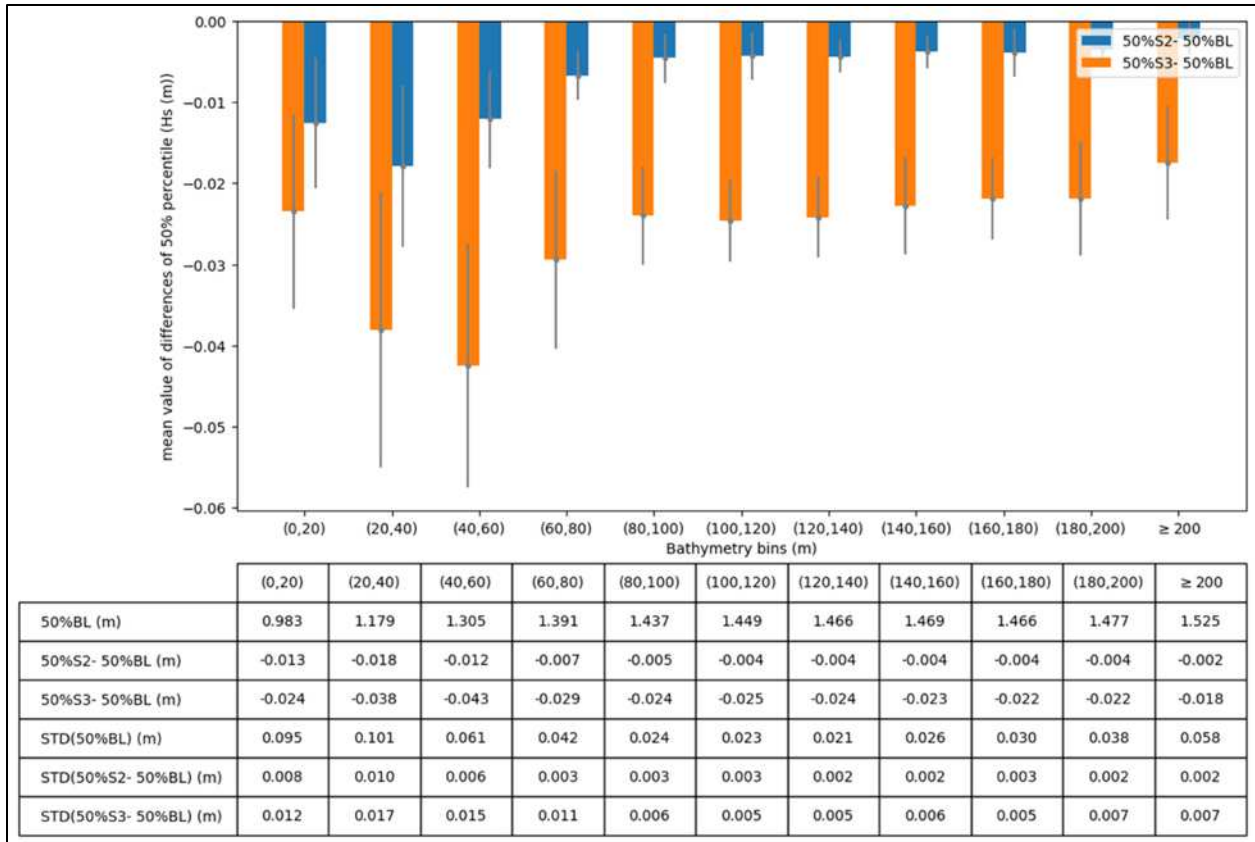


Figure 199. Mean value of the difference between the median wave heights of OWT Scenarios and Baseline for every bathymetric bin. Blue bar is for Scenario 2 – Baseline and orange bar is for Scenario 3 – Baseline. Depth-bin definition provided in Figure 51.

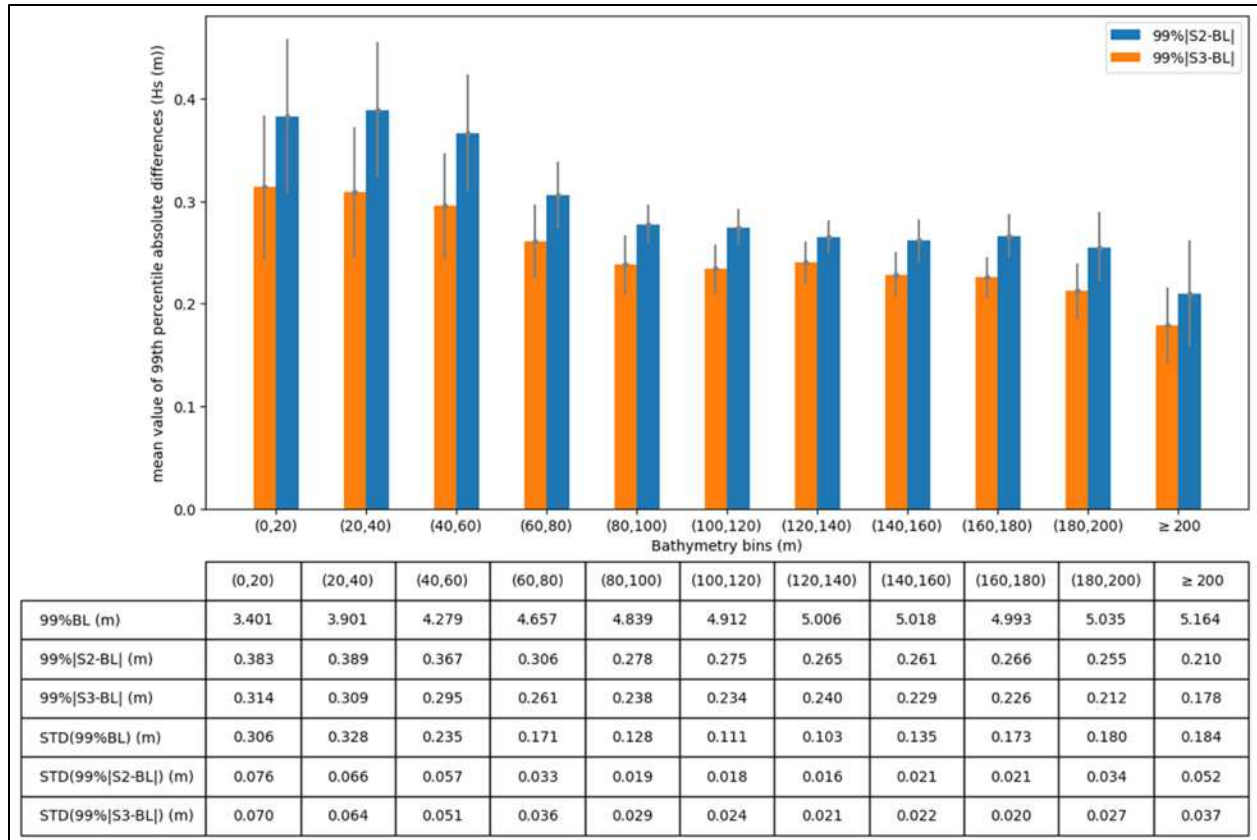


Figure 200. Mean value of 99th percentile of OWTs Scenarios and Baseline significant wave height instantaneous absolute differences for every bathymetry bin.

Blue bar is for 99th percentile of |Scenario 2 – Baseline| and orange bar is for 99th percentile of |Scenario 3 – Baseline| instantaneous differences. Depth-bin definition provided in Figure 51.

We also investigated significant wave height differences of 1st, 10th, 90th, and 99th percentiles to obtain a better insight on OWTs impacts on wave height and its spatial variation. Figure 197 indicates the 1st and 10th percentiles of significant wave height (E1 & F1) in addition to the differences of the 1st and 10th significant wave height percentiles of Scenario 2 and baseline (E2 & F2) and Scenario 3 and baseline (E3 & F3). A similar figure for the 90th and 99th is presented in Figure 198. A summary for the decreases in the 90th and 99th percentiles of significant wave height is also provided in Figure 199 and Figure 200, respectively, for each bathymetric depth bin depicted in Figure 51. The pattern of wave height reduction in 1st, 10th and, 90th percentile (E2, E3 & F2, F3 & G2, G3) is almost the same as the pattern observed in the median wave height differences analysis: highest reductions occur where the turbines are located and especially near the OWT that are aligned with the dominant wind direction. The 99th percentile difference maps for scenarios 2 and 3 (H2, H3) also show wave height reduction for the most areas; however, areas with higher increase in wave height are captured near the northern boundary (darker red areas) which indicates we have higher Hs in scenarios 2 and 3 than baseline at high wave height events there (higher than 99% of the overall wave height at that location). Figure 201 shows significant wave height and peak wave direction time series at point F which is located within the darker red area; when the event occurs (March 13, 2018, red circle) the wave direction is from Northeast which indicates dominant swell coming from the open boundary. The OWT driven wind reduction in this area thus does not interact directly with the incoming swell, but it may interact with local wind-wave conditions that are reduced and which, in turn, may decrease destructive interference against the incoming waves from outside the domain; therefore, higher wave height occurs in scenarios 2 and 3 there at the 99% level. Although this can be an explanation for these local incidents, it should also be noted that for all scenarios the same wave boundary

conditions are used for baseline and scenarios 2 and 3 originating from ERA5 so the wind reduction is not indicated in the boundary forcings. This is a limitation that may then also contribute to capturing higher wave heights in Scenario 2 and 3 at the 99th percentile level during wave height spikes at the northeastern region of the grid.

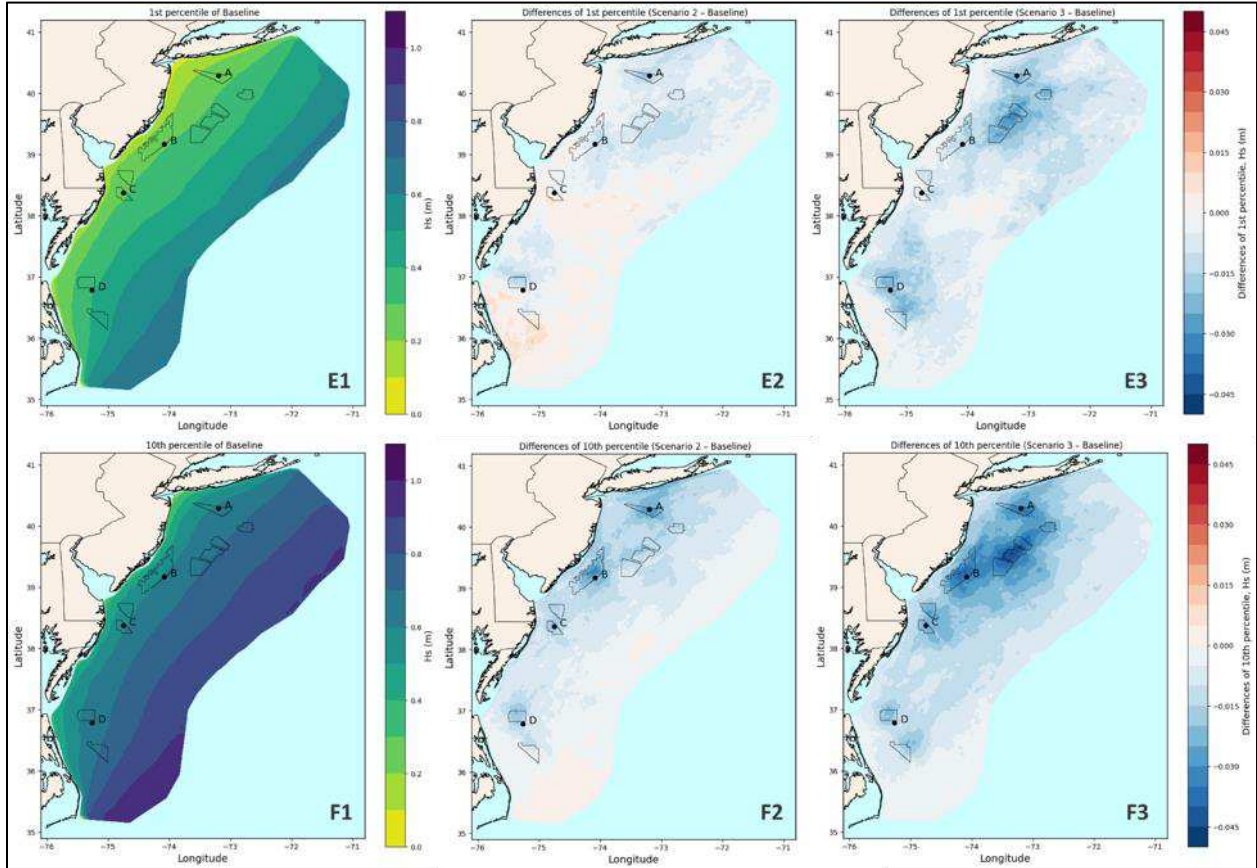


Figure 201. Changes to 1% and 10% significant wave height. Top row: 1st percentile significant wave height for Feb-01-2018 to Jan-31-2020 (E1) and OWT scenario changes: 1st percentile of Scenario 2 - 1st percentile of Baseline (E2) and 1st percentile of Scenario 3 - 1st percentile of Baseline (E3). Bottom row: The same as top row but for the 10th percentile (F1) and the differences of 10th percentile for each OWT scenario to the baseline: Scenario 2 (F2) and Scenario 3 (F3).

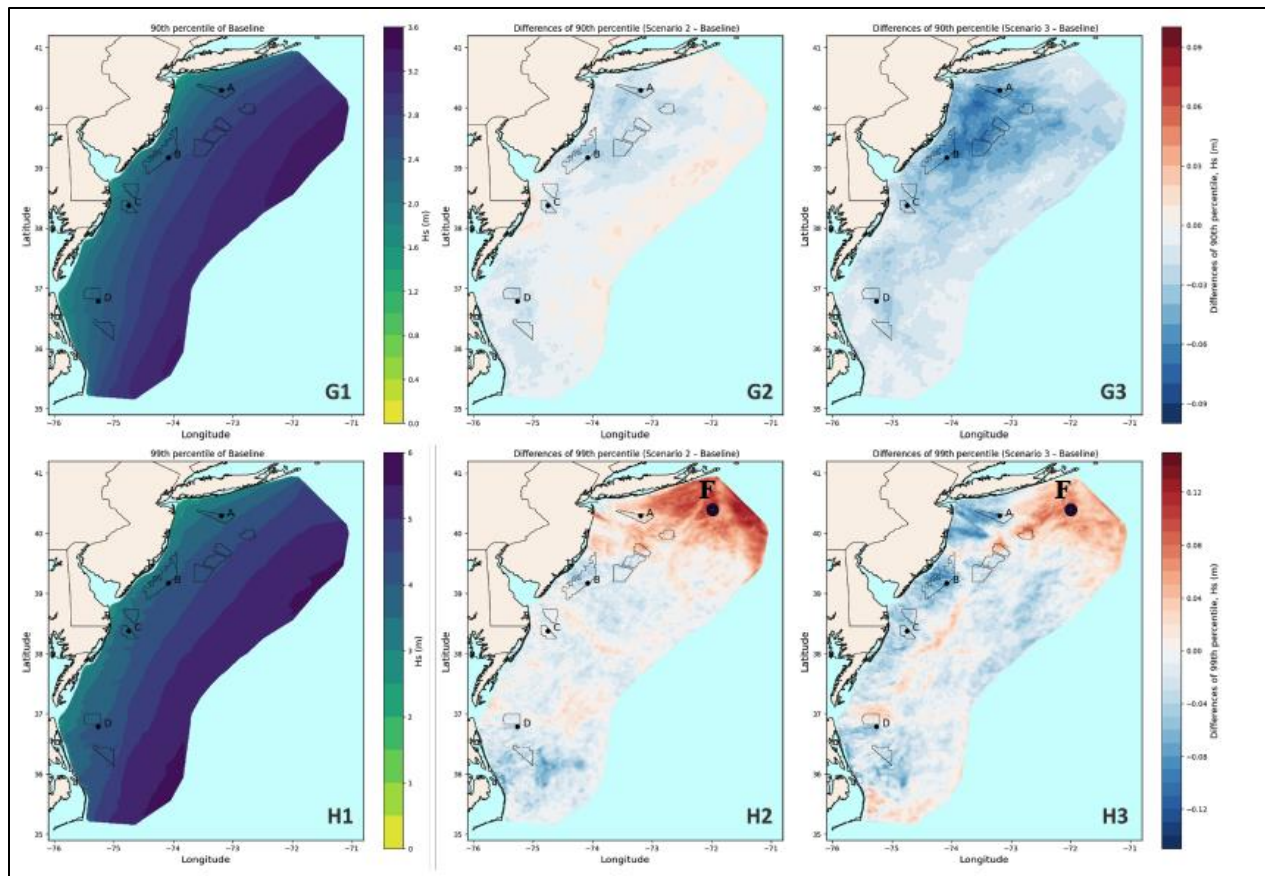


Figure 202. Changes to 90% and 99% significant wave height.

Top row: 90th percentile significant wave height for Feb-01-2018 to Jan-31-2020 (G1) and OWT scenario changes: 90th percentile of Scenario 2 - 90th percentile of Baseline (G2) and 90th percentile of Scenario 3 - 90th percentile of Baseline (G3). Bottom row: The same as top row but for the 99th percentile (H1) and the differences of 99th percentile for each OWT scenario to the baseline: Scenario 2 (H2) and Scenario 3 (H3).

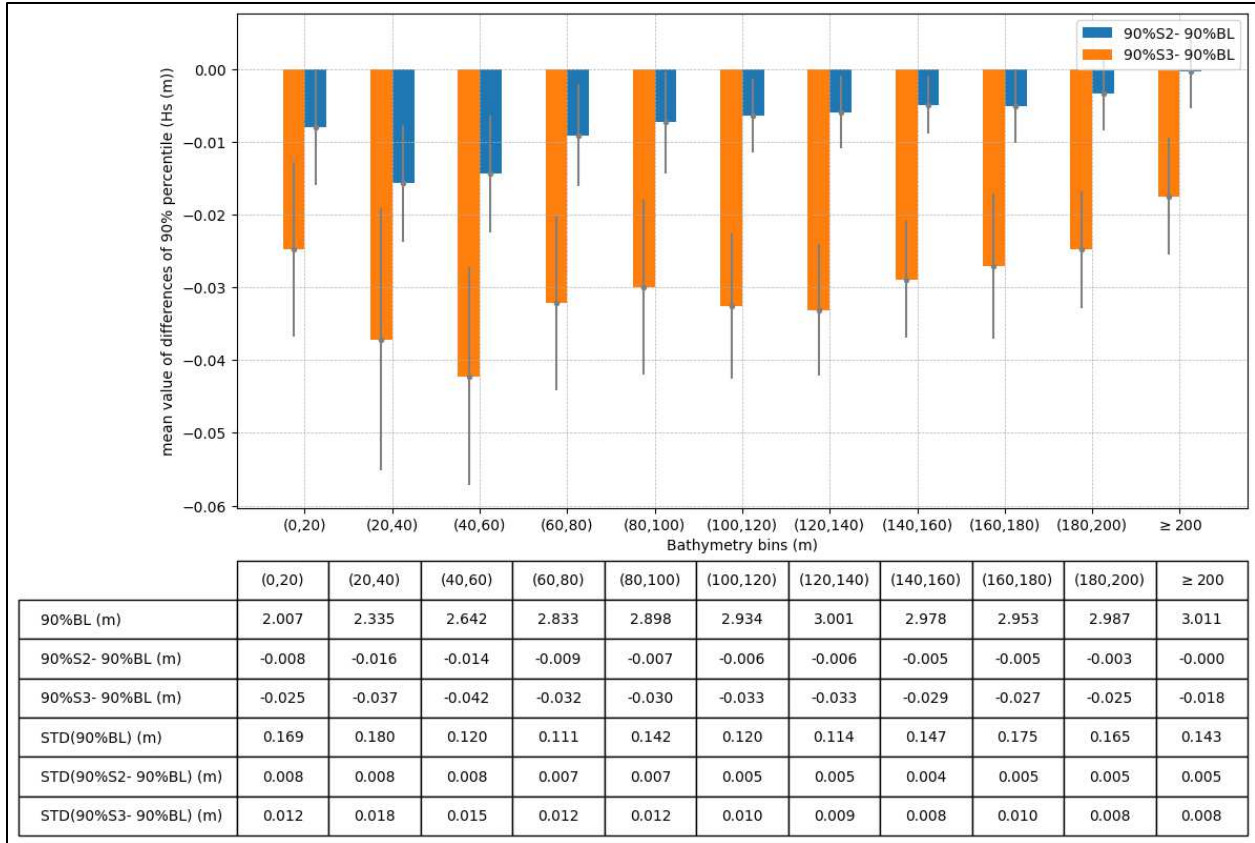


Figure 203. Mean value of the difference between the 90th percentile wave heights of OWT Scenarios and Baseline for every bathymetry bins. Blue bar is for Scenario 2 – Baseline and orange bar is for Scenario 3 – Baseline. Depth-bin definition provided in Figure 51.

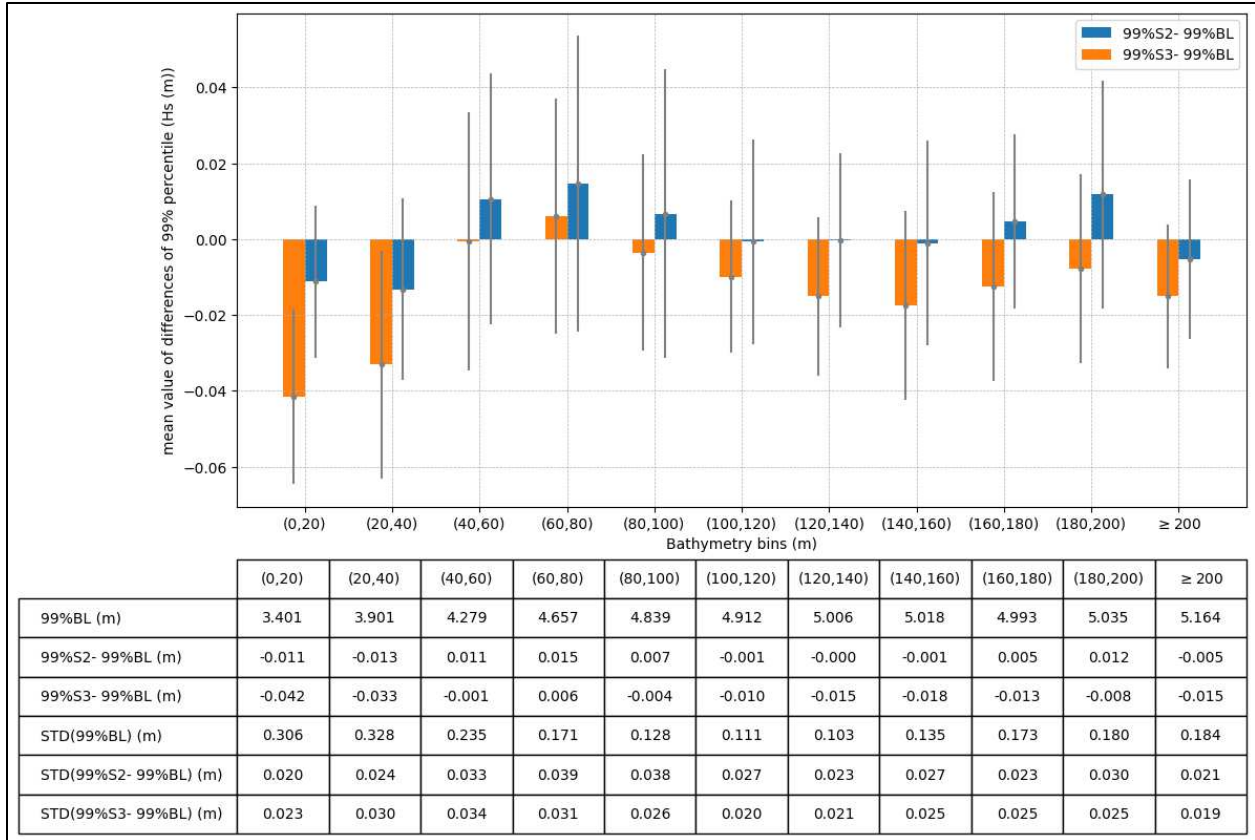


Figure 204. Mean value of the difference between the 99th percentile wave heights of OWT Scenarios and Baseline for every bathymetry bins. Blue bar is for Scenario 2 – Baseline and orange bar is for Scenario 3 – Baseline. Depth-bin definition provided in Figure 51.

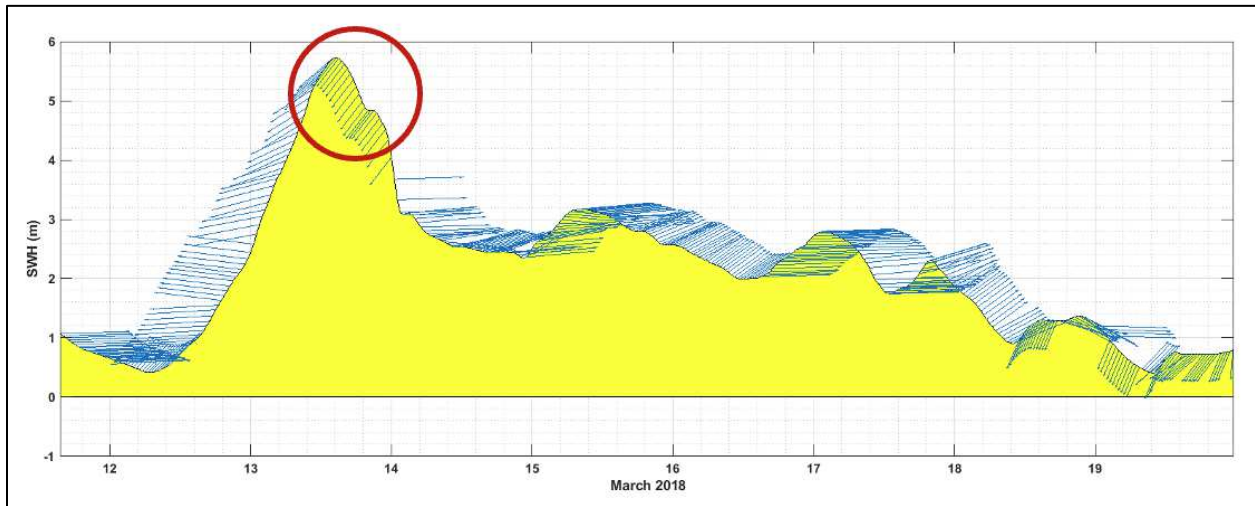


Figure 205. Stick plot of significant wave height and peak wave direction at Point F shown in Figure 198.

8.2 Impact to Mean Wave Period

The simulated wake effects of the offshore wind turbines on the Mean Wave Period, T_m , are illustrated in the scenario-difference maps of Figure 202, Figure 205, and Figure 206 for each OWT scenario. Two-year-Median mean wave period (T_m) varies from 4.6 s to 5.6 s from coastline to further offshore while the 99% percentile of T_m is as high as 10s offshore (Figure 202, C1, and D1). As expected, the highest impact of wind wake reduction on T_m occurs where the turbines are located; The maximum impact is 0.16 s increase (3.2%) in median T_m for both Scenario 2 and 3 (Figure 202, C2, and C3). Like with median and quantile significant wave height maps, the simulated two-year-median T_m is seen to change (here, mostly increase) more for the full-build-out Scenario 3, compared to Scenario 2. The same pattern is observed in difference maps of T_m 1st, 10th percentiles in Figure 205 and 90th, and 99th percentiles in Figure 206. These difference quantile maps indicate localized increases in T_m where the OWT are located. It is hypothesized that this very small (relative to the present-day mean or standard deviation), localized increase in T_m is due to the WEA-related decrease in wind waves relative to the longer period swells. A summary for the changes in the median and 99th percentiles of the instantaneous T_m differences between scenarios and baseline is presented in Figure 203 and Figure 204, respectively. Similarly, the differences between the 90th, and 99th percentiles of T_m for each scenario against baseline are also summarized in Figure 207 and Figure 208, respectively, for each bathymetric depth bin in Figure 51.

Figure 202, panels D2 & D3, show the 99th percentile of the T_m instantaneous absolute differences for Scenario 2 and 3, respectively. They indicate the same order of impact for both scenarios (larger impact near the coastline and turbines' locations and less impact further offshore. Figure 202 shows that, for the high percentiles of instantaneous differences that are more influenced by individual events, the more limited Scenario 2 is shown to have a higher impact, similarly to the finding for significant wave height.

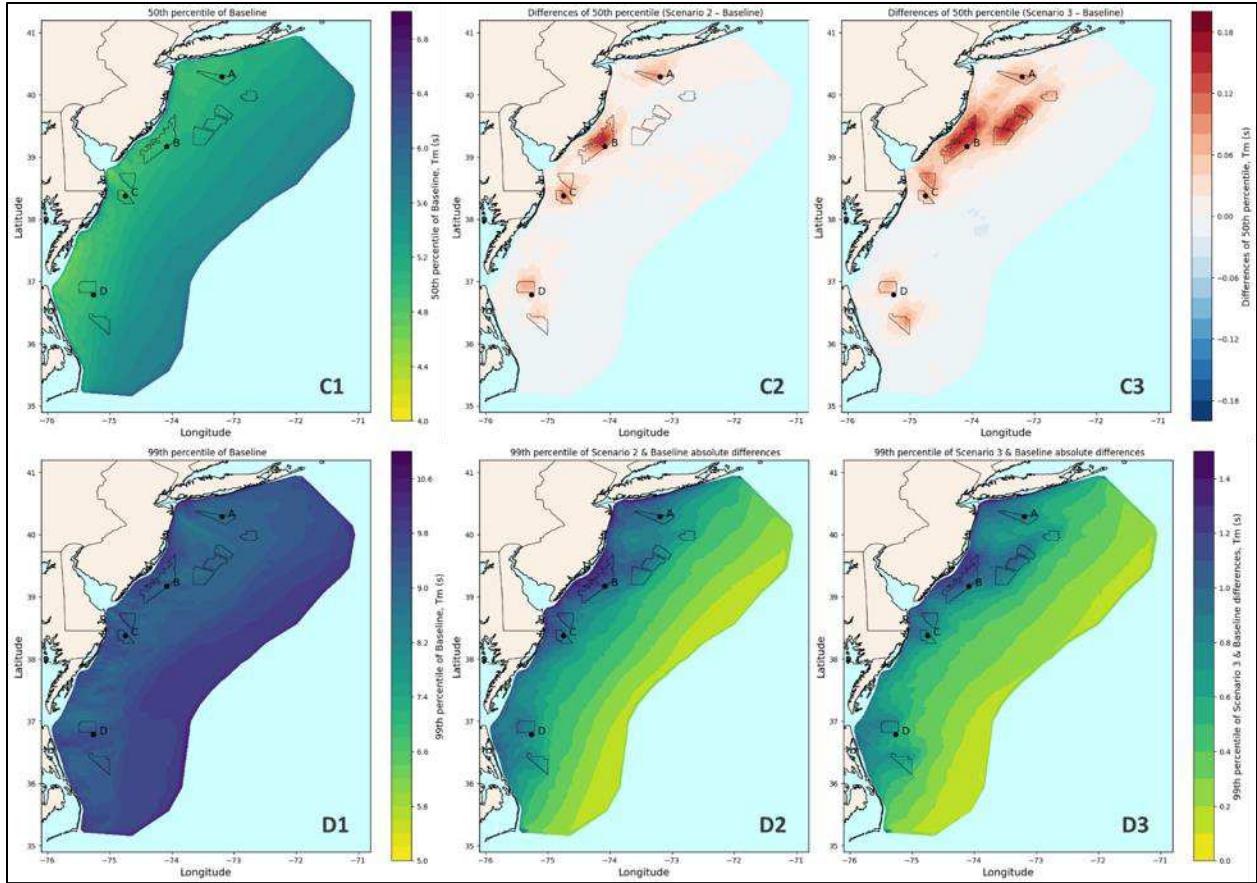


Figure 206. Median mean wave period change and the 99th percentile of the instantaneous difference. Top row: Median Mean Wave Period for Feb-01-2018 to Jan-31-2020 (C1) and OWT scenario changes: Median of Scenario 2 - Median of Baseline (C2) and Median of Scenario 3 - Median of Baseline (C3). Bottom row: The same as top row but for the 99th percentile (D1) and the 99th percentile of instantaneous absolute differences for each OWT scenario to the baseline: Scenario 2 (D2) and Scenario 3 (D3).

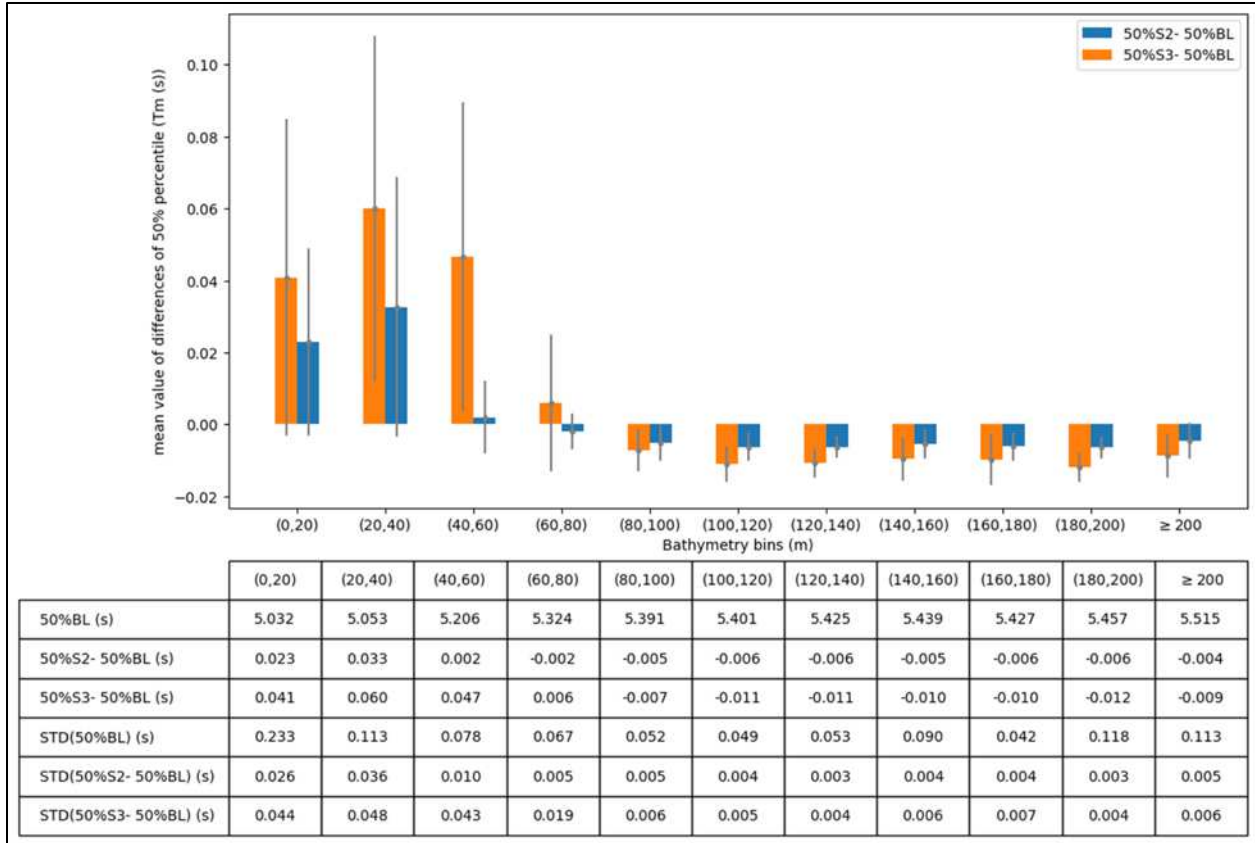


Figure 207. Mean value of the difference between the median Mean Wave Period of OWT Scenarios and Baseline for every bathymetry bin. Blue bar is for Scenario 2 – Baseline and orange bar is for Scenario 3 – Baseline. Depth-bin definition provided in Figure 51.

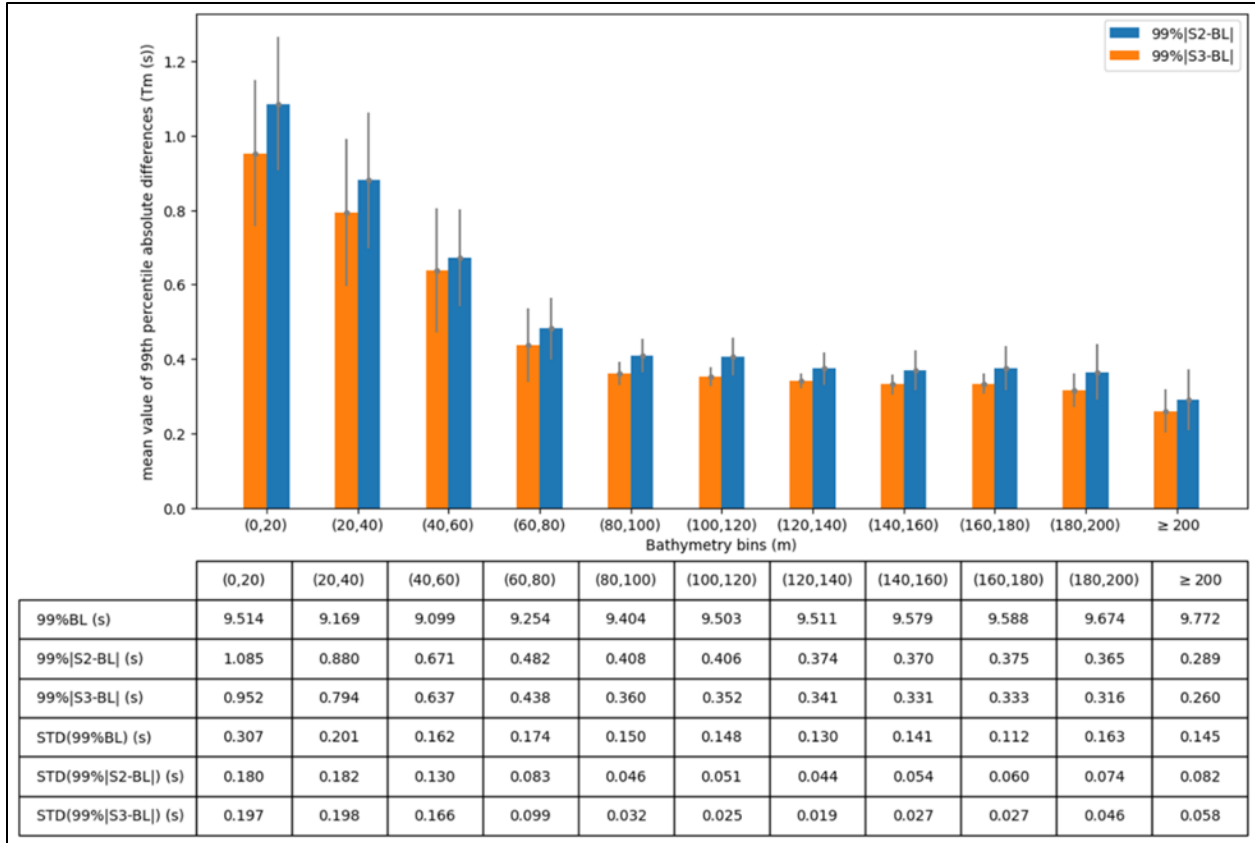


Figure 208. Mean value of 99th percentile of OWTs Scenarios and Baseline mean wave period absolute instantaneous differences for every bathymetry bins.
 Blue bar is for 99th percentile of |Scenario 2 – Baseline| and orange bar is for 99th percentile of |Scenario 3 – Baseline| instantaneous differences. Depth-bin definition provided in Figure 51.

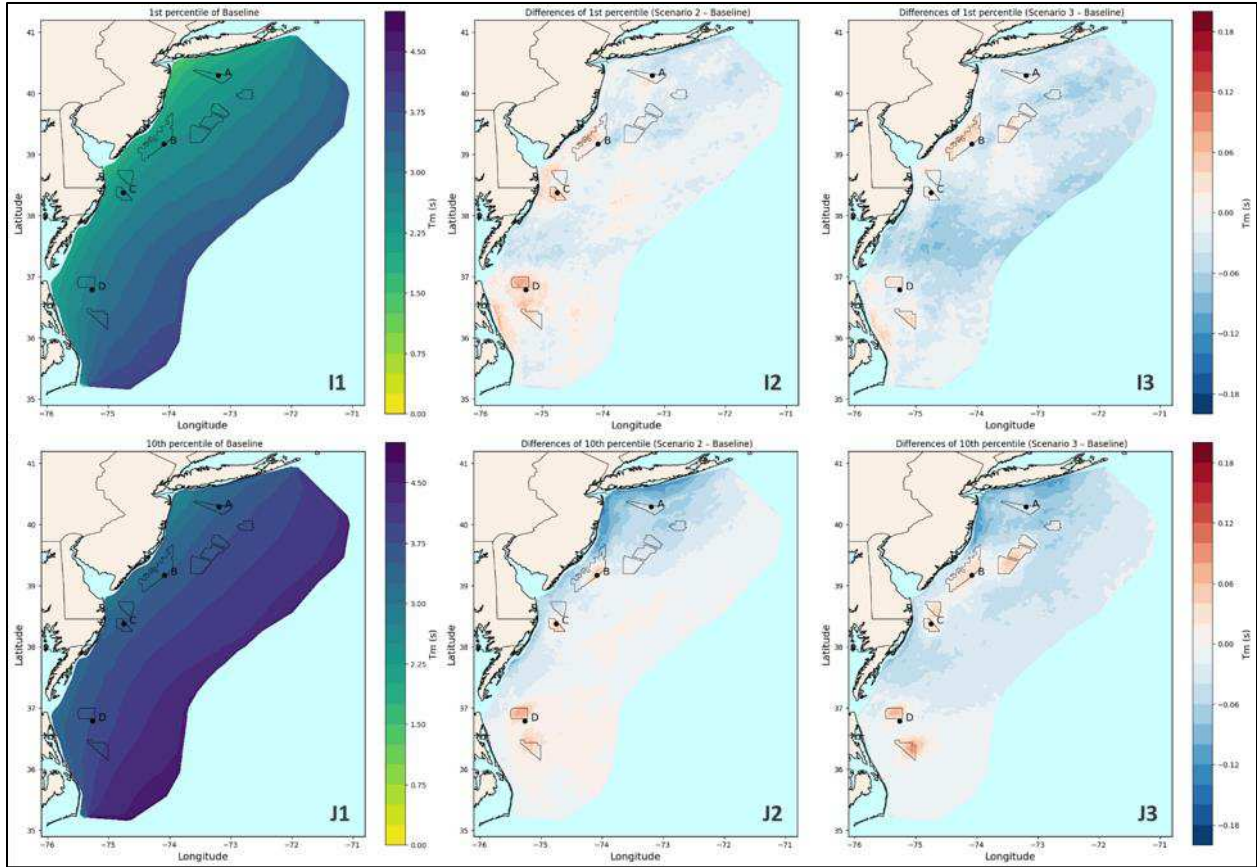


Figure 209. Change in 1st percentile and 10th percentile mean wave period.

Top row: 1st percentile mean wave period for Feb-01-2018 to Jan-31-2020 (I1) and OWT scenario changes: 1st percentile of Scenario 2 - 1st percentile of Baseline (I2) and 1st percentile of Scenario 3 - 1st percentile of Baseline (I3). Bottom row: The same as top row but for the 10th percentile (J1) and the differences of 10th percentile for each OWT scenario to the baseline: Scenario 2 (J2) and Scenario 3 (J3).

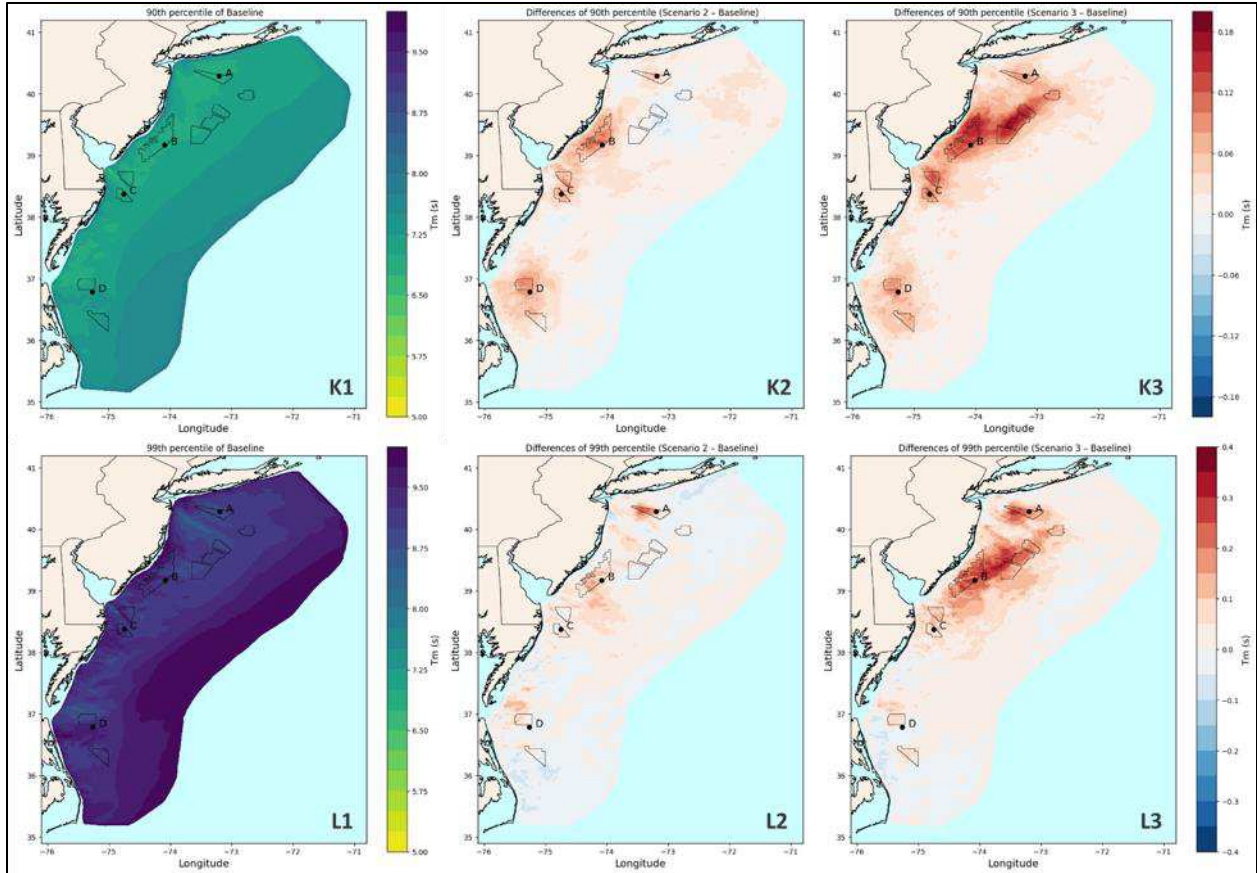


Figure 210. Change in 90th percentile and 99th percentile mean wave period. Top row: 90th percentile mean wave period for Feb-01-2018 to Jan-31-2020 (K1) and OWT scenario changes: 90th percentile of Scenario 2 - 90th percentile of Baseline (K2) and 90th percentile of Scenario 3 - 90th percentile of Baseline (K3). Bottom row: The same as top row but for the 99th percentile (L1) and the differences of 99th percentile for each OWT scenario to the baseline: Scenario 2 (L2) and Scenario 3 (L3).

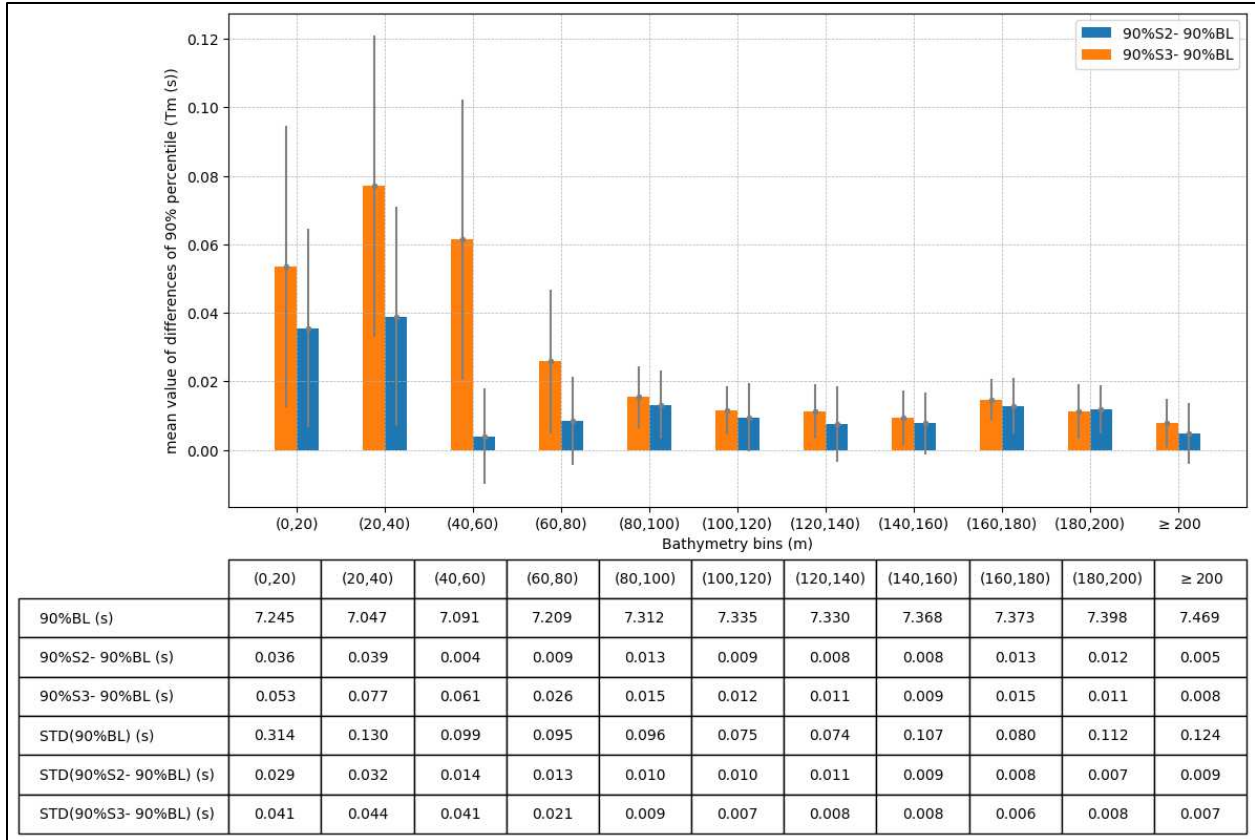


Figure 211. Mean value of the difference between the 90th percentile of Mean Wave Period of OWT Scenarios and Baseline for every bathymetry bins. Blue bar is for Scenario 2 – Baseline and orange bar is for Scenario 3 – Baseline. Depth-bin definition provided in Figure 51.

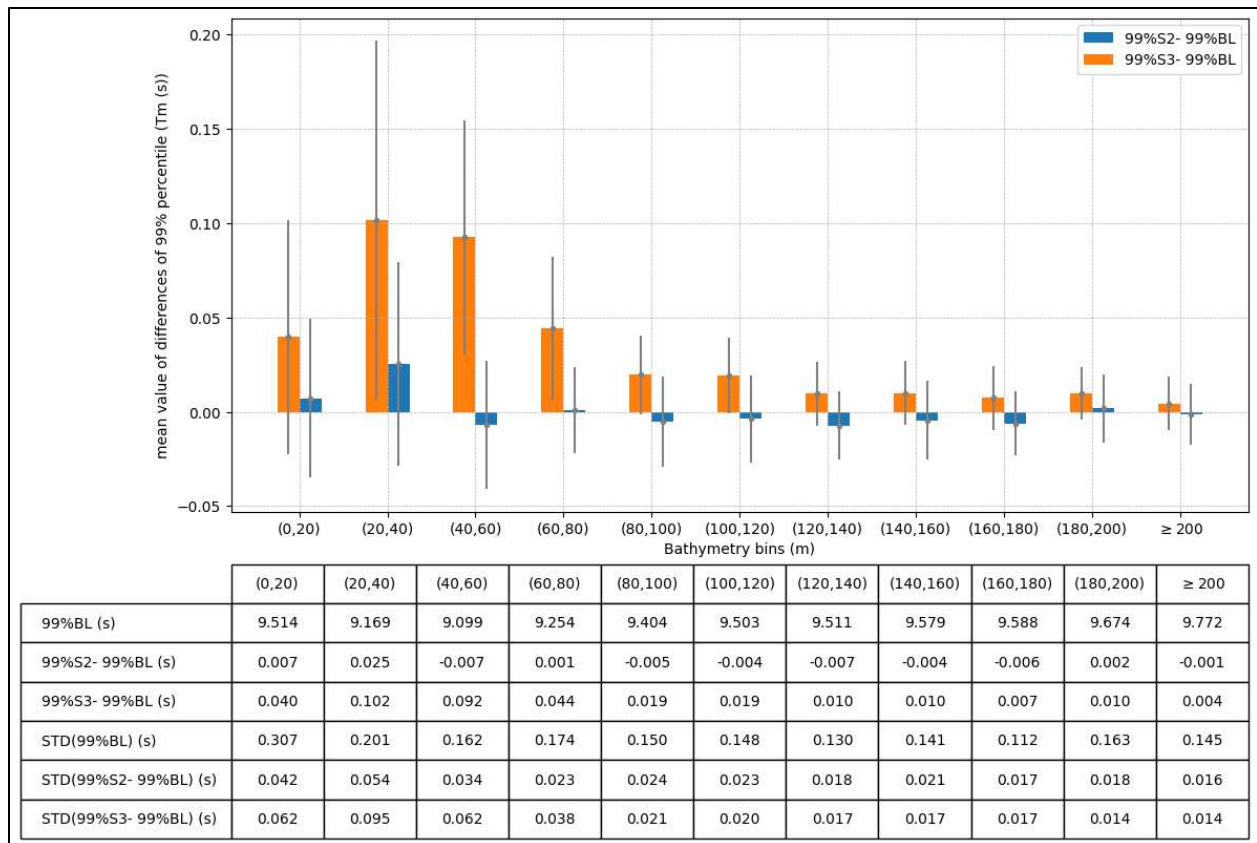


Figure 212. Mean value of the difference between the 99th percentile of Mean Wave Period of OWT Scenarios and Baseline for every bathymetry bins. Blue bar is for Scenario 2 – Baseline and orange bar is for Scenario 3 – Baseline. Depth-bin definition provided in Figure 51.

9 Impact Of Offshore Wind Farms on Hydrodynamics

9.1 Background

9.1.1 Middle-Atlantic Bight General Circulation

Based on high frequency (HF) radar data collected in the New Jersey inner Shelf, Kohut et al. (2004) found that the annual mean current measured between May 1999 and May 2000 showed a weak alongshore southwestward flow (Figure 209). This study discussed the seasonal variation of the New Jersey Shelf current, where stratification caused by freshwater runoff and warmer temperatures can be seen during the summer season. However, during the winter season, the transient current is more variable, shows relatively less correlation with the wind and is strongly correlated with the topography of the inner shelf through vorticity dynamics (Kohut et al., 2004).

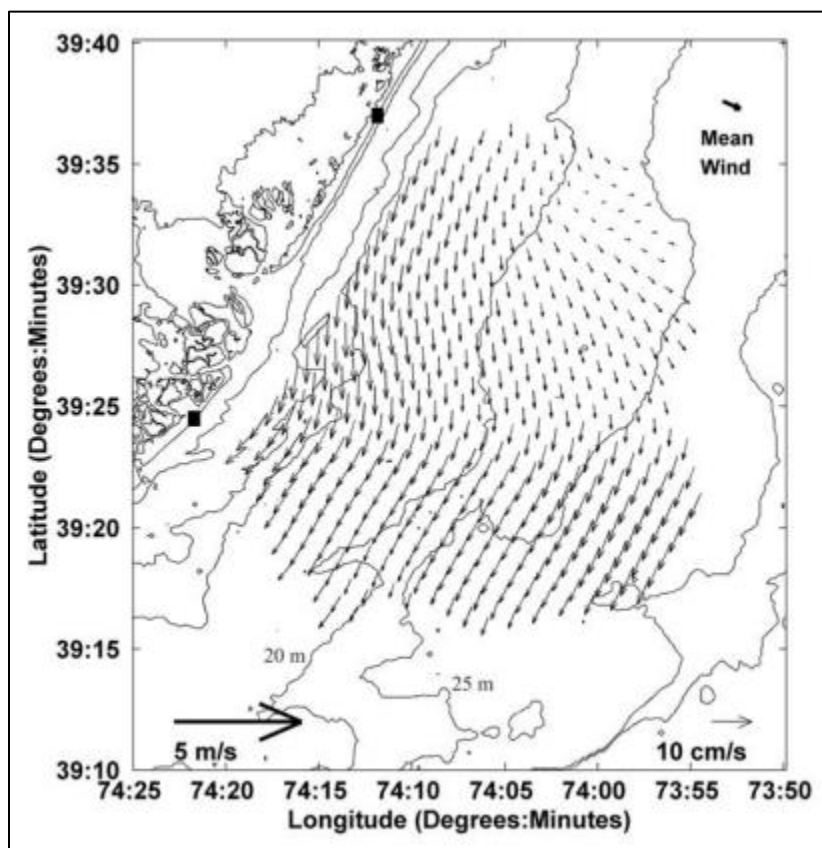


Figure 213. Annual mean currents recorded by High Frequency Radar system between May 1999 and May 2000 (Kohut et al., 2004).
Reproduced with permission.

Gong et al. (2010) also characterized the spatial structure of the mean current and of the seasonal surface circulation in the New Jersey Shelf, using long-range HF radar data from 2002 to 2007. The mean surface flow over the New Jersey Shelf is between 2 and 12 cm/s down shelf and towards the south, while the detided root-mean-square (RMS) velocity variability ranges from 11 to 20 cm/s, being the same magnitude as the mean offshore current, but much larger than the mean current nearshore. The study also suggested that the surface flow in the New Jersey Shelf is a function of topography, seasonal stratification, and wind forcing. The current is in the same direction as the wind during the unstratified/mixed (winter) season, as

dominant northwesterly (cross-shelf) winds drive cross-shelf offshore flows. However, during the stratified season (summer), the flow direction is to the right of the wind due to Ekman forcing, as dominant southwesterly wind drives upwelling favorable cross-shelf offshore flow. During the transition seasons (spring and autumn), northeasterly winds drive energetic along-shelf flows.

Roarty et al. (2020) also analyzed circulation over the Mid-Atlantic Bight (MAB) using HF radar data and found that the 10-year (2007–2016) annual mean surface currents are weaker and mostly cross-shelf near the coast, (about 3–6 cm/s) while the current speeds increase to about 8–10 cm/s and rotate to an alongshore direction near the shelf break.

The nature of tides on the MAB shelf is semi-diurnal (i.e., tidal currents change direction about twice a day) and rotary. In offshore regions, tidal currents are weak (< 0.05 m/s); however, near the shore especially in the embayments and shoal areas tidal currents could reach velocities of 1.5 m/s (USDOI 1982). Delft3D simulated cross-domain mean surface currents over the two year simulation period are generally consistent with the abovementioned magnitudes for the mean, transient low-pass filtered variability, and tidal current range (Figure 210), as well as with the general current directions and circulation patterns as shown in Appendix A (A-7 to A-9), with the New Jersey Shelf confined between the Hudson Valley and the southward flowing Shelf Break Jet (Gong et al, 2010 and Forsyth et al, 2020).

Lentz (2008) found that the depth-averaged alongshelf flow in the Mid-Atlantic Bight is primarily driven by an alongshelf pressure gradient (sea surface slope of 3.7×10^{-8} increasing to the north) and an opposing mean wind stress that also drives the near-surface offshore flow. Thus, changes in wind stress are expected to have an impact on the alongshore residual flow in the MAB: a reduction in the wind stress may lead to an increased southward flow and upwelling-favorable surface offshore flow. This impact would also be consistent with the findings of Chen and Yang (2024).

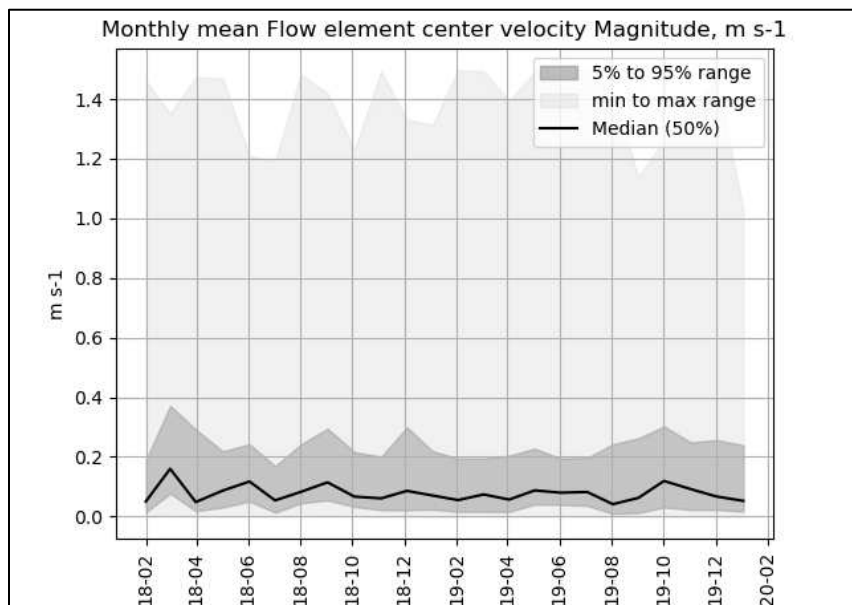


Figure 214. Delft3D FM modeled mean surface currents from Feb 2018 to Jan 2020.

9.1.2 Cold Pool

The Cold Pool in the Middle Atlantic Bight (MAB) and New York Bight forms from remnant winter water as the thermocline develops in spring (Chen et al., 2024) and persists between April and September.

During this period, the bottom waters remain cold due to the development of the seasonal stratification that separates them from the warmer surface waters. The Cold Pool undergoes significant seasonal warming during the summer, influenced by surface heating, horizontal advection of warmer waters, and mixing processes. Additionally, the Cold Pool moves southwest following the mean alongshore current at a rate of approximately 5 cm/s. The rate of warming varies spatially, ranging from 0.02°C to 0.06°C per day (Lentz, 2017). In the fall, the cooling of surface waters and wind mixing lead to the dissolution and destratification of the Cold Pool.

The Cold Pool is a crucial habitat for various marine species, including the yellowtail flounder, which thrive in the cooler temperatures. Changes in the Cold Pool's temperature can significantly impact the distribution and recruitment success of these species (Sullivan et al., 2005 and Miller et al., 2016). Therefore, understanding the warming trends and dynamics of the Cold Pool is essential for predicting future changes in the MAB ecosystem, especially considering climate change and anthropogenic activity, which is expected to further alter temperature regimes. Recent studies have shown that the cold pool is warming and shrinking (Friedland et al., 2022).

Four monthly vertical temperature transects taken across the continental shelf (Figure 211) display model-simulated seasonal cold pool evolution for 2018 (Figure 212, Figure 214, Figure 216, and Figure 218) and 2019 (Figure 213, Figure 215, Figure 217, and Figure 219). In the winter months colder temperatures are distributed across the water column and in the spring and summer months the presence of a thermocline creates pockets of water colder than the surface. The temperature contours for the month of March are vertically distributed from the nearshore to offshore areas. The initial cold pool formation is shown in the month of May and more defined in the summer months of June and July. Regional temperature variations across the four temperature transects are expressed in higher surface temperatures in the southern transects.

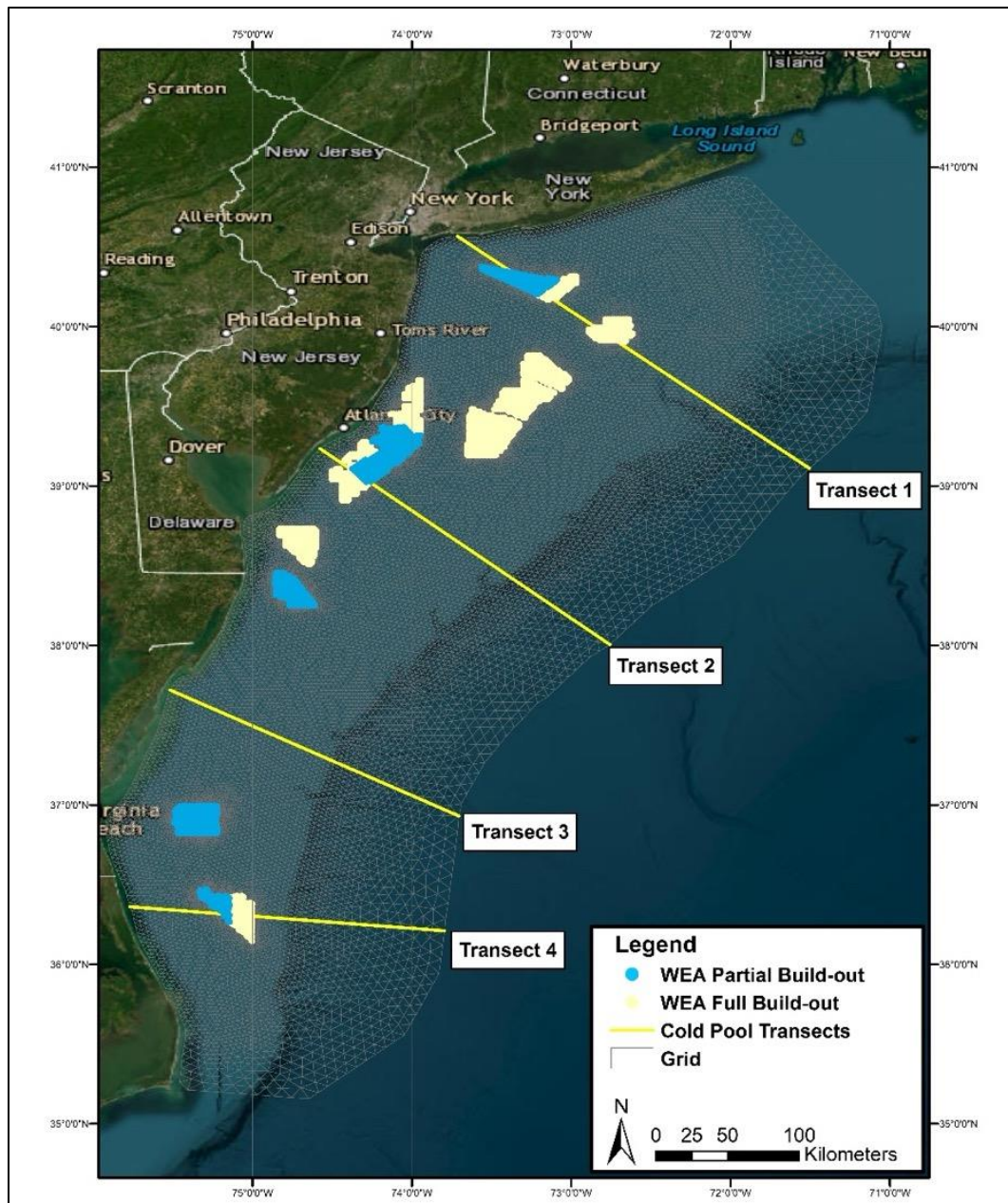


Figure 215. Locations of cross-shelf temperature transects.

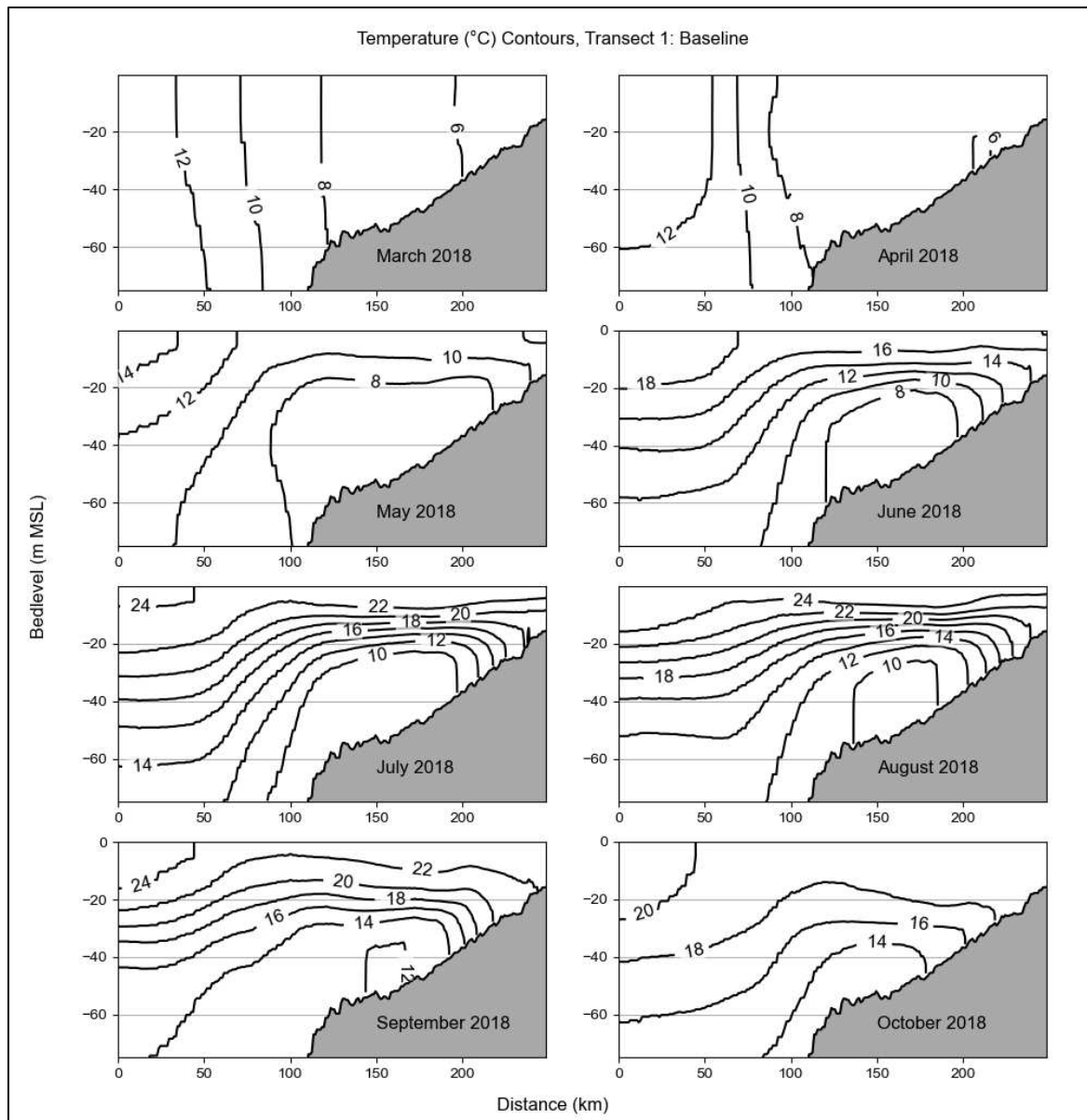


Figure 216. Temperature contours under baseline conditions from March to October 2018 at transect 1.

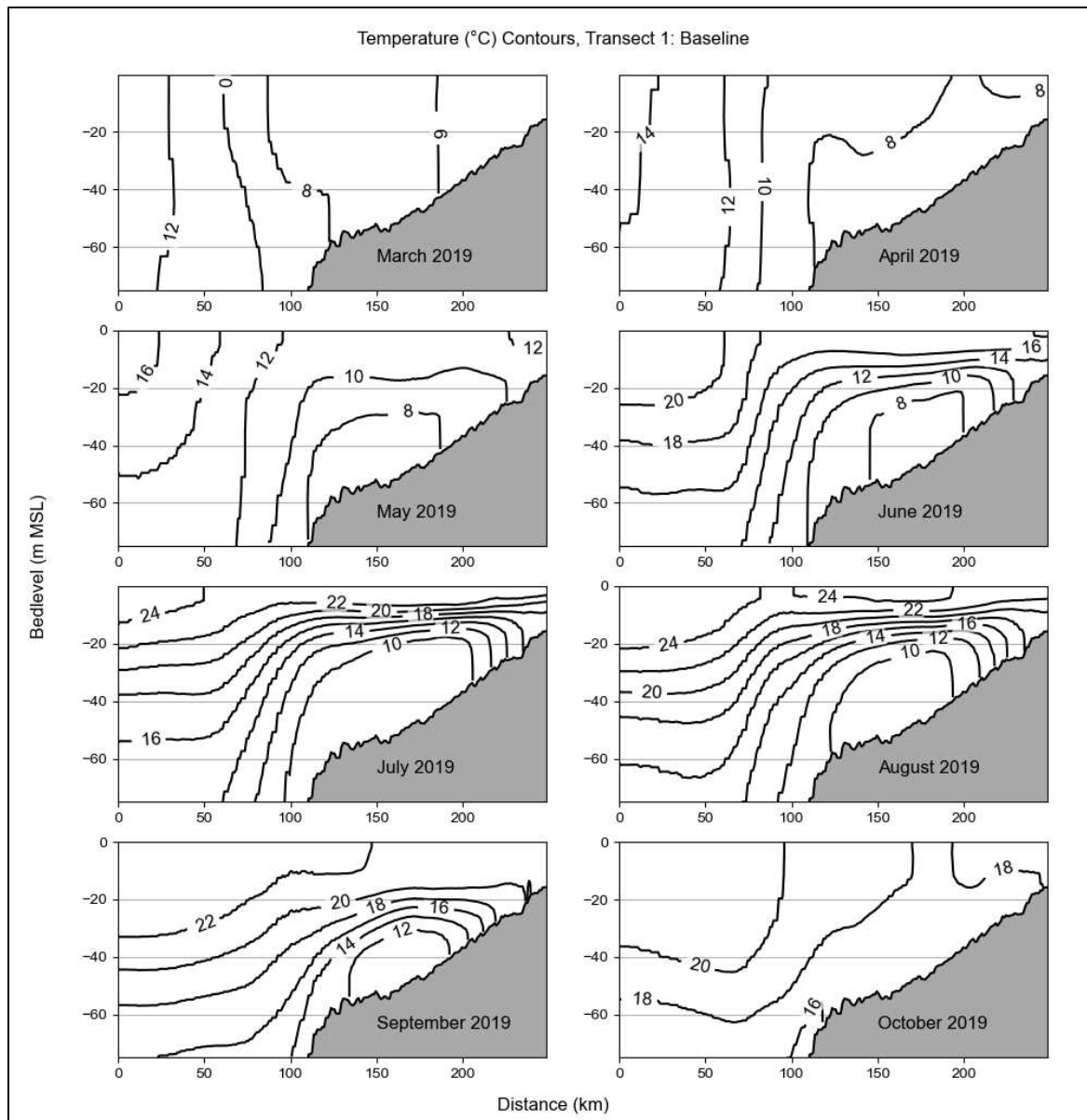


Figure 217. Temperature contours under baseline conditions from March to October 2019, at transect 1.

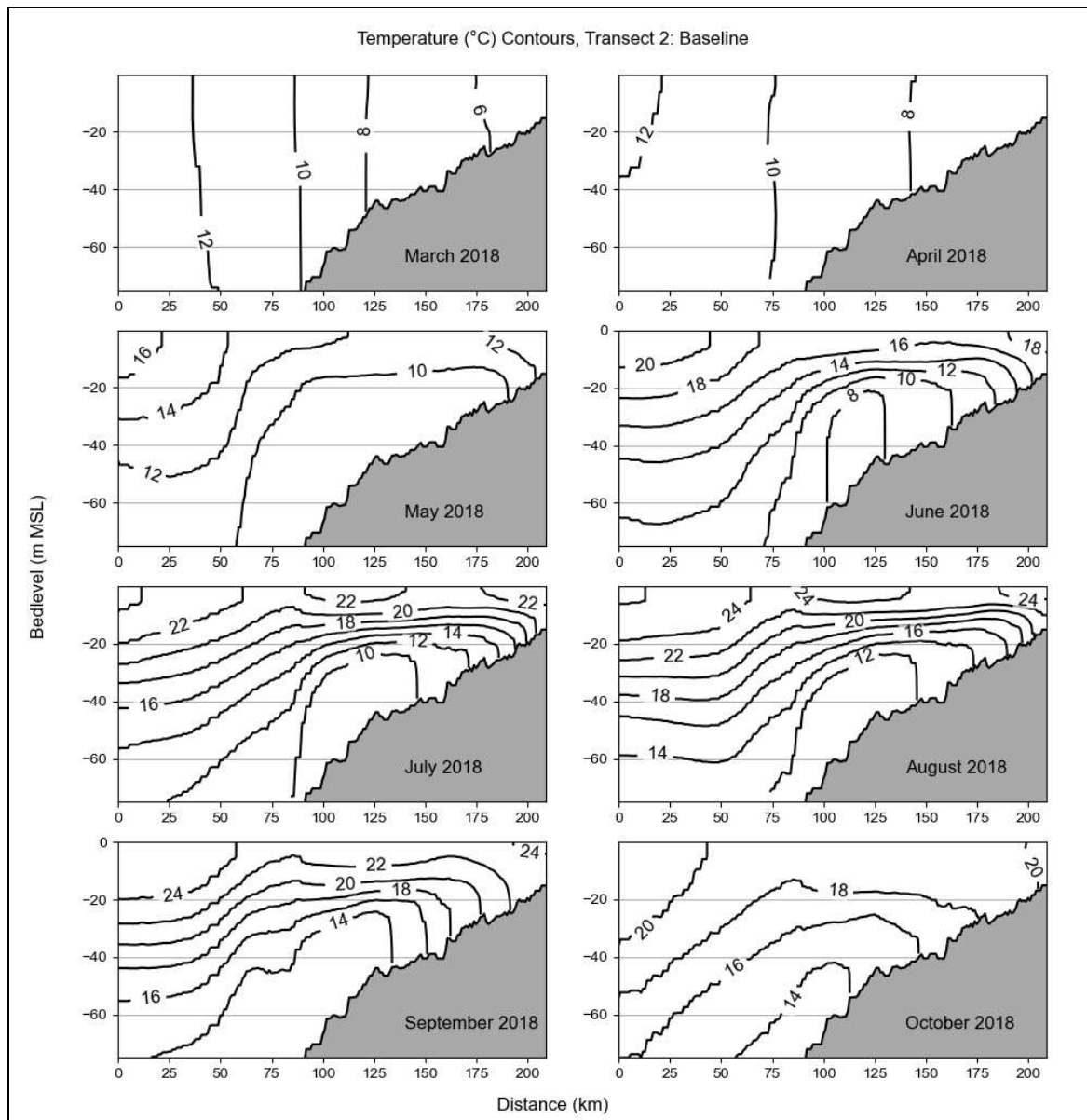


Figure 218. Temperature contours under baseline conditions from March to October 2018, at transect 2.

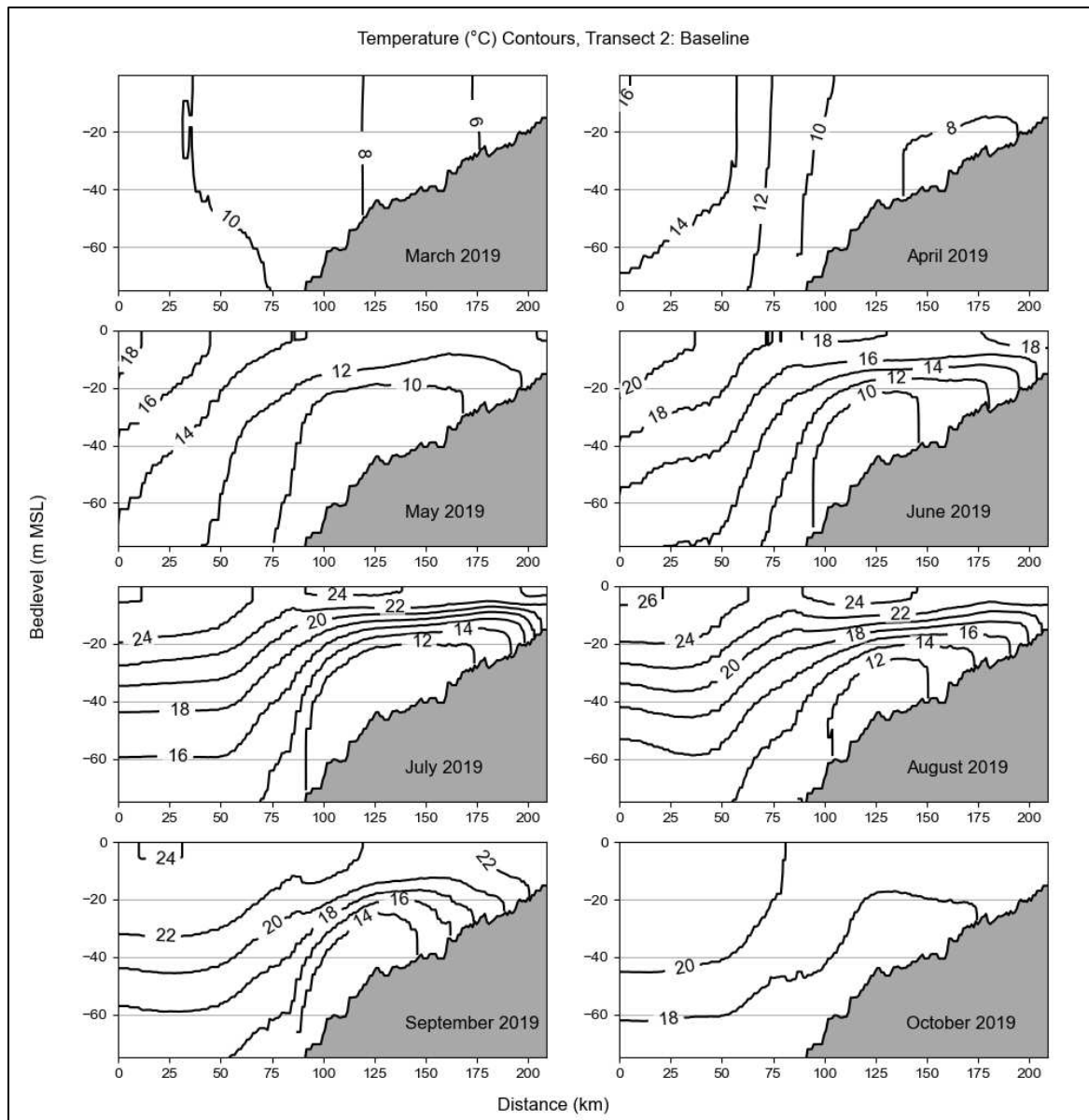


Figure 219. Temperature contours under baseline conditions from March to October 2019, at transect 2.

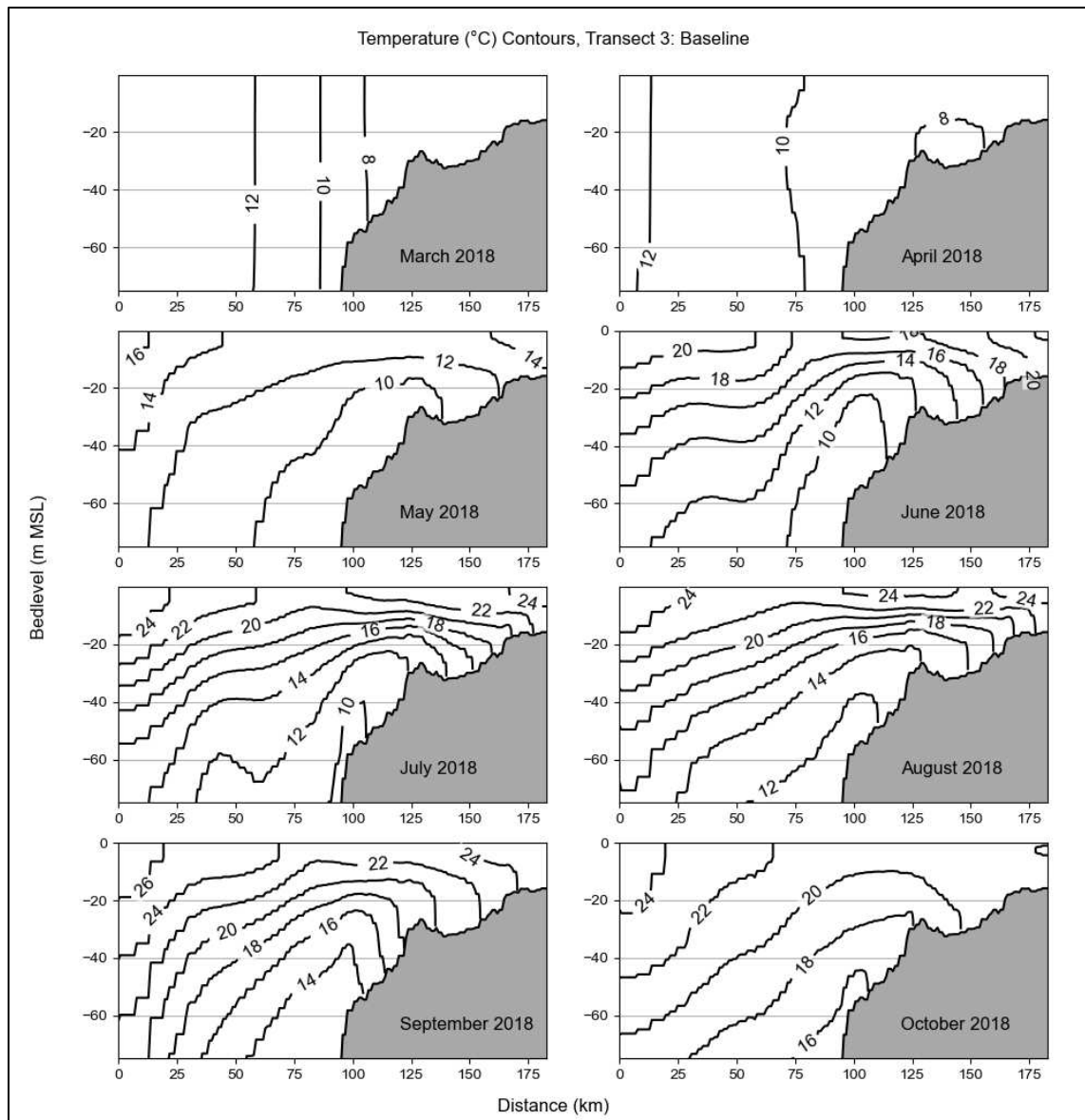


Figure 220. Temperature contours under baseline conditions from March to October 2018, at transect 3.

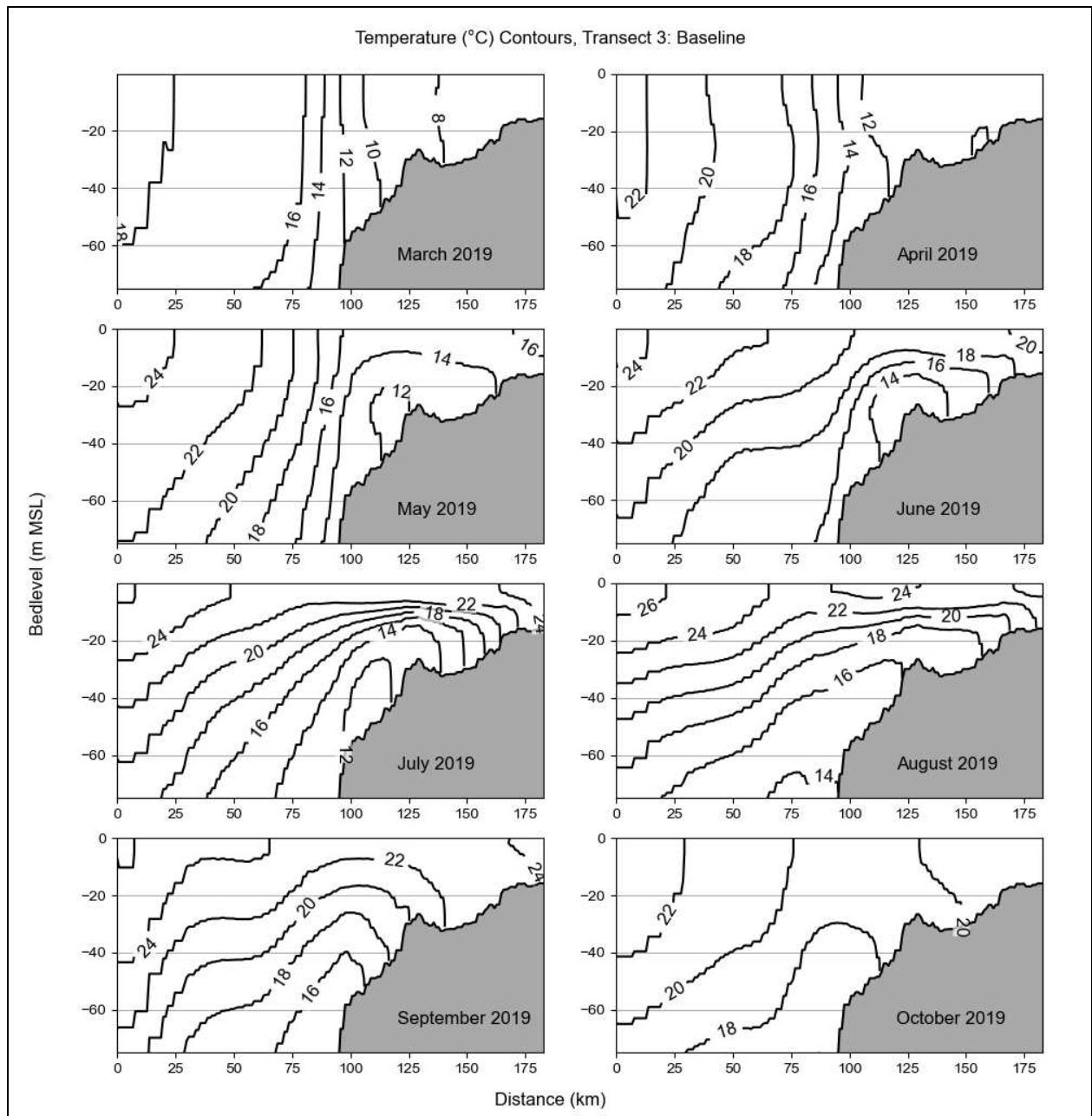


Figure 221. Temperature contours under baseline conditions from March to October 2019, at transect 3.

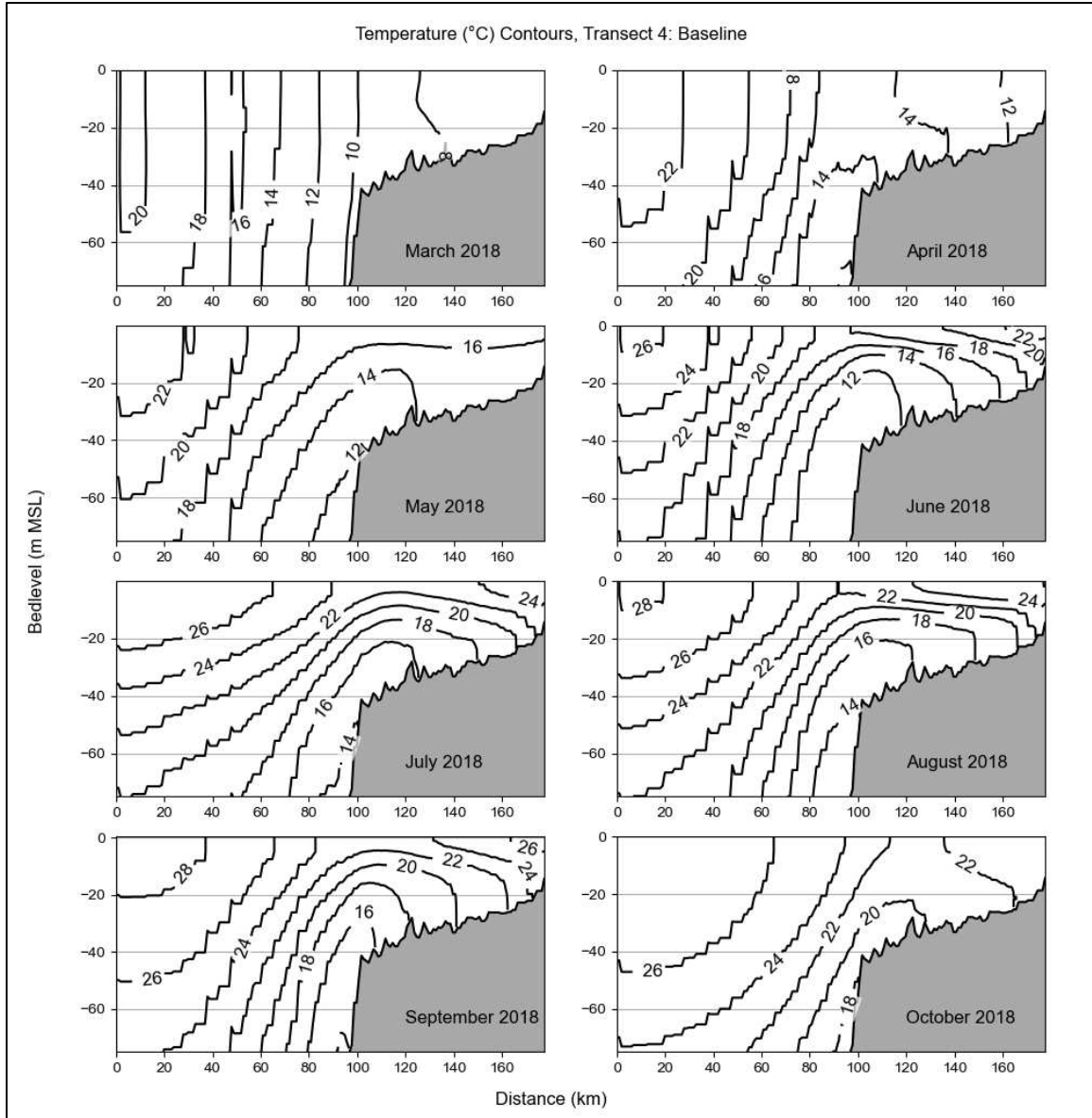


Figure 222. Temperature contours under baseline conditions from March to October 2018, at transect 4.

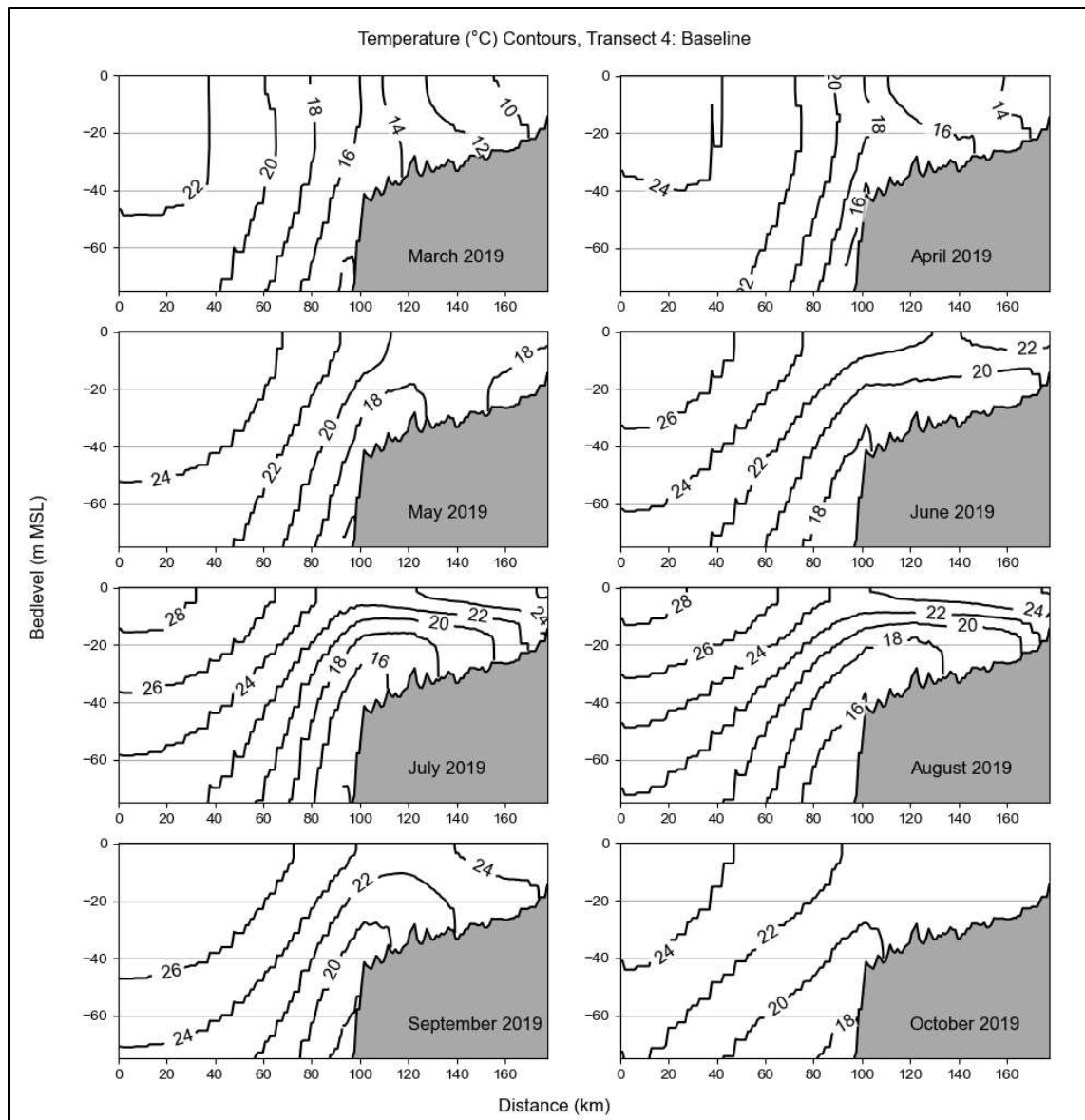


Figure 223. Temperature contours under baseline conditions from March to October 2019, at transect 4.

9.1.3 Hydrodynamic Effects of Offshore Wind Developments

Based on a recent literature view from the National Academies of Science (NAS 2023), the potential effects of offshore wind turbines on the ocean can be due to the physical presence of the structures (WTG monopiles here) across the water column and from the effects of wind energy extraction (wind wake) on wind-driven ocean circulation. In the water, at the turbine scale, monopile drag and flow obstruction can produce stronger separated currents, vortex shredding, vortex streets, and production of turbulent wakes downstream (NAS 2023, Chen et al., 2024). These phenomena are known to be present at length scales less than 1km, which is the size of the numerical mesh elements containing turbine foundation in this study, and thus are parameterized with the bridge pillar subgrid formulation (Section 5.8) in Delft3D-FM based on the CFD experiments of Johnson et al. (2021). At the wind farm scale (10-100km, depending on footprint), cumulative effects of the combined drag of monopiles in the literature include current speed reductions, increase in stratification, and doming of the pycnocline (e.g., Floeter et al., 2022, Christiansen

et al., 2023, Chen et al., 2024). Christiansen et al. (2023) found that the reduction in time-averaged North Sea residual currents were roughly 10%, though wind wake effects were not considered (NAS 2023).

Observations and modeling show that wind wakes from the wind energy extraction at hub height can extend to the sea surface and can reach 10s and, in times of constructive farm to farm interactions, 100s of km downstream of wind farms (Hasager et al., 2015, Platis et al., 2018, Cañadillas et al., 2022, Christiansen et al., 2022, Golbazi et al., 2022). Peak events were found to occur during stable atmospheric conditions, which, over the MAB occur mostly in the spring and summer (Debnath et al., 2021). At these wind farm to regional scales, it can be hypothesized that the decrease of surface stress from wind energy extraction may dominate the response of the ocean.

9.2 Effects of WEA Development on Cold Pool and Regional Currents

9.2.1 Cold Pool

Comparison of cold pool contours between the baseline scenario, Scenario 2 (partial wind farm) and Scenario 3 (full wind farm buildout) show the effect the proposed wind farm construction will have on the temperature dynamics over the water column. The largest impact to the cold pool dynamics is predicted under the full buildout of WEAs (Scenario 3). Contour comparisons at Transect 2 for the 2018 cold-pool season are shown in Figure 220 (for Scenario 2) and Figure 221 (for Scenario 3) against baseline. Cold pool contour comparisons at the other transects and for both years are included in Appendix D. Among four transects in Figure 211, the transect with the highest changes is Transect 2 and thus it is highlighted here. At other transects (included in the Appendix) changes are smaller. The figures also indicate that the installation of offshore wind farms raises the thermocline and shifts warmer bottom water toward the coast, likely as a result of increased coastal upwelling, as discussed in the final paragraph of section 9.1.1.

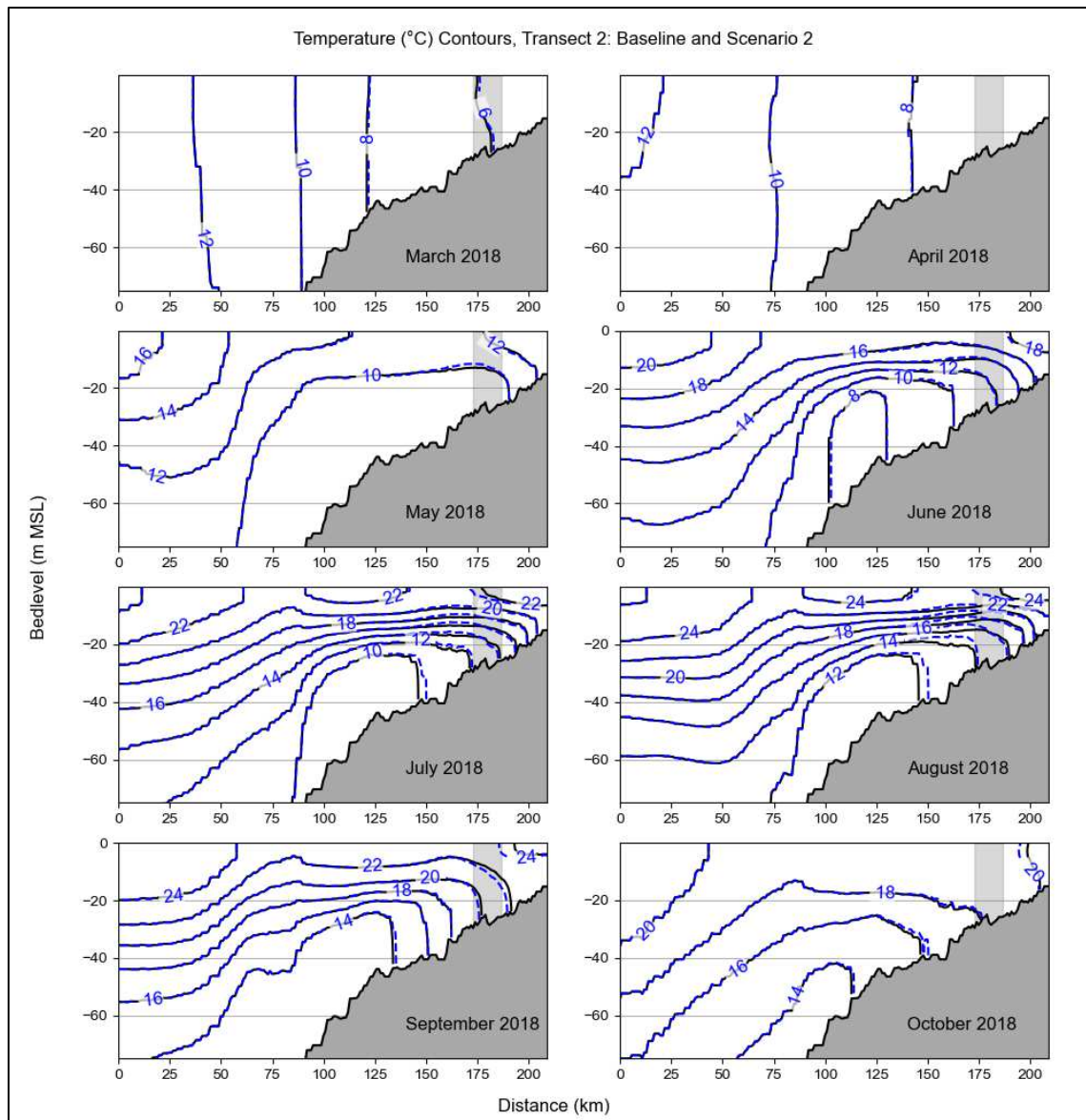


Figure 224. Temperature contours under baseline (solid black line) and Scenario 2 (dashed blue line) conditions, from March to October 2018, at transect 2.

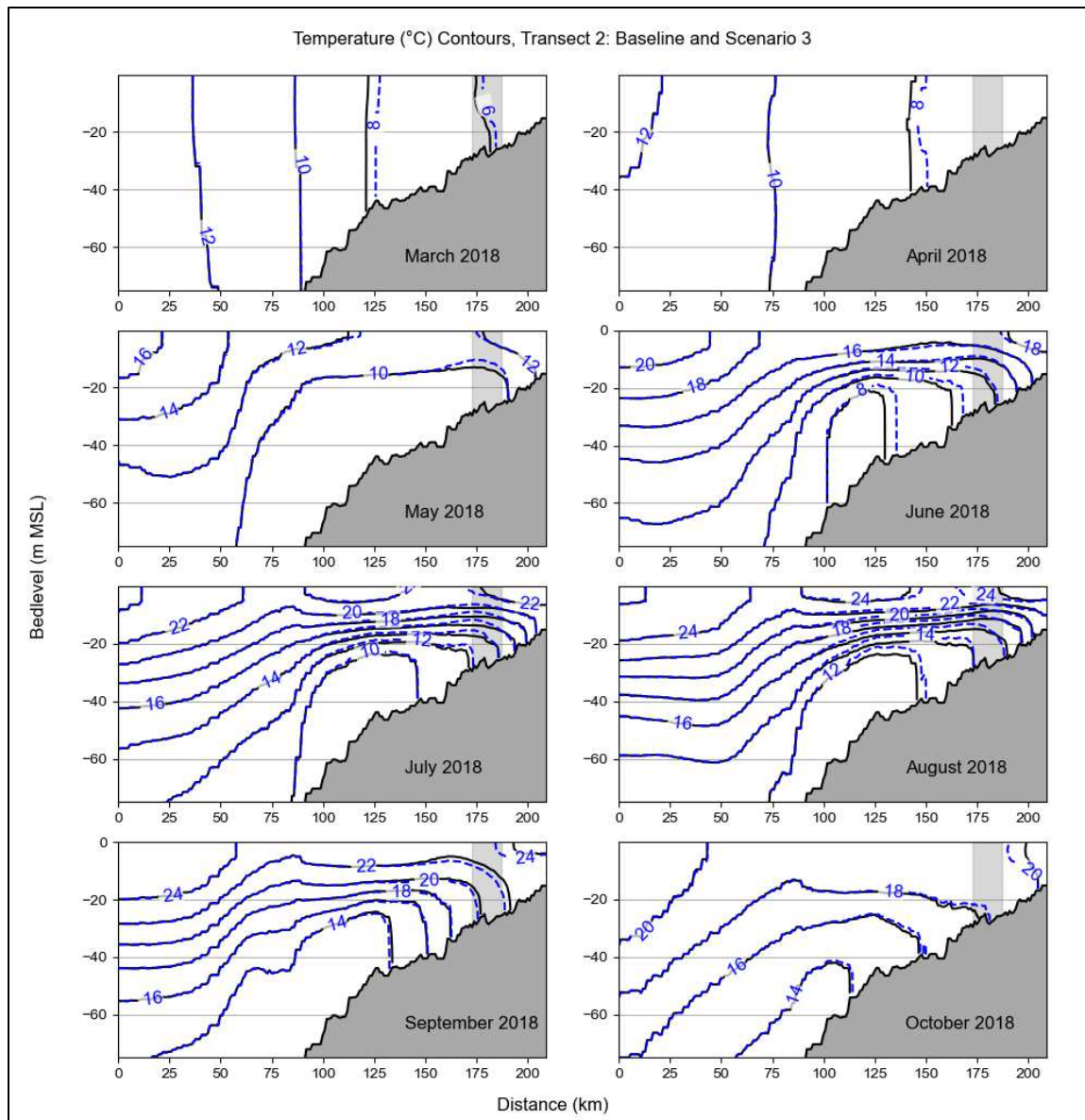


Figure 225. Temperature contours under baseline (solid black line) and Scenario 3 (dashed blue line) conditions, from March to October 2018, at transect 2.

9.2.2 Effects on Currents

The simulated installation of the wind turbines in the WEAs contributes to changes in depth-averaged current. To assess this impact to the overall strength of the general circulation, including the tidal components, the 50th, 95th, and 99th percentile of the simulated depth-averaged current speed (magnitude) were calculated and differences going from baseline to Scenario 2, and Scenario 3 were analyzed (Figure 222). For instance, 99th percentile difference plot for Scenario 2 and Scenario 1 shows the 99th percentile of Scenario 2 - 99th percentile of Scenario 1 (not the 99th percentile of the instantaneous differences). The differences in 50th, 95th, and 99th percentile currents between the scenarios show mostly a relatively small decrease in current speed (less than 1 cm/s) after WEA development. Local increases in current speed (also less than 1cm/s) are also seen, especially shoreward of the northern WEAs along the New York Bight and New Jersey Coast. This can be attributed to

increased turbulence and mixing around the turbines. Furthermore, alterations in larger-scale circulation resulting from wake effects may also influence the variations in current speed.

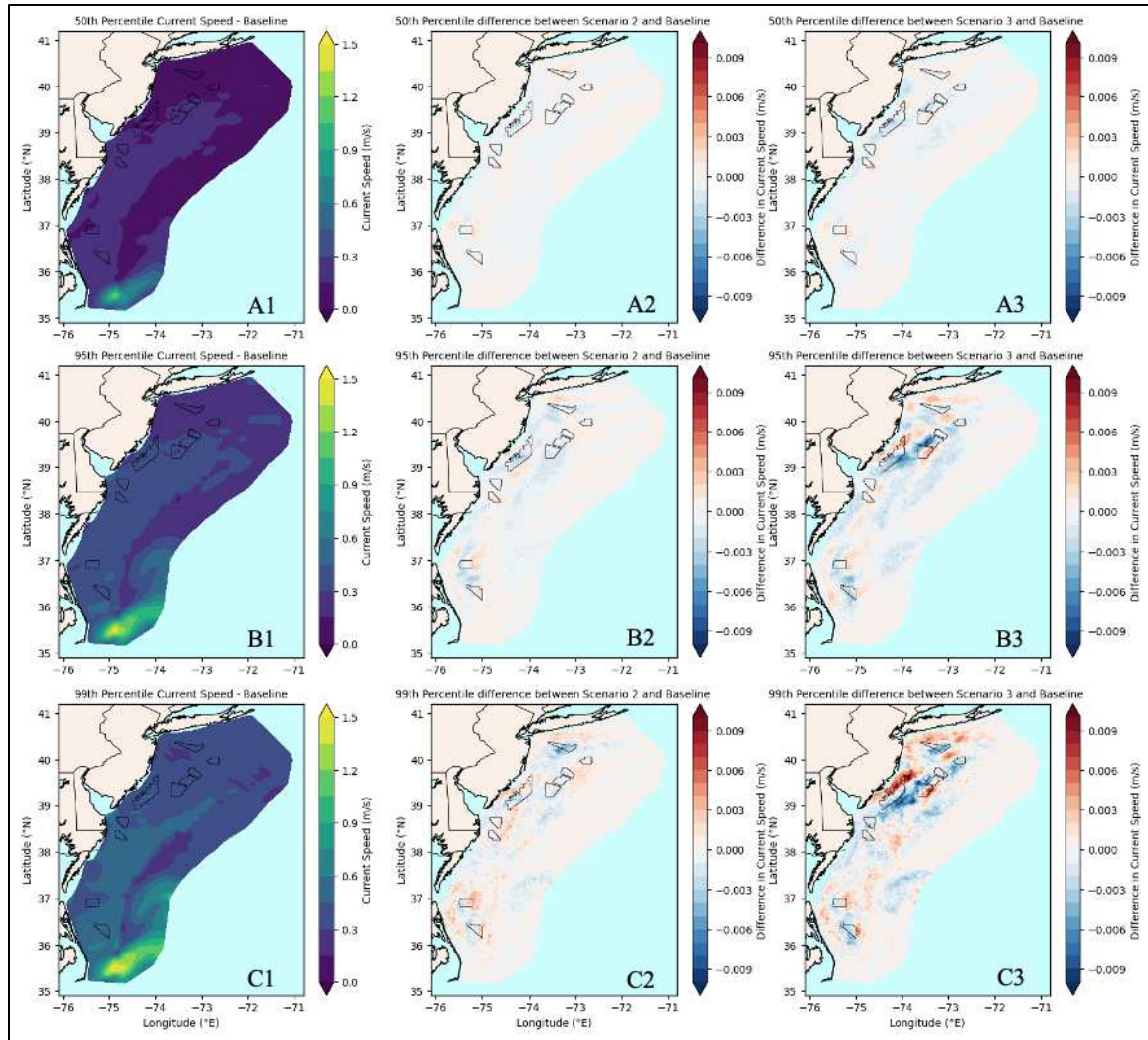


Figure 226. Change in the median and 99th percentile depth-averaged current speed. 50th percentile depth-averaged current speed for baseline scenario (A1), difference of 50th percentile between Scenario 2 and baseline (A2), and between Scenario 3 and baseline (A3). Middle row: The same as top row but 95th percentile depth-averaged current speed (B1), difference of 95th percentile between Scenario 2 and baseline (B2), and between Scenario 3 and baseline (B3). Bottom row: The same as top row but 99th percentile depth-averaged current speed (C1), difference of 99th percentile between Scenario 2 and baseline (C2), and between Scenario 3 and baseline (C3).

Figure 222 involves statistics including tidal components in depth-averaged current. However, after tidal excursions and inertial oscillations are filtered out, particle motion is primarily controlled by the mean current. Thus, a similar analysis was conducted after applying a low-pass filter (LPF) to the current time series. The 50th, 95th, and 99th percentile residual currents were calculated and differences going from baseline to Scenario 2, and Scenario 3 were analyzed (Figure 223). The difference in the 50th percentile between the scenarios show mostly an increase in tidal residual current speed inside and along the WEAs in both scenarios and depending on the buildout of WEAs in each scenario. This, in relative terms against baseline currents, is more significant, as can be deduced by comparing the left column of Figure 223 to Figure 222, where the magnitude of the total current is much higher than that of the residual. However, as the effect of stronger events becomes more significant in the 95th and 99th percentiles of the residual current in Figure 223, a pattern consistent with the one in Figure 222 for the total current emerges, with

relatively significant increases closer to the coastal zone, shoreward of the WEAs, and decreases further offshore.

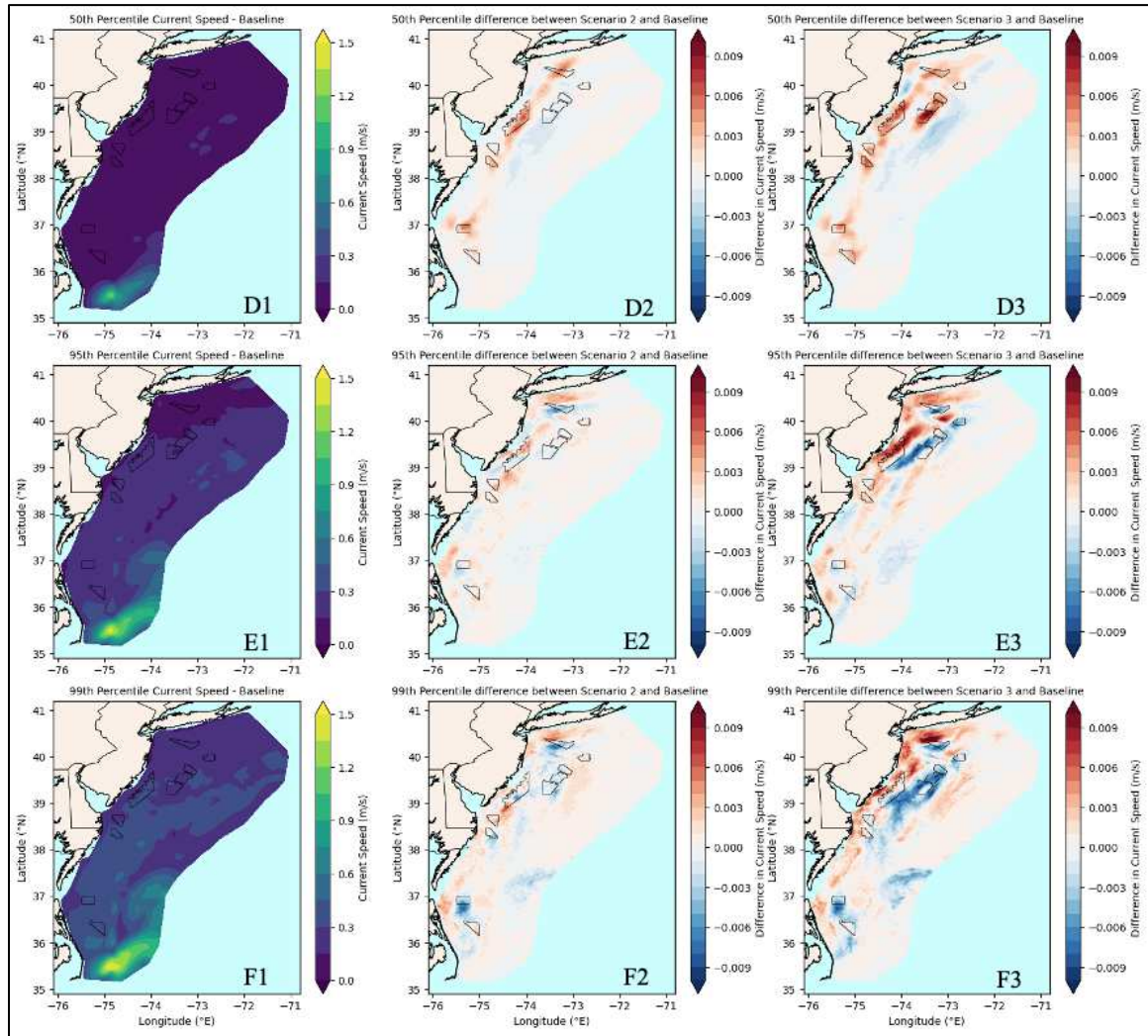


Figure 227. Change in the median and 99th percentile Low-Pass-Filtered depth-averaged current speed. 50th percentile depth-averaged current speed (LPF applied) for baseline scenario (D1), difference of 50th percentile between Scenario 2 and baseline (D2), and between Scenario 3 and baseline (D3). Middle row: The same as top row but 95th percentile depth-averaged current speed (LPF applied) (E1), difference of 95th percentile between Scenario 2 and baseline (E2), and between Scenario 3 and baseline (E3). Bottom row: The same as top row but 99th percentile depth-averaged current speed (LPF applied) (F1), difference of 99th percentile between Scenario 2 and baseline (F2), and between Scenario 3 and baseline (F3).

Figure 224 illustrates the mean difference in current speed and direction between the scenarios. Results indicate that the presence of offshore wind farms enhances the southward subtidal flow over most wind farms, consistent with the dynamics described in Lentz (2010) and Chen and Young (2024), whereas the mean regional alongshore water level gradient (positive toward the south) becomes less balanced from the decreased mean wind. The general circulation in the MAB retains its alongshore southward flow, but with increased shear around the WEAs.

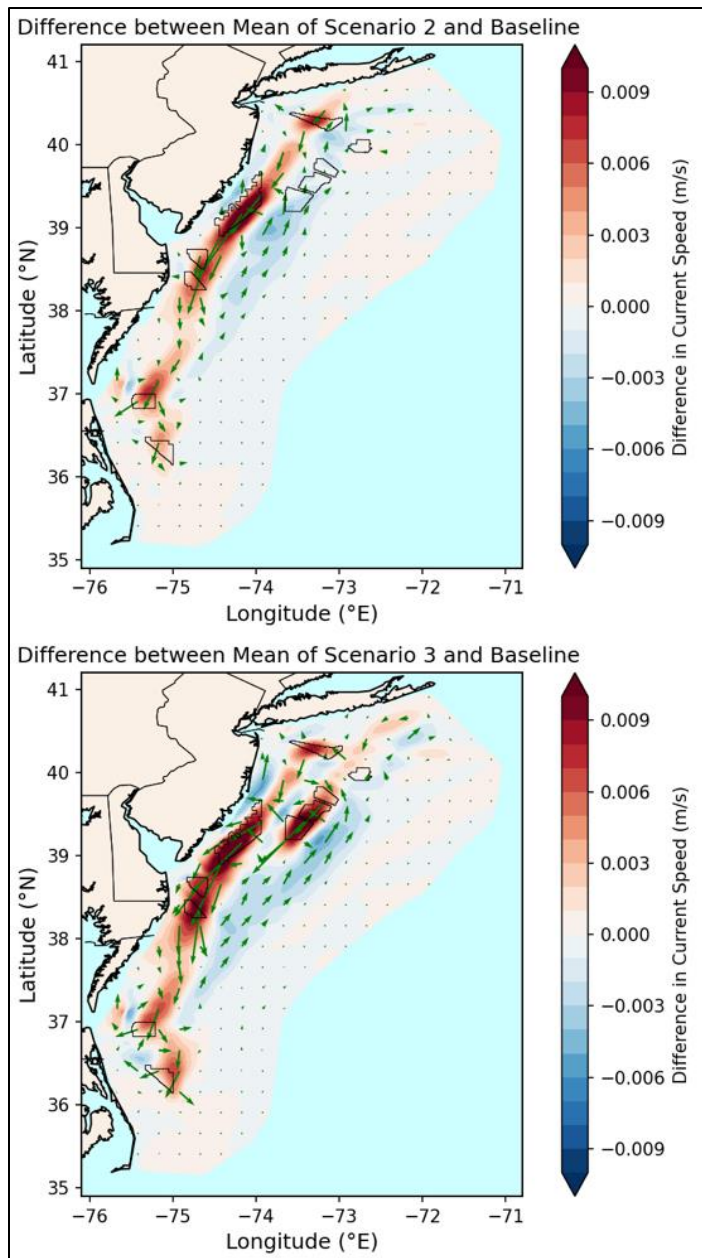


Figure 228. Difference of depth-averaged velocity between Scenario 2 and baseline (upper panel), and Scenario 3 and baseline (lower panel). The green arrows indicate the direction of the changes (vector difference) in depth-averaged velocity.

9.3 Impact Analysis at Specific Locations

Figure 225 shows locations of stations in the model domain at which time series of several parameters were extracted for more detailed analysis. In Figure 225:

- the cyan stations are located within the wind farms that are in both the partial buildout (Scenario 2) and full buildout (Scenario 3) scenarios,
- the yellow stations are within the expanded farm field of Scenario 3 but not in Scenario 2, and

- the white stations are not located within a wind farm in either scenario.

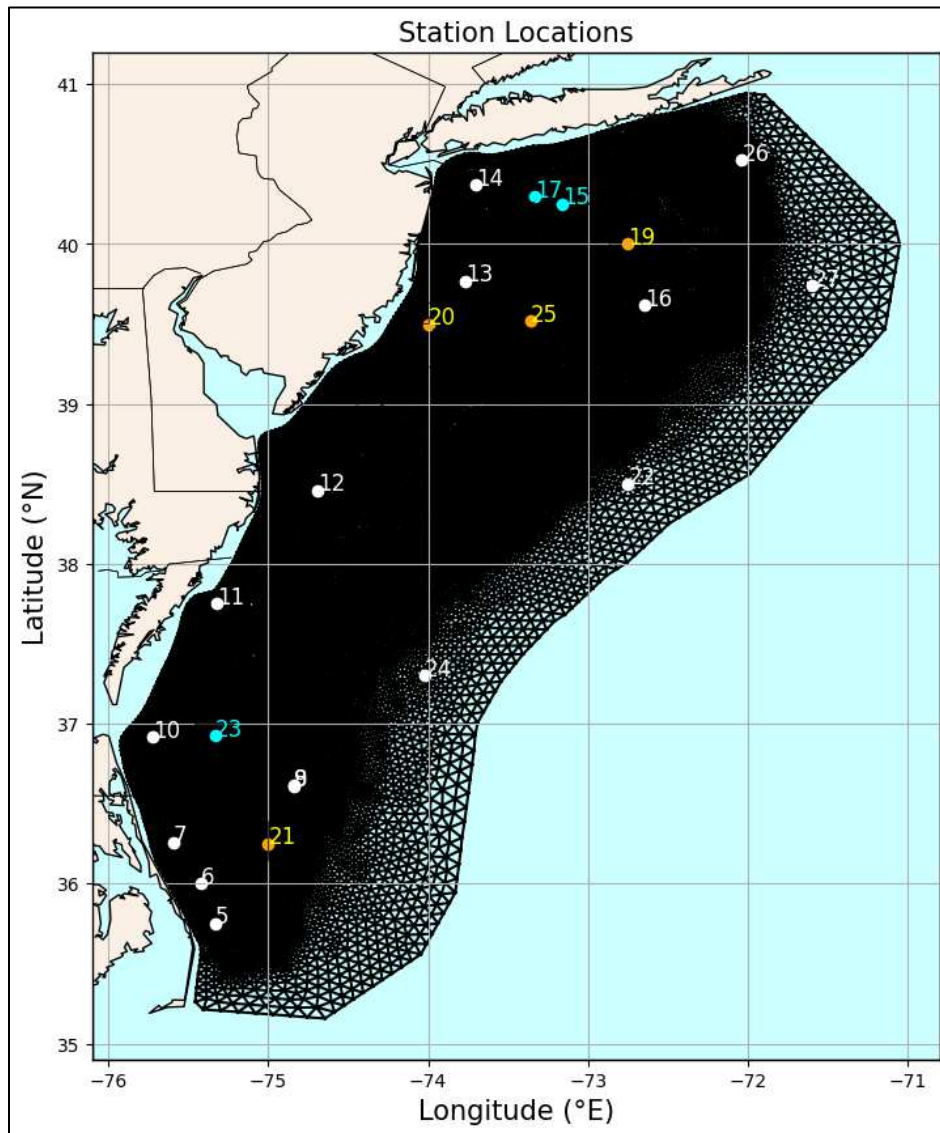


Figure 229. Locations of time series stations used in oceanographic impact analyses. Among these locations, the ones inside the WEAs (bright blue and yellow stations) are discussed in this section. The time series along with bi-annual mean and standard deviation (the average and standard deviation of all values within the two-year modeling period) for all stations in Figure 225 are provided in Appendix B. Although Figure 225 includes numbers from 5 to 27, only 21 stations are shown. This is because some of the original stations, including 8 and 18, were situated very close to each other and exhibited similar temporal variations.

9.3.1 Annualized and Seasonal Changes

To investigate impacts of WEA development to seasonal and annual-mean conditions at these locations, seasonal and annual means of model parameters were calculated from the extracted time series of the three simulated scenarios. For annualized means, all 24 simulated months were averaged together. With regard to seasonal means, and regardless of year:

- Winter considered data in December, January, and February,
- Spring in March, April, and May,
- Summer in June, July, and August, and
- Fall in September, October, November.

To test whether annualized and/or seasonal means of oceanographic parameters are simulated to differ significantly from baseline after WEA developments, we employed hypothesis testing for equality of means based on the student-t test. If the calculated t-statistic of the compared sets corresponded to a probability value (p-value) smaller or equal to 0.05, the null hypothesis of equality of means was rejected, and the differences were deemed statistically significant (at the 95% confidence level). Simulated annualized mean parameters for Scenario 1 (Baseline) and their difference between scenario 3 (Full Buildout) and Baseline for the cyan and yellow stations of Figure 225 are tabulated in Table 27. The relative percent change of simulated seasonal mean parameters between Scenario 3 (Full Buildout) and Scenario 1 (Baseline) at the same stations is tabulated in Table 28. Results for wind and current speed, water temperature and heat flux are discussed in the following sections. Analysis of the summer means for the gradient Richardson number of the surface layer, and the thermocline depth, are also included in Table 27 and are discussed in the corresponding subsections of section 9.3.2.

9.3.1.1 Mean and Seasonal Wind Speed

As winds are higher in fall through winter, maximum absolute reductions due to the simulated wind farms occurred then, compared to summer when winds tend to be weaker. Maximum reductions in the annual wind speed above 10% of baseline were found at stations 15 (S2: 10% to S3: 14%), 17 (S2 and S3: 11%), 19 (S2:1% to S3: 12%), 20 (S2:4% to S3: 13%), 21 (S2:1% to S3: 9%), 23 (S2 and S3: 11%) with max reduction at station 25 (S2:1% to S3: 16%).

9.3.1.2 Mean and Seasonal Current Speed

Maximum relative bottom current speed reductions reached up to 5-6% annually at stations 15, 25, and 12 (S3), though most reductions at other stations were less than 1%.

Annual mean surface current speeds increased offshore New Jersey (stations 12, 13, and 20) up to 6–7%, as well as at stations 21 and 23 near the southern WEAs (2-3% for S3), although they were weaker at some other points. On the other hand, by far the strongest surface current weakening is at station 15, up to -8% for S3, yet the depth-averaged current increased somewhat there as well. The depth-averaged current was mostly stronger in scenarios with WEAs at the stations, with peak increase around 6% at stations 13 and 20, and 4% at station 17. It was weaker by 1% at station 19. Results are consistent with the changes in the mean currents seen in Figure 224.

9.3.1.3 Mean and Seasonal Temperature

Mean annual and seasonal surface temperatures increase in simulations with developed WEAs compared to the baseline, more in Scenario 3 than Scenario 2. In absolute terms the increase is higher in the summer at most stations, and in the winter and spring at some stations. Surface waters are colder in the winter, and, in relative terms, highest % increases compared to baseline conditions are simulated for that season. They reach as high as 4% of baseline at station 15, from 8.89° C to 9.24° C in winter. Out of all stations evaluated, the highest simulated seasonal surface temperature increase is from 20.9° C to 21.5° C at station 25 in the summer, a 0.6° C change in surface temperature there in Scenario 3 compared to baseline. At these two stations, annual mean surface temperatures increase by 0.2° C at Station 15 and 0.3° C at Station 25. Stations 17 and 20 also see their annual surface temperatures increase by about 0.2° C. These four stations are all within northern WEAs in Scenario 3.

Simulated changes in mean seasonal bottom temperatures vary by station and season and are generally smaller than at surface. As with surface temperatures, highest relative changes are found in the winter at stations 15 (+3%) and 20 (+4%) located within WEAs in Scenario 3 but are lower at other stations. Changes in annual mean bottom temperatures are usually within a percent of baseline.

9.3.1.4 Mean and Seasonal Heat Flux

Statistically significant changes in the seasonal means of surface heat fluxes in the scenarios with developed WEAs compared to baseline conditions are found mostly in seasons with stronger winds (fall-winter-spring) with lesser changes in the spring, and mostly on the stations that are closer to WEAs. As expected, statistically significant differences in the seasonal means were only found for sensible, evaporative, and total heat flux, and not in solar influx nor longwave back radiation.

The seasonal mean of the sensible surface heat flux over the shelf (all stations in Figure 229, except for 22, 24, and 27) is positive (incoming) in the spring and summer when the atmosphere is warmer than the ocean, and becomes negative (outgoing) in (mid-) fall and over the winter when the atmosphere is colder. With wind farms present (Scenarios 2 and 3), the sensible surface heat fluxes weaken at most stations, becoming less positive in the spring and summer, and less negative in the fall and winter. Accumulated over the two years, the change in sensible heat flux at most stations is cooling, from the ocean to the atmosphere (it becomes more negative in Table 27).

The seasonal mean of evaporative surface heat flux is always negative, with peaks in fall (primarily) and winter; the exception is that it can be positive at stations closest to the Gulf Stream in the spring. With wind farms present (scenarios 2 and 3), the evaporative flux showed a tendency to become proportionally less negative in the fall, winter, and spring, and more negative in the summer. Accumulated over the two years, the change in evaporative heat flux is warming, from the atmosphere to the ocean.

The total heat flux is positive (incoming) in the spring and summer and becomes negative (outgoing) in the fall and over the winter. The most significant changes in total surface heat flux between the scenarios with developed WEAs against baseline, mostly associated with the - greater, compared to the other terms - changes in evaporative heat flux, is a decrease in the outgoing total heat flux in the fall and winter, followed by a smaller decrease in the incoming total heat flux in the spring and/or summer, at most stations. Accumulated over the two years, the mean effect is a tendency to reduce the magnitude (exchange strength, either net incoming or outgoing) of total surface heat flux.

Table 27. Simulated annualized mean Scenario 1 (Baseline) parameters and their difference between Scenario 3 (Full buildout) and Scenario 1 at 7 of the stations shown in Figure 225.

Station #	15	15	17	17	19	19	20	20	21	21	23	23	25	25
	S1 = Baseline	Delta (S3-S1)												
Surface T	14.12	+0.24	13.84	+0.16	14.69	+0.13	14.07	+0.19	18.53	-0.03	16.37	+0.06	14.25	+0.32
Bottom T	9.72	+0.11	10.30	+0.12	9.84	+0.01	11.39	+0.07	15.85	-0.04	14.07	-0.07	10.52	+0.04
Wind speed	6.961	-0.965	6.766	-0.768	7.190	-0.843	6.282	-0.830	6.708	-0.594	6.558	-0.734	7.028	-1.145
Surface Cur	0.093	-0.007	0.092	+0.001	0.092	-0.006	0.122	+0.009	0.167	+0.004	0.140	+0.002	0.116	-0.002
Bottom Cur	0.032	-0.001	0.034	-0.001	0.037	+0.000	0.045	+0.001	0.064	-0.001	0.053	-0.001	0.042	-0.002
D-Ave Cur	0.060	+0.000	0.063	+0.003	0.058	-0.001	0.079	+0.005	0.114	+0.001	0.092	+0.002	0.073	+0.000
Sensible	-10.1	-0.7	-8.3	-0.6	-11.9	-0.2	-2.0	-2.5	-0.4	+1.0	+3.3	-1.2	-2.3	-3.1
Evaporative	-58.3	+5.5	-53.7	+4.2	-62.8	+4.7	-42.8	+1.0	-53.3	+5.8	-41.9	+3.1	-46.8	+2.2
Total HF	-10.1	+3.0	-2.7	+2.5	-16.8	+3.5	+23.0	-2.6	+16.0	+6.9	+40.3	+1.5	-17.4	-2.6
Richardson*	1.78	+1.36	1.27	+0.20	0.50	+1.30	-	-	2.22	+1.00	0.15	+0.01	0.08	+0.25
Therm. D*	12.23	-0.50	11.06	-0.27	12.96	-0.30	9.29	-0.06	9.67	-1.04	10.06	-0.11	11.60	-0.61

S1=Baseline: Annualized (2-simulated-year) mean of baseline (Scenario 1) conditions. Delta (S3-S1): Difference between annualized mean of Scenario 3 (Full buildout) and Scenario 1 (Baseline).

Changes that are not statistically significant at the 95% level ($p > 0.05$) are denoted with hyphen (-).

Explanation of columns: Surface T: Surface Temperature, °C. Bottom T: Bottom Temperature, °C. Surface Cur: Surface Current Speed, m/s. Bottom Cur: Bottom Current Speed, m/s. D-Ave Cur: Depth-Averaged Current Speed, m/s. Sensible: Sensible Heat Flux, W/m². Evaporative: Evaporative Heat Flux, W/m². Total HF: Total Heat Flux, W/m². Richardson: Gradient Richardson number (Summer only). Therm. D: Thermocline depth, m from surface (Summer only).

* Summer Only

Table 28. Relative percent increase (+) or decrease (-) of simulated seasonal mean parameters between Scenario 3 (Full buildout) and Scenario 1 (Baseline) at 7 of the stations shown in Figure 225.

Station #	15	15	15	15	17	17	17	17	19	19	19	19	20	20	20	20	21	21	21	21	23	23	23	23	25	25	25	25
Season	W	Sp	Su	F																								
Surface T	+4	+3	+1	+1	+2	+2	+1	-	+1	+1	+1	+1	+2	+1	+2	+1	+0	-1	-	+0	-	-	+1	-	+2	+3	+3	+1
Bottom T	+3	+2	+1	+0	+2	+2	+2	-	+1	-1	-	-	+4	+1	-1	-	-	-1	+0	-	+0	-	-2	-	+2	+1	-1	-
Wind speed	-13	-14	-16	-13	-11	-11	-13	-11	-10	-12	-15	-11	-10	-13	-19	-12	-9	-9	-11	-7	-10	-11	-14	-10	-14	-16	-22	-15
Surface Cur	-16	-6	+8	-15	-4	+2	+6	-2	-11	-8	-	-5	-4	+9	+17	+3	-2	+3	+7	+2	-4	-	+10	+1	-12	-7	+17	-5
Bottom Cur	-	-8	-3	-6	-	-3	-5	-4	-	-2	-1	-2	+2	+3	-2	-	-	-3	-	-	-	-3	-4	-2	-8	-4	-	-7
D-Ave Cur	-2	-1	+10	-7	+4	+5	+8	+2	-2	-3	+1	-2	-	+8	+13	+4	-	-	+5	-	-2	-	+8	-	-9	-3	+26	-6
Sensible	-4	-30	-37	-9	-5	-24	-29	-8	-7	-28	-38	-	+15	-31	-36	-	-17	+16	-10	-18	-	-13	-22	-7	-	-43	-43	-
Evaporative	-9	-6	-	-13	-8	-4	+3	-11	-9	-5	-	-8	-	-	+17	-7	-12	-14	-	-9	-9	-8	+4	-9	-10	-	+61	-11
Total HF	-3	-	-4	-13	-4	-	-4	-11	-6	-	-	-8	-	-5	-6	-7	-11	+12	-	-20	-7	-	-3	-16	-5	-7	-10	-11

W: Winter (Dec-Feb). Sp: Spring (Mar-May). Su: Summer (Jun-Aug). F: Fall (Sep-Nov).

Percent values shown are rounded to nearest integer.

Changes that are not statistically significant at the 95% level ($p > 0.05$) are denoted with hyphen (-).

Explanation of columns: Surface T: Surface Temperature. Bottom T: Bottom Temperature. Surface Cur: Surface Current Speed. Bottom Cur: Bottom Current Speed. D-Ave Cur: Depth-Averaged Current Speed. Sensible: Sensible Heat Flux. Evaporative: Evaporative Heat Flux. Total HF: Total Heat Flux.

9.3.2 Impacts at Weekly Timescale Relative to Baseline Variability

To analyze temporal and spatial variation of windfarm effects on oceanographic parameters, time series of weekly means for the different scenarios and the weekly z-score statistic were calculated for different locations across the model. The z-score, a statistical measure of the relative difference between the weekly mean of a parameter between a scenario and the baseline, normalized over the weekly variability in the baseline (the present natural variability of each week), was calculated using the following formula:

$$Z_{scenario-baseline} = \frac{\bar{X}_{scenario} - \bar{X}_{baseline}}{\sigma_{baseline}} \quad \text{Eq. 6}$$

where:

$Z_{scenario-baseline}$
= Z - score based on the difference of a Scenario (2 or 3) and the baseline (Scenario 1)

$\bar{X}_{scenario}$
= Weekly mean value of scenario

$\bar{X}_{baseline}$
= Weekly mean value of baseline

and $\sigma_{baseline}$ = Weekly standard deviation of baseline

A significant z-score indicates the magnitude of the windfarm effects on the weekly mean is comparable to the temporal variability of the baseline conditions for that week of the year.

The scenario evaluated above is either Scenario 2 (partial buildout) or Scenario 3 (full buildout). Note that the sign of the z-score reveals the increase (positive) or decrease (negative) of a weekly mean parameter in a scenario against baseline, but its magnitude depends on the variability of the natural condition (baseline) within a specific week. Thus, greater weekly z-score magnitudes do not necessarily translate to greater absolute changes in a weekly-mean parameter value.

To quantify the instances the z-score value exceeds 95th percentile and is significantly different than present natural (baseline) weekly variability at that level, Table 29 and Table 30 list the percentage of time when the z-score is beyond ± 1.96 for Scenario 2-baseline, and Scenario 3-baseline, respectively. The parameters shown in the tables are wind speed, current speed, water temperature, turbulent vertical eddy viscosity, turbulent kinetic energy, gradient Richardson number (a measure of water column stability, explained in Section 9.3.2.6), thermocline depth and thermocline depth. The heat flux parameters are not shown in the tables as for them the z-score never exceeded the 95th percentiles (see Section 9.3.2.3 below). The tables illustrate how, for temperature, the increased instances of z-scores exceeding ± 1.96 at certain stations (e.g., stations 15 and 17) affect the thermocline in both Scenario 2 and Scenario 3. In terms relative to transient weekly natural variability, the impact of the wind farms is found to mostly influence stability (Richardson number), water temperatures, and thermocline depth. Note however, that current speed here includes the main tidal component, while, and as mentioned earlier, tidal residual flows are the ones most impacted by the wind farms.

Also note that, on a mean bi-annual basis (for the 24-month period treated) relatively smaller changes can be seen in other variables. For some parameters and some stations, these changes in the mean z-scores are sometimes consistently positive or negative throughout seasonal to annual time scales (Tables 27 and Table 28), and though they may tend to be small relative to intra-week variability, that is not always the case against interannual variability. An example is mean annual surface water temperature, which, as

mentioned, may surpass a quarter degree Celsius in some stations, in simulations with wind turbines, a change that is approaching the order of magnitude expected because of long-term climate forcing.

Table 29. Percentage of weeks that the z-score exceeds 95th percentile for Scenario 2 - baseline.

Station	Wind Speed	Current Speed	Current Speed	Current Speed	Temp	Temp	Viscosity	Viscosity	TKE	TKE	Ri	Ri	Thermocline	Thermocline
-	-	Surface	Bottom	Depth-Averaged	Surface	Bottom	Surface	Bottom	Surface	Bottom	Surface	Bottom	Depth	Strength
6											1	1		
7												1		
9														1
10						1.9								1
12						1.9							1.9	1
13													1	1
14										1			1.9	
15	1	1			7.6	13.3							11	3.8
16													1	
17		1		1.9	1.9	5.7							9.5	
19													1.9	1
20						1								1
21											1		1	
23		1.9				5.7	1		1		4.8		2.9	
24														1
25												1	1	

Note: Only stations with > 0% for any parameter are shown. For the remaining listed stations, only parameters with > 0% are shown.
 TKE = Turbulent Kinetic Energy. Ri = Richardson number.

Table 30. Percentage of weeks that the z-score exceeds 95th percentile for Scenario 3 - baseline.

Station	Wind Speed	Current Speed	Current Speed	Current Speed	Temp	Temp	Viscosity	Viscosity	TKE	TKE	Ri	Ri	Thermocline	Thermocline
-	-	Surface	Bottom	Depth-Averaged	Surface	Bottom	Surface	Bottom	Surface	Bottom	Surface	Bottom	Depth	Strength
5														1
6												1		
7						1						1		
9												1	1	1
10						1								1
11												1		
12						7.6							1.9	3.8
13						4.8							1.9	2.9
14						2.9							1.9	
15		1		1	14.3	18.1					1		11.4	6.7
16		1									1.9		3.8	
17		1		1	4.8	15.2					1		8.6	1.9
19		1			1.9	5.7			1		4.8		5.7	3.8
20		2.9			1.9	16.2					1	1.9	2.9	4.8
21						1					5.7	1	2.9	
23		1				7.6	1		1		1.9		2.9	1
24														1
25		1.9		5.7	5.7	7.6					1.9		7.6	6.7
26											1			1

Note: Only stations with > 0% for any parameter are shown. For the remaining listed stations, only parameters with > 0% are shown.
 TKE = Turbulent Kinetic Energy. Ri = Richardson number.

The following subsections present time series plots showing detailed results for the full range of parameters. In the figures, months when the water column is typically vertically mixed (November to March, inclusive) are highlighted with gray to visually separate them from transition and stratified months (April to October) of the seasonal cycle of the Mid-Atlantic Bight cold pool.

9.3.2.1 Effects on Surface Wind and Currents

Wind speed and current (surface, bottom, and depth-averaged) magnitude time series for stations located in the WEAs are presented in Figure 226 - Figure 232. The top left panels of these figures show that winds are stronger during the autumn and winter season (from October to March), when they contribute to destratification and mixing. Yet, except perhaps at the station closest to the NY Bight Apex (Station 17, Figure 227), the larger differences in current speeds due to WEA development are seen during the spring and summer, when the MAB shelf is stratified. The change in magnitude (left panels) and difference time series (middle and right panels) for wind speed both are consistent with both Scenario 2 and 3 experiencing reduction in wind speed compared to baseline due to wind wakes (as also seen in Table 27 and Table 28 and discussed in Section 9.3.1).

The differences in current speed (primarily depth-average and surface current) show both positive and negative peaks. In the difference plots the surface and depth-averaged currents show more positive peaks compared to bottom-current which is more decoupled from the wind stress changes, and there is a small net decrease in bottom current speed, consistent with Table 27 and Table 28.

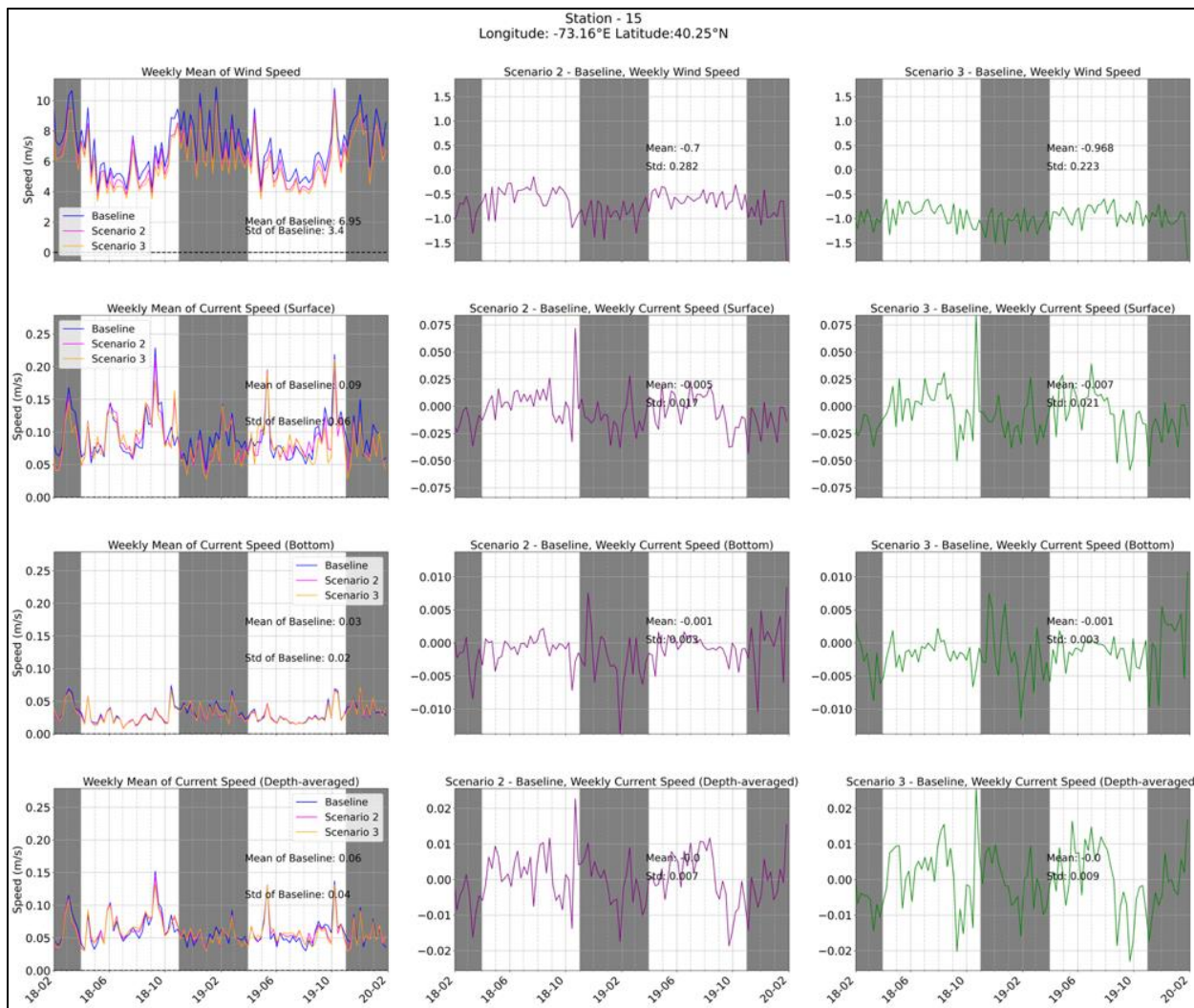


Figure 230. Weekly mean (left panels), and weekly differences for Scenario 2-baseline (middle panels) and Scenario 3-baseline (right panels) for wind speed and current speed (surface, bottom, and depth-averaged) at station 15.

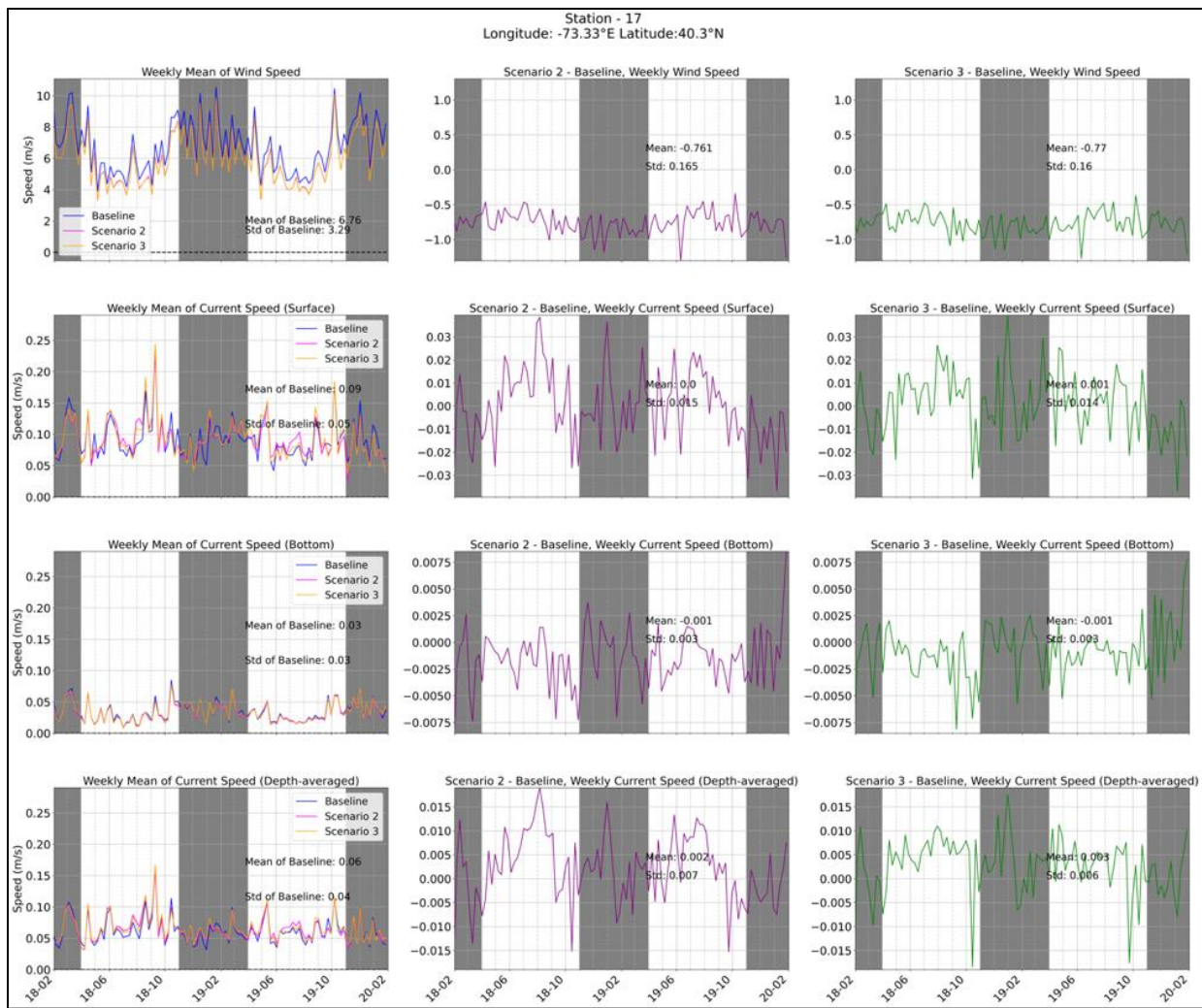


Figure 231. Weekly mean (left panels), and weekly differences for Scenario 2-baseline (middle panels) and Scenario 3-baseline (right panels) for wind speed and current speed (surface, bottom, and depth-averaged) at station 17.

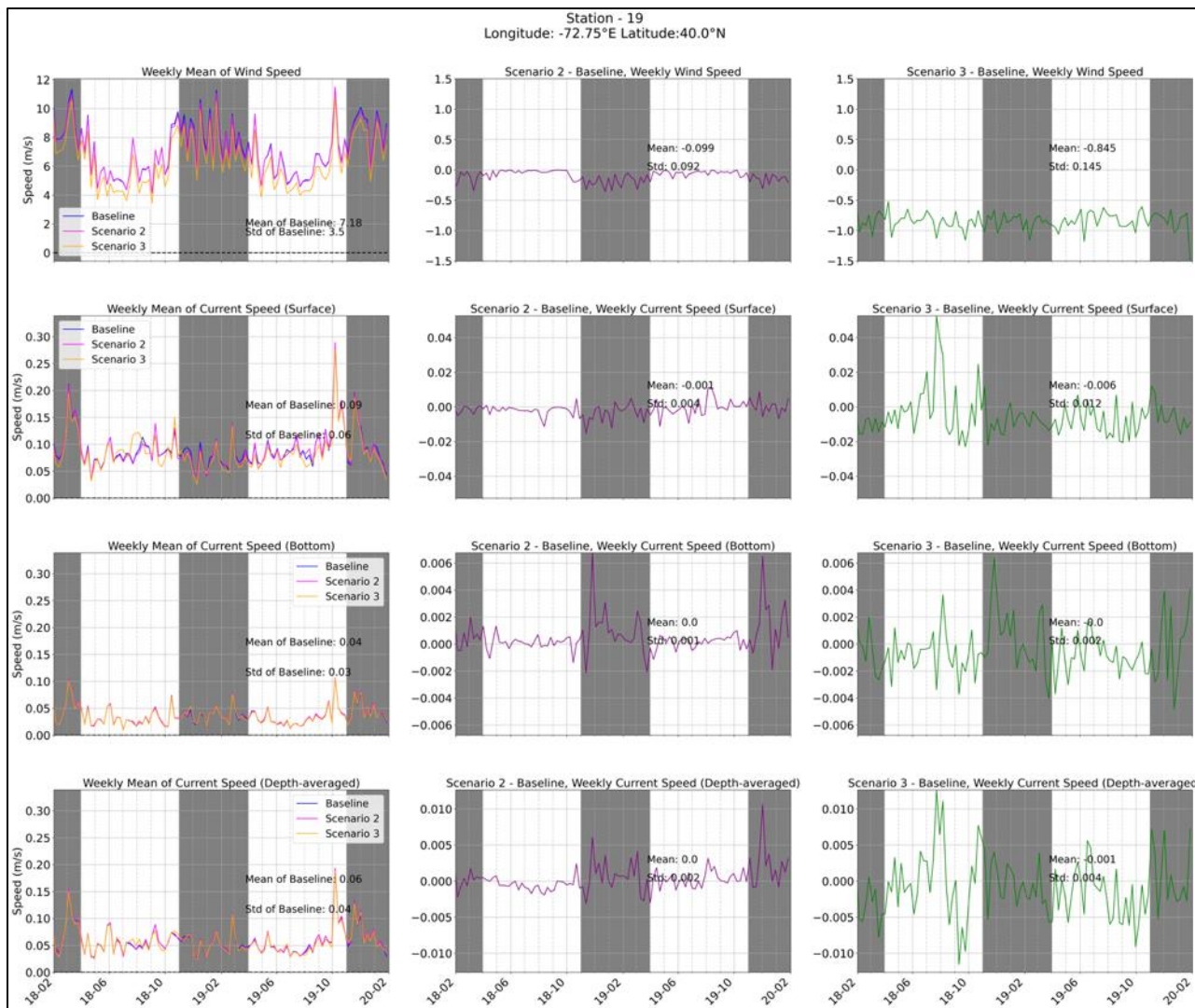


Figure 232. Weekly mean (left panels), and weekly differences for Scenario 2-baseline (middle panels) and Scenario 3-baseline (right panels) for wind speed and current speed (surface, bottom, and depth-averaged) at station 19.

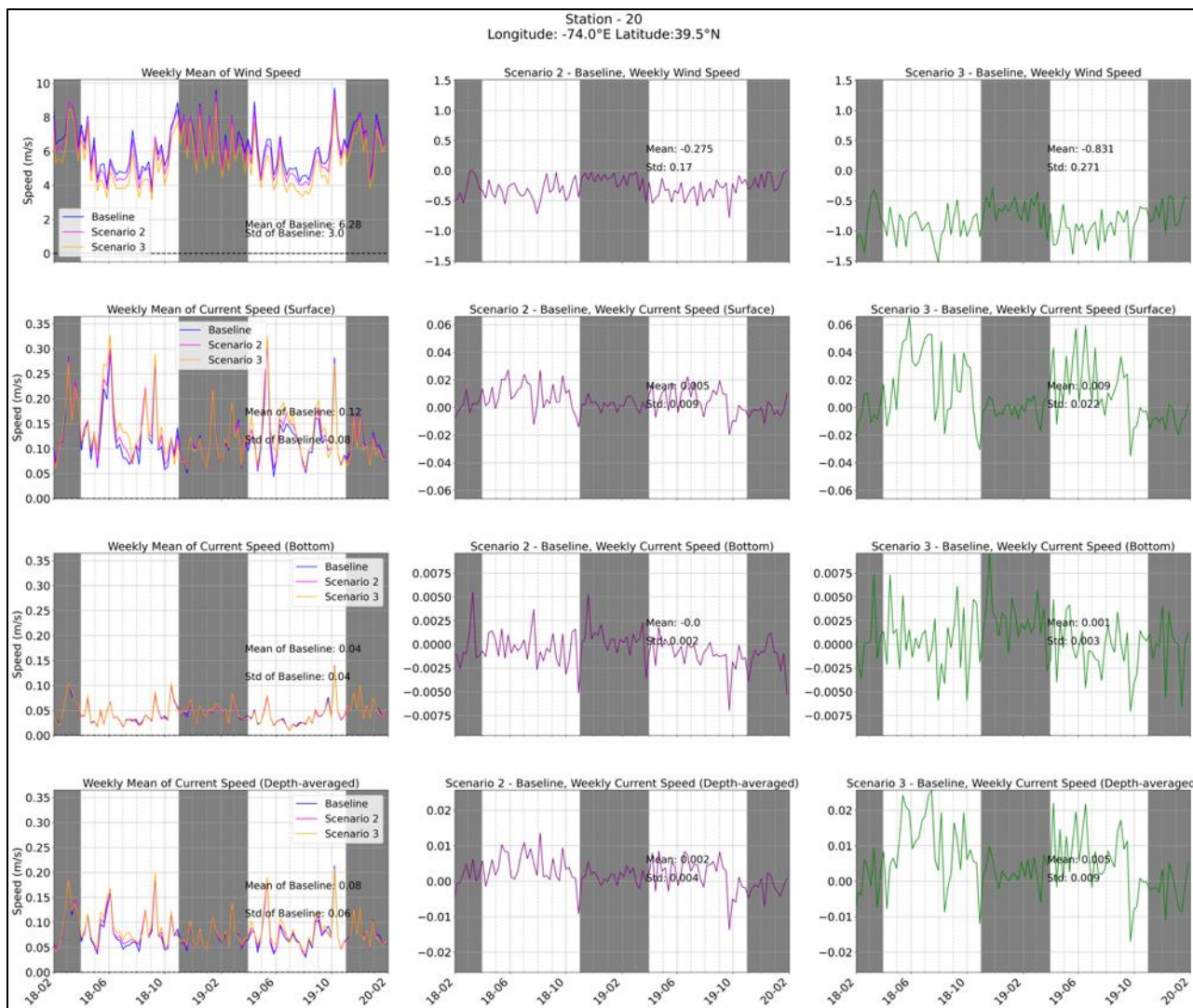


Figure 233. Weekly mean (left panels), and weekly differences for Scenario 2-baseline (middle panels) and Scenario 3-baseline (right panels) for wind speed and current speed (surface, bottom, and depth-averaged) at station 20.

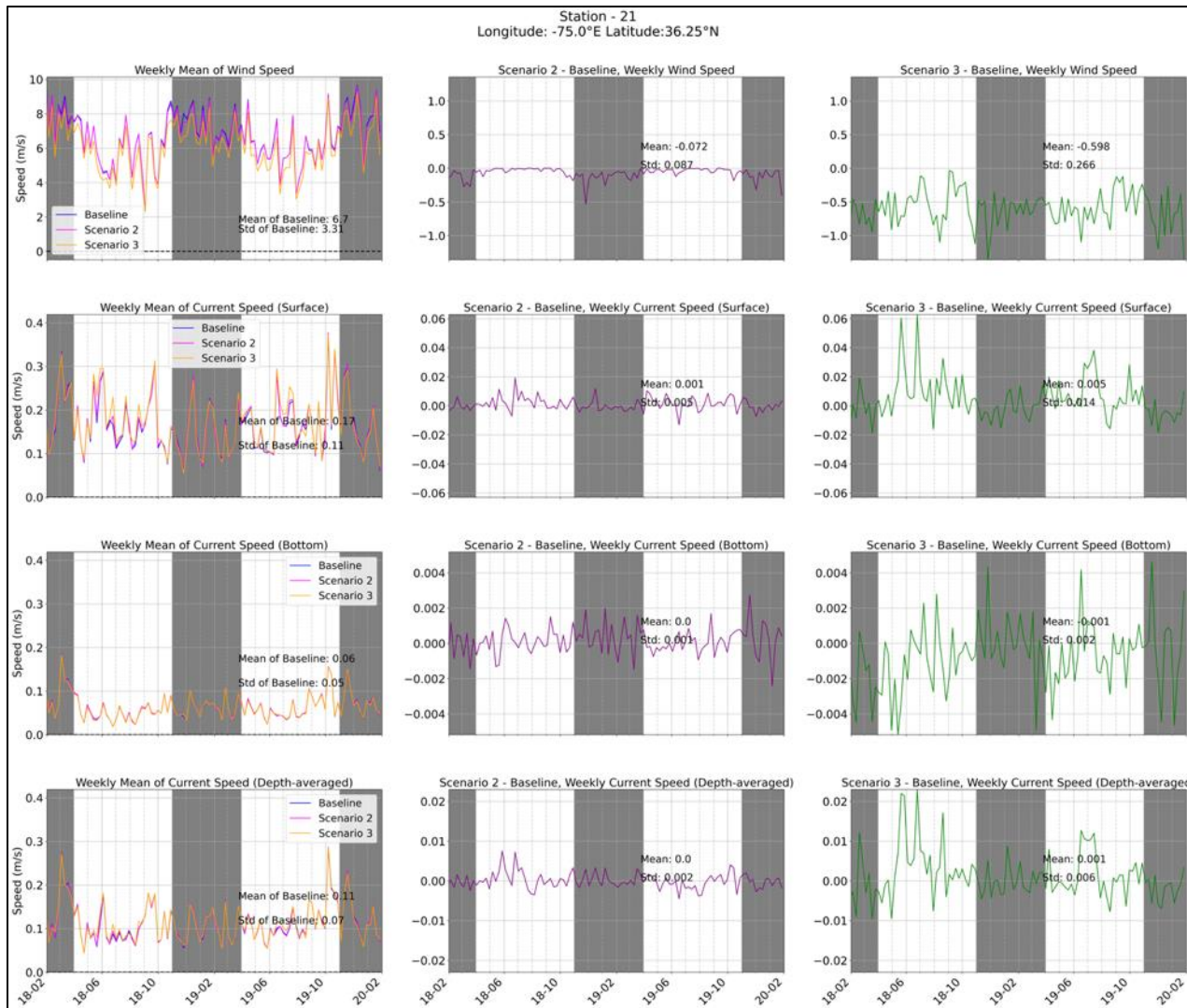


Figure 234. Weekly mean (left panels), and weekly differences for Scenario 2-baseline (middle panels) and Scenario 3-baseline (right panels) for wind speed and current speed (surface, bottom, and depth-averaged) at station 21.

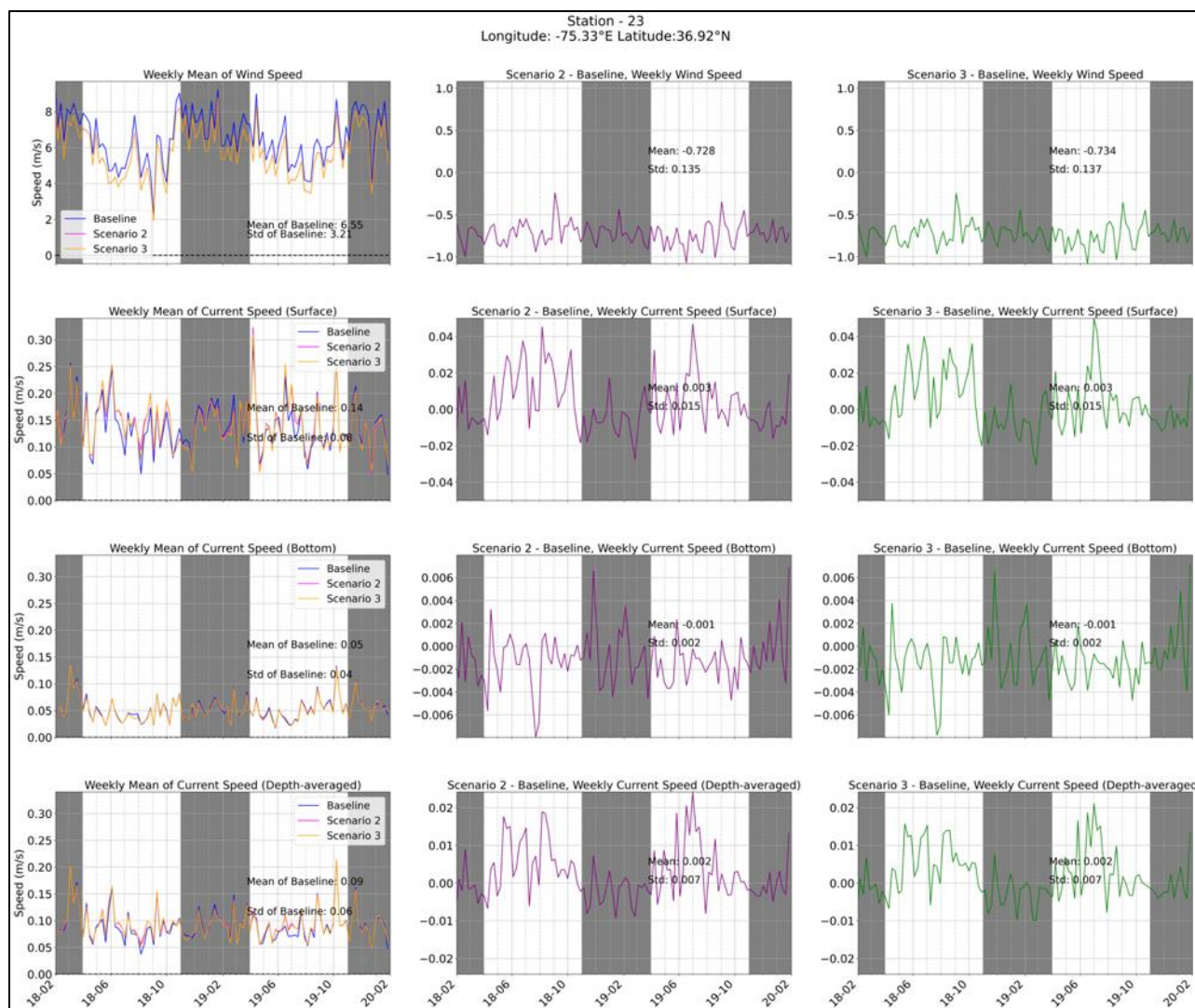


Figure 235. Weekly mean (left panels), and weekly differences for Scenario 2-baseline (middle panels) and Scenario 3-baseline (right panels) for wind speed and current speed (surface, bottom, and depth-averaged) at station 23.

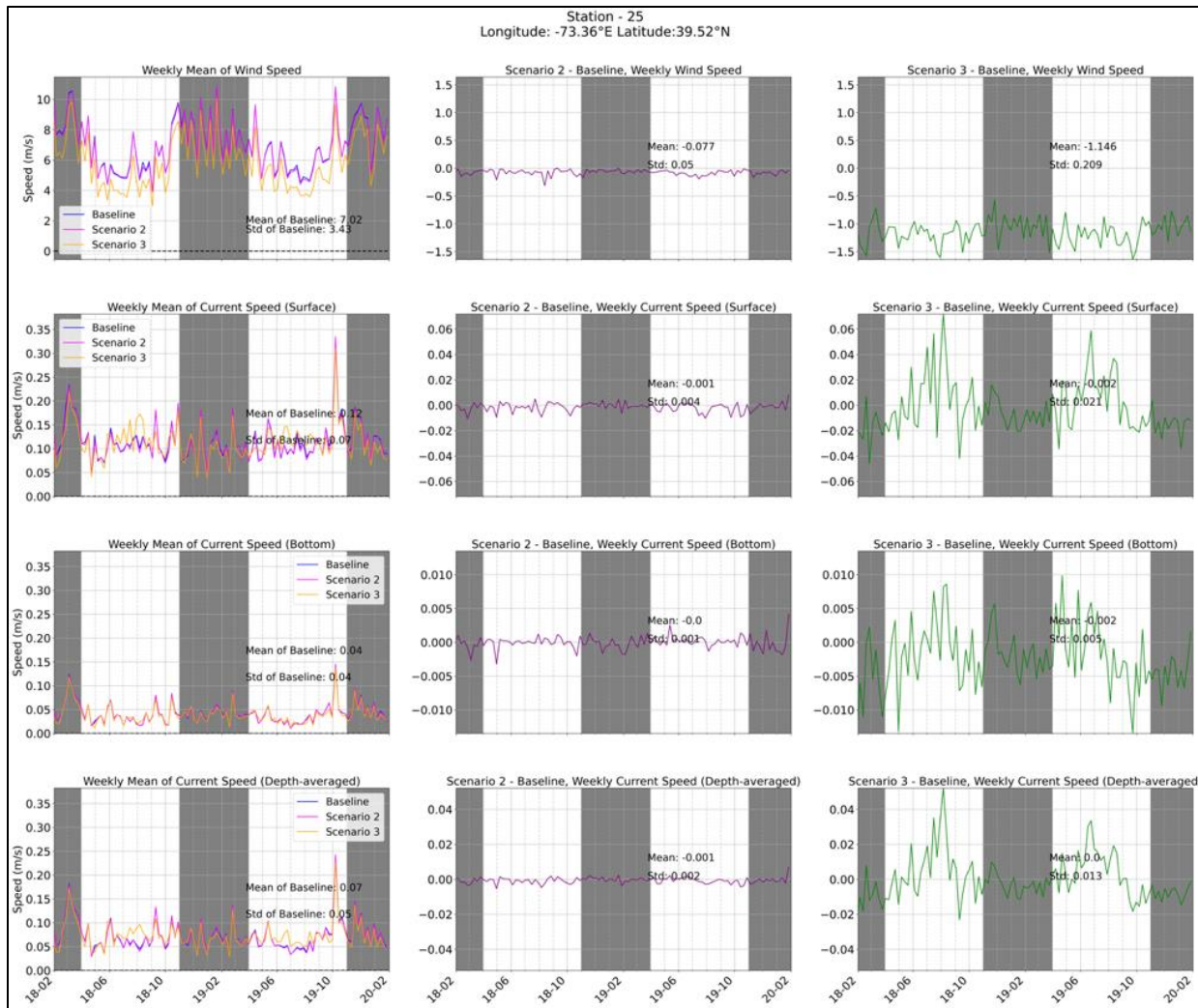


Figure 236. Weekly mean (left panels), and weekly differences for Scenario 2-baseline (middle panels) and Scenario 3-baseline (right panels) for wind speed and current speed (surface, bottom, and depth-averaged) at station 25.

9.3.2.2 Effects on Water Temperature

Simulated surface and bottom temperature time series at stations located in the WEAs are presented in Figure 233 to Figure 239. Overall, and for both baseline conditions but also the two wind farm development scenarios, surface temperatures tend to rise in April–June (resulting in higher weekly natural variability), peak in the summer for both years (2018 and 2020), start falling between August–September until mid-winter and be at their lowest between February and March. Bottom waters warm slower and reach their peak in early fall (September–October) after which time overturning occurs and bottom temperatures drop following surface cooling.

Comparing wind farm scenarios and baseline, Scenario 3 (full buildout) has greater magnitude changes from baseline compared to Scenario 2 (partial buildout). A rise in SST is simulated by the model, which can at times reach about 1° C at stations 20 and 25 east of the NJ Shore for full-buildout conditions under Scenario 3. Station 25 also exhibits the highest annualized increase in SST at 0.32° C for Scenario 3 (Table 27). The difference panels also show positive peaks across the two years for surface temperature, and increasingly so between Scenario 2 and Scenario 3, especially at stations with wind turbines only in Scenario 3. The exception is the southern-most station of the ones shown, station 21, where the differences from baseline are small (Table 27), and the differences fluctuate the least from week to week. In general, the difference panels for surface temperature mostly show positive weekly peaks with few exceptions. For bottom temperature, they show both positive (relative warming) and negative (relative cooling) peaks. Stations 15 (Figure 233), 17 (Figure 234), and 23 (Figure 238) appear in WEAs of both scenarios (Scenario 2 and 3) the differences do not change significantly going from Scenario 2-baseline to Scenario 3-baseline. However, the rest of the stations (shown by yellow in Figure 225) show different variations.

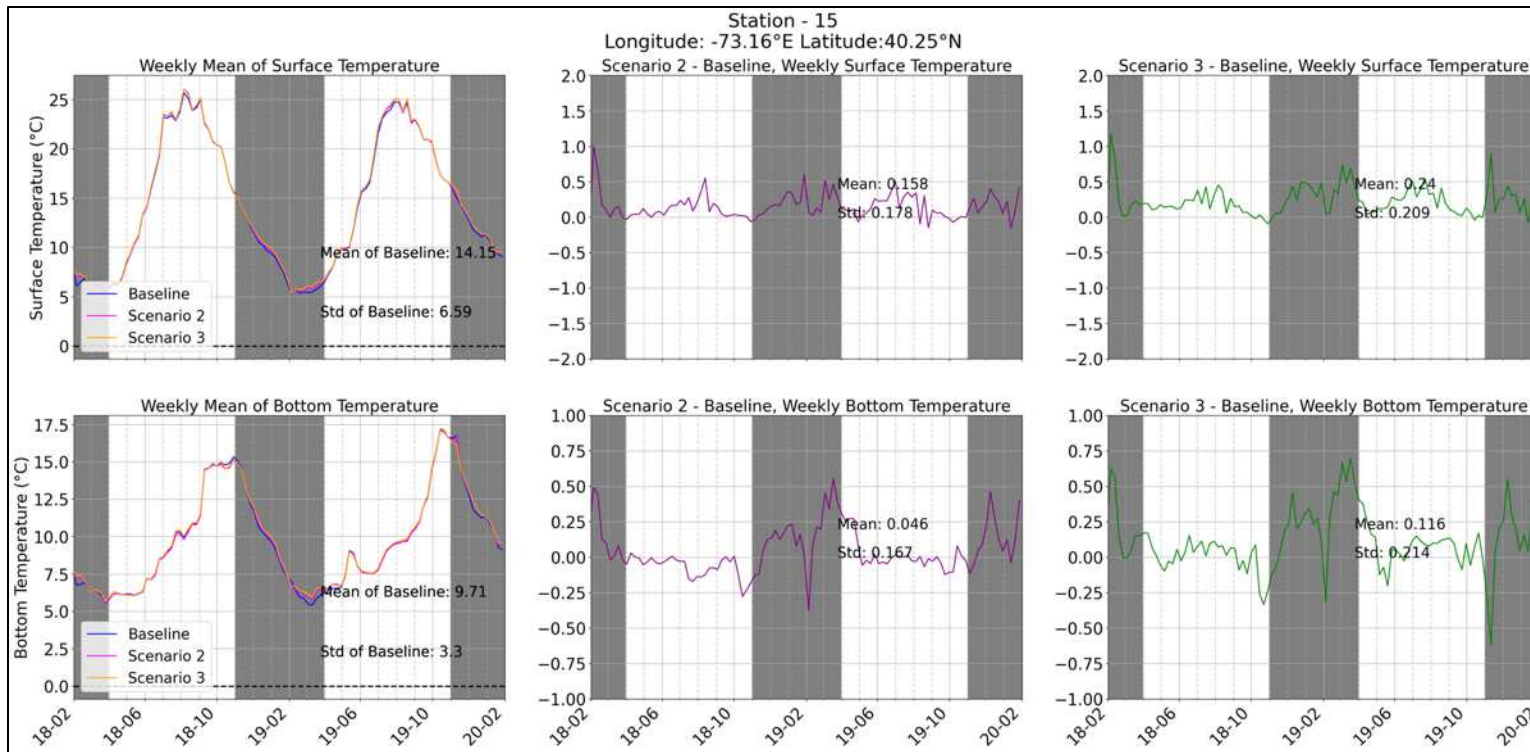


Figure 237. Weekly mean (left panels), and weekly differences for Scenario 2-baseline (middle panels) and Scenario 3-baseline (right panels) for surface (upper panels) and bottom temperature (lower panels) at station 15.

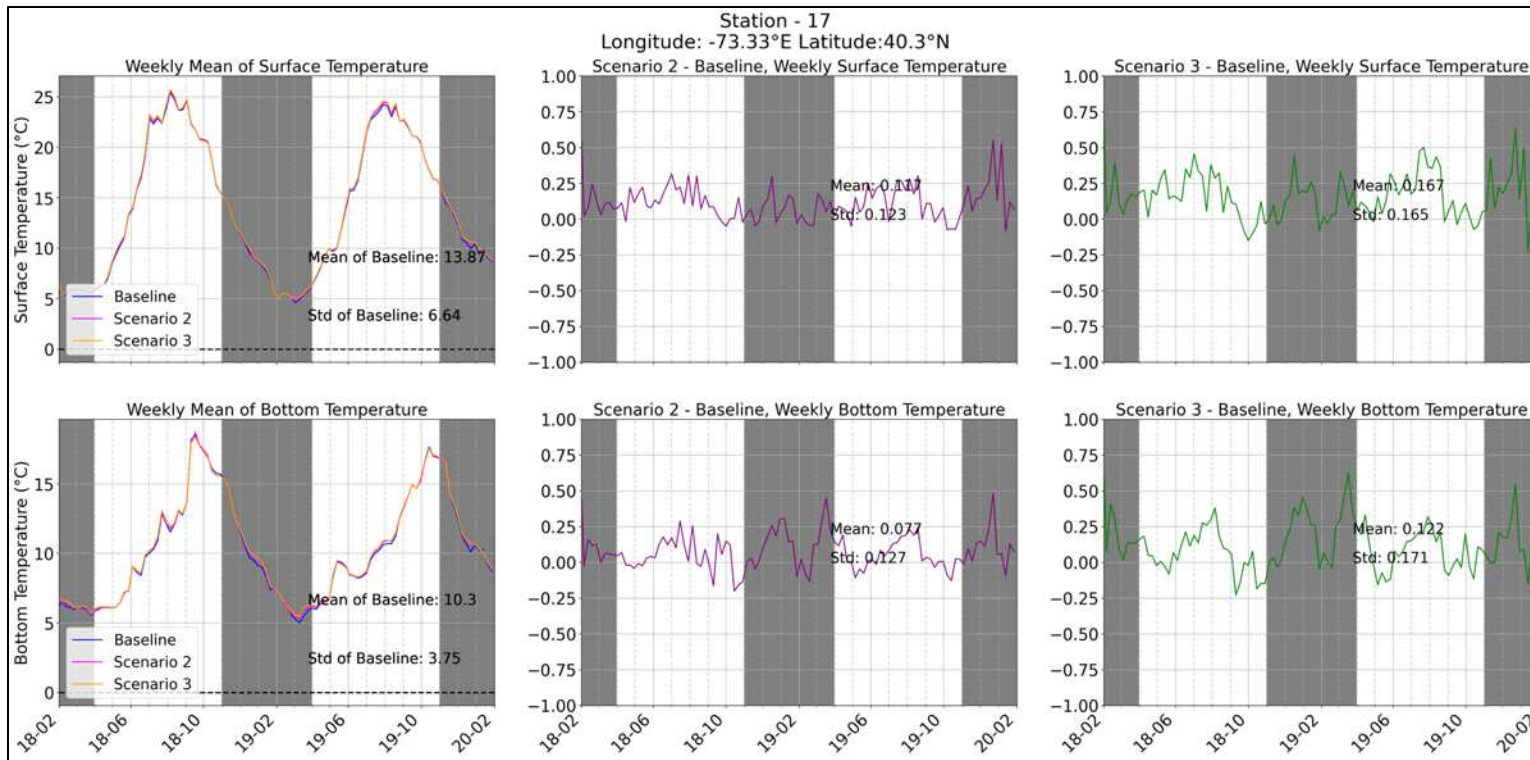


Figure 238. Weekly mean (left panels), and weekly differences for Scenario 2-baseline (middle panels) and Scenario 3-baseline (right panels) for surface (upper panels) and bottom temperature (lower panels) at station 17.

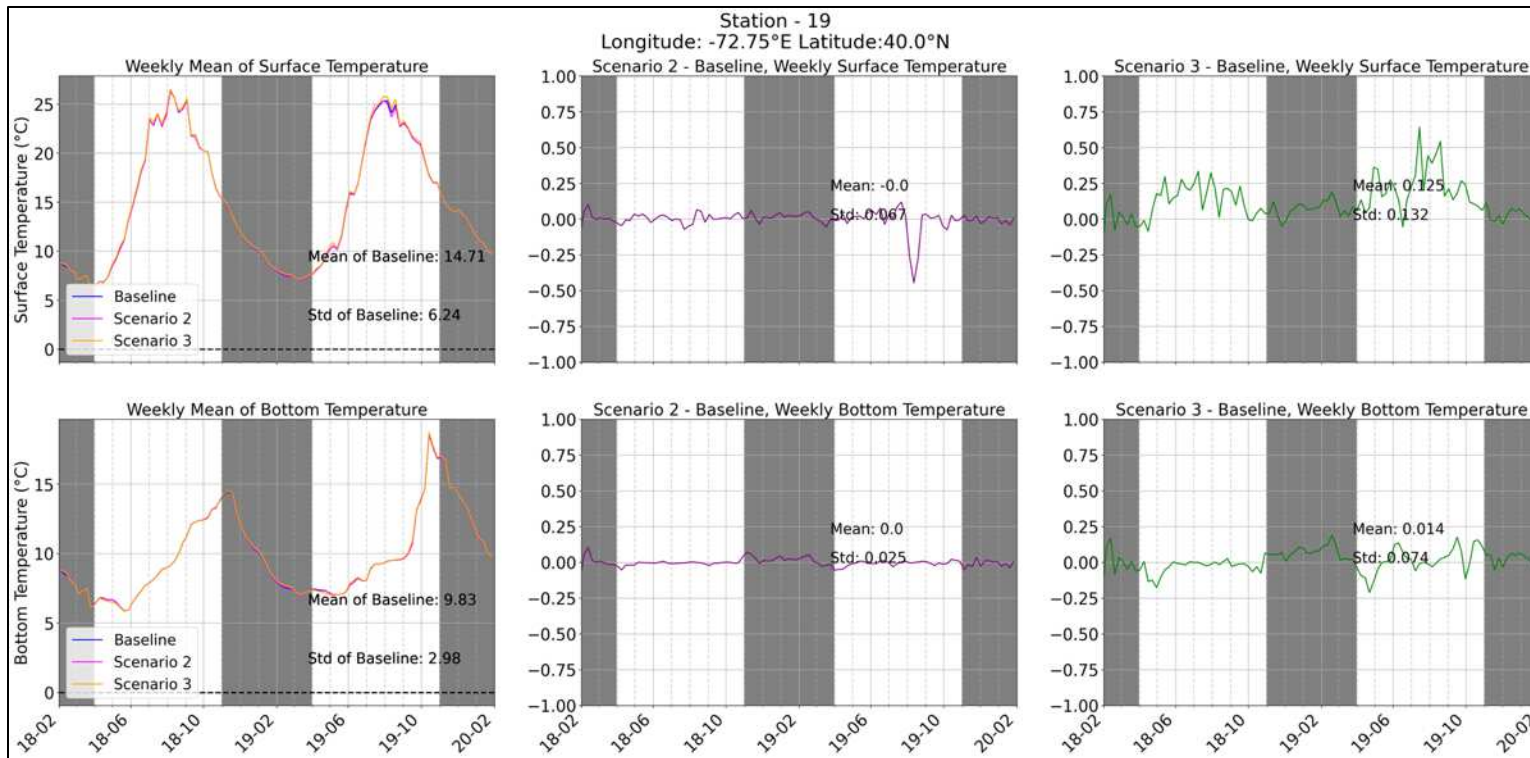


Figure 239. Weekly mean (left panels), and weekly differences for Scenario 2-baseline (middle panels) and Scenario 3-baseline (right panels) for surface (upper panels) and bottom temperature (lower panels) at station 19.

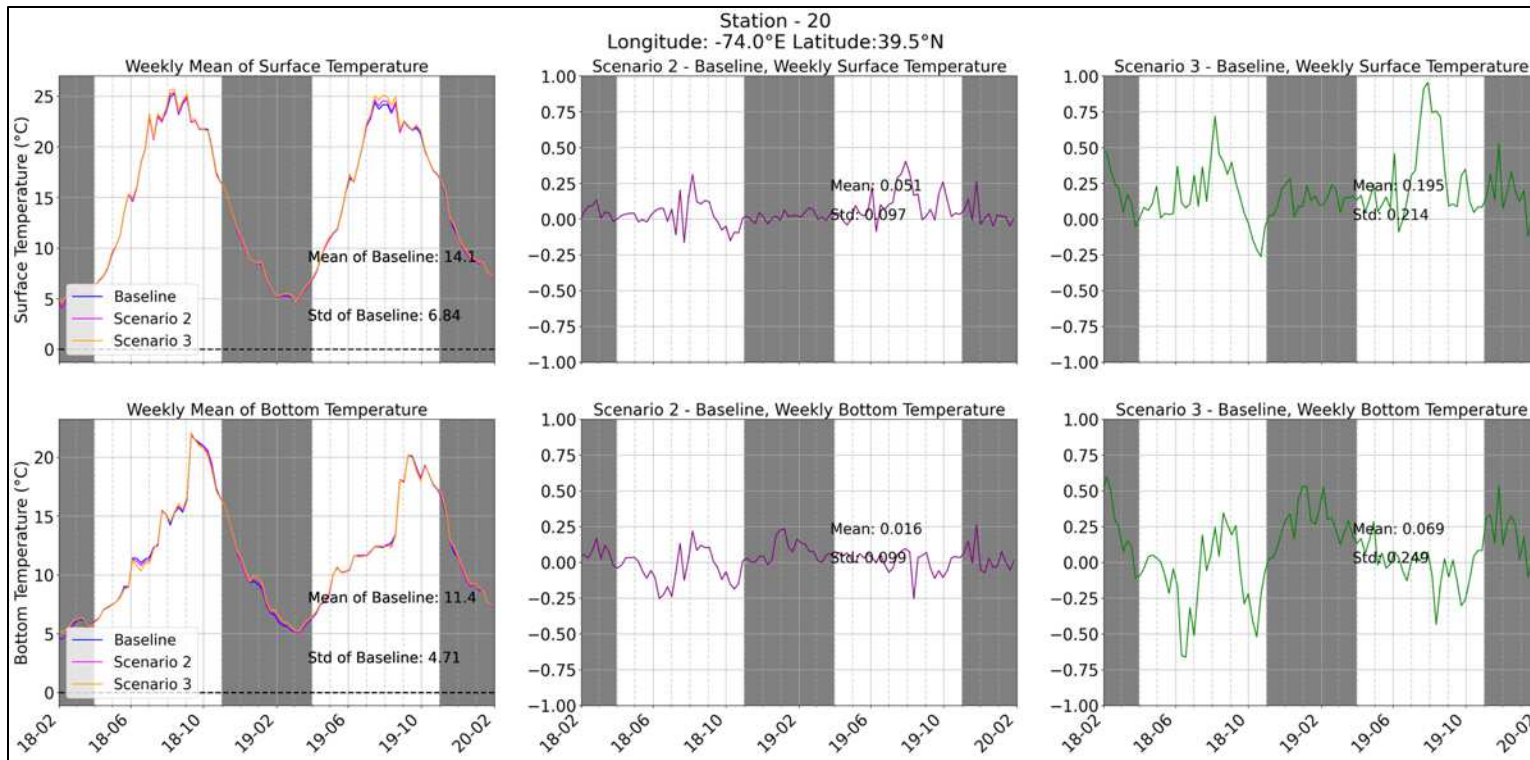


Figure 240. Weekly mean (left panels), and weekly differences for Scenario 2-baseline (middle panels) and Scenario 3-baseline (right panels) for surface (upper panels) and bottom temperature (lower panels) at station 20.

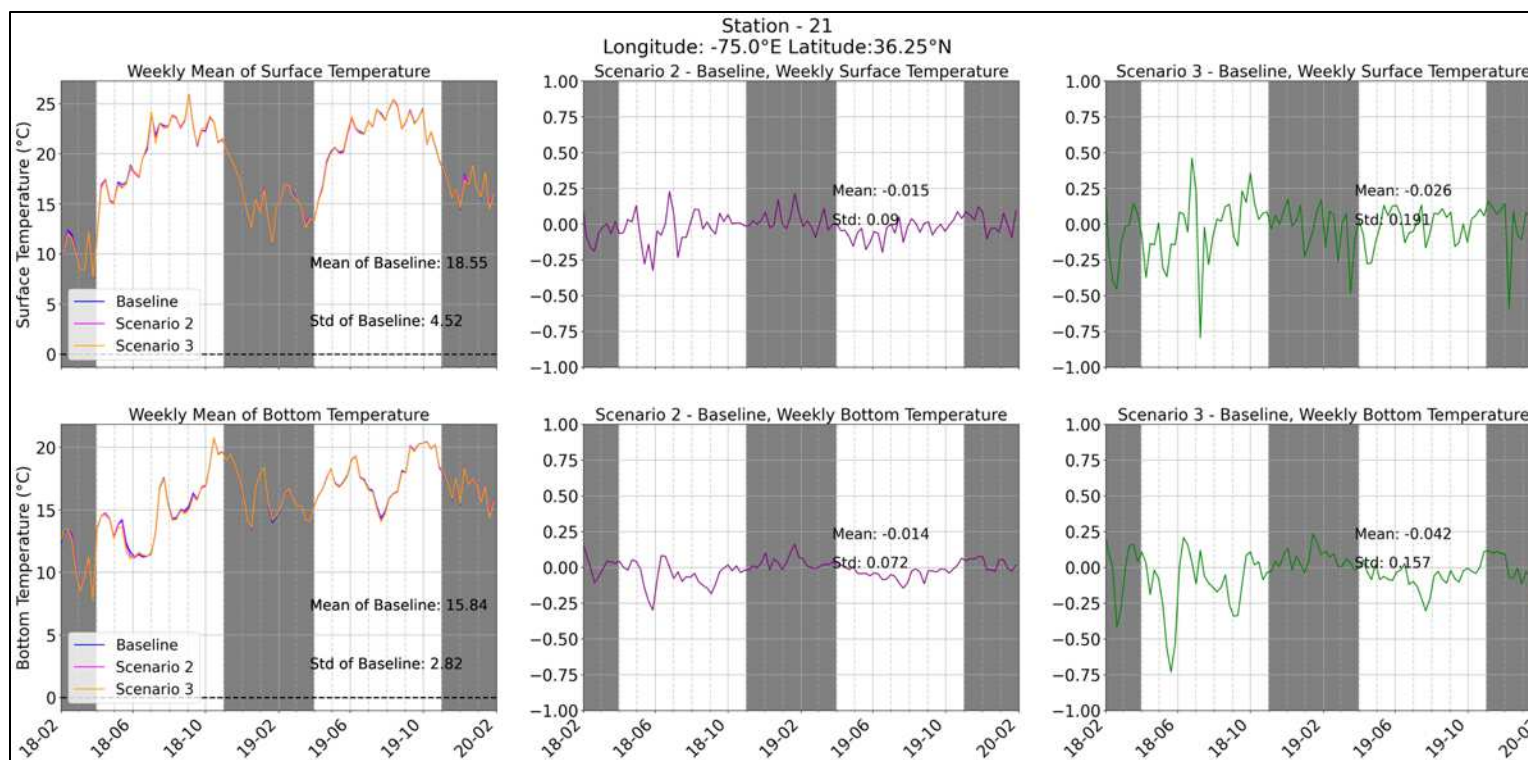


Figure 241. Weekly mean (left panels), and weekly differences for Scenario 2-baseline (middle panels) and Scenario 3-baseline (right panels) for surface (upper panels) and bottom temperature (lower panels) at station 21.

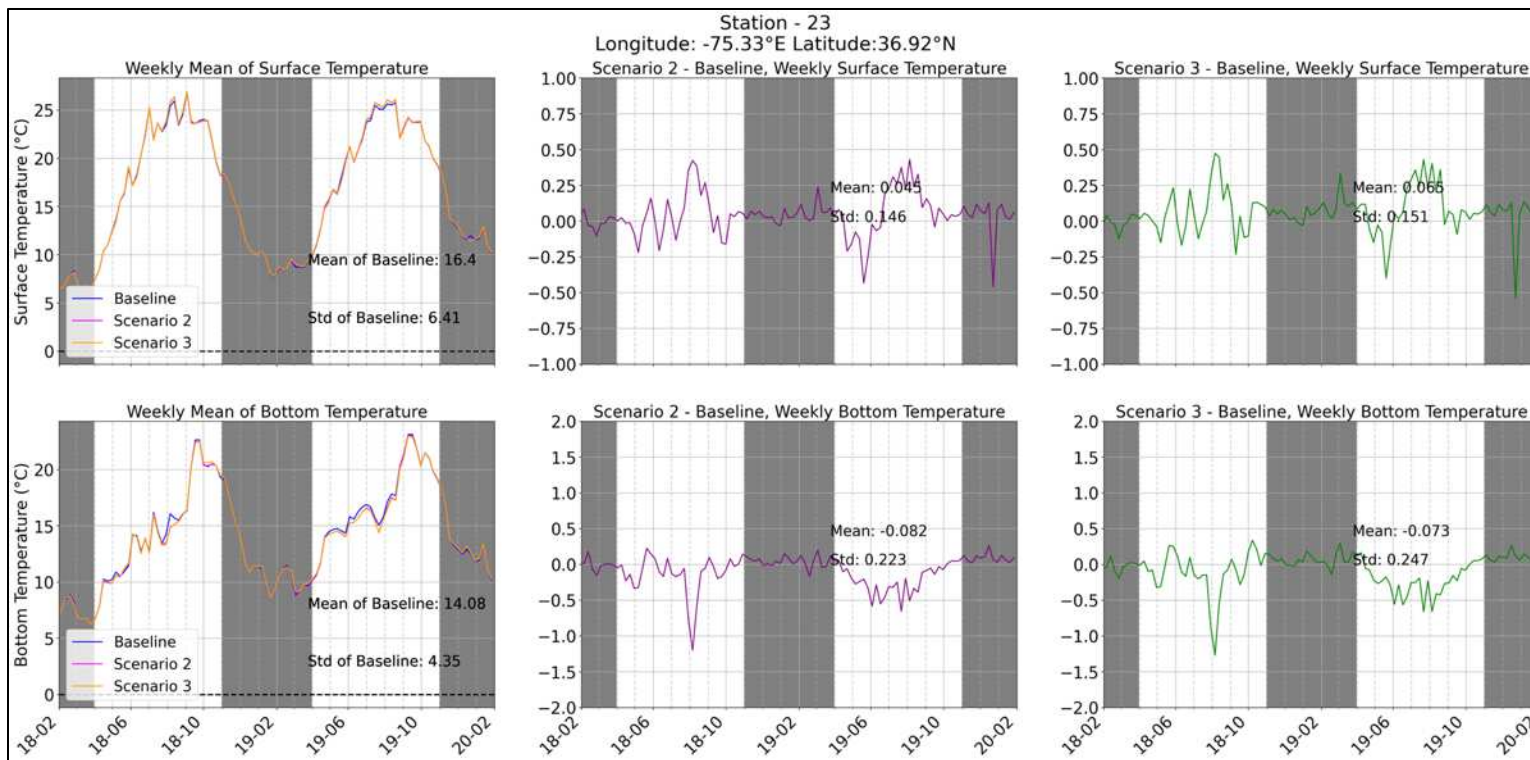


Figure 242. Weekly mean (left panels), and weekly differences for Scenario 2-baseline (middle panels) and Scenario 3-baseline (right panels) for surface (upper panels) and bottom temperature (lower panels) at station 23.

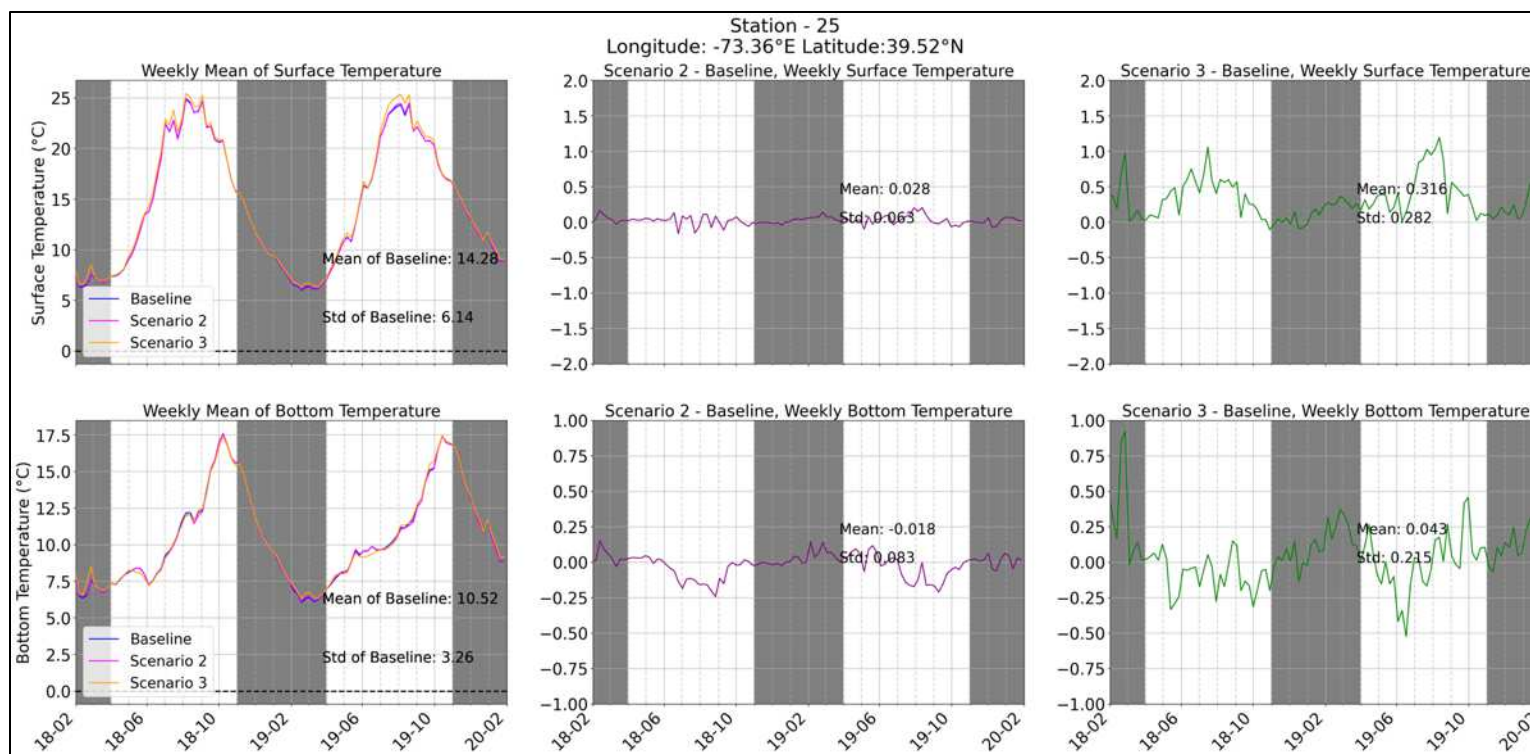


Figure 243. Weekly mean (left panels), and weekly differences for Scenario 2-baseline (middle panels) and Scenario 3-baseline (right panels) for surface (upper panels) and bottom temperature (lower panels) at station 25.

9.3.2.3 Effects on Surface Heat Fluxes

Time series of surface heat fluxes at the air-sea interface located in the WEAs are presented in Figure 240 through Figure 246, positive being downward to the water column (e.g., solar incoming heat flux year round and total heat flux in the spring and summer months), and negative being upward (e.g., total heat flux in the fall and winter months, and longwave back radiation). It is important to note that the wind wake effect was taken into account when calculating the sensible and latent heat fluxes for Scenario 2 and Scenario 3. For solar and longwave heat fluxes, the differences in Scenario 2 or 3 relative to Baseline are null or insignificant as they are not directly impacted by the change in wind; the longwave heat flux emitted back to the atmosphere increases (becomes more negative), but slightly, due to the simulated increase in sea surface temperature. The differences for the evaporative heat flux time series show both positive and negative values (caused by change in moisture transport near the sea surface) while, for sensible heat flux, difference time series are almost always negative, meaning water receive relatively less sensible heat flux in Scenario 2 and 3 compared to baseline (as explained in Section 9.3.1.4). This can occur because, with lower wind speeds, the mechanisms of sensible and latent heat transfer become less efficient, and their magnitude (both downward and upward) decreases. For example, the waters may receive less heat through convection but may also lose less heat through evaporation. Even though the changes in total heat flux are overall small, the differences of water temperature (section 9.3.2.2) shows temperature is relatively higher in Scenario 2 and 3.

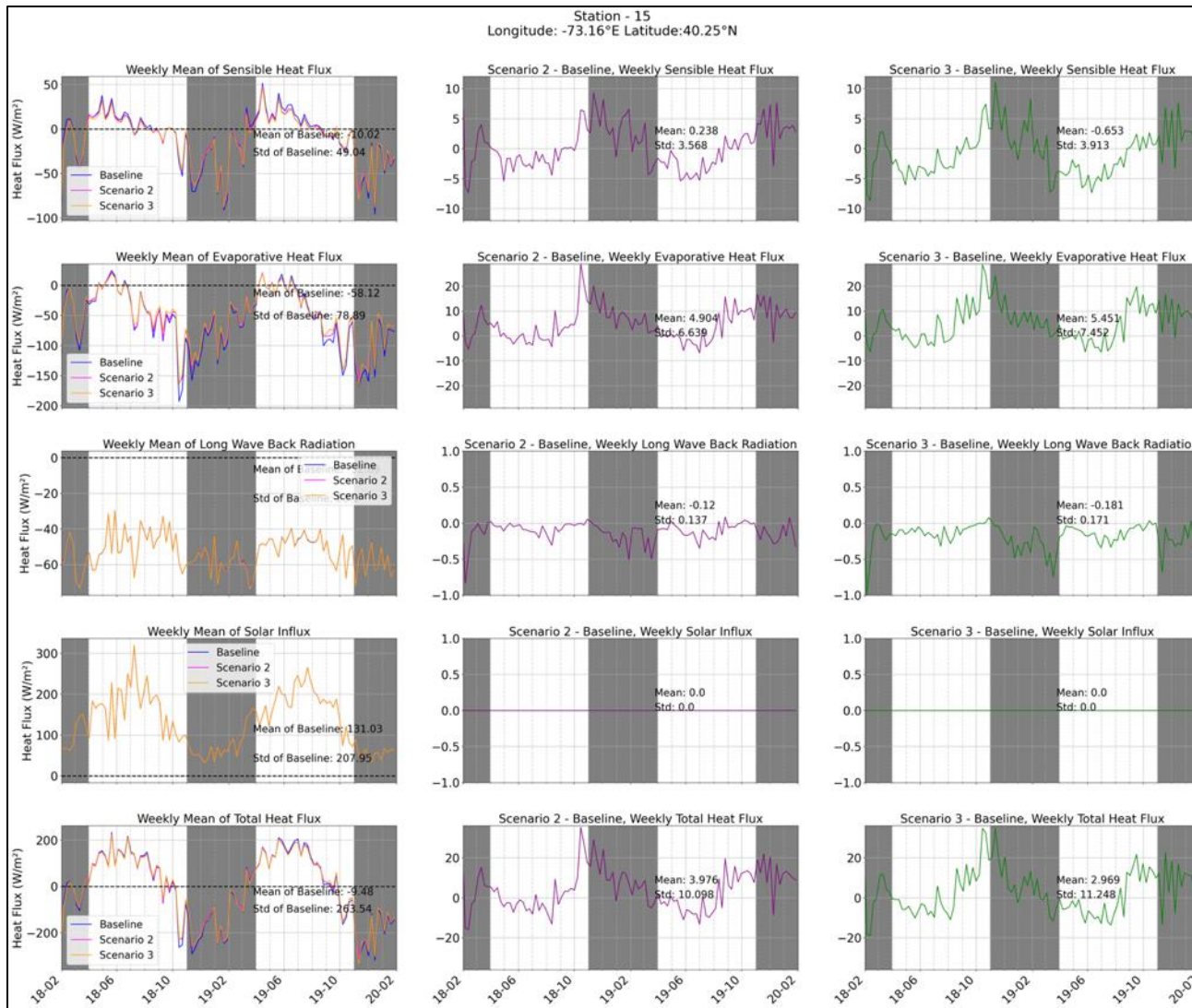


Figure 244. Weekly mean (left panels), and weekly differences for Scenario 2-baseline (middle panels) and Scenario 3-baseline (right panels) for different heat fluxes at station 15.

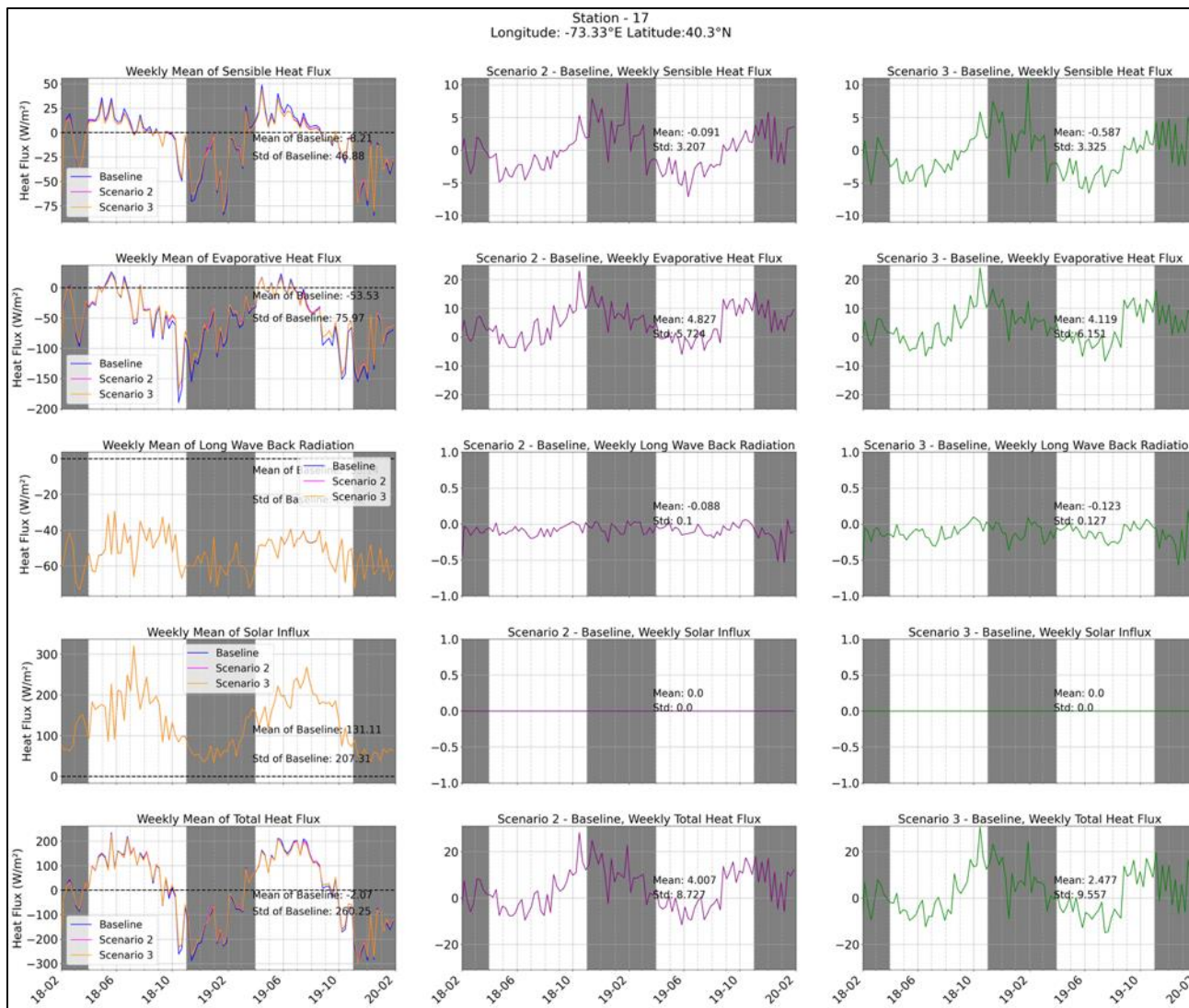


Figure 245. Weekly mean (left panels), and weekly differences for Scenario 2-baseline (middle panels) and Scenario 3-baseline (right panels) for different heat fluxes at station 17.

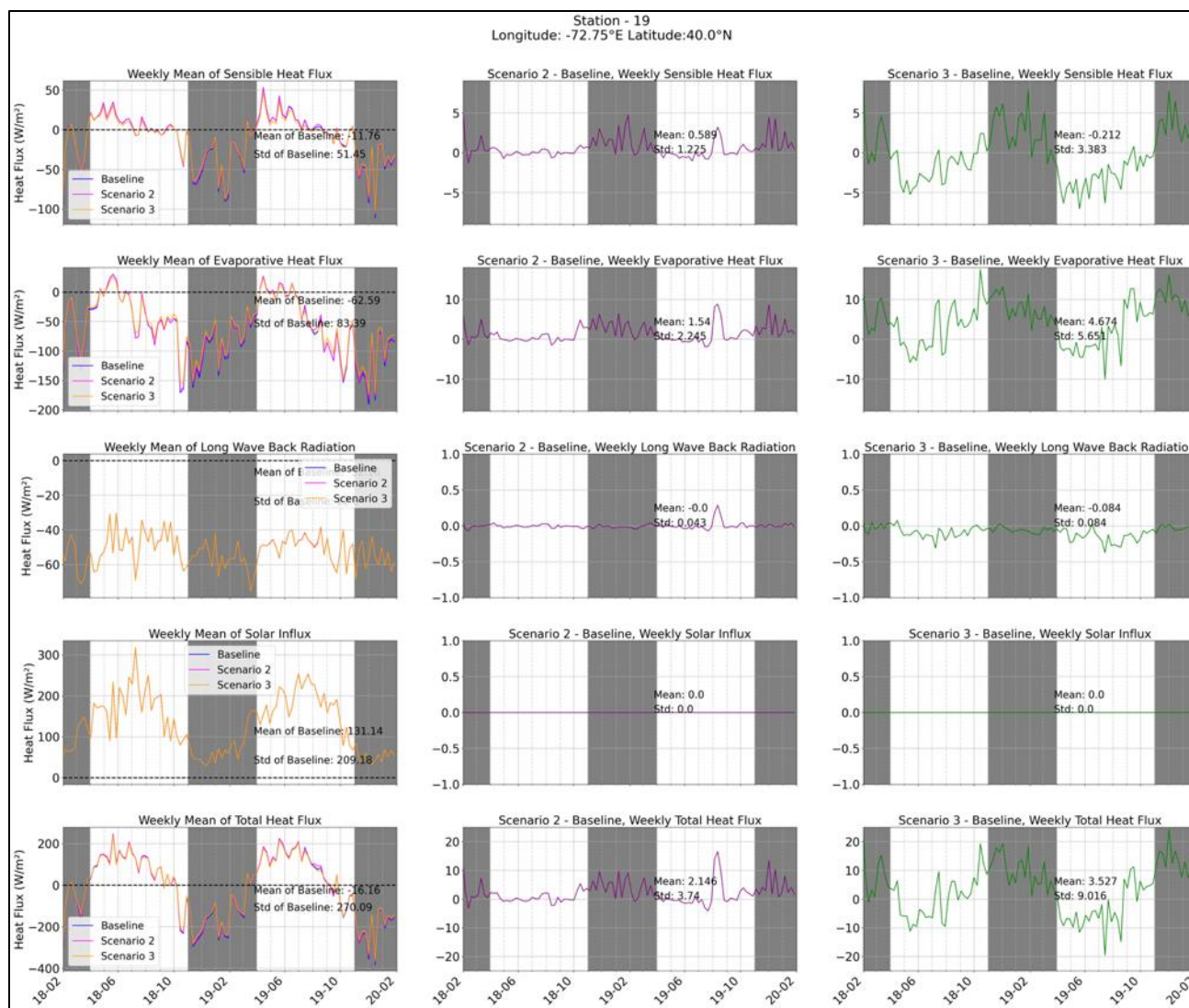


Figure 246. Weekly mean (left panels), and weekly differences for Scenario 2-baseline (middle panels) and Scenario 3-baseline (right panels) for different heat fluxes at station 19.

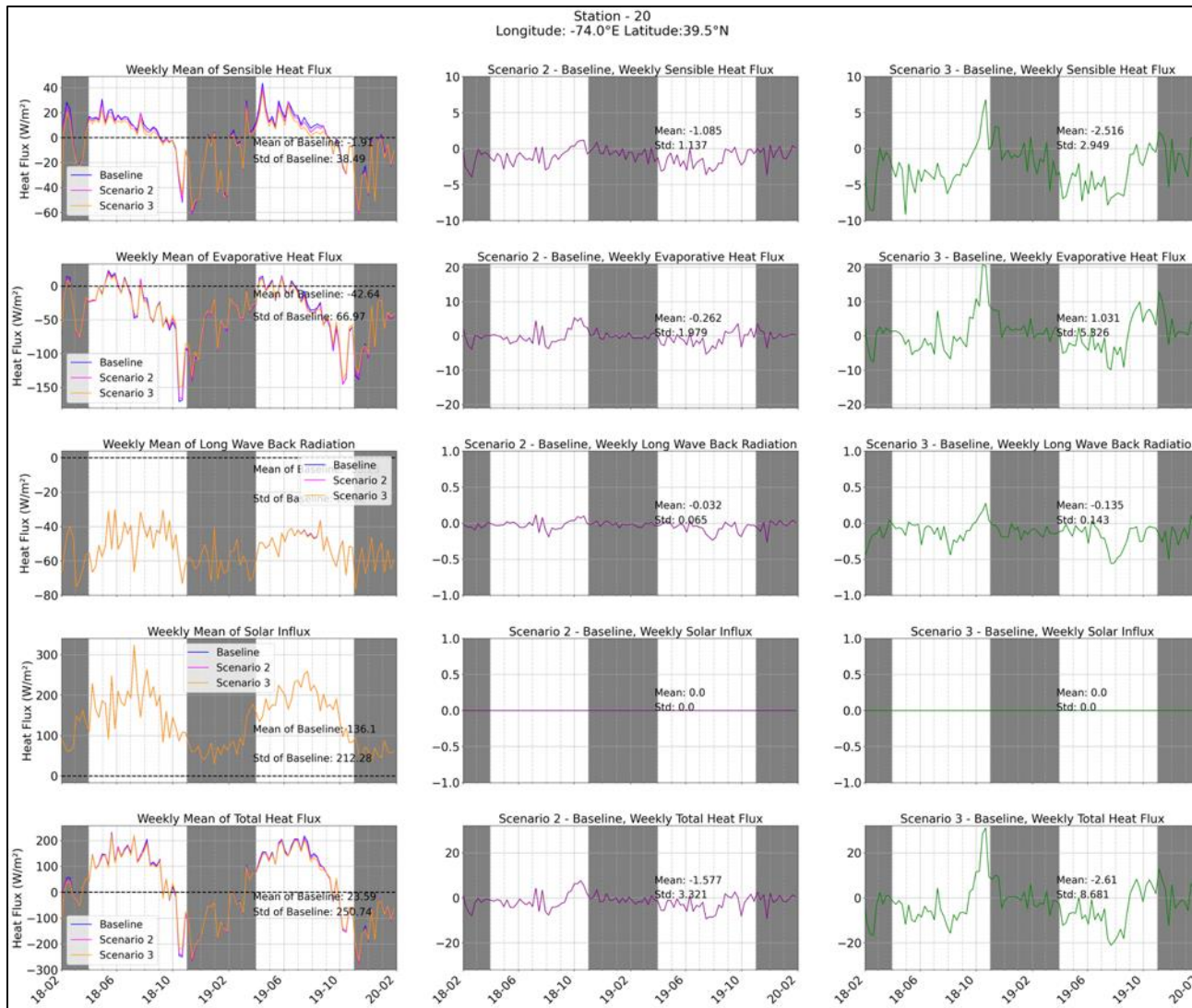


Figure 247. Weekly mean (left panels), and weekly differences for Scenario 2-baseline (middle panels) and Scenario 3-baseline (right panels) for different heat fluxes at station 20.

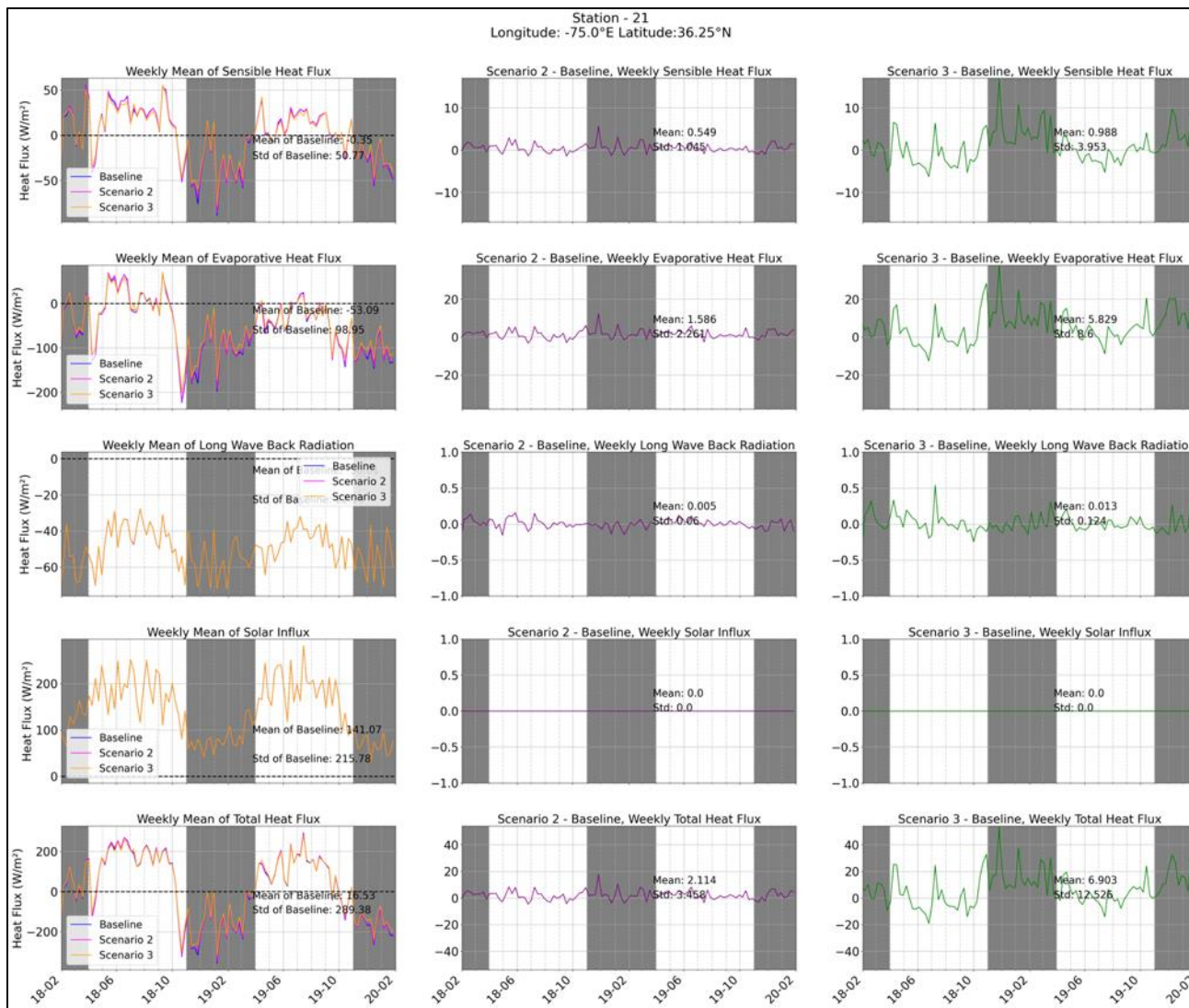


Figure 248. Weekly mean (left panels), and weekly differences for Scenario 2-baseline (middle panels) and Scenario 3-baseline (right panels) for different heat fluxes at station 21.

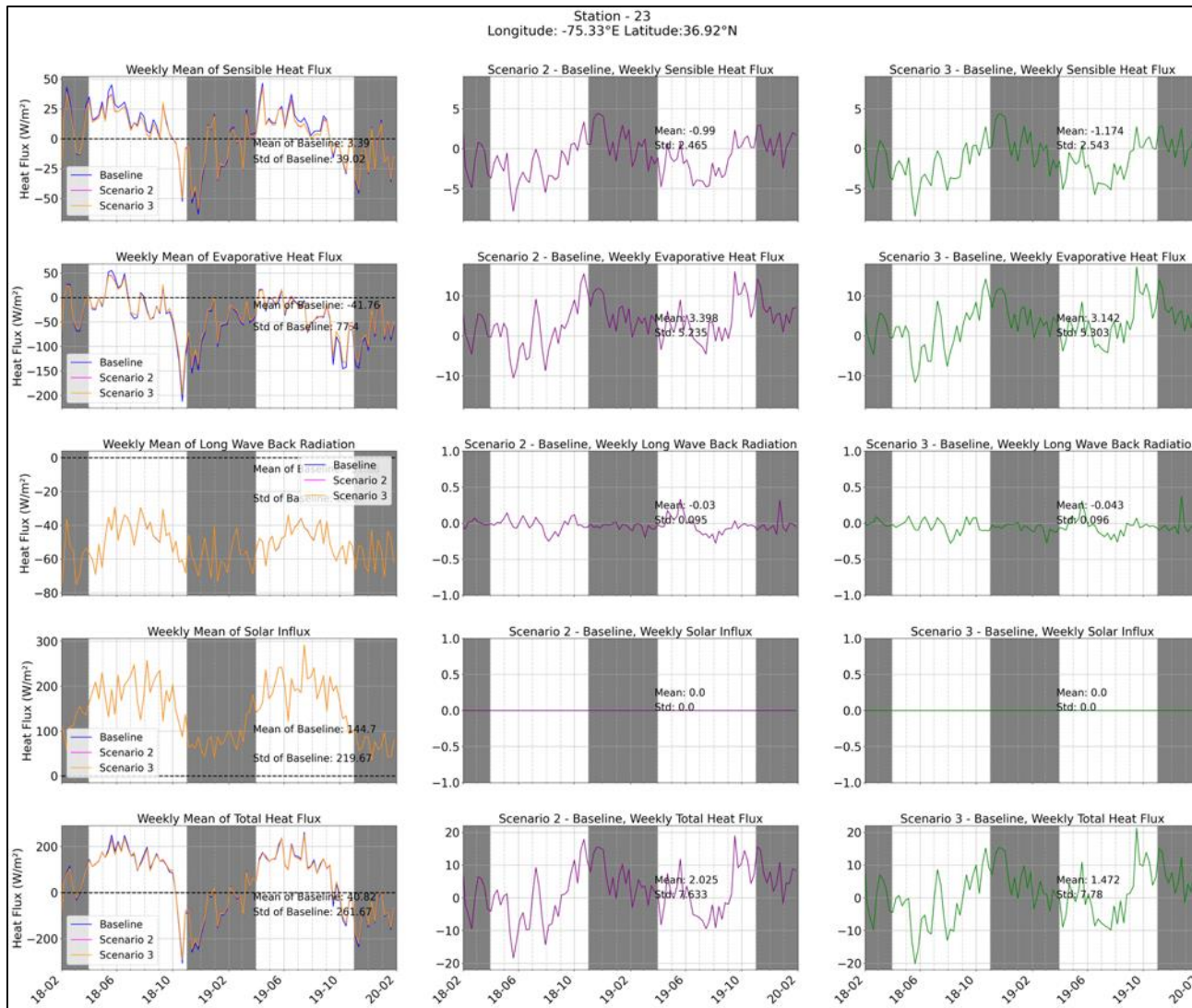


Figure 249. Weekly mean (left panels), and weekly differences for Scenario 2-baseline (middle panels) and Scenario 3-baseline (right panels) for different heat fluxes at station 23.

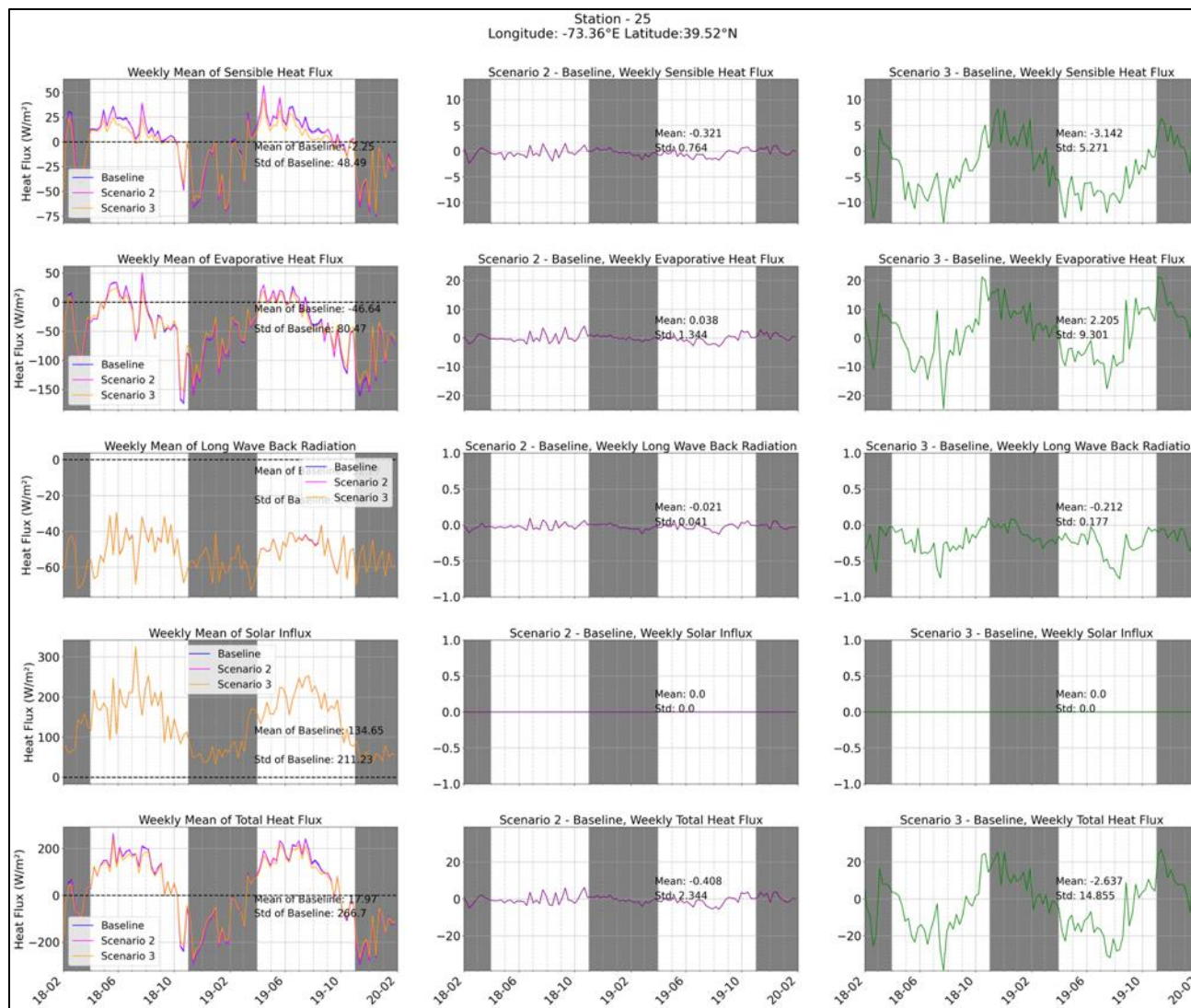


Figure 250. Weekly mean (left panels), and weekly differences for Scenario 2-baseline (middle panels) and Scenario 3-baseline (right panels) for different heat fluxes at station 25.

9.3.2.4 Effects on Turbulent Vertical Eddy Viscosity

Time series of turbulent vertical eddy viscosity located in the WEAs are presented in Figure 247 through Figure 253. The seasonality of vertical eddy viscosity is driven by strong vertical mixing during winter, due to stronger winds, whereas in summer, there is reduced mixing and increased stratification. The difference time series for eddy viscosity shows mostly negative peaks, especially at the surface layer. This is expected, since turbulent vertical eddy viscosity scales with surface wind at the surface mixed layer, and linearly with near-bottom current at the bottom, both of which, and especially surface wind, have been shown to also decrease in WEA development scenarios. Some of the negative peaks in the surface viscosity difference time series can also be correlated to the difference time series of the surface current. For instance the trough for viscosity at station 17 (Figure 248) in June 2019 can be associated to the trough in the surface current speed difference at the same station in Figure 227, as well as the trough in surface wind in the same figure.

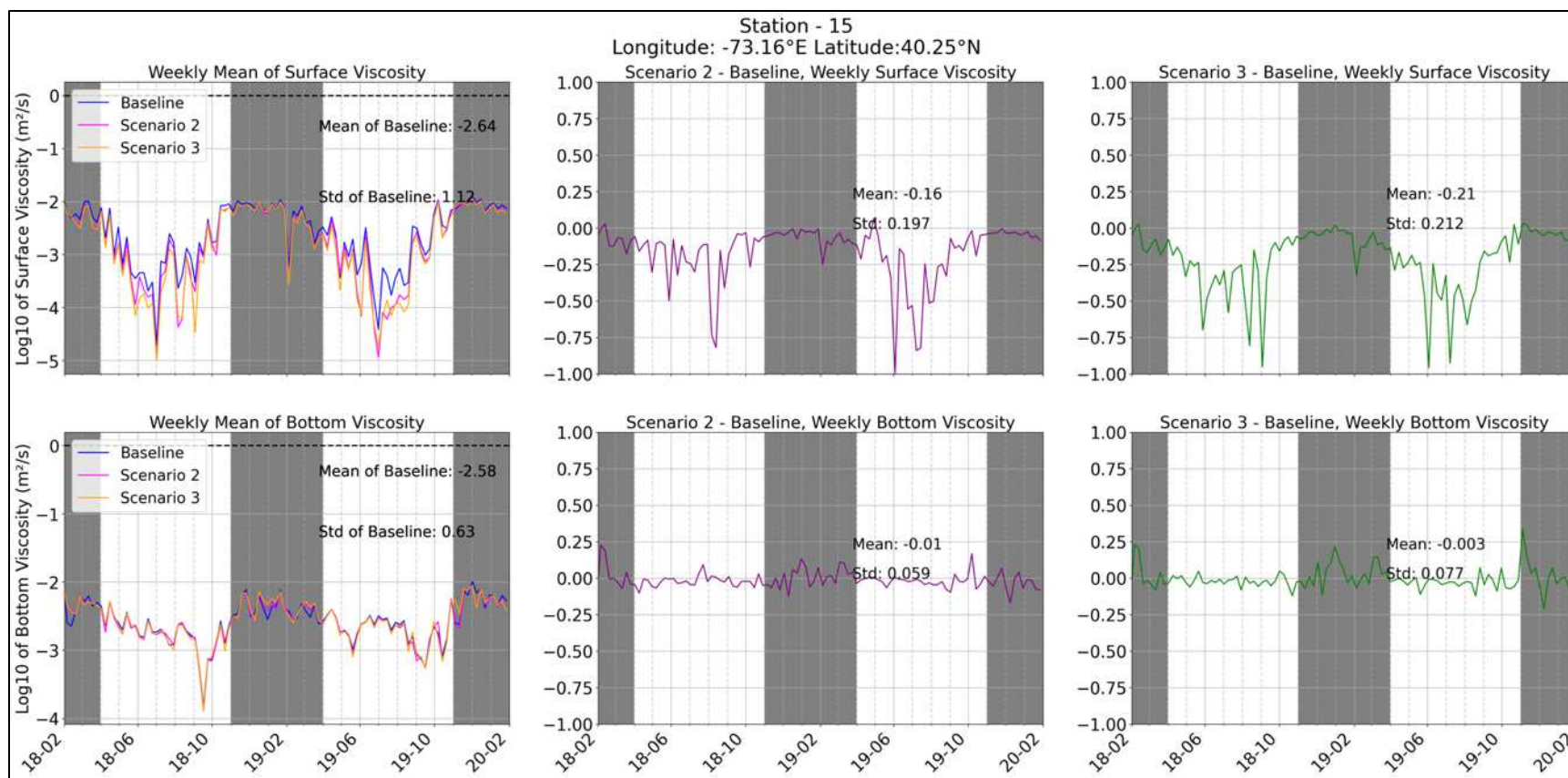


Figure 251. Weekly mean (left panels), and weekly differences for Scenario 2-baseline (middle panels) and Scenario 3-baseline (right panels) for turbulent vertical eddy viscosity (surface and bottom) at station 15.

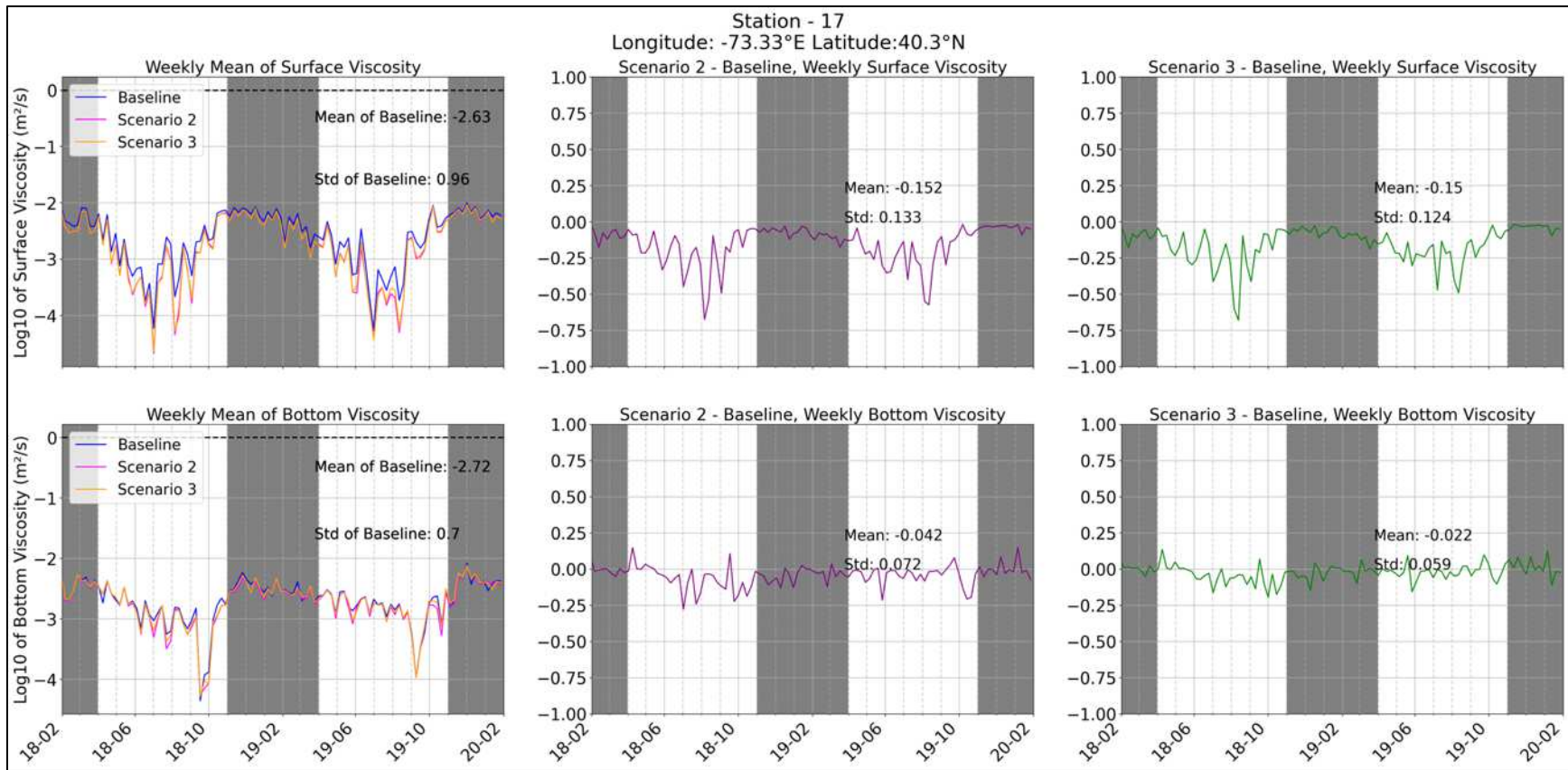


Figure 252. Weekly mean (left panels), and weekly differences for Scenario 2-baseline (middle panels) and Scenario 3-baseline (right panels) for turbulent vertical eddy viscosity (surface and bottom) at station 17.

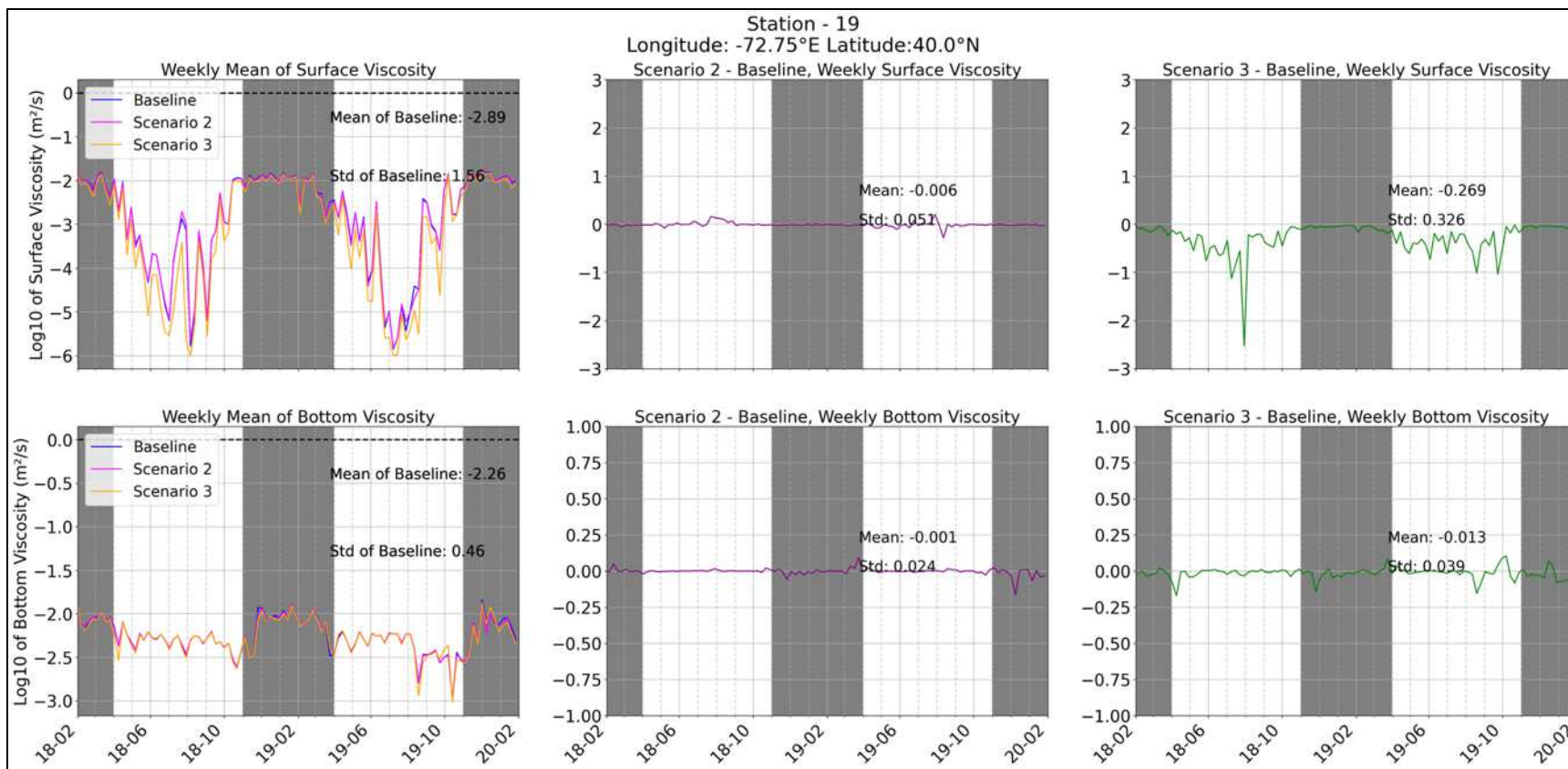


Figure 253. Weekly mean (left panels), and weekly differences for Scenario 2-baseline (middle panels) and Scenario 3-baseline (right panels) for turbulent vertical eddy viscosity (surface and bottom) at station 19.

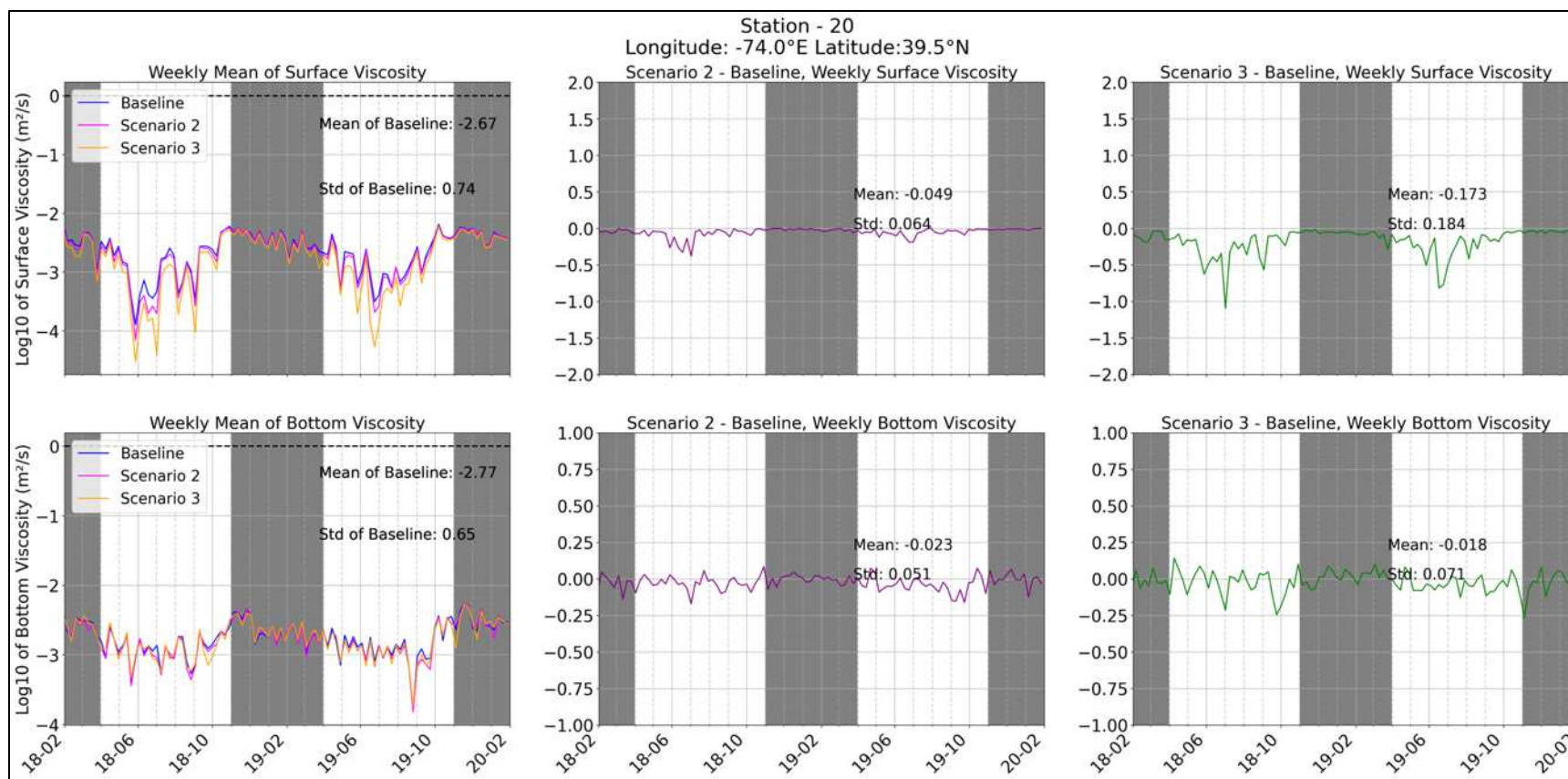


Figure 254. Weekly mean (left panels), and weekly differences for Scenario 2-baseline (middle panels) and Scenario 3-baseline (right panels) for turbulent vertical eddy viscosity (surface and bottom) at station 20.

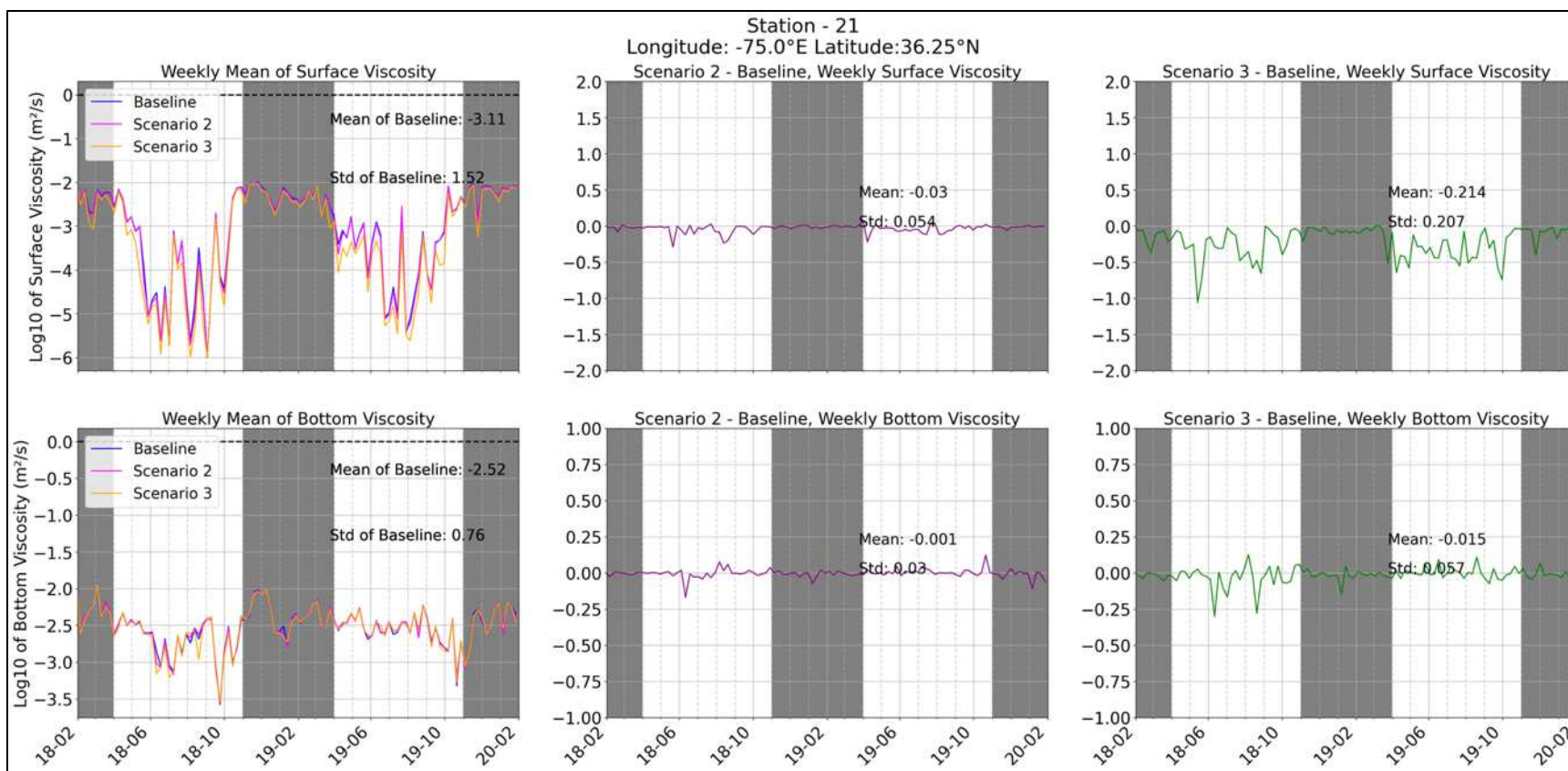


Figure 255. Weekly mean (left panels), and weekly differences for Scenario 2-baseline (middle panels) and Scenario 3-baseline (right panels) for turbulent vertical eddy viscosity (surface and bottom) at station 21.

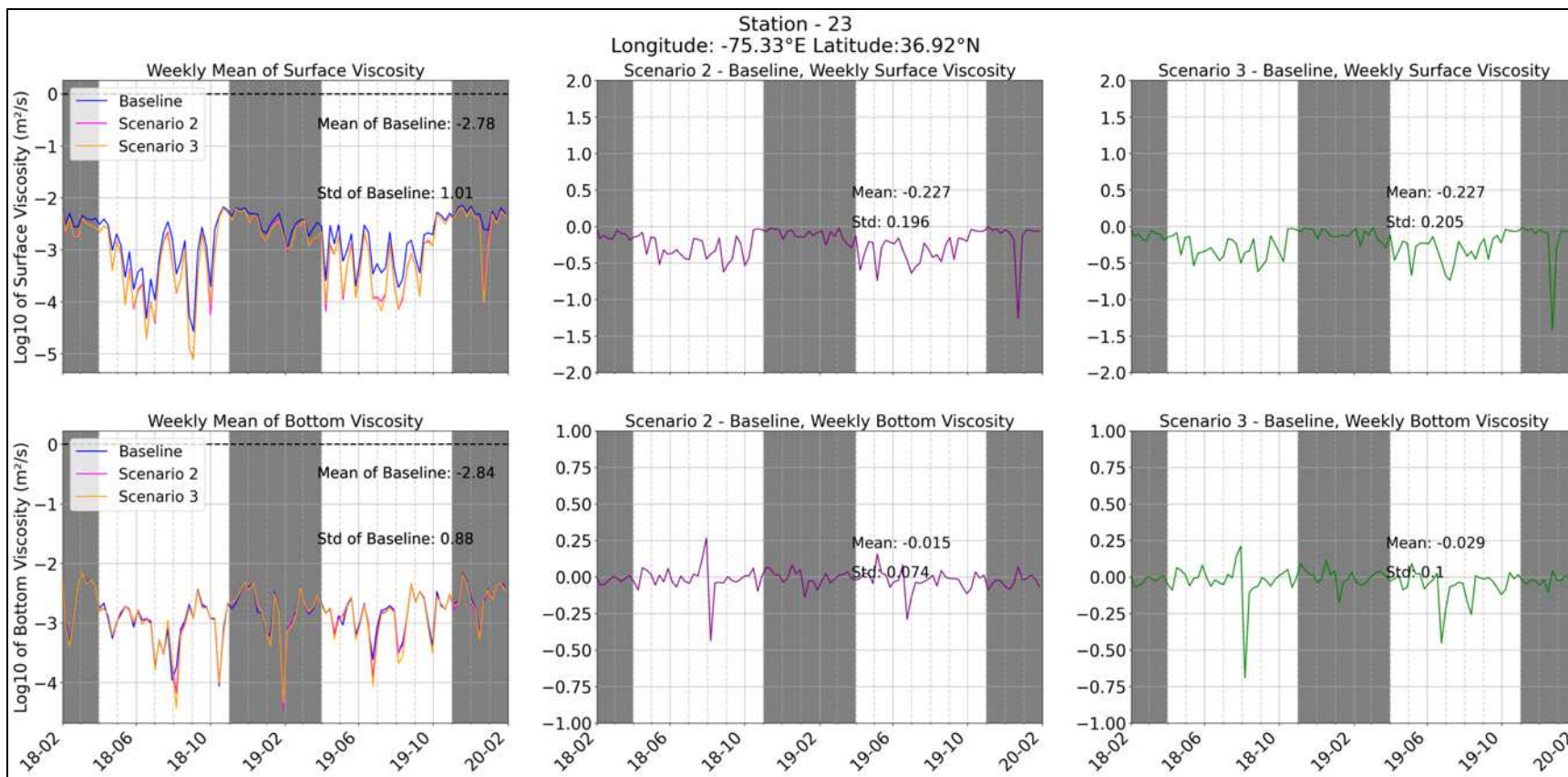


Figure 256. Weekly mean (left panels), and weekly differences for Scenario 2-baseline (middle panels) and Scenario 3-baseline (right panels) for turbulent vertical eddy viscosity (surface and bottom) at station 23.

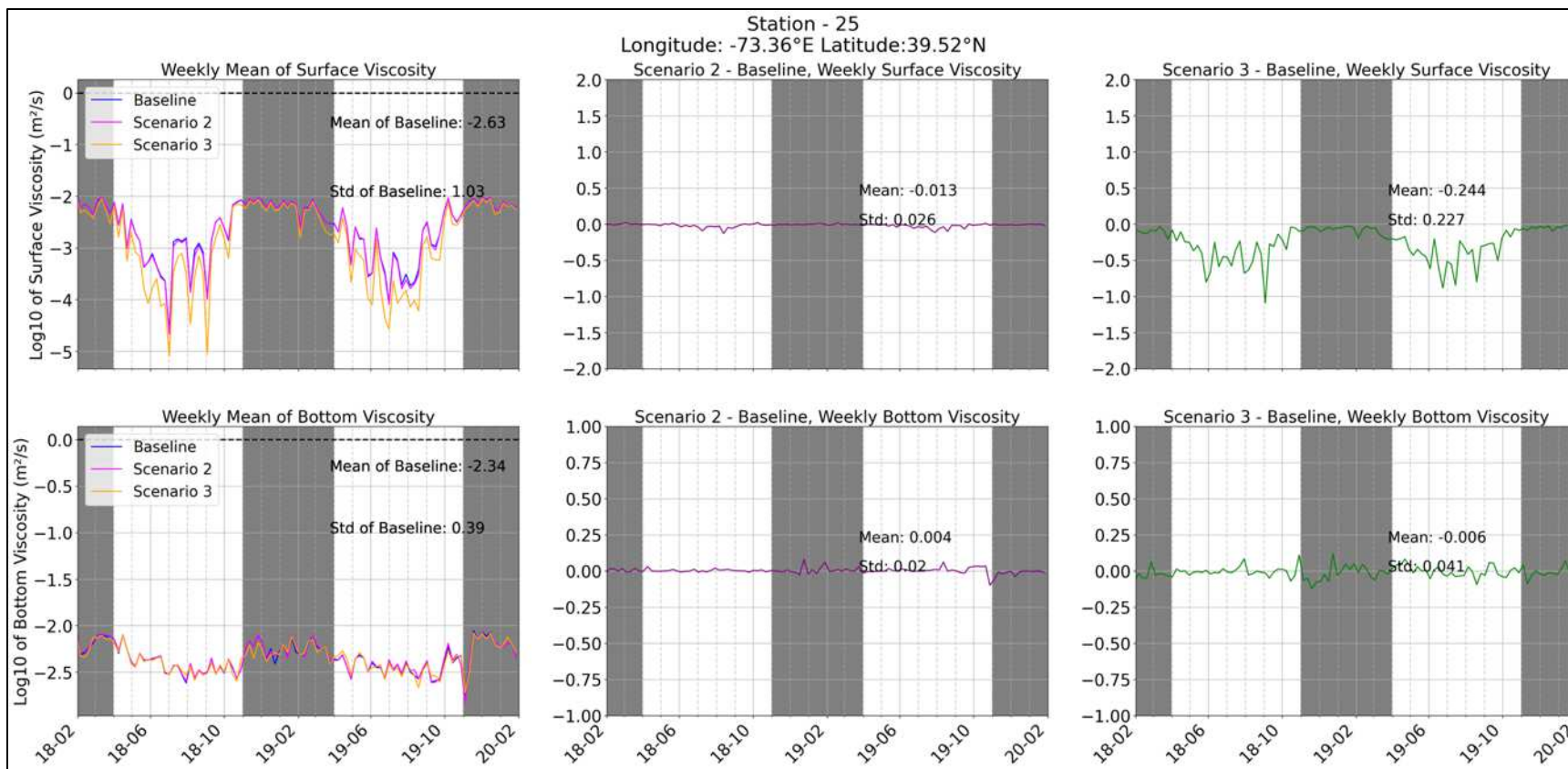


Figure 257. Weekly mean (left panels), and weekly differences for Scenario 2-baseline (middle panels) and Scenario 3-baseline (right panels) for turbulent vertical eddy viscosity (surface and bottom) at station 25.

9.3.2.5 Effects on Turbulent Kinetic Energy

Time series of Turbulent Kinetic Energy (TKE) located in the WEAs are presented in Figure 254 through Figure 260. The difference time series for TKE shows mostly negative values, especially at the surface layer. These time series follow similar seasonal patterns to the corresponding results for vertical eddy viscosity (Figure 247 through Figure 253) as TKE directly influences eddy viscosity (based on the k-epsilon closure model). Overall, mixing, especially surface mixing, is simulated to decrease within the WEAs, as driven by the decrease in surface wind stress, primarily, and bottom current, secondarily.

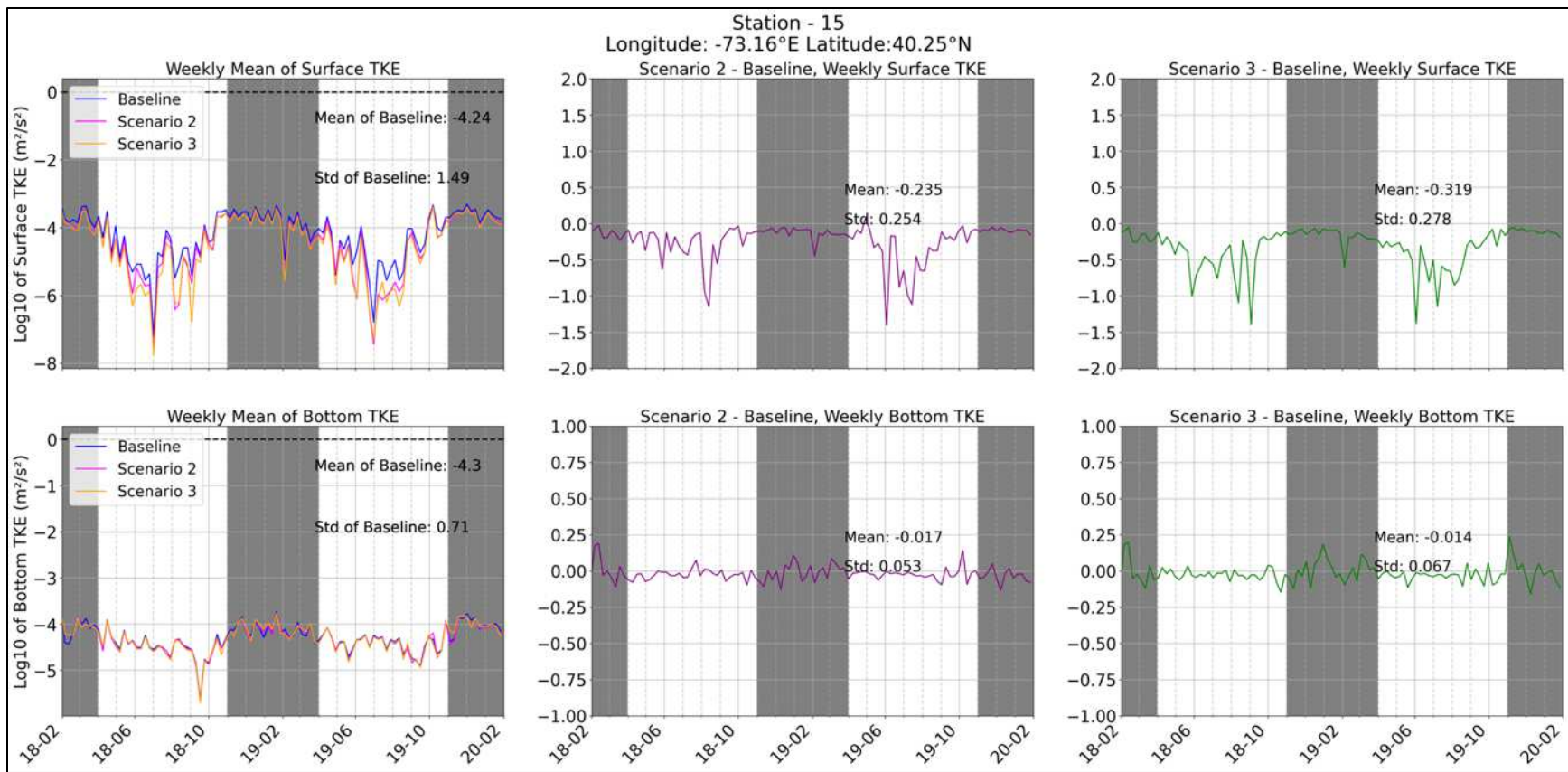


Figure 258. Weekly mean (left panels), and weekly differences for Scenario 2-baseline (middle panels) and Scenario 3-baseline (right panels) for TKE (surface and bottom) at station 15.

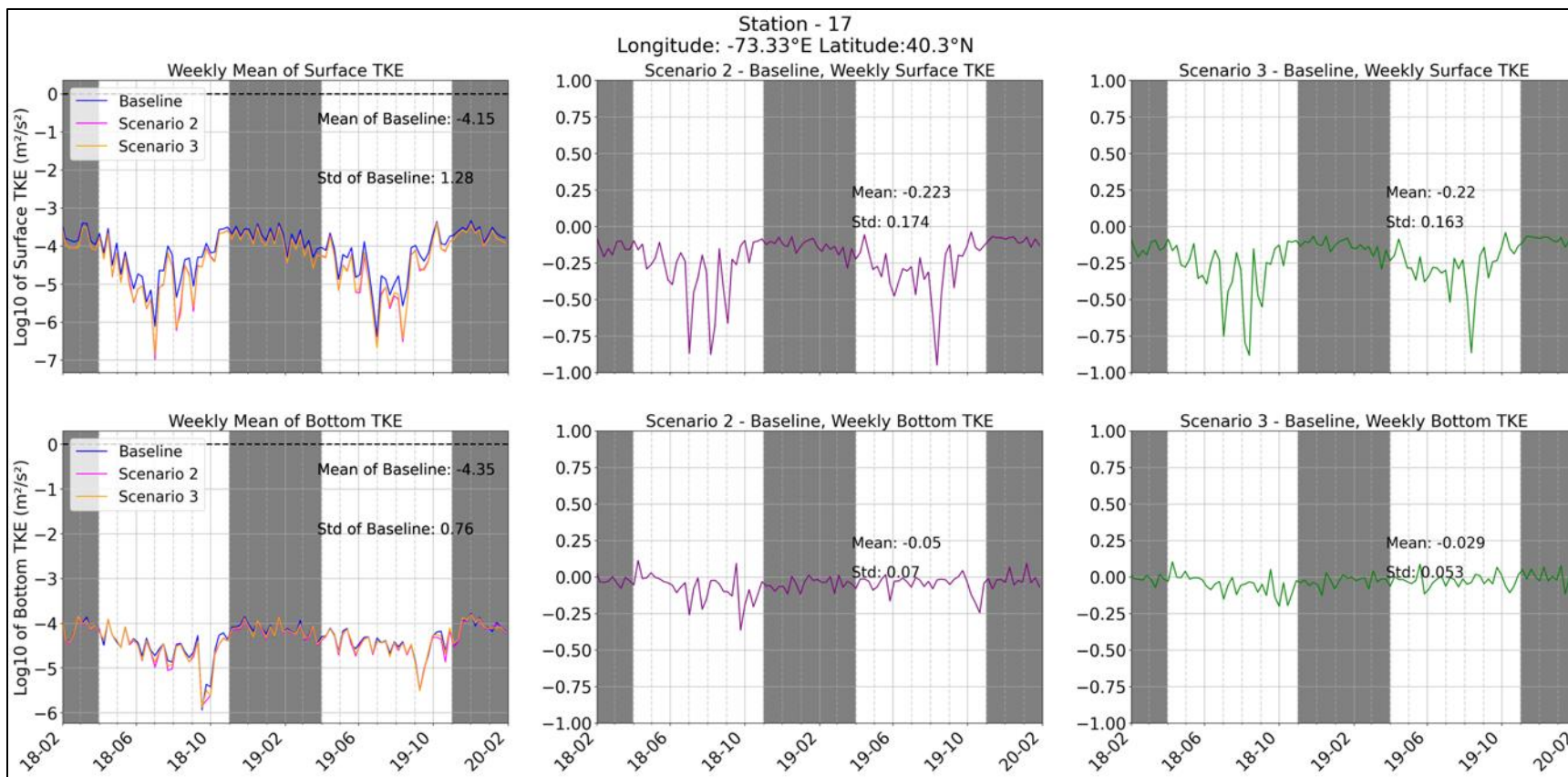


Figure 259. Weekly mean (left panels), and weekly differences for Scenario 2-baseline (middle panels) and Scenario 3-baseline (right panels) for TKE (surface and bottom) at station 17.

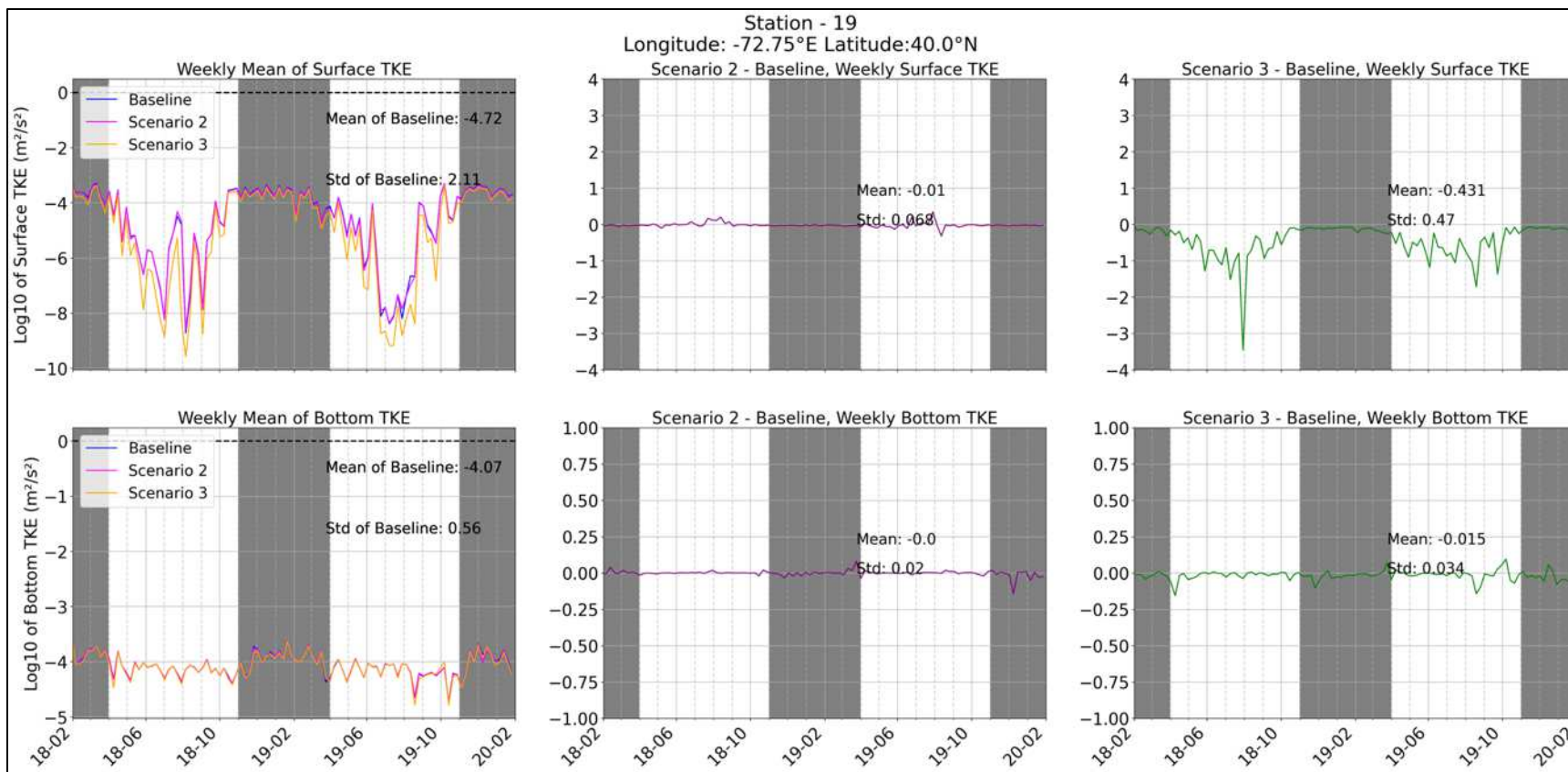


Figure 260. Weekly mean (left panels), and weekly differences for Scenario 2-baseline (middle panels) and Scenario 3-baseline (right panels) for TKE (surface and bottom) at station 19.

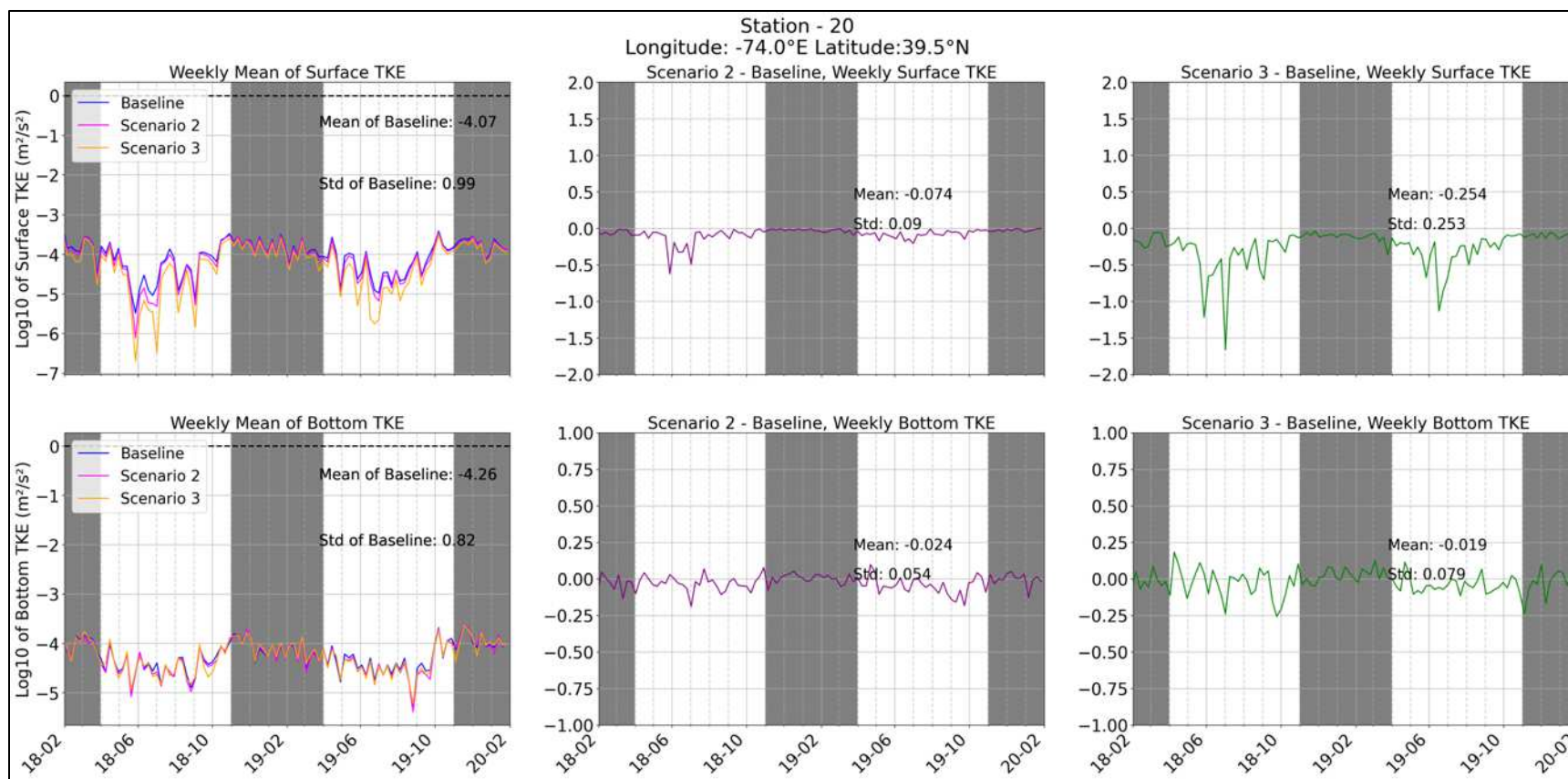


Figure 261. Weekly mean (left panels), and weekly differences for Scenario 2-baseline (middle panels) and Scenario 3-baseline (right panels) for TKE (surface and bottom) at station 20.

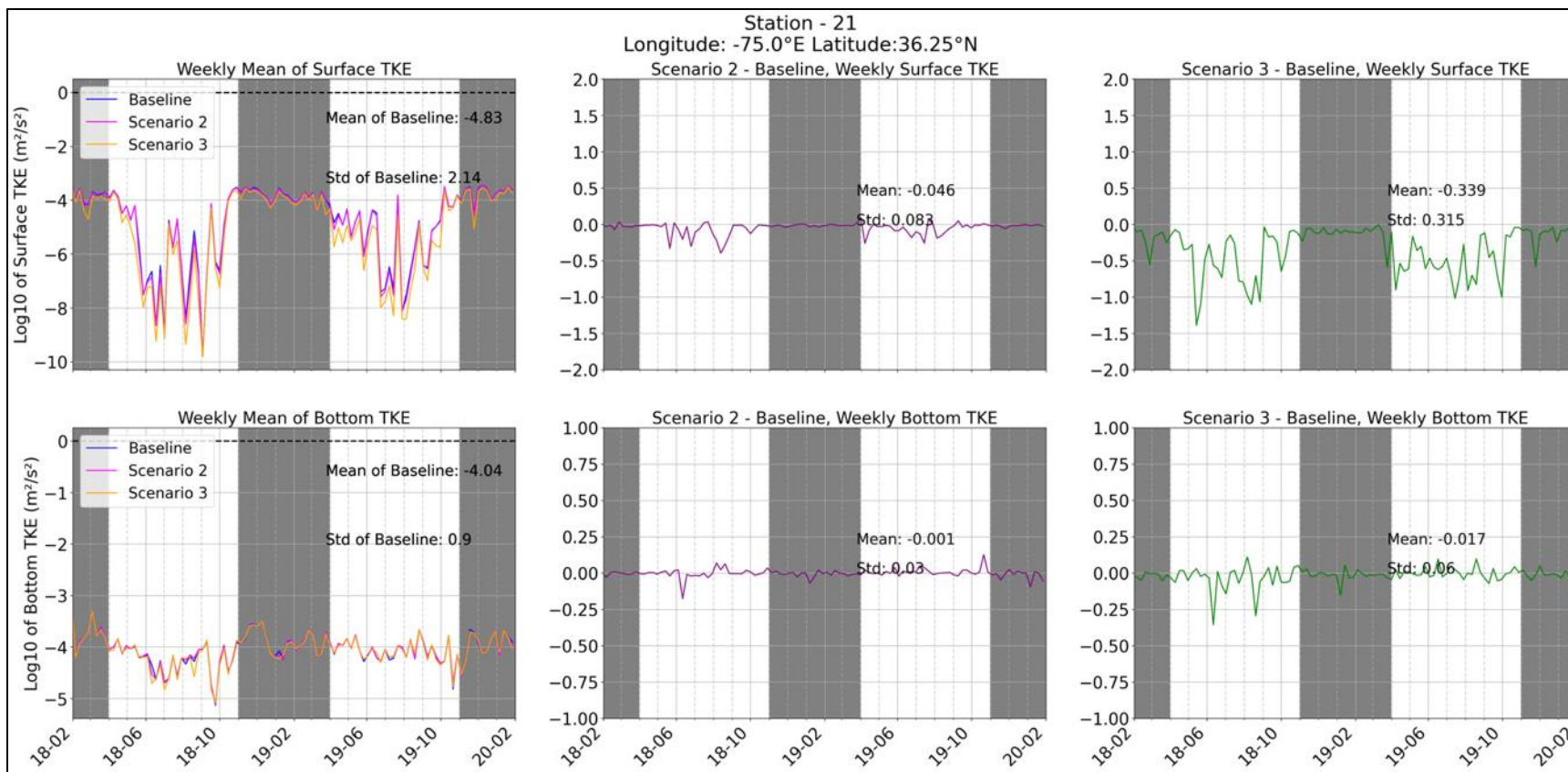


Figure 262. Weekly mean (left panels), and weekly differences for Scenario 2-baseline (middle panels) and Scenario 3-baseline (right panels) for TKE (surface and bottom) at station 21.

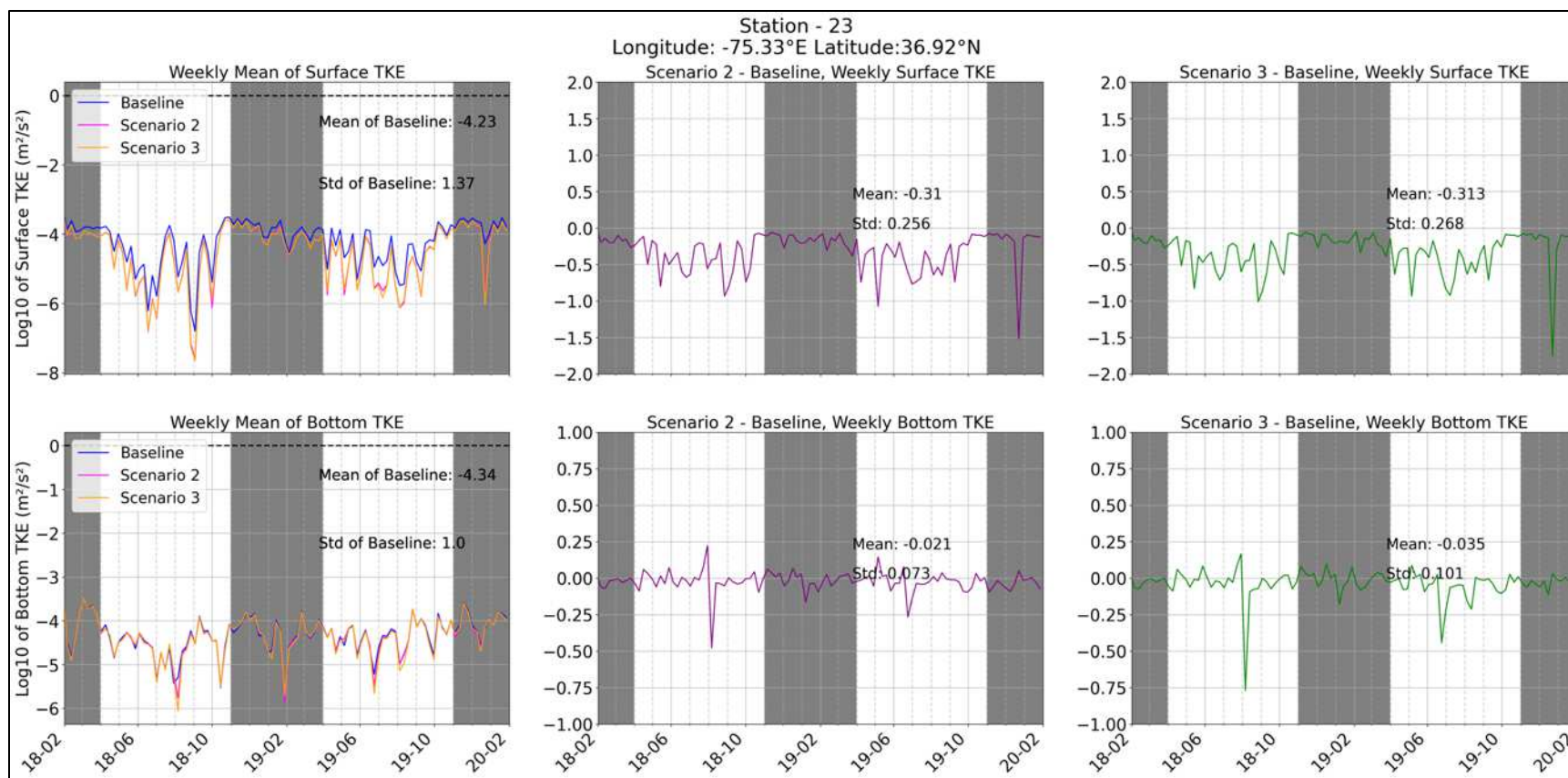


Figure 263. Weekly mean (left panels), and weekly differences for Scenario 2-baseline (middle panels) and Scenario 3-baseline (right panels) for TKE (surface and bottom) at station 23.

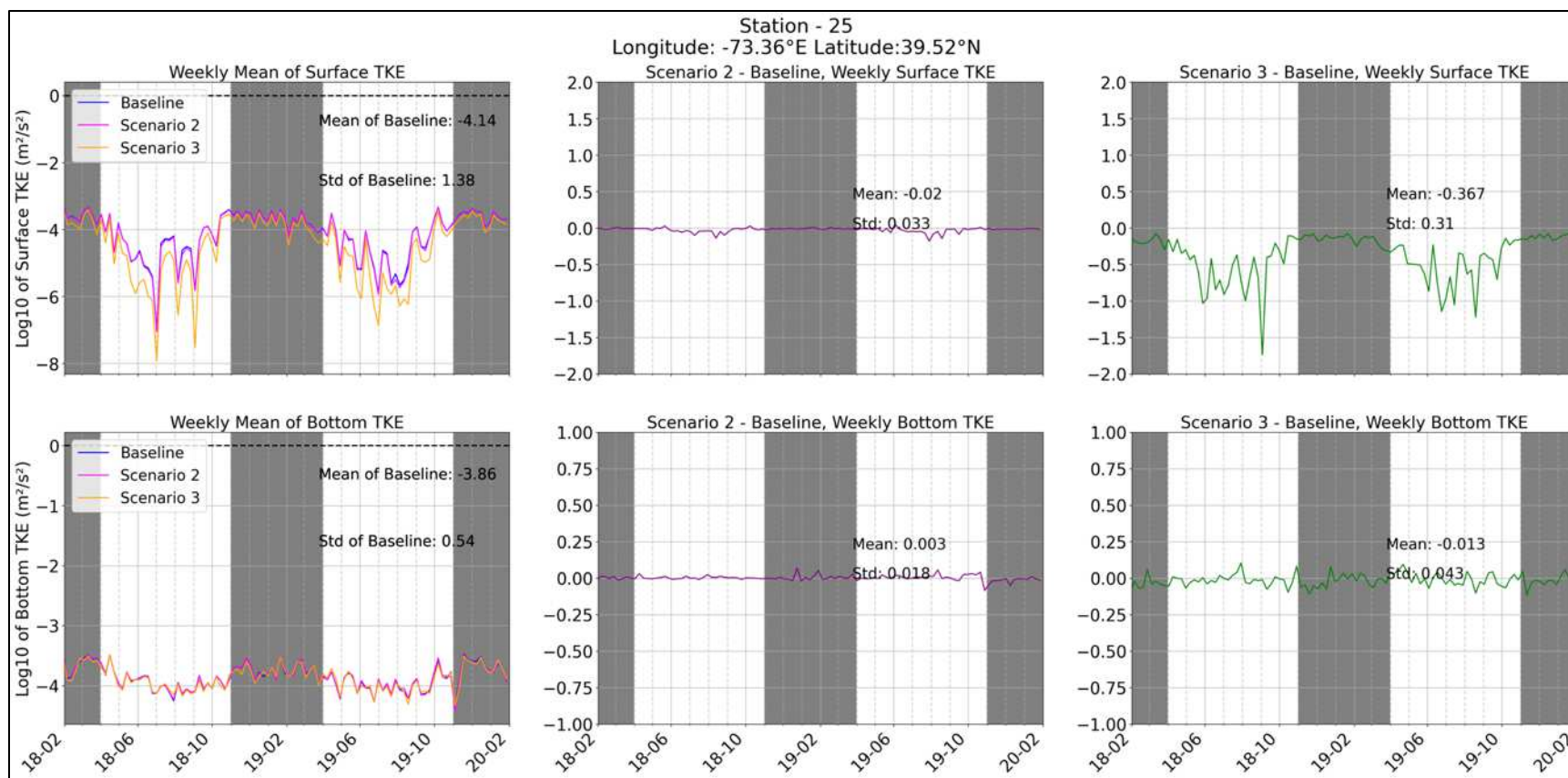


Figure 264. Weekly mean (left panels), and weekly differences for Scenario 2-baseline (middle panels) and Scenario 3-baseline (right panels) for TKE (surface and bottom) at station 25.

9.3.2.6 Effects on Stability (Richardson Number)

Time series of the gradient Richardson number (Ri) located in the WEAs are presented in Figure 261 through Figure 267 where –

$$Ri = \frac{-g \frac{\partial \rho}{\partial z}}{\rho \left[\left(\frac{\partial u}{\partial z} \right)^2 + \left(\frac{\partial v}{\partial z} \right)^2 \right]}$$

Eq. 7

for g = gravitational constant 9.8 m s^{-2} , ρ = density as a function of depth z , and (u,v) are eastward and northward horizontal velocity components. For $Ri \geq 0$ the stratification is stable, while for $Ri < 0$ the stratification is unstable. Stable stratification reduces turbulent mixing, whereas unstable stratification results in increased mixing.

The difference time series for the gradient Richardson number shows mostly positive peaks (beside winter) for most of the stations in the WEAs. The gradient Richardson number is a dimensionless number that quantifies the balance between potential energy (due to stratification) and kinetic energy (due to shear or turbulence) in a fluid flow. In other words, it is the ratio of buoyancy (stratification production) divided by shear (mixing production). Thus, increases in the Richardson number represent a more stable water column, and these positive differences in the stratified season, though transient and at times reversible, indicate that the water column is more stratified for Scenarios 2 and 3, compared to the baseline, at most stations. This is further corroborated by the increase in the summertime Richardson numbers tabulated in Table 27.

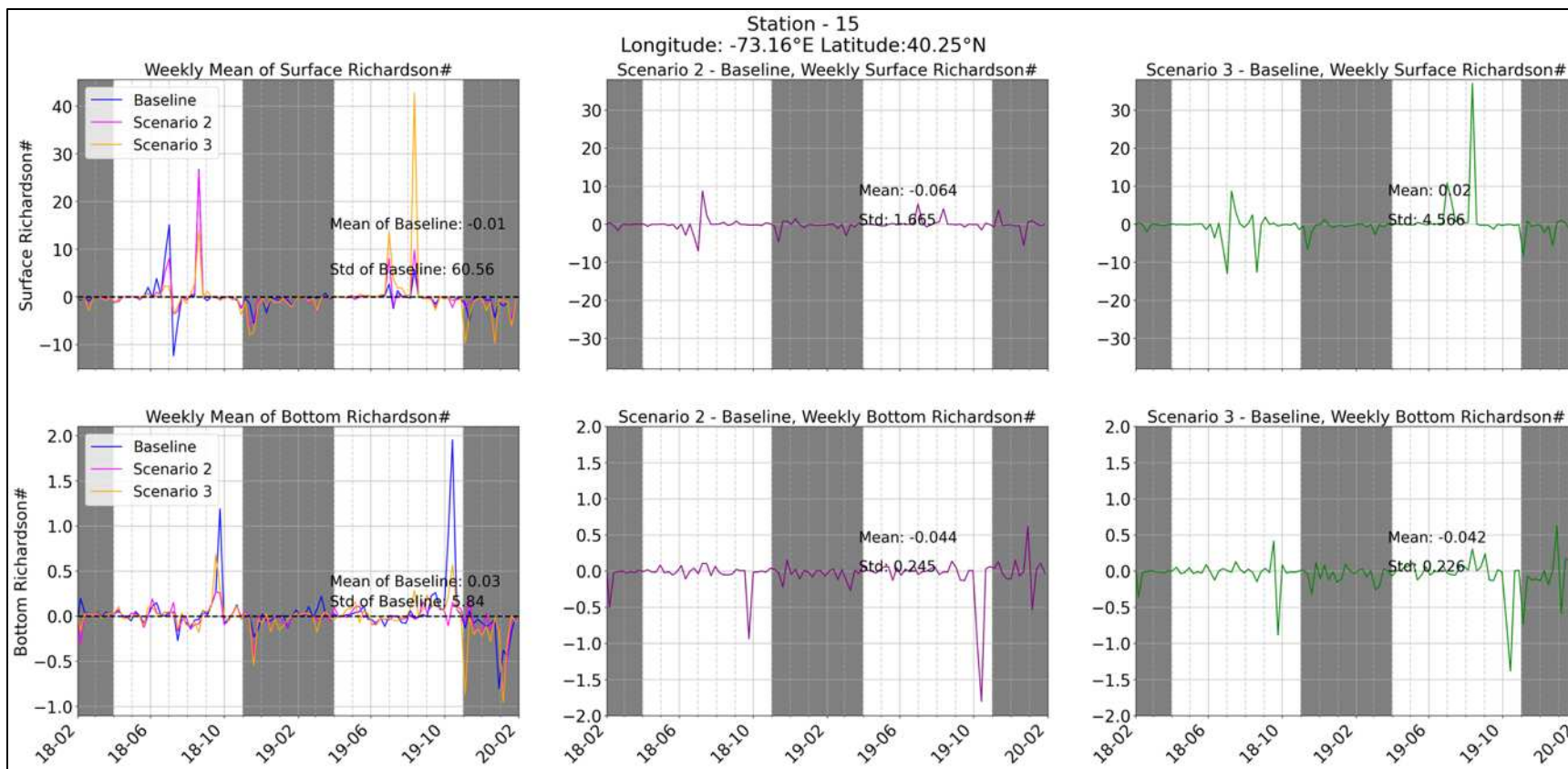


Figure 265. Weekly mean (left panels), and weekly differences for Scenario 2-baseline (middle panels) and Scenario 3-baseline (right panels) for Richardson Number (surface and bottom) at station 15.

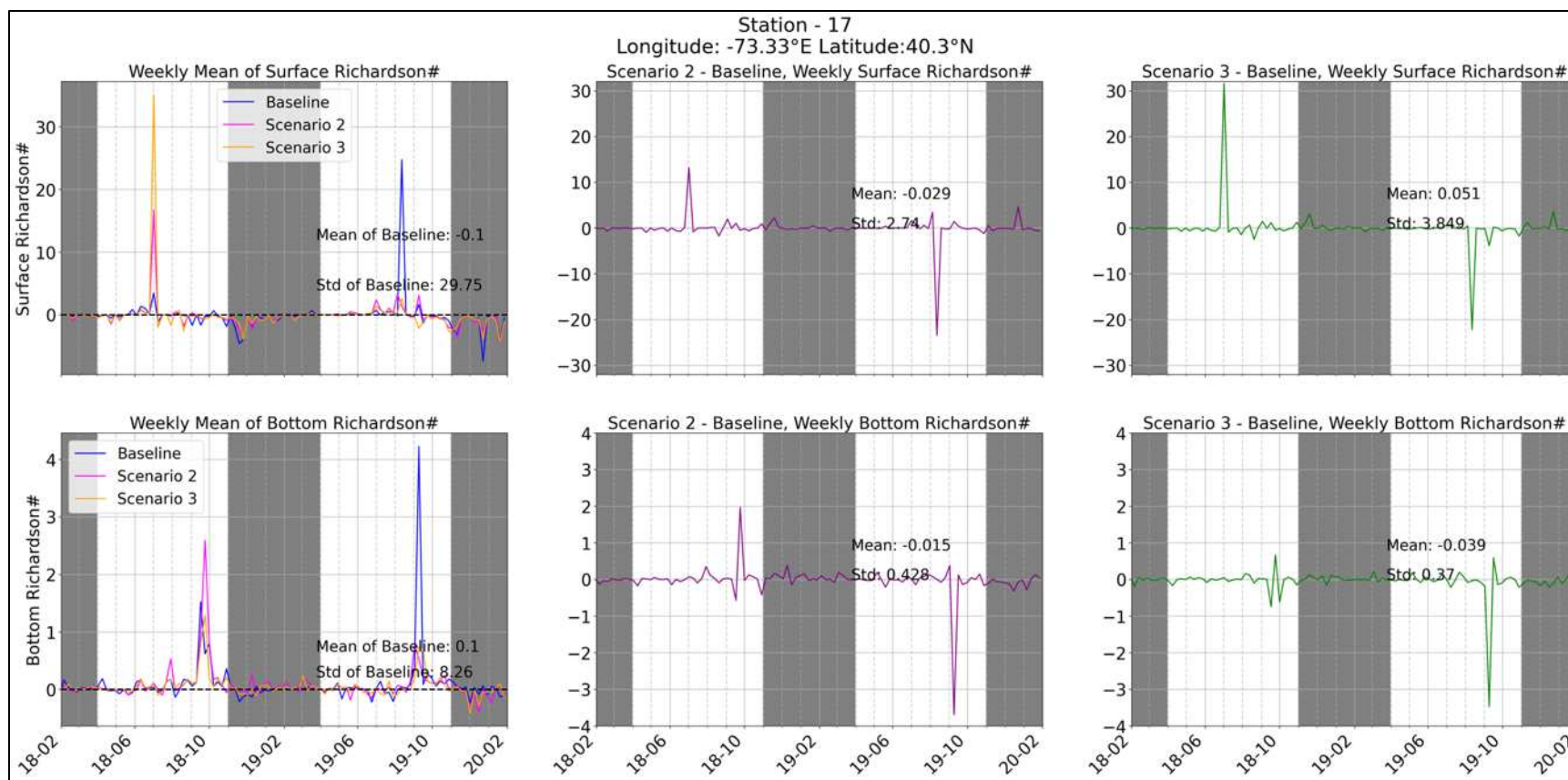


Figure 266. Weekly mean (left panels), and weekly differences for Scenario 2-baseline (middle panels) and Scenario 3-baseline (right panels) for Richardson Number (surface and bottom) at station 17.

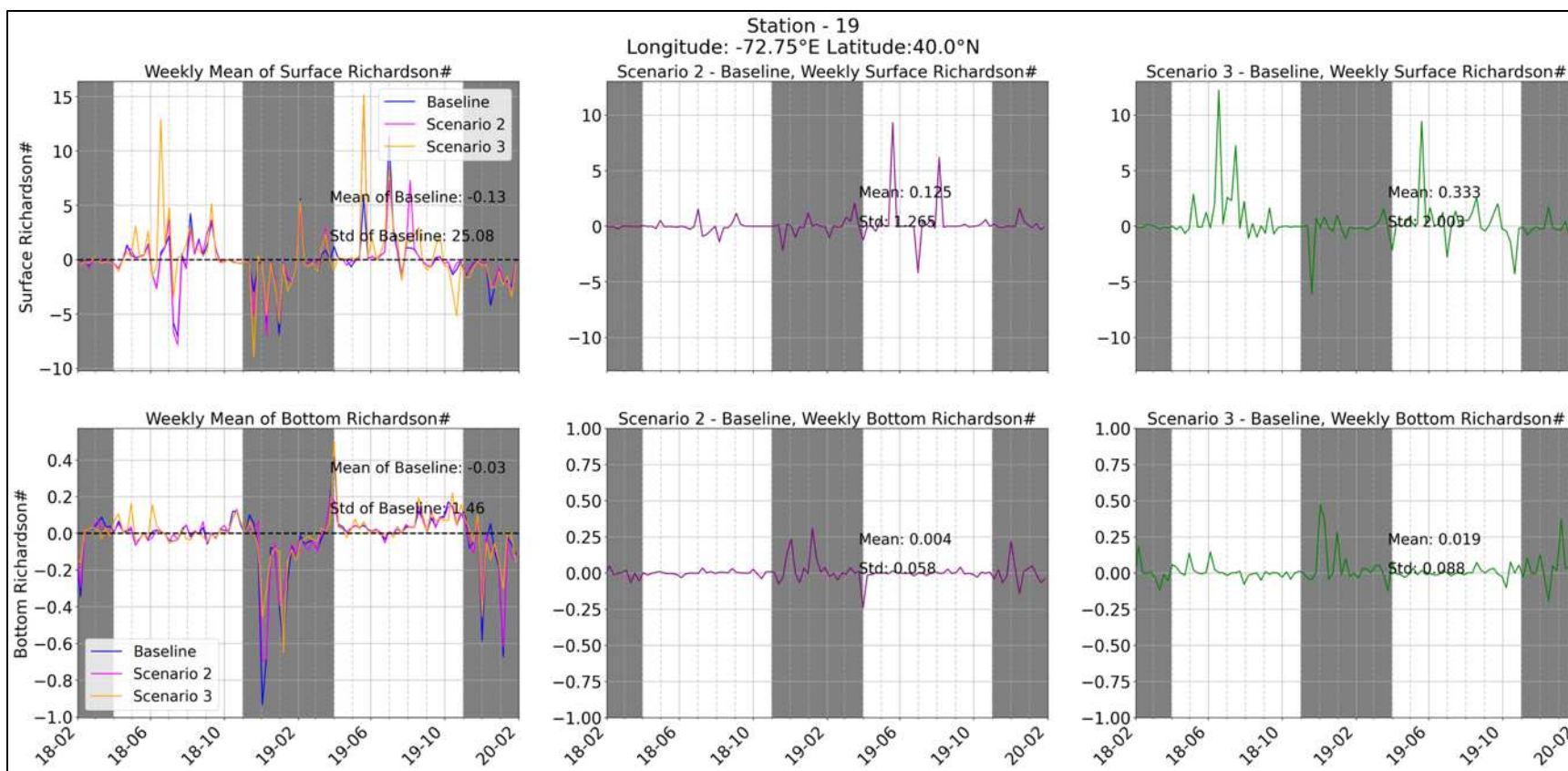


Figure 267. Weekly mean (left panels), and weekly differences for Scenario 2-baseline (middle panels) and Scenario 3-baseline (right panels) for Richardson Number (surface and bottom) at station 19.

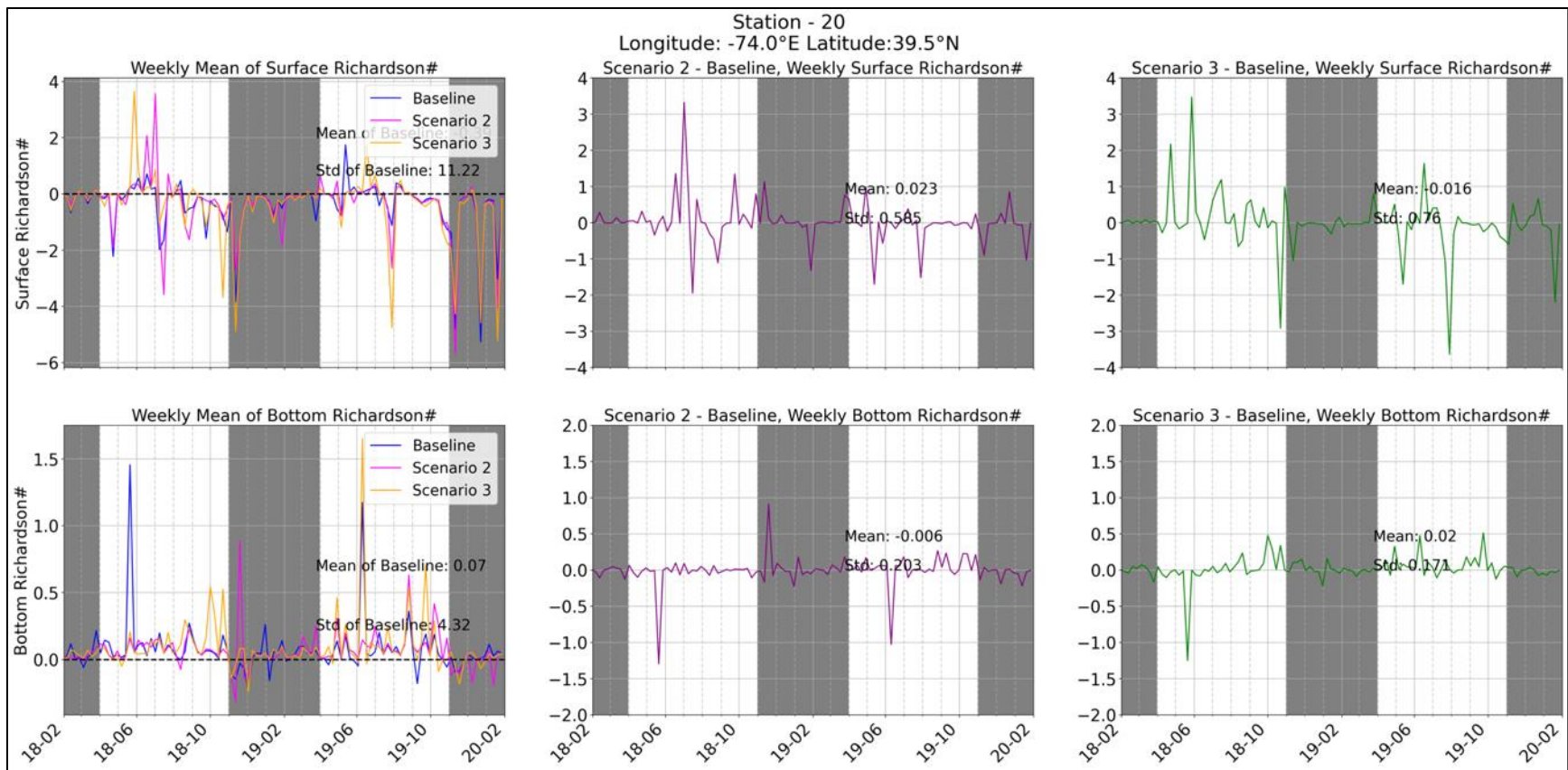


Figure 268. Weekly mean (left panels), and weekly differences for Scenario 2-baseline (middle panels) and Scenario 3-baseline (right panels) for Richardson Number (surface and bottom) at station 20.

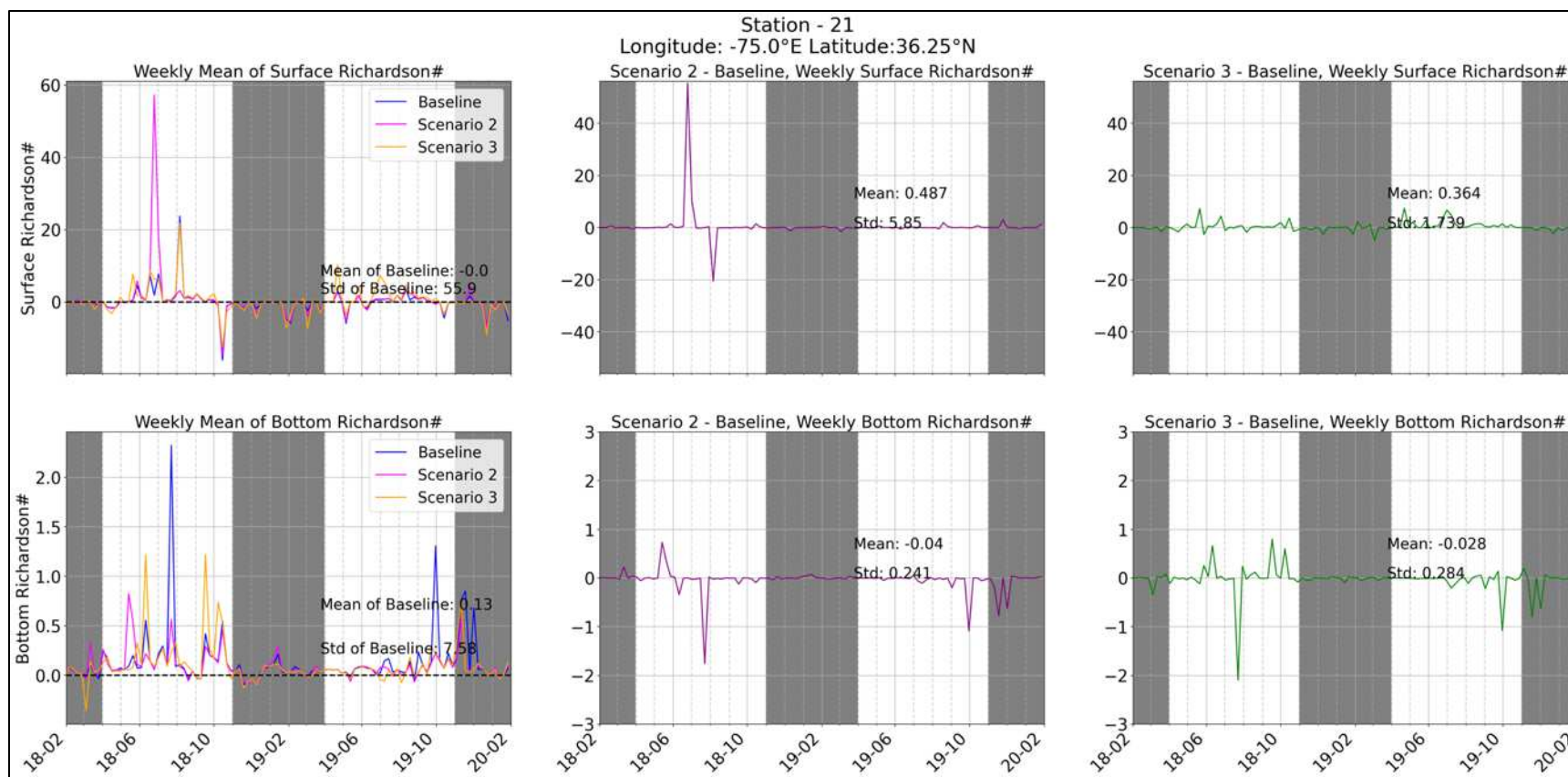


Figure 269. Weekly mean (left panels), and weekly differences for Scenario 2-baseline (middle panels) and Scenario 3-baseline (right panels) for Richardson Number (surface and bottom) at station 21.

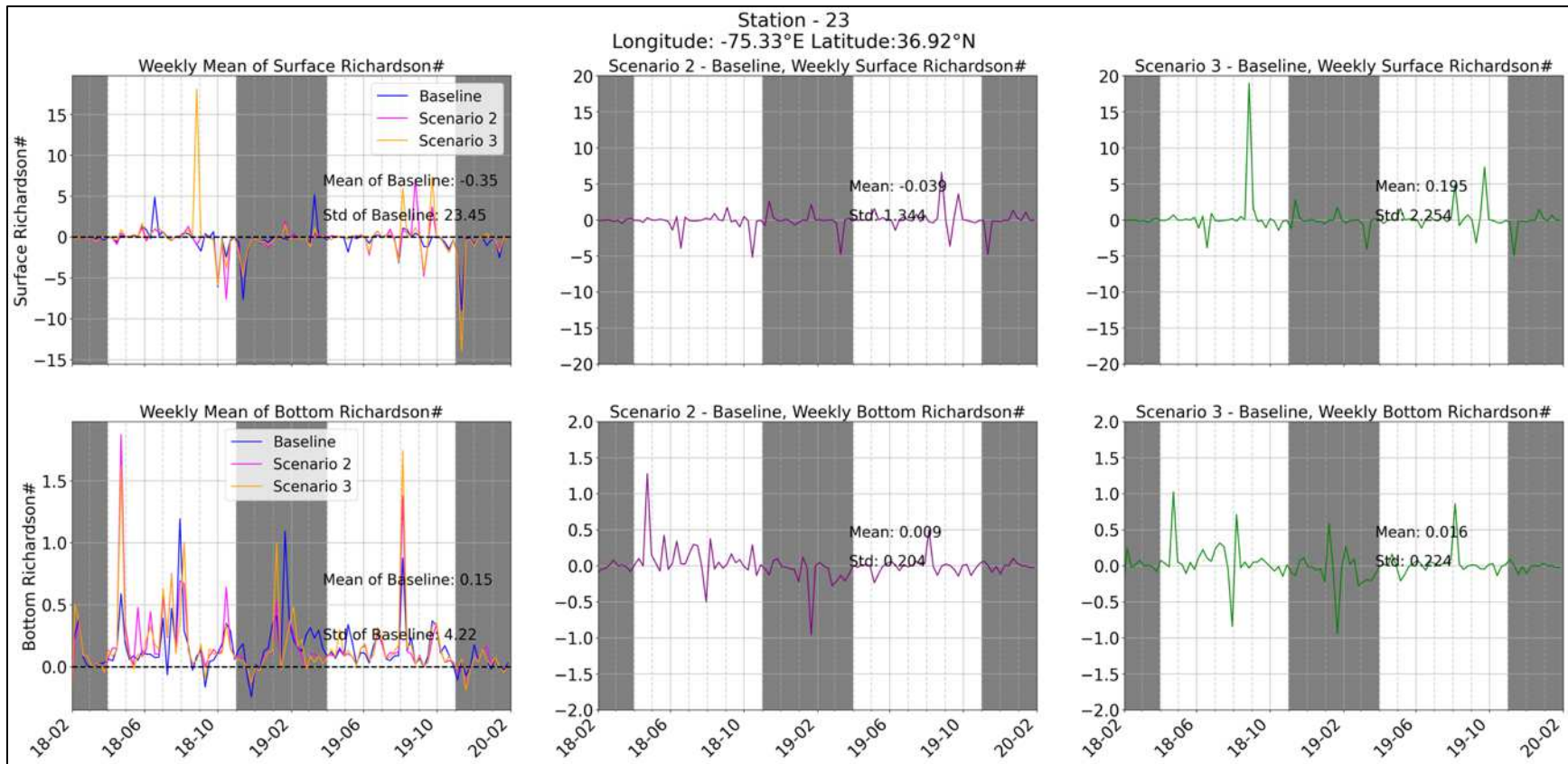


Figure 270. Weekly mean (left panels), and weekly differences for Scenario 2-baseline (middle panels) and Scenario 3-baseline (right panels) for Richardson Number (surface and bottom) at station 23.

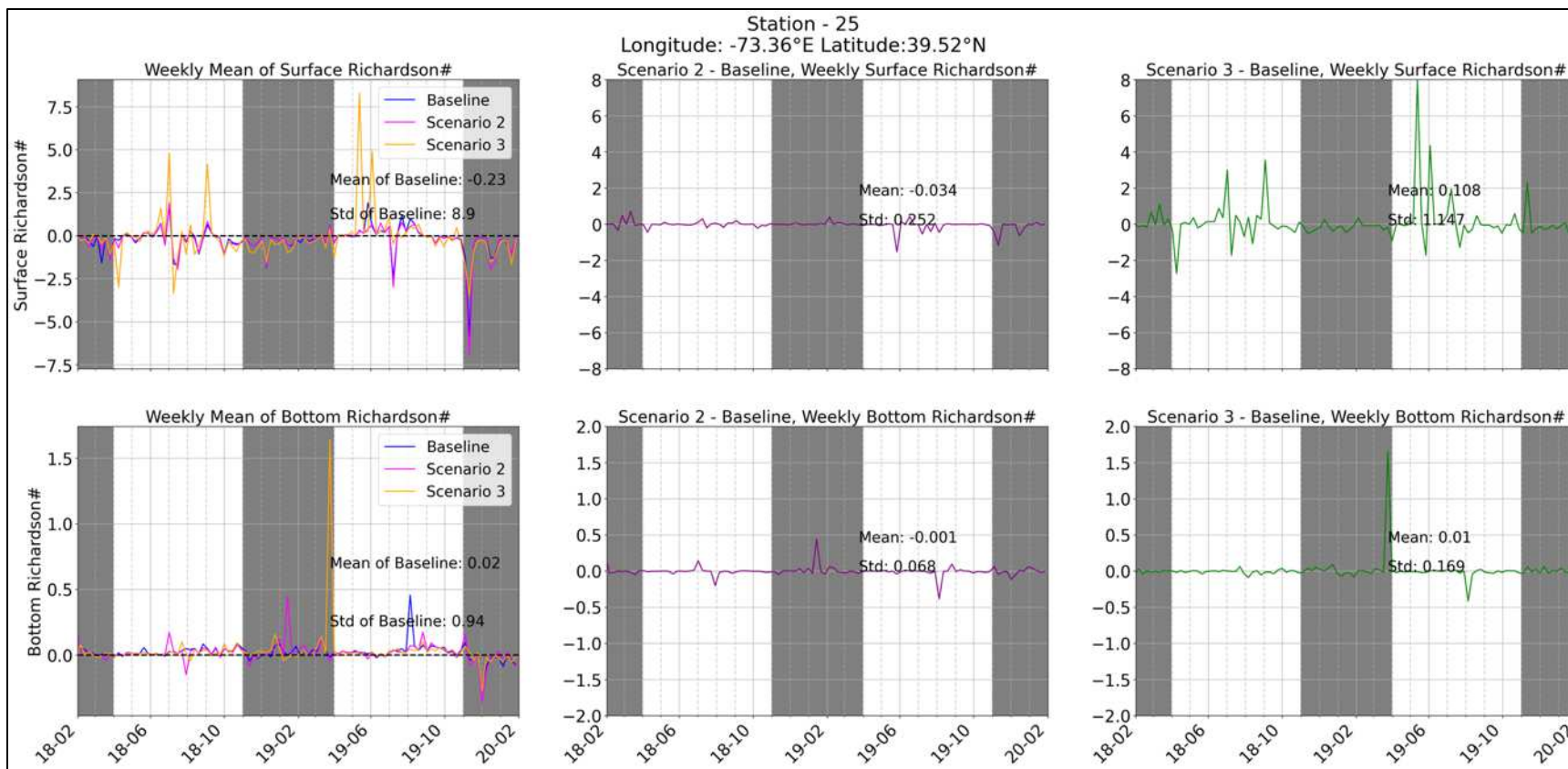


Figure 271. Weekly mean (left panels), and weekly differences for Scenario 2-baseline (middle panels) and Scenario 3-baseline (right panels) for Richardson Number (surface and bottom) at station 25.

9.3.2.7 Effects on the Thermocline

Time series of thermocline depth (the depth of the peak thermal gradient) and strength (the thermal gradient at that depth) at stations located in the WEAs are presented in Figure 268 through Figure 274. The difference time series for thermocline depth shows mostly negative peaks (beside winter) for most of the stations in developed WEAs. These negative changes are consistent with a phenomenon known in the offshore wind farm literature as “thermocline shoaling” (“doming” or uplifting) linked to the wind wake (Floeter et al., 2022) and are likely caused by less mixing and potential changes in shear and Ekman pumping due to the reduction in wind speed for Scenario 2 and 3, which leads to decrease in thermocline depth over the summer (as also seen in Table 27). The figures also demonstrate that the thermocline strength drops to zero in the winter, indicating a well-mixed water column, making the thermocline depth an irrelevant metric in this condition.

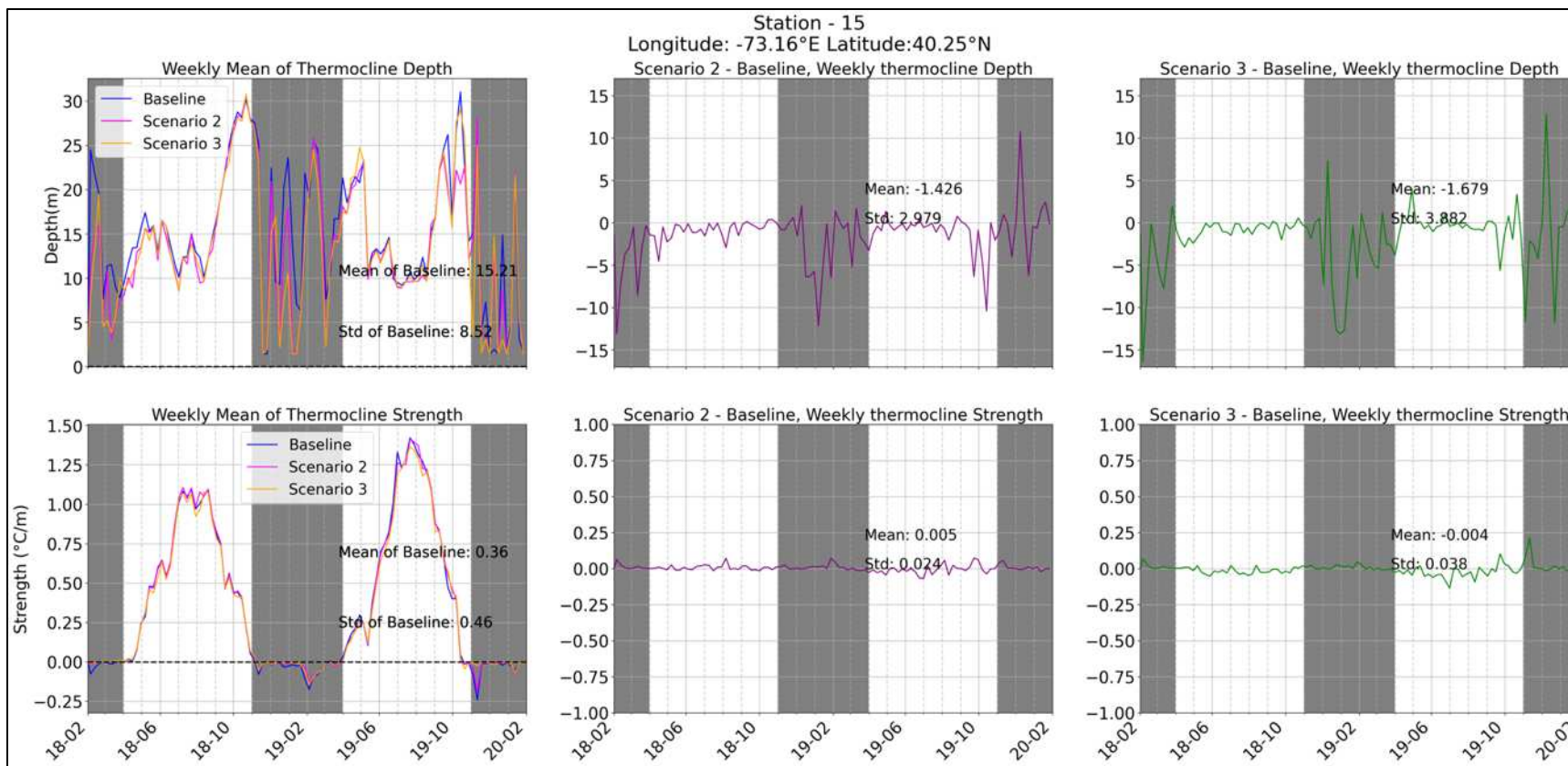


Figure 272. Weekly mean (left panels), and weekly differences for Scenario 2-baseline (middle panels) and Scenario 3-baseline (right panels) for thermocline depth and strength at station 15.

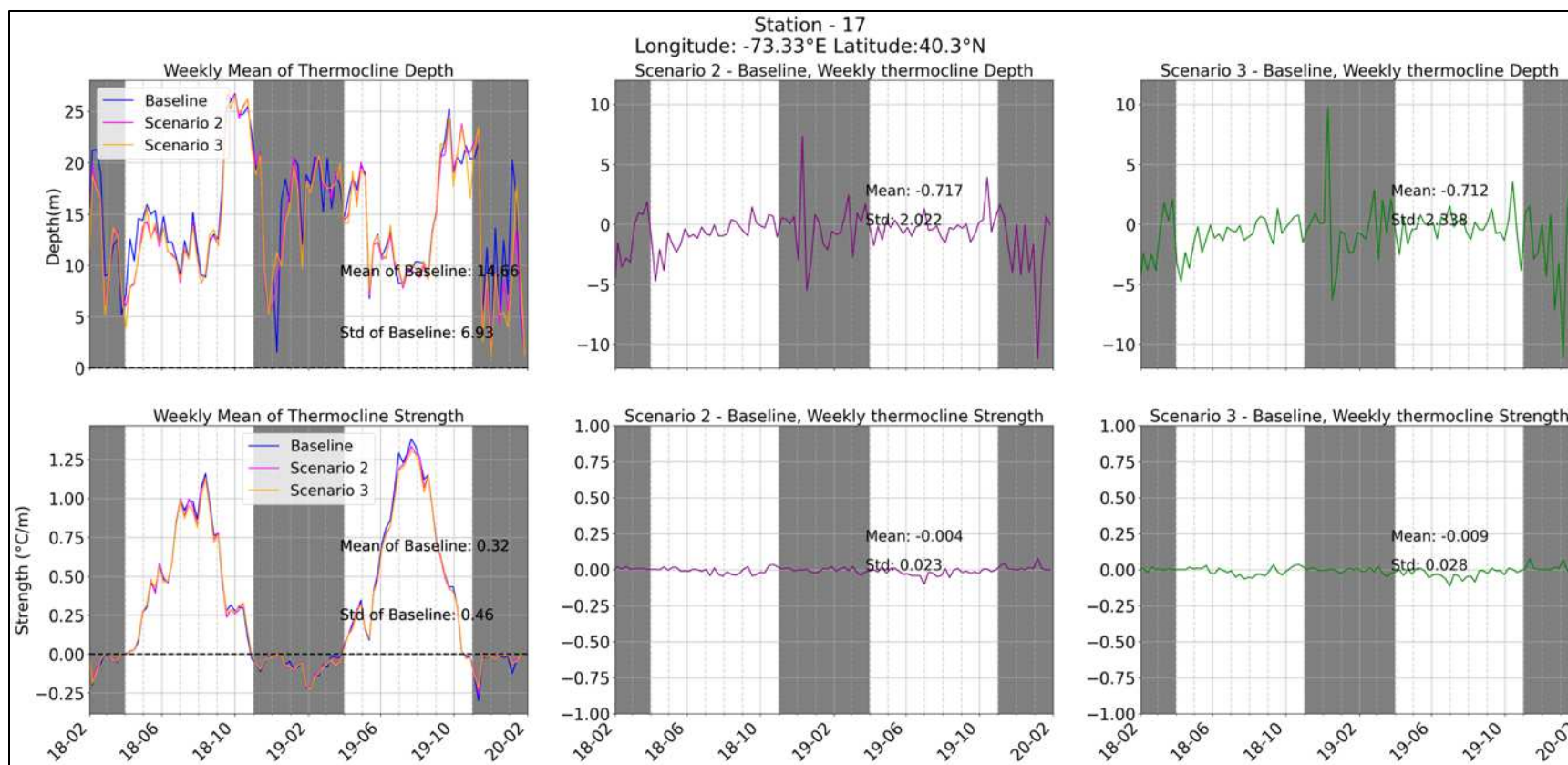


Figure 273. Weekly mean (left panels), and weekly differences for Scenario 2-baseline (middle panels) and Scenario 3-baseline (right panels) for thermocline depth and strength at station 17.

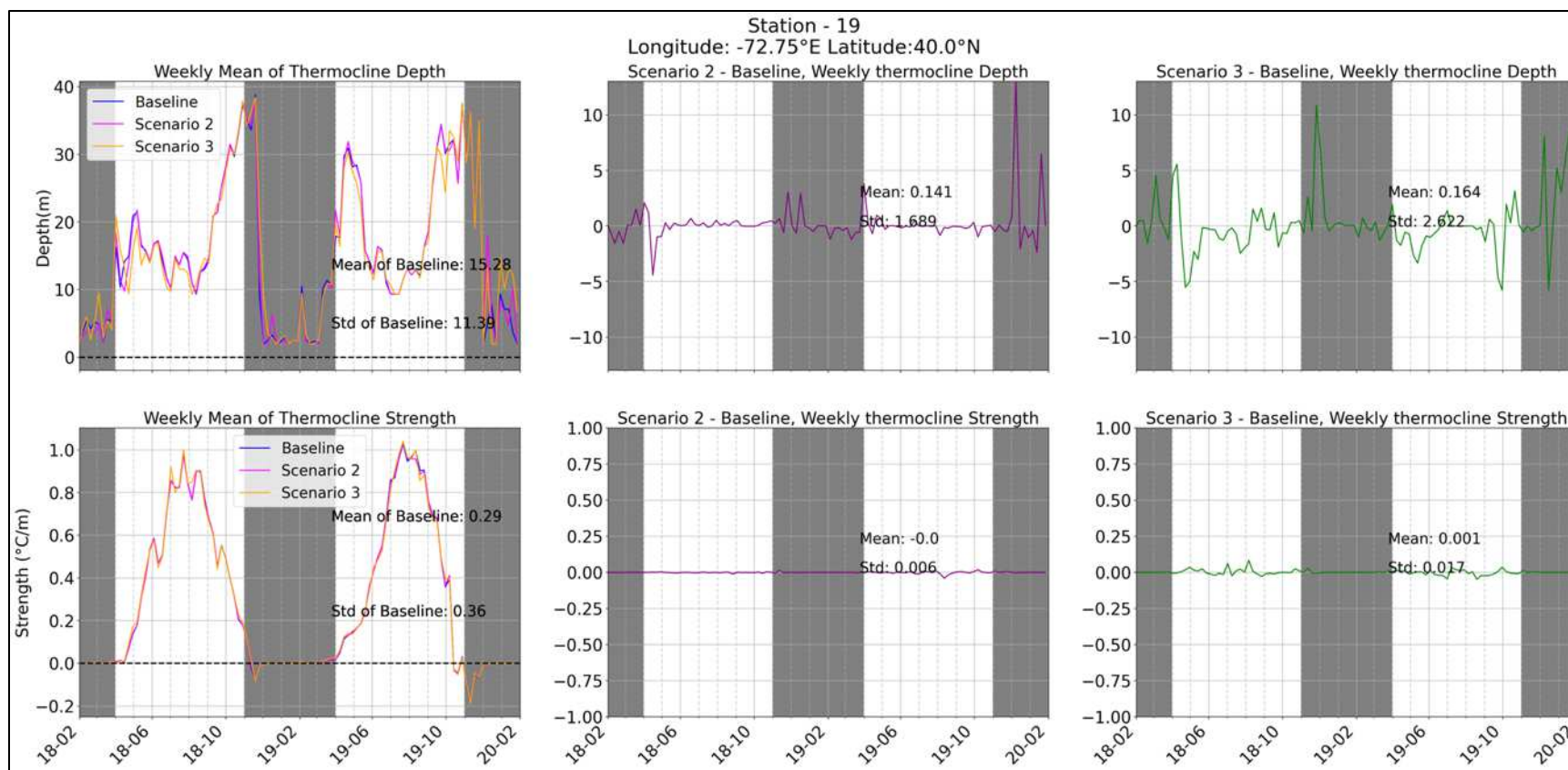


Figure 274. Weekly mean (left panels), and weekly differences for Scenario 2-baseline (middle panels) and Scenario 3-baseline (right panels) for thermocline depth and strength at station 19.

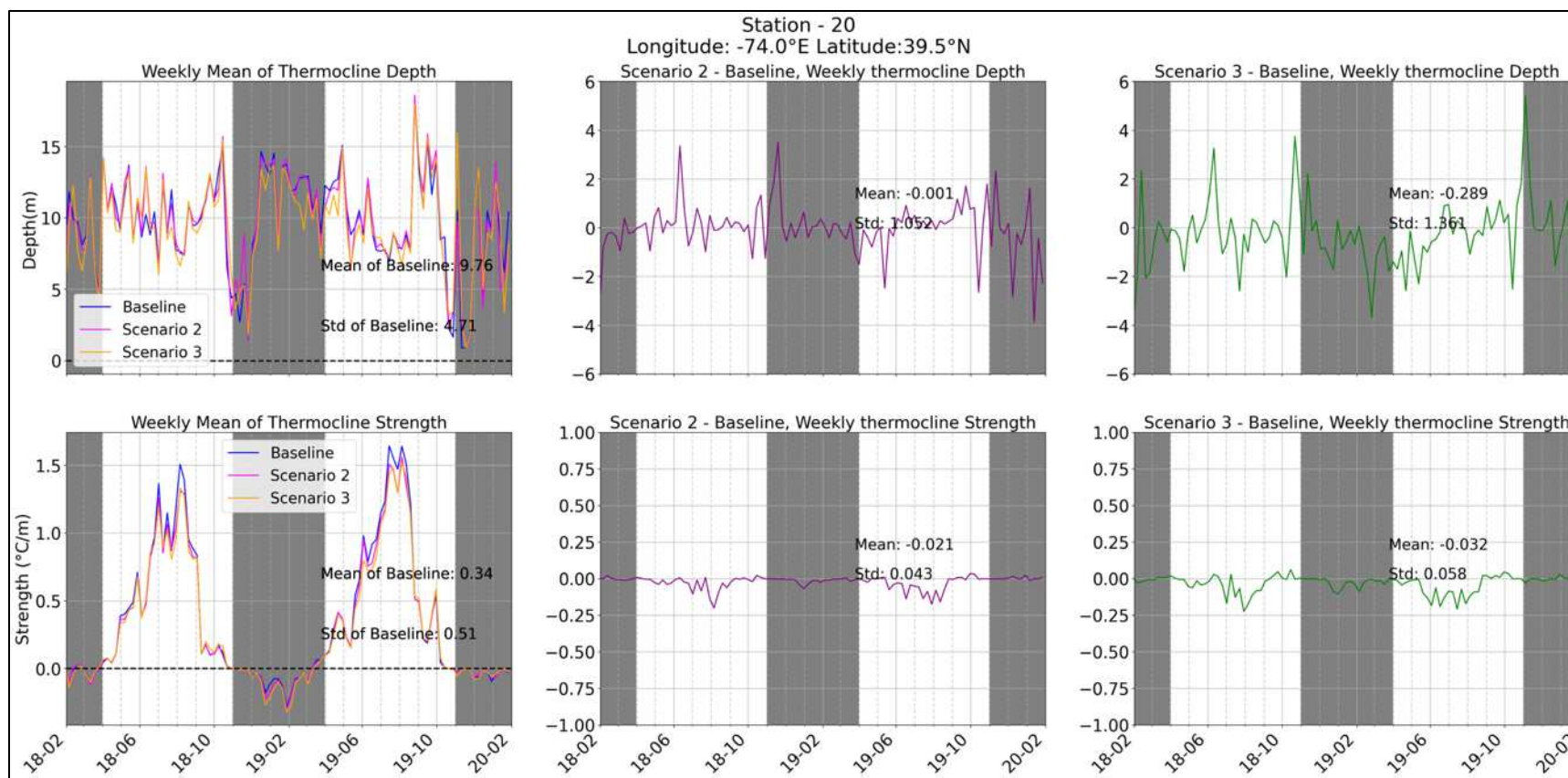


Figure 275. Weekly mean (left panels), and weekly differences for Scenario 2-baseline (middle panels) and Scenario 3-baseline (right panels) for thermocline depth and strength at station 20.

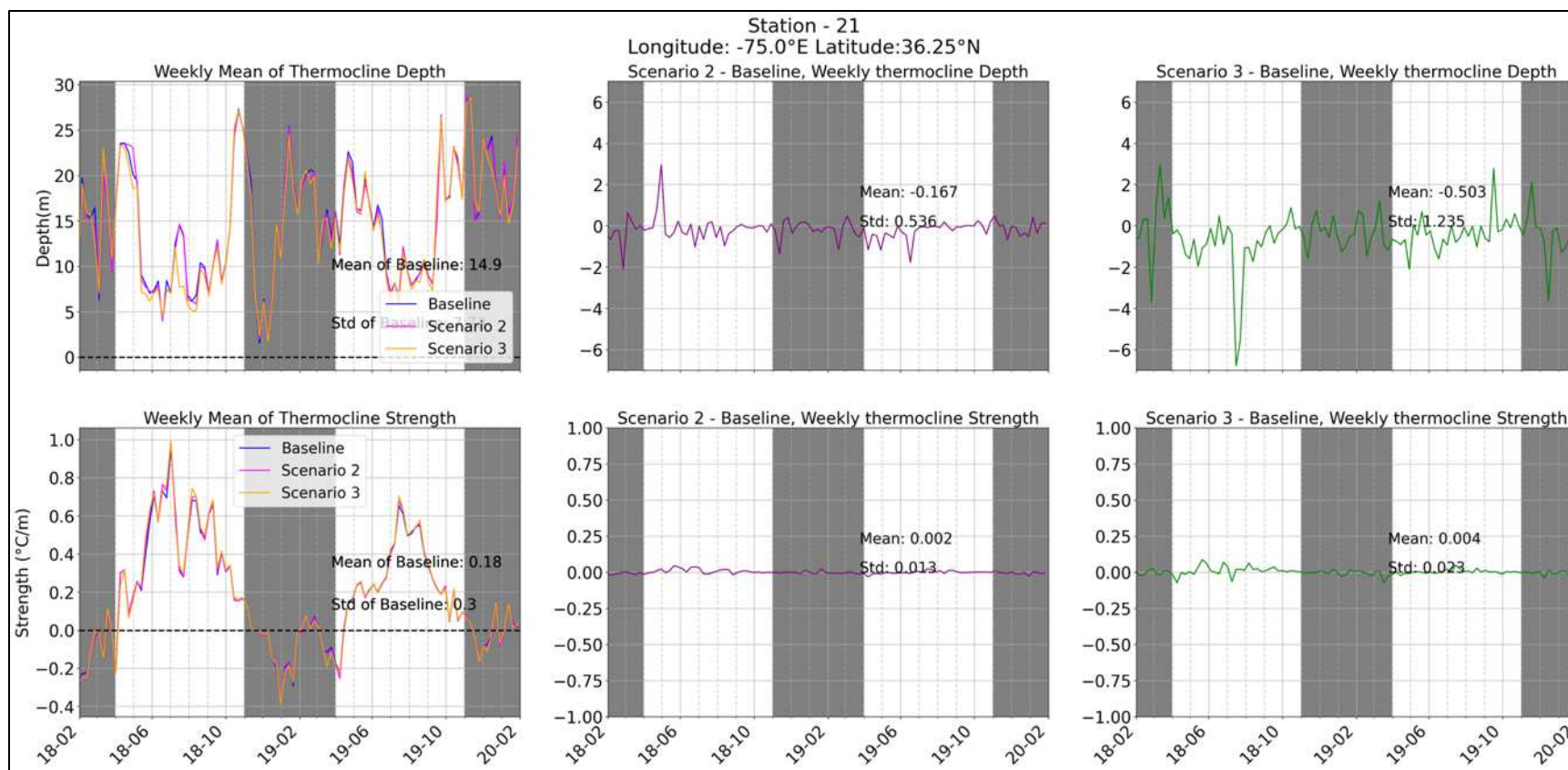


Figure 276. Weekly mean (left panels), and weekly differences for Scenario 2-baseline (middle panels) and Scenario 3-baseline (right panels) for thermocline depth and strength at station 21.

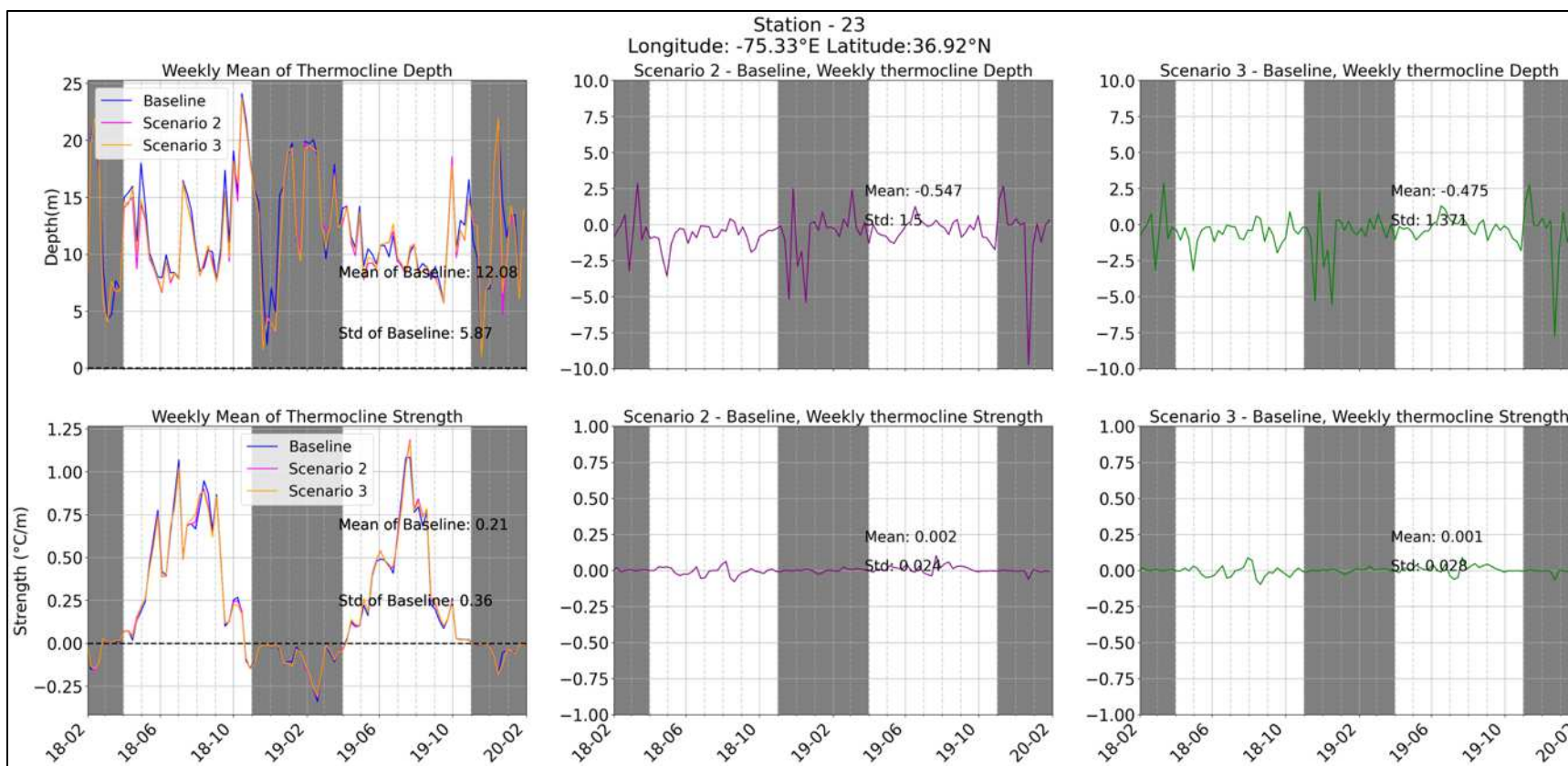


Figure 277. Weekly mean (left panels), and weekly differences for Scenario 2-baseline (middle panels) and Scenario 3-baseline (right panels) for thermocline depth and strength at station 23.

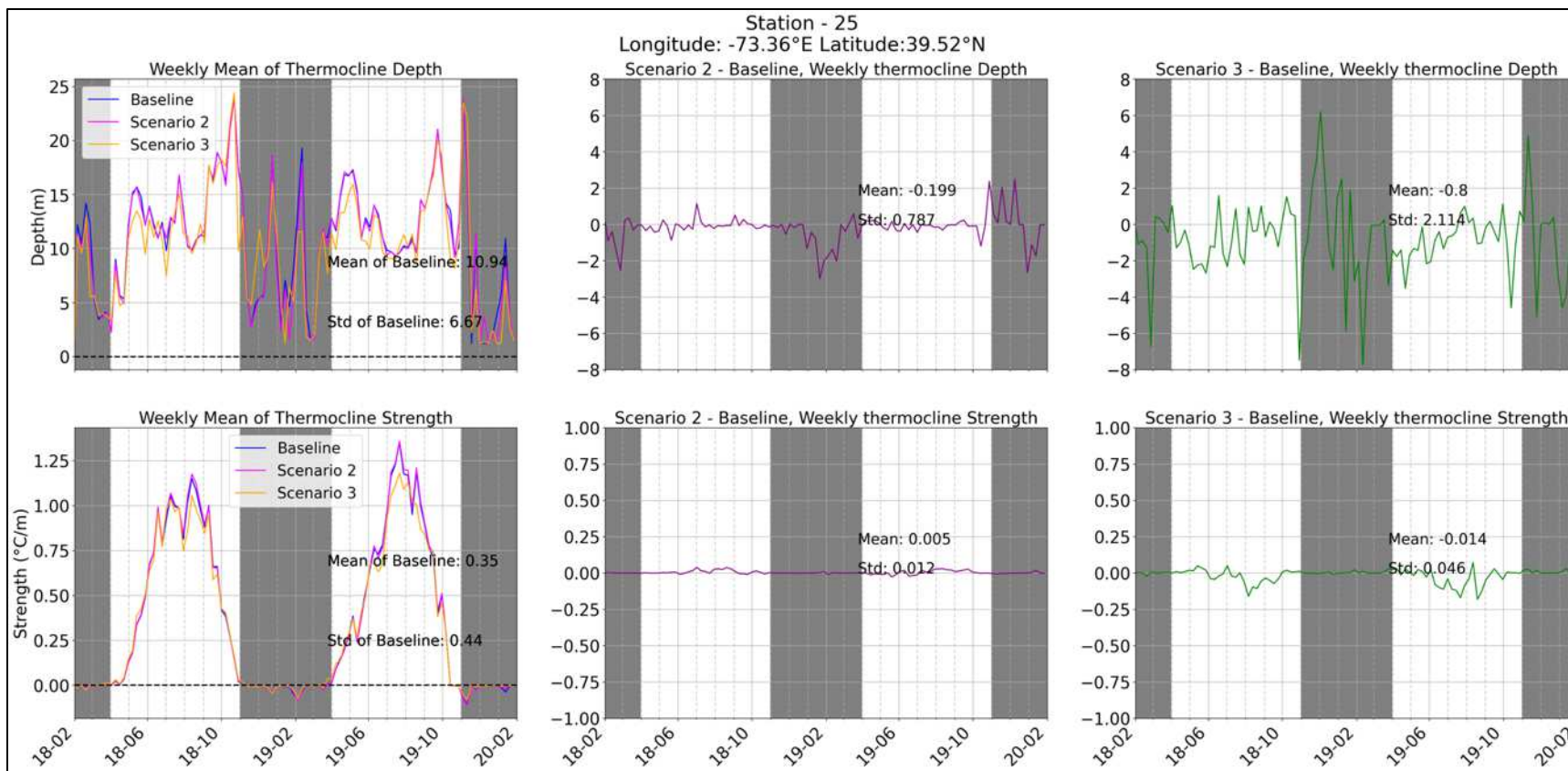


Figure 278. Weekly mean (left panels), and weekly differences for Scenario 2-baseline (middle panels) and Scenario 3-baseline (right panels) for thermocline depth and strength at station 25.

9.4 Effects on Stratification and Thermocline

The addition of the WEA turbines effects the temperature throughout the water column. This is exhibited in the cold pool dynamics, temperature time series analysis, and the difference (delta) in temperature between the surface and bottom levels of the water column. A positive (negative) change between this temperature delta between wind farm scenarios and baseline conditions indicates the areas of increased (decreased) thermal stratification under the partial (Scenario 2) and full build out (Scenario 3).

The full build out of the WEA turbines (Scenario 3) has the largest area of increased temperature delta (increased thermal stratification) compared to baseline conditions. The model results display increased variability in temperature during the summer season. An increase in thermal stratification in the wind farms located in the Mid-Atlantic region, offshore of New Jersey, is predicted in August 2018 (Figure 221). The cold pool dynamics of the region in August 2018, are consistent with the temperature change. Transect 2 cold pool contours in August 2018, show an increase in the cold pool area towards the nearshore region (Figure 221). The temperature analysis conducted at station 25 is also consistent with these findings. Station 25 displays large changes in temperature in the bottom of the water column under full build out conditions compared to baseline conditions in August 2018.

Monthly thermal stratification maps over the model duration are included in Appendix C.

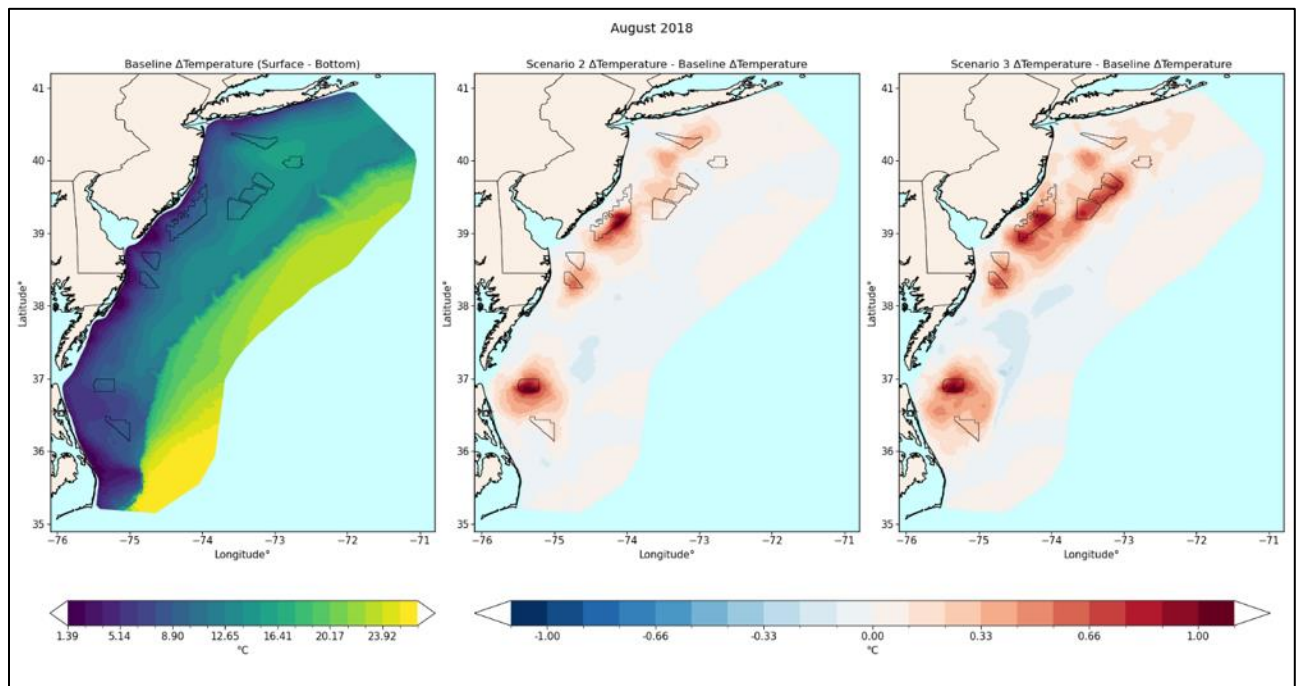


Figure 279. Change in thermal stratification for Scenario 2 (partial build out) and Scenario 3 (full buildout) against baseline conditions for August 2018.

In the previous subsections, it is shown how wind wakes affect surface and bottom temperature (see Section 9.3.2.2), which result in a change in thermocline depth and strength (Section 9.3.2.7). Two example scenarios are discussed next, to analyze how the change in wind speed influences change in temperature in the water column. For Scenario 3-baseline analysis at station 19, a significant change was seen in the z-score for temperature (Figure 235) as well as thermocline depth and strength (Figure 270) at the end of April, 2019. The wind velocity, current velocity, and temperature throughout the water column for all three scenarios are presented in Figure 276. The wind time series show that around April 28, the wind speed during Scenario 3 was lower compared to Scenario 2 and baseline. This reduction in wind

speed causes more stratification and decrease in thermocline depth (Figure 270). Thus, the volume of water susceptible to heat flux warming through mixing decreases and that leads to increased temperature of surface water at station 19. The temperature plot for Scenario 3 around the same time shows that near the surface, temperature increased compared to Scenario 2 and baseline.

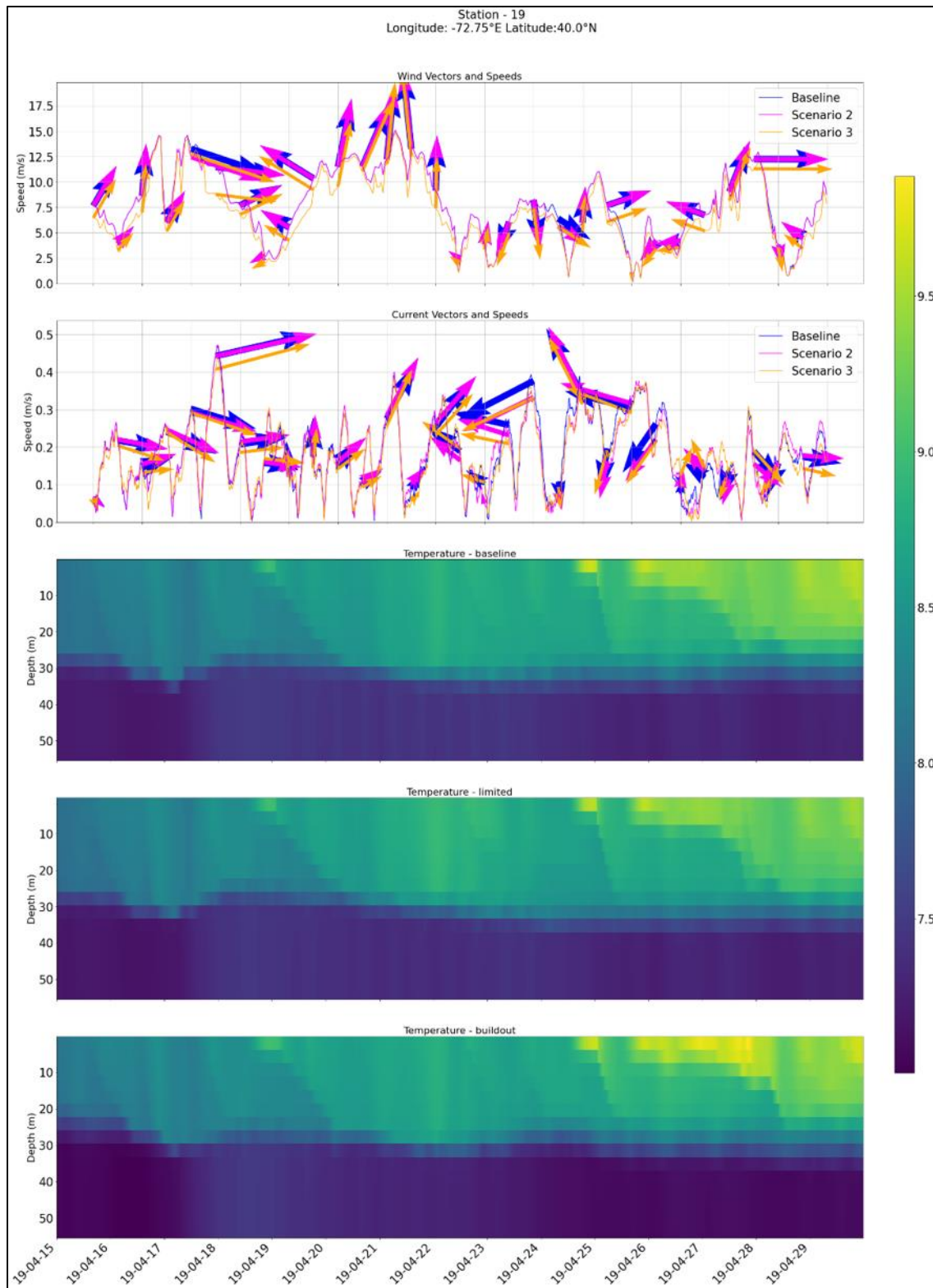


Figure 280. Wind velocity (top first panel), current velocity (second panel), and temperature with depth (panels 3 through 5) for all three scenarios during April 15–April 30, 2019 at station 19. Another similar analysis based on the relationship of wind velocity and temperature is presented in Figure 277 for station 25. A significant change was seen in Scenario 3-baseline calculation for temperature

(Figure 239) as well as thermocline (Figure 273) at the start of August, 2019. The wind velocity, current velocity, and temperature throughout the water column for all three scenarios are presented in Figure 277. The wind time series show that around August 2, the wind speed during Scenario 3 was lower compared to Scenario 2 and baseline. This subsequently causes more stratification/higher thermocline and warmer surface water. The temperature plot for Scenario 3 around the same time shows that near the surface, temperature was relatively higher compared to Scenario 2 and baseline.

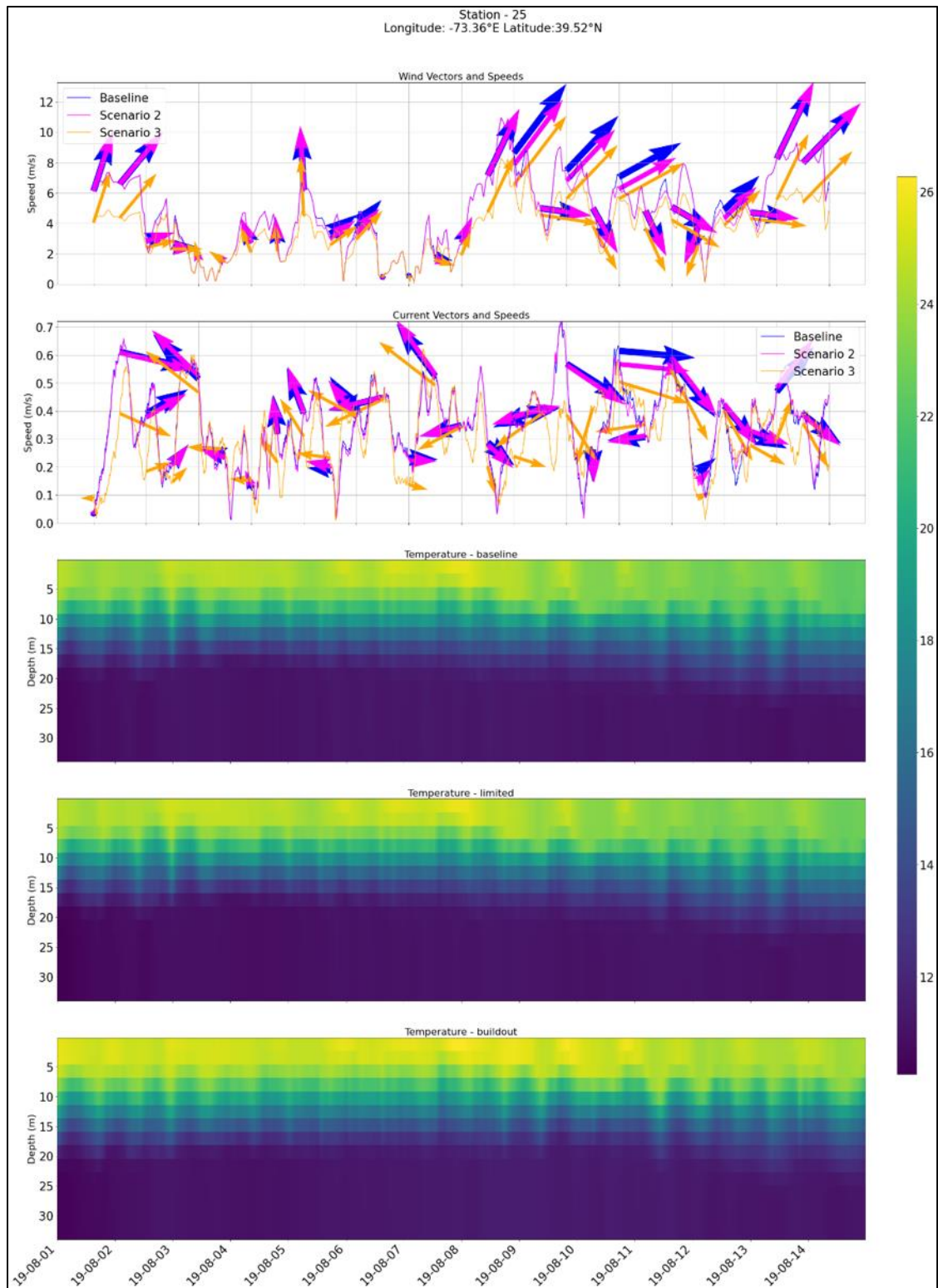


Figure 281. Wind velocity (first panel), current velocity (second panel), and temperature with depth (panels 3 through 5) for all three scenarios during August 1–August 15, 2019 at station 25.

10 Impact Of Offshore Wind Farms on Bed Shear Stress and Sediment Mobility

10.1 Methodology

Ocean current and wave forces produce bed shear stress, which represents the friction exerted by the moving water against the seabed. Constructing offshore wind energy facilities may impact the marine environment by altering bottom shear stress, thereby affecting sediment movement. These alterations in bottom stress may stem from changes in current velocity and wave parameters in and around the offshore wind farm.

The impacts were analyzed by separately employing hydrodynamic and wave models, and then integrating them by superimposing their effects for every time-step. The calculations for bed shear stress and sediment mobility were conducted for fully forced 3D baroclinic simulations of Scenario 1 (baseline), Scenario 2 (limited), and Scenario 3 (buildout). The bed shear stress was calculated using the methodology developed by Soulsby and Clarke (2005). For sediment mobility analysis, the Shields criterion for the critical bed shear stress was applied, following the approach of van Rijn (2018).

10.2 Bed Shear Stress

The following plots show the 50th, 95th, and 99th percentile bed shear stress results for currents and waves separately and for combined currents and waves.

In the model's domain, bed shear stresses arising from currents are generally low for baseline (Scenario 1) (Figure 278) with an exception in the southern region where the Gulf Stream current produces a significant shear stress. Except in the area north of 40° N, where the northern-most assessed windfarm is located, high bed shear stress at the 99th percentile is observed to some extent across the shelf. Going from baseline to Scenario 2, and Scenario 3 no significant change in bed shear stress is detected.

The 50th percentile bed shear stress generated by waves for Scenario 1 (Figure 279) is relatively small. However, 95th and 99th percentile stresses induced by wave, are more significant in the shelf compared to deep water. Among the areas shown, the northern wind farms (north of Hudson Canyon at ~40°N) located in a relatively deeper region (Figure 39) with lower currents (Figure 222 and Figure 223) experience relatively lower bed shear stress compared to the rest of the MAB shelf. For the 99th percentile current this area also experiences an increase in bed shear stress going from baseline to Scenario 2. For baseline to Scenario 3, this area shows a decrease, but the bed shear increases around the southernmost wind farm. The rest of MAB mostly shows decrease in bed shear for both Scenario 2, and Scenario 3.

The RMS bed shear stress for waves-plus-current (Figure 280) is mostly dominated by shear stress induced by wave especially on the shelf. The 50th percentile bed shear stress is small while the 95th percentile stress for baseline is relatively bigger. The decrease in shear stress is higher from baseline to Scenario 3 when compared to baseline-Scenario 2 for 95th percentile stress. This greater reduction in stress is caused by the presence of additional wind farm in Scenario 3. Similar to the differences in wave induced 99th percentile stress between different scenarios, changes in RMS of wave-plus-current from baseline to Scenario 2, and Scenario 3, also depicts increased stress in some areas. This may be due to nonlinear changes in transient wave heights and periods of individual events.

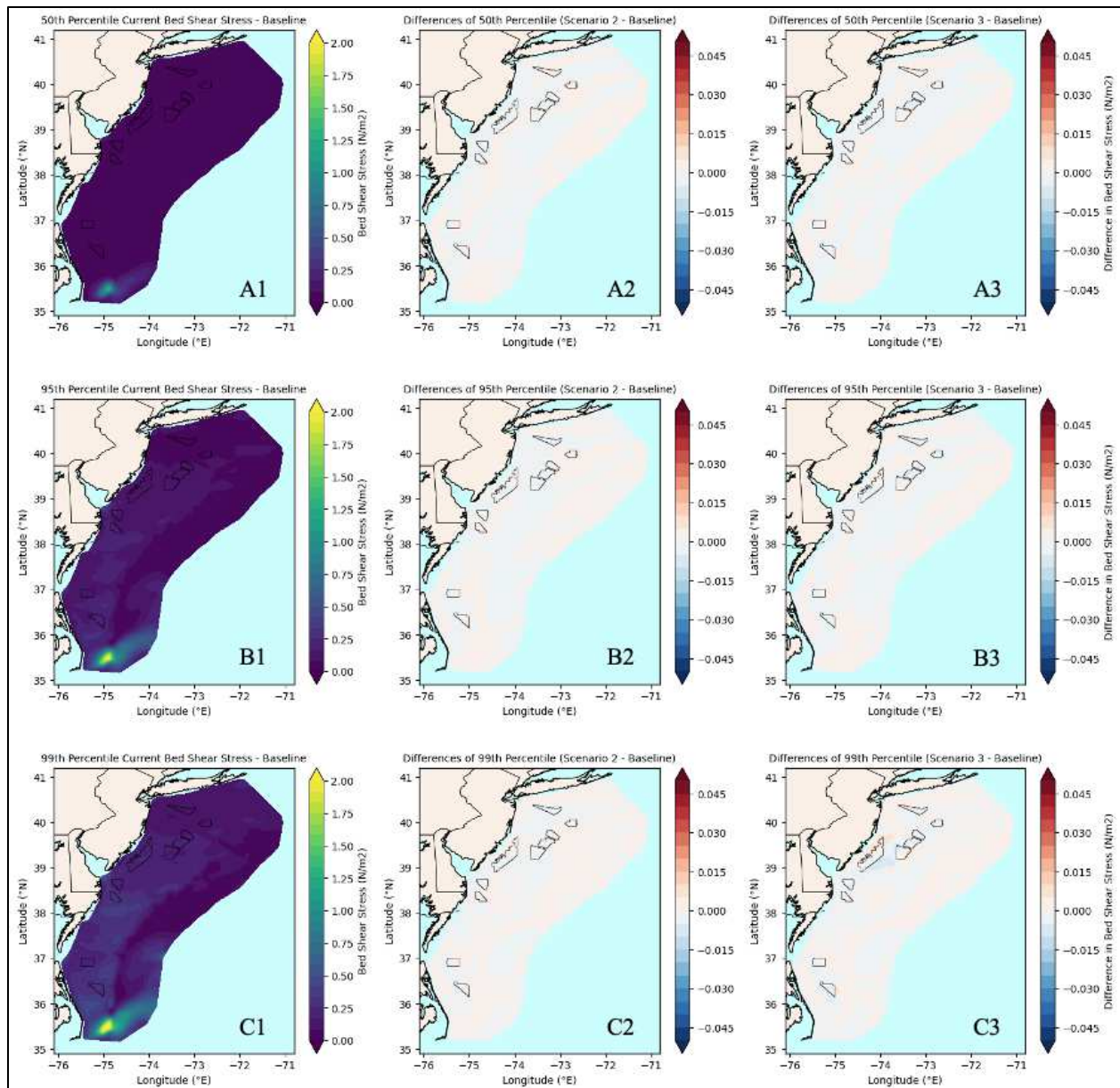


Figure 282. Change in median, 95th percentile, and 99th percentile of bed shear stress due to currents. Top row: 50th percentile bed shear stress due to current (A1) and OWT scenario changes: 50th percentile of Scenario 2 - 50th percentile of Baseline (A2) and 50th percentile of Scenario 3 - 50th percentile of Baseline (A3). Middle row: The same as top row but for the 95th percentile (B1) and the differences of 95th percentile for each OWT scenario to the baseline: Scenario 2 (B2) and Scenario 3 (B3). Bottom row: The same as top row but for the 99th percentile (C1) and the differences of 99th percentile for each OWT scenario to the baseline: Scenario 2 (C2) and Scenario 3 (C3).

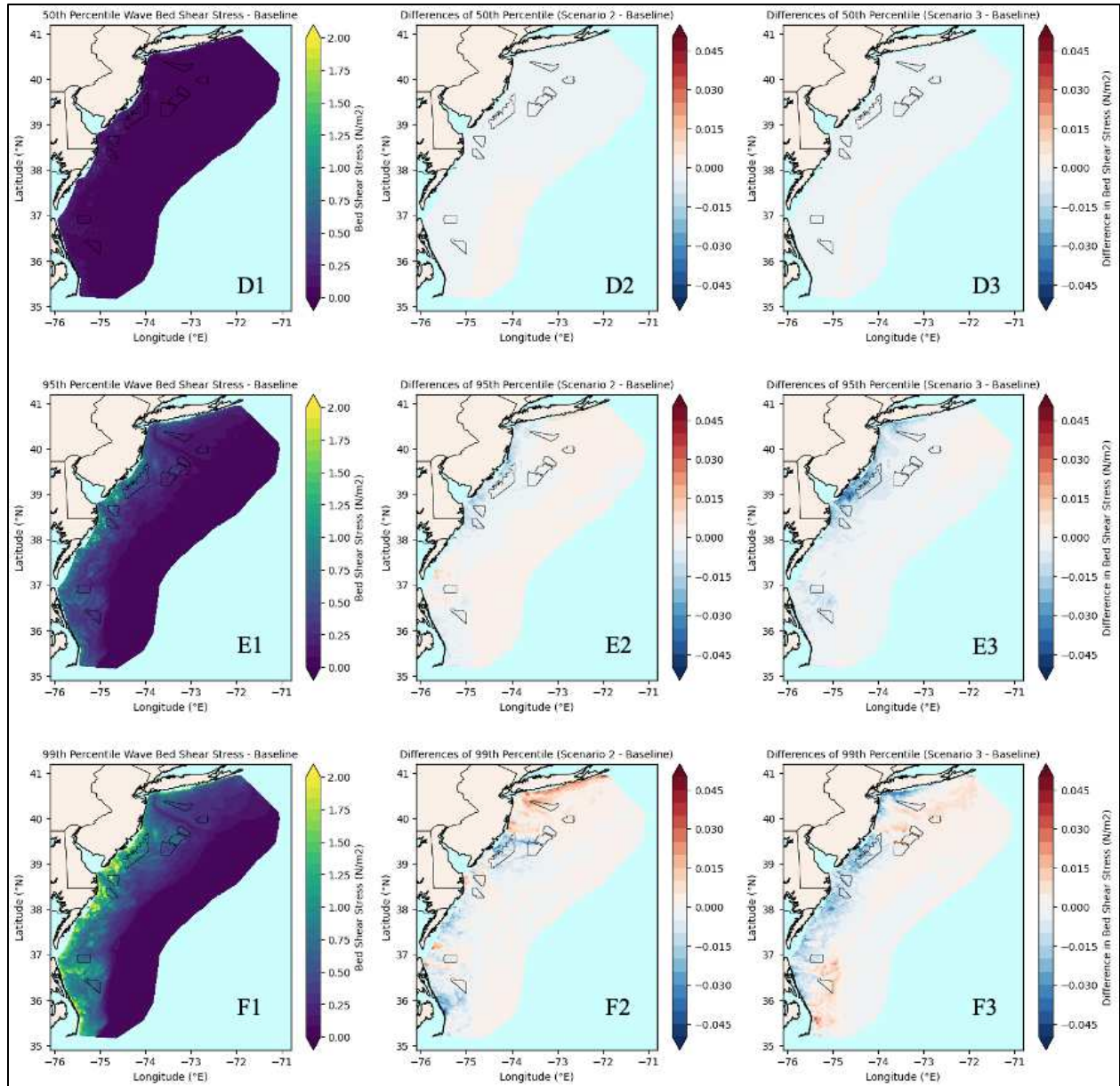


Figure 283. Change in median, 95th percentile, and 99th percentile of bed shear stress due to waves. Top row: 50th percentile bed shear stress due to wave (D1) and OWT scenario changes: 50th percentile of Scenario 2 - 50th percentile of Baseline (D2) and 50th percentile of Scenario 3 - 50th percentile of Baseline (D3). Middle row: The same as top row but for the 95th percentile (E1) and the differences of 95th percentile for each OWT scenario to the baseline: Scenario 2 (E2) and Scenario 3 (E3). Bottom row: The same as top row but for the 99th percentile (F1) and the differences of 99th percentile for each OWT scenario to the baseline: Scenario 2 (F2) and Scenario 3 (F3).

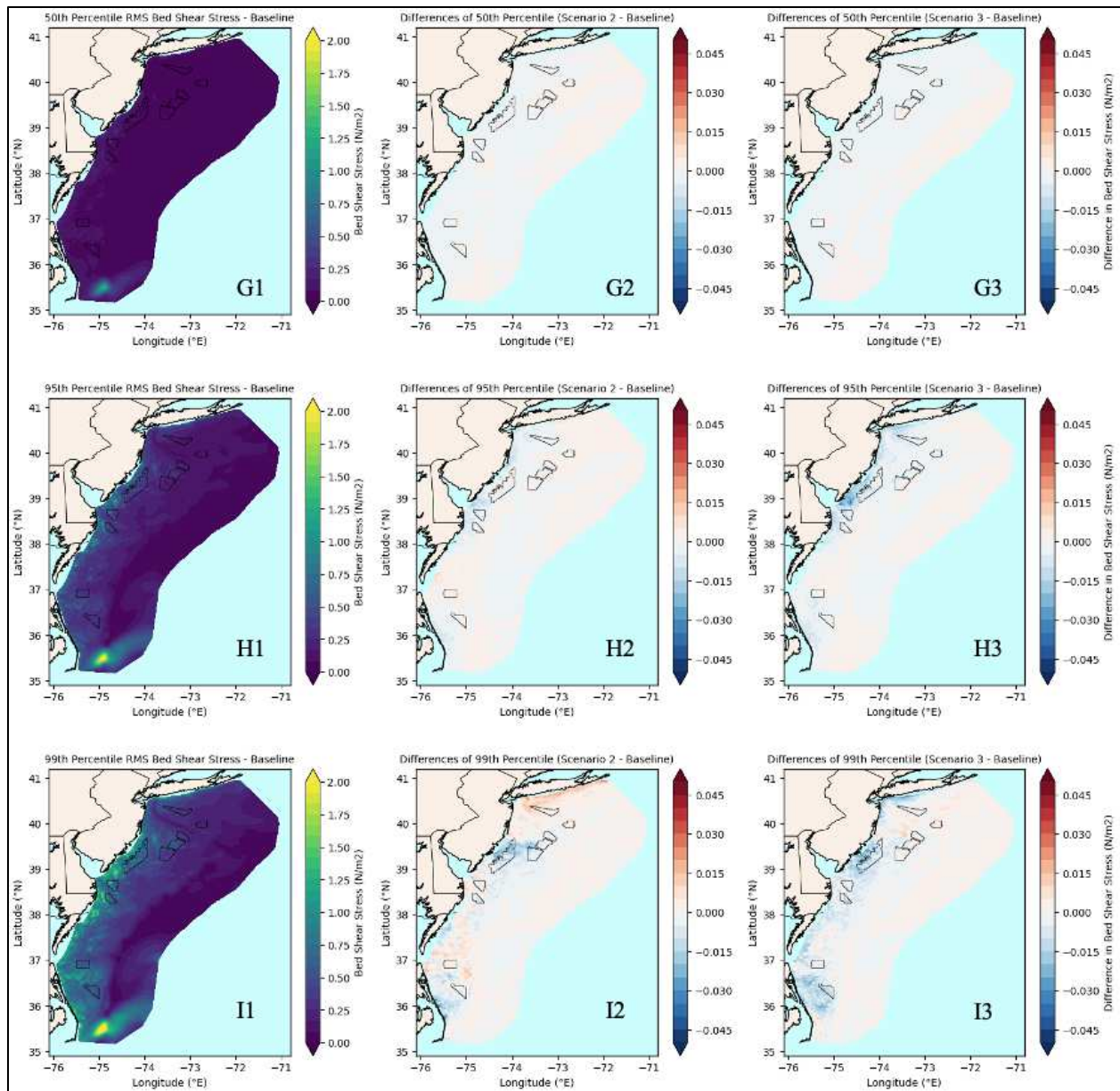


Figure 284. Change in median, 95th percentile, and 99th percentile of bed shear stress due to combined currents and waves.

Top row: 50th percentile RMS bed shear stress for waves-plus-current (G1) and OWT scenario changes: 50th percentile of Scenario 2 - 50th percentile of Baseline (G2) and 50th percentile of Scenario 3 - 50th percentile of Baseline (G3). Middle row: The same as top row but for the 95th percentile (H1) and the differences of 95th percentile for each OWT scenario to the baseline: Scenario 2 (H2) and Scenario 3 (H3). Bottom row: The same as top row but for the 99th percentile (I1) and the differences of 99th percentile for each OWT scenario to the baseline: Scenario 2 (I2) and Scenario 3 (I3).

10.3 Sediment Mobility

Sediment mobility was calculated based on the Shields relation which utilized the RMS bed shear stress for waves-plus-current depicted in the previous section. First, the grain size diameters that can be

mobilized under 50th/95th/99th percentile RMS bed shear stresses, were calculated at all the cells of the model, consistent with the bottom roughness used in the model (van Rijn, 2018). If the calculated diameter of the grain size that can be mobilized exceeded the equivalent model grain size diameter, then sediment is set in motion. Based on this criterion, if a location of the model shows moving sediment during Scenario 1 but not in Scenario 2 or Scenario 3, it experiences decreased mobility. On the other hand, if sediment was not moving in Scenario 1 but shows movement in Scenario 2 or Scenario 3, then the location would undergo increased mobility. Figure 281 shows the minimum mobile grain size diameters based on 50th, 95th, and 99th percentile RMS bed shear stresses (waves-plus-current) for the baseline as well as changes in sediment mobility going from baseline to Scenario 2, and Scenario 3.

The minimum mobile grain size diameters based on different RMS bed shear stresses for waves-plus-current show that larger grain diameter can be moved with increasing shear stress on the shelf (Figure 281). Also, the footprints of change in sediment mobility are consistent with the RMS bed shear stresses for waves-plus-current shown in Figure 280.

For the 50th percentile RMS bed shear stresses for waves-plus-current, no change of mobility is seen in Scenario 2 and Scenario 3 as the change in shear stress/grain size diameter is minimum. However, for the 95th percentile stress, decrease in mobility is detected from baseline to Scenario 2 and Scenario 3. Scenario 2 also shows few locations where mobility is increased. For the 99th percentile stress, the decrease in mobility is seen going from baseline to Scenario 2 in more cells of the model while some of the locations depict increased mobility (mostly in between 37°N and 38°N, and 40°N to around 41°N which is consistent with the increase in shear stress (Figure 280). For 99th percentile stress change from baseline to Scenario 3, more places show decrease in mobility while few places show increase.

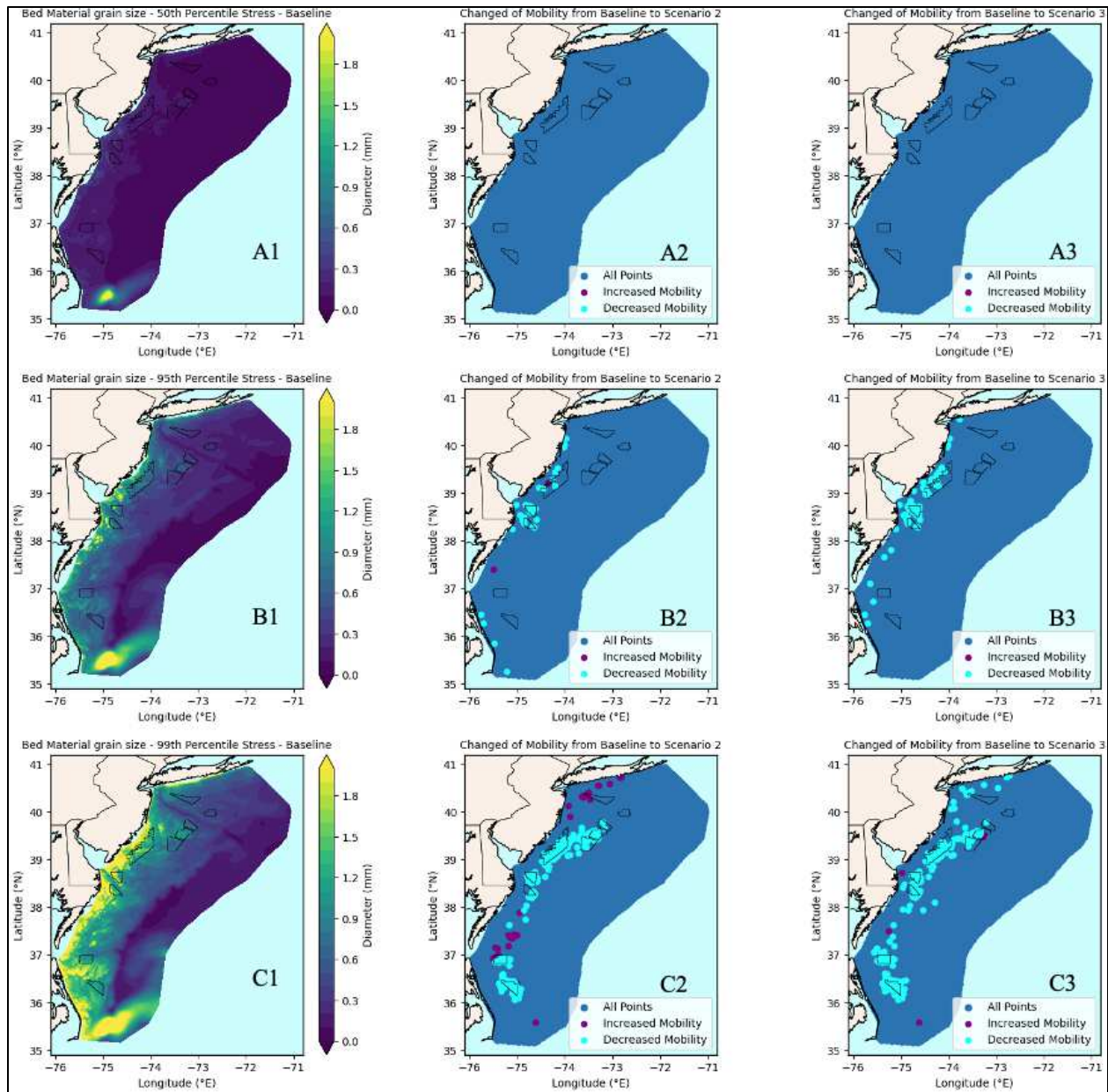


Figure 285. Sediment mobility changes.

Bed material grain size diameter (A1) for baseline that can be moved by 50th percentile RMS bed shear stresses for waves-plus-current, change in sediment mobility from baseline to Scenario 2 (A2), and from baseline to Scenario 3 (A3). Middle row: The same as top row but by 95th percentile RMS bed shear stresses (B1), change in sediment mobility caused by 95th percentile RMS bed shear stress from baseline to Scenario 2 (B2), and from baseline to Scenario 3 (B3). Bottom row: The same as top row but by the 99th percentile RMS bed shear stresses (C1), change in sediment mobility caused by 99th percentile RMS bed shear stress from baseline to Scenario 2 (C2), and from baseline to Scenario 3 (C3).

11 Selection of Species of Interest

11.1 Literature Review and Species Selection

Planktonic organisms, including the larval life stages of fish, bivalves, and arthropods, are highly susceptible to changes in hydrodynamic circulation. Changes in circulation, stratification, and mixing, such as that which may be caused by the presence of offshore wind turbines (OWTs) within WEAs, may potentially alter larval dispersion dynamics and lead to a reduction in recruitment success and survival (Iles and Sinclair, 1982). Larval position in the water column may also be affected causing deviations in prey availability and vulnerability to predation. Incorporating species-specific ontogenetic behaviors for potentially affected organisms via individual-based models is important for capturing individual-level mechanisms that influence populations (DeAngelis and Grimm, 2014).

Commercial species with high economic interest in the Mid-Atlantic Bight were considered for this study. The initial list of potential candidate species included the Atlantic sea scallop (*Placopecten magellanicus*), Atlantic surfclam (*Spisula solidissima*), summer flounder (*Paralichthys dentatus*), black sea bass (*Centropristis striata*), and longfin inshore squid (*Loligo pealeii*). In 2021, commercial landings of these species ranged between 1,300 to 7,000 metric tons in the middle Atlantic, accounting for 8 to 43 percent of total landings (NOAA commercial landings database). Atlantic cod (*Gadus morhua*) and American lobster (*Homarus americanus*) were excluded from consideration as they are small contributors to the Mid-Atlantic economy, making up 1 percent or less of total landings. The *Calanus* copepod (*Calanus* spp.) was another planktonic organism of interest due to its importance in the diet of North Atlantic right whales. However, it was determined that the geographic region and scope of this study did not warrant inclusion of copepods in the analysis.

An extensive literature review was conducted for the five candidate species to consolidate information on species-specific spawning locations and timing, larval life stages and characteristics, larval distributions and behavior, larval stage duration, and settlement habitats. The summer flounder, which was the focus of a recent BOEM larval modeling study (Johnson et al., 2021), was removed from the target species list after consultation with BOEM. Larval information on the longfin inshore squid was limited and insufficient for use in a particle tracking model. Attempts were made to acquire recent larval longfin inshore squid data from NOAA's Northeast Fisheries Science Center (NEFSC), but this dataset was still unavailable as of the writing of this report. The three remaining species with adequate information for larval transport modeling were the Atlantic sea scallop, Atlantic surfclam, and black sea bass. Previous modeling work has been done for each of these species, with the following publications serving as additional resources to inform biological parameters for modeling:

1. Atlantic sea scallop – Munroe et al. (2018) and Chen et al. (2021)
2. Atlantic surfclam – Zhang et al. (2016)
3. Black sea bass – Edwards et al. (2008)

11.2 Larval Biological Parameters

A summary of the larval biological parameters to be used in the larval transport model can be found in Table 31. The parameters presented include spawning location, spawning depth, spawning time, fecundity, larval dispersal duration, temperature tolerance, onset of metamorphosis to juvenile stage, settlement depth, settlement habitat, and vertical swimming velocity. In addition, Figure 282, Figure 283 and Figure 284 show the distribution of sea scallop spawning beds (Hart and Chute, 2004), the distribution of adult surfclam (Fay et al., 1983), and the distribution of black sea bass eggs from NOAA-NEFSC ichthyoplankton surveys (Drohan et al., 2007), respectively. All three target species exhibit active

spawning in shallower continental shelf waters of the Mid-Atlantic Bight. Spawning typically occurs yearly between the spring and fall for the Atlantic surfclam and black sea bass while the Atlantic sea scallop follows a semi-annual spawning cycle occurring first from May to June then followed by a second spawning from September to November. Both bivalve species produce eggs in the order of millions per reproductive individual. Atlantic sea scallop can reach 270 million eggs per individual, compared to 13 million eggs per individual for Atlantic surfclam. Black sea bass shows the lowest fecundity, with reproductive females producing approximately 200,000 to 300,000 eggs per individual in the Mid-Atlantic Bight. The duration of each species' larval stays in a planktonic phase also varies. Black sea bass has the shortest larval dispersal duration of up to 24 days, Atlantic surfclam follows at 35 days, and Atlantic sea scallop has the longest larval dispersal duration of up to 82 days. Settlement, which ensues once larvae metamorphose to juveniles, occurs over low to medium complexity substrates at depths of less than 60-meters for Atlantic sea scallop and surfclam while black sea bass settles in high complexity habitats at depths shallower than 20-meters. Data sources are listed as footnotes of the table and provided in the reference section.

Table 31. Summary of pertinent larval biological parameters for each target species specific to the Mid Atlantic Bight

--	Atlantic sea scallop 1 (<i>Placopecten magellanicus</i>)	Atlantic surfclam 2 (<i>Spisula solidissima</i>)	Black sea bass 3 (<i>Centropristis striata</i>)
Spawning locations	Shallower coastal waters (Figure 2)	Shallow subtidal depths to 60 m (Figure 3)	Nearshore continental shelf (Figure 4)
Spawning depth	18 to 110 m	shallow up to 60 m	20 to 50 m
Spawning season	May to June; September to November	May to October	April to October
Fecundity	1–270 million eggs per individual	0.14–13 million eggs per individual	191,000–369,500 eggs per individual
Larval dispersal duration	28 to 82 days	35 days	21 to 24 days
Temperature tolerance	10 to 18 C	14 to 30 C	11 to 26 C
Metamorphosis to juvenile	30 to 40 days	19 to 35 days	21 to 24 days
Settlement depth	15 to 60 m	< 60 m	< 20 m
Settlement habitat	Coarse substrates over clay or sand	Medium to coarse sand to gravel bottoms	Complex microtopographies
Vertical swimming velocity	1 to 1.5 mm/s	0.2 to 0.5 mm/s	10 to 20 mm/s

1 Hart and Chute (2004), DuPaul et al. (1989), Schmitzer et al. (1991), Langton et al. (1987), Culliney (1974), McGarvey et al. (1992), Pearce et al. (2004), Tremblay and Sinclair (1990), Tremblay et al. (1994), Thouzeau et al. (1991), Manuel et al. (2000).

2 Fay et al. (1983), Cargnelli et al. (1999), Walker et al. (1996), Rumrill (1990), Loosanoff and Davis (1963), Hoffman et al. (2018), Mann et al. (1991).

3 Drohan et al. (2007), Mercer (1978), Berrien and Sibunka (1999), Able and Fahay (1998), Berlinsky et al. (2000), Able et al. (1995), Edwards et al. (2008).

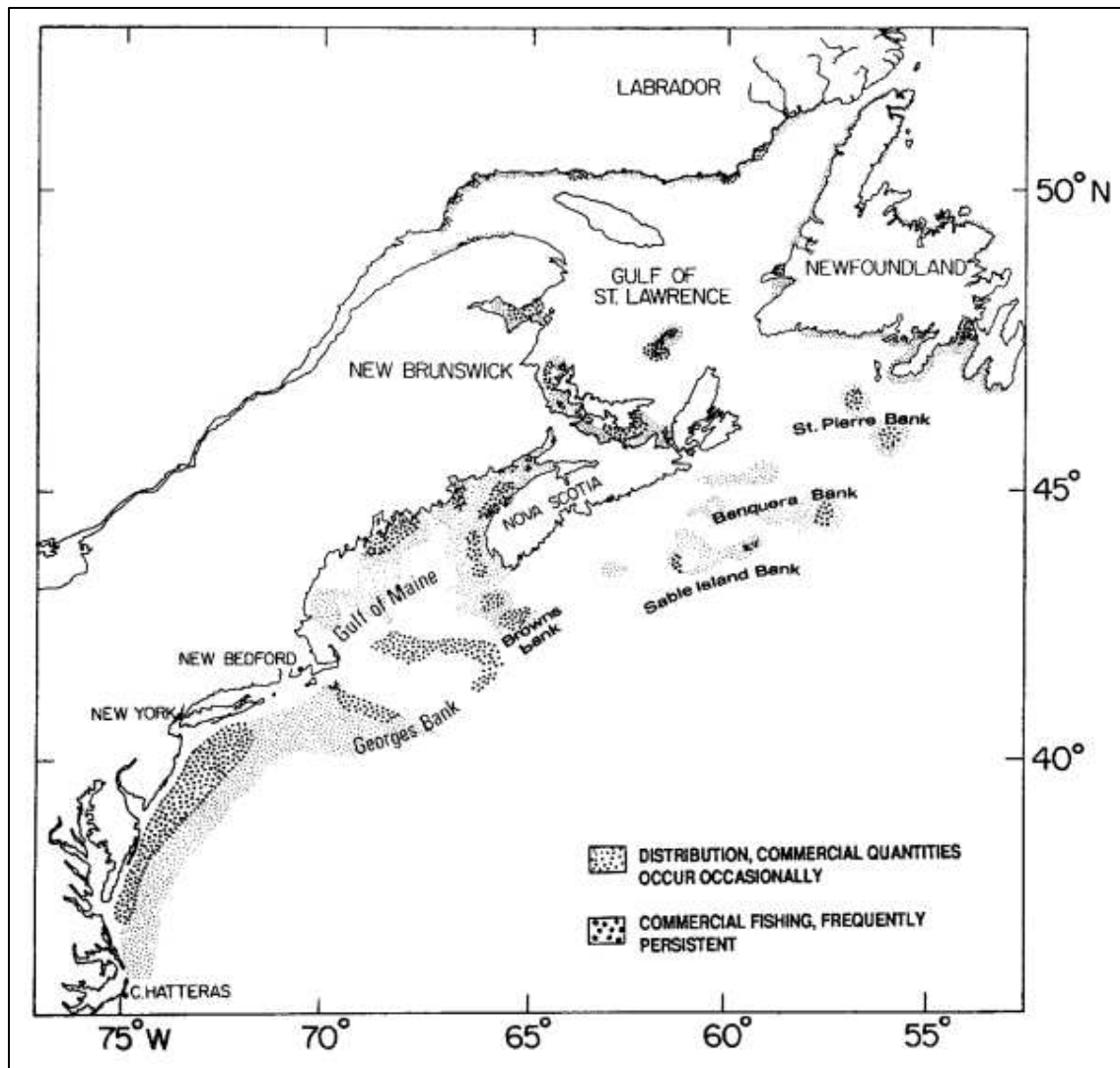


Figure 286. Distribution of Atlantic sea scallop (*Placopecten magellanicus*) spawning beds off the Northeast coast of North America. Figure from Hart and Chute, 2004.

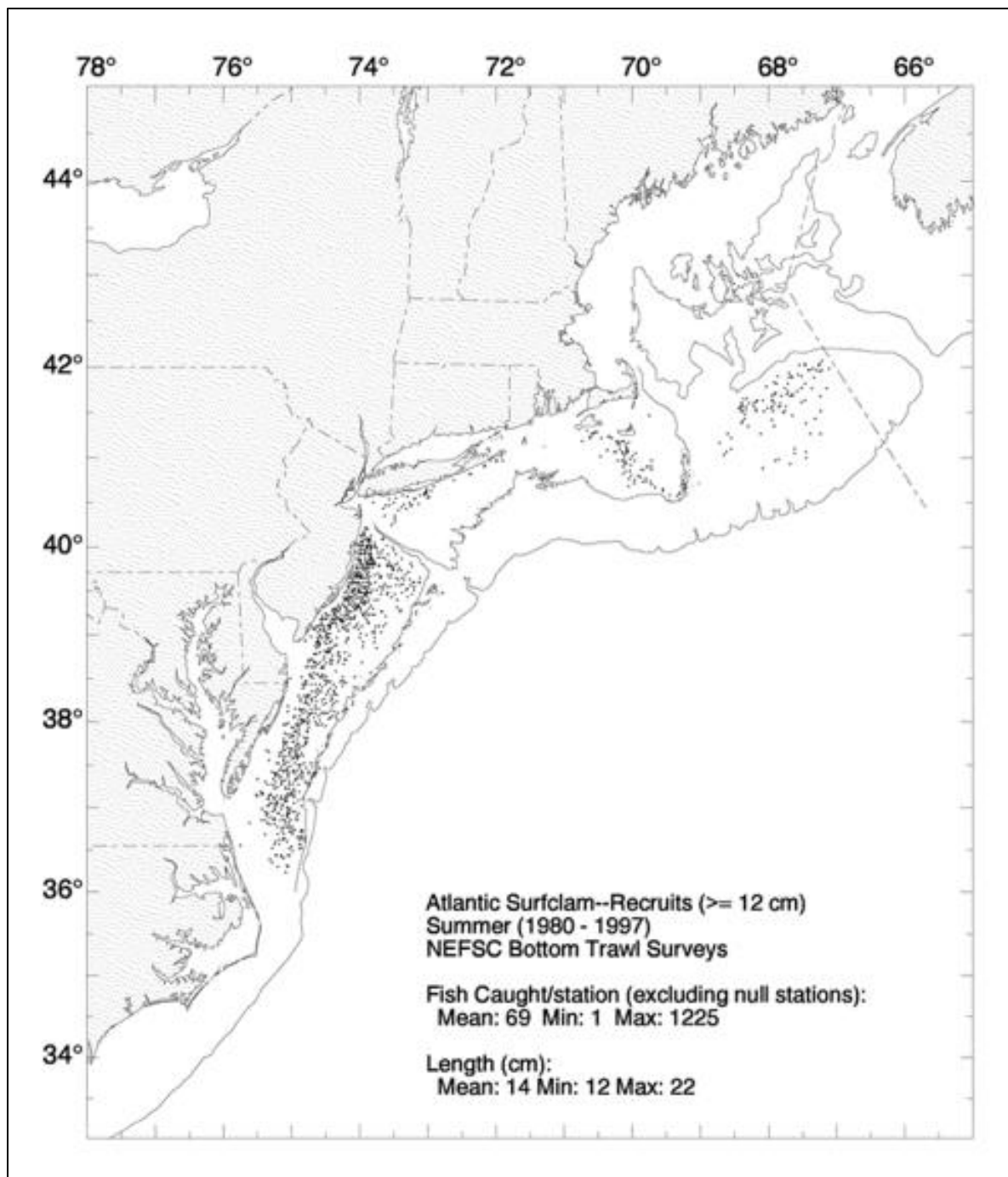


Figure 287. Distribution of Atlantic surfclam (*Spisula solidissima*) in the Mid-Atlantic. Figure from Cargnelli et al., 1999.

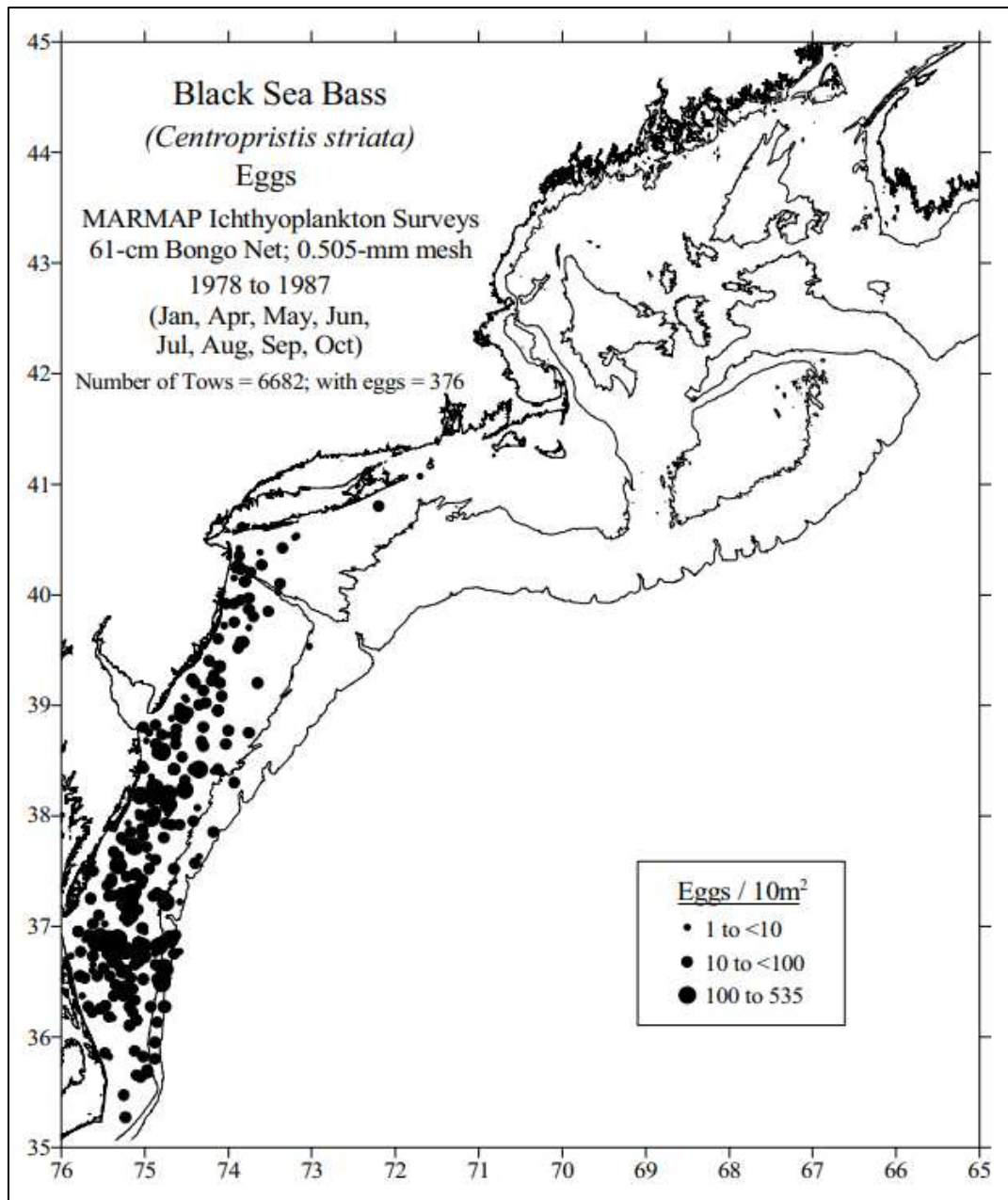


Figure 288. Distribution of black sea bass (*Centropristis striata*) eggs collected during NOAA-NEFSC ichthyoplankton surveys.
 Figure from Drohan et al., 2007

12 Larval Transport Modeling and Impact of Offshore Wind Farms on Larval Connectivity

12.1 Introduction

For offshore WEA development to be sustainable, it is necessary to investigate its potential impacts on marine species, particularly their ecological functions. Many species exhibit complex life cycles with a pelagic larval stage and a benthic or pelagic adult stage. Understanding how different sub-populations within a species range are interconnected through the exchange of larvae (i.e., larval connectivity) (Palumbi, 2003) is key to understanding population dynamics and the spatial management of marine species (Burgess et al., 2014). Maintaining larval connectivity is crucial for local stock persistence (Garavelli et al., 2018) and for preserving the structure and functioning of the ecosystems that species inhabit (Bergström et al., 2013).

Larval dispersal between spawning and settlement habitats is mainly influenced by hydrodynamic processes such as currents, turbidity, and temperature (Cowen & Sponaugle, 2009). These processes may be locally or regionally affected by the presence of developed WEAs, consequently altering larval dispersal dynamics (Iles & Sinclair, 1982). On a local scale, turbulence and stratification can be increased with the presence of WEAs (Schultze et al., 2020), potentially affecting temperature and nutrients (Daewel et al., 2022; Dorrell et al., 2022). On a regional scale, the presence of WEAs has been shown to decrease stratification and create wind wake effects (van Berkel et al., 2020). These hydrodynamic changes associated with WEA development could impact larval survival and connectivity (Daewel et al., 2011). The success of larval connectivity through larval dispersal also depends on several biological factors such as larval behavior, larval mortality, and the availability of spawning and settlement habitats (Pineda et al., 2007).

To investigate the effects of WEA development on both the physical and biological processes driving larval connectivity, biophysical individual-based models can be used to incorporate species-specific behavior and capture the mechanisms influencing populations (DeAngelis & Grimm, 2014). Biophysical models are frequently used to assess the importance of biotic and abiotic processes for larval connectivity and the spatial management and conservation of marine species (Garavelli et al., 2018; Munroe et al., 2018). The application of such models to assess the impact of WEA development on larval connectivity is less common, but biophysical models have been used in two recent studies to assess the impacts of WEA development on larval connectivity of different species along the U.S. Atlantic coast (Chen et al., 2024; Johnson et al., 2021).

Johnson et al. (2021) assessed the effects of WEA development off Massachusetts and Rhode Island on the larval distribution and settlement of Atlantic sea scallop (*Placopecten magellanicus*), silver hake (*Merluccius bilinearis*), and summer flounder (*Paralichthys dentatus*) for one year using an agent-based model developed with ABM Lab. Reduced current speeds associated with the presence of WEA turbines were identified as causing a decrease in larval settlement for Atlantic scallop and summer flounder, and a change in larval distribution for silver hake. Chen et al. (2024) also assessed the effects of WEA development in the same region for Atlantic sea scallop larvae from September to November for three years using the larval model Scallop-IBM. Their model predicted that the presence of one offshore wind farm increases offshore subtidal flow, contributing to larvae being transported further offshore, compared to when the farm is not considered in the model.

To understand the impacts of WEA development on larval connectivity, it is essential to identify which environmental processes might be influenced and how potential changes compare to the natural variability of the ecosystem. These effects will likely differ among species, depending on their life cycle and habitats. In this study, we developed a biophysical larval dispersal model to investigate the effects of

WEAs on the larval connectivity of three commercial species in the Mid-Atlantic Bight (MAB), from New York to North Carolina: Atlantic sea scallop, Atlantic surfclam (*Spisula solidissima*), and black sea bass (*Centropristis striata*). To identify the influence of physical and biological processes on larval connectivity, different model simulations were performed for three scenarios: one baseline scenario without WEA, one with partial WEA development, and one with full WEA development.

12.2 Methods

12.2.1 Hydrodynamic Model

The MAB hydrodynamic modeling was performed using the Deltares Delft3D Flexible Mesh (Delft3D FM) Modeling Suite, specifically using its hydrodynamic module, DFLOW (Delft, 2023) (see previous Chapter 5 for full details of the model). Three scenarios of the hydrodynamic simulations were conducted to allow for the direct comparison of larval connectivity: one baseline scenario without WEA turbines (Scenario 1), one with partial WEA development (Scenario 2), and one with full WEA development (Scenario 3) (Table 1).

12.2.2 Biophysical Larval Dispersal Model

To model the larval dispersal of the three species of interest (Atlantic sea scallop, Atlantic surfclam, and black sea bass), a biophysical larval dispersal model was developed using the individual-based Lagrangian model Ichthyop (Barrier et al., 2023; Lett et al., 2008). Ichthyop is commonly used to model transport processes and assess the effects of hydrodynamics on plankton dynamics (Amorim et al., 2024; Garavelli et al., 2016; Garavelli et al., 2014; Marchessaux et al., 2023). In the model, the virtual larvae are characterized by their latitude, longitude, and depth in three dimensions.

Ichthyop (Barrier et al., 2023; Lett et al., 2008) was primarily developed to work with the Regional Ocean Modeling System (ROMS). It has also been expanded to work with the following ocean models: the Model for Applications at Regional Scale (MARS), the Nucleus for European Modelling of the Ocean (NEMO), SYMPHONIE, and most recently the Finite Volume Community Ocean Model (FVCOM) (Chen et al., 2003), but not Delft3D. We modified the version of Ichthyop adapted to FVCOM to be able to read and work with Delft3D FM outputs using the following steps. We expanded the FVCOM version of Ichthyop because of the similarity of the mesh-style grid and sigma-layering between FVCOM and Delft3D FM.

We implemented an inverse weighted distance average interpolation for all location-dependent variables (i.e., velocity, bathymetry, surface water level, and temperature), following what Delft3D FM uses for its own internal particle tracking model (Delft, 2023). As these variables are saved on the center of the triangle, we first interpolate to the edge of the triangle and then interpolate to the point of interest. We interpolate in a two-step process to reduce skewness error. For example, to determine the velocity at a given point within a triangle, we first perform an inverse weighted average of the velocity at the center of the triangle to each of the edges of the triangle (Eq. 8, Figure 285a and b):

$$\mathbf{u}_{E1} = \frac{\frac{\mathbf{u}_1}{d_1} + \frac{\mathbf{u}_2}{d_2}}{\frac{1}{d_1} + \frac{1}{d_2}} = \frac{d_2 * \mathbf{u}_1 + d_1 * \mathbf{u}_2}{d_1 + d_2} \quad \text{Eq. 8}$$

Where vector \mathbf{u} is the horizontal (u) and vertical (v) velocity components as shown in Figure 285 located at position 1, 2, or along the edge (E1) and d is the relevant distance. We then perform an inverse weighted average from each of the edges to our point of interest (Eq. 9 and Figure 285c):

$$\mathbf{u}_p = \frac{\frac{\mathbf{u}_{E1}}{d_1} + \frac{\mathbf{u}_{E2}}{d_2} + \frac{\mathbf{u}_{E3}}{d_3}}{\frac{1}{d_1} + \frac{1}{d_2} + \frac{1}{d_3}} = \frac{d_2 * d_3 * \mathbf{u}_{E1} + d_1 * d_3 * \mathbf{u}_{E2} + d_1 * d_2 * \mathbf{u}_{E3}}{d_2 * d_3 + d_1 * d_3 + d_1 * d_2} \quad \text{Eq. 9}$$

where subscript p denotes the position of interest and other parameters are the same as in Eq. 8.

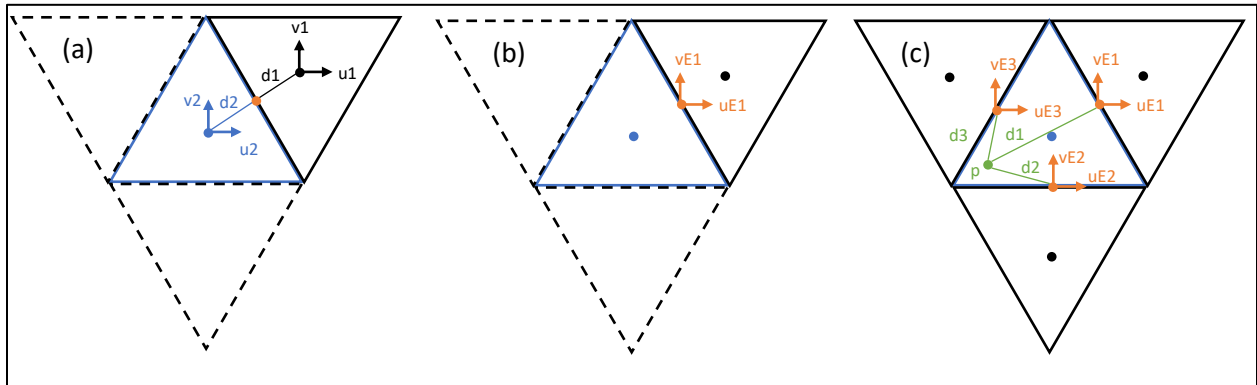


Figure 289. Plot a shows the center points on two adjoining triangles (blue or black dot) of the mesh grid with distances from the edge that connects them, d_1 and d_2 . Inverse distance interpolation of those initial two center points gives the velocities at the center of the edge (orange dot, plot b). Using these edge velocities (orange), we then interpolate with the same formula to a random point in the triangle (green, plot c).

12.2.3 Larval Dispersal Model Setup

Biological parameters of the Atlantic sea scallop, Atlantic surfclam, and black sea bass are reviewed in Table 31 and discussed in the previous Chapter 11. We selected a subset of those parameters for the larval dispersal model (Table 32). Biological parameters included in the model were the spawning location, spawning depth, spawning time, larval dispersal duration, temperature tolerance, settlement depth, settlement habitat, and diel vertical migration (DVM) behavior. For each species, the value of each parameter was based on the literature (Table 32).

Table 32: Relevant biological parameters for the larval dispersal model for each species.

--	Atlantic sea scallop (<i>Placopecten magellanicus</i>)	Atlantic surfclam (<i>Spisula solidissima</i>)	Black sea bass (<i>Centropristis striata</i>)
Larvae spawning (release) and settlement areas (Figure 286)	--	--	--
-Bathymetry	15 to 110 m (Hart & Chute, 2004)	15 to 60 m (Cargnelli, 1999)	20 to 50 m (Drohan et al., 2007)

--	Atlantic sea scallop (<i>Placopecten magellanicus</i>)	Atlantic surfclam (<i>Spisula solidissima</i>)	Black sea bass (<i>Centropristis striata</i>)
-Release/ settlement Area	From 36.5 N to 40.5 N Virginia Beach to Long Island (Hart & Chute, 2004)	From 37 N to 40.5 N (Cargnelli, 1999)	From 36.5 N to 40.5 N Nearshore Continental Shelf (Drohan et al., 2007)
-Release Depth	Bottom	Bottom	20 to 50 m (Drohan et al., 2007)
-Settlement Depth	15 to 60 m (Hart & Chute, 2004)	< 20 m (Cargnelli, 1999)	< 20 m (Able & Fahay, 1998)
Larvae release times	--	--	--
-Seasons	First day of the week from May to October, inclusive (Hart & Chute, 2004)	First day of the week from May to November, inclusive (Cargnelli, 1999)	First day of the week from April to October, inclusive (Able & Fahay, 1998)
-Years	2018 and 2019	2018 and 2019	2018 and 2019
Larval dispersal duration	45 days (Chen et al., 2024; Hart & Chute, 2004)	35 days (Rumrill, 1990)	24 days (Berlinsky et al., 2007)
Pre-competency period (minimum settlement age)	28 days (John Tremblay et al., 1994)	19 days (Fay et al., 1983)	21 days (Berlinsky et al., 2007)
# Larvae released per event	1,000	1,000	1,000
Diel Vertical Migration (DVM)	3 to 20 m (Chen et al., 2021)	3 to 20 m	5 to 20 m (Edwards et al., 2008)
Temperature tolerance range	10 to 18°C (Tremblay & Sinclair, 1990)	14 to 30° C (Fay et al., 1983)	11 to 26° C (Drohan et al., 2007)

In the model, spawning and settlement areas were designed based on the habitat of each species along the shallow continental shelf waters of the MAB (Figure 286). Release (spawning) and settlement areas for each species were defined by equally dividing up the habitat for each species. The bathymetry of each area and the release depth of larvae were based on habitat preference and species distribution in the water column, respectively (Figure 286). For example, scallop and surfclam larvae were released at the bottom of the water column in the model because both species are benthic. Sea bass larvae were released between 20 and 50 m depth because the species rise in the water column to spawn.

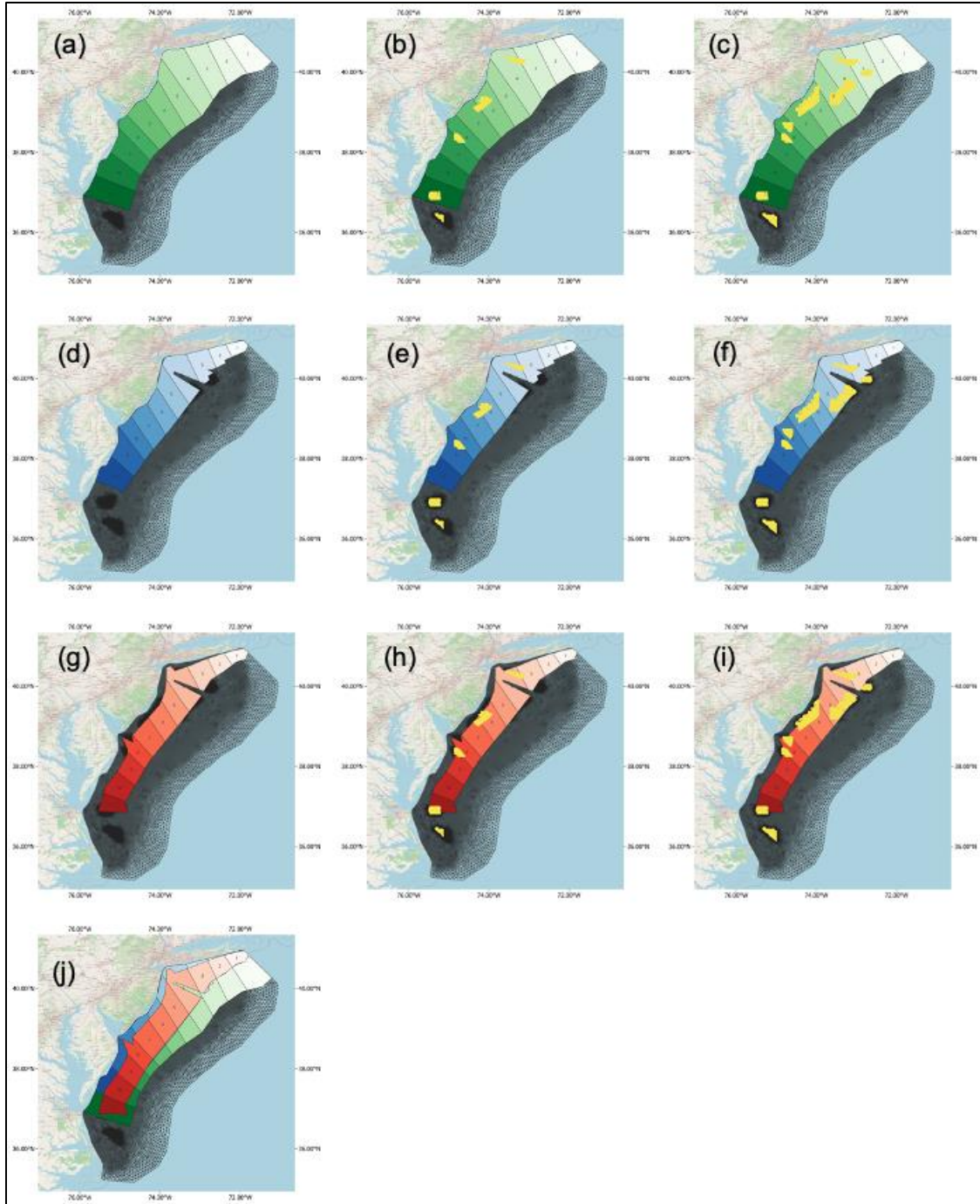


Figure 290. Larvae release (spawning) and settlement zones for sea scallop (green, a, b, c), surfclam (blue, d, e, f), and sea bass (red, g, h, i). Turbines are shown in yellow: Scenario 1 (no turbines) are the maps in the left-most column (plots a, d, g), Scenario 2 (partial buildout) are the maps in the center column (plots b, e, h), and Scenario 3 (full buildout) are the maps in the right-most column (plots c, f, i). The grid of the hydrodynamic model is shown with the black mesh in each map. Zones numbers and color shading are to help visualize the different zones but do not hold specific significance. Plot j is an image of all zones for each of the species together.

In the model, larvae were released weekly from the defined release areas (Figure 286) during the spawning season for two years (from February 2018 to January 2020) (see Table 32 for details). Larvae

were tracked every half hour (time step of the hydrodynamic model) using a forward-Euler advection scheme. Following Peliz et al. (2007), horizontal diffusion was included in the model with a turbulent dissipation rate $\epsilon = 10^{-9} \text{ m}^2\text{s}^{-3}$. The larval dispersal duration (maximum of time during which the larvae can be transported by currents in the model) was set to 45 days for sea scallop, 35 days for surfclam, and 24 days for sea bass. The pre-competency period, or the minimum age at settlement, was set to 28 days for sea scallop, 19 days for surfclam, and 21 days for sea bass. Settlement ensues before larvae metamorphose into juveniles. In the model, larvae were considered settled when located in a settlement area after the pre-competency period (see Table 32).

To represent the vertical behavior of larvae in the water column (i.e., nighttime at the water surface to feed and daytime at depth to avoid predators), DVM was included as follows: sea scallop and surfclam at 3 m depth during nighttime (6:00 PM to 6:00 AM) and 20 m depth during daytime (6:00 AM to 6:00 PM); sea bass at 5 m depth during nighttime (6:00 PM to 6:00 AM) and 20 m depth during daytime (6:00 AM to 6:00 PM).

12.2.4 Model Configurations

Five sets of model configurations (referred to as M1 through M5) were performed for each of the three hydrodynamic scenarios to test the sensitivity of the model (Table 33). Models M1 and M2 do not include behavior (passive) and were designed to study the effect of hydrodynamics on larval connectivity for the three species and to test the sensitivity of the model to the number of larvae released: 1,000 in M1 and 10,000 in M2. M2 was only performed for Atlantic sea scallop because of computing constraints. M3 aimed at investigating the effect of DVM on larval connectivity (see Table 32 for DVM amplitudes for each species). M4 was designed to assess the effects of temperature-dependent larval mortality on larval connectivity and was performed for each species. Finally, M5 includes DVM and temperature dependence for all species.

Table 33: Summary of parameters included in the different model configurations.

Model configurations M2 was performed for Atlantic sea scallop only due to computing constraints.

Model configurations	Behavior	Number of larvae released	Temperature-dependent larval mortality	Species
M1	Passive	1,000	No	Atlantic sea scallop, Atlantic surfclam, Black sea bass
M2	Passive	10,000	No	Atlantic sea scallop
M3	Diel vertical migration	1,000	No	Atlantic sea scallop, Atlantic surfclam, Black sea bass
M4	Passive	1,000	Yes	Atlantic sea scallop, Atlantic surfclam, Black sea bass
M5	Diel vertical migration	1,000	Yes	Atlantic sea scallop, Atlantic surfclam, Black sea bass

12.2.5 Analysis

Connectivity matrices were primarily used to interpret the model results. Values of the connectivity matrix represent the larval settlement success $C_{i,j}$, which is the number of larvae released from zone i that successfully settled to zone j . To calculate the percentage of larval settlement success between two zones, $C_{i,j}$ was normalized to the total larvae released per zone, $C_{i,j}/n_i*100$, where n_i is the number of larvae

released in zone i . The total percentage of successfully settled larvae in one given settlement zone was calculated as the row sum of the matrix normalized to the number of larvae released, or $\sum_j C_{i,j}/N*100$, where N is the total larvae released per event (i.e., 1,000 or 10,000 released weekly during the species spawning time; see Table 32). Lastly, mean connectivity was calculated by summing all values in the connectivity matrix and then normalizing to the total larvae released, $\sum_i \sum_j C_{i,j}/N*100$. Larval dispersal distances were also calculated, representing the distance traveled by larvae from the time of release in one given spawning zone to the time of settlement in one given settlement zone. To compare the results between the hydrodynamic scenarios, we performed a multifactor analysis of variance (ANOVA) of the simulated values of larval dispersal distances (minimum, mean, maximum) and mean connectivity for all simulations for each species.

12.3 Results

12.3.1 Influence of Hydrodynamics on Larval Connectivity

In Figure 287 to Figure 291 results are described for the model configuration M1 (passive transport of 1,000 particles) for each hydrodynamic scenario as outlined in Table 1. Figure 287 only shows the trajectories of all larvae released on May 1, 2018. Overall, most of the larvae followed a southward trajectory from their release to their settlement zones. Scallop larvae trajectories are observed further offshore than surfclam and sea bass. For all species, larvae trajectories are observed up to 36° N, with some larvae being transported offshore, particularly for sea scallop and surfclam. Between the three hydrodynamic scenarios, slight changes in larval trajectories are observed for each species. For sea scallop (Figure 287a, b, c), in all scenarios, some offshore trajectories move south throughout the study domain. In Scenario 3, fewer trajectories are observed between 39 and 40° N, where the WEAs are present. For surfclam (Figure 287d, e, f), larvae released north of 40° N do not travel south of the study domain. In scenarios 2 and 3, larvae released close to the shore and north of 40° N were transported southward and went around the northernmost WEA. In Scenario 3, fewer trajectories are observed at 39.6° N, close to the eastern WEAs, and fewer larvae were transported towards the southern areas, between 37 and 38° N. For black sea bass, larvae trajectories are located further from the shore compared to scallop and surfclam and are similar between the three scenarios, with fewer trajectories observed around the WEAs.

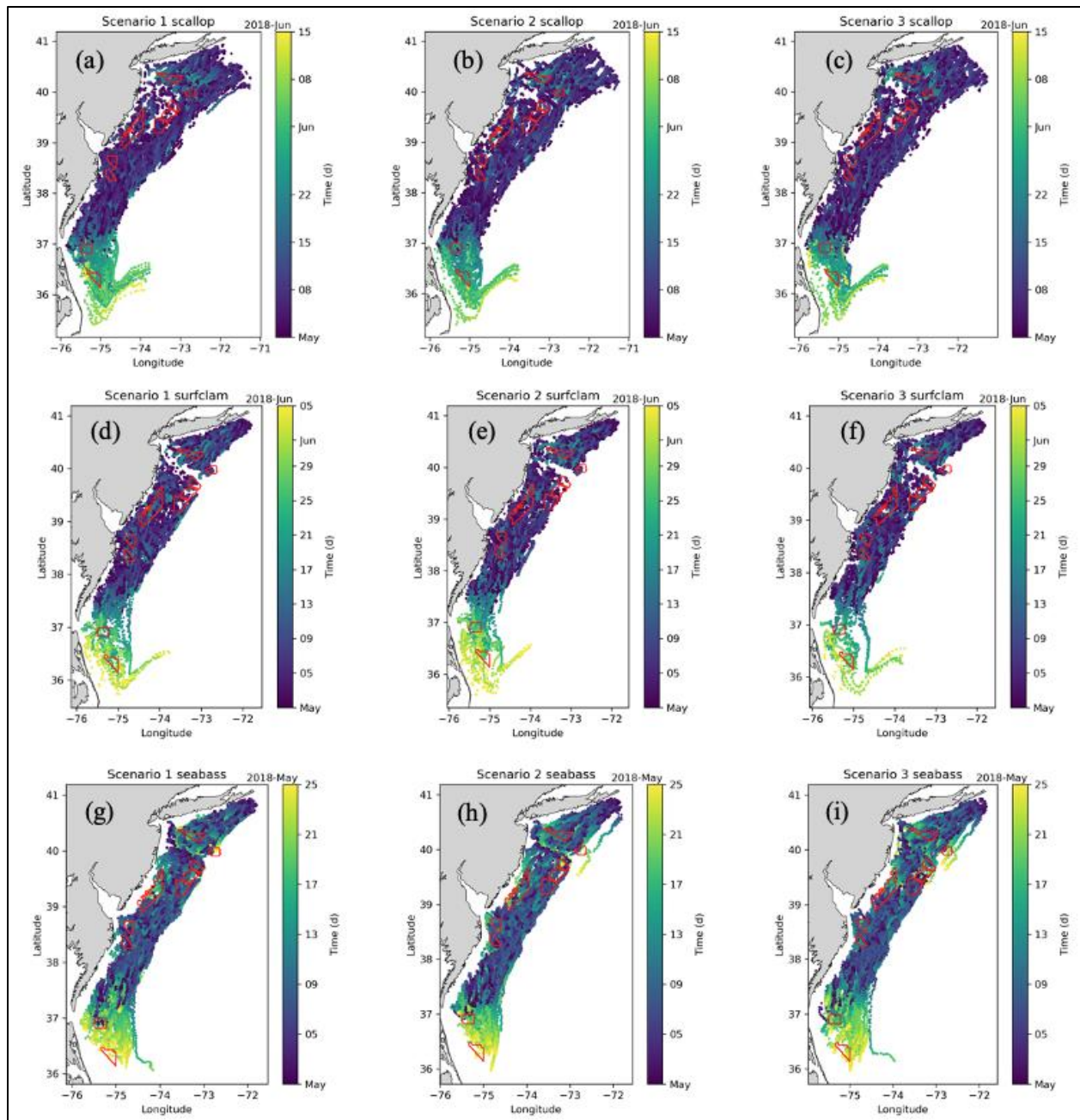


Figure 291. Trajectories of all larvae released on May 1, 2018 for simulation M1. Top row (a, b, c) sea scallop, middle row (d, e, f) surfclam, and bottom row (g, h, i) sea bass. WEAs from Scenario 3 are shown with red outlines in each plot. Left column (a, d, g) is Scenario 1 (no turbines), middle column (b, e, h) is Scenario 2 (partial buildout), and right column (c, f, i) is Scenario 3 (full buildout).

Figure 288 shows the density of successfully settled larvae binned in hexagons with color corresponding to the number of larvae in that bin for simulation M1. The maps are zoomed in on the northern portion of the domain. Sea scallop (Figure 288a, b, and c) shows a higher density of larvae around 40.5° N for all scenarios. There are gaps in the density map for all three scenarios, highlighting the patchiness of scallop settlement. Surfclam (Figure 288d, e, and f) has less gaps and a hotspot around 40.5° N. This hotspot is not discernably different between the three scenarios. Sea bass (Figure 288g, h, and i) has the least amount of gaps in the density plot and the hot spot is further south than scallop and surfclam, occurring

between 40 and 40.5° N. There is not a discernable difference between the densities for the three scenarios.

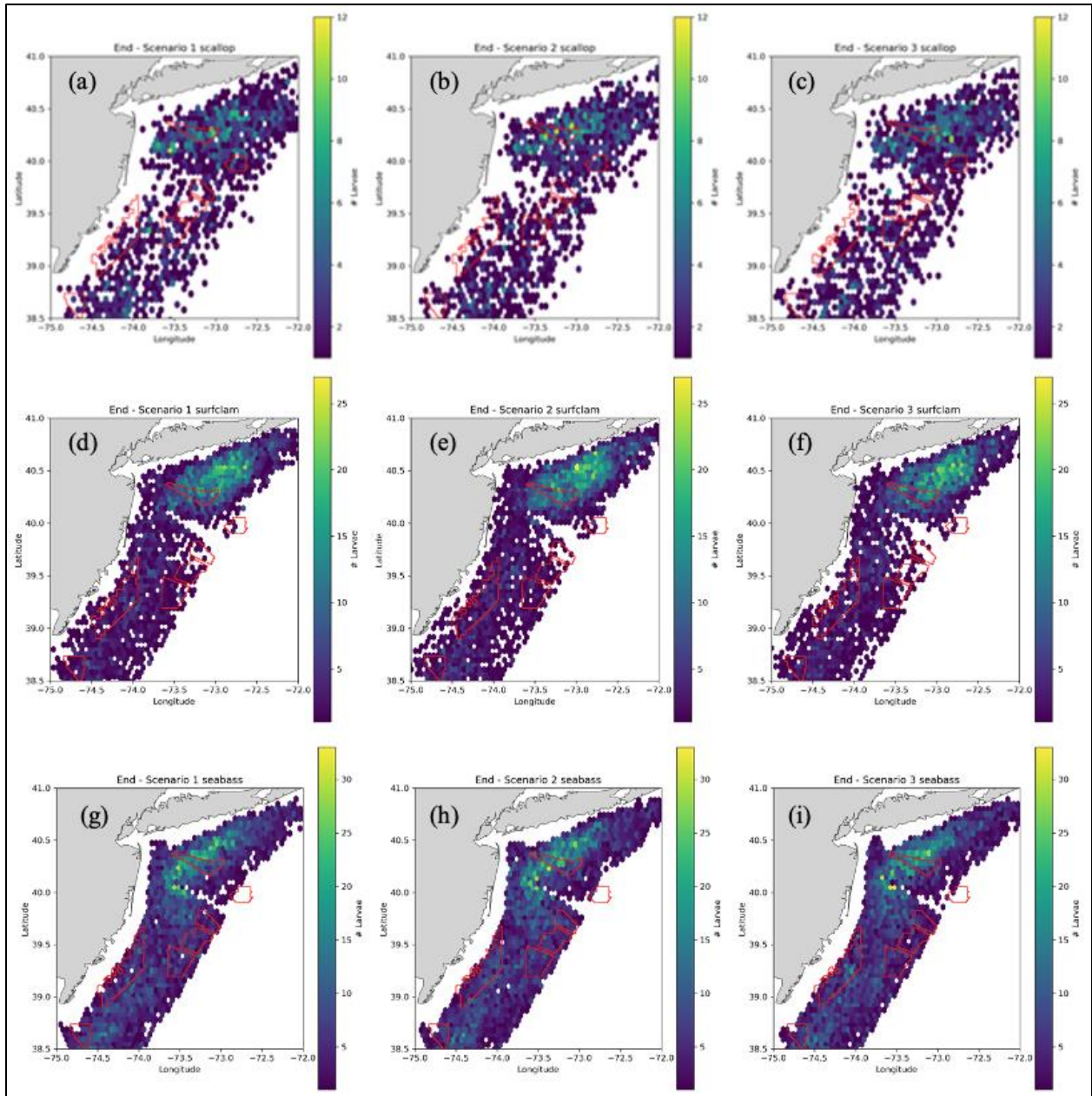


Figure 292. Density of all successfully settled larvae for simulation M1. This image is a zoomed-in portion of the total domain near the northern WEAs. Top row (a, b, c) sea scallop, middle row (d, e, f) surfclam, and bottom row (g, h, i) sea bass. WEAs from scenario 3 are shown with red outlines in each plot. Left column (a, d, g) is scenario 1 (no turbines), middle column (b, e, h) is scenario 2 (partial buildout), and right column (c, f, i) is scenario 3 (full buildout).

Dispersal distances of larvae from their release areas to their settlement areas are shown in Figure 289. Larval dispersal distances are mostly between 25 and 100 km for sea scallop and surfclam and between 25 and 200 km for sea bass. Around 45% of scallop and 70% of surfclam larvae were transported 50 km

or less from their release locations. Overall, compared to Scenario 1, larvae disperse slightly further when WEA turbines are included. Summary statistics on the distance traveled of successfully settled larvae for sea scallop, surfclam, and sea bass are in Table 34, Table 35, and Table 36, respectively. For sea scallop, the mean larval dispersal distance slightly increases from scenarios 1 to 3 (from 88.3 km to 89.28 km). The minimum larval dispersal distance is greater for Scenario 2 (1.91 km) than the other scenarios, and the maximum dispersal is higher in Scenario 1 (494.67 km; Table 34). For surfclam, the mean and maximum dispersal distances increase from scenarios 1 to 3 (mean = 45.53 km for Scenario 1 and 48.18 km for Scenario 3; max = 256.56 km for Scenario 1 and 285.55 km for Scenario 3; Table 35). The lowest minimum dispersal distance occurs in Scenario 2. For sea bass, the minimum dispersal distance is lowest for Scenario 1 (Table 36). From scenarios 1 to 3, the mean dispersal distance increases (from 78.93 km to 82.88 km), and the maximum dispersal distance decreases (from 339.87 km to 333.4 km).

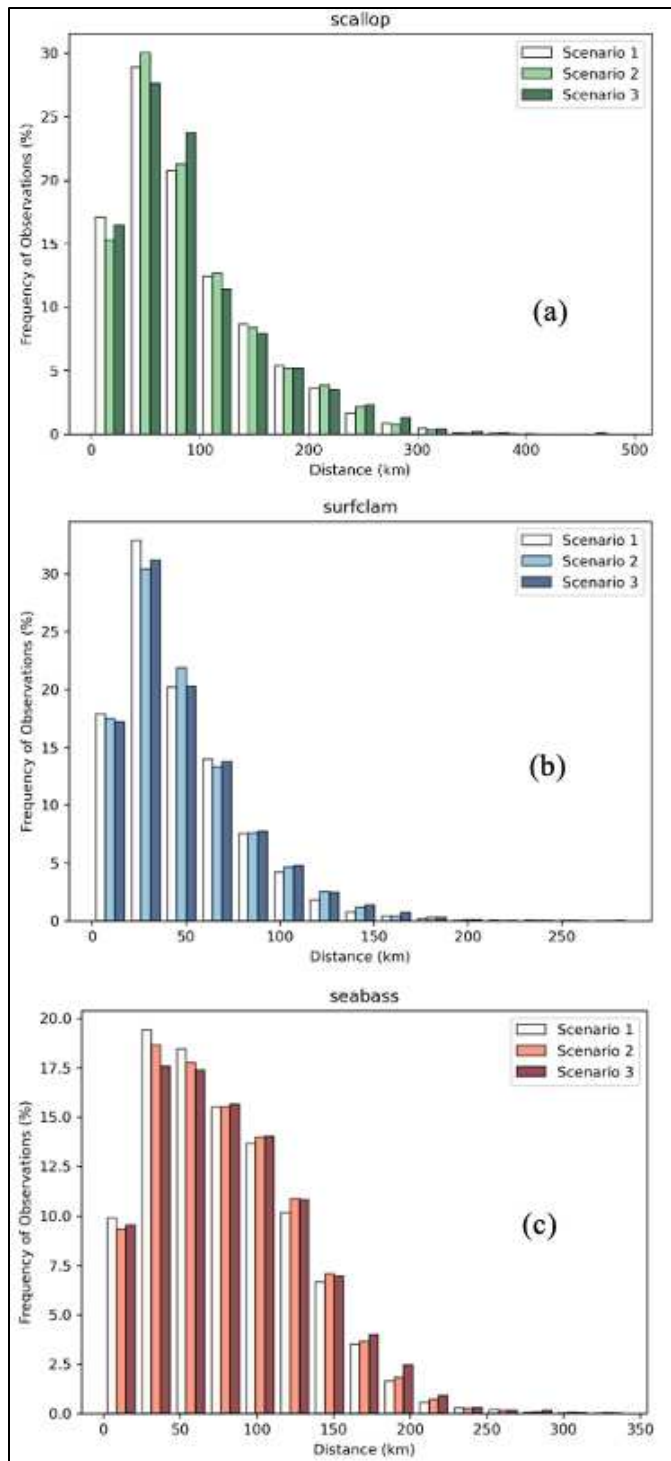


Figure 293. Larval dispersal distance between release and settlement locations for Scenario 1 (no turbines, white), Scenario 2 (partial buildout; light shading), and Scenario 3 (full buildout; dark shading). For sea scallop (a, green), surfclam (b, blue), and sea bass (c, red) for simulation M1.

The larval settlement success (% , as defined in Section 12.2.5) between release and settlement areas is represented for each species and the three hydrodynamic scenarios (Figure 290). For Scenario 1, the larval settlement success is higher for surfclam and sea bass (up to 12%) compared to scallop (up to 4%) (Figure 290 a, d, g). For the three species, larvae are generally transported from the northern to the southern part of the study domain and larval connectivity is higher in the northern part with a hotspot of connectivity (brighter colors on the matrix) between 39.9° N and 40.35° N (zones 2 to 4). Higher local retention (ratio of locally produced settlement to total local larval release; (Lett et al., 2015)) is noted in zones 2 and 3 for sea scallop and zone 3 for surfclam. For scenarios 2 and 3, the positive and negative differences in larval settlement success with Scenario 1 are relatively low: around 0.5% for sea scallop, 1% for surfclam, and 1.5% for sea bass. For Scenario 2, the larval connectivity increases in the northern part for all species and local retention decreases in some zones (for sea scallop: zones 1–3, 5–8, 11; for surfclam: 1, 3, 5–6, 8–9; for sea bass: 1, 4–9). For Scenario 3, the connectivity observations from Scenario 2 remain and are generally more accentuated (Figure 290c, f, i). Some key differences between scenarios 1 and 3 are a decrease in local retention in the northern zones and an increase in larval settlement success from north to south. Mean connectivity is consistent across the three scenarios for each species (Table 34, Table 35, and Table 36).

Larval settlement success within each settlement zone is represented in Figure 291. For Scenario 1, more larvae settled in zones 3 and 4. Larval settlement success in the zones located south of 40° N is higher for sea bass (Figure 291g) compared to scallop and surfclam (Figure 291a, d). In Scenario 2, more larvae were transported to the northern settlement zones (above 39° N) and less to the southern ones for sea scallop. Differences in larval settlement success for surfclam and sea bass vary depending on the zone. For Scenario 3, higher settlement success of scallop larvae is observed in zones 4 and 10, compared to Scenario 1 (Figure 291c). Larval settlement success is generally lower for surfclam, except in the southernmost zone (Figure 291f). For sea bass, settlement success decreases typically in the northern settlement zones and increases in the southern ones (Figure 291i).

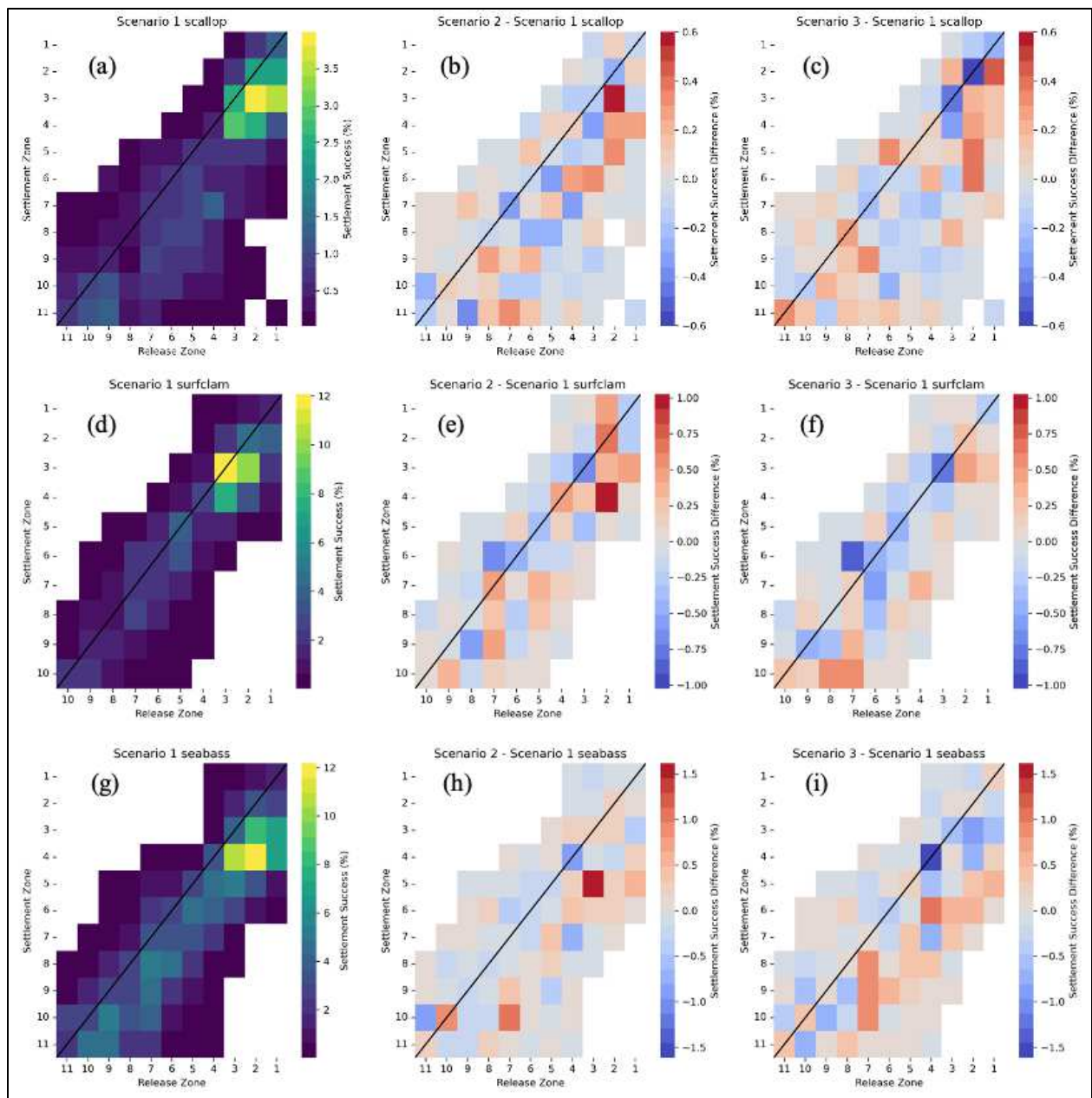


Figure 294. Connectivity matrix for each species for simulation M1; top row (a, b, c) is sea scallop, middle row (d, e, f) is surfclam, and bottom row (g, h, i) is sea bass. Left column (a, d, g) is the connectivity matrix for Scenario 1 (baseline). Center (b, e, h) and right-most column (c, f, i) are the difference between the connectivity matrices of either Scenario 2 or 3 and Scenario 1, respectively, with red reflecting a positive difference and blue a negative difference.

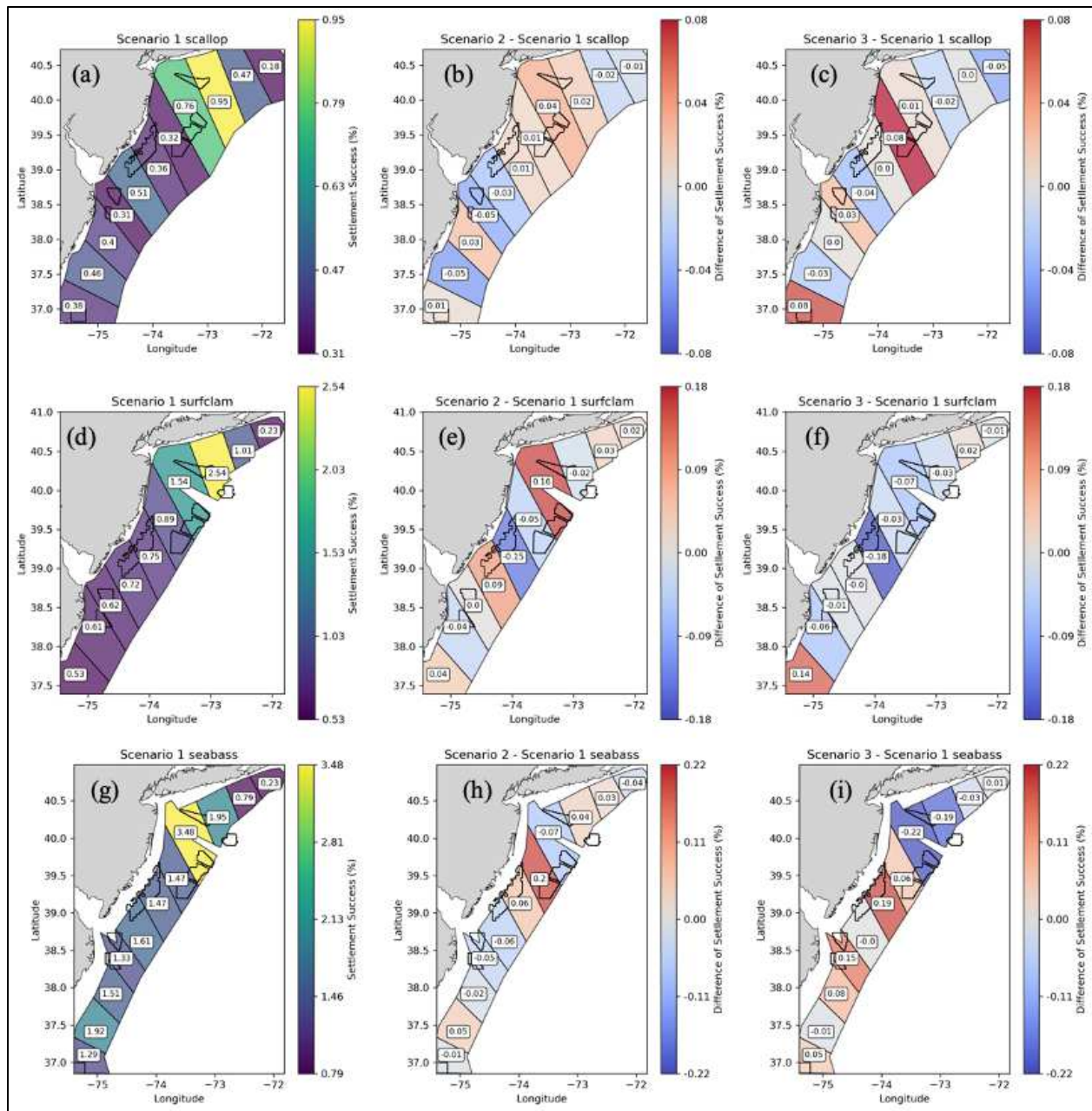


Figure 295. Maps of settlement success per settlement zone for Scenario 1 (baseline, left column, a, d, g) for each species – top row sea scallop (a, b, c), center row surfclam (d, e, f), bottom row sea bass (g, h, i) for simulation M1.

Settlement success here is the total number of larvae in each settlement zone (sum of the columns of the connectivity matrix) normalized to the total released (in all areas and during all runs) * 100. Center (b, e, h) and right (c, f, i) column are the difference between the settlement success maps of either Scenario 2 or 3 and Scenario 1, respectively, with red reflecting a positive difference and blue a negative difference. The color bar for the Scenario 3 panels is the same as Scenario 2 for each species. WEAs from Scenario 3 are outlined in black on all plots.

With 10,000 larvae included in the model configurations (M2), trajectories of scallop larvae released on May 1, 2018, (Figure 292a through c) are overall similar to the ones observed in M1 (1,000 larvae; Figure 287a through c), with more larvae being transported in the northern part of the study domain. Larval connectivity from north to south increases in M2 compared to M1; settlement zones between 38.66° N and

37.04° N receive larvae from all the release zones of the study domain and larvae released in the northern zones were transported further south. Similar connectivity patterns are observed in M2 compared to M1 with a decrease in local retention in the northern zones (except zones 1 and 2) and an increase in larval settlement success from north to south. Mean connectivity is also consistent across the three scenarios for each species (Table 34, Table 35, Table 36). The range of larval dispersal distances in M2 (Figure 292g) is similar to M1 (Figure 289a) with most larvae settling within 100 km of their release zone. In M2, Scenario 2 increases larval dispersal distances around 50 km range and Scenario 3 increases distances around 100 km range. As in M1, the mean larval dispersal distance slightly increases from scenarios 1 to 3 (from 88.82 km to 89.3 km) and the maximum dispersal is higher in Scenario 1 (495.4 km for Scenario 1; 465.07 km for Scenario 2; 471.77 km for Scenario 3). Minimum and maximum distances are more extreme than in M1, particularly for scenarios 2 and 3 (min = 0.3 km for Scenario 2, 0.73 km for Scenario 3; max = 465.07 km for Scenario 2, 471.77 km for Scenario 3). Figure 292h, i, and j show that with 10,000 larvae (M2) the density of successfully settled scallop isn't as patchy as it was with 1,000 larvae (Figure 288a, b, and c). The hot spot is more clearly defined and occurs between 40.0° N and 40.5° N.

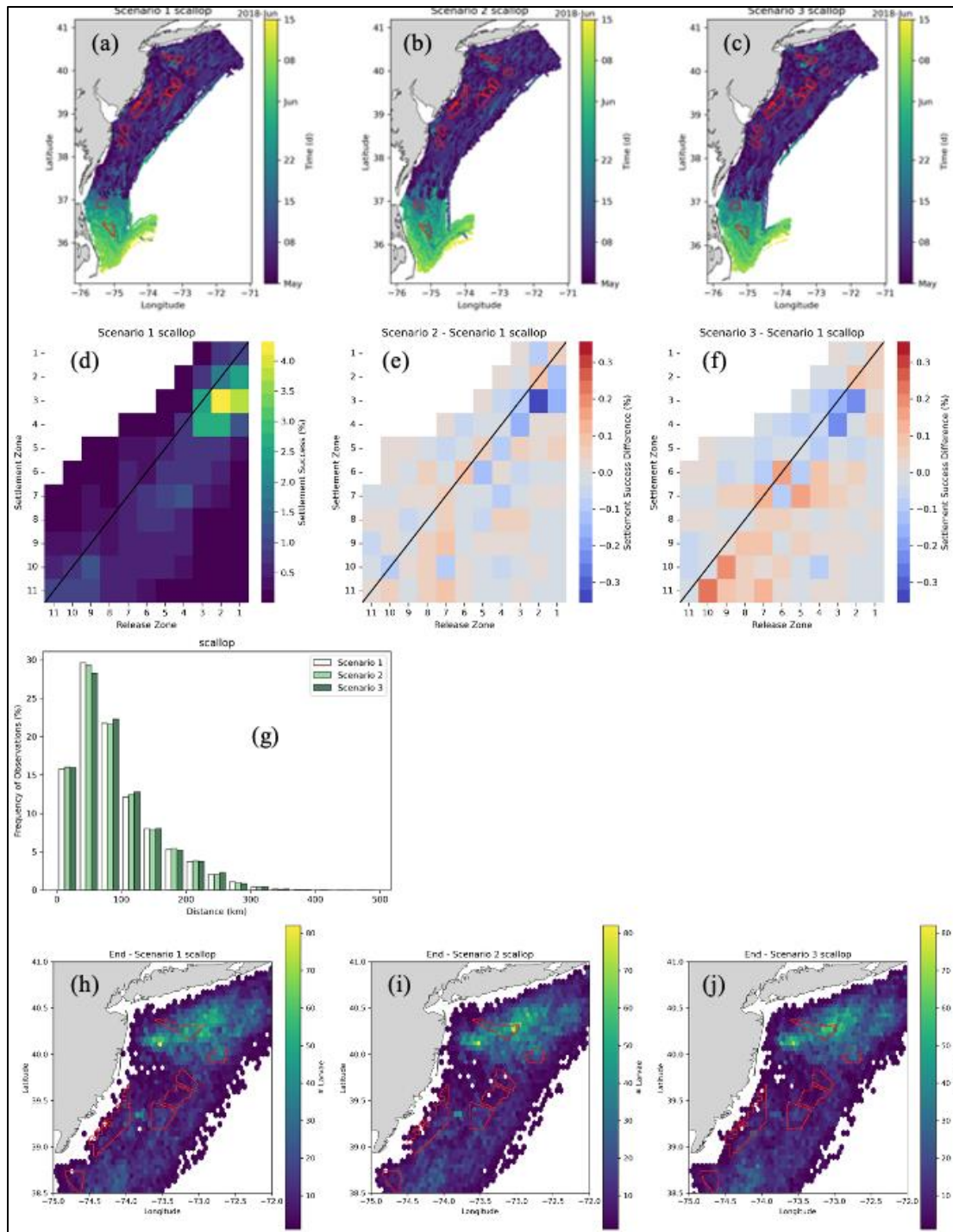


Figure 296. Scallop trajectories (a, b, c), connectivity matrices (d, e, f), distance distribution (g), and successfully settled end location density plot (h, i, j) for 10,000 released larvae (M2). Left column (a, d) is scenario 1 (baseline). Plot (b) and (c) are the trajectories for scenario 2 and 3 with the WEAs from scenario 3 outlined in red. Plot (e) and (f) are the difference between the connectivity matrices of either scenario 2 or 3 and scenario 1, respectively, with red reflecting a positive difference and blue a negative difference.

12.3.2 Effect of DVM on Larval Connectivity

When including DVM (model configuration M3), the trajectories between the three species are comparable. Figure 293 only shows the trajectories of all larvae released on May 1, 2018. Scallop and surfclam larval trajectories follow a similar path with more scallop larvae transported to the eastern model boundary than surfclam (Figure 293). Sea bass larvae do not travel as far south in Scenario 3 compared to scenarios 1 and 2. Compared to the model without DVM (M1; Figure 287), most larvae released in the northern areas (above 40°N) were transported further offshore with scallop larvae reaching the southern boundary of the study domain, surfclam larvae being transported to around 38°N, and sea bass larvae being transported to around 39°N. With DVM, larvae trajectories stopped before the southernmost WEAs.

Looking at settlement density, scallop with DVM (simulation M3, Figure 294a, b, and c) shows a higher density of larvae around 39.0°N for all scenarios. This is further south than simulation M1 (Figure 288a, b, and c). There are less gaps in the density map for all three scenarios than the M1 case, highlighting the reduction in patchiness of scallop settlement with DVM. Surfclam (Figure 294d, e, and f) has relatively consistent larval density throughout the domain across the scenarios with slightly higher density on the edge of the zone definitions. Sea bass (Figure 294g, h, and i) shows a relatively consistent larval density across the domain, with slightly increased density further offshore. There is higher density further south in scenario 3 than scenario 1.

DVM increased the similarity of the distribution of the larval dispersal distances between species (Figure 295). With DVM, larval dispersal distances are more evenly distributed across a wider range of distances compared to those without DVM showing higher frequency near shorter distances (Figure 289). The maximum frequency of larval dispersal distances is lower with DVM compared to without, with a broader peak spread over 100–200 km for sea scallop and 50–125 km for surfclam and sea bass. A large percentage of scallop larvae (82%) settle between 25 and 200 km from their release areas. Similarly, a large proportion of surfclam larvae (77%) and sea bass larvae (75%) settle between 15 and 150 km from their release areas. For the three species, larvae settle further with Scenario 3 than with scenarios 1 and 2, particularly for distances longer than 100km. Across all the species, Scenario 2 has the lowest mean dispersal distance (Table 34, Table 35, Table 36). For all scenarios, the mean dispersal distance is greater with DVM than without (e.g., for surfclam and Scenario 3: 48.18 km without DVM and 87.6 km with DVM), and for scenarios 2 and 3, maximum dispersal distance is greater for larvae with DVM than without.

When including DVM, larval connectivity largely increases for all the species (Figure 296). In Scenario 1, the larval settlement success in zone 4 is multiplied by around seven for sea scallop and is double for surfclam and sea bass compared to M1 (Figure 296a, d, g). The hotspot of larval connectivity is larger compared to M1 with larvae being transported between 40.28°N (zone 3) and 38.61°N (zone 7). Local retention of larvae is qualitatively similar in all the zones. The differences in connectivity for scenarios 2 and 3 are also higher compared to M1. Overall, for Scenario 2, more scallop larvae are successfully transported in the northern part of the domain, and local retention increases in the northern zones. For surfclam and sea bass, less connectivity is observed except between zones 3 and 6. For Scenario 3, larval connectivity increases in the hotspot observed in Scenario 1 for the three species, and local retention decreases mainly for surfclam and sea bass. Mean connectivity is higher for larvae with DVM than larvae without DVM by six times, and mean connectivity increases from Scenario 1 to 3 (Table 34, Table 35, Table 36). Mean connectivity is highest for sea bass with DVM, but all species have a mean connectivity of around 3–3.5% with DVM and 0.5–1.5% without DVM.

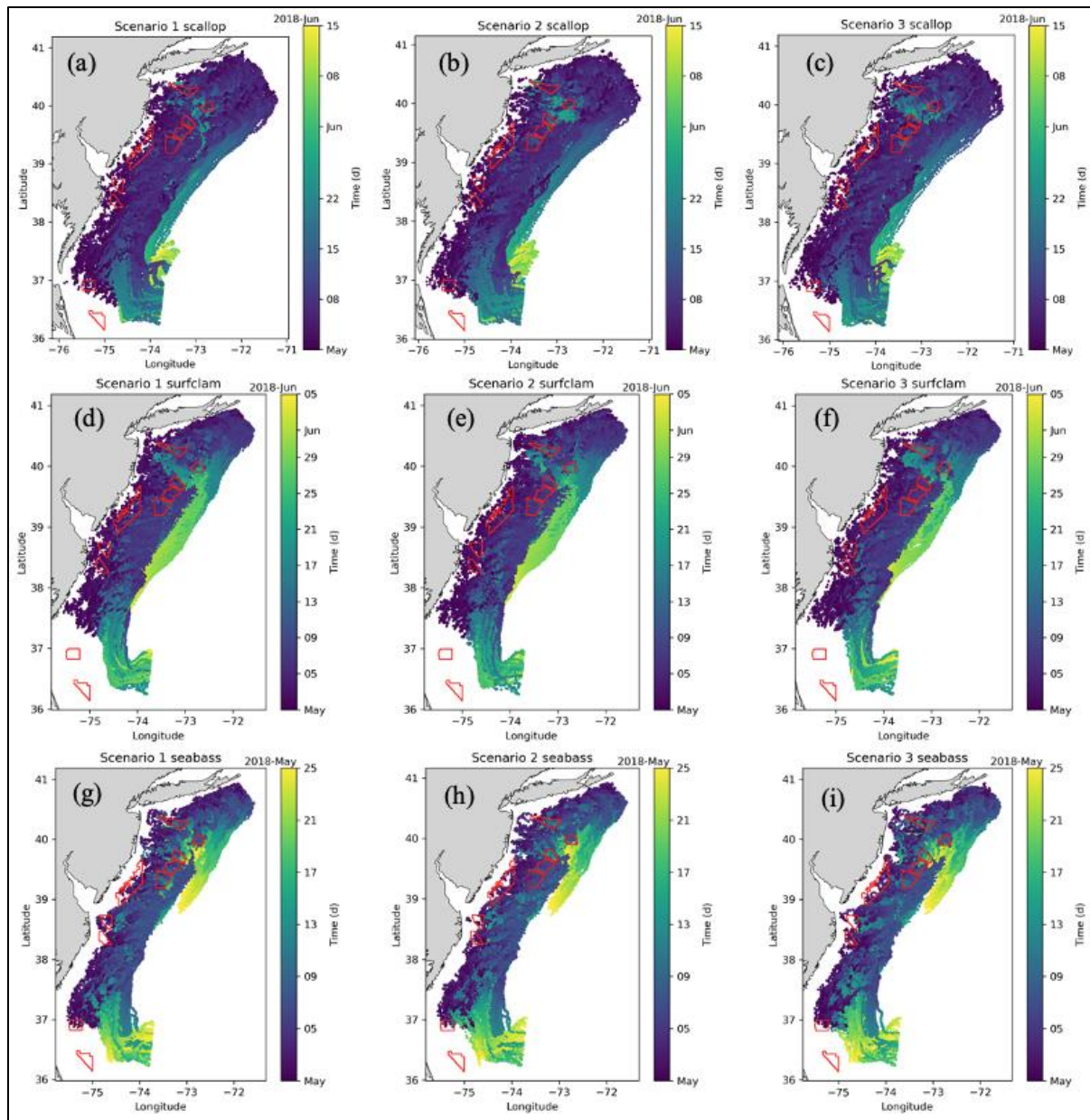


Figure 297. Trajectories over time for all larvae released on May 1, 2018 with DVM (simulation M3). Top row (a, b, c) sea scallop, middle row (d, e, f) surfclam, and bottom row (g, h, i) sea bass. WEAs from Scenario 3 outlined in red in each plot. Left-most column (a, d, g) is the base scenario (no turbines), middle column (b, e, h) is Scenario 2 (partial buildout), and right-most column (c, f, i) is full buildout.

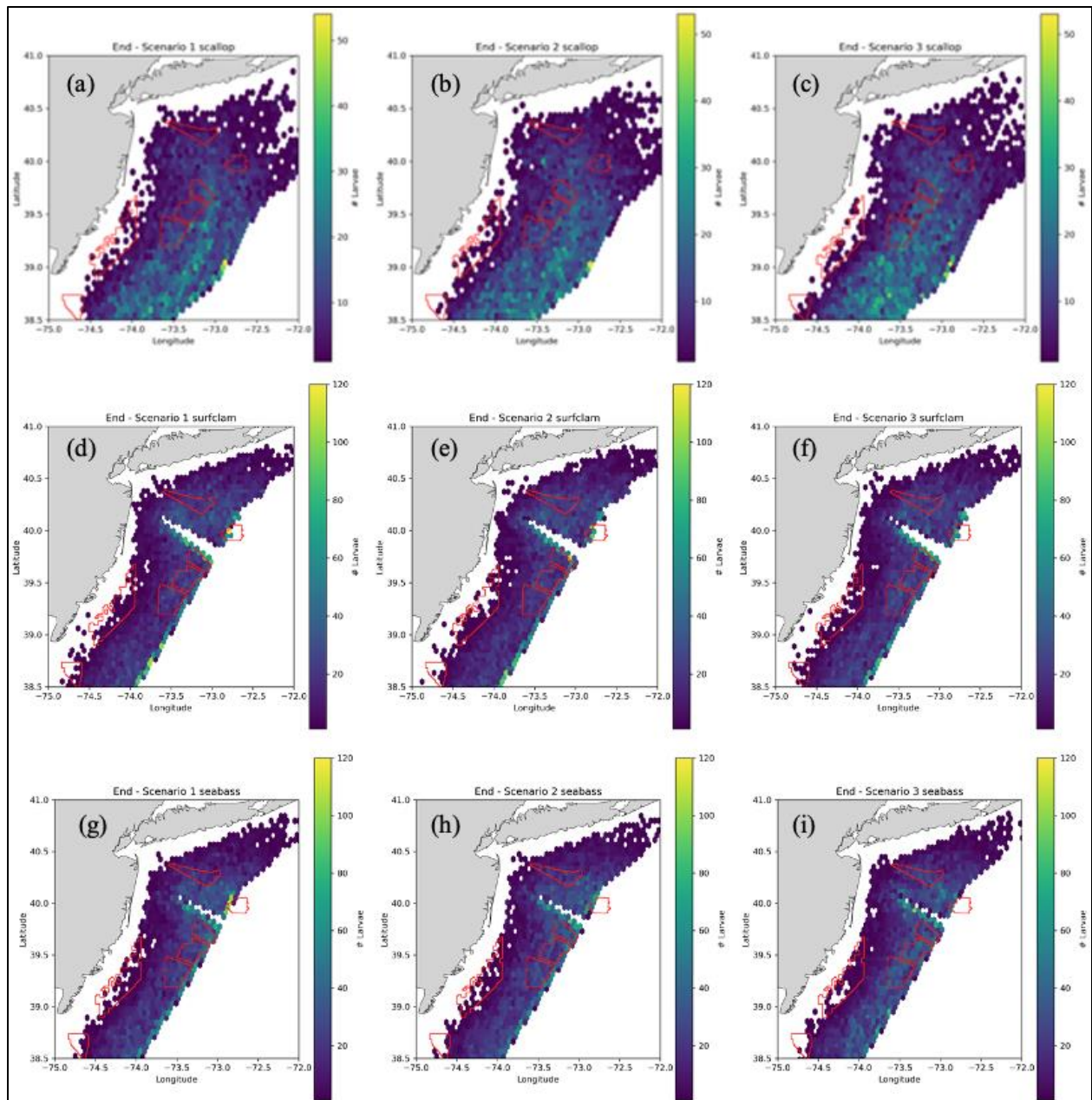


Figure 298. Density of all successfully settled larvae for simulation M3. This image is a zoomed in portion of the total domain near the northern WEAs. Top row (a, b, c) sea scallop, middle row (d, e, f) surfclam, and bottom row (g, h, i) sea bass. WEAs from scenario 3 are shown with red outlines in each plot. Left column (a, d, g) is scenario 1 (no turbines), middle column (b, e, h) is scenario 2 (partial buildout), and right column (c, f, i) is scenario 3 (full buildout).

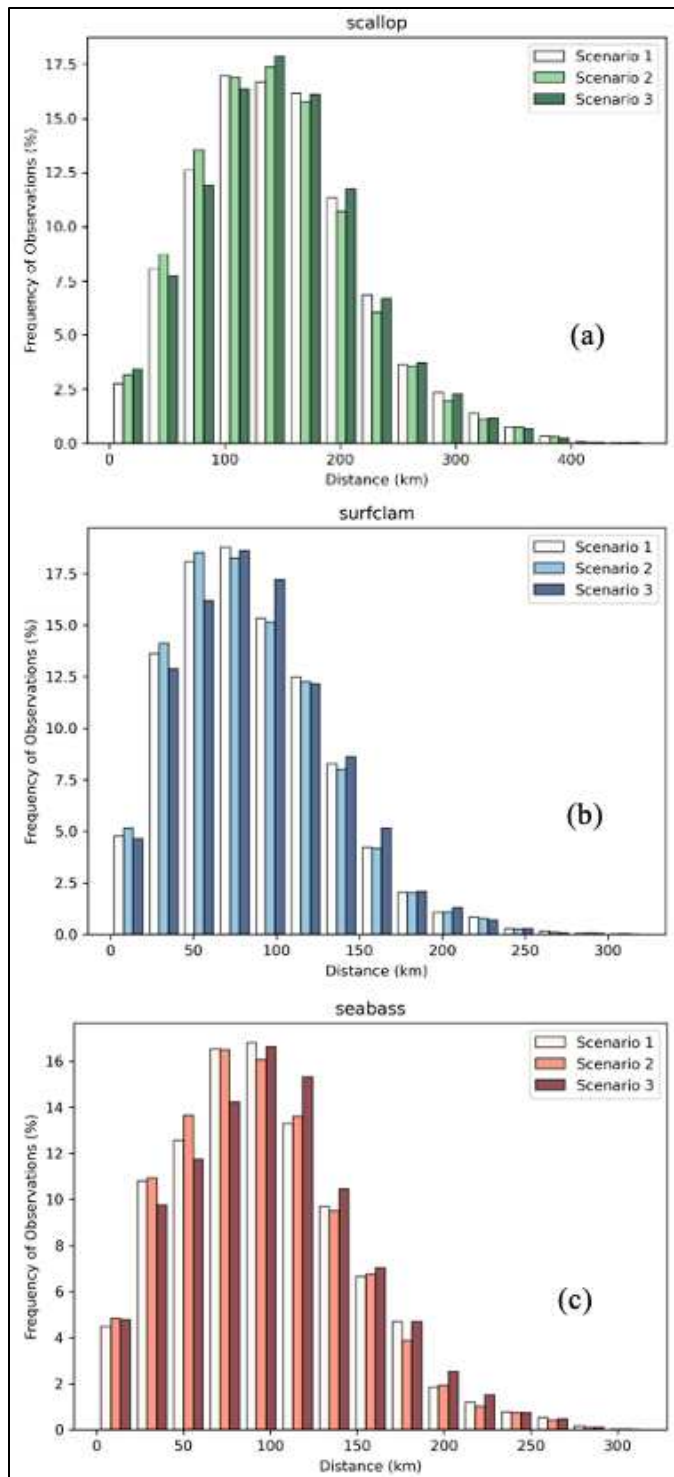


Figure 299. Distance between larvae release and settle for Scenario 1 (baseline, no turbines, white), Scenario 2 (partial buildout, light shading), and Scenario 3 (full buildout, dark shading). For sea scallop (a, greens), surfclam (b, blues), and sea bass (c, reds) with DVM (simulation M3).

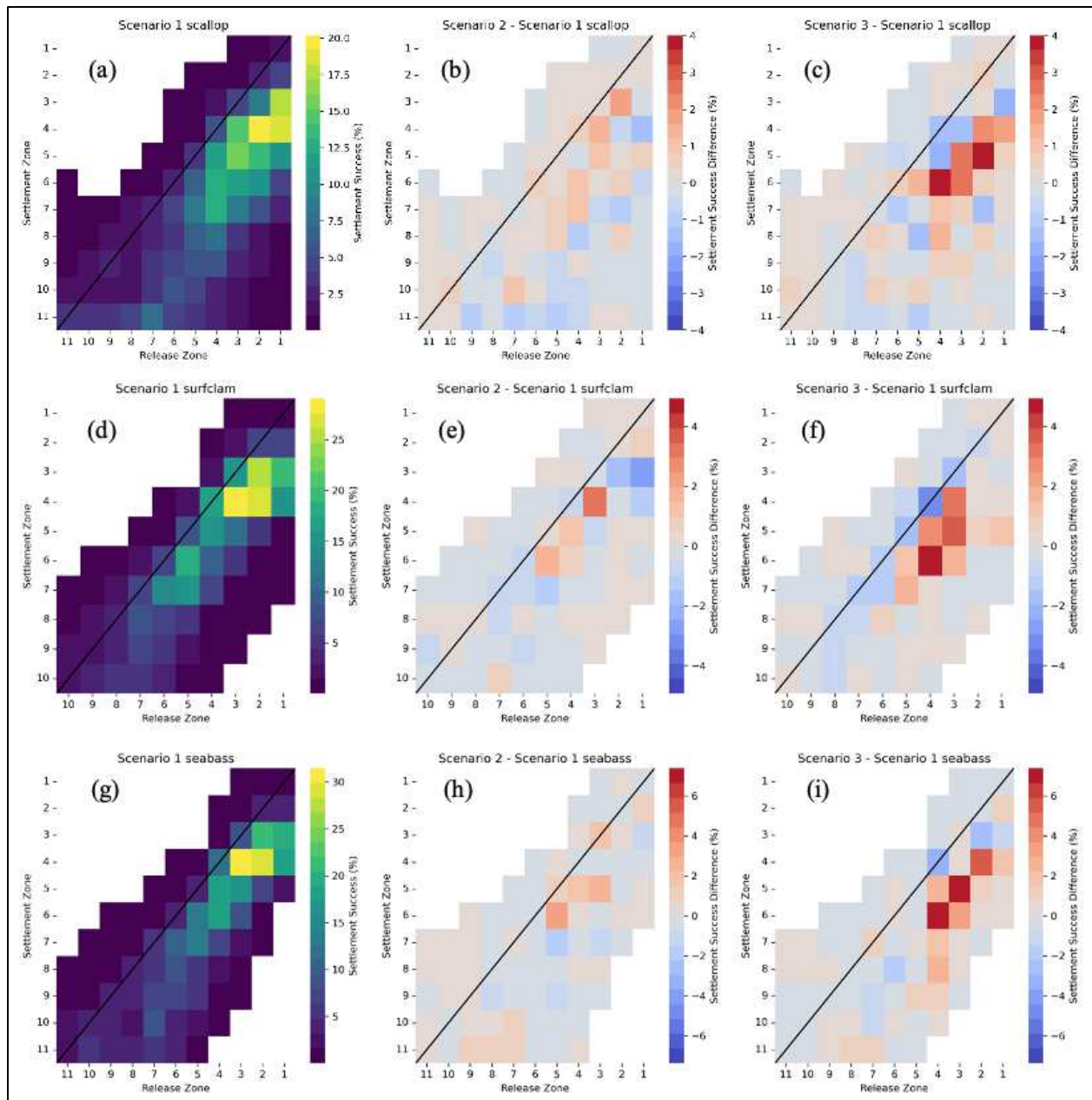


Figure 300. Connectivity matrix for each species with DVM (simulation M3); top row (a, b, c) is sea scallop, middle row (d, e, f) is surfclam, and bottom row (g, h, i) is sea bass. Left column (a, d, g) is the connectivity matrix for the Scenario 1 (baseline). Center (b, e, h) and right columns (c, f, i) are the difference between the connectivity matrices of either Scenario 2 or 3 and Scenario 1, respectively, with red reflecting a positive difference and blue a negative difference.

12.3.3 Effect of Temperature Tolerance on Larval Connectivity

When including larval temperature dependence for sea scallop (model configuration M4), most larvae released on May 1, 2018 exhibit short trajectories (Figure 297a, b, and c), likely due to their narrow range of temperature tolerance (10 to 18° C; see Table 32). In scenarios 2 and 3, some trajectories are longer. Figure 298a, b, and c shows that significantly less scallop successfully settle in the northern portion of the study domain with temperature dependence (M4) than without it (M1, Figure 288a, b, and c). There is not

much discernable difference between the three scenarios. Larval dispersal distances (Figure 299a) range from 0 to 250 km for sea scallop. In Scenario 1, the distance distribution for less than 50 km is uniform, whereas in scenarios 2 and 3, it steadily declines with increasing distance. Typically, scallop larval dispersal distances in scenarios 2 and 3 are greater than those in Scenario 1. Larval connectivity also decreases with only two spots of connectivity observed, one between 40.48°N and 39.91°N (zones 1 to 4) and one between 38.66° N and 37.5° N (zones 7-10) (Figure 300a, b, c). The difference in connectivity is low for scenarios 2 and 3 compared to Scenario 1 with higher larval settlement success of scallop observed in the northern connectivity spot and more larvae that settled in 39.45° N (zone 5). When larval temperature dependence is included in the model, the mean dispersal distance, maximum dispersal distance, and mean connectivity are low compared to the other simulations by 50% or more (Table 34). There is no significant difference between the three scenarios for the temperature dependence case, except that the maximum dispersal distance is higher for Scenario 3 than for scenarios 1 or 2.

When including larval temperature dependence for surfclam (model configuration M4), larvae similarly have short trajectories. Surfclam settled larval density (Figure 298d, e, and f) is much less dense with temperature dependence than without (M1, Figure 288d, e, and f). Larval dispersal distances (Figure 299b) range from 0 to 200 km for surfclam. All three scenarios follow a right-skewed normal distribution; the frequency of observations increases to 25 km and then steadily decreases for greater distances. Typically, larval dispersal distances in scenarios 2 and 3 are greater than those in Scenario 1. Mean dispersal distance is similar between the M4 and the model including passive behavior (M1) (Table 35). The connectivity matrices for surfclam larvae with a temperature dependence (Figure 300d, e, f) appear much more similar to the connectivity matrix with passive behavior included in the model (Figure 290d, e, f; configuration M1). With the temperature dependence, the connectivity hotspot occurs in zone 5 (latitude 40° N) and there is high local retention for many of the zones in Scenario 1. Scenario 2 increases local retention in zone 10 and there is less larval connectivity from zone 6 to zone 5. In Scenario 3, local retention decreases in zone 9, with a slight increase in settlement success in the surrounding zones. Mean connectivity is lower for simulation M4 than simulation M1 by a factor of 5 or M3 by more than an order of magnitude (Table 35).

Sea bass trajectories when larvae temperature dependence is included in the model (M4) are longer than for sea scallop or surfclam (Figure 297g, h, i). There are more trajectories around 40° N in Scenario 1 than in Scenario 2 or 3, otherwise the trajectories are similar across the scenarios. The sea bass larval density with temperature dependence (Figure 298g, h, and i) appears very similarly to how it did without temperature dependence (Figure 288g, h, and i). The sea bass dispersal distances (Figure 299c) follow a similar pattern to surfclam (Figure 299b): the frequency of observations increases from 0 to 50km and then steadily decreases. Larval dispersal distances in scenarios 2 and 3 are greater than those in Scenario 1. The upper bound of distance is higher for sea bass than the other species (300 km). Mean dispersal distance is lower for sea bass with temperature dependence (configuration M4) than with passive behavior (M1, by about 10 km) or DVM (M3, by about 30 km) (Table 36). The connectivity of sea bass larvae with temperature dependence (Figure 300g, h, i) shows a hotspot of connectivity from release zones 2 and 3 to settlement zones 3 and 4, which is a slightly expanded hotspot from when passive behavior is included (M1) (Figure 290g, h, i). Introducing WEAs reduces connectivity for scenarios 2 and 3. Mean connectivity for temperature-dependent sea bass larvae (M4) is more than half that of the passive (M1) and a fifth of the DVM (M3) (Table 36).

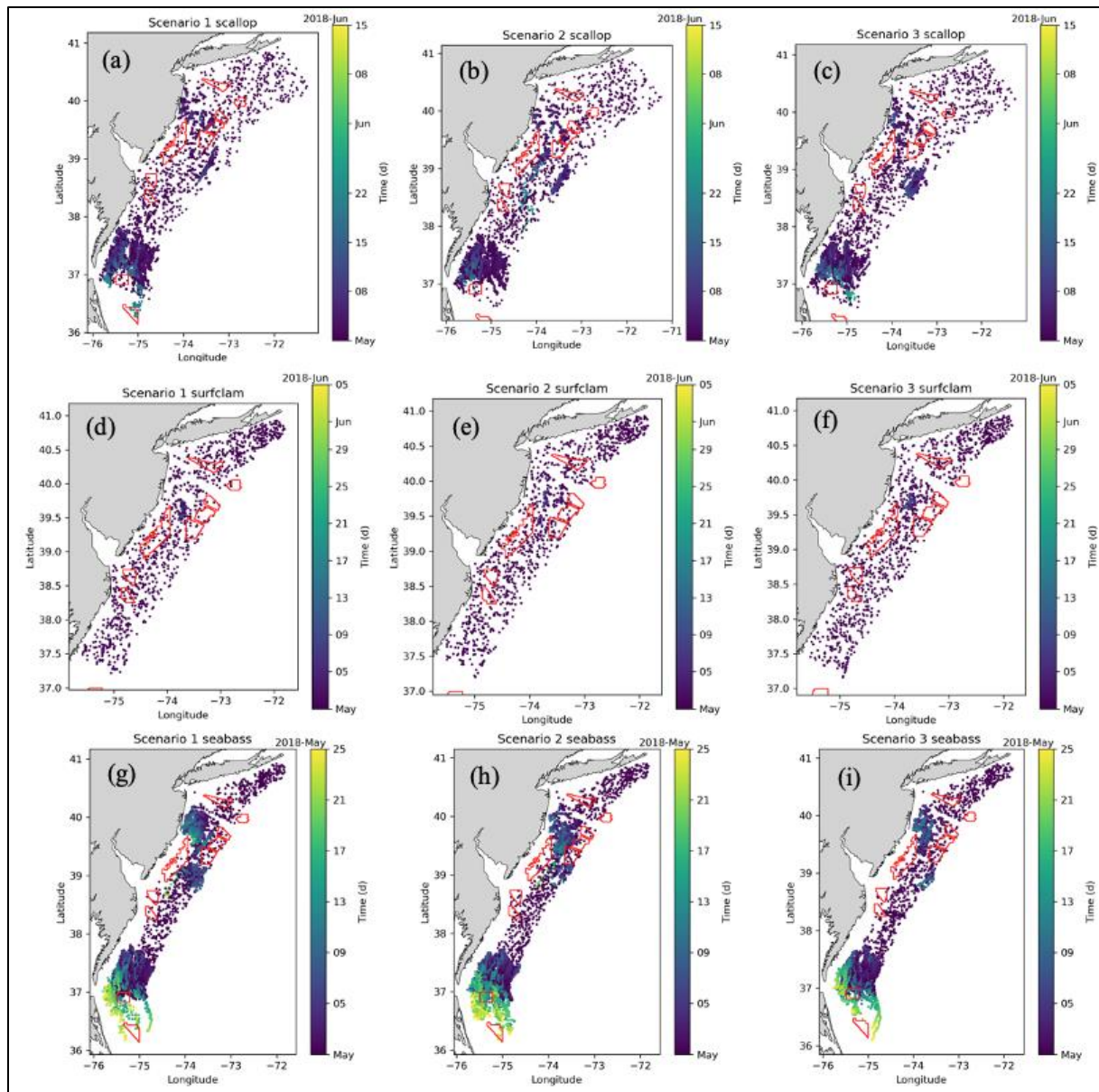


Figure 301. Trajectories over time for all larvae released on May 1, 2018 with temperature dependence (simulation M4).

Top row (a, b, c) sea scallop, middle row (d, e, f) surfclam, and bottom row (g, h, i) sea bass. WEAs from Scenario 3 outlined in red in each plot. Left-most column (a, d, g) is the base scenario (no turbines), middle column (b, e, h) is Scenario 2 (partial buildout), and right-most column (c, f, i) is full buildout.

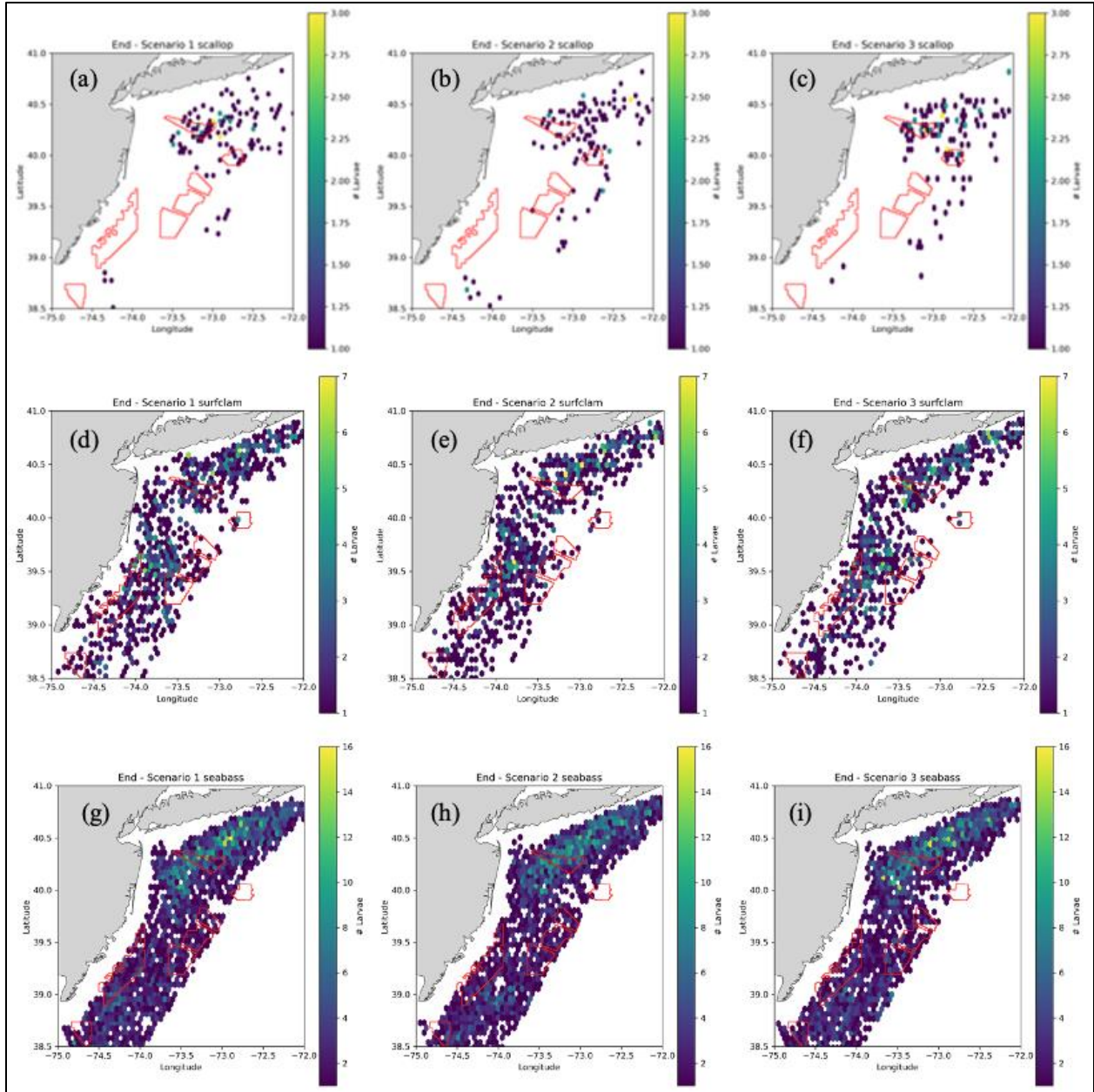


Figure 302. Density of all successfully settled larvae for simulation M4. This image is a zoomed in portion of the total domain near the northern WEAs. Top row (a, b, c) sea scallop, middle row (d, e, f) surfclam, and bottom row (g, h, i) sea bass. WEAs from scenario 3 are shown with red outlines in each plot. Left column (a, d, g) is scenario 1 (no turbines), middle column (b, e, h) is scenario 2 (partial buildout), and right column (c, f, i) is scenario 3 (full buildout).

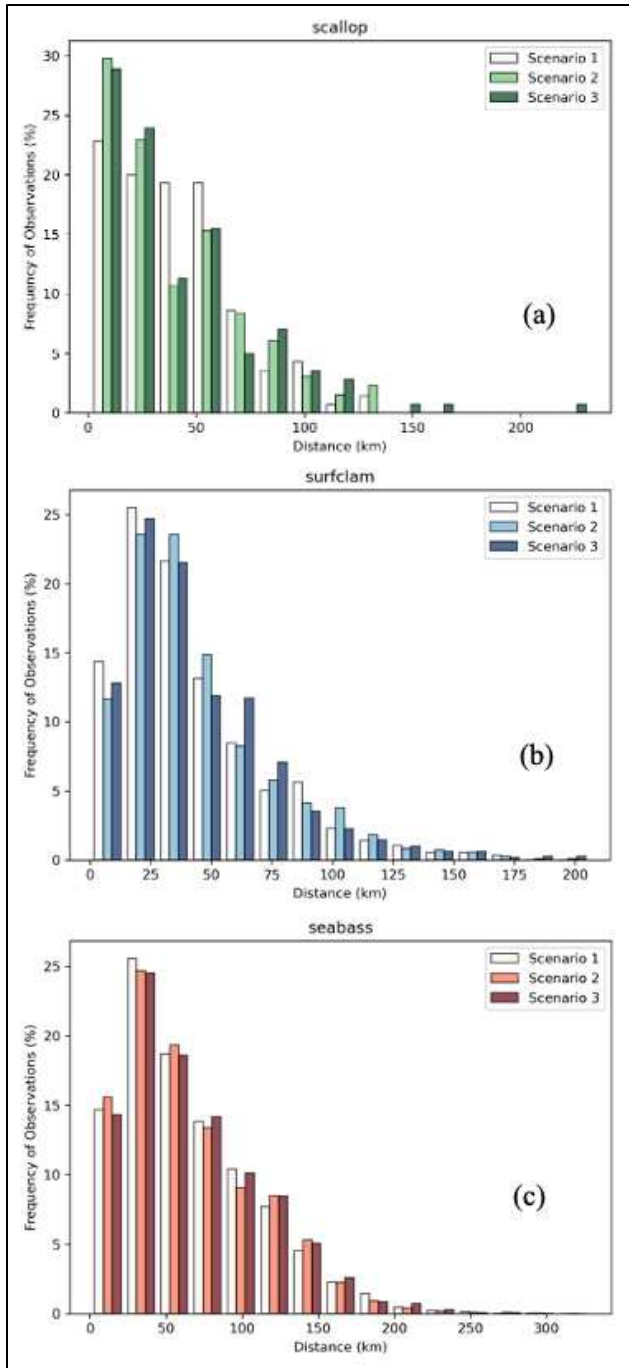


Figure 303. Larval dispersal distance between larvae release and settlement for Scenario 1 (baseline, no turbines, white), Scenario 2 (partial buildout, light shading), and Scenario 3 (full buildout, dark shading). For sea scallop (a, greens), surfclam (b, blues), and sea bass (c, reds) with temperature dependence (simulation M4).

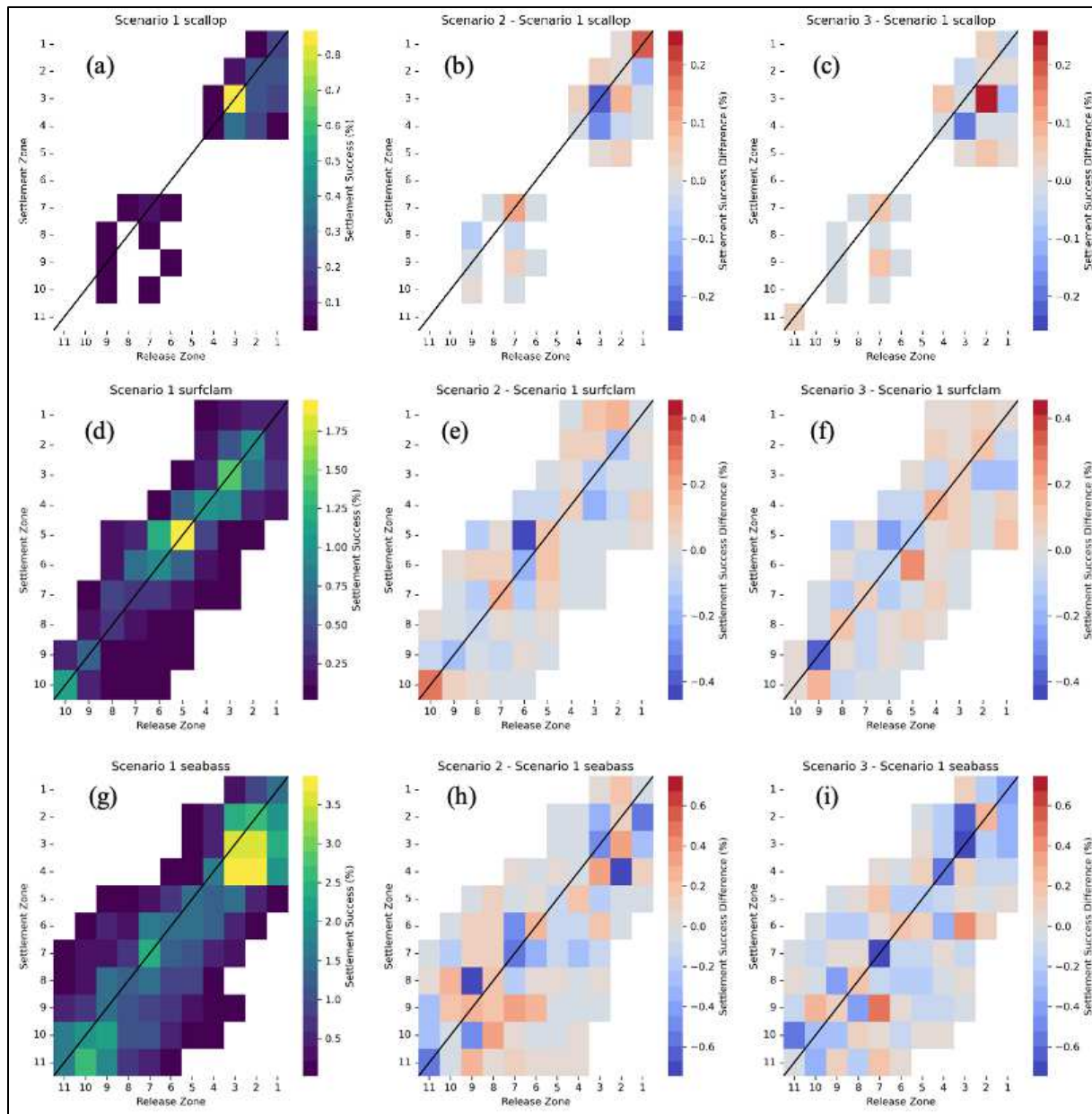


Figure 304. Connectivity matrix for each species with temperature dependence (simulation M4); top row (a, b, c) is scallop, middle row (d, e, f) is surfclam, and bottom row (g, h, i) is sea bass. Left column (a, d, g) is the connectivity matrix for the Scenario 1 (baseline). Center (b, e, h) and right columns (c, f, i) are the difference between the connectivity matrices of either Scenario 2 or 3 and Scenario 1, respectively, with red reflecting a positive difference and blue a negative difference.

12.3.4 Effect of DVM and Temperature Tolerance on Larval Connectivity

When including DVM and larval temperature dependence for scallop (model configuration M5), most larvae released on May 1, 2018 exhibit short trajectories (Figure 301a, b, and c), likely due to their narrow range of temperature tolerance (10 to 18° C; see Table 32). However, trajectories extend further south for scallop with DVM and temperature dependence (Figure 301a, b, and c) compared to passive larvae with temperature dependence only (Figure 297a, b, and c). Figure 302a, b, and c show even less larval density for scallop with DVM and temperature dependence (simulation M5) than just temperature dependence

(Figure 298a, b, and c, M4). Larval dispersal distances (Figure 303a) range from 0 to 225 km for scallop. For all scenarios, the distance distribution is bimodal: peaks occur between 25–50 km and 75–150 km. This matches the trajectories (Figure 301), larvae either move short distances or medium distances. Typically, scallop larval dispersal distances in scenarios 2 and 3 are greater than those in scenario 1. Larval connectivity also decreases with only two spots of connectivity observed, one between 40.48° N and 39.91° N (zones 1 to 4) and one between 38.66° N and 38.0° N (zones 6–7) (Figure 304a, b, c). The difference in connectivity is low for scenarios 2 and 3 compared to scenario 1 with higher larval settlement success of scallop observed in the northern connectivity spot and more larvae that settled in 39.91° N (zone 4) released from zone 1 but less larvae released from zone 1 settling in zones 2 and 3. When DVM and larval temperature dependence is included in the model, mean connectivity is slightly lower than larval temperature dependence alone (M4 vs M5 in Table 34), whereas the min, mean, and max dispersal distances are all higher than simulation M4. Between the three scenarios for the DVM and temperature dependence case, the mean dispersal distance is higher for scenarios 2 and 3 than for scenario 1 and mean connectivity is reduced for scenario 3 than scenarios 1 or 2.

When including DVM and larval temperature dependence for surfclam (model configuration M5), larvae similarly have short trajectories (Figure 301d, e, and f), similar to when larval temperature dependence only is included (Figure 297d, e, and f). Surfclam show a decrease in larval density with DVM and temperature dependence (M5, Figure 302d, e, and f) than just temperature dependence (M4, Figure 298d, e, and f). Larval dispersal distances (Figure 303b) range from 0 to 250 km for surfclam. All three scenarios follow a right-skewed normal distribution; the frequency of observations increases to 25 km and then steadily decreases for greater distances. Typically, larval dispersal distances in scenarios 2 and 3 are greater than those in scenario 1, but very slightly. Mean dispersal distance is similar between M5 and the model including DVM (M3) (Table 35). The connectivity matrices for surfclam larvae with DVM and temperature dependence (Figure 304d, e, f) appear similar to the connectivity matrix with DVM behavior included in the model (Figure 296d, e, f; configuration M3). With DVM and temperature dependence, the connectivity hotspot occurs in zone 2 (latitude 40.5° N) and there is high connectivity moving southward. Scenario 2 increases local retention in zones 4–6 and there is less larval connectivity from zone 2 to zone 3. In scenario 3, local retention decreases in zones 2–4, with a slight increase in settlement success in the surrounding zones, especially from zone 4 to zone 6. Mean connectivity is about the same for simulation M5 as simulation M1 (Table 35).

Sea bass trajectories when DVM and larvae temperature dependence are included in the model (M5) are longer than for scallop or surfclam, especially around 37° N (Figure 301g, h, i). There are more trajectories around 39° N in scenario 1 than in scenario 2 or 3, otherwise the trajectories are similar across the scenarios. Sea bass show a decrease in larval density with DVM and temperature dependence (M5, Figure 302g, h, and i) than just temperature dependence (M4, Figure 298g, h, and i). The sea bass dispersal distances (Figure 303c) follow a similar pattern to surfclam Figure 303b): the frequency of observations increases from 0 to 75 km and then steadily decreases. Larval dispersal distances in scenarios 2 and 3 are greater than those in scenario 1. The upper bound of distance is higher for sea bass than the other species (300 km). Mean dispersal distance is higher for sea bass with DVM and temperature dependence (configuration M5) than with passive behavior (M1, by about 5 km) and lower than with DVM (M3, by about 10 km) (Table 36). The connectivity of sea bass larvae with DVM and temperature dependence (Figure 304g, h, i) shows a hotspot of connectivity from release zones 2 and 3 to settlement zones 3 and 4, which is a slightly expanded hotspot from when passive behavior is included (M1) (Figure 290g, h, i) and very similar to when only temperature dependence is included (Figure 300g, h, i). Introducing WEAs reduces connectivity for scenarios 2 and 3. Mean connectivity for DVM temperature-dependent sea bass larvae (M5) is slightly more than with temperature dependence only (M4, Table 36).

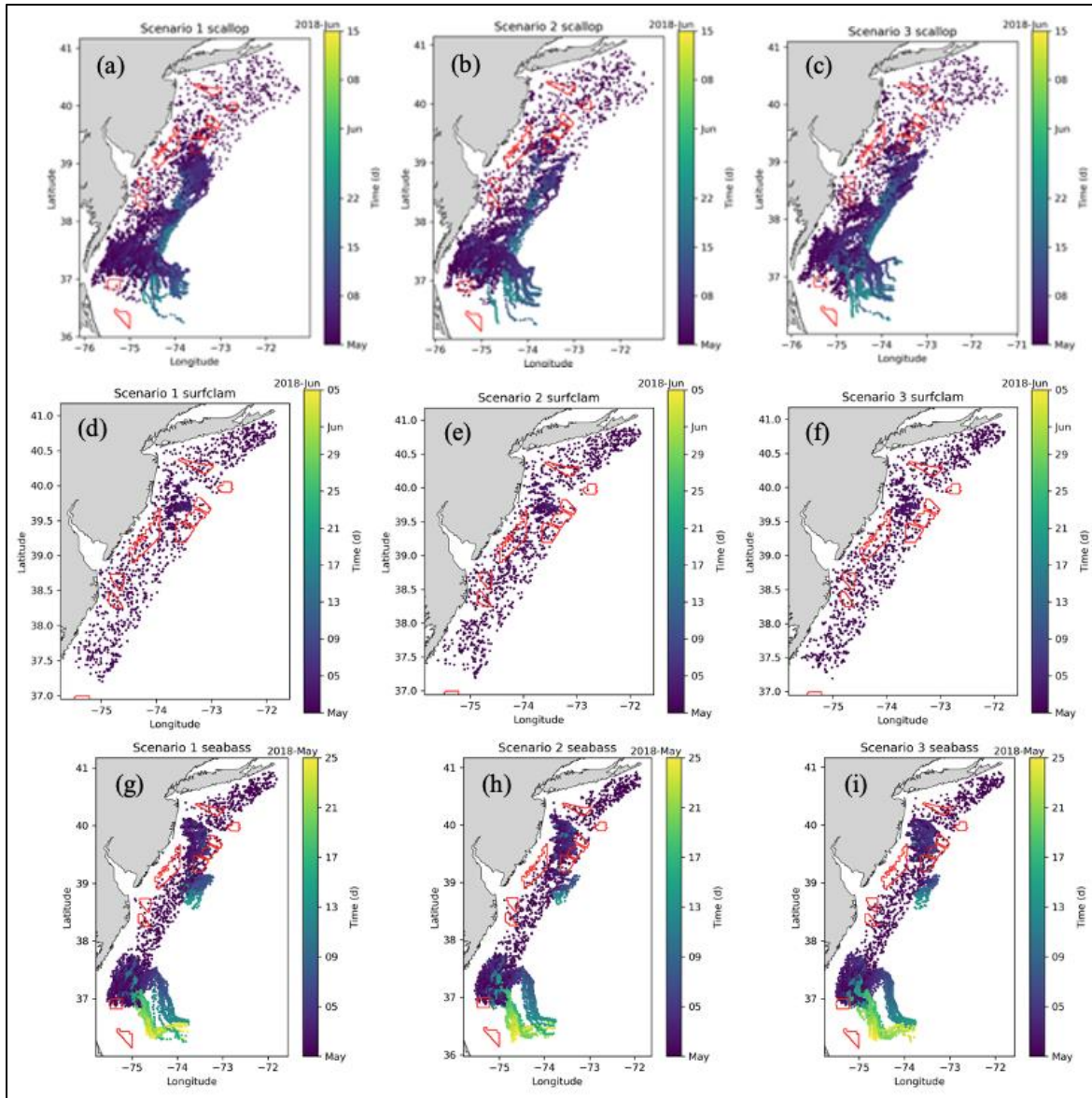


Figure 305. Trajectories over time for all larvae released on May 1, 2018 with DVM and temperature dependence (simulation M5).

Top row (a, b, c) sea scallop, middle row (d, e, f) surfclam, and bottom row (g, h, i) sea bass. WEAs from scenario 3 outlined in red in each plot. Left-most column (a, d, g) is the base scenario (no turbines), middle column (b, e, h) is scenario 2 (partial buildout), and right-most column (c, f, i) is full buildout.

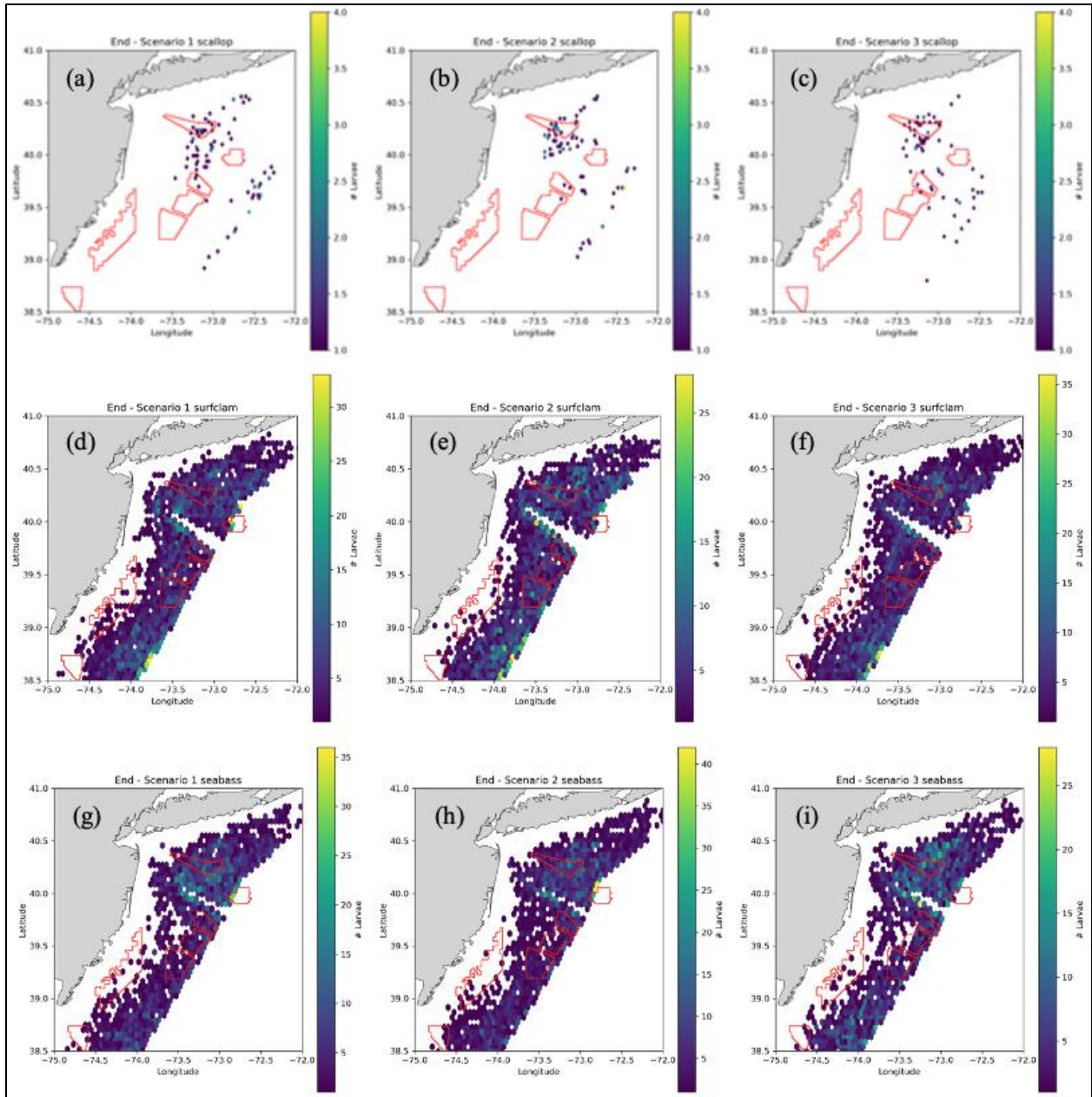


Figure 306. Density map of all successfully settled larvae for simulation M5. This image is a zoomed in portion of the total domain near the northern WEAs. Top row (a, b, c) sea scallop, middle row (d, e, f) surfclam, and bottom row (g, h, i) sea bass. WEAs from scenario 3 are shown with red outlines in each plot. Left column (a, d, g) is scenario 1 (no turbines), middle column (b, e, h) is scenario 2 (partial buildout), and right column (c, f, i) is scenario 3 (full buildout).

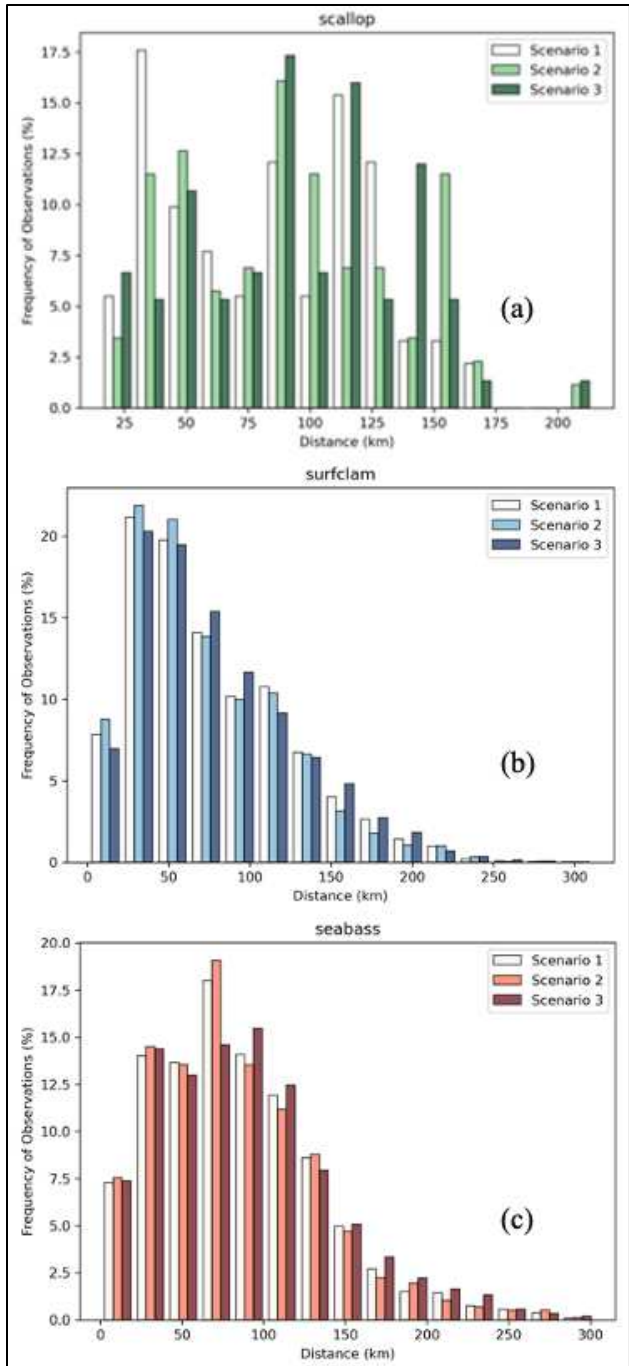


Figure 307. Larval dispersal distance between larvae release and settlement for scenario 1 (baseline, no turbines, white), scenario 2 (partial buildout, light shading), and scenario 3 (full buildout, dark shading). For sea scallop (a, greens), surfclam (b, blues), and sea bass (c, reds) with DVM and temperature dependence (simulation M5).

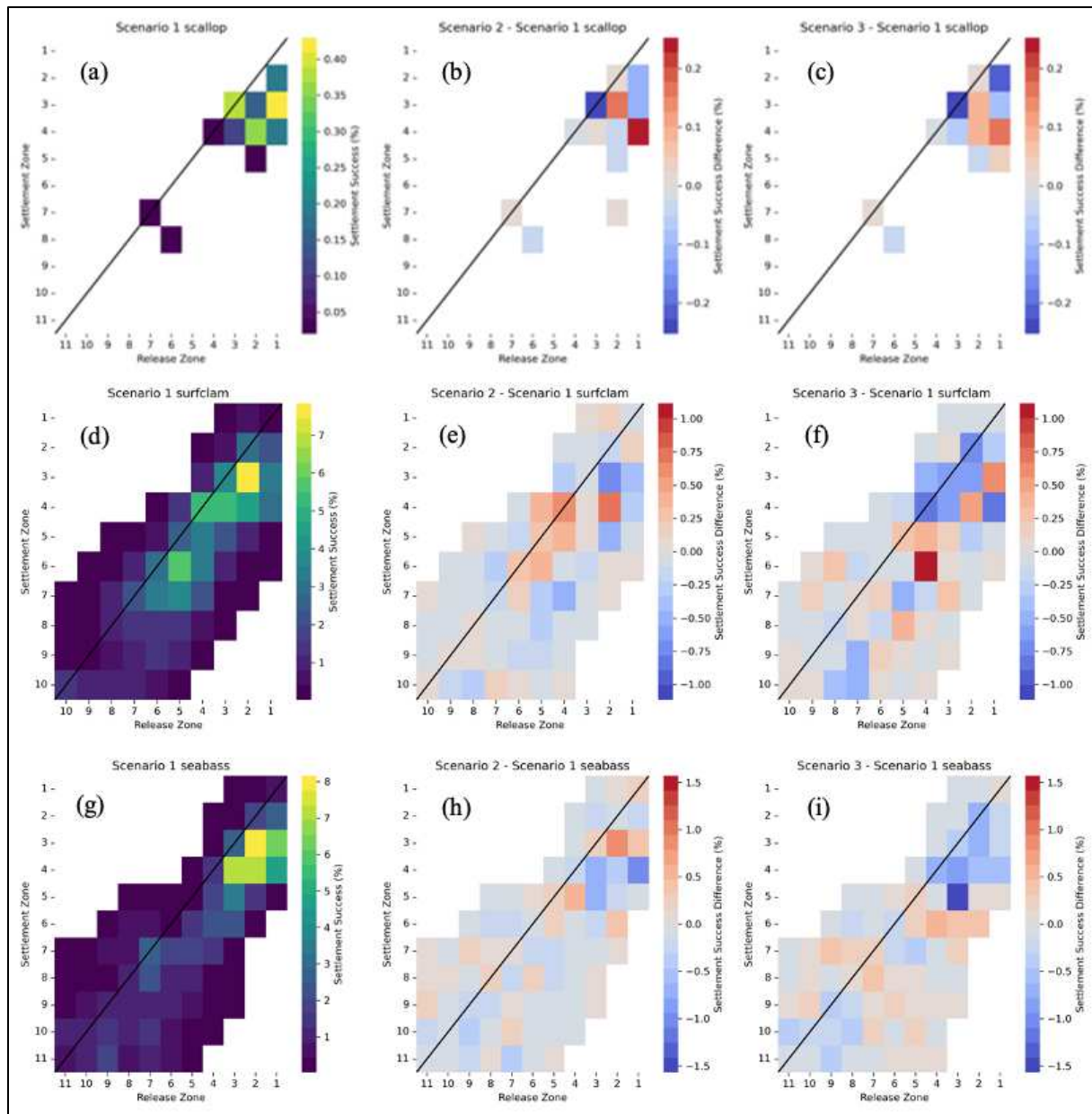


Figure 308. Connectivity matrix for each species with DVM and temperature dependence (simulation M5); top row (a, b, c) is sea scallop, middle row (d, e, f) is surfclam, and bottom row (g, h, i) is sea bass. Left column (a, d, g) is the connectivity matrix for the scenario 1 (baseline). Center (b, e, h) and right columns (c, f, i) are the difference between the connectivity matrices of either scenario 2 or 3 and scenario 1, respectively, with red reflecting a positive difference and blue a negative difference.

12.3.5 Summary of Larval Connectivity Statistics

When comparing model outputs across all simulations (Table 34–Table 36), introducing WEAs does not lead to a statistically significant difference for minimum dispersal distance, mean dispersal distance, maximum dispersal distance, or mean connectivity for any of the species; all p-value statistics from an analysis of variance test are greater than 0.05 (Table 37). The lowest p-value statistics occur for minimum dispersal distance of Atlantic surfclam and black sea bass and maximum dispersal distance of black sea bass.

Table 34. Summary of results obtained for all model simulations for Atlantic sea scallop.

See Table 3 for details. Disp. Dist. is dispersal distance, min is minimum, max is maximum.

Species and Simulations	Metric	Unit	Scenario 1 (Baseline)	Scenario 2 (Partial)	Scenario 3 (Full)
Scallop – M1	Min Disp. Dist.	km	0.87	1.91	0.54
Scallop – M1	Mean Disp. Dist.	km	88.3	88.8	89.28
Scallop – M1	Max Disp. Dist.	km	494.67	380.57	369.63
Scallop – M1	Mean Connectivity	%	0.46	0.45	0.46
Scallop – M2	Min Disp. Dist.	km	0.09	0.3	0.73
Scallop – M2	Mean Disp. Dist.	km	88.82	88.75	89.3
Scallop – M2	Max Disp. Dist.	km	495.4	465.07	471.77
Scallop – M2	Mean Connectivity	%	0.46	0.45	0.46
Scallop – M3	Min Disp. Dist.	km	1.45	0.83	0.83
Scallop – M3	Mean Disp. Dist.	km	147.03	142.88	146.58
Scallop – M3	Max Disp. Dist.	km	459.87	462.47	460.96
Scallop – M3	Mean Connectivity	%	3.09	3.11	3.21
Scallop – M4	Min Disp. Dist.	km	1.67	1.16	1.38
Scallop – M4	Mean Disp. Dist.	km	41.37	39.37	41.35
Scallop – M4	Max Disp. Dist.	km	132.67	138.93	231.63
Scallop – M4	Mean Connectivity	%	0.03	0.02	0.03
Scallop – M5	Min Disp. Dist.	km	15.69	22.42	19.01
Scallop – M5	Mean Disp. Dist.	km	84.03	91.66	94.55
Scallop – M5	Max Disp. Dist.	km	169.45	214.06	202.49
Scallop – M5	Mean Connectivity	%	0.02	0.02	0.01

Table 35. Summary of results obtained for all model simulations for Atlantic surfclam.

See Table 3 for details. Disp. Dist. is dispersal distance, min is minimum, max is maximum.

Species and Simulations	Metric	Unit	Scenario 1 (Baseline)	Scenario 2 (Partial)	Scenario 3 (Full)
Surfclam – M1	Min Disp. Dist.	km	0.38	0.08	0.64
Surfclam – M1	Mean Disp. Dist.	km	45.53	47.52	48.18
Surfclam – M1	Max Disp. Dist.	km	256.56	265.48	285.55
Surfclam – M1	Mean Connectivity	%	0.94	0.95	0.92
Surfclam – M3	Min Disp. Dist.	km	0.46	0.69	0.08
Surfclam – M3	Mean Disp. Dist.	km	85.5	84.39	87.6
Surfclam – M3	Max Disp. Dist.	km	318.31	320.94	319.16
Surfclam – M3	Mean Connectivity	%	3.69	3.62	3.75
Surfclam – M4	Min Disp. Dist.	km	0.59	0.37	1.59
Surfclam – M4	Mean Disp. Dist.	km	41.95	44.12	43.52
Surfclam – M4	Max Disp. Dist.	km	171.2	205.7	200.39
Surfclam – M4	Mean Connectivity	%	0.2	0.19	0.2
Surfclam – M5	Min Disp. Dist.	km	0.69	1.38	1.28
Surfclam – M5	Mean Disp. Dist.	km	75.81	72.66	77.52
Surfclam – M5	Max Disp. Dist.	km	297.54	297.19	310.82
Surfclam – M5	Mean Connectivity	%	0.95	0.93	0.92

Table 36. Summary of results obtained for all model simulations for black sea bass.

See Table 3 for details. Disp. Dist. is dispersal distance, min is minimum, max is maximum.

Species and Simulations	Metric	Unit	Scenario 1 (Baseline)	Scenario 2 (Partial)	Scenario 3 (Full)
Sea bass – M1	Min Disp. Dist.	km	1.06	0.3	0.38
Sea bass – M1	Mean Disp. Dist.	km	78.93	80.94	82.88
Sea bass – M1	Max Disp. Dist.	km	339.87	337.36	333.4
Sea bass – M1	Mean Connectivity	%	1.53	1.54	1.54
Sea bass – M3	Min Disp. Dist.	km	0.66	0.41	0.47
Sea bass – M3	Mean Disp. Dist.	km	96.33	94.34	99.37
Sea bass – M3	Max Disp. Dist.	km	306.54	315.11	303.02
Sea bass – M3	Mean Connectivity	%	3.32	3.36	3.52
Sea bass – M4	Min Disp. Dist.	km	0.63	0.94	1.08
Sea bass – M4	Mean Disp. Dist.	km	65.66	65.59	66.93
Sea bass – M4	Max Disp. Dist.	km	286.72	328.87	299.92
Sea bass – M4	Mean Connectivity	%	0.66	0.63	0.61
Sea bass – M5	Min Disp. Dist.	km	0.56	0.46	0.91
Sea bass – M5	Mean Disp. Dist.	km	84.71	83.62	87.66
Sea bass – M5	Max Disp. Dist.	km	299.69	301.47	302.48
Sea bass – M5	Mean Connectivity	%	0.78	0.75	0.73

Table 37. P-value statistics for each of the metrics shown in Table 34, Table 35, and Table 36 calculated over all simulations for each species comparing the variance between the hydrodynamic scenarios.

A p-value above 0.05 means there is no statistical difference between the three hydrodynamic scenarios for that summary statistic for that species.

Species	Min Disp. Dist.	Mean Disp. Dist.	Max Disp. Dist.	Mean Connectivity
Atlantic sea scallop	0.9652	0.9945	0.9803	0.9995
Atlantic surfclam	0.5940	0.9878	0.9025	0.9997
Black sea bass	0.5695	0.9309	0.5943	0.9993

12.4 Discussion

Larval dispersal models were run for three hydrodynamic scenarios (baseline without WEAs, with partial WEA development, and with full WEA development) for each of the three species of interest (Atlantic sea scallop, Atlantic surfclam, and black sea bass). These three scenarios were conducted for different model configurations that included more larvae released per week (10,000 vs 1,000), larval behavior (DVM), and larval temperature dependence.

For all model simulations and scenarios for the three species, some similar connectivity patterns are identified. The model predicts the transport of larvae between their spawning and settlement zones mainly from north to south. In the MAB region, the southwestward flow along the continental shelf (Lentz, 2008) likely drives the larval connectivity patterns in the region (Zhang et al., 2015) and is captured by the hydrodynamic model. A hotspot of larval connectivity is observed for all three species in the northern zones of the study area, between 39.9° N and 40.35° N, with also high local retention. Higher larval settlement in this region was also observed for sea scallop (Munroe et al., 2018) and surfclam (Zhang et al., 2016) larvae compared to the southern regions of the MAB. The higher settlement rate in this region indicates a source of larvae for local and southern regions, as proposed by Zhang et al. (2016) for surfclam. The hydrodynamic model predicts lower currents in this region (the shelf north of the Hudson River canyon), which likely explains the connectivity hotspot.

Between the three species, the varying bathymetry of the release zones influences larval trajectories. Scallop and surfclam larvae are mainly transported along the continental shelf for the three hydrodynamic scenarios. Sea bass larvae trajectories are located further from the coast. Compared to scallop and surfclam larvae released at the bottom of the water column in the model, sea bass larvae were released all along 20–50 m of the water column. This biological characteristic of sea bass and hydrodynamics features likely explain their larval distribution in the entire study area even if their larval dispersal duration is shorter than scallop and surfclam. Currents weaken with depth; the larvae released near the bottom will be influenced by the weakest currents and the ones released higher in the water column will encounter stronger currents. For all model configurations, scenarios, and species, larvae are mainly transported south and toward the coast. For all species, larvae released in the northern zones, north of 40° N, get caught in eddies and remain in the region. Larvae released south of 40° N are transported south and some are retained in mesoscale eddies around 36° N and transported offshore to the eastern model boundary or, upon exiting the shelf, get entrained into the Gulf Stream and are lost.

The inclusion of WEAs along the coast in the model suggests relatively similar connectivity patterns in the MAB between the three scenarios for each of the three species. However, the model predicted

differences at the regional scale, particularly in the zones where WEAs are present, and an increase in larval dispersal distances. The effect of WEAs is not uniform along the release zones with both an increase and decrease in larval settlement and local retention observed for all the species. In the partial WEA scenario, larval connectivity increases in the northern zones. In the full WEA scenario, local retention decreases in most of the zones with WEAs, particularly for sea scallop and surfclam in the northern zones. The decrease in local retention is associated with increased larval dispersal distances with the full WEA scenario, expanding the larval transport from north to south. The noticeable differences in larval connectivity patterns with the full WEA scenario could be explained by the larger spatial footprint of WEAs compared to the partial scenario, as well as the cumulative impacts of multiple WEAs along the coastline (Methratta et al. 2020). While cumulative effects from the operation of multiple large wind farms on adult fish are expected to be negligible (Ecology and Environment Engineering, P.C. 2017), cumulative hydrodynamic effects on larval dynamics remain uncertain. In our study, larval trajectories show that some larvae are transported away from the WEA areas but stay in the study domain. The predicted increase in larval dispersal distance and their offshore transport in our model aligns with the findings of Chen et al. (2024)'s study, which found that larvae were transported further offshore when wind turbines were included in their model. Chen et al. (2024) explained the offshore transport observed by the presence of a downwind wake associated with the presence of offshore wind turbines. In our study, downstream-depth averaged currents increase where WEAs are present, likely explaining the higher dispersal distances observed.

Larval behavior accentuates the differences in larval connectivity observed with passive behavior when WEAs are present. Unlike passive larvae that are dependent on the release location and depth in the model, the inclusion of DVM forces the larvae to stay at a given depth range during the entire larval dispersal duration. The depth range of DVM tested in the model was very similar for each species (between 3 and 20 m), explaining the similarities in larval trajectories and distances compared to without behavior. Larval settlement success and mean dispersal distances are higher when DVM is included for all the species. With the partial WEA scenario, the larval settlement success between spawning and settlement zones did not change significantly overall. A slight decrease in larval supply from the north is observed in the northern area for surfclam and a slight increase around 39.9° N is observed for the three species. With the full WEA scenario, differences in larval connectivity are mainly observed between 39.1° N and 40.2° N with a decrease in local retention and an increase in larval transport from north to south. The hydrodynamic features related to the presence of WEA turbines (i.e., increase of stratification, reduction of mixing, and strong mean depth-averaged tidal residual currents, Figure 224) transport the larvae away from their spawning zones, which is also noted by longer larval dispersal distances.

Including the temperature dependence of larvae in the model significantly decreases the success of settlement for all the species. This is particularly observed for sea scallop larvae because of their high larval mortality. Scallop larvae have the narrowest temperature tolerance, from 10 to 18° C, contributing to their mortality during both colder (April and May) and warmer months (July and August) of the scallop spawning season. Surfclam and sea bass larvae have a higher upper-bound temperature tolerance. Their survival is then higher in the summer and their overall connectivity is less affected. As observed in the other model configurations, a northern hotspot of connectivity is identified for each species. Compared to other model configurations, the local retention is higher and larval dispersal distances are shorter. When including WEAs, local retention decreases. The survival temperature ranges of larvae are based on laboratory studies. In the open ocean, larvae encounter a high variability of temperature. Marine species can adapt to temperature changes, to a certain level, and potentially delay spawning events until conditions are more favorable (Bonardelli et al., 1996) or tolerate a suboptimal temperature for a short period. This is not represented in the model as the model immediately kills the larvae when the temperature is outside their survival range. Temperatures tend to increase slightly in the hydrodynamic simulations with WEA buildout, which may lead to increased larval dispersal distance with WEAs as larvae can survive longer. Regardless of the presence of WEAs, climate change is expected to lead to a

change of species distribution in the MAB (Hare et al., 2016; Hofmann et al., 2018). When both larval behavior and temperature dependence are included, more settlement success is observed, particularly in the northern zones, compared to when larval behavior is not included. DVM forces the larvae to stay closer to the surface in the model, where waters are warmer, therefore decreasing the larval mortality. When WEAs are included in the model, the main difference observed is a decrease in local retention in the northern zones.

Differences in larval connectivity patterns were noted for sea scallop, surfclam, and sea bass with and without the presence of WEAs depending on the biological processes included in the model. Biological processes included in the model were based on the available literature. Larval mortality was driven by seawater temperature only, but other factors can influence larval mortality such as food availability and predation (Morgan, 2020). Because of computing limitations when running a model over a large domain, only 1,000 larvae were included in most model configurations (except M2). Although the connectivity results are overall qualitatively similar between releasing 1,000 and 10,000 larvae weekly in the model, further simulations are needed for all species and scenarios to compare the model sensitivity to the number of larvae released. Furthermore, the biophysical model only provides a snapshot of the larval dynamics of scallop, surfclam, and sea bass in the MAB. Johnson et al. (2021) performed their model simulations for one year and Chen et al. (2024) included three non-consecutive years of hydrodynamics in their model. Running the biophysical larval dispersal model over more than a couple of years would enable to account for annual variability in hydrodynamic patterns and gain a better understanding of how these patterns influence larval connectivity. Increasing the number of modeled years would enable assessing the potential of WEAs in the MAB to act as steppingstones (Adams et al., 2014) and evaluating their effects on larval spillover into surrounding habitats (Halouani et al., 2020).

13 Study Conclusions

To investigate potential impacts of proposed offshore wind energy development on marine environmental conditions of the Mid-Atlantic Bight continental shelf from North Carolina to New York, we developed a calibrated and validated modeling system incorporating multiple wind energy areas with clusters of individual 15 MW wind turbines on monopile foundations. We treated three modeling scenarios: baseline conditions with no wind energy areas; partial buildout, five clusters with 1,852 total turbines at sites in publicly available Construction and Operation Plans; and complete buildout, eight clusters with 6,353 total turbines augmenting the partial buildout to span all lease areas. We examined effects of wind energy areas on wind conditions; wave characteristics; oceanographic processes including currents, water temperature, stratification, and cold pool evolution; bed shear stress and sediment mobility; and larval connectivity for Atlantic sea scallop, Atlantic surfclam, and black sea bass.

The wind energy areas cause reductions in the wind field within and downwind from clusters of turbines. The complete buildout has stronger reductions, which span larger areas, than partial buildout. Owing to the thrust vs wind speed curves characterizing the turbines, the deficits are strongest for wind speeds between the cut-in speed of about 3 m/s and the speed at which the rated power is reached, about 11 m/s. Maximum reductions of climatological wind speed at 10 m height (used to force the model) for complete buildout reach about 20% in limited areas within wind energy areas and about 10% on their downwind edge. They weaken rapidly with distance from wind energy arrays but can extend up to 100–200 km downwind. There is some overlap of wind reductions due to nearby wind energy arrays, depending on the orientation of the wind direction relative to the clusters of turbines. Relatively rare and transient maximal wind reductions, occurring about 1% of the time, can reach 30–50% for 10 m/s wind speeds, and are more widespread across the domain. Golbazi et al. (2022) used 1.33 km-resolution WRF numerical simulations to model wind wakes of Mid-Atlantic Bight wind energy areas and reported 10% maximum deficits and wake lengths near 50 km downwind, extending up to 150 km during days with farm-to-farm interactions. Our PyWake-based results have stronger wake effects, which could be because Golbazi et al. used power and thrust curves for 10 MW turbines and we used 15 MW turbines.

The wind deficits change wave conditions, with the main effect to reduce the wind-wave component of the total wave field. This mainly occurs within the wind energy areas where the wind deficits are strong, particularly clusters of turbines aligned with the wind direction, and in areas farther inshore. Median significant wave heights are reduced by up to 4 cm and 7 cm for the partial and complete build-out scenarios, respectively, which is about 5% of climatology or less in the wind energy areas nearer to the coast and relatively less further offshore. These results are consistent with the 3.5% max reduction and reductions reaching about 50 km downstream reported in Fischereit et al. (2022) and Bärfus et al. (2021) for smaller turbines (5–10 MW) than in the present study. We also find reduced wind-waves cause swell to be a relatively larger contribution to the total wave field, so dominant wave periods in the most strongly affected areas increase slightly by 0.16 s. In general, these effects are stronger and occur over a larger area for complete buildout than partial buildout.

Oceanographic circulation processes also are changed by wind energy arrays. In this study, the effect of wind deficits has the dominant influence, with the effects of monopile turbine foundations more minor; for the latter, this study chose parameterization using a C_D (hydrodynamic drag) equation available in Delft3D (Delft, 2023), with C_D values based on CFD model experiments from Johnson et al. (2021). These results differ from the findings of Chen et al. (2024) for the area just to the northwest of this study, which found that water column vortex shredding from the monopile foundations was the dominant effect on ocean circulation. It should be noted however that wind wake calculation subgrid methodologies (1 km subgrid Delft with PyWake here compared to > 1 m FVCOM with 1 km subgrid WRF in Chen et al., 2023), turbine specifications (larger 15 MW turbines here versus smaller 10 MW ones with simplified thrust in Chen et al., 2024), and domains (NY to NC here vs RI to MA in Chen et al., 2024) differ

between the two studies. It should also be noted that Chen et al. (2024) calculated much smaller wind wakes with their subgrid WRF-based study: maximum 0.2–0.3m/s deficits and size about the length of a wind farm. Their findings were similar in spatial scale to the ones produced in Golbazi et al. (2022) and—through other methods—used in Johnson et al. (2021). However, those findings appear to differ from other studies and experiments—including SAR and LiDAR data in the literature that show larger and longer wind wake deficits more similar to the present study (e.g., Christiansen et al. 2013, Platis et al. 2018, Fischereit et al. 2021, Christiansen et al. 2022, Raghukumar et al. 2022, Cañadillas et al. 2022). The latter group of studies, for lower power turbines than the ones consider here, show wind-wake length scales exceeding 50 km downstream of farms and 30% reductions at 10m/s wind speeds (3 m/s), especially during stably stratified atmospheric conditions (mostly during spring and summer in the MAB, Debnath et al., 2021).

Our results indicate that wind farms cause statistically significant changes in annual- and seasonal-mean winds; surface heat fluxes; surface and bottom temperatures; surface, bottom, and vertical-mean currents; water column stability; and thermocline depth. Scenario results indicate wind energy areas cause 50th, 95th, and 99th percentile total current (not low-pass filtered) speeds to decrease modestly (less than 2 mm/s on the median, less than 1 cm/s on the upper percentiles), with smaller-magnitude (less than 1 cm/s) local increases also seen especially shoreward of the northern wind energy areas along the NY Bight and NJ coast at the 99th percentile level.

The main characteristic of Mid-Atlantic Bight general circulation is a 2–12 cm/s alongshore southward flowing mean current over the shelf, driven mainly by the southward regional alongshore pressure gradient and influenced by wind stress (Lentz, 2010; Chen and Yang, 2024). The Scenario 2 and 3 tidal residual, low-passed, mean current vectors of the southward general circulation strengthen along the wind energy areas. These changes appear to be due to alterations in larger-scale circulation patterns resulting from wind wake effects, rather than increased turbulence and mixing around the turbine foundations. A consistent interpretation is that weaker winds due to wind energy areas shift the dynamical balance of alongshore flow to enhance its southward component. Another feature in the scenario results is increased horizontal shear of currents, due to weakening of southward flow adjacent to wind energy areas where it has increased.

In the two scenarios with reduced winds due to wind energy area buildout, surface temperatures are higher over most of the domain, and the thermocline shoals, both characteristics that are consistent with suppressed wind-driven vertical turbulence in the surface mixed layer. The strength of the seasonal thermocline increases, with surface to bottom temperature stratification increasing in the full buildout scenario by as much as 1° C in certain areas during summer. These scenarios also have higher bottom temperatures at the New Jersey shelf. These changes affect the seasonal cold pool formation and evolution, but do not fundamentally alter it. Consistent with these effects, statistical analysis of representative stations shows that parameters most likely to have weekly-mean values that differ between complete buildout and baseline by more than baseline variability (weekly standard deviations) are temperature, near-surface stability, and thermocline depth and strength. In contrast, this is less likely for wind speed, current speed, vertical turbulent eddy viscosity, and turbulent kinetic energy.

Changes in waves and currents due to wind energy areas affect bed shear stress and sediment mobility. The main influence is the changes in winds, not currents, even though bottom currents decrease slightly within the WEAs. The reductions in waves lead to smaller bed shear stress and sediment mobility, particularly within wind energy areas and farther inshore. These changes are stronger for complete buildout than partial buildout, and most pronounced for the 95th and 99th percentiles of bed shear stress and sediment mobility.

Larval connectivity results for passive larvae under baseline conditions indicate that, for Atlantic sea scallop, Atlantic surfclam, and black sea bass, transport occurs from the northern to the southern region of the study area consistent with the regional residual currents. The consistent connectivity patterns and the

effects of WEAs observed across model configurations suggest that larval connectivity for Atlantic sea scallop, Atlantic surfclam, and black sea bass is primarily influenced by hydrodynamic processes in the MAB. While the calculated larval connectivity values did not differ significantly between the tested hydrodynamic scenarios, the larval dispersal model for these three commercial species predicted reduced local retention, especially in the northern region, and increased larval dispersal distances in some regions where WEAs are present. These effects are more pronounced with complete buildout compared to partial buildout. They are likely due to the alteration of hydrodynamic conditions by wind energy areas, including stronger along-shelf flow in some areas, reduced mixing, and increased stratification. The increased larval dispersal distances in the presence of WEAs may prevent larvae from settling in habitats close to their spawning areas, potentially altering the species' distribution range over time. Although regional connectivity remains qualitatively similar with and without WEAs, the model indicates that WEAs have the potential to modify preferred spawning and settlement habitats of scallop, sea bass, and surfclam. When adding diel vertical migration behavior in the larval dispersal model, the mean and range of larval dispersal distances are larger and mean larval connectivity increases (to about 3.0–3.5% from 0.5–1.5%), consistent with larvae spending more time higher in the water column where currents are generally stronger. Simulations adding temperature-dependent mortality show a decrease in larval connectivity due to high mortality, likely because of exposure to a wider range of temperatures than in laboratory studies on which threshold temperatures are based.

Overall, the impact of wind energy areas on marine environmental conditions is stronger for the complete buildout scenario, with some exceptions due to variations in local conditions. The changes in waves, bed shear stress, and sediment mobility are likely not of sufficient magnitude to be important relative to natural variability. Furthermore, because the effects of buildout are more pronounced within wind energy arrays and weaker outside them, impacts generally are minor on regionwide water column oceanographic processes, for example the seasonal development of stratification, and formation and evolution of the cold pool. However, the increases in water temperature and stratification strength are of sufficient magnitude to potentially alter ecology, particularly when superposed on climate warming (Georgas et al., 2016, Brickman et al., 2021, Wang 2023) that is causing warm-water species guilds to displace cold-water guilds northward. The decreased local retention in the NY Bight north of 40°N is consistent with formulating a hypothesis of offshore wind development having the potential to change estuarine mouth dynamics in the Hudson River bulge recirculation area. More work is needed to fully evaluate the importance of the changes identified.

Data availability: The larval dispersal model is a modification of the original Ichthyop². To recreate the larval dispersal modeling results in this report, use the following GitHub repository which includes the Ichthyop-Delft3D-FM modifications with the hydrodynamic modeling data mentioned above³. Delft Model Inputs to Ichthyop for each scenario and Ichthyop model outputs are in the Azure share folder.

14 References

References

² See GitHub: [ichthyop/ichthyop](https://github.com/ichthyop/ichthyop)

³ See [Imengel422/ichthyop, branch: feature/delft](https://github.com/Imengel422/ichthyop/branch:feature/delft)

- Abkar M, Porté-Agel F. 2015. A new wind-farm parameterization for large-scale atmospheric models. *J Renewable and Sustainable Energy*. 7(1): 013121.
- Able KW, Fahay MP, Sheperd GR. 1995. Early life history of black sea bass, *Centropristis striata*, in the Mid-Atlantic Bight and a New Jersey estuary. *Fish Bull*. 93:429–445.
- Able KW, Fahay MP. 1998. The first year in the life of estuarine fishes in the Middle Atlantic Bight. New Brunswick (NJ): Rutgers University Press. 342 p.
<https://books.google.com/books?id=3a92QgAACAAJ>
- Adams TP, Miller R, Aleynik D, Burrows MT. 2014. Offshore marine renewable energy devices as steppingstones across biogeographical boundaries. *J Applied Ecol*. 51(2): 330–338.
- Allahdadi M, Nabi B, Gunawan B, Lai J, He R, Neary VS. 2019. Development and validation of a regional-scale high-resolution unstructured model for wave energy resource characterization along the US east coast. *Renewable Energy*. 136: 500–511.
- Amorim FN, Caetano M, Bastos L, Iglesias I. 2024. Deep-sea mining rock-fragment dispersal scenarios associated with submesoscale forcings: a case study in the Atlantic. *Heliyon*. 10(14): e34174.
<https://doi.org/10.1016/j.heliyon.2024.e34174>
- Aydoğan B, Ayat B. 2021. Performance evaluation of SWAN ST6 physics forced by ERA5 wind fields for wave prediction in an enclosed basin. *Ocean Eng*. 240: 109936.
- Bärfuss K, Schulz-Stellenfleth J, Lampert A. 2021. The impact of offshore wind farms on sea state demonstrated by airborne LiDAR measurements. *J Mar Sci Eng*. 9(6): 644.
- Barrier N, Verley P, Andres G, Lett C. 2023. Ichthyop: a Lagrangian tool for modelling ichthyoplankton dynamics. Version 3.3.16. <https://doi.org/10.5281/zenodo.7986365>
- Bastankhah M, Porté-Agel F. 2014. A new analytical model for wind-turbine wakes. *Renewable Energy*. 70: 116–123.
- Bergström L, Sundqvist F, Bergström U. 2013. Effects of an offshore wind farm on temporal and spatial patterns in the demersal fish community. *Mar Ecol Prog Ser*. 485: 199–210.
- Berlinsky D, Watson M, Nardi G, Bradley T. 2000. Investigations of selected parameters for growth of larval and juvenile black sea bass *Centropristis striata* L. *J World Aquacult Soc*. 31: 426–435.
<https://doi.org/0.1111/j.1749-7345.200.tb0892.x>
- Berrien P, Sibunka J. 1999. Distribution patterns of fish eggs in the United States northeast continental shelf ecosystem, 1977-1987. Seattle (WA): National Oceanic and Atmospheric Administration, National Marine Fisheries Service. NOAA Technical Report NMFS-145. 310 p. [accessed 3 March 2025]; https://repository.library.noaa.gov/view/noaa/3083/noaa_3083_DS1.pdf
- Bonardelli JC, Himmelman JH, Drinkwater K. 1996 Relation of spawning of the giant scallop, *Placopecten magellanicus*, to temperature fluctuations during downwelling events. *Mar Biol*. 24(4): 637–649. <https://doi.org/10.1007/BF00351045>
- Bhushan S, Blumberg AF, Georgas N. 2010. Comparison of NYHOPS hydrodynamic model SST predictions with satellite observations in the Hudson River tidal, estuarine, and coastal plume region.

In: Spaulding, Malcolm, editor. Estuarine and Coastal Modeling (2009): Proceedings of the Eleventh International Conference, November 4-6, 2009, Seattle, Washington. Reston (VA): American Society of Civil Engineers. p. 11–26.

Bratton D, Womeldorf C. 2011. The wind shear exponent: comparing measured against simulated values and analyzing the phenomena that affect the wind shear. ASME 2011 5th International Conference on Energy Sustainability, August 7–10, 2011, Washington, DC. p. 2245-2251.
<https://doi.org/10.1115/ES2011-54823>

Burgess SC, Nickols KJ, Griesemer CD, Barnett LA, Dedrick AG, Satterthwaite EV, Yamane L, Morgan SG, White JW, Botsford LW. 2014. Beyond connectivity: how empirical methods can quantify population persistence to improve marine protected-area design. *Ecol Appl.* 24(2): 257–270.

Brickman D, Alexander MA, Pershing A, Scott JD, Wang Z. 2021. Projections of physical conditions in the Gulf of Maine in 2050. *Elementa.* 9 (1): 00055.

Campos RM, Gramcianinov CB, Camargo R, daSilv Dias PL. 2022. Assessment and calibration of ERA5 severe winds in the Atlantic ocean using satellite data. *Remote Sens.* 14(19): 4918.

Cañadillas B, Foreman R, Barth V, Siedersleben S, Lampert A, Platis A. 2020. Offshore wind farm wake recovery: Airborne measurements and its representation in engineering models. *Wind Energy.* 23: 1249–1265. doi:10.1002/we.2484

Cañadillas B, Beckenbauer M, Trujillo JJ, Dörenkämper M, Foreman R, Neumann T, Lampert A. 2022. Offshore wind farm cluster wakes as observed by long-range-scanning wind lidar measurements and mesoscale modeling. *Wind Energy Sci.* 7(3): 1241–1262.

Cargnelli LM, Griesbach SJ, Packer DB, Weissberger E. 1999. Essential fish habitat source document: Atlantic surfclam, *Spisula solidissima*, life history and habitat characteristics. Woods Hole (MA): National Marine Fisheries Service. NOAA Technical Memorandum NMFS-NE-42. 22 p.
<https://epository.library.noaa.gov/view/noaa/3144>

Charles E, Idier D, Delecluse P, Déqué M, Le Cozannet G. , 2012. Climate change impact on waves in the Bay of Biscay, France. *Ocean Dynamics.* 62: 831–848. <https://doi.org/10.1007/s10236-012-0534-8>

Chen K, Yang J. 2024. What drives the mean along-shelf flow in the Northwest Atlantic coastal ocean? *J Geophys Res: Oceans.* 129, e2024JC021079. <https://doi.org/10.1029/2024JC021079>

Chen C, Zhao L, Gallger S, Ji R, He P, Davis C, Beardsley RC, Hart D, Gentleman WC, Wang L, Li S, Lin H, Stokesbury K, Bethoney D. 2021. Impact of larval behaviors on dispersal and connectivity of sea scallop larvae over the northeast U.S. shelf. *Prog Oceanogr.* 195: 102604.
<https://doi.org/10.1016/j.pocean.2021.102604>

Chen C, Liu H, Beardsley RC. 2003. An unstructured grid, finite-volume, three-dimensional, primitive equations ocean model: application to coastal ocean and estuaries. *J Atmos Oceanic Techno.* 20(1): 159–186.

Chen C, Zha L, Lin H, He P, Li S, Wu Z, Qi J, Xu Q, Stokesbury K, Wang L. 2024. Potential impacts of offshore wind energy development on physical processes and scallop larval dispersal over the US Northeast shelf. *Prog Oceanogr.* 224: 103263. <https://doi.org/10.1016/j.pocean.2024.103263>

- Christiansen N, Daewel U, Djat B, Schrum C. 2022. Emergence of large-scale hydrodynamic structures due to atmospheric offshore wind farm wakes. *Front Mar Sci.* 9: 818501.
- Christiansen N, Carpenter JR, Daewel U, Suzuki N, Schrum C. 2023. The large-scale impact of anthropogenic mixing by offshore wind turbine foundations in the shallow North Sea. *Front Mar Sci.* 10: 1178330. doi:10.3389/fmars.2023.1178330
- Christiansen MB., Hasager CB. 2005. Wake effects of large offshore wind farms identified from satellite SAR. *Remote Sens Env.* 98: 251–268. doi: 10.1016/j.rse.2005.07.009
- Christiansen MB, Hasager CB. 2006. Using airborne and satellite SAR for wake mapping offshore. *Wind Energ.* 9: 437–455. doi: 10.1002/we.196
- Cowen RK, Sponaugle S. 2009. Larval dispersal and marine population connectivity. *Ann Rev Mar Sci.* 1(1): 443–466.
- Culliney JL. 1974. Larval development of the giant scallop *Placopecten magellanicus* (Gmelin). *Biol Bull.* 147: 321–332.
- Daewel U, Akhtar N, Christiansen N, Schrum C. 2022. Offshore wind farms are projected to impact primary production and bottom water deoxygenation in the North Sea. *Comm Earth Environ.* 3(1): 292. <https://doi.org/10.1038/s43247-022-00625-0>
- Daewel U, Peck MA, Schrum C. 2011. Life history strategy and impacts of environmental variability on early life stages of two marine fishes in the North Sea: an individual-based modelling approach. *Can J Fish Aquatic Sci.* 68(3): 426–443.
- DeAngelis DL, Grimm V. 2014. Individual-based models in ecology after four decades. *F1000prime Reports*, 6.
- Debnath, M, Doubrawa P, Optis M, Hawbecker P, Bodini N. 2021. Extreme wind shear events in US offshore wind energy areas and the role of induced stratification. *Wind Energy Science.* 6(4): 1043–1059.
- Deltares D. 2022. *Delft3D-FLOW user manual*. Deltares Delft, The Netherlands: 330.
- Delft H. 2023. *D_Flow flexible mesh computational cores and user interface user manual*. Deltares. https://content.oss.deltares.nl/delft3d/D-Flow_FM_User_Manual.pdf
- Dörenkämper M, Steinfeld G. 2021. Wind farm cluster wakes. In: *Handbook of wind energy aerodynamics*. Cham (CH): Springer International Publishing. p. 1–38.
- Dorrell RM, Lloy CJ, Lincoln BJ, Rippeth TP, Taylor JR, Caulfield C-CP, Sharples J, Polton JA, Scannell BD, Greaves DM, Hall RA, Simpson JH. 2022. Anthropogenic mixing in seasonally stratified shelf seas by offshore wind farm infrastructure. *Front Mar Sci.* 9: 830927. <https://doi.org/10.3389/fmars.2022.830927>
- Drohan AF, Manderson JP, Packer DB. 2007. Essential fish habitat source document: Black sea bass, *Centropristis striata*, life history and habitat characteristics. Woods Hole (MA): National Marine Fisheries Service. NOAA Technical Memorandum NMFS-N-200. 78 p. <https://repository.library.noaa.gov/view/noaa/4038>

- Ecology and Environment Engineering, P.C. 2017. New York State Offshore Wind Master Plan: consideration of potential cumulative effects. Final report. Prepared for New York State Energy Research and Development Authority. New York, NY.
- Edwards KP, Hare JA, Werner F. 2008. Dispersal of black sea bass (*Centropristis striata*) larvae on the southeast U.S. continental shelf: results of a coupled vertical larval behavior – 3 circulation model. *Fish Oceanogr* 17(4): 299–315. <https://doi.org/10.1111/j.1365-2419.2008.00480.x>
- Eldeberky Y, Battjes JA. 1996. Spectral modeling of wave breaking: Application to Boussinesq equations. *J Geophys Res: Oceans*. 101(C1): 1253–1264.
- Eldeberky Y, Polnikov V, Battjes JA. 1997. A statistical approach for modeling triad interactions in dispersive waves. In: Edge, BL, editor. *Proceedings of the 25th International Conference on Coastal Engineering*, held in Orlando, Florida, September 2-6, 1996. Reston (VA): ASCE. p.1088-1101.
- Emeis S. 2010. A simple analytical wind park model considering atmospheric stability. *Wind Energy*. 13: 459–469.
- Fay CW, Neves RJ, Pardue GB. 1983. Species profiles: life histories and environmental requirements of coastal fishes and invertebrates (Mid-Atlantic): surfclam. Report FWS/ OBS-82/11.13. Washington (DC): U.S. Fish Wildlife Service. <https://www.nrc.gov/docs/ML0720/ML072070388.pdf>
- Fischereit J, Schaldemose Hansen K, Larsén XG, van der Laan MP, Réthoré PE, MurciaLeon JP. 2022. Comparing and validating intra-farm and farm-to-farm wakes across different mesoscale and high-resolution wake models. *Wind Energy Sci*. 7: 1069–1091.
- Fischereit, J, Larsén XG, Hahmann AN. 2022. Climatic Impacts of wind-wave-wake interactions in offshore wind farms. *Front Energy Res*. 10: 881459. doi:10.3389/fenrg.2022.881459. <https://www.frontiersin.org/articles/10.3389/fenrg.2022.881459>
- Fitch AC, Olson JB, Lundquist JK, Dudhia J, Gupta AK, Michalakes J, Brstad I. 2012. Local and mesoscale impacts of wind farms as parameterized in a mesoscale NWP model. *Month Weather Rev*. 140(9): 3017-3038.
- Floeter J, Pohlmann T, Harmer A, Möllmann C. 2022. Chasing the Offshore Wind farm wind-wake-induced upwelling/downwelling dipole. *Front Mar Sci*. 9: 884943. <https://doi.org/10.3389/fmars.2022.884943>
- Forsyth J, Andres M, Gawarkiewicz G. 2020. Shelfbreak jet structure and variability off new jersey using ship of opportunity data from the CMV *Oleander*. *J Geophys Res: Oceans*.. 125(9): e2020JC016455. <https://doi.org/10.1029/2020jc016455>
- Frandsen ST. 1992. On the wind speed reduction in the center of large clusters of wind turbines. *J Wind Eng Ind Aerodyn*. 39: 251-6.
- Frandsen S, Barthelmie R, Pryor S, Rathmann O, Larsen S. 2006. Analytical modelling of wind speed deficit in large offshore wind farms. *Wind Energy*. 9: 39-53, <https://doi.org/10.1002/we.189>
- Friedland, KD, Miles T, Goode AG, Powell EN, Brady DC. 2022. The Middle Atlantic Bight Cold Pool is warming and shrinking: indices from in situ autumn seafloor temperatures. *Fish Ocean*. 31(2): 217–223.

- Gaertner E, Rinker J, Sethuraman L, Zahle F, Anderson B, Barter G, Abbas N, Meng F, Bortolotti P, Skrzypinski W, Scott G. 2020. Definition of the IEA 15-megawatt offshore reference wind. Golden (CO): National Renewable Energy Laboratory. NREL/TP-5000-75698.
- Garavelli L, Colas F, Verley P, Kaplan DM, Yannicelli B, Lett C. 2016. Influence of biological factors on connectivity patterns for *Concholepas concholepas* (loco) in Chile. PLOS ONE. 11(1): e0146418. <https://doi.org/10.1371/journal.pone.0146418>
- Garavelli L, Kaplan D, Colas F, Stotz W, Yannicelli B, Lett C. 2014. Identifying appropriate spatial scales for marine conservation and management using a larval dispersal model: the case of *Concholepas concholepas* (loco) in Chile. Prog Oceanogr. 124: 42–53. <https://doi.org/1.1016/j.pocean.2014.03.11>
- Garavelli L, White JW, Chollett I, Chérubin LM. 2018. Population models reveal unexpected patterns of local persistence despite widespread larval dispersal in a highly exploited species. Conserv Lett 11(5): e12567. <https://doi.org/10.1111/conl.12567>
- Georgas N. 2010. Establishing confidence in marine forecast systems: The design of a high-fidelity marine forecast model for the NY/NJ Harbor Estuary and its adjoining coastal waters [dissertation]. Hoboken (NJ): Stevens Institute of Technology. 272 p.
- Georgas N, Blumberg AF. 2010. Establishing confidence in marine forecast systems: The design and skill assessment of the New York Harbor Observation and Prediction System, version 3 (NYHOPSv3). Estuarine Coast Model. (2009). [https://ascelibrary.org/doi/abs/10.1061/41121\(388\)39](https://ascelibrary.org/doi/abs/10.1061/41121(388)39)
- Georgas N, Yin L, Jiang Y, Wang Y, Howell P. 2016. An open-access, multi-decadal, three-dimensional, hydrodynamic hindcast dataset for the Long Island Sound and New York/New Jersey Harbor Estuaries. J Mar Sci Eng. 4(3): 48. <https://www.mdpi.com/2077-1312/4/3/48/htm>
- Gill AE. 1982. Atmosphere-ocean dynamics. San Diego (CA): Academic Press. International Geophysics Series, volume 30. 681 p.
- Golbazi, M, Archer CL, Alessandrini S. 2022. Surface impacts of large offshore wind farms. Environ Res Lett. 17(6): 064021.
- Gong D, Kohut JT, Glenn SM. 2010. Seasonal climatology of wind-driven circulation on the New Jersey Shelf. J Geophys Res: Oceans. 115(C4). <https://agupubs.onlinelibrary.wiley.com/doi/pdfdirect/10.1029/2009JC005520>
- Halouani G, Vilanueva C-M, Raoux A, Dauvin JC, Lasram FBR, Foucher E, Le Loc'h F, Safi G, Araignous E, Robin JP. 2020. A spatial food web model to investigate potential spillover effects of a fishery closure in an offshore wind farm. J Mar Sys. 212: 103434.
- Hare JA, Morrison WE, Nelson MW, Stachura MM, Teeters EJ, Griffis RB, Alexander MA, Scott JD, Alade L, Bell RJ. 2016. A vulnerability assessment of fish and invertebrates to climate change on the Northeast US Continental Shelf. PLOS ONE. 11(2), e0146756.
- Hart DR, Chute AS. 2004. Essential fish habitat source document: Sea scallop, *Placopecten magellanicus*, life history and habitat characteristics. Second edition. Woods Hole (MA): National

- Marine Fisheries Service. NOAA Technical Memorandum NMF-NE-189. 32 p.
<https://repository.library.noaa.gov/view/noaa/4031>
- Hasager, C, Vincent P, Badger J, Badger M, Di Bella A, Peña A, Husson R, Volker P. 2015. Using satellite SAR to characterize the wind flow around offshore wind farms. *Energies*. 8(6): 5413–5439.
- Hasselmann KF, Barnett TP, Bouws E, Carlson H, Cartwright DE, Eake K, Euring JA, Gicnapp A, Hasselmann DE, Kruseman P, Meerburg A. 1973. Measurements of wind-wave growth and swell decay during the Joint North Sea Wave Project (JONSWAP). *Ergaenzungsheft zur Deutschen Hydrographischen Zeitschrift, Reihe A*.
- Hersbach H, Bell B, Berrisford P, Biavati G, Horányi A, Muñoz Sabater J, Nicolas J, Peubey C, Radu R, Rozum I, Schepers D, Simmons A, Soci C, Dee D, Thépaut, J-N. 2023. ERA5 hourly data on single levels from 1940 to present. Copernicus Climate Change Service (C3S) Climate Data Store (CDS). DOI: 10.24381/cds.adbb2d47
- Hofmann EE, Powell EN, Klinck JM, Munroe DM, Mann R, Hadvogel DB, Narváez DA, Zhang X, Kuykendall KM. 2018. An overview of factors affecting distribution of the Atlantic surfclam (*Spisula solidissima*), a Continental Shelf biomass dominant, during a period of climate change. *J Shellfish Res*. 37(4): 821-831. <https://doi.org/10.2983/035.037.0412>
- Holthuijsen H, Booij N, Ris RC, Andork Gal JH, de Jong JCM. 1999. A verification of the third-generation wave model SWAN along the southern North Sea coast. *J Geophys Res*. 104:7667–7681. https://falk.ucsd.edu/modeling/swan2_jgr99.pdf
- Iles TD, Sinclair M. 1982. Atlantic herring: stock discreteness and abundance. *Science*. 15(4533): 627-633.
- Jensen NO. 1983. A note on wind generator interaction. No 2411. Roskilde (DE): Risø National Laboratory.
- Jiménez PA, Dudhia, J, González-Rouco JF, Navarro J, Montávez JP, García-Bustamante E. 2012. A revised scheme for the WRF surface layer formulation. *Mon Weather Rev*. 140(3): 898-918.
- Johnson TL, van Berkel, JJ, Mortensen LO, Bel MA, Tiong I, Hernande B, Snyder DB, Thomsen F, Petersen OS (DHI Water & Environment, Lakewood, CO). 2021. Hydrodynamic modeling, particle tracking and agent-based modeling of larvae in the U.S. Mid-Atlantic Bight. Sterling (VA): U.S. Department of the Interior, Bureau of Ocean Energy Management. 232 p. Obligation No.: 140M120C0004. Report No.: BOEM 2021-049. https://epis.boem.gov/final%20reports/BOEM_2021-049.pdf
- Katic I, Højstrup J, Jensen NO. 1986. A simple model for cluster efficiency. In: Palz W, Sesto E, editors. *Proceedings: EWEC '86 : European Wind Energy Association Conference and Exhibition; 7-9 October 1986, volume 1*. Rome (IT): A Raguzzi. p. 407-410.
- Kohut JT, Glenn SM, Chant RJ. 2004. Seasonal current variability on the New Jersey inner shelf. *J Geophys Res: Oceans*. 109(C7). <https://agupubs.onlinelibrary.wiley.com/doi/full/10.1029/2003JC001963>
- Lane A. 1989. The heat balance of the North Sea. Report No. 8. Merseyside (UK): Proudman Oceanographic Laboratory. 46 p. <https://nora.nerc.ac.uk/id/eprint/3872/>

- Langton RW, Robinson WE, Schick D. 1987. Fecundity and reproductive effort of sea scallops *Placopecten magellanicus* from the Gulf of Maine. *Mar Ecol Prog Ser.* 37: 19–25.
- Lentz SJ. 2008. Observations and a model of the mean circulation over the Middle Atlantic Bight Continental Shelf. *J Phys Oceanogr.* 38(6): 1203–21.
- Lentz SJ. 2017. Seasonal warming of the Middle Atlantic Bight Cold Pool. *J Geophys Res: Oceans.* 122: 941–954. doi:10.1002/2016JC012201
- Levin J, Arango HG, Laughlin B, Hunter E, Wilkin J, Moore AM. 2020. Observational impacts on the mid-Atlantic Bight front and cross-shelf transport in 4D-var ocean state estimates: part I—multiplatform analysis. *Ocean Model.* 156, 101721. <https://doi.org/10.1016/j.ocemod.2020.101721>
- Loosanoff VL, Davis HC. 1963. Rearing of bivalve mollusks. *Adv Mar Biol.* 1: 1–136.
- López AG, Wilkin JL, Levin JC. 2020. Doppio—a ROMS (v3.6)-based circulation model for the Mid-Atlantic Bight and Gulf of Maine: configuration and comparison to integrated coastal observing network observations. *Geosci Model Dev.* 13: 3709–3729. <https://doi.org/10.5194/gmd-13-3709-2020>
- Ma Y, Archer CL, Vassel-Bé-Hagh A. 2022. The Jensen wind farm parameterization. *Wind Energy Sci.* 7(6): 2407-2431.
- Mann R, Campos BM, Luckenbach MW. 1991. Swimming rate and responses of larvae of three mactrid bivalves to salinity discontinuities. *Mar Ecol Prog Ser.* 68: 257–269.
- Manuel JL, Pearce, CM, Manning DA, O’Dor K. 2000. The response of sea scallop (*Placopecten magellanicus*) veligers to a weak thermocline in 9-m deep mesocosms. *Mar Biol.* 17: 169–175.
- Mao M, Van Der Westhuysen AJ, Xia M, Schwab DJ, Chawla A. 2016. Modeling wind waves from deep to shallow waters in Lake Michigan using unstructured SWAN. *J Geophys Res: Oceans.* 121(6): 3836-3865.
- Marchessaux G, Chevalier C, Magano MC, Sarà G. 2023. Larval connectivity of the invasive blue crabs *Callinectes sapidus* and *Portunus segnis* in the Mediterranean Sea: a step toward improved cross border management. *Mar Poll Bull.* 194: 115272. <https://doi.org/10.1016/j.marpolbul.2023.115272>
- McGarvey R, Serchuk FM, McLaren A. 1992. Statistics of reproduction and early life history survival of the Georges Bank sea scallop (*Placopecten magellanicus*) population. *J Northwest Atl Fish Sci.* 13: 83–99.
- Medina G, Shaw WJ, Zang Z, Newsom RK. 2020. Mid-Atlantic Bight wave hindcast to support DOE lidar buoy deployments: model validation. Richland (WA): Department of Energy, Pacific Northwest National Laboratory. Obligation No.: DE-AC05-76RL01830. Report No.: PNNL-29814. <https://doi.org/10.2172/1635751>
- Mercer LP. 1978. The reproductive biology and population dynamics of black sea bass, *Centropristis striata* (dissertation). Williamsburg (VA): College of William and Mary, Williamsburg. 195 p.
- Methratta ET, Hawkins A, Hooker BR, Lipsky A, Hare JA. 2020. Offshore wind development in the Northeast US Shelf Large Marine Ecosystem: ecological, human, and fishery management dimensions. *Oceanography.* 33(4): 16–27. <https://doi.org/10.5670/oceanog.2020.402> .

- Mills KE, Kemberling A, Kerr LA, Lucey SM, McBride RS, Nye JA, Pershing AJ, Barajas M, Lovas CS. 2024. Multispecies population-scale emergence of climate change signals in an ocean warming hotspot. *ICES J Mar Sci.* 81(2): 375–389.
- Morgan SG. 2020. Life and death in the plankton: larval mortality and adaptation. In: McEdward L, editor. *Ecology of marine invertebrate larvae*. Boca Raton (FL): CRC Press. 279-321.
- Mudiyanselage Basnayake V. 2021. Application of local and global sensitivity analysis methods to a North Sea hydrodynamic model – study case of offshore Blue Mussels and seaweed farms (thesis). Barcelona (ES): Escola de Camins. 132 p.
- Munroe DM, Haidvogel D, Caracappa JC, Klick JM, Powell EN, Hofmann EE, Shank BV, Hart DR. 2018. Modeling larval dispersal and connectivity for Atlantic sea scallop (*Placochelys magellanicus*) in the Middle Atlantic Bight. *Fish Res.* 208: 7–15.
- [NAS] National Academies of Sciences, Engineering, Medicine. 2023. Potential hydrodynamic impacts of offshore wind energy on Nantucket Shoals regional ecology: an evaluation from wind to whales. Washington (DC): The National Academies Press. 106 p. <https://doi.org/10.17226/27154>.
- Niayifar A, Porté-Agel F. 2016. Analytical modeling of wind farms: a new approach for power prediction. *Energies* 9(9): 741.
- NOAA Fisheries. 2023. Commercial Landings database. Accessed January 2, 2023. <https://www.fisheries.noaa.gov/foss/>
- Palumbi SR. 2003. Population genetics, demographic connectivity, and the design of marine reserves. *Ecol Appl.* 13(sp1), 146-158.
- Pan Y, Archer CL. 2018. A hybrid wind-farm parameterization for mesoscale ad climate models. *Boundary Layer Meteorol.* 168:469-495.
- Pawlowicz R, Beardsley B, Lentz S. 2002. Classical tidal harmonic analysis including error estimates in MATLAB using T_TIDE. *Comput Geosci.* 28: 929-937.
- Pearce CM, Manuel JL, Gallager SM, Manning DA, O'Dor RK, Bourget E. 2004. Depth and timing of settlement of veligers from different populations of giant scallop, *Placochelys magellanicus* (Gmelin), in thermally stratified mesocosms. *J Exp Mar Biol Ecol.* 12: 187–214.
- Pedersen JG, Svensson E, Pulsen L, Nygaard NG. 2022. Turbulence optimized park model with Gaussian wake profile. *J Phys Conf Ser.* 2265(2): 022063).
- Pedersen M, Forsting A, van der Laan P, Riva R, Romàn L, Risco J, Friis-Møller M, Quick J, Christiansen J, Rodrigues Olsen B, Réthoré P. 2023. PyWake 2.5.0: An open-source wind farm simulation tool. [Kongens Lyngby](https://www.kongenslyngby.dk) (DK): DTU Wind, Technical University of Denmark.
- Peña A, Schaldemose Hansen K, Ott S, van der Lan MP. 2018. On wake modeling, wind-farm gradients, and AEP predictions at the Anholt wind farm. *Wind Energy Sci.* 3(1):191-202.
- Peliz A, Dubert J, Marchesiello P, Teles-Machado A. 2007. Surface circulation in the Gulf of Cadiz: Model and mean flow structure. *J Geophys Res: Oceans.* 112(C11). <https://doi.org/10.1029/2007jc004159>

- Pineda J, Hare J, Sponaugle S. 2007. Larval transport and dispersal in the coastal ocean and consequences for population connectivity. *Oceanogr.* 20(3): 22-39. <https://doi.org/10.5670/oceanog.2007.27>
- Platis A, Siedersleben SK, Bange J, Lampert A, Bärfuss K, Hankers R, Cañadillas B, Foreman R, Schulz-Stellenfleth J, Djath B, et al. 2018. First in situ evidence of wakes in the far field behind offshore wind farms. *Scientific Reports.* 8(1): 2163.
- Platis A, Bange J, Bärfus K. Cañadillas B, Hundhausen M, Djath B, Lampert A, Schulz-Stellenfleth J, Siedersleben S, Neumann T, Emeis S. 2020. Long-range modifications of the wind field by offshore wind parks—results of the project WIPAFF. *Meteorologische Zeitschrift.* 29: 355–376.
- Platis A, Hundhausen M, Mauz M, Siedersleben S, Lampert A, Brfuss K, Djath B, Schulz-Stellenfleth J, Canadillas B, Neumann T, Emeis S. 2021. Evaluation of a simple analytical model for offshore wind farm wake recovery by in situ data and weather research and forecasting simulations. *Wind Energy.* 24(3): 212-228.
- Roarty H, Glenn S, Brodie J, Nazzaro L, Smith M, Handel E, Kohut J, Updyke T, Atkinson L, Boicourt W, Brown W. 2020. Annual and seasonal surface circulation over the Mid-Atlantic Bight Continental Shelf derived from a decade of high frequency radar observations. *J Geophys Res: Oceans.* 125(11), e2020JC016368. <https://agupubs.onlinelibrary.wiley.com/doi/pdf/10.1029/2020JC016368>
- Rumrill SS. 1990. Natural mortality of marine invertebrate larvae. *Ophelia.* 32: 163–198. <https://doi.org/10.1080/00785236.1990.10422030>
- Schmitzer AC, DuPaul WD, Kirkley JE. 1991. Gametogenic cycle of sea scallops (*Placopecten magellanicus* (Gmelin, 1791)) in the mid-Atlantic Bight. *J Shellfish Res.* 10: 221–228.
- Schultze L, Merckelbach L, Horstmann J, Raasch S, Carpenter J. 2020. Increased mixing and turbulence in the wake of offshore wind farm foundations. *J Geophys Res: Oceans.* 125(8): e2019JC015858.
- Soulsby RL, Clarke S. 2005. Bed shear-stress under combined waves and currents on smooth and rough beds. Oxfordshire (GB): HR Wallingford. Technical report 137. <https://eprints.hrwallingford.com/558/1/TR137.pdf>
- Sun Y, Chen C, Beardsley RC, Ullman D, Butman B, Lin H. 2016. Surface circulation in Block Island Sound and adjacent coastal and shelf regions: A FVCOM-CODAR comparison. *Prog Oceanogr.* 143: 26–45.
- Thouzeau G, Robert G, Smith SJ. 1991. Spatial variability in distribution and growth of juvenile and adult sea scallops *Placopecten magellanicus* (Gmelin) on eastern Georges Bank (northwest Atlantic). *Mar Ecol Prog Ser.* 74: 205–28.
- Tremblay MJ, Sinclair M. 1990. Sea scallop larvae *Placopecten magellanicus* on Georges Bank: vertical distribution in relation to water column stratification and food. *Mar Ecol Prog Ser.* 61(1/2): 1-15. <http://www.jstor.org/stable/24842243>
- Tremblay MJ, Loder JW, Werner FE, Naimi CE, Page FH, Sinclair MM. 1994. Drift of sea scallop larvae *Placopecten magellanicus* on Georges Bank: a model study of the roles of mean advection, larval behavior and larval origin. *Deep Sea Res Part II: Oceanogr.* 41: 7–49. [https://doi.org/10.1016/09670645\(94\)90061-2](https://doi.org/10.1016/09670645(94)90061-2)

- Troen I, Petersen EL. 1989. European wind atlas. Roskilde, (DK): Risø National Laboratory.
- USDOJ. 1982. Final environmental impact statement: proposed 1983 Outer Continental Shelf Oil and Gas Lease Sale No. 76. (NY): US Department of the Interior, Minerals Management Service. [accessed 4 March 2025]; <https://rucore.libraries.rutgers.edu/rutgers-lib/32148/PF/1/play/>
- Van der Laan MP, Pena A, Volker P, Hansen KS, Sørensen NN, Ott S, Hasager CB. 2017. Challenges in simulating coastal effects on an offshore wind farm. *J Phys Conf Ser.* 854 (1):012046
- Van der Wethuysen AJ, Zijlema M, Battjes JA. 2007. Nonlinear saturation-based whitecapping dissipation in SWAN for deep and shallow water. *Coastal Eng.* 54(2): 151-170.
- Van Rijn LC. 2018. Design and bed protections; stability and movement of cobbles, boulders and rocks. viewed 28 February 2024, <https://www.leovanrijn-sediment.com/papers/Bedprotections2017.pdf>
- Volker PJ, Badger J, Hahmann AN, Ott S. 2015. The Explicit Wake Parameterization V1. 0: a wind farm parameterization in the mesoscale model WRF. *Geosci Model Develop.* 8(11): 3715-3731.
- Walker RL, Hurley DH, Jansen ML. 1996. Fecundity estimates of the southern surfclam *Spisula solidissima similis*. *J Shellfish Res.* 15: 531.
- Wang L. 2023. Simulating ocean acidification in the Northeast U.S. region using a fully coupled three-dimensional and ecosystem model (dissertation). Boston (MA): University of Massachusetts. 277 p.
- Wilkin J, Levin J, Moore A, Arango H, López A, Hunter E. 2022. A data-assimilative model reanalysis of the U.S. Mid Atlantic Bight and Gulf of Maine: configuration and comparison to observations and global ocean models. *Prog Oceanogr.* 209: 102919.
- Willmott CJ. 1981. On the validation of models. *Phys Geogr.* 2 (2):184–194.
- Zhang X, Munroe D, Haidvogel D, Powell EN. 2016. Atlantic surfclam connectivity within the Middle Atlantic Bight: mechanisms underlying variation in larval transport and settlement. *Estuarine Coastal Shelf Sci.* 173: 65–78.
- Zhang X, Munroe D, Haidvogel D, Powell EN, Klinck J, Mann R, Castruccio FS. 2015. Modeling larval connectivity of the Atlantic surfclams within the Middle Atlantic Bight: Model development, larval dispersal and metapopulation connectivity. *Estuarine Coastal Shelf Sci.* 153: 38–53. <https://doi.org/10.1016/j.ecss.2014.11.033>
- Zijlma M. 2010. Computation of wind-wave spectra in coastal waters with SWAN on unstructured grids. *Coastal Eng* 57(3):267-277.

15 Appendices

Please see Supplementary File (Volume 2) containing Appendices A, B, C, and D.



U.S. Department of the Interior (DOI)

DOI protects and manages the Nation's natural resources and cultural heritage; provides scientific and other information about those resources; and honors the Nation's trust responsibilities or special commitments to American Indians, Alaska Natives, and affiliated island communities.



Bureau of Ocean Energy Management (BOEM)

BOEM's mission is to manage development of U.S. Outer Continental Shelf energy and mineral resources in an environmentally and economically responsible way.

BOEM Environmental Studies Program

The mission of the Environmental Studies Program is to provide the information needed to predict, assess, and manage impacts from offshore energy and marine mineral exploration, development, and production activities on human, marine, and coastal environments. The proposal, selection, research, review, collaboration, production, and dissemination of each of BOEM's Environmental Studies follows the DOI Code of Scientific and Scholarly Conduct, in support of a culture of scientific and professional integrity, as set out in the DOI Departmental Manual (305 DM 3).